Thèse n° 10 556

Development of strategies to improve 1H resolution in NMR of solids at 100 kHz magic-angle spinning

Présentée le 15 décembre 2023

Faculté des sciences de base
Laboratoire de résonance magnétique
Programme doctoral en chimie et génie chimique

pour l'obtention du grade de Docteur ès Sciences

par

Bruno SIMÕES DE ALMEIDA

Acceptée sur proposition du jury

Prof. S. Gerber, présidente du jury
Prof. D. L. Emsley, directeur de thèse
Dr Y. Nishiyama, rapporteur
Dr E. Salager, rapporteuse
Prof. M. Ernst, rapporteur

École
polytechnique
fédérale
de Lausanne

2023

Acknowledgments

The acknowledgments are the hardest section of the thesis to write. You want to find the right words to express gratitude towards the people who contributed and helped on such an important endeavor.
First, I want to thank my supervisor, Professor Lyndon Emsley. Thank you for offering me the opportunity to do science at a high level at EPFL and welcoming me to a brilliant group full of brilliant people. You were a great supervisor who was always available for the people in the group. I grew so much in these four years and I am taking all my learnings for my future career. Thank you for all the discussions and pieces of advice. I will always cherish my time at LRM.
I want to thank Nadia for everything. You made the Ph.D. marathon a lot easier by always helping with the administrative part of this work. More importantly, stopping at your office for a quick chat was always a nice part of the day.
I want to thank Professor Sandrine Gerber for accepting to be the jury president of my thesis. I want to thank Doctor Yusuke Nishiyama, Doctor Elodie Salager, and Professor Matthias Ernst for accepting to be the jury examiners. Thank you for reading my thesis and for coming to EPFL for my defense. It was a privilege to have such an interesting discussion with you about my work.
I want to thank Doctor Anne-Sophie Chauvin for all the support during these four years. It was a pleasure to have done a lot of my teaching hours in your courses.

Thanks to the amazing NMR platform team (Aurélien, Laura and Anto) for their constant support and help. You made my Ph.D. studies easier and I really enjoyed all our discussions.
I could write another thesis to thank all my LRM colleagues, to whom I wish all the best. First, a special word to the “Protons team”, as Lyndon used to call us. Thank you, Pinelopi, for being the best supervisor I could have asked for. All the patience and help can never be repaid and if I know a bit about NMR, it is mainly thanks to you. Thank you for your constant support. Thank you, Daria, for being the best company at the spectrometer and for all the time we spent at the lab. It was amazing to have you during your Masters and to witness how brilliant you are during your Ph.D. Thank you, Manuel, for the computer magic and the amazing cooking. I am very happy to have shared this journey at the same time as you. Thank you for your help and support.
I also want to thank Federico for all the support and help at the beginning of my Ph.D. and all our discussions and encounters in conferences ever since.

I want to thank my fellow Ph.D. students at LRM for your support. Thank you, Aditya, for being a great office colleague and for all the support and discussions we had during our time together. Thank you, Yu, for your support and all the discussions about football. After writing your thesis, I hope you could write a travel guide for non-mainstream European destinations. Thank you, Anna, for hearing my broken Spanish for four years, that was very kind of you, making me believe that I actually speak it. Thank you, Ray, I hope I did not leave a big mess in the office. Thank you, Ummugulsum, for all the support and the Turkish sweets.
I also want to thank Baptiste, Snaedis, Martins, and Albert for our time together at LRM, particularly some of the drinks at SAT and the biggest nightclub in Renens, Baptiste’s house.
I want to thank all the postdocs at LRM for your constant help and support, particularly those who took some time to read my thesis. Thank you, Michael, for all the support and help during these four years we spent together. I hope you left some Switzerland to visit for you to come back. Thank you for actually watching my film recommendations. I wish you and Georgia all the best in Warwick. Thank you, Saumya, for all the support and discussions. It was always fun to discuss with you during lunch and thank you for the amazing trip to Euromar in Glasgow with Rahul. I wish you both all the best.
I am not sure if I want to thank the guy who replied “Bruno” when he was asked what was the most bizarre creature he saw in Australia. But I really laughed at that joke, and some other ones made by that same person. So, thank you, Federico, for the amazing time in Brisbane and all the time at LRM. I wish you and Federica the best. Thank you, Jacob, for all the support It was really fun to go for lunch with you, thank you for laughing at some of my jokes and the discussions about the most random and mundane topics. Thank you, Ran, for all the support and your constant good mood. Thank you for the new favorite Chinese restaurant in Renens. And if you are still passionate about heavy machinery and agricultural manual labor, the job offer still stands.
Thank you, Amrit, for your constant support and help. It was a real pleasure to have shared some of my LRM time with you. I hope you are enjoying your time in Florida and I wish you and Malvika all the best. Thank you, Gabriele, for the big support and kindness at the beginning of my Ph.D. You were a great help on those average Hamiltonians and it was always great to discuss with you. To my first office mates, Pierrick and Andrea, also a big

thank you for your support and help. The lunches with you and Pinelopi were also a highlight of my time at LRM and it was always fun to spend time with you all. Me and Pierrick were at SCS 2022 when we learned about the passing of the Queen, and since it was almost a full member of our lab, and out of respect for Pierrick, I am also writing a few words here.
I also want to thank Annika, Yufei, Yuxuan, and Ruben for the time we spent together at LRM and I wish you all the best.
I want to thank everyone I met during my Ph.D., remotely connected to EPFL or NMR and academic research in general, particularly all the people I met during the NMR summer school and the conferences I attended. They were great experiences that I remember fondly.

There is another thesis to be written to properly acknowledge the following people. They don't understand English but I am sure they will know how to translate it. They are my foundation and nothing I accomplished could have been done without them. Although they are not remotely close to NMR, this Ph.D. is also theirs. They have been my bedrock since the beginning. With their love and support. I always knew I was a step closer to my goal. I cannot thank them enough for all the sacrifices they have made. Thank you for everything, you are the best I could ask for. Thank you, Mãe e Pai. The family is only complete if I add the two funniest people I know, my brother Edgar and my sister Beatriz. One of my life joys is to be your brother and thank you for your constant support, I love you. From now on, you have to call me Dr. Handsome.
I want to thank my grandmothers, Adelaide e Albina, who were always loving and kind to me since I was a kid. A special thanks to my whole family in Portugal and Switzerland, who I love very dearly.
Thank you, Sérgio and Sylvie, and particularly the cutest goddaughter, Adeline. I want to thank Vítor, Isabel, Luís, and Aida for their constant support and all the laughs. I want to thank my cousins Dany, Lino, Cindia, and Stacy for all the time spent together and the support. I want to thank all my aunts, uncles, and cousins for all the support and love all over the years.

One of my points of pride in life is the friends I made along the way. I want to thank them for their love and support.
A special thanks to António and João, who promised to learn English and read my thesis. I love you for all the laughs with a single look and the shared memories. Thank you, Johnathan and Mércia. The wedding and the trip to Rio were among the best experiences I had during my Ph.D. years. Thank you, André, for the friendship since we arrived in Switzerland back in 2007. Thank you, Elodie, for the friendship and the hangouts during the Unige years. Talking about Unige, of course, I want to thank all my pals from the chemistry and biochemistry bachelor. Particularly, Romain, Antoine, and Nik, your friendship is something I value very much. For all the chemistry, inside and outside of the lab, thank you. Romain, you were the best roommate ever.

Finally, I want to acknowledge the uncertain and hard times we lived through the pandemic. In the midst of the first lockdown, I found the love of my life. These last sentences are for you, Jenny. To meet you has been the best thing that happened to me. The three years and a half have been the happiest of times and your love and support were essential to complete my Ph.D. All the moments and laughs we shared are unforgettable. I also thank your parents for their support. I am excited to continue to share my life with you. I love you.

Abstract

In the last decade, ^{1}H solid-state NMR has become more preponderant in structure elucidation of solids. The availability of faster magic-angle spinning (MAS) rates (100-200 kHz) has improved ^{1}H detected experiments, which has greatly contributed to the assignment of different materials.

However, for many compounds, the ^{1}H spectral resolution is relatively poor, even at the fastest spinning rates. The observed linewidths are a few hundred Hz broad, impeding any reliable assignment. Despite detecting the ideal NMR nucleus due to its natural abundance and high gyromagnetic ratio, ^{1}H NMR has not reached a widespread application in solids due to its resolution limitations.

This thesis focuses on understanding the different sources that contribute to the ^{1}H linewidth under fast MAS, and developing new strategies that improve the spectral resolution.

The homonuclear dipolar coupling is the internal spin interaction contributing the most to ^{1}H lineshapes. Here, we develop an analytical expression up to third order of the average Hamiltonian for two and three spins systems. We find that the higher order terms result in both residual shift and splitting. The full Hamiltonian without any secular approximation or truncation agrees the best with full numerical simulations. The MAS dependence of the residual shift and splitting is found to be polynomial.

Following the theoretical studies, we adapt the anti-z COSY pulse sequence to the context of solids under fast MAS in order to remove the residual secular coupling terms. Comparing to conventional echo experiments, the anti-z COSY spectrum provides up to 50 % line narrowing. An accelerated version of this sequence based on a two-dimensional one pulse (TOP) transformation is also designed

Another type of strategy for resolution improvement is then presented, based on error mapping. The residual homogeneous broadening due to imperfect averaging is parametrically mapped in such a way that it can be removed in a multidimensional correlation, leaving only the pure isotropic proton (PIP) signal. This method is applied to experiments at variable spinning rates on six different solids. The average resolution improvement factor is 7.

The PIP strategy is then also implemented with a deep learning approach (PIPNET), which overcomes some of the limitations of the previous model, while achieving the same level of resolution. In addition, PIPNET was extended to ^{1}H-^{1}H two dimensional experiments, also acquired at different MAS frequencies. The resolution improvement in 2D spectra allows identification and assignment on previously overlapped correlation peaks.

All these new methods focus on removing the residual homogeneous broadening, that is MAS dependent. The last part of this thesis focusses on detailing and assessing the inhomogeneous factors liming the linewidth. We find that the overall width and the nature of the different contributions can vary very considerably. Faster spinning always yields narrower lines but at 100 kHz MAS, the dipolar contribution is no longer dominant for some resonances. When the inhomogeneous contributions, such as anisotropic bulk magnetic susceptibility (ABMS) and chemical shift disorder are dominant, two dimensional ^{1}H-^{1}H correlation experiments yield better resolution for assignment. Particularly the extraction of the antidiagonal of a 2D peak will remove any correlated inhomogeneous broadening, giving substantially narrower ^{1}H linewidths.

Keywords

solid-state NMR, ^{1}H NMR, fast MAS, resolution, homonuclear dipolar coupling, anti-z COSY, TAZ COSY, PIP, PIPNET, ABMS

Résumé

Au cours de la dernière décennie, la RMN ^{1}H à l'état solide est devenue plus prépondérante dans l'élucidation de la structure des solides. La disponibilité de hautes vitesses de rotation à angle magique (MAS) (100-200 kHz) a amélioré les expériences de détection de ^{1}H, ce qui a grandement contribué à l'attribution de différents matériaux.

Cependant, pour un grand nombre de composés, la résolution spectrale du proton est relativement faible, même aux vitesses de rotation les plus rapides. Les largeurs de raies observées sont de quelques centaines de Hz, ce qui empêche toute attribution fiable. Malgré que le proton soit le noyau RMN idéal en raison de son abondance naturelle et de son rapport gyromagnétique élevé, la RMN du ^{1}H n'a pas atteint une application généralisée dans les solides en raison de ses limites de résolution.

Cette thèse se concentre sur la compréhension des différentes sources qui contribuent à la largeur de raie ^{1}H dans le contexte de MAS rapide, et sur le développement de nouvelles stratégies qui améliorent la résolution spectrale.

Le couplage dipolaire homonucléaire est l'interaction de spin qui contribue le plus à la forme des lignes du proton. Nous développons ici l'expression analytique jusqu'au troisième ordre de l'hamiltonien moyen des systèmes à deux et trois spins. Nous constatons que les termes d'ordre supérieur entraînent à la fois un shift et un élargissement résiduels. L'hamiltonien complet sans approximation correspond le mieux aux simulations numériques. La dépendance du MAS sur le déplacement and élargissement résidues est polynomiale.

À la suite des analyses théoriques, nous adaptons la séquence anti-z COSY au contexte des solides soumis à une MAS rapide afin d'éliminer les termes résiduels de couplage. Par rapport aux expériences d'écho conventionnelles, le spectre anti-z COSY permet un rétrécissement de la raie de 50 % pour certains pics. Une version accélérée de cette séquence basée sur une transformation “two dimension one pulse” (TOP) a également été conçue.

Un autre type de stratégie d'amélioration de la résolution est également présenté, basé sur la cartographie des erreurs. L'élargissement homogène résiduel est cartographié de manière paramétrique de telle sorte qu'il peut être supprimé dans une corrélation multidimensionnelle, ne laissant que le signal protonique isotrope pur (PIP). Cette méthode a été appliquée à des expériences d'écho conventionnel à des vitesses de rotation croissantes sur six solides différents. Le facteur moyen d'amélioration de la résolution est de 7.

La stratégie PIP est également mise en œuvre avec une approche d'apprentissage profond (PIPNET), qui permet de surmonter certaines des limites du modèle précédent, tout en atteignant le même niveau de résolution. En outre, PIPNET a été étendu aux expériences bidimensionnelles ^{1}H-^{1}H, également acquises à différentes fréquences MAS. L'amélioration de la résolution des spectres 2D permet d'identifier et d'attribuer des pics de corrélation qui se chevauchaient auparavant.

Toutes ces nouvelles méthodes se concentrent sur l'élimination de l'élargissement homogène résiduel, qui dépend du MAS. La dernière partie de cette thèse détaille et évalue les facteurs inhomogènes limitant la largeur de raie. Nous constatons que la largeur globale et la nature des différentes contributions peuvent varier considérablement. Une rotation plus rapide produit toujours des raies plus étroites, mais à 100 kHz MAS, la contribution dipolaire n'est plus dominante pour certaines résonances. Lorsque les contributions inhomogènes, telles que la susceptibilité magnétique globale anisotrope (ABMS) et le désordre du déplacement chimique, sont dominantes, les expériences de corrélation ^{1}H-^{1}H bidimensionnelles offrent une meilleure résolution pour l'attribution. En particulier, l'extraction de l'antidiagonale d'un pic 2D élimine tout élargissement inhomogène corrélé, ce qui permet d'obtenir des largeurs de raies ^{1}H nettement plus étroites.

Table of contents

Acknowledgments **2**

Abstract **4**

Keywords **5**

Résumé **6**

Table of contents **7**

Publications **10**

Chapter 1 Introduction **11**

1.1 Structure resolution *11*

1.2 Solid state NMR *11*

1.3 Dipolar coupling *12*

1.4 Magic-Angle Spinning *14*

1.5 ^{1}H NMR of solids in the fast-spinning regime *15*

1.6 The Quest for Resolution *18*

1.7 Outline of the thesis *20*

Chapter 2 Understanding the residual broadening in ^{1}H NMR spectra under MAS **21**

2.1 Introduction *21*

2.2 Theory and Simulations of homonuclear three-spin systems in rotating solids *22*

2.2.1 Introduction 22
2.2.2 Methods 22
2.2.3 Theory 23
2.2.4 Effect of MAS on Powder Line Shapes 37
2.2.5 Connection to Experiment 38
2.2.6 Conclusion 40
2.2.7 Appendix I 41

2.3 Conclusion and Perspectives *58*

Chapter 3 Improved ^{1}H resolution combining MAS and multiple pulse sequences **59**

3.1 Introduction *59*

3.2 Homonuclear Decoupling in ^{1}H NMR of Solids by Remote Correlation *60*

3.2.1 Introduction 60
3.2.2 Methods 60
3.2.3 Results & Discussion 60
3.2.4 Conclusion 63
3.2.5 Appendix II 64

3.3 Fast Remote Correlation Experiments for ^{1}H Homonuclear Decoupling in Solids *77*

3.3.1 Introduction 77
3.3.2 Methods 77
3.3.3 Results and Discussion 79

3.3.4 Conclusion 80
3.3.5 Appendix III 81

3.4 Conclusion and Perspectives 84

Chapter 4 Improved ^{1}H resolution exploiting error mapping 80

4.1 Introduction 80

4.2 Pure Isotropic Proton Solid State NMR (PIP) 81
4.2.1 Introduction 81
4.2.2 Methods 81
4.2.3 Results and Discussion 85
4.2.4 Conclusions 88
4.2.5 Appendix IV 90

4.3 Pure Isotropic Proton NMR Spectra in Solids using Deep Learning 115
4.3.1 Introduction 115
4.3.2 Results and Discussion 115
4.3.3 Conclusion 121
4.3.4 Appendix V 122

4.4 Two -dimensional Pure Isotropic Proton Solid State NMR 138
4.4.1 Introduction 138
4.4.2 Results and Discussion 138
4.4.3 Conclusion 144
4.4.4 Appendix VI 145

4.5 Conclusion and Perspectives 157

Chapter 5 Remaining Barriers 158

5.1 Introduction 158

5.2 Barriers to Resolution in ^{1}H of Rotating Solids 159
5.2.1 Introduction 159
5.2.2 Theory 159
5.2.3 Experimental 161
5.2.4 Results & Discussion 162
5.2.5 Conclusion 171
5.2.5 Appendix VII 173

5.3 Conclusion and Perspectives 202

Chapter 6 Conclusion 203

6.1 Results Achieved 203

6.2 Future Developments 203

Supplementary Information 205

Homonuclear Decoupling in ^{1}H NMR of Solids by Remote Correlation 205
Pulse sequences 205
Scripts 206

Fast Remote Correlation Experiments for ^{1}H Homonuclear Decoupling in Solids 215
Pulse sequences 215
Scripts 221

Barriers to Resolution in ^{1}H of Rotating Solids 228
Scripts 228

Bibliography 231

Curriculum Vitae 245

Publications

The present thesis is based on the following publications:

1. Moutzouri, P.; Paruzzo, F. M.; Simões de Almeida, B.; Stevanato, G.; Emsley, L., Homonuclear Decoupling in ^{1}H NMR of Solids by Remote Correlation. *Angew Chem Int Ed Engl* **2020,** *59* (15), 6235-6238.
2. Moutzouri, P.; Simões de Almeida, B.; Emsley, L., Fast remote correlation experiments for ^{1}H homonuclear decoupling in solids. *J Magn Reson* **2020,** *321*, 106856.
3. Simões de Almeida, B.; Moutzouri, P.; Stevanato, G.; Emsley, L., Theory and simulations of homonuclear three-spin systems in rotating solids. *J Chem Phys* **2021,** *155* (8), 084201.
4. Moutzouri, P.; Simões de Almeida, B.; Torodii, D.; Emsley, L., Pure Isotropic Proton Solid State NMR. *J Am Chem Soc* **2021,** *143* (26), 9834-9841.
5. Cordova, M.; Moutzouri, P.; Simões de Almeida, B.; Torodii, D.; Emsley, L., Pure Isotropic Proton NMR Spectra in Solids using Deep Learning. *Angew Chem Int Ed Engl* **2023,** *62* (8), e202216607.
6. Moutzouri, P.; Cordova, M.; Simões de Almeida, B.; Torodii, D.; Emsley, L., Two-dimensional Pure Isotropic Proton Solid State NMR. *Angew Chem Int Ed Engl* **2023,** *62* (21), e202301963.
7. Simões de Almeida, B.; Torodii, D.; Moutzouri, P.; Emsley, L., Barriers to Resolution in ^{1}H NMR of Rotating Solids, *J Magn Reson*, **2023**, 233, 107557

During my PhD, I have also participated in other projects related to solid-state NMR, one linked to structure determination of an amorphous compound and another on assignment of chemical shifts. I have also had the opportunity to write a small review on resolution improvement in ^{1}H NMR of solids, after having been awarded the Junior Prize of the SCS Fall Meeting 2022. These results are not part of the present thesis, but can be found in the following publications:

8. Cordova, M.; Balodis, M.; Hofstetter, A.; Paruzzo, F.; Nilsson Lill, S. O.; Eriksson, E. S. E.; Berruyer, P.; Simoes de Almeida, B.; Quayle, M. J.; Norberg, S. T.; Svensk Ankarberg, A.; Schantz, S.; Emsley, L., Structure determination of an amorphous drug through large-scale NMR predictions. *Nat Commun*, **2021,** *12* (1), 2964.
9. Cordova, M. Balodis, M.; Simões de Almeida, B.; Ceriotti, M.; Emsley, L., Bayesian probabilistic assignment of chemical shifts in organic solids. *Science Advances*, **2021,** *7*, eabk2341.
10. Simões de Almeida, B.; Emsley, L., Improvements in Resolution of 1H NMR of solids. *Chimia*, **2023,** *77* (4).

Chapter 1 Introduction

1.1 Structure resolution

At the heart of chemistry lie atoms and molecules. Deciphering their structure is a key step, if not the reason, of a chemist's scientific work. The arrangement of atoms and molecules in a given material determines its behaviour. To know the chemical structure is to understand (and to predict) properties.

Widely used atomic-level characterization techniques include X-Ray crystallography[1-5], cryogenic electronic microscopy[6-10] and nuclear magnetic resonance (NMR) spectroscopy[11-13]. Single Crystal X-Ray Diffraction (SCXRD) is the gold standard method for crystalline materials. However, a single crystal of the studied material (minimum size of a hundred microns) is required in SCXRD, which often is difficult to obtain.[4-5] Powder diffraction (with X-Rays or Neutrons) can be used for crystalline samples, but structure elucidation is challenging.[14-19] Diffraction can be also be extend to amorphous samples, but data interpretation is even more difficult.[20-23]

Also, X-ray diffraction cannot always accurately determine the position of nuclei which are poor in electrons, such as ^{1}H, because X-rays are scattered by electron density.

NMR is a complementary technique that overcomes many of the limitations of conventional diffraction methods. NMR is able to probe local atomic environments without the need for long range order in the samples, and can use any NMR active nuclei (see in section 1.2) as a probe. Therefore, it is applicable on a variety of systems, ranging from liquids[24-25] and semi solids[26-29] to solids, both crystalline and amorphous samples. NMR methods have been successfully applied a plethora of materials, ranging from inorganic battery materials[30-31], cements[32-33] and perovskites[34-35] to organic solids[36-58], proteins[59-61] and pharmaceuticals.[36-40, 62-68]

Unrestricted by particle size, phase or mobility of the sample, solid state NMR has a pivotal role in modern structural elucidation challenges, providing atomic resolution that other techniques cannot offer.

In the following section, some fundamental aspects of solid state NMR will be briefly introduced in order to better understand the challenges that have been addressed during this thesis. More detailed explanations of these concepts can be found in several textbooks.[69-74]

1.2 Solid state NMR

NMR detects the response from nuclei with a non-zero spin ($I > 0$), when placed in a magnetic field (B_0). The external magnetic field lifts the degeneracy of the nuclear spin states. The difference in energy (ΔE) will depend on the strength of the magnetic field and the gyromagnetic ratio (γ) of the observed nucleus. Transitions between the states are induced with radiofrequency radiation. According to the Planck relation, any energy/energy transition is associated with a specific frequency.

In NMR, these transition frequencies are called the Larmor frequencies. They are nuclei specific because each nuclear isotope has a distinct gyromagnetic ratio, γ. The two most routinely used nuclei in the context of organic, biological and pharmaceutical compounds are ^{1}H ($\gamma/2\pi$= 42.577 MHz·T^{-1}) and ^{13}C ($\gamma/2\pi$= 10.708 MHz·T^{-1}).

Commercially available high resolution NMR systems use magnetic fields ranging from 7 to 28 T, which correspond to ^{1}H Larmor frequencies from 300 to 1200 MHz. For reference, the 21.14 T spectrometer mainly used in this thesis work corresponds to ^{1}H and ^{13}C Larmor frequencies of 900 MHz and 226 MHz, respectively.

Besides distinguishing different nuclei, NMR is sensitive to the smallest perturbations of the magnetic environment surrounding the nucleus, which are caused by the molecular structure (both neighbouring nuclei and electrons). The NMR frequency is not just affected by the large applied magnetic field, i.e., the Zeeman interaction, but additionally by weaker nuclear spin interactions, which are defined by the chemical structure.

The NMR Hamiltonian describing the energy of spins I = 1/2 (^{1}H, ^{13}C) in an external magnetic field is defined as:

$$\hat{H}_{NMR} = \hat{H}_{Zeeman} + \hat{H}_{\sigma} + \hat{H}_{DD} + \hat{H}_{J} \qquad (1.1)$$

$\widehat{H}_{\sigma}$ describes the chemical shielding interaction, which is between the nucleus and the induced field from the surrounding electrons. The absolute shielding is not directly measured, but is measured relative to a reference compound, which gives the chemical shift δ. The electron distribution tends to shield the nucleus from the magnetic field (at least for light elements), causing a shift in NMR frequency for every nucleus of the same isotope in a molecule. For example, a proton in an aromatic group will resonate at a different frequency from one in a methyl group.

In addition to the chemical shift, which is a single nuclear spin interaction, there are also the couplings between spins to take into account. The two spins involved in the coupling interaction can be homo- or hetero-nuclear. It is worth noting that homonuclear dipolar couplings between nuclei from isotopes that have a very low percentage of natural abundance (such as ^{13}C) can typically be neglected due to the low probability of having two neighbouring nuclei in a natural abundance compound.

$\widehat{H}_{J}$ represents the scalar coupling, also named J-couplings, which is a spin-spin interaction mediated through bonding electrons.

$\widehat{H}_{DD}$ describes the through space dipolar coupling. The first spin interacts with the magnetic field generated by the second spin. The coupling can be intra or and inter-molecular, but the strength of the coupling decreases rapidly with distance.

All three interactions are anisotropic, meaning they are dependent on the sample orientation with respect to the magnetic field. Therefore, they are not defined by a single value (scalar), but a second rank tensor.

The bifurcation between experimental NMR of liquids and solids arises from this distinction. In an isotropic liquid, the rotational diffusion of the molecule averages out any anisotropic interaction and only the isotropic value of the interaction is observed in the spectrum.

Typically, a 1D NMR spectrum of a liquid is defined by the different isotropic chemical shifts of a given element and a series of isotropic J couplings, which translates to peaks with multiplet structures. The isotropic value of the dipolar coupling is zero, which is explored in detail in section 1.3.

The variety and relatively easy implementation of ^{1}H and ^{13}C 1D and 2D correlation experiments[75-83] have made solution-state NMR a widely applied method, through the wealth of knowledge offered from chemical shifts and J couplings. The chemical shift ranges are 10-20 ppm for ^{1}H and 200 ppm for ^{13}C., with peak resolution generally being 0-1 Hz in a properly homogenised (shimmed) magnet. Typical J couplings are between 0-1 kHz. The success of solution-state NMR hinges on the random tumbling of molecules in liquids which allows high resolution spectra.

In solids, there is no molecular rotation. The full effects of anisotropy are visible in the 1D spectrum of a static solid[70, 84]. However, the anisotropic contribution is a probe of the chemical structure and orientation, providing information not readily accessible with solution NMR. With ^{13}C NMR, homonuclear couplings are much weaker and heteronuclear coupling to ^{1}H can be removed with decoupling schemes.[85-88] Therefore, only chemical shift anisotropy (CSA) information is present in the spectrum. The observed signal will depend on the orientation of the principal axis of the chemical shift tensor with respect to B_0. If the splitting caused by the homonuclear dipolar coupling is negligible in natural abundance sample and the size of the homonuclear couplings is small, the ^{13}C spectrum of a static single crystal of five different nuclei will present five distinct signals, and the frequency of each peak will depend on the crystallite orientation.[70, 84] In a powdered sample, with crystallites randomly oriented, the spectrum will be a sum of spectra arising from each present crystallite in the sample.[70] This will correspond to five continuous powder patterns, one for each distinct spin. If the molecular structure is relatively simple, with a handful of different spins, the CSA principal values can be derived from each powder pattern and they will be a sensitive reporter of the electronic structure.[89-98]

However, with an increasing number of different spins, powder patterns will overlap with each other and resolution will be lost.

In the case of ^{1}H spins, homonuclear dipolar coupling also needs to be considered. The description of this interaction and its effect on the spectrum is detailed in the next section.

1.3 Dipolar coupling

Considering a pair of spins ½, I and S, at a distance r, $\widehat{H}_{DD}$ is defined as[72]:

$$\widehat{H}_{DD} = -\frac{\mu_0}{4\pi}\gamma_I\gamma_S\hbar\left(\frac{\hat{I}\cdot\hat{S}}{\boldsymbol{r}^3}\right) - 3\frac{(\hat{I}\cdot\boldsymbol{r})(\hat{S}\cdot\boldsymbol{r})}{\boldsymbol{r}^5} \tag{1.2}$$

where μ_0 is the vacuum permeability constant and $\hbar$ is the reduced Planck constant. Using spherical polar coordinates

$$\boldsymbol{r} = (r\,sin\,\theta\,cos\,\phi\,, r\,sin\,\theta\,sin\,\phi\,, r\,cos\,\theta) \tag{1.3}$$

the dipolar coupling Hamiltonian becomes

$$\widehat{H}_{DD} = -\frac{\mu_0}{4\pi}\frac{\gamma_I\gamma_S\hbar}{r^3}[A + B + C + D + E + F] \tag{1.4}$$

where

$$\begin{aligned} A &= \hat{I}_z\hat{S}_z(3\cos^2\theta - 1) \\ B &= -\frac{1}{4}[\hat{I}_+\hat{S}_- + \hat{I}_-\hat{S}_+](3\cos^2\theta - 1) \\ C &= -\frac{3}{2}[\hat{I}_z\hat{S}_+ + \hat{I}_+\hat{S}_z](\sin\theta\cos\theta\, e^{-i\phi}) \\ D &= -\frac{3}{2}[\hat{I}_z\hat{S}_- + \hat{I}_-\hat{S}_z](\sin\theta\cos\theta\, e^{+i\phi}) \\ E &= -\frac{3}{4}[\hat{I}_+\hat{S}_+](\sin^2\theta\, e^{-2i\phi}) \\ F &= -\frac{3}{4}[\hat{I}_-\hat{S}_-](\sin^2\theta\, e^{+2i\phi}) \end{aligned} \tag{1.5}$$

This is known as the dipolar alphabet. θ represents the angle between the internuclear vector and B_0.

In the presence of a large static magnetic field, the Zeeman interaction is much larger than the local fields originating from dipolar couplings. Therefore, a secular approximation reduces the Hamiltonian to terms that only commute with the Zeeman interaction.[72] For a homonuclear dipolar coupling, this corresponds to A and B terms, whereas for a heteronuclear spin pair only the A term is considered.

$$\widehat{H}_{DD} = DD_{IS}[A + B] = -\frac{\mu_0}{4\pi}\frac{\gamma_I\gamma_S\hbar}{r^3}[A + B] \tag{1.6}$$

The strength of the dipolar coupling DD_{IS} (typically given in units of rad/s) has a cubic dependence on the internuclear distance. For a ^{1}H spin pair, the dipolar coupling constant $DD_{IS}/(2\pi)$ is 35.5kHz at 1.5 Å, 15.0 kHz at 2 Å and 0.96 kHz at 5 Å. The size of the dipolar coupling is normally orders of magnitude larger than the J coupling and, for each spin pair, induces large splittings in the spectrum.

In isotropic liquids, the rapid random tumbling time averages the coupling to zero. This is seen by integrating the orientational dependence over the surface of a sphere [72]:

$$\int_0^\pi d\theta\,\sin\theta\,(3\cos^2\theta - 1) = 0 \tag{1.7}$$

However, in static solids, the dipolar coupling is not averaged out. Every proton pair with a non-negligible $DD_{IS}/(2\pi)$ will produce splittings. [99] In a powdered sample containing a dense network of protons, the cumulative effect of all proton pairs in all crystallites is a large broadening in the whole spectrum. For instance, Figure 1.1 shows the ^{1}H 1D NMR spectrum of a static sample of ritonavir:

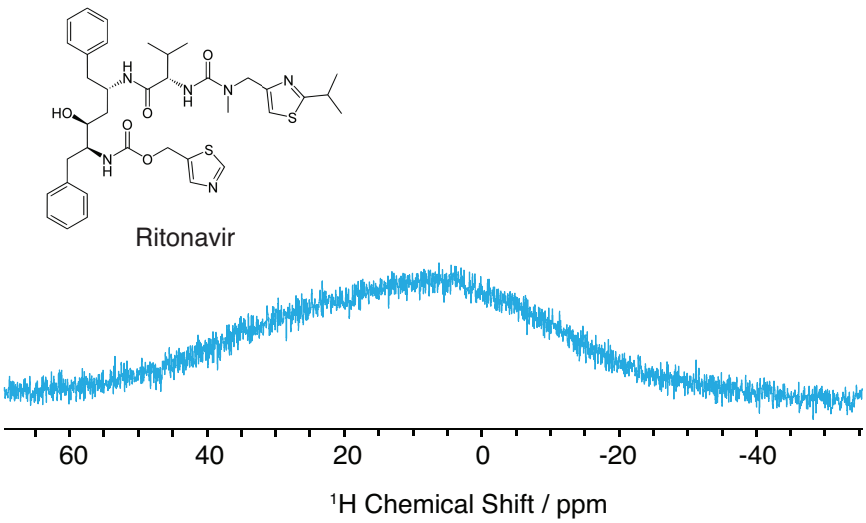

Figure 1.1. Molecular structure of ritonavir and the ^{1}H NMR spectrum of a static sample recorded for a powder sample of ritonavir form II.

The resulting spectrum is featureless and little to no structural information can be retrieved. Although dipolar couplings encode distance between spins, it is usually preferable to remove the broadening due to dipolar coupling, and obtain atomic-site resolved spectra.

1.4 Magic-Angle Spinning

The $(3\cos^2\theta - 1)$ orientation dependence is not specific to dipolar coupling, but to any anisotropic NMR interaction that is defined by a second-rank tensor[70, 100], such as the chemical shift tensor. The value of the interaction is equal to zero when the angle between the spin interaction principal axis frame and the magnetic field B_0 is set at the magic-angle (θ_m).

$$\theta = \theta_m = \left(\tan^{-1}\sqrt{2}\right) = 54.7° \qquad (1.8)$$

This crucial property revolutionized NMR of solids with the implementation of magic-angle spinning (MAS). Introduced in the 1950s[101-102], MAS consists of physically spinning the sample around an axis tilted at 54.7° with respect to the magnetic field.

To first order, MAS yields an average orientation of the interaction along the magic angle, and removes all anisotropy from second rank tensor interactions[103], such as dipolar coupling and CSA, leading to substantial line narrowing in the spectrum. Higher order terms are dependent on the MAS frequency[103-108] as will be discussed in detail below. Therefore, the degree of coherent averaging is determined by the spinning rate (given in kHz).

However, under MAS, the effect of the different Hamiltonian terms on the spectrum is not the same. Maricq and Waugh[103], in their seminal paper, introduced the formalism of "inhomogeneous" and "homogeneous" interactions. Due to the sample rotation, the Hamiltonian becomes time-dependent and Maricq and Waugh considered any interaction that commutes with itself at different times as inhomogeneous. This is the case for the chemical shift and heteronuclear dipolar couplings. The NMR signal is detected during MAS rotation and the inhomogeneous interactions, being rotor-modulated, are dephased and perfectly refocused within a rotor period. This results in the appearance of rotational echoes in the free induction decay (FID). After Fourier-Transform (FT), the frequency spectrum is composed of a sideband pattern.[70] The sideband pattern consists of a series of narrow lines positioned at integer multiples of the spinning rate centered around the isotropic chemical shift position. Therefore, MAS splits the inhomogeneously broadened lines into a pattern of narrow spinning sidebands.[109] As the spinning rate increases, the spinning sidebands intensities are attenuated and positioned at further away from the isotropic peaks in the spectrum. Simultaneously, the center band intensity is increased because the integrated signal of all sidebands is the same at all rates. At slow spinning rates, the sidebands are

useful and, in favorable cases, can be analyzed to retrieve the CSA tensor principal values. Moderate spinning rates (~10-20 kHz) are enough to suppress most of the spinning sidebands, since, typically for ^{1}H and ^{13}C, CSA is not larger than a few kHz.

On the other hand, homogeneous interactions, such as homonuclear dipolar couplings, do not commute with themselves at different times during the rotor period. The full refocusing of homogeneous interactions is not possible, resulting in a faster decay of the FID and consequently more line broadening in the frequency domain.[109] The residual broadening can be very large and hide the underlying chemical shifts.[107, 109-113] For effective line narrowing, the spinning rate needs to be larger than the effective dipolar strength.[103, 106, 108] In ^{1}H dense systems, this implies spinning at 100 kHz MAS or higher. In the past, such spinning rates were unavailable and the inability to sufficiently reduce or suppress the ^{1}H-^{1}H dipolar coupling prevented the application of ^{1}H NMR detection methods. For this reason, MAS spectroscopy originally strongly focused on dilute spins such as ^{13}C and ^{15}N, where the CSA is the only major interaction in the spectrum.

At faster MAS rates (> 40 kHz), the CSA is effectively averaged out and a routine 1D cross-polarization ^{13}C experiment[114] can provide strikingly high resolution spectra[115], as it is seen below with Ritonavir.

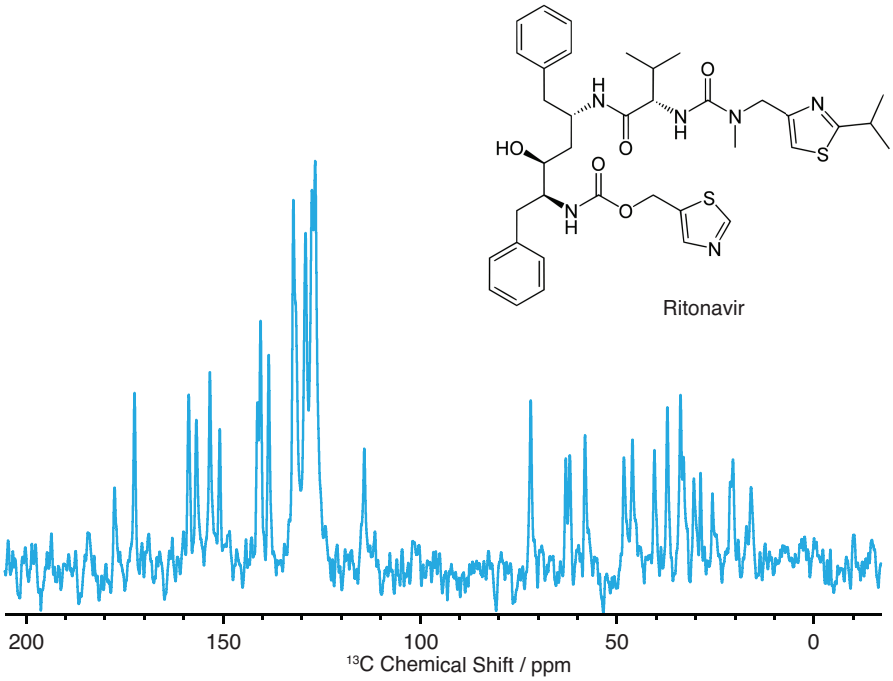

Figure 1.2. Molecular structure of ritonavir and the ^{13}C 1D Cross-Polarization 100 kHz MAS spectrum recorded for a powder sample of ritonavir form II.

The sidebands are not visible in the spectrum, due to the high spinning rate, therefore the CSA information is lost. However, removing this information allows to obtain a single peak for each distinct nuclei, leading to the desired atomic site resolution. A lot of effort was put into MAS equipment design over the last decades and fast spinning probes are commercially available today (100-150 kHz).[110, 116-119] The effect of fast MAS on ^{1}H is discussed in the next section.

1.5 ^{1}H NMR of solids in the fast-spinning regime

As mentioned in the previous section, a ^{1}H spin pair 1.5 Å apart has a $DD_{IS}/(2\pi)$ of 35.5 kHz. Therefore, a MAS rate significantly above that frequency would be necessary in order to effectively average out that particular coupling. If stronger couplings are present in the sample (1.1 Å would correspond to 90.2 kHz), faster rates are required. In a dense network of ^{1}H spins with various dipolar couplings and the multispin effect, the MAS rate needs to be significantly greater than the largest dipolar couplings present in the network in order to be considered to be in the fast-spinning regime.

The residual homogeneous broadening of every distinct spin of a given sample can be estimated from a pseudo 2D spin-echo experiment.[120] The spin echo intensities are measured at different echo durations (2τ) (Figure 1.3) and the decay is defined by the transverse spin-spin dephasing time (T_2').[112, 121]

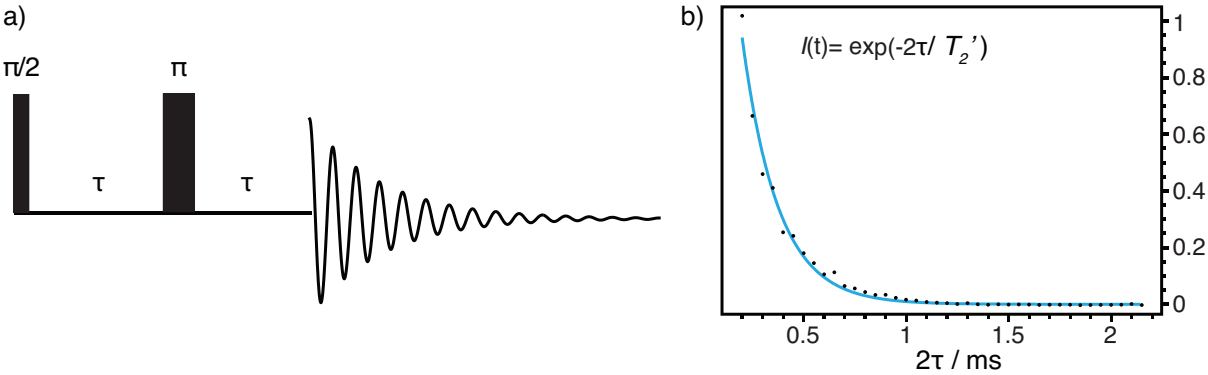

Figure 1.3. a) spin-echo pulse sequence. The homogeneous linewidth is determined from the intensity of the spin echo as a function of the spin-echo delay τ. (b) the spin echo decay I is fitted to a simple exponential and T_2' is extracted.

Typically, in rigid organic solids, T_2' is in the order of a few milliseconds. The corresponding homogeneous broadening in Hz (Δ') is defined as

$$\Delta' = \frac{1}{\pi T_2'} \qquad (1.9)$$

On the other hand, the inhomogeneous broadening is refocused during the spin echo[122]. The linewidth obtained by FT of the regular FID is the sum of the homogeneous and inhomogeneous linewidth, therefore, the inhomogeneous linewidth can be obtained by the difference of the regular FID and the spin echo decay.

The sources of inhomogeneous broadening and their contribution to the total linewidth at fast MAS have been discussed in the literature and are also detailed in **Chapter 5**. The dependence of the total linewidth and Δ' dependence on MAS rate have also been the subject of investigation and are discussed in **Chapter 2**.

As the spinning rate increases, elongation of T_2' is expected because of the improved coherent averaging of the dipolar couplings, which translates to a longer ^{1}H coherence lifetime.[112-113, 123]

Alternatively, reducing the number of protons by deuteration also diminishes the dipolar coupling effect. For ^{1}H diluted samples, proton detection methods are useful, even at moderate MAS frequencies.[124-130] Although a cost in sensitivity is expected with deuteration, the gain in line narrowing can be preferred. At fast MAS rates, deuteration is still recommended, particularly for protein samples, where deuteration is relatively straightforward. Combined with a high magnetic field, fast MAS rate and deuteration, linewidths of 50–100 Hz can be obtained and assignment of proteins was possible with proton detection.[129-130]

When the experimental MAS rates available were in the slow to moderate spinning regime ($\omega_r << DD_{IS}/(2\pi)$), ^{1}H resolution was improved but far from resolving atomic sites in powdered samples. However, sophisticated NMR methods achieved further decoupling, which consisted of combining rotation and multiple pulse sequence methods (CRAMPS)[119, 131-136]. Introduced by Gerstein *et al.*. in 1977 at 2.5 kHz MAS[131], several decoupling schemes achieved impressive line narrowing, up to 65 kHz MAS.

Even if these techniques introduce additional noise, and chemical shift scaling and artifacts, they are the state-of-the-art methods for ^{1}H detection for MAS rates up to 65 kHz.

Today, MAS in the fast spinning regime ($\omega_r >> DD_{IS}/(2\pi)$) has significantly improved ^{1}H resolution. The fastest commercially available rates are in the range 100-150 kHz[110, 116-119], while rates up to 200 kHz[137] have been demonstrated at laboratory level. The linewidths at 100 kHz MAS are comparable to the ones obtained with CRAMPS at slower frequencies, but without the inconveniences related to CRAMPS methods mentioned above.

As an example, the relatively simple organic solid L-Tyrosine hydrochloride is spun at 40 and 100 kHz MAS and the corresponding 1D ^{1}H spectra are presented in Figure 1.4.

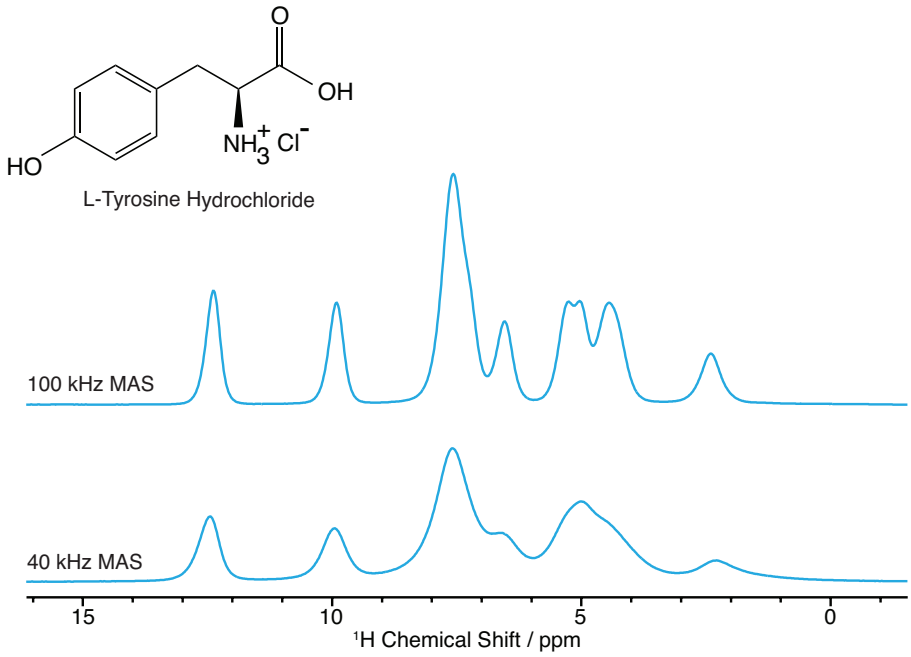

Figure 1.4. Molecular structure of L-Tyrosine Hydrochloride and 1D ^{1}H NMR spectra of powdered sample of L-tyrosine Hydrochloride, acquired at 40 kHz and 100 kHz MAS.

The resolution improvement is substantial from 40 kHz to 100 kHz MAS. Compared to a static spectrum, as seen in the previous section, the 40 kHz MAS spectrum has linewidths 125 times narrower. Nonetheless, it is visible that the linewidths are still relatively large and severe overlap is still present in the 3-5 ppm regions. The 100 kHz MAS spectrum has better resolved peaks overall, but it is particularly notable around 5 ppm: what was an unresolved "blob" at 40 kHz becomes three distinct peaks at 100 kHz. This spinning rate is attainable by using a 0.7 mm diameter rotor.

Indeed, faster MAS rates are associated with smaller rotors and restricted sample amount.[123] Although abundant spins such as ^{1}H are not particularly handicapped by this, the reduced sample quantity leads to a substantial sensitivity loss for direct detection of rare heteronuclei with a lower γ.

This loss is compensated by using one of the most common techniques in MAS, cross-polarization (CP).[114] CP involves polarization transfer between abundant spins (^{1}H) and dilute spins (^{13}C), which are dipolar coupled. The sensitivity improvement allows detection for rare nuclei, even at natural abundance, such as ^{15}N. The signal enhancement is defined by the ratio of γ_{1H}/γ_{13C} and the relaxation delay is dependent on ^{1}H T_1, which is generally shorter than the T_1 of dilute spins. In addition, faster MAS elongates both $T_{1\rho}$ [138-139] and T_2'[112], which facilitates the magnetization transfer.

For these reasons, several heteronuclear and multidimensional (2D[140-142], 3D[143-151] and 4D[152-161]) correlation experiments based on CP contacts are been developed and are largely used on different classes of materials: inorganics[162-167], polymers[168-173], pharmaceuticals[36-40, 62-68] and proteins[59-61]. The hCH/hNH sequence based on double CP contacts is extensively used for 2D HETCOR experiments[174-175]. HETCOR spectra can be acquired for proteins in minutes, and if fast MAS is combined with a high B_0, larger complex proteins can be studied.

In terms of homonuclear multidimensional correlation experiments, a plethora of dipolar recoupling methods have been developed in the past decades, for different spinning regimes and specific radiofrequency irradiation requirements. Double-Quantum (DQ) and Zero-Quantum (ZQ) recoupling sequences are the first order homonuclear dipolar recoupling techniques and are generally for short-distance correlation. Although not detailed here, there are also the second-order recoupling sequences based on spin-diffusion (SD) to detect long-range correlations.[176-182]

The classic ZQ recoupling sequence is radio frequency driven recoupling (RFDR)[183-184] and its variation finite pulse radio frequency driven recoupling (fpRFDR) at fast MAS[185-191]. The latter version accounts for the fact that at fast MAS, the pulse has considerable width compared to the short rotor period. Consequently, the spin evolution during the pulse width can no longer be neglected and needs to be taken into account in the pulse sequence

design. The RF irradiation scheme requirement combined with the robust recoupling performance renders this sequence highly suitable for homonuclear correlation experiments.

On the other hand, several DQ recoupling methods have been developed to determine the proximity between spins.[192-210] At fast MAS, sequences requiring low RF field strength are preferred and the most common DQ recoupling sequences[189] are POST C7,[198] $\mathrm{SR14}_5^4$,[199] $\mathrm{SR26}_{11}^4$,[211] $\mathrm{BR2}_2^1$,[202] BABA_{xy16},[203] $\mathrm{SR2}_{2p}^1$ and $[\mathrm{SR2}_{2p}^1]$.[189] BABA_{xy16} is a phase cycled scheme based on the simpler original BABA (Back-to-.Back) sequence, but it is more broadband, robust and more adapted for faster MAS rates and ^{1}H detection.[203] It has been applied to host-guest systems such as PDMS@ɣ-cyclodextrin, but also polymers and organic solids. In this body of work, the BABA_{xy16} experiment will be the go-to method for ^{1}H-^{1}H correlations at fast MAS. Nevertheless, it is worthy to note that symmetry-based sequences have also been demonstrated recently to be more robust than BABA_{xy16}, by reducing significantly t_1 noise.[119, 212]

1.6 The Quest for Resolution

The equipment mainly used in this body of work is a probe using 0.7 mm diameter rotors in a magnetic field of 21.1 T, which spins routinely at 100 kHz. The ^{1}H 1D spectrum of L-tyrosine HCl in Figure 1.4 demonstrated the capabilities of this system and how ^{1}H resolution is improved when fast MAS is combined with a high B_0.

Nevertheless, the obtained linewidths are still a few hundred Hz and not all resonances are resolved (according to the literature assignment, based on ^{13}C detection experiments), experiencing substantial overlap. This is a sample with 10 different ^{1}H sites, a relatively simple spin system, which demonstrates the current limitations on resolution.

These limitations are exacerbated for ritonavir, with 48 protons. Figure 1.5 shows the corresponding 40 and 100 kHz 1D ^{1}H spectra.

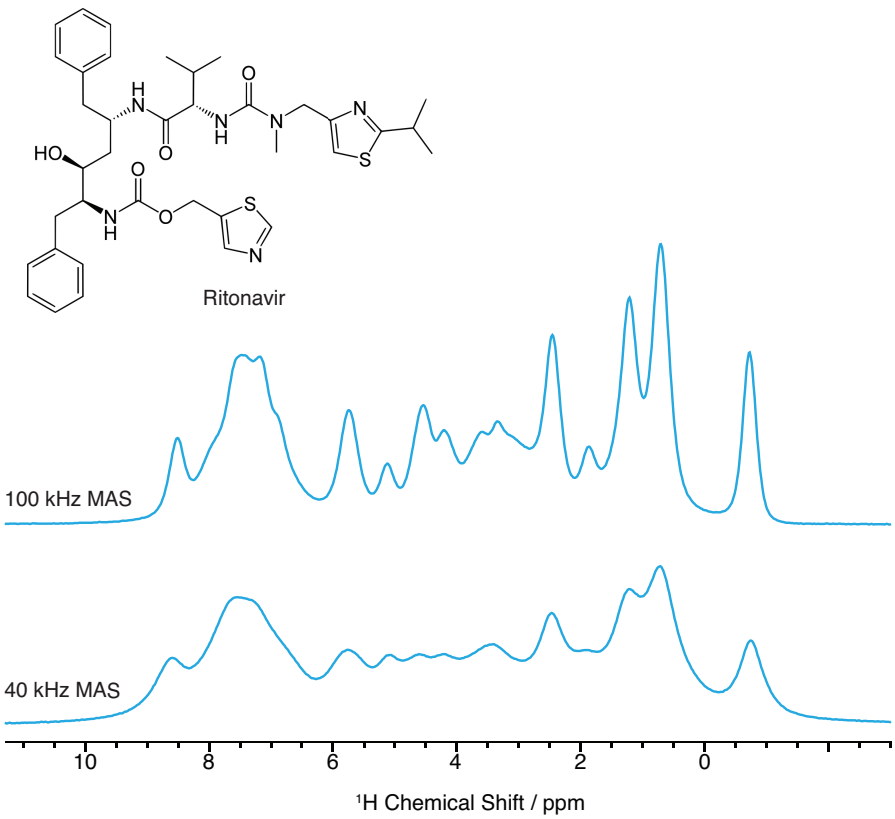

Figure 1.5. Molecular structure of Ritonavir and 1D 900 MHz ^{1}H NMR spectra of a powdered sample of Ritonavir (II), acquired at 40 kHz and 100 kHz MAS.

Again, the narrowing is substantial between the 40 and 100 kHz MAS spectra, and some distinct resonances are resolved. Yet, the residual broadening remains significant, rendering assignment difficult, if not impossible. In

recent literature, other examples include strychnine[213], ampicillin[214], molnupiravir[215], AZD5718[216], Lorlatinib.[217] These examples all illustrate the need for further decoupling and faster MAS rates.

Great resolution improvement is possible by adding a second dimension to the spectrum. As mentioned above, DQ/SQ correlation experiments are typically used for homonuclear ^{1}H-^{1}H correlation and several pulse sequences have been developed for NMR of solids under fast MAS. Figure 1.6 shows the DQ/SQ ^{1}H-^{1}H spectrum of ritonavir at 40 and 100 kHz MAS using the BABA$_{xy16}$ pulse sequence.[203] The difference between the two MAS rates is again striking.

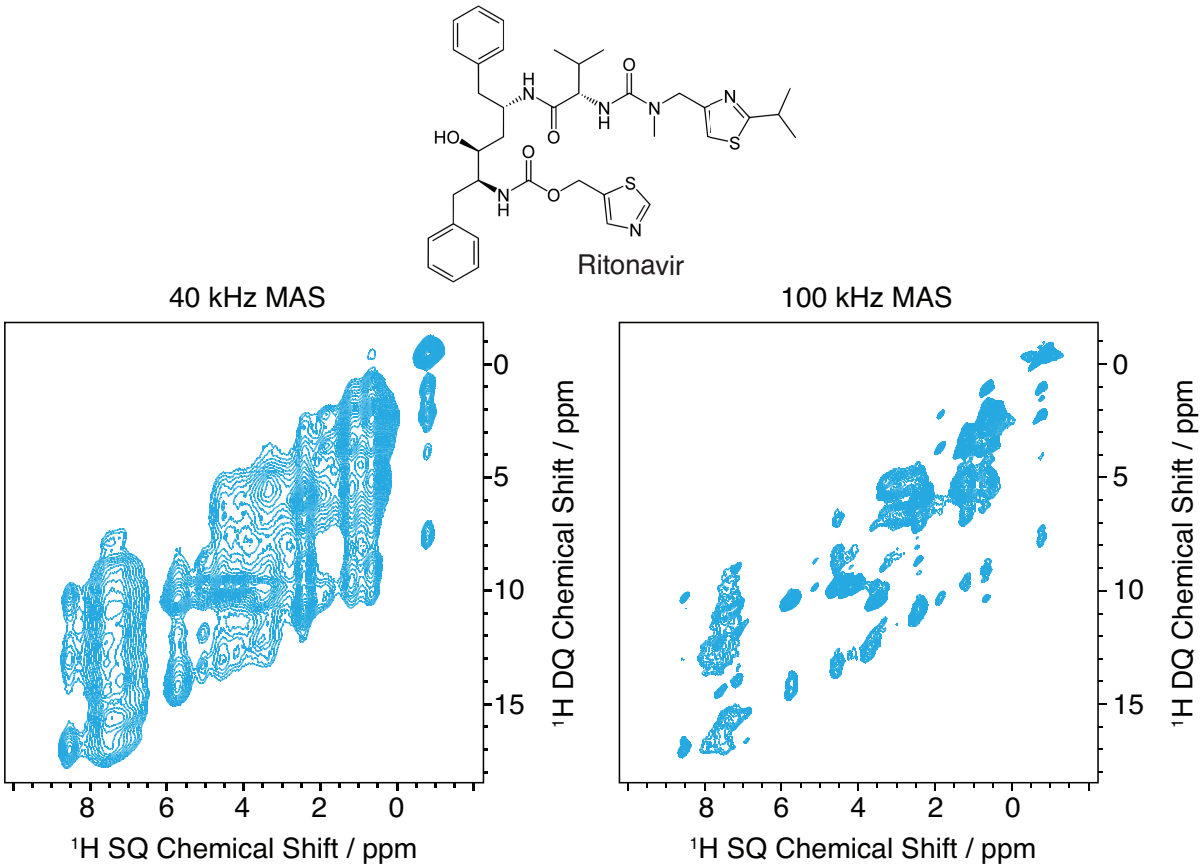

Figure 1.6. Molecular structure of Ritonavir and 2D 900 MHz ^{1}H-^{1}H DQ/SQ NMR spectra of a powdered sample of Ritonavir (II), acquired at 40 kHz and 100 kHz MAS with the BABA$_{xy16}$ pulse sequence.

The improvement in resolution compared to the one-dimensional spectrum is obvious and more resonances can be assigned. Although, DQ/SQ spectra at fast spinning rates offer better ^{1}H experimental resolution for structural assignment in ^{1}H NMR of solids, the technique is still underwhelming due to the severe residual broadening. The residual linewidths only represent 1% of the static linewidth, but they are still not narrow enough for confident assignment in the majority of cases. The reliance on ^{13}C detection methods is still necessary for the structural assignment of ritonavir.

Until the residual homogeneous broadening by MAS alone is negligible, the development of alternative strategies to improve the resolution are required to expand the domain of applicability of ^{1}H solid state NMR. These strategies require a theoretical understanding of what contributes to the linewidth, as focused on in this thesis.

1.7 Outline of the thesis

The core of my PhD has been understanding the sources of residual broadening in ^{1}H NMR under fast magic-angle spinning, and developing new methods to increase the spectral resolution in order to make ^{1}H NMR a more preponderant actor in NMR crystallography. The thesis will present both theoretical studies and new methodology developed in our lab to access narrower ^{1}H linewidths.

Chapter 2 describes analytical integration up to third order using Average Hamiltonian Theory of two and three spin systems under MAS. The study is focused on two nuclear spin interactions: isotropic chemical shift and homonuclear dipolar coupling. Each order of the Hamiltonian is detailed and their relevance at different MAS rates is compared to numerical simulations. The residual terms are found to produce residual shifts and splittings in the spectrum, which is supported by experimental results.

Chapter 3 presents the first two new methods that further improve ^{1}H resolution under fast MAS. Commonly used for homonuclear J decoupling in liquid state, the Anti-Z COSY experiment is here adapted to rotating solids to remove the residual dipolar coupling terms found in Chapter 2. A faster version (TAZ-COSY) is also described. Both of them achieve a narrowing up to a factor of two when compared to 1D conventional experiment.

Chapter 4 then discusses pure isotropic proton (PIP) approaches. Based on error mapping instead of coherent averaging, PIP methods are introduced that are in principle able to remove all residual homogeneous broadening, reaching the highest ^{1}H resolution on organic solids to date. PIP is first implemented with a parameter fitting approach on conventional 1D spectra. Then, PIPNET is developed, which can be seen as PIP with a machine learning model that overcomes previous assumptions and limitations, while attaining similar levels of resolution. Finally, PIPNET is extended to PIPNET2D, where pure isotropic spectra are obtained for ^{1}H-^{1}H 2D correlation experiments.

Chapter 5 reflects on the previous methods and investigates the different contributions to the ^{1}H linewidth at fast MAS, with a particular focus on the inhomogeneous broadening sources. Five different samples are studied, each one with a particular distribution of the different contributions to the lineshape. The analysis is done with the help of DQ/SQ spectra, which show that all correlated inhomogeneous broadening can be removed with the extraction of antidiagonals. ABMS is revealed to be an important source of broadening at the fast-spinning regime, therefore becoming the target to suppress in future methods that will continue the quest for more ^{1}H resolution.

Chapter 6 concludes on the achieved results and puts into perspective a possible outlook on next paths to follow to improve ^{1}H resolution.

Chapter 2 Understanding the residual broadening in ^{1}H NMR spectra under MAS

2.1 Introduction

The homonuclear dipolar coupling is the internal spin interaction that contributes the most to the broad line shapes in ^{1}H NMR spectra of static solids at natural isotopic abundance. This broadening can extend over several kHz, obscuring information from smaller interactions, such as chemical shifts. Therefore, a lot of effort has been made into: i) analysing the dipolar based contributions to the ^{1}H spectrum and ii) reducing those contributions in order to increase spectral resolution, leading to richer chemical information on the sample structure.[218]

At the centre of the quest for the best possible resolution is MAS. [101-102], which averages second-rank tensor interactions, such as the homonuclear dipolar interaction. Generally, even at the fastest MAS rates possible today (100-150 kHz)[110, 116-118], the linewidths are reduced to a few hundreds of Hz. These values are limiting to resolve all ^{1}H resonances for an accurate assignment, and part of this residual broadening is coming from the dipolar terms which are not completely removed by MAS at these rates.

To further narrow the linewidths, a myriad of techniques combining multiple-pulse sequences and MAS have been developed.

Simultaneously with the progress in resolution, great research has been done on theorizing the ^{1}H linewidth under MAS considering the chemical shift and the homonuclear dipolar coupling as the main spin interactions in the Hamiltonian. The Hamiltonian is time-dependent due to the sample rotation around the magic angle. Also, the homonuclear dipolar terms do not commute within a rotor period. Consequently, it is not possible to exactly propagate the Hamiltonian over a rotor period or a pulse sequence without resorting to numerical simulations or some analytical approximations. For the latter approach, Floquet Theory and Average Hamiltonian Theory have been greatly used in NMR to describe different problems in solid state NMR.

By having the MAS as the sole time-dependent process, Average Hamiltonian Theory is suitable for the analysis of the dipolar contributions to the ^{1}H spectrum.[103] The time-dependent Hamiltonian is replaced with a time-independent effective Hamiltonian over a time interval (a rotor period in our case), which is approximated through a series expansion. Every integrated order of this expansion will give a physical comprehension of the spin behavior.

In **Chapter 2.2**, the Average Hamiltonian is fully analytically integrated up to third order for the case of both two and three spin dipolar coupled systems including chemical shift differences. Both of these cases are treated for single orientation with isotropic chemical shifts and homonuclear dipolar couplings. The analysis starts with the two-spin case, comparing it with fully numerical integration methods, and then extends to the three spin case. The comparisons (Figure 2.4 and Figure 2.9) show that only the full average Hamiltonian considering all terms (both non secular and secular terms) completely agrees with numerical simulation across all MAS rates. The two spin simulations are in line with the literature[103, 106, 108] and the higher order terms produce a residual shift in the spectrum that has a polynomial dependence. For the three spin case, on top of the residual shift the higher order terms produce also a residual splitting (in third order, there are even residual secular $\boldsymbol{I_{kz}I_{lz}}$ terms that contribute to the lineshape). Again, the residual shift and residual splitting have an overall polynomial MAS dependence. In order to diminish the gap between simulations and experiments, the effect on powders is also studied, for which a residual shift and broadening from the higher order terms is also observed.

2.2 Theory and Simulations of homonuclear three-spin systems in rotating solids

This chapter has been adapted with permission from: Simões de Almeida, B.; Moutzouri, P.; Stevanato, G.; Emsley, L., Theory and simulations of homonuclear three-spin systems in rotating solids. *J Chem Phys* **2021,** *155* (8), 084201.

My contribution was to develop and apply the method, and to analyse the results obtained. I also wrote the manuscript, with contributions of all authors.

2.2.1 Introduction

A detailed analysis of the contributions to spectral lineshapes under MAS with an average Hamiltonian theory (AHT) treatment to third order for 2 and 3 inequivalent spins I = ½ is presented. We describe complete analytical expressions for the lineshapes, considering only the isotropic chemical shifts (Ω_{iso}) and the homonuclear dipolar coupling. We compare the predictions from AHT to numerical simulations of the complete density matrix. We find that the all terms in the AHT description up to third order are required to obtain good agreement with the numerical simulations, and that restriction to only secular terms leads to significant errors. The analysis confirms that the residual dipolar broadening for three unlike spins is composed of shift-like and coupling-like terms, and we show the full orientation- and spinning-rate-dependence of these terms. The effect of MAS on the homonuclear dipolar interactions, has been studied previously in 2 spin systems, notably by Maricq and Waugh[103], Nakai and McDowell[108] and Levitt *et al.*.[106]

Maricq and Waugh treated the case of two equivalent dipolar coupled spins (no chemical shift difference), using average Hamiltonian theory. Both Nakai and McDowell, and Levitt *et al.*., treated the case of two inequivalent dipolar coupled spins, using Floquet Theory, in different spinning regimes. We compare and contrast the three-spin behaviour found here with the prior two spin results, that we reproduce here with AHT. For the three spins case, Brunner *et al..* [104] investigated the residual linewidth under MAS using average Hamiltonian theory to second order using a second moment analysis for three spin systems experiencing homonuclear dipolar coupling. The moment analysis is a powerful tool to simply the analytical problem, and predict overall linewidths, for example, but it has the disadvantage of masking the detailed description of the lineshape. Challoner and McDowell[105] also studied the evolution of the linewidth under MAS with AHT to second order (in the fast spinning regime) for three spin systems, where one of the spins has significantly different chemical shift (ABX spin system). Both these approaches predicted a $1/\omega_r$ dependence for the residual linewidth. Spiess and coworkers[109, 111] used Floquet theory to do a general treatment of dipolar multi-spin systems under MAS, again using a moment analysis for the linewidhts. Ray *et al..* [219] have numerically simulated spectra using Floquet theory for six spin systems at high fields and fast spinning regimes. Zorin *et al..* [113] also used numerical simulations for multi-spin systems to analyse the residual linewidths.

More recently, Sternberg *et al..* [112] analysed the proton linewidth as a function of MAS rate by comparing experiments and simulations using the Fokker-Plank approach, and Malar *et al..*[107] and Schledron *et al..*[220] analysed linewidths for fast MAS using a second moment approach. Hellwagner *et al..*[221] studied the different contributions to the residual broadening in FSLG decoupled proton spectra with Floquet theory. For a homonuclear coupled three spin system with two dipolar couplings, their analysis of the second-order cross terms showed that the three spin operators [70] make a strong contribution to the residual linewidth. They also found that, in a homonuclear two spin system, the third order terms yield a contribution to the FSLG linewidths. Several approaches, including perturbation theory[222-223] , numerical simulations[224-225], AHT[226-227] and Floquet theory[228-229] have been used to study the related problem of spin diffusion in multi spin systems.

2.2.2 Methods

Symbolic calculations and propagation of the average Hamiltonians was carried out using the SpinDynamica package (Version 3.4.2)[230] in Mathematica. Numerical full density matrix simulations were carried out using the SPINACH package (Version 2.4.5157)[231] in Matlab. The same spins systems were used in both packages and their corresponding spectra compared. The details of each spin system used in the following are given in the Appendix I.

2.2.3 Theory

2.2.3.1 Tensor notation

In a spherical tensor basis, the isotropic chemical shift Hamiltonian for a given spin is[70, 100, 103, 106, 108]

$$H_{\Omega_{iso}} = \Omega_{iso1}\, T_{1,0}^{\Omega_{iso1}} = \Omega_{iso}\, I_{1z} \tag{2.1}$$

Where Ω_{iso1} is the isotropic chemical shift value in radians for spin 1. Note that in the following we have chosen to neglect contributions due to the anisotropy of the chemical shift. The secular high-field dipolar coupling Hamiltonian between two spins (1 and 2) is given by a product of orientation dependent and spin dependent parts[70, 230]:

$$H_A = \mathrm{A}_{12} D_{0,0}^2(\Omega) T_{2,0}^A = -\sqrt{6}\frac{\gamma_1\gamma_1\hbar\mu_0}{4\pi r^3} D_{0,0}^2(\Omega^D) T_{2,0}^A \tag{2.2}$$

where A_{12} .is the dipolar coupling constant, that depends on the gyromagnetic ratio γ of the two spins and the internuclear distance. If the coupling is homonuclear, then, $\gamma_1 = \gamma_2$. Being a second rank spin interaction [70, 100], the spin part of the dipolar coupling Hamiltonian in the spherical tensor basis is

$$T_{2,0}^A = \sqrt{\frac{2}{3}}\left(4I_{1z}I_{2z} - (I_1^+ I_2^- — I_1^- I_2^+)\right) \tag{2.3}$$

The Wigner matrixes [232] $\boldsymbol{D}^l(\Omega)$ rotate the spherical tensor operators between frames, which are linked by a set of three Euler angles (Ω). They are unitary matrixes of size (2l+1)x(2l +1), where *l* is the rank of the interaction. $D_{0,0}^2(\Omega)$ is the second rank Wigner rotation matrix element describing the transformation from the principal axes systems (PAS) of the dipolar tensor to the laboratory frame.

$$D_{0,0}^2(\Omega) = e^{i\gamma 0} e^{i\alpha 0} d_{00}^{(2)}(-\beta) = 3\frac{cos^2(\beta) - 1}{2} \tag{2.4}$$

and where in general

$$D_{mm'}^2(\Omega) = D_{mm'}^2(\alpha,\beta,\gamma) = e^{i\gamma m} e^{i\alpha m'} d_{mm'}^{(2)}(-\beta) \tag{2.5}$$

The second rank reduced Wigner elements, $d_{mm'}^{(2)}(-\beta)$ are recalled in the Appendix I. The Euler angles are defined with the ZYZ convention, where α refers to the rotation of the tensor around the frame z-axis[230].

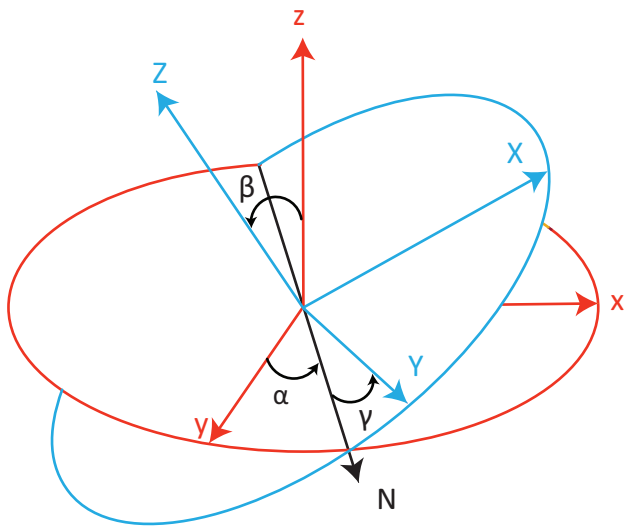

Figure 2.1 Two orthogonal 3D cartesian coordinate systems, xyz and XYZ.The Euler angles α, β and γ define the relative orientation between them. Adapted from https://en.wikipedia.org/wiki/Euler_angles

Orientation and time dependences can conveniently be expressed by decomposing $D^2_{0,0}(\Omega)$ into a series of consecutive frame transformations:

$$\mathrm{PAS} \xrightarrow{D(\Omega_P^C)} \mathrm{CRYSTAL} \xrightarrow{D(\Omega_C^R)} \mathrm{ROTOR} \xrightarrow{D(\Omega_R^L)} \mathrm{LAB} \tag{2.6}$$

where $D(\Omega_P^C)$ is a rotation of the interaction from its principal axis system (P) to a crystal fixed frame (C). $D(\Omega_C^R)$ rotates the interaction from the crystal frame to a rotor fixed frame (R), and finally $D(\Omega_R^L)$rotates the dipolar coupling from the rotor to the laboratory fixed frame (L).

In the general case, we have for each rotation the following set of Euler angles:

$$\Omega_P^C = \{\alpha_P^C, \beta_P^C, \gamma_P^C\} \tag{2.7}$$

$$\Omega_P^R = \{\alpha_P^R, \beta_P^R, \gamma_P^R\} \tag{2.8}$$

$$\Omega_R^L = \{\omega_r t, \theta_m, 0\} \tag{2.9}$$

Where Ω_P^C and Ω_P^R are the Euler angles for the principal axys system to the crystal fixed frame, and the crystal frame to the rotor frame, respectively. The changing relative rotor orientation to the laboratory frame, Ω_R^L, is defined, for exact magic-angle spinning, with $\alpha_R^L = \omega_r t$, $\beta_R^l = \theta_m$, where ω_r is the spinning rate and θ_m is the magic angle ($\tan^{-1}\sqrt{2}$), and γ_R^L is arbitrary.

For a two-spin system, we can assume that the crystal frame is coincident with the PAS without loss of generality, and only two frame transformations are necessary. For a rotating sample, the orientation of the rotor frame with respect to the laboratory frame (Eq. 2.9) is time-dependent. For MAS the rotor frame z-axis is tilted at the magic angle, $\theta = \theta m = 54.74°$, relative to the lab frame z-axis, which is parallel to the static field B_0, so that

$$d_{00}^{(2)}(-\theta_m) = 0 \tag{2.10}$$

Considering the spin part of the homonuclear dipolar interaction operators ($T_{l,m}$), only $T_{2,0}$ contributes to the high-field Hamiltonian. Therefore, we obtain a full time-dependent Hamiltonian for three-spin systems under MAS:

$$\begin{aligned} H(t) = \; & \Omega_{iso1} I_{1z} + \Omega_{iso2} I_{2z} + \Omega_{iso2} I_{3z} \\ & + \sqrt{\frac{2}{3}} \sum_{m'=-2}^{2} \sum_{m=-2}^{2} D_{m0}^{(2)}(\Omega^{RL})\, D_{0m'}^{(2)}(\Omega^{PR}) \mathrm{A}_{12} \left(4 I_{1z} I_{2z} - (I_1^+ I_2^- - I_1^- I_2^+)\right) \\ & + \sqrt{\frac{2}{3}} \sum_{m'=-2}^{2} \sum_{m=-2}^{2} D_{m0}^{(2)}(\Omega^{RL})\, D_{0m'}^{(2)}(\Omega^{PR}) \mathrm{A}_{13} \left(4 I_{1z} I_{3z} - (I_1^+ I_3^- - I_1^- I_3^+)\right) \\ & + \sqrt{\frac{2}{3}} \sum_{m'=-2}^{2} \sum_{m=-2}^{2} D_{m0}^{(2)}(\Omega^{RL})\, D_{0m'}^{(2)}(\Omega^{PR}) \mathrm{A}_{23} \left(4 I_{2z} I_{3z} - (I_2^+ I_3^- - I_2^- I_3^+)\right) \end{aligned} \tag{2.11}$$

2.2.3.2 Average Hamiltonian Theory

Due to MAS, H_A has a periodic time-dependence such that

$$H_A(t) = H_A(t + NT) \tag{2.12}$$

In addition, the dipolar interaction is homogeneous in the sense of Maricq and Waugh [103]: $[H(t), H(t')] \neq 0$. Consequently, the propagator describing the time evolution of the system cannot in general be derived analytically. Average Hamiltonian theory[103, 233-234] can be used to approximate the Hamiltonian to any given order. AHT uses the Magnus expansion to replace H(t) with a time-independent average. Maricq and Waugh noted that the Magnus expansion will converge when the interaction strengths ϵ are small enough compared to the MAS rate, i.e. $\omega r / \epsilon >> 1$ with for two-spin systems,

$$\epsilon = \sqrt{(\Omega_{iso1} - \Omega_{iso2})^2 + \left(\mathrm{A}_{12} D_{0,0}^2(\Omega)\right)^2} \tag{2.13}$$

The average Hamiltonian is then given up to 3rd order by:

$$\bar{H}(1) = \frac{\omega_r}{2\pi} \int_0^{2\pi/\tau_r} dt H(t) \tag{2.14}$$

$$\bar{H}(2) = \frac{\omega_r}{4\pi i} \int_0^{2\pi/\tau_r} dt \int_0^t dt' [H(t), H(t')] \tag{2.15}$$

$$\begin{aligned} \bar{H}(3) = -\frac{\omega_r}{12\pi} \int_0^{2\pi/\tau_r} dt \int_0^t dt' \int_0^{t'} dt'' \; \{ & [H(t), [H(t'), H(t'')]] \\ & + [[H(t), H(t')], H(t'')] \} \end{aligned} \tag{2.16}$$

where $\tau_r = 2\pi/\omega_r$, corresponding to a rotor period. For the sake of simplicity, from this point onwards, ω_r in equations refers to $\frac{\omega_r}{2\pi}$.

2.2.3.3 AHT treatment for two-spin systems

The average Hamiltonian is expressed in the Zeeman eigenbasis $|\mathrm{m_{I1z}}, \mathrm{m_{I2z}}\rangle$ of the operators I_{1z} and I_{2z}, where:

$$\mathrm{I}_{1z} |\mathrm{m_{I1z}}, \mathrm{m_{I2z}}\rangle = \mathrm{m_{I1z}} |\mathrm{m_{I1z}}, \mathrm{m_{I2z}}\rangle \tag{2.17}$$

with the eigenstates:

$$|1\rangle = \left|+\frac{1}{2},+\frac{1}{2}\right\rangle, |2\rangle = \left|-\frac{1}{2},+\frac{1}{2}\right\rangle, |3\rangle = |+\frac{1}{2},-\frac{1}{2}\rangle, |4\rangle = |-\frac{1}{2},-\frac{1}{2}\rangle \tag{2.18}$$

1st order

Evaluation of the first order term for 2-spin systems spinning around an arbitrary axis yields:

$$\begin{aligned}\bar{H}(1) = \Omega_1 I_{1z} + \Omega_2 I_{2z} \\ -\frac{A_{12}}{64}(3cos^2(\beta_{PR})-1)(3cos^2(\beta_{RL})-1)\left(4I_{1z}I_{2z} - (I_1^+I_2^- - I_1^-I_2^+)\right)\end{aligned} \tag{2.19}$$

If the rotor is spinning at the magic angle, then $\beta_{RL} = \theta_m$ and the dipolar coupling term vanishes, and only the isotropic chemical shift terms survive.

$$\bar{H}(1)^{MAS} = \Omega_1 I_{1z} + \Omega_2 I_{2z} \tag{2.20}$$

2nd order

In 2nd order, the dipolar couplings do not vanish even under MAS.

$$\bar{H}(2)^{MAS}_{nonsec} = \Delta\mathrm{R}(2)^{MAS}_{nonsec} i(I_1^+I_2^- - I_1^-I_2^+) \tag{2.21}$$

$$\begin{aligned}\Delta\mathrm{R}(2)^{MAS}_{nonsec} &= \frac{f_2(\Omega)}{\omega_r}\mathrm{A}_{12}(\Omega_{iso1} - \Omega_{iso2}) \\ &= \frac{3}{32\omega_r}\mathrm{A}_{12}(\Omega_{iso1} - \Omega_{iso2})\sin(\beta_{PR})\sin(\theta_m) \\ &\times (8\,cos(\beta_{PR})\,cos(\theta_m)\sin(\alpha_{PR})) + sin(2\alpha_{PR})\,sin(\beta_{PR})\,sin(\theta_m))\end{aligned} \tag{2.22}$$

Where $f_2(\Omega)$ is a trigonometric function of the Euler angles. At second order, a zero-quantum term adds to the isotropic shifts of the first order term. The amplitude of this term has a $1/\omega_r$ dependence. The expression for spinning at an arbitrary angle is given in the Appendix I.

In the matrix representation of the average Hamiltonian, this second order term is a "flip-flop", and connects eigenstates $|2\rangle$ and $|3\rangle$. This term is denoted non-secular since it does not commute with the chemical shift terms. The effect on the spectrum is discussed in section 2.2.3.4.

3rd order

The analytical expression at third order gets more intricate, as the number of integrations and commutators increase. There is a zero-quantum contribution:

$$\bar{H}(3)^{MAS}_{nonsec} = \Delta\mathrm{R}(3)^{MAS}_{nonsec}(I_1^+I_2^- + I_1^-I_2^+) \tag{2.23}$$

$$\begin{aligned}\Delta\mathrm{R}(3)_{nonsec}^{MAS} &= \frac{f_{3ns}(\Omega)}{{\omega_r}^2} A_{12}(\Omega_{iso1} - \Omega_{iso2})^2 \\ &= \frac{3}{64{\omega_r}^2} A_{12}(\Omega_{iso1} - \Omega_{iso2})^2 \sin(\beta_{PR}) \sin(\theta_m) \\ &\times (16\, cos(\alpha_{PR})\, cos(\beta_{PR})\, cos(\theta_m) + cos(\alpha_{PR})^2\, sin(\beta_{PR})\, sin(\theta_m) \\ &- sin(\alpha_{PR})^2\, sin\,(\beta_{PR}) sin\,(\theta_m))\end{aligned} \tag{2.24}$$

and a term with single spin operators:

$$\overline{H}(3)_{sec}^{MAS} = \Delta\mathrm{R}(3)_{sec}^{MAS}(I_{1z} - I_{2z}) \tag{2.25}$$

$$\begin{aligned}\Delta\mathrm{R}(3)_{sec}^{MAS} &= \frac{f_{3s}(\Omega)}{{\omega_r}^2} {A_{12}}^2(\Omega_{iso1} - \Omega_{iso2}) \\ &= \frac{1}{512{\omega_r}^2} {A_{12}}^2(\Omega_{iso1} - \Omega_{iso2})\, sin(\beta_{PR})^2\, (-33 \\ &+ 32\, cos(2\alpha_{PR})\, cos(\beta_{PR})^2 - 31\, cos(2\beta_{PR}) + cos(4\alpha_{PR})\, sin(\beta_{PR})^2 \\ &+ 8\sqrt{2} si\, n(\alpha_{PR})\, si\, n(2\alpha_{PR})\, sin(2\beta_{PR}))\end{aligned} \tag{2.26}$$

We denote these terms as non-secular and secular respectively, since the zero-quantum term does not commute with the chemical shift terms, whereas the second term does. Both terms can be minimized by fast MAS, as the expressions have a ω_r^{-2} dependence. On the other hand, the expression for the secular term shows a $A_{12}^2(\Omega_{iso1}-\Omega_{iso2})$ dependence. Within the fast MAS convergence regime of Eq. 2.13, a stronger dipolar coupling interaction and/or a larger chemical shift difference enhances the value of the residual shift (ΔR) at a given spinning rate.

The non-secular zero-quantum term has a similar MAS dependence, but has a linear dependence on the dipolar coupling and a squared dependence on the chemical shift difference. As with the second order term, this term is off-diagonal term in the matrix representation of the average Hamiltonian, and connects |2⟩ and |3⟩.

In summary, to third order, in addition to the isotropic chemical shift terms, the two-spin Hamiltonian contains a zero-quantum term at second order, and a secular shift term and a zero-quantum term at third order,

$$\begin{aligned}\overline{H}^{MAS} = (\Omega_{\mathrm{iso1}} + \Delta\mathrm{R}(3)_{sec}^{MAS})I_{1z} + (\Omega_{\mathrm{iso2}} - \Delta\mathrm{R}(3)_{sec}^{MAS})I_{2z} + \mathrm{i}\Delta\mathrm{R}(2)_{nonsec}^{MAS}\,(I_1^+I_2^- - I_1^-I_2^+) \\ + \Delta\mathrm{R}(3)_{nonsec}^{MAS}\,(I_1^+I_2^- + I_1^-I_2^+)\end{aligned} \tag{2.27}$$

By secularizing the average Hamiltonian with respect to the chemical shift difference, only the third order shift term would remain, in addition to the isotropic chemical shift terms.

The effect on the NMR spectrum, and the accuracy of AHT for the two-spin systems is treated in the next section with numerical examples.

2.2.3.4 Effect on the MAS NMR spectrum – two spins

The effect of magic angle spinning on two-spin systems is shown with numerical simulations in Figure 2.2, with the underlying shifts and couplings given in the caption yielding ϵ = 13 kHz (Eq. 2.13), and spectra shown from 40 – 100 kHz MAS rates. The spectrum of a static sample depicted in Fig. 2.2 presents the splittings caused by the dipolar interaction ($A_{12}D_{0,0}^2(\Omega)$ = 12990 Hz). The spectrum of the isotropic shifts alone is also shown. The dipolar interaction in the lab frame is larger than the chemical shift difference, in this strong coupling regime. The inner peak intensities are weaker than the outer peaks and are barely visible in the spectrum of the static sample.

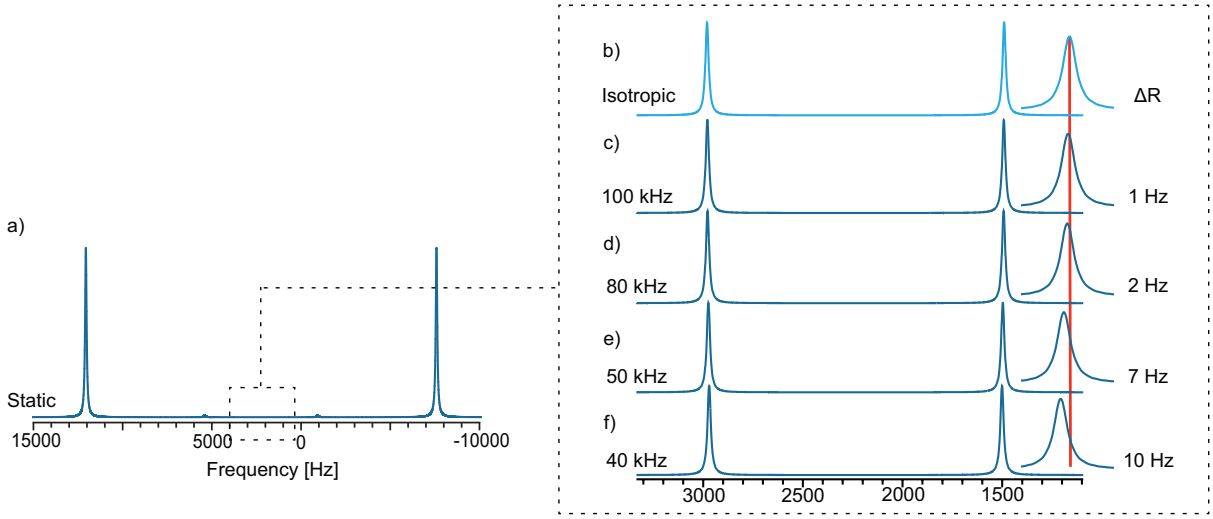

Figure 2.2 a) Static, b) Isotropic and c-f) MAS spectra and spectra of an AB systems for a single orientation. Ω_{iso1} = 1490 Hz, Ω_{iso2} = 2980 Hz. The coupling in the PAF was set to A_{12} = 30 kHz. The Euler angles for the crystal to rotor frame transformation are: $\{\alpha_{12}, \beta_{12}, \gamma_{12}\} = \{45°, 60°, 30°\}$. The zoom on the right shows to the Ω_1 region, with the red line at Ω_{iso1}. On the right, the values of the residual shift (the difference between Ω_{iso1} and the apparent peak position) are reported. Exponential linebroadening of 20 Hz was applied to the simulated free induction decays prior to Fourier transformation. Simulated with SPINACH as described in the Appendix I.

Despite the presence of two-spin operators in the average Hamiltonian, the resulting MAS spectra only contain two resonances, as MAS completely removes the splittings, and a zoom on the Ω_{iso1} region shows the effect of the higher order corrections to be a residual shift ΔR which decreases with increasing MAS. At 100 kHz, the residual shift is almost zero.

These numerical simulations (carried out using the SPINACH platform as described in detail in Appendix I) can be compared to the predictions of the second and third order AHT analysis above. Fig. 2.3 shows comparisons of the spectra, at 40 kHz MAS, obtained with different levels of AHT (propagated using the SpinDynamica platform as described in Appendix I) and the full numerical simulation. At this MAS rate and with this spin system, the full third-order Hamiltonian from AHT of Eq. 2.27 is in essentially complete agreement with the numerical simulation, with both of them indicating a ΔR of 11 Hz. Removing the non-secular terms leads to a small deviation from the exact simulation, and to a ΔR of 15 Hz. Finally, truncating the Hamiltonian to second order leads to a relatively large error in the prediction, and predicts ΔR of -3 Hz.

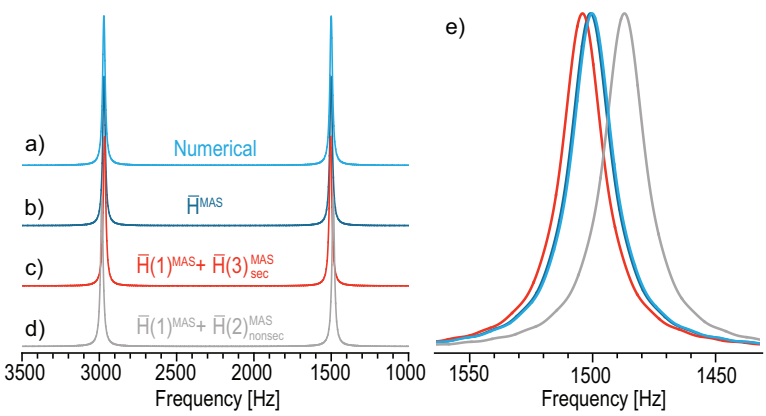

Figure 2.3 Comparison of spectrum obtained with full numerical simulation (a)) and the spectra obtained with the different AHT versions: the full Hamiltonian up to third order (b)), the secular part of the Hamiltonian up to third order (c)), and the second order Hamiltonian (d)). The spectra were simulated at 40 kHz MAS and the spin system used is the same as in Figure 2.2 The zoom in e) shows the Ω_{iso1} region.

To understand better the MAS dependence of the residual shift, Figure 2.4 shows the evolution of ΔR as a function of the MAS rate, ranging from 10 to 100 kHz, for the exact simulation and the three AHT versions. The

full third-order Hamiltonian agrees essentially completely with the numerical simulation from 20 kHz MAS upwards. As seen at 40 kHz in Figure 2.3, the secular Hamiltonian has slightly different residual shifts. The difference is greater at slower MAS but negligible at the fastest MAS rates. The average Hamiltonian truncated to second order has a significantly larger error and converges much more slowly. Notably, all three average Hamiltonians in Figure 2.3 and 2.4 produce a residual shift. For the secular average Hamiltonian, the third order shift term is diagonal in the eigenbasis of $|\mathrm{m_{I1z}}, \mathrm{m_{I2z}}\rangle$, and therefore the residual shift observed in the spectra is identical to the magnitude of the coefficient of the third order secular term in Eq. 2.26, and consequently follows a ω_r^{-2} dependence.

However, for the average Hamiltonian truncated to second order, the observed residual shift does not follow a ω_r^{-1} dependence, and is different from the magnitude of the coefficient of the second order non secular term in Eq.s 2.21 and 2.22. This is because the zero-quantum term is non-secular in the eigenbasis (Eq. 2.28), and is then diagonalized to yield the resulting eigenvalue that gives the residual shift observed (Eq. 2.29). Since the smaller the off-diagonal terms are, the less they will contribute to the eigenvalues, for a fixed chemical shift difference, as the spinning speed is increased, the terms decrease as ω_r^{-1}, but the observed shift in the spectrum will in general drop off faster than that.

$$\bar{\boldsymbol{H}}(1)^{MAS} + \bar{\boldsymbol{H}}(2)^{MAS} = \begin{pmatrix} \frac{\Omega_{iso1}+\Omega_{iso2}}{2} & 0 & 0 & 0 \\ 0 & \frac{-\Omega_{iso1}+\Omega_{iso2}}{2} & \frac{-f_2(\Omega)\mathrm{A}_{12}(\Omega_{iso1}-\Omega_{iso2})}{\omega_r} & 0 \\ 0 & \frac{f_2(\Omega)\mathrm{A}_{12}(\Omega_{iso1}-\Omega_{iso2})}{\omega_r} & \frac{\Omega_{iso1}-\Omega_{iso2}}{2} & 0 \\ 0 & 0 & 0 & \frac{-\Omega_{iso1}-\Omega_{iso2}}{2} \end{pmatrix} \tag{2.28}$$

After diagonalization, the eigenstates $\{|1\rangle, |2\rangle, |3\rangle$ and $|4\rangle\}$ of the 2 spin systems are:

$$\begin{pmatrix} \frac{\Omega_{iso1}+\Omega_{iso2}}{2} \\ \frac{(\Omega_{iso1}-\Omega_{iso2})\sqrt{4{A_{12}}^2 f_2(\Omega^D)^2+{\omega_r}^2}}{\omega_r} \\ -\frac{(\Omega_{iso1}-\Omega_{iso2})\sqrt{4{A_{12}}^2 f_2(\Omega^D)^2+{\omega_r}^2}}{\omega_r} \\ \frac{-\Omega_{iso1}-\Omega_{iso2}}{2} \end{pmatrix} \tag{2.29}$$

The eigenvalues are identical but of opposite sign, therefore the four allowed transitions will give only two different transition frequencies, and no splittings, as observed in the spectrum of Figure 2.3. The eigenvalue $|2\rangle$ and the $|2\rangle$-$|1\rangle$ transition frequency as a function of ω_r for the second-order truncated average Hamiltonian, for the two-spin systems example in Figure 2.2, is displayed in Figure 2.15.

In the full average Hamiltonian, on top of the second order zero quantum term and the secular shift term, there is the non-secular zero-quantum term. The eigenstates $\{|1\rangle, |2\rangle, |3\rangle$ and $|4\rangle\}$ for the full average Hamiltonian are:

$$\begin{pmatrix} \frac{\Omega_{iso1}+\Omega_{iso2}}{2} \\ \frac{(\Omega_{iso1}-\Omega_{iso2})\sqrt{4{A_{12}}^4 f_{3s}(\Omega)^2+{\omega_r}^4+4{A_{12}}^2(f_{3ns}^2(\Omega)^2+(f_2^2(\Omega)^2+f_{3s}^2(\Omega)^2){\omega_r}^2)}}{{\omega_r}^2} \\ -\frac{(\Omega_{iso1}-\Omega_{iso2})\sqrt{4{A_{12}}^4 f_{3s}(\Omega)^2+{\omega_r}^4+4{A_{12}}^2(f_{3ns}^2(\Omega)^2+(f_2^2(\Omega)^2+f_{3s}^2(\Omega)^2){\omega_r}^2)}}{{\omega_r}^2} \\ \frac{-\Omega_{iso1}-\Omega_{iso2}}{2} \end{pmatrix} \quad (2.30)$$

The eigenvalue |2⟩ and the |2⟩-|1⟩ transition frequency as a function of ω_r are shown in Figure 2.16 The ΔR of Ω_{iso1} is also plotted as a function of ω_r and compared to the numerical results in Figure 2.17.

In general, the full ω_r dependence of the shifts is a sum of an ω_r^2 and ω_r^4 term, divided by ω_r^2. Nakai and McDowell[108] and Levitt *et al..*[106] have previously considered that in the fast MAS limit in a two-spin systems the overall dependence of the secular terms is expected to be ω_r^{-2}. In this limit Levitt *et al..*[106] obtain the same dipolar coupling and chemical shift difference dependence as $\Delta R(3)_{sec}^{MAS}$ of Eq. 2.26 here.

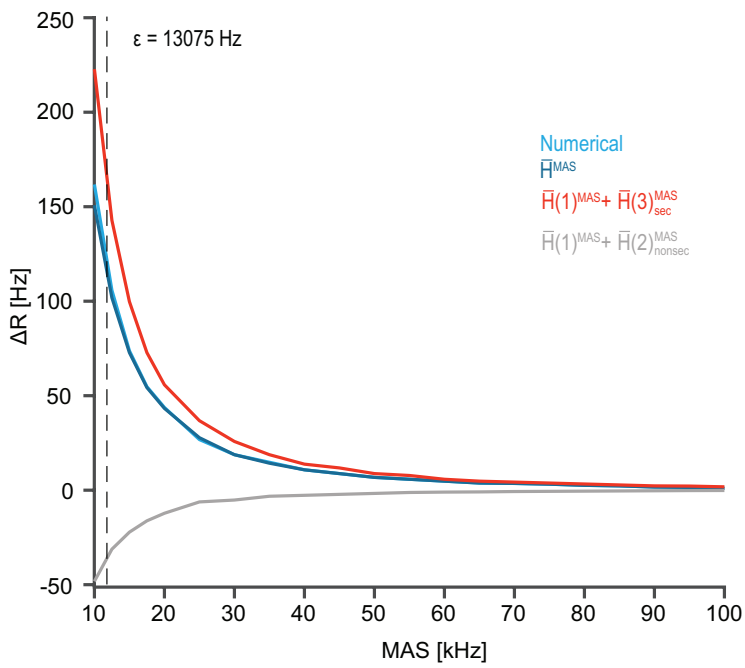

Figure 2.4 Residual shift evolution(ΔR) as function of the MAS rate of the peak in the Ω_{iso1} region of a two-spin systems in a single orientation, with the parameters given in Figure 2.3. The blue line is the exact numerical simulation, the red line represents the secular Hamiltonian until third order, the gray line represents the full Hamiltonian until second order and and the black lines are the full representation of the Hamiltonian to 3rd order, including the non-secular terms.

The dependence on the chemical shift difference predicted by AHT is also confirmed in exact simulations. Figure 2.19 shows the evolution of the residual shift at a MAS rate of 40 kHz as the chemical shift difference (Ω_{iso1}-Ω_{iso2}) is increased. The observed residual shift increases linearly with (Ω_{iso1}-Ω_{iso2}), as shown by Figure 2.18, indicating that the secular term of Eq. 2.26 is dominant, and the square term of the eigenvalue has a small contribution to the residual shift. Similarly, the analysis was extended to the dipolar coupling dependence in Figure 2.20. The residual shift increases in a more strongly coupled systems as predicted by Eq. 2.22, 2.24 and 2.26. The dipolar coupling strength was increased from 0 to 40 kHz, and the fitting in Figure 2.19 shows the good agreement to the dependence found in the eigenvalue of Eq. 2.30.

These dependencies are valid in the fast-spinning regime (Eq. 2.13). In the slow to intermediate spinning regime, the numerical simulations show the opposite effect with the chemical shift difference and the MAS rate on the residual shift evolution (Figure 2.20 and 2.21).

In summary, it is important to note that the Hamiltonian terms of Eq. 2.27 lead to shifts in the resonance positions, and not to splittings (even if the underlying operators include two-spin terms). This is in agreement with the previous work on two-spin systems in references 104 and 105.

These crystallite orientation dependent shifts cause broadening in a powder sample (see below) and prevent the obtention of a pure isotropic spectrum at fast MAS. In the fast-spinning regime, the full Hamiltonian description agrees essentially completely with the numerical simulation. The analytical integration to fourth order is computational demanding, however for numerical example of two spins system at 50 kHz MAS, the fourth order integration gives ($I_1^+I_2^- - I_1^-I_2^+$) as spin operators, but with a space part negligible compared to the lower orders. The magnitude of the space part, for this case, is 100 times smaller than the second order terms.

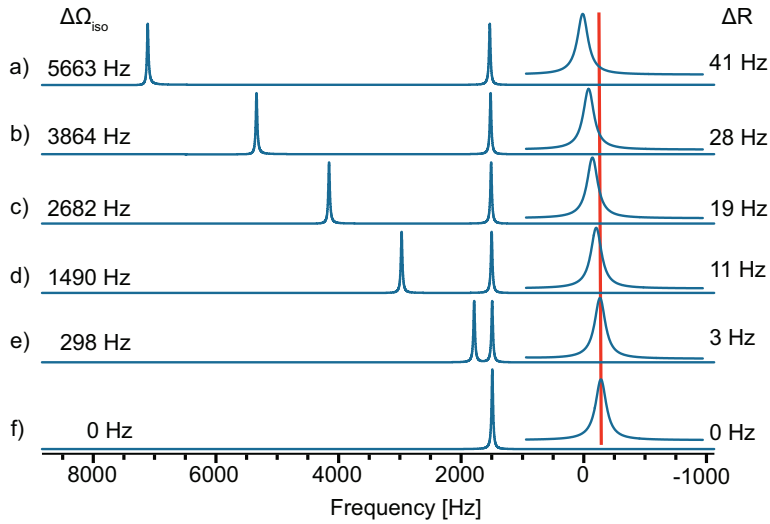

Figure 2.5 Effect of the chemical shift difference for a two-spin systems. The isotropic shift Ω_{iso1} was set to 1490 Hz, while Ω_{iso2} is varied. The difference in chemical shift between the two spins ($\Delta\Omega_{iso}$) is shown for each spectrum (a)-f)), as well the observed residual shift (ΔR) for Ω_{iso1}. The other parameters are the same as in Figure 2.2. The zoom on the right refers to the Ω_{iso1} region. The red line refers to isotropic shift of Ω_{iso1}. In all spectra, the MAS rate was set to 40 kHz.

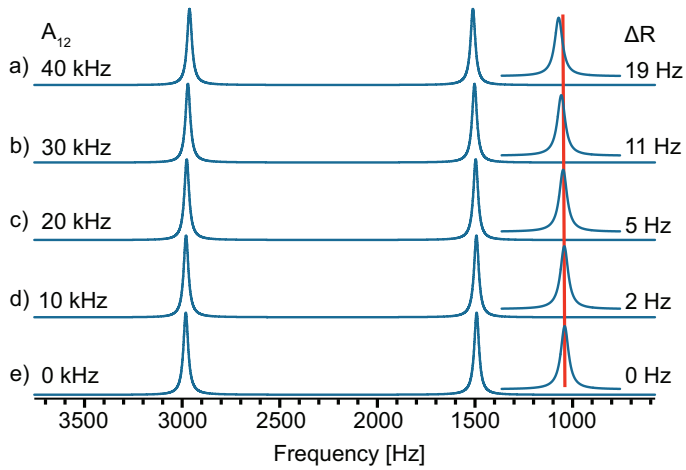

Figure 2.6 Effect of the magnitude of the dipolar coupling on the spectra of a two spin systems. The isotropic shift of Ω_{iso1} was set to 1490 Hz and Ω_2 to 2980 Hz. The dipolar coupling between the two spins ($A_{12}D^2_{0,0}(\Omega^D)$) is shown for each spectrum, as well the observed residual shift (ΔR) for Ω_{iso1}. The other parameters are the same as in Figure 2.2. The zoom on the right refers to the Ω_{iso1} region. The red line refers to isotropic shift of Ω_1. In all spectra, the MAS was set to 40 kHz.

Following these results, the AHT treatment is now extended to three spin systems.

2.2.3.5 AHT Treatment for 3 Spin Systems

We consider again a single orientation of a three-spin dipolar coupled system, with inequivalent isotropic chemical shifts, neglecting CSA. This time, the average Hamiltonian is expressed in the eigenbasis $|\mathrm{m_{I1z}}, \mathrm{m_{I2z}}, \mathrm{m_{I3z}}\rangle$ of the operators I_{1z}, I_{2z} and I_{3z}.

1st order

Similarly, to the 2-spin case, the dipolar interactions vanish at first order for MAS, and the resulting Hamiltonian only contains the isotropic terms:

$$\bar{H}(1)^{MAS} = \Omega_1 I_{1z} + \Omega_2 I_{2z} + \Omega_3 I_{3z} \tag{2.31}$$

2nd order

The compact expression of the second order term for spinning at the magic angle is

$$\begin{aligned}\bar{H}(2)^{MAS}_{nonsec} = -\frac{i}{\omega_{MAS}}(&\Delta D(2)_{12}(I_1^- I_2^+ - I_1^+ I_2^-) + \Delta D(2)_{13}(I_1^- I_3^+ - I_1^+ I_3^-) \\ &+ \Delta D(2)_{23}(I_2^- I_3^+ - I_2^+ I_3^-) + \Delta D(2)_{1z23}(I_{1z} I_2^+ I_3^- - I_{1z} I_2^- I_3^+) \\ &+ \Delta D(2)_{12z3}(I_1^+ I_{2z} I_3^- - I_1^- I_{2z} I_3^+) + \Delta D(2)_{123z}(I_1^+ I_2^- I_{3z} - I_1^- I_2^+ I_{3z}))\end{aligned} \tag{2.32}$$

where

$$\Delta D(2)_{\mathrm{ij}} = A_{ij}\left(\Omega_{iso\mathrm{i}} - \Omega_{iso\mathrm{j}}\right) f(\alpha_{PR}^{ij}, \beta_{PR}^{ij}) \tag{2.33}$$

and

$$\begin{aligned}\Delta D(2)_{\mathrm{ijkz}} = (A_{ij}A_{ikz}) f_1\left(\alpha_{PR}^{ij}, \beta_{PR}^{ij}, \alpha_{PR}^{ikz}, \beta_{PR}^{ikz}\right) + (A_{ij}A_{jkz}) f_2\left(\alpha_{PR}^{ij}, \beta_{PR}^{ij}, \alpha_{PR}^{jkz}, \beta_{PR}^{jkz}\right) \\ + (A_{ikz}A_{jkz}) f_3\left(\alpha_{PR}^{ikz}, \beta_{PR}^{jkz}, \alpha_{PR}^{ikz}, \beta_{PR}^{jkz}\right)\end{aligned} \tag{2.34}$$

and where $f(\alpha, \beta)$ are trigonometric functions of the Euler angles.The ΔD terms originate both shift and splitting in the spectrum. The full expressions for the ΔD terms are given in the Appendix I. These terms show the same MAS rate dependence as in the 2 spin case, and the corresponding operators do not commute with the Zeeman interaction. The amplitudes depend on the chemical shift differences and dipolar couplings for the two spins involved in the ZQ term. In addition, for the three-spin case, we see new three spin operator terms, which are a product between a longitudinal single spin operator and the zero-quantum terms of the two other spins. In the fast MAS regime considered these terms do not depend on the chemical shift differences. The space part in Eq. 2.34 consists of a sum of 2x3 terms, where each pair depends on the product of two different dipolar couplings ($A_{12}A_{13}$, $A_{12}A_{23}$ and $A_{13}A_{23}$).

3rd order

The analytical expression in 3rd order for three spins starts to be more computationally demanding. There are more operators and their space part becomes more intricate. The full expressions of the space part of each term are presented in the Appendix I. The secular condensed part is

$$\begin{aligned}\bar{H}(3)^{MAS}_{sec} = \frac{1}{\omega_{MAS}^2}(&\Delta R(3)_1 I_{1z} + \Delta R(3)_2 I_{2z} + \Delta R(3)_3 I_{3z} + \Delta C(3)_{\mathrm{sec12}} I_{1z} I_{2z} \\ &+ \Delta C(3)_{\mathrm{sec13}} I_{1z} I_{3z} + \Delta C(3)_{\mathrm{sec23}} I_{2z} I_{3z})\end{aligned} \tag{2.35}$$

where

$$\Delta R(3)_i = A_{ij}{}^2(\Omega_{iso\mathrm{i}} - \Omega_{iso\mathrm{j}})f(\alpha_{PR}^{ij}, \beta_{PR}^{ij}) + A_{ik}{}^2(\Omega_{iso\mathrm{i}} - \Omega_{isok})f(\alpha_{PR}^{ik}, \beta_{PR}^{ik}) \tag{2.36}$$

and

$$\begin{aligned}\Delta C(3)_{\mathrm{secij}} = {} & A_{ij}{}^2 A_{ik} f_1(\alpha_{PR}^{ij}, \beta_{PR}^{ij}, \alpha_{PR}^{ik}, \beta_{PR}^{ik}) + A_{ij}{}^2 A_{jk} f_1(\alpha_{PR}^{ij}, \beta_{PR}^{ij}, \alpha_{PR}^{jk}, \beta_{PR}^{jk}) \\ & + A_{ik}{}^2 A_{jk} f_1(\alpha_{PR}^{ik}, \beta_{PR}^{ik}, \alpha_{PR}^{jk}, \beta_{PR}^{jk}) \\ & + A_{ij} A_{ik} A_{jk} f_1(\alpha_{PR}^{ij}, \beta_{PR}^{ij}, \alpha_{PR}^{ik}, \beta_{PR}^{ik}, \alpha_{PR}^{jk}, \beta_{PR}^{jk}) \\ & + A_{ij} A_{ik}{}^2 f_1(\alpha_{PR}^{ij}, \beta_{PR}^{ij}, \alpha_{PR}^{ik}, \beta_{PR}^{ik}) + A_{ij}\, A_{jk}{}^2 f_1(\alpha_{PR}^{ij}, \beta_{PR}^{ij}, \alpha_{PR}^{jk}, \beta_{PR}^{jk}) \\ & + A_{ik}\, A_{jk}{}^2 f_1(\alpha_{PR}^{ik}, \beta_{PR}^{ik}, \alpha_{PR}^{jk}, \beta_{PR}^{jk})\end{aligned} \tag{2.37}$$

with the non-secular part

$$\begin{aligned}\overline{H}(3)_{nonsec}^{MAS} = {} & \frac{1}{\omega_{MAS}{}^2}(\Delta D(3)_{\mathrm{nonsec12}}(I_1^- I_2^+ + I_1^+ I_2^-) + \Delta D(3)_{\mathrm{nonsec13}}(I_1^- I_3^+ + I_1^+ I_3^-) \\ & + \Delta D(3)_{\mathrm{nonsec23}}(I_2^- I_3^+ + I_2^+ I_3^-) + \Delta D(3)_{\mathrm{nonsec1z23}}(I_{1z} I_2^+ I_3^- + I_{1z} I_2^- I_3^+) \\ & + \Delta D(3)_{\mathrm{nonsec12z3}}(I_1^+ I_{2z} I_3^- + I_1^- I_{2z} I_3^+) + \Delta D(3)_{\mathrm{nonsec123z}}(I_1^+ I_2^- I_{3z} \\ & + I_1^- I_2^+ I_{3z}\end{aligned} \tag{2.38}$$

where

$$\begin{aligned}\Delta D(3)_{\mathrm{nonsecij}} = {} & A_{ij}\, A_{ik}{}^2 f_1(\alpha_{PR}^{ij}, \beta_{PR}^{ij}, \alpha_{PR}^{jk}, \beta_{PR}^{jk}) + A_{ij}\, A_{jk}{}^2 f_1(\alpha_{PR}^{ij}, \beta_{PR}^{ij}, \alpha_{PR}^{jk}, \beta_{PR}^{jk}) \\ & + A_{ik}\, A_{jk}{}^2 f_1(\alpha_{PR}^{ik}, \beta_{PR}^{ik}, \alpha_{PR}^{jk}, \beta_{PR}^{jk}) + A_{jk}\, A_{ik}{}^2 f_1(\alpha_{PR}^{xy}, \beta_{PR}^{xy}, \alpha_{PR}^{yz}, \beta_{PR}^{yz}) \\ & + A_{ij} A_{ik} A_{jk} f_1(\alpha_{PR}^{ij}, \beta_{PR}^{ij}, \alpha_{PR}^{ik}, \beta_{PR}^{ik}, \alpha_{PR}^{jk}, \beta_{PR}^{jk}) + A_{ij}(\, 2\Omega_{isoi}\Omega_{isoj} - \Omega_{isoi}^2 \\ & - \Omega_{isoj}^2) f_1(\alpha_{PR}^{ij}, \beta_{PR}^{ij})\end{aligned} \tag{2.39}$$

and

$$\begin{aligned}\Delta D(3)_{\mathrm{nonsecijkz}} = {} & A_{ij} A_{ikz}(\Omega_{isoi} - \Omega_{isoj}) f_1(\alpha_{PR}^{ij}, \beta_{PR}^{ij}, \alpha_{PR}^{ikz}, \beta_{PR}^{ikz}) \\ & + A_{ij} A_{jkz}(\Omega_{isoi} - \Omega_{isoj}) f_1(\alpha_{PR}^{ij}, \beta_{PR}^{ij}, \alpha_{PR}^{jkz}, \beta_{PR}^{jkz}) \\ & + A_{ikz} A_{jkz}(\Omega_{isoi} + \Omega_{isoj} + \Omega_{isokz}) f_1(\alpha_{PR}^{ikz}, \beta_{PR}^{ikz}, \alpha_{PR}^{jkz}, \beta_{PR}^{jkz})\end{aligned} \tag{2.40}$$

In the secular part, each residual shift term in Eq. 2.36 now consists of a sum of two terms, with each depending on the interaction with the one of the other spins. These dependences are analogous to the two spins case. Spin 2 has the opposite dependence on $A_{12}{}^2(\Omega_{iso2}-\Omega_{iso1})$ but now depends on $A_{23}{}^2(\Omega_{iso3}-\Omega_{iso2})$. Therefore, unlike in the two spins case, spin 1 and spin 2 will have different absolute residual shifts. Additionally, in the three-spin-case there is the appearance of new residual two-spin $I_{iz}I_{jz}$ type terms. Their full orientation dependence is given in the Appendix I, and has a series of dependences on the different dipolar couplings and their Euler angles. In the nonsecular terms there also zero-quantum terms analogous to the two-spin case, and new three-spin operator terms, as obtained in second order but with a more intricate orientation dependence. Notably, in the fast MAS regime, these zero quantum terms do not depend on the chemical shift differences.

In summary, compared to the two-spin case, the average Hamiltonian of the three-spin systems presents additional secular terms at third order and new non-secular three-spin operator terms, both in second and third order.

2.2.3.6 Effect on the MAS spectrum - three spins

The spin systems parameters used for the numerical examples are given in the caption to Figure 2.7 The Nakai parameters ϵ of Eq. 2.13 for the three pairwise dipolar interactions are 14 kHz for A_{12}, 15 kHz for A_{13} and 20 kHz for A_{23}. In this strongly coupled system, the single-orientation spectrum of a static sample shown in Figure 2.7 and contains the expected transitions for three-spin systems. The pure isotropic spectrum (Figure 2.7) naturally consists of only the three isotropic resonances.

The effect of MAS on the single orientation three spin systems is shown in Figure 2.7. As for the two spins case, the spectra contain residual shifts from the isotropic frequency. The magnitude of these shifts is now a sum of terms, and in general is likely to be larger than seen in the two-spin systems. For example, at 100 kHz MAS, the residual shift of spin 1, shown in the Figure, is still 26 Hz.

Most notably, in contrast to the 2-spin case, there are now also residual splittings on all three resonances, as predicted by the appearance of $I_{iz}I_{jz}$ type terms at third order in the AHT analysis (Eq. 2.35). The non-secular second and third order terms also lead to both shifts and splittings. The ensemble leads to all three spins showing a doublet of doublets, corresponding to the twelve principal transition frequencies from the eigenbasis $|m_{I1z}, m_{I2z}, m_{I3z}\rangle$. As expected, the splitting due to the couplings decreases with increasing MAS rate.

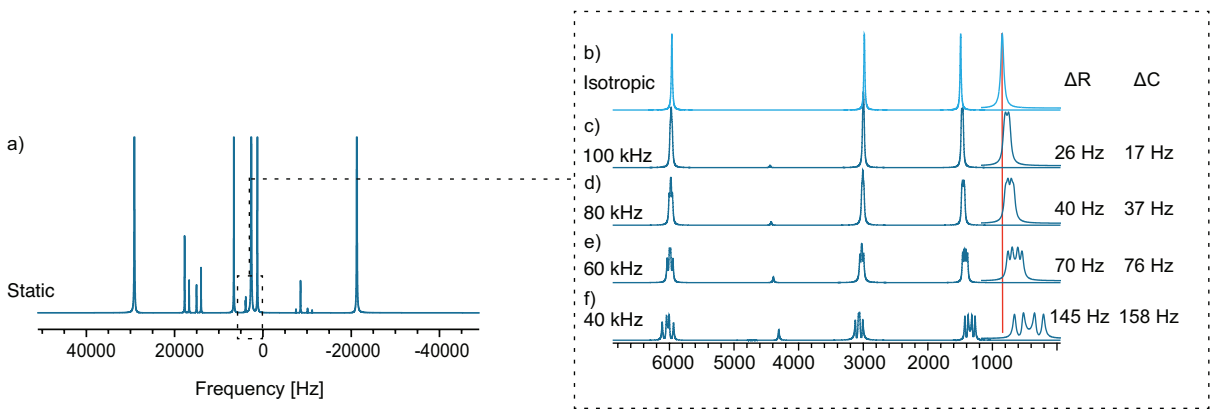

Figure 2.7 Static (a)), Isotropic(b)) and MAS (c-f)) spectra of three-spin systems in a single orientation. Ω_{iso1} = 1490 Hz, Ω_{iso2} = 2980 Hz and Ω_{iso3} = 5960 Hz. The couplings are A_{12} = 30 kHz , A_{13} = 35 kHz and A_{23} = 40 kHz. The corresponding Euler angles for the crystal to rotor frame transformation are: $\{\alpha_{12}, \beta_{12}, \gamma_{12}\} = \{60°, 45°, 30°\}$; $\{\alpha_{13}, \beta_{13}, \gamma_{13}\} = \{45°, 60°, 60°\}$; $\{\alpha_{23}, \beta_{23}, \gamma_{23}\} = \{30°, 36°, 30°\}$. In this orientation, in the lab frame, the couplings correspond to 14.3 kHz , 15.2 kHz and 19.8 kHz. The zoom on the right shows the Ω_1 region. The red line indicates the isotropic shift Ω_1. The spectra were calculated with SPINACH as detailed in the Appendix. An exponential linebroadening of 20 Hz was applied to all the FIDs prior to Fourier transformation.

As for the two spin cases, the ω_r dependence in general does not simply follow the amplitude of the coefficient for the non-secular off-diagonal terms, whose effect will decay more rapidly as ω_r is increased. The matrix representation of the full Hamiltonian and the resulting eigenvalues are not displayed due to the complexity and length of the terms but, as for the two spins, the eigenstates have both a polynomial ω_r dependence, up to the sixth power, and a ω_r^{-2} dependence.

Figure 2.8 shows comparisons of the spectra, at 80 kHz MAS, obtained with different levels of AHT and the full numerical simulation, as in Figure 2.3. At this MAS rate and with this spin system, the full third-order Hamiltonian from AHT is in essentially complete agreement with the numerical simulation, with both of them indicating a ΔR of 40 Hz. The numerical simulation presents a ΔC of 37 Hz, whereas the full Hamiltonian shows a ΔC of 40 Hz. The secular Hamiltonian presents a different lineshape from the exact simulation, with a ΔR of -22 Hz and a ΔC of 99 Hz. Finally, truncating the Hamiltonian to second order leads to a relatively large error in the prediction, and predicts ΔR of 58 Hz and a ΔC of 60 Hz.

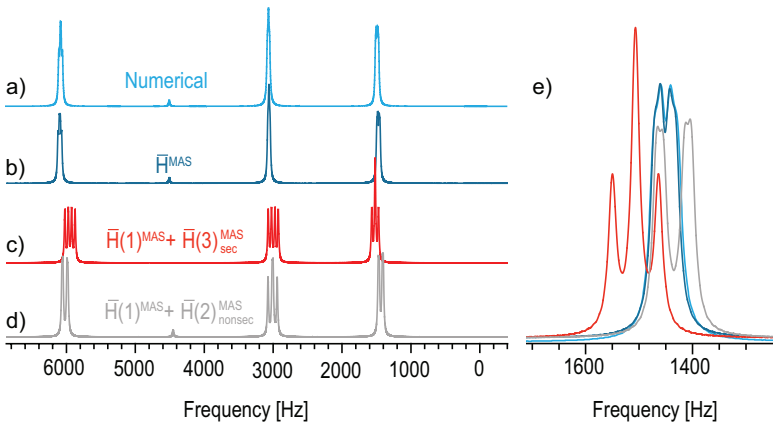

Figure 2.8 Comparison of spectrum obtained with full numerical simulation (a)) and the spectra obtained with the different AHT versions: the full Hamiltonian up to third order (b)), the secular part of the Hamiltonian up to third order (c)), and the second order Hamiltonian (d)). The spectra were simulated at 80 kHz MAS and the spin systems used is the same as in Figure 2.7. The zoom on e) shows the Ω_{iso1} region.

As in the two-spins case, Figure 2.9 shows the evolution of ΔR and ΔC as a function of the MAS rate, ranging from 40 to 100 kHz, for the exact simulation and the three AHT versions. As expected, the full third order average Hamiltonian once again shows the best agreement with the exact simulation. The second order truncated version has better agreement than the secularised approach, but are still significantly different from the full Hamiltonian. The full description of the average Hamiltonian is again needed in order to simulate accurate spectra, and the ω_r dependence is that of the eigenvalues from the full average Hamiltonian.

Looking in more detail at the behaviour, the observed ΔR (the difference between Ω_{iso} and the center of gravity of the multiplet) and ΔC (the width of the multiplet) for Ω_{iso1} are shown in Figure 2.9. For the other two spins, the evolution is shown in the Appendix, Figure 2.22 and 2.23.

Since ΔR and ΔC have different orientation dependencies, each spin presents a different absolute ratio between the two effects, here varying between 1.00 and 0.36.

The chemical shift difference is also an important parameter. In the two spins systems, we saw that when the spins are equivalent, all the higher order terms (N>1) vanish. However, in a three-spin system, we see that some of the terms do not depend on the chemical shift difference [e.g., in Eqs. 2.34, 2.37 and 2.39], and so they remain even when the chemical shift difference is zero. Conventionally, a larger chemical shift difference should render the system inhomogeneous. The chemical shift difference needs to be associated with a non-negligible homonuclear dipolar coupling in order for the higher order terms dependent on the chemical shift difference to be relevant. If the chemical shift difference is very large then usually the dipolar coupling of that spin pair is much weaker than couplings associated with spin pairs that a have a more similar chemical shift. Additionally, there are no higher order terms solely dependent on the chemical shift difference, unlike terms only dependent on the dipolar couplings.

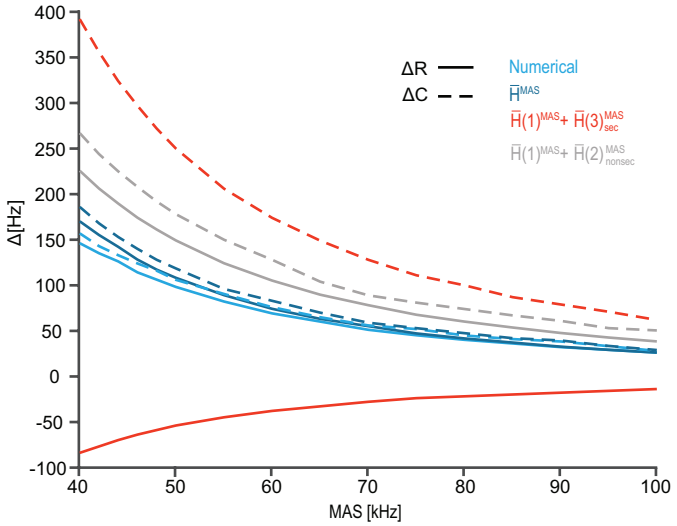

Figure 2.9 Residual shift (ΔR) and residual coupling (ΔC) evolution as function of the MAS rate (from 40 kHz to 100 kHz, in steps of 5 kHz.) of the peak in the Ω_{iso1} region of three-spin systems in a single orientation, with the parameters given in Figure 2.7. The blue line is the exact numerical simulation, the red line represents the secular Hamiltonian until third order, the gray blue line represent the full Hamiltonian until second order and and the dark blue lines are the full representation of the Hamiltonian until 3rd order, with the non-secular terms. The ΔR and ΔC evolution for the two other spins are available in the Appendix I, Figure 2.20 and 2.21.

We see that, in the regime of fast MAS, as for the two-spin case, increasing the chemical shift difference will lead to larger residuals, and this is confirmed in the SpinDynamica simulations of the residual couplings as a function of MAS rate shown in figure 2.24, and where we see that the residual couplings have a polynomial dependence on the MAS rate.

In summary, third order AHT provides an accurate description of the three-spin systems in the fast MAS regime. In comparison to the two-spin systems we see that faster MAS rates are necessary to provide the same level of averaging, as might be expected for a more strongly coupled system. More interestingly, while the residuals in the two-spin systems only led to shifts away from the isotropic positions, in the three-spin systems we see in addition the appearance of residual splittings. The two effects have similar magnitudes.

2.2.3.7 Effects of a π pulse

There is an important distinction between the linewidth observed in the spectrum, which is the focus of this study, and the dephasing time observed in a spin-echo experiment (often referred to as T_2'). This difference can be explained if we calculate the effect of a spin-echo (τ-π- τ) on the average Hamiltonian of Eq.s 2.31 to 2.40, which yields

$$\bar{H}(2)^{echo}_{nonsec} = -\frac{i}{\omega_{MAS}}(\Delta D(2)_{1z23}(I_{1z}I_2^+I_3^- - I_{1z}I_2^-I_3^+) + \Delta D(2)_{12z3}(I_1^+I_{2z}I_3^- - I_1^-I_{2z}I_3^+) + \Delta D(2)_{123z}(I_1^+I_2^-I_{3z} - I_1^-I_2^+I_{3z}))$$

$$\bar{H}(3)^{echo}_{sec} = \frac{1}{\omega_{MAS}^2}(\Delta C(3)_{\mathrm{sec}12}I_{1z}I_{2z} + \Delta C(3)_{\mathrm{sec}13}I_{1z}I_{3z} + \Delta C(3)_{\mathrm{sec}23}I_{2z}I_{3z}) \qquad (2.41)$$

$$\bar{H}(3)^{MAS}_{nonsec} = \frac{1}{\omega_{MAS}{}^2}(\Delta D(3)_{\mathrm{nonsec}12}(I_1^-I_2^+ + I_1^+I_2^-) + \Delta D(3)_{\mathrm{nonsec}13}(I_1^-I_3^+ + I_1^+I_3^-) + \Delta D(3)_{\mathrm{nonsec}23}(I_2^-I_3^+ + I_2^+I_3^-))$$

We see that the Hamiltonian has been considerably simplified, as expected, and that the chemical shifts, and several of the residual terms, are refocused. For example, at second order the two spin terms, that depend on the difference in chemical shifts, are refocused as compared to Eq. 2.32, but the three spin terms, which only depend on products of dipolar couplings, are retained. Similar trends are seen in the third order terms.

2.2.4 Effect of MAS on Powder Line Shapes

Figure 2.10 shows the spectral lineshapes we expect from powders under fast MAS. Here we show exact numerical simulations, but they can also be calculated by summing spectra for different orientations using the third-order AHT expressions, and the results are found to be essentially identical. A two-angle REPULSION[235] grid of orientations was used to simulate the powder spectra.

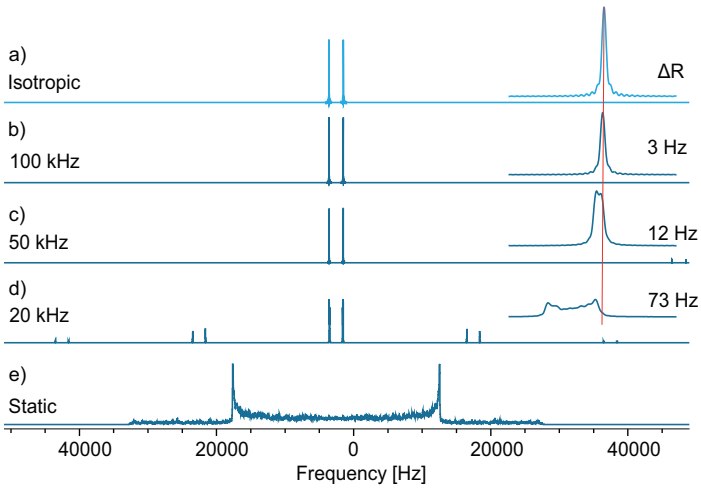

Figure 2.10 Effect of MAS on the spectrum of a two-spin systems summed over 200 different orientations on a two-angle repulsion grid. The spin system parameters were otherwise the same as in Figure 2.2. The zoom on the right shows the Ω_{iso1} (1490 Hz). The red line refers indicates Ω_{iso1}. An exponential linebroadening of 20 Hz was applied to all the FIDs prior to Fourier transformation. The spectra were calculated with SPINACH as detailed in the Appendix.

The static spectrum shows the expected Pake doublet[99]. As predicted in the AHT expressions for the single orientations, MAS removes the splitting in a powder, and reduces the spectrum to two single peaks and their spinning sidebands. Most importantly, since the residual shift ΔR is orientation dependent, the residual spectra are now made of narrow powder patterns, with characteristic lineshapes for mixed second and fourth rank interactions. The width of the powder patterns decreases with increasing MAS rates. Again, this is in full agreement with the previous treatments for two spin systems.[103, 106, 108] Perhaps most importantly, the center of gravity of the residual powder pattern is not at the isotropic chemical shift position, i.e., the ΔR tensor does not have a zero average. This leads to a residual shift ΔΔR of the whole resonance peak in the powder spectrum away from the isotropic value.

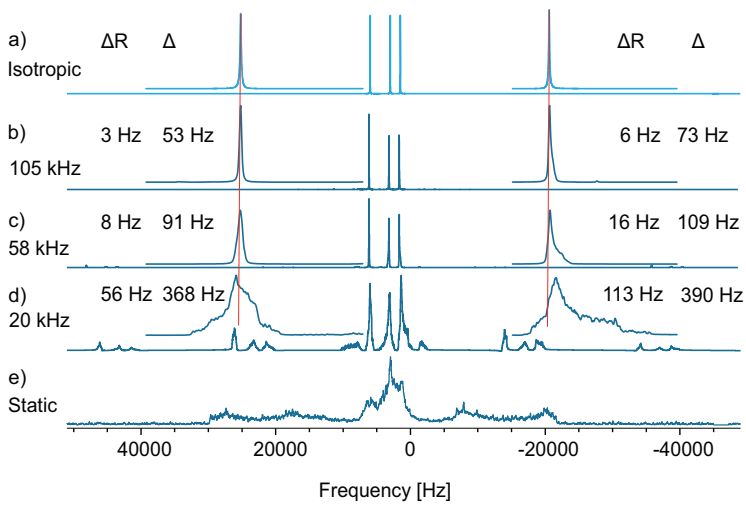

Figure 2.11 Effect of MAS on the spectrum of three-spin systems summed over 800 different orientations on a two-angle repulsion grid. The spin system parameters were otherwise the same as in Figure 2.7. The zooms on the left and the right show

the Ω_{iso3} (5960 Hz) and Ω_{iso1} (1490 Hz) regions respectively. The red line shows the isotropic shifts. An exponential linebroadening of 40 Hz was applied to all the FIDs prior to Fourier transformation. The spectra were calculated with SPINACH as detailed in the Appendix.

Figure 2.11 shows the powder lineshapes simulated for fast MAS spectra in the three-spin systems. In the fast MAS regime, we see asymmetric lineshapes that here are made up of the orientation dependent residual shifts, as well as the orientation dependent residual couplings. The patterns are thus broader than in the two-spin case. Again, perhaps most importantly, the center of gravity of the residual powder pattern is not at the isotropic chemical shift position. This again leads to a spin system and MAS rate dependent residual shift $\Delta\Delta R$ of the whole resonance peak in the powder spectrum away from the isotropic value.

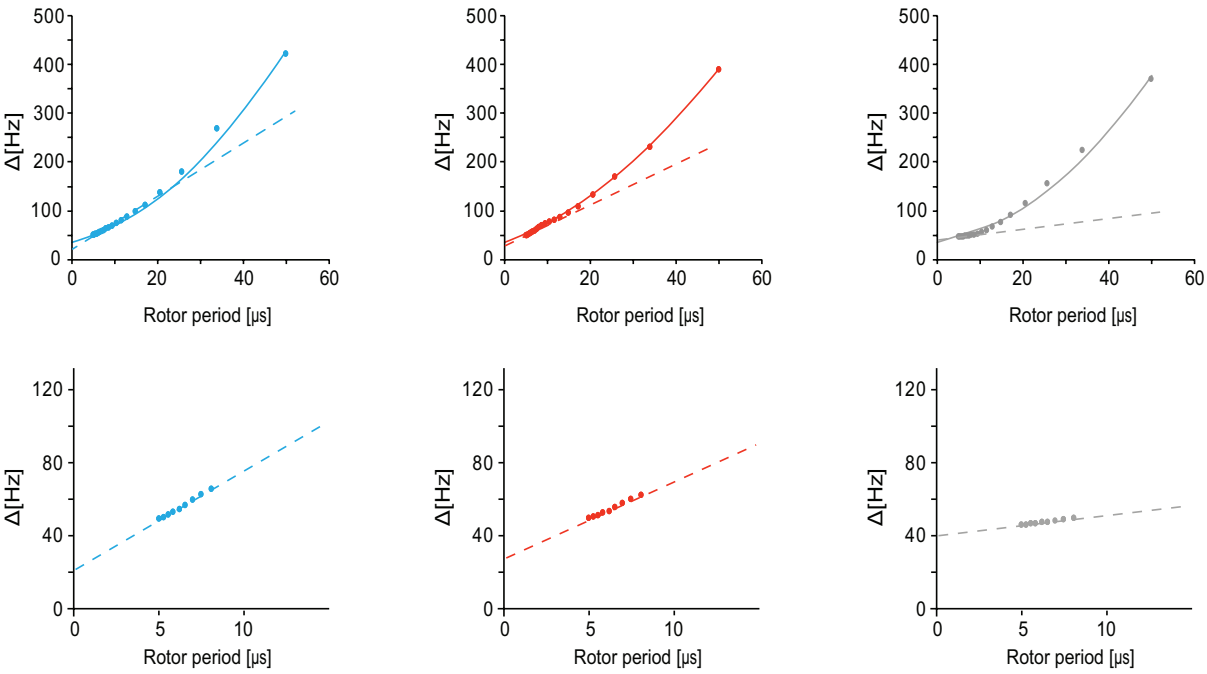

Figure 2.12 Residual linewidths as a function of the rotor period for Ω_{iso1} (red), Ω_{iso2} (blue), and Ω_{iso3} (gray) for the three-spin system simulated in Fig.2. 11. The MAS rates range from 20 to 200 kHz. In the upper panels, the whole range is plotted and they are fitted to a polynomial dependence (solid line). The dotted line corresponds to the fit of the 9 rates from 120 to 200 kHz MAS to a linear function. The lower panels show a zoomed-in image of this region. The spectra are obtained after applying an exponential line broadening of 40 Hz. The fit parameters are given in Table 2.2.

Figure 2.12 shows the MAS rate dependence of the linewidth at half-height (Δ) measured from the powder simulations for the three-spin system. In general, we observe that the linewidths show a polynomial behaviour. We note that for spin 3, there is a clear inverse linear regime at fast spinning rates, which intercepts at the value of the intrinsic linewidth (here 40 Hz due to the exponential broadening added to the simulations prior to Fourier transform). We also see that if we only look at the rates over a range from 90-200 kHz (lower panel), all three spins fit well to an inverse linear dependence. However, for spins 1 and 2, the intercept is at less than 40 Hz, which belies the underlying polynomial dependence. This is discussed further below.

2.2.5 Connection to Experiment

We note that the shifts of the peaks in MAS spectra of powders discussed above should be experimentally observable. Figure 2.13 shows the H1 and H3 regions of the echo detected ^{1}H MAS spectra of powdered L-tyrosine hydrochloride, with MAS rates from 82 to 90 kHz. All the spectra were acquired with a VT control set to 280 K. Both resonances shift to lower ppm as the MAS rate is increased.

We note that these measurements could easily be confounded by a systematic increase in the sample temperature as the MAS rate increases, due to frictional heating, if the chemical shifts are temperature dependent. To account for this, Figure 2.13 also shows the spectra recorded at a constant MAS rate (80 kHz), and as a function of the VT temperature. In this case there is also a shift of the two peaks observed, but in the

opposite direction. We believe this is a clear demonstration of the presence of MAS rate dependent shifts. Finally we note that very recently pure isotropic ^{1}H spectra have been recorded from variable MAS rate data, in which MAS rate dependent shifts were also observed, including in experiments with active temperature control.[236]

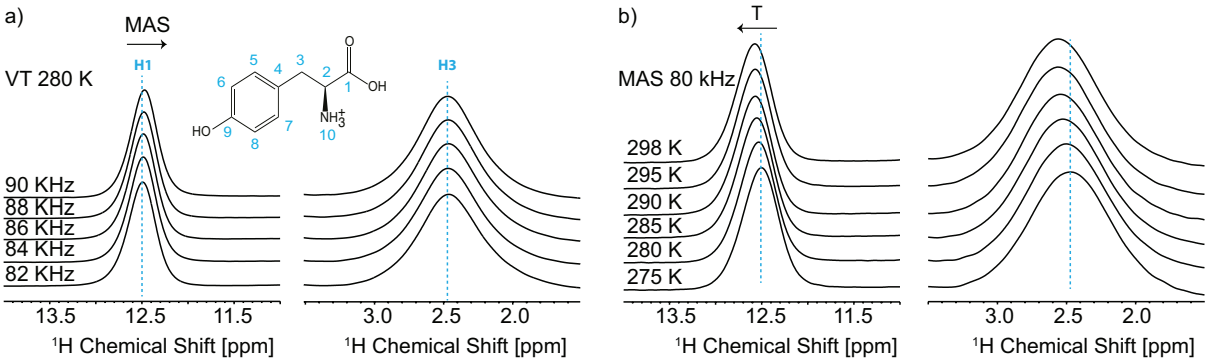

Figure 2.13 Echo-detected ^{1}H MAS spectra of powdered L-Tyrosine hydrochloride. Only the regions of protons H1 and H3 are displayed. (A) The VT temperature was set at 280 K, and the MAS rate was increased from 82 kHz to 90 kHz in steps of 2 kHz. (B) The MAS rate was set to 80 kHz and the VT temperature was increased from 275 K to 298K. All the spectra were acquired using a Bruker 0.7 mm room temperature HCN CP-MAS probe at a magnetic field of 18.8 T, corresponding to a ^{1}H frequency of 800 MHz.

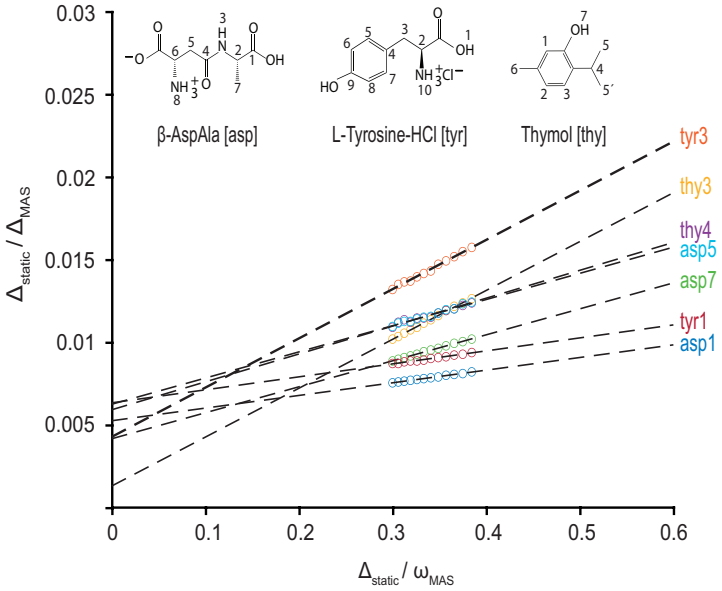

Figure 2.14 . Measured ^{1}H linewidths vs MAS rate from 78 to 100 kHz for selected resolved resonances in β-AspAla, L-Tyrosine-HCl and Thymol. The measured linewidth is scaled relative to the linewidth observed in a static sample whch was estimated to be 30 kHz. All the spectra were acquired using a Bruker 0.7 mm room temperature HCN CP-MAS probe at a magnetic field of 18.8 T, corresponding to a ^{1}H frequency of 800 MHz.

In addition to the residual shift, we have also investigated the evolution of the residual linewidth as function of the MAS rate in experimental data. Figure 2.14 shows the measured linewidth (scaled by the linewidth in the static sample) for resolved resonances in β-AspAla, L-tyrosine-hydrochloride and thymol. In each case the experimental residual linewidths fit well to an inverse linear dependence on MAS rate over the range from 78 to 100 kHz used here. However, as noted above in the discussion of Figure 2.12, a polynomial dependence is likely to fit well to an inverse linear behaviour over a given range, with the only indication being that the intercept would be underestimated. Since the exact intrinsic linewidth is not known in the experimental case, this might only become apparent if the polynomial dependence was strong enough to produce an intercept at less than zero.

2.2.6 Conclusion

The average Hamiltonian to third order was fully integrated for two and three spin systems in a single orientation, with isotropic chemical shifts and homonuclear dipolar couplings. For both two and three spin integrations, results showed that the full third-order expression of the Hamiltonian, without secular approximations or truncation to second-order, is the description that agrees the best, by far, with full numerical calculations. In particular, we consider the effect on the spectrum of the different residual terms as a function of the spinning rate, and of the dipolar coupling constant and the chemical shift difference.

For the two spins case, we confirm that the effect of the dipolar coupling is removed in first order, and a zero-quantum term appears both in second and third order, and a secular shift term appears in third order. These terms lead to the appearance of a residual shift in the fast MAS spectrum. The spinning rate dependence of the shift terms is not trivial, and the amplitude of the shift decreases as the spinning rate increases in general with as sum of an ω_r^2 and ω_r^4 term, divided by ω_r^2. In the fast MAS regime this leads to a behaviour that is well described by an overall ω_r^{-2} dependence.

In the three-spin case, on top of the zero quantum and residual shifts terms, there are also three spin operators, both in second and third order. Finally, there are also secular residual two-spin coupling terms in third order. The effect on the spectrum is now to produce a residual shift and residual splittings. Both the shift and splittings have a fairly complex dependence on spinning rate with the eigenstates having a polynomial ω_r dependence, up to the sixth power, and a ω_r^{-2} dependence.

In our simulations, for the spin system parameters and the spinning rates used here in these small two- and three-spin systems, the behaviour is well fit by an overall polynomial dependence. For one case we observe an inverse linear dependence on the MAS rate at the faster MAS rates.

The effect on powder patterns is also shown, and we find that the anisotropic residual shift does not have zero average, so that the powder lineshape is broadened and shifted from the isotropic position. This suggests that in ^{1}H MAS spectra, even at the fastest MAS attainable today, the positions observed are not exactly the isotropic shifts. The residual terms will be removed completely only at infinite MAS rate.

The spinning rate dependence found here, and the regimes observed in simulation and experiment in Figures 2.12 and 2.14, might explain some of the debate that can be found in the experimental literature. Brunner et al.[104], Challoner and McDowell[105], Spiess and coworkers[109, 111] and Zorin et al[113] reported an ω_r^{-1} dependence for the proton residual linewidth, while Ray et al[219], Sternberg et al[112] and Malar et al[107] and Schledron *et al.*.[220] observed good fits to polynomial ω_r^{-1} and ω_r^{-2} dependences.

Finally, we note that the some of the terms observed here are not refocused by a π pulse, and will be successfully removed with the anti-Z COSY and TAZ-COSY experiments, [213, 237] leading to narrower ^{1}H MAS spectra, whereas others are not. In constrast, in the very recently introduced pure-isotropic-proton (PIP) spectra, since both the shifts and the couplings are modulated by changing the MAS rate both sources of broadening are removed.[236]

2.2.7 Appendix I

2.2.7.1 Two Spins full expression terms at arbitrary angle

Second order

Spin part	Space part
$i(I_1^+I_2^- - I_1^-I_2^+)$	$\frac{3}{32\omega_r}\mathrm{A}_{12}(\Omega_{iso1} - \Omega_{iso2})\sin(\beta_{PR})\sin(\theta)\,(8\,cos(\beta_{PR})\,cos(\theta)\sin(\alpha_{PR}) + sin(2\alpha_{PR})\,sin(\beta_{PR})\,sin(\theta))$

Third order

Spin part	Space part
$(I_1^+I_2^- + I_1^-I_2^+)$	$\frac{3}{64{\omega_r}^2}A_{12}(\Omega_{iso1} - \Omega_{iso2})^2\sin(\beta_{PR})\sin(\theta)\,(16\,cos(\alpha_{PR})\,cos(\beta_{PR})\,cos(\theta) + cos(\alpha_{PR})^2\,sin(\beta_{PR})\,sin(\theta) - sin(\alpha_{PR})^2\,sin\,(\beta_{PR})sin\,(\theta))$
$(I_{1z} - I_{2z})$	$\frac{1}{512{\omega_r}^2}{A_{12}}^2(\Omega_{iso1} - \Omega_{iso2})\,sin(\beta_{PR})^2\,(-33 + 32\,cos(2\alpha_{PR})\,cos(\beta_{PR})^2 - 31\,cos(2\beta_{PR}) + cos(4\alpha_{PR})\,sin(\beta_{PR})^2 + 8\sqrt{2}sin\,(\alpha_{PR})sin\,(2\alpha_{PR})sin(2\beta_{PR})$

Fourth order (Numerically integrated)

Spin part
$(I_1^+I_2^- + I_1^-I_2^+)$

2.2.7.2 Three spins full expression terms at the magic angle

Second order

$(I_1^- I_2^+ - I_1^+ I_2^-)$	$-\frac{1}{\omega\mathrm{rot}} i \sin(\alpha\mathrm{A12})\,(\Omega 1 - \Omega 2)\left(0.353553\,\mathrm{A12}\sin(\beta\mathrm{A12})\cos(\beta\mathrm{A12}) - 0.125\,\mathrm{A12}\cos(\alpha\mathrm{A12})\sin^2(\beta\mathrm{A12})\right)$
$(I_1^- I_3^+ - I_1^+ I_3^-)$	$-\frac{1}{\omega\mathrm{rot}} i \sin(\alpha\mathrm{A13})\,(\Omega 1 - \Omega 3)\left(0.353553\,\mathrm{A13}\sin(\beta\mathrm{A13})\cos(\beta\mathrm{A13}) - 0.125\,\mathrm{A13}\cos(\alpha\mathrm{A13})\sin^2(\beta\mathrm{A13})\right)$
$(I_2^- I_3^+ - I_2^+ I_3^-)$	$-\frac{1}{\omega\mathrm{rot}} i \sin(\alpha\mathrm{A23})\,(\Omega 2 - \Omega 3)\left(0.353553\,\mathrm{A23}\sin(\beta\mathrm{A23})\cos(\beta\mathrm{A23}) - 0.125\,\mathrm{A23}\cos(\alpha\mathrm{A23})\sin^2(\beta\mathrm{A23})\right)$
$(I_{1z} I_2^+ I_3^- - I_{1z} I_2^- I_3^+)$	$-\frac{1}{2\,\omega\mathrm{rot}}$ $i\,(0.015625\,\mathrm{A12}\,\mathrm{A13}\sin^2(\beta\mathrm{A12})\sin^2(\beta\mathrm{A13})\sin(2\,(\alpha\mathrm{A12}-\alpha\mathrm{A13})) + 0.25\,\mathrm{A12}\,\mathrm{A13}\sin(\beta\mathrm{A12})\cos(\beta\mathrm{A12})\sin(\beta\mathrm{A13})\cos(\beta\mathrm{A13})\sin(\alpha\mathrm{A12}-\alpha\mathrm{A13}) + 0.03125\,\mathrm{A12}\,\mathrm{A23}\sin^2(\beta\mathrm{A12})\sin^2(\beta\mathrm{A23})\sin(2\,(\alpha\mathrm{A12}-\alpha\mathrm{A23})) + 0.5\,\mathrm{A12}\,\mathrm{A23}\sin(\beta\mathrm{A12})\cos(\beta\mathrm{A12})\sin(\beta\mathrm{A23})\cos(\beta\mathrm{A23})\sin(\alpha\mathrm{A12}-\alpha\mathrm{A23}) - 0.03125\,\mathrm{A13}\,\mathrm{A23}\sin^2(\beta\mathrm{A13})\sin^2(\beta\mathrm{A23})\sin(2\,(\alpha\mathrm{A13}-\alpha\mathrm{A23})) - 0.5\,\mathrm{A13}\,\mathrm{A23}\sin(\beta\mathrm{A13})\cos(\beta\mathrm{A13})\sin(\beta\mathrm{A23})\cos(\beta\mathrm{A23})\sin(\alpha\mathrm{A13}-\alpha\mathrm{A23}))$
$(I_1^+ I_{2z} I_3^- - I_1^- I_{2z} I_3^+)$	$-\frac{1}{2\,\omega\mathrm{rot}}$ $i\,(0.03125\,\mathrm{A12}\,\mathrm{A13}\sin^2(\beta\mathrm{A12})\sin^2(\beta\mathrm{A13})\sin(2\,(\alpha\mathrm{A12}-\alpha\mathrm{A13})) + 0.5\,\mathrm{A12}\,\mathrm{A13}\sin(\beta\mathrm{A12})\cos(\beta\mathrm{A12})\sin(\beta\mathrm{A13})\cos(\beta\mathrm{A13})\sin(\alpha\mathrm{A12}-\alpha\mathrm{A13}) + 0.015625\,\mathrm{A12}\,\mathrm{A23}\sin^2(\beta\mathrm{A12})\sin^2(\beta\mathrm{A23})\sin(2\,(\alpha\mathrm{A12}-\alpha\mathrm{A23})) + 0.25\,\mathrm{A12}\,\mathrm{A23}\sin(\beta\mathrm{A12})\cos(\beta\mathrm{A12})\sin(\beta\mathrm{A23})\cos(\beta\mathrm{A23})\sin(\alpha\mathrm{A12}-\alpha\mathrm{A23}) + 0.03125\,\mathrm{A13}\,\mathrm{A23}\sin^2(\beta\mathrm{A13})\sin^2(\beta\mathrm{A23})\sin(2\,(\alpha\mathrm{A13}-\alpha\mathrm{A23})) + 0.5\,\mathrm{A13}\,\mathrm{A23}\sin(\beta\mathrm{A13})\cos(\beta\mathrm{A13})\sin(\beta\mathrm{A23})\cos(\beta\mathrm{A23})\sin(\alpha\mathrm{A13}-\alpha\mathrm{A23}))$
$(I_1^+ I_2^- I_{3z} - I_1^- I_2^+ I_{3z})$	$-\frac{1}{2\,\omega\mathrm{rot}}$ $i\,(-0.03125\,\mathrm{A12}\,\mathrm{A13}\sin^2(\beta\mathrm{A12})\sin^2(\beta\mathrm{A13})\sin(2\,(\alpha\mathrm{A12}-\alpha\mathrm{A13})) - 0.5\,\mathrm{A12}\,\mathrm{A13}\sin(\beta\mathrm{A12})\cos(\beta\mathrm{A12})\sin(\beta\mathrm{A13})\cos(\beta\mathrm{A13})\sin(\alpha\mathrm{A12}-\alpha\mathrm{A13}) + 0.03125\,\mathrm{A12}\,\mathrm{A23}\sin^2(\beta\mathrm{A12})\sin^2(\beta\mathrm{A23})\sin(2\,(\alpha\mathrm{A12}-\alpha\mathrm{A23})) + 0.5\,\mathrm{A12}\,\mathrm{A23}\sin(\beta\mathrm{A12})\cos(\beta\mathrm{A12})\sin(\beta\mathrm{A23})\cos(\beta\mathrm{A23})\sin(\alpha\mathrm{A12}-\alpha\mathrm{A23}) + 0.015625\,\mathrm{A13}\,\mathrm{A23}\sin^2(\beta\mathrm{A13})\sin^2(\beta\mathrm{A23})\sin(2\,(\alpha\mathrm{A13}-\alpha\mathrm{A23})) + 0.25\,\mathrm{A13}\,\mathrm{A23}\sin(\beta\mathrm{A13})\cos(\beta\mathrm{A13})\sin(\beta\mathrm{A23})\cos(\beta\mathrm{A23})\sin(\alpha\mathrm{A13}-\alpha\mathrm{A23}))$

Third order

Non secular

$(I_1^- I_2^+ + I_1^+ I_2^-)$
$\frac{1}{16\,\omega\mathrm{rot}^2}\big(0.00976563\ \mathrm{A12}\ \mathrm{A13}^2 \cos(2\,(\alpha\mathrm{A12} - 2\,\alpha\mathrm{A13}))\sin^2(\beta\mathrm{A12})\sin^4(\beta\mathrm{A13}) -$ $0.0078125\ \mathrm{A13}^2\ \mathrm{A23}\cos(2\,\alpha\mathrm{A23})\sin^2(\beta\mathrm{A23})\sin^4(\beta\mathrm{A13}) +$ $0.0078125\ \mathrm{A13}^2\ \mathrm{A23}\cos(4\,\alpha\mathrm{A13} - 2\,\alpha\mathrm{A23})\sin^2(\beta\mathrm{A23})\sin^4(\beta\mathrm{A13}) +$ $0.0552427\ \mathrm{A12}\ \mathrm{A13}^2\cos(2\,\alpha\mathrm{A12} - \alpha\mathrm{A13})\cos(\beta\mathrm{A13})\sin^2(\beta\mathrm{A12})\sin^3(\beta\mathrm{A13}) -$ $0.0552427\ \mathrm{A12}\ \mathrm{A13}^2\cos(2\,\alpha\mathrm{A12} - 3\,\alpha\mathrm{A13})\cos(\beta\mathrm{A13})\sin^2(\beta\mathrm{A12})\sin^3(\beta\mathrm{A13}) +$ $0.0441942\ \mathrm{A13}^2\ \mathrm{A23}\cos(\alpha\mathrm{A13} - 2\,\alpha\mathrm{A23})\cos(\beta\mathrm{A13})\sin^2(\beta\mathrm{A23})\sin^3(\beta\mathrm{A13}) -$ $0.0441942\ \mathrm{A13}^2\ \mathrm{A23}\cos(3\,\alpha\mathrm{A13} - 2\,\alpha\mathrm{A23})\cos(\beta\mathrm{A13})\sin^2(\beta\mathrm{A23})\sin^3(\beta\mathrm{A13}) +$ $0.15625\ \mathrm{A12}\ \mathrm{A13}^2\cos(\alpha\mathrm{A12} - \alpha\mathrm{A13})\cos(\beta\mathrm{A12})\cos(\beta\mathrm{A13})\sin(\beta\mathrm{A12})\sin^3(\beta\mathrm{A13}) -$ $0.15625\ \mathrm{A12}\ \mathrm{A13}^2\cos(\alpha\mathrm{A12} + \alpha\mathrm{A13})\cos(\beta\mathrm{A12})\cos(\beta\mathrm{A13})\sin(\beta\mathrm{A12})\sin^3(\beta\mathrm{A13}) +$ $0.15625\ \mathrm{A12}\ \mathrm{A13}^2\cos(\alpha\mathrm{A12} - 3\,\alpha\mathrm{A13})\cos(\beta\mathrm{A12})\cos(\beta\mathrm{A13})\sin(\beta\mathrm{A12})\sin^3(\beta\mathrm{A13}) +$ $0.125\ \mathrm{A13}^2\ \mathrm{A23}\cos(\alpha\mathrm{A13} - \alpha\mathrm{A23})\cos(\beta\mathrm{A13})\cos(\beta\mathrm{A23})\sin(\beta\mathrm{A23})\sin^3(\beta\mathrm{A13}) +$ $0.125\ \mathrm{A13}^2\ \mathrm{A23}\cos(3\,\alpha\mathrm{A13} - \alpha\mathrm{A23})\cos(\beta\mathrm{A13})\cos(\beta\mathrm{A23})\sin(\beta\mathrm{A23})\sin^3(\beta\mathrm{A13}) -$ $0.125\ \mathrm{A13}^2\ \mathrm{A23}\cos(\alpha\mathrm{A13} + \alpha\mathrm{A23})\cos(\beta\mathrm{A13})\cos(\beta\mathrm{A23})\sin(\beta\mathrm{A23})\sin^3(\beta\mathrm{A13}) -$ $0.0078125\ \mathrm{A13}\ \mathrm{A23}^2\cos(2\,\alpha\mathrm{A13})\sin^4(\beta\mathrm{A23})\sin^2(\beta\mathrm{A13}) +$ $0.0078125\ \mathrm{A13}\ \mathrm{A23}^2\cos(2\,(\alpha\mathrm{A13} - 2\,\alpha\mathrm{A23}))\sin^4(\beta\mathrm{A23})\sin^2(\beta\mathrm{A13}) +$ $0.0441942\ \mathrm{A13}\ \mathrm{A23}^2\cos(2\,\alpha\mathrm{A13} - \alpha\mathrm{A23})\cos(\beta\mathrm{A23})\sin^3(\beta\mathrm{A23})\sin^2(\beta\mathrm{A13}) -$ $0.0441942\ \mathrm{A13}\ \mathrm{A23}^2\cos(2\,\alpha\mathrm{A13} - 3\,\alpha\mathrm{A23})\cos(\beta\mathrm{A23})\sin^3(\beta\mathrm{A23})\sin^2(\beta\mathrm{A13}) -$ $0.15625\ \mathrm{A12}\ \mathrm{A13}^2\cos(2\,(\alpha\mathrm{A12} - \alpha\mathrm{A13}))\cos^2(\beta\mathrm{A13})\sin^2(\beta\mathrm{A12})\sin^2(\beta\mathrm{A13}) -$ $0.125\ \mathrm{A13}^2\ \mathrm{A23}\cos(2\,(\alpha\mathrm{A13} - \alpha\mathrm{A23}))\cos^2(\beta\mathrm{A13})\sin^2(\beta\mathrm{A23})\sin^2(\beta\mathrm{A13}) -$ $0.125\ \mathrm{A13}\ \mathrm{A23}^2\cos(2\,(\alpha\mathrm{A13} - \alpha\mathrm{A23}))\cos^2(\beta\mathrm{A23})\sin^2(\beta\mathrm{A23})\sin^2(\beta\mathrm{A13}) -$ $0.0078125\ \mathrm{A12}\ \mathrm{A13}\ \mathrm{A23}\cos(2\,(\alpha\mathrm{A12} - \alpha\mathrm{A13} - \alpha\mathrm{A23}))\sin^2(\beta\mathrm{A12})\sin^2(\beta\mathrm{A23})\sin^2(\beta\mathrm{A13}) +$ $0.00390625\ \mathrm{A12}\ \mathrm{A13}\ \mathrm{A23}\cos(2\,(\alpha\mathrm{A12} + \alpha\mathrm{A13} - \alpha\mathrm{A23}))\sin^2(\beta\mathrm{A12})\sin^2(\beta\mathrm{A23})\sin^2(\beta\mathrm{A13}) +$ $0.00390625\ \mathrm{A12}\ \mathrm{A13}\ \mathrm{A23}\cos(2\,(\alpha\mathrm{A12} - \alpha\mathrm{A13} + \alpha\mathrm{A23}))\sin^2(\beta\mathrm{A12})\sin^2(\beta\mathrm{A23})\sin^2(\beta\mathrm{A13}) -$ $0.883883\ \mathrm{A12}\ \mathrm{A13}^2\cos(\alpha\mathrm{A12} - 2\,\alpha\mathrm{A13})\cos(\beta\mathrm{A12})\cos^2(\beta\mathrm{A13})\sin(\beta\mathrm{A12})\sin^2(\beta\mathrm{A13}) +$ $0.0220971\ \mathrm{A12}\ \mathrm{A13}\ \mathrm{A23}\cos(2\,\alpha\mathrm{A12} - 2\,\alpha\mathrm{A13} - \alpha\mathrm{A23})\cos(\beta\mathrm{A23})\sin^2(\beta\mathrm{A12})\sin(\beta\mathrm{A23})\sin^2(\beta\mathrm{A13}) -$ $0.0220971\ \mathrm{A12}\ \mathrm{A13}\ \mathrm{A23}\cos(2\,\alpha\mathrm{A12} - 2\,\alpha\mathrm{A13} + \alpha\mathrm{A23})\cos(\beta\mathrm{A23})\sin^2(\beta\mathrm{A12})\sin(\beta\mathrm{A23})\sin^2(\beta\mathrm{A13}) -$ $0.707107\ \mathrm{A13}^2\ \mathrm{A23}\cos(2\,\alpha\mathrm{A13} - \alpha\mathrm{A23})\cos^2(\beta\mathrm{A13})\cos(\beta\mathrm{A23})\sin(\beta\mathrm{A23})\sin^2(\beta\mathrm{A13}) +$ $0.707107\ \mathrm{A13}^2\ \mathrm{A23}\cos(\alpha\mathrm{A23})\cos^2(\beta\mathrm{A13})\cos(\beta\mathrm{A23})\sin(\beta\mathrm{A23})\sin^2(\beta\mathrm{A13}) +$ $0.0625\ \mathrm{A12}\ \mathrm{A13}\ \mathrm{A23}\cos(\alpha\mathrm{A12} + 2\,\alpha\mathrm{A13} - \alpha\mathrm{A23})\cos(\beta\mathrm{A12})\cos(\beta\mathrm{A23})\sin(\beta\mathrm{A12})\sin(\beta\mathrm{A23})\sin^2(\beta\mathrm{A13}) -$ $0.0625\ \mathrm{A12}\ \mathrm{A13}\ \mathrm{A23}\cos(\alpha\mathrm{A12} - 2\,\alpha\mathrm{A13} - \alpha\mathrm{A23})\cos(\beta\mathrm{A12})\cos(\beta\mathrm{A23})\sin(\beta\mathrm{A12})\sin(\beta\mathrm{A23})\sin^2(\beta\mathrm{A13}) -$ $0.0625\ \mathrm{A12}\ \mathrm{A13}\ \mathrm{A23}\cos(\alpha\mathrm{A12} - 2\,\alpha\mathrm{A13} + \alpha\mathrm{A23})\cos(\beta\mathrm{A12})\cos(\beta\mathrm{A23})\sin(\beta\mathrm{A12})\sin(\beta\mathrm{A23})\sin^2(\beta\mathrm{A13}) +$ $0.125\ \mathrm{A13}\ \mathrm{A23}^2\cos(\alpha\mathrm{A13} - \alpha\mathrm{A23})\cos(\beta\mathrm{A13})\cos(\beta\mathrm{A23})\sin^3(\beta\mathrm{A23})\sin(\beta\mathrm{A13}) -$ $0.125\ \mathrm{A13}\ \mathrm{A23}^2\cos(\alpha\mathrm{A13} + \alpha\mathrm{A23})\cos(\beta\mathrm{A13})\cos(\beta\mathrm{A23})\sin^3(\beta\mathrm{A23})\sin(\beta\mathrm{A13}) +$ $0.125\ \mathrm{A13}\ \mathrm{A23}^2\cos(\alpha\mathrm{A13} - 3\,\alpha\mathrm{A23})\cos(\beta\mathrm{A13})\cos(\beta\mathrm{A23})\sin^3(\beta\mathrm{A23})\sin(\beta\mathrm{A13}) +$ $0.707107\ \mathrm{A13}\ \mathrm{A23}^2\cos(\alpha\mathrm{A13})\cos(\beta\mathrm{A13})\cos^2(\beta\mathrm{A23})\sin^2(\beta\mathrm{A23})\sin(\beta\mathrm{A13}) -$ $0.707107\ \mathrm{A13}\ \mathrm{A23}^2\cos(\alpha\mathrm{A13} - 2\,\alpha\mathrm{A23})\cos(\beta\mathrm{A13})\cos^2(\beta\mathrm{A23})\sin^2(\beta\mathrm{A23})\sin(\beta\mathrm{A13}) +$ $0.0220971\ \mathrm{A12}\ \mathrm{A13}\ \mathrm{A23}\cos(2\,\alpha\mathrm{A12} - \alpha\mathrm{A13} - 2\,\alpha\mathrm{A23})\cos(\beta\mathrm{A13})\sin^2(\beta\mathrm{A12})\sin^2(\beta\mathrm{A23})\sin(\beta\mathrm{A13}) -$ $0.0220971\ \mathrm{A12}\ \mathrm{A13}\ \mathrm{A23}\cos(2\,\alpha\mathrm{A12} + \alpha\mathrm{A13} - 2\,\alpha\mathrm{A23})\cos(\beta\mathrm{A13})\sin^2(\beta\mathrm{A12})\sin^2(\beta\mathrm{A23})\sin(\beta\mathrm{A13}) +$ $0.0625\ \mathrm{A12}\ \mathrm{A13}\ \mathrm{A23}\cos(\alpha\mathrm{A12} - \alpha\mathrm{A13} + 2\,\alpha\mathrm{A23})\cos(\beta\mathrm{A12})\cos(\beta\mathrm{A13})\sin(\beta\mathrm{A12})\sin^2(\beta\mathrm{A23})\sin(\beta\mathrm{A13}) -$ $0.0625\ \mathrm{A12}\ \mathrm{A13}\ \mathrm{A23}\cos(\alpha\mathrm{A12} - \alpha\mathrm{A13} - 2\,\alpha\mathrm{A23})\cos(\beta\mathrm{A12})\cos(\beta\mathrm{A13})\sin(\beta\mathrm{A12})\sin^2(\beta\mathrm{A23})\sin(\beta\mathrm{A13}) -$ $0.0625\ \mathrm{A12}\ \mathrm{A13}\ \mathrm{A23}\cos(\alpha\mathrm{A12} + \alpha\mathrm{A13} - 2\,\alpha\mathrm{A23})\cos(\beta\mathrm{A12})\cos(\beta\mathrm{A13})\sin(\beta\mathrm{A12})\sin^2(\beta\mathrm{A23})\sin(\beta\mathrm{A13}) +$ $0.125\ \mathrm{A12}\ \mathrm{A13}\ \mathrm{A23}\cos(2\,\alpha\mathrm{A12} - \alpha\mathrm{A13} - \alpha\mathrm{A23})\cos(\beta\mathrm{A13})\cos(\beta\mathrm{A23})\sin^2(\beta\mathrm{A12})\sin(\beta\mathrm{A23})\sin(\beta\mathrm{A13}) +$ $0.707107\ \mathrm{A12}\ \mathrm{A13}\ \mathrm{A23}\cos(\alpha\mathrm{A12} - \alpha\mathrm{A13} - \alpha\mathrm{A23})\cos(\beta\mathrm{A12})\cos(\beta\mathrm{A13})\cos(\beta\mathrm{A23})\sin(\beta\mathrm{A12})\sin(\beta\mathrm{A23})$ $\sin(\beta\mathrm{A13}) - 0.353553\ \mathrm{A12}\ \mathrm{A13}\ \mathrm{A23}\cos(\alpha\mathrm{A12} + \alpha\mathrm{A13} - \alpha\mathrm{A23})\cos(\beta\mathrm{A12})\cos(\beta\mathrm{A13})\cos(\beta\mathrm{A23})\sin(\beta\mathrm{A12})$ $\sin(\beta\mathrm{A23})\sin(\beta\mathrm{A13}) - 0.353553\ \mathrm{A12}\ \mathrm{A13}\ \mathrm{A23}\cos(\alpha\mathrm{A12} - \alpha\mathrm{A13} + \alpha\mathrm{A23})\cos(\beta\mathrm{A12})\cos(\beta\mathrm{A13})\cos(\beta\mathrm{A23})$ $\sin(\beta\mathrm{A12})\sin(\beta\mathrm{A23})\sin(\beta\mathrm{A13}) + 0.00976563\ \mathrm{A12}\ \mathrm{A23}^2\cos(2\,(\alpha\mathrm{A12} - 2\,\alpha\mathrm{A23}))\sin^2(\beta\mathrm{A12})\sin^4(\beta\mathrm{A23}) +$ $0.0552427\ \mathrm{A12}\ \mathrm{A23}^2\cos(2\,\alpha\mathrm{A12} - \alpha\mathrm{A23})\cos(\beta\mathrm{A23})\sin^2(\beta\mathrm{A12})\sin^3(\beta\mathrm{A23}) -$ $0.0552427\ \mathrm{A12}\ \mathrm{A23}^2\cos(2\,\alpha\mathrm{A12} - 3\,\alpha\mathrm{A23})\cos(\beta\mathrm{A23})\sin^2(\beta\mathrm{A12})\sin^3(\beta\mathrm{A23}) +$ $0.15625\ \mathrm{A12}\ \mathrm{A23}^2\cos(\alpha\mathrm{A12} - \alpha\mathrm{A23})\cos(\beta\mathrm{A12})\cos(\beta\mathrm{A23})\sin(\beta\mathrm{A12})\sin^3(\beta\mathrm{A23}) -$ $0.15625\ \mathrm{A12}\ \mathrm{A23}^2\cos(\alpha\mathrm{A12} + \alpha\mathrm{A23})\cos(\beta\mathrm{A12})\cos(\beta\mathrm{A23})\sin(\beta\mathrm{A12})\sin^3(\beta\mathrm{A23}) +$ $0.15625\ \mathrm{A12}\ \mathrm{A23}^2\cos(\alpha\mathrm{A12} - 3\,\alpha\mathrm{A23})\cos(\beta\mathrm{A12})\cos(\beta\mathrm{A23})\sin(\beta\mathrm{A12})\sin^3(\beta\mathrm{A23}) -$ $0.15625\ \mathrm{A12}\ \mathrm{A23}^2\cos(2\,(\alpha\mathrm{A12} - \alpha\mathrm{A23}))\cos^2(\beta\mathrm{A23})\sin^2(\beta\mathrm{A12})\sin^2(\beta\mathrm{A23}) -$ $0.883883\ \mathrm{A12}\ \mathrm{A23}^2\cos(\alpha\mathrm{A12} - 2\,\alpha\mathrm{A23})\cos(\beta\mathrm{A12})\cos^2(\beta\mathrm{A23})\sin(\beta\mathrm{A12})\sin^2(\beta\mathrm{A23}) +$ $1.41421\ \mathrm{A12}\cos(\alpha\mathrm{A12})\cos(\beta\mathrm{A12})\sin(\beta\mathrm{A12})$ $\big(-4\,(\Omega1 - \Omega2)^2 + 0.625\ \mathrm{A13}^2\cos^2(\beta\mathrm{A13})\sin^2(\beta\mathrm{A13}) + 0.625\ \mathrm{A23}^2\cos^2(\beta\mathrm{A23})\sin^2(\beta\mathrm{A23})\big) -$ $0.125\ \mathrm{A12}\cos(2\,\alpha\mathrm{A12})\sin^2(\beta\mathrm{A12})\big(0.078125\ \mathrm{A13}^2\sin^4(\beta\mathrm{A13}) + 0.078125\ \mathrm{A23}^2\sin^4(\beta\mathrm{A23}) - 4\,(\Omega1 - \Omega2)^2\big)\big)$

$(I_1^- I_3^+ + I_1^+ I_3^-)$
$-\frac{1}{16\,\omega\mathrm{rot}^2}\big(0.00976563\,\mathrm{A12}^2\,\mathrm{A13}\cos(2\,\alpha\mathrm{A13})\sin^2(\beta\mathrm{A13})\sin^4(\beta\mathrm{A12}) -$ $0.00976563\,\mathrm{A12}^2\,\mathrm{A13}\cos(4\,\alpha\mathrm{A12} - 2\,\alpha\mathrm{A13})\sin^2(\beta\mathrm{A13})\sin^4(\beta\mathrm{A12}) +$ $0.0078125\,\mathrm{A12}^2\,\mathrm{A23}\cos(2\,\alpha\mathrm{A23})\sin^2(\beta\mathrm{A23})\sin^4(\beta\mathrm{A12}) -$ $0.0078125\,\mathrm{A12}^2\,\mathrm{A23}\cos(4\,\alpha\mathrm{A12} - 2\,\alpha\mathrm{A23})\sin^2(\beta\mathrm{A23})\sin^4(\beta\mathrm{A12}) -$ $0.0552427\,\mathrm{A12}^2\,\mathrm{A13}\cos(\alpha\mathrm{A12} - 2\,\alpha\mathrm{A13})\cos(\beta\mathrm{A12})\sin^2(\beta\mathrm{A13})\sin^3(\beta\mathrm{A12}) +$ $0.0552427\,\mathrm{A12}^2\,\mathrm{A13}\cos(3\,\alpha\mathrm{A12} - 2\,\alpha\mathrm{A13})\cos(\beta\mathrm{A12})\sin^2(\beta\mathrm{A13})\sin^3(\beta\mathrm{A12}) -$ $0.0441942\,\mathrm{A12}^2\,\mathrm{A23}\cos(\alpha\mathrm{A12} - 2\,\alpha\mathrm{A23})\cos(\beta\mathrm{A12})\sin^2(\beta\mathrm{A23})\sin^3(\beta\mathrm{A12}) +$ $0.0441942\,\mathrm{A12}^2\,\mathrm{A23}\cos(3\,\alpha\mathrm{A12} - 2\,\alpha\mathrm{A23})\cos(\beta\mathrm{A12})\sin^2(\beta\mathrm{A23})\sin^3(\beta\mathrm{A12}) -$ $0.15625\,\mathrm{A12}^2\,\mathrm{A13}\cos(\alpha\mathrm{A12} - \alpha\mathrm{A13})\cos(\beta\mathrm{A12})\cos(\beta\mathrm{A13})\sin(\beta\mathrm{A13})\sin^3(\beta\mathrm{A12}) -$ $0.15625\,\mathrm{A12}^2\,\mathrm{A13}\cos(3\,\alpha\mathrm{A12} - \alpha\mathrm{A13})\cos(\beta\mathrm{A12})\cos(\beta\mathrm{A13})\sin(\beta\mathrm{A13})\sin^3(\beta\mathrm{A12}) +$ $0.15625\,\mathrm{A12}^2\,\mathrm{A13}\cos(\alpha\mathrm{A12} + \alpha\mathrm{A13})\cos(\beta\mathrm{A12})\cos(\beta\mathrm{A13})\sin(\beta\mathrm{A13})\sin^3(\beta\mathrm{A12}) -$ $0.125\,\mathrm{A12}^2\,\mathrm{A23}\cos(\alpha\mathrm{A12} - \alpha\mathrm{A23})\cos(\beta\mathrm{A12})\cos(\beta\mathrm{A23})\sin(\beta\mathrm{A23})\sin^3(\beta\mathrm{A12}) -$ $0.125\,\mathrm{A12}^2\,\mathrm{A23}\cos(3\,\alpha\mathrm{A12} - \alpha\mathrm{A23})\cos(\beta\mathrm{A12})\cos(\beta\mathrm{A23})\sin(\beta\mathrm{A23})\sin^3(\beta\mathrm{A12}) +$ $0.125\,\mathrm{A12}^2\,\mathrm{A23}\cos(\alpha\mathrm{A12} + \alpha\mathrm{A23})\cos(\beta\mathrm{A12})\cos(\beta\mathrm{A23})\sin(\beta\mathrm{A23})\sin^3(\beta\mathrm{A12}) +$ $0.0078125\,\mathrm{A12}\,\mathrm{A23}^2\cos(2\,\alpha\mathrm{A12})\sin^4(\beta\mathrm{A23})\sin^2(\beta\mathrm{A12}) -$ $0.0078125\,\mathrm{A12}\,\mathrm{A23}^2\cos(2\,(\alpha\mathrm{A12} - 2\,\alpha\mathrm{A23}))\sin^4(\beta\mathrm{A23})\sin^2(\beta\mathrm{A12}) -$ $0.0441942\,\mathrm{A12}\,\mathrm{A23}^2\cos(2\,\alpha\mathrm{A12} - \alpha\mathrm{A23})\cos(\beta\mathrm{A23})\sin^3(\beta\mathrm{A23})\sin^2(\beta\mathrm{A12}) +$ $0.0441942\,\mathrm{A12}\,\mathrm{A23}^2\cos(2\,\alpha\mathrm{A12} - 3\,\alpha\mathrm{A23})\cos(\beta\mathrm{A23})\sin^3(\beta\mathrm{A23})\sin^2(\beta\mathrm{A12}) +$ $0.15625\,\mathrm{A12}^2\,\mathrm{A13}\cos(2\,(\alpha\mathrm{A12} - \alpha\mathrm{A13}))\cos^2(\beta\mathrm{A12})\sin^2(\beta\mathrm{A13})\sin^2(\beta\mathrm{A12}) +$ $0.125\,\mathrm{A12}^2\,\mathrm{A23}\cos(2\,(\alpha\mathrm{A12} - \alpha\mathrm{A23}))\cos^2(\beta\mathrm{A12})\sin^2(\beta\mathrm{A23})\sin^2(\beta\mathrm{A12}) +$ $0.125\,\mathrm{A12}\,\mathrm{A23}^2\cos(2\,(\alpha\mathrm{A12} - \alpha\mathrm{A23}))\cos^2(\beta\mathrm{A23})\sin^2(\beta\mathrm{A23})\sin^2(\beta\mathrm{A12}) -$ $0.00390625\,\mathrm{A12}\,\mathrm{A13}\,\mathrm{A23}\cos(2\,(\alpha\mathrm{A12} - \alpha\mathrm{A13} - \alpha\mathrm{A23}))\sin^2(\beta\mathrm{A13})\sin^2(\beta\mathrm{A23})\sin^2(\beta\mathrm{A12}) -$ $0.00390625\,\mathrm{A12}\,\mathrm{A13}\,\mathrm{A23}\cos(2\,(\alpha\mathrm{A12} + \alpha\mathrm{A13} - \alpha\mathrm{A23}))\sin^2(\beta\mathrm{A13})\sin^2(\beta\mathrm{A23})\sin^2(\beta\mathrm{A12}) +$ $0.0078125\,\mathrm{A12}\,\mathrm{A13}\,\mathrm{A23}\cos(2\,(\alpha\mathrm{A12} - \alpha\mathrm{A13} + \alpha\mathrm{A23}))\sin^2(\beta\mathrm{A13})\sin^2(\beta\mathrm{A23})\sin^2(\beta\mathrm{A12}) +$ $0.883883\,\mathrm{A12}^2\,\mathrm{A13}\cos(2\,\alpha\mathrm{A12} - \alpha\mathrm{A13})\cos^2(\beta\mathrm{A12})\cos(\beta\mathrm{A13})\sin(\beta\mathrm{A13})\sin^2(\beta\mathrm{A12}) -$ $0.883883\,\mathrm{A12}^2\,\mathrm{A13}\cos(\alpha\mathrm{A13})\cos^2(\beta\mathrm{A12})\cos(\beta\mathrm{A13})\sin(\beta\mathrm{A13})\sin^2(\beta\mathrm{A12}) +$ $0.0220971\,\mathrm{A12}\,\mathrm{A13}\,\mathrm{A23}\cos(2\,\alpha\mathrm{A12} - 2\,\alpha\mathrm{A13} - \alpha\mathrm{A23})\cos(\beta\mathrm{A23})\sin^2(\beta\mathrm{A13})\sin(\beta\mathrm{A23})\sin^2(\beta\mathrm{A12}) -$ $0.0220971\,\mathrm{A12}\,\mathrm{A13}\,\mathrm{A23}\cos(2\,\alpha\mathrm{A12} - 2\,\alpha\mathrm{A13} + \alpha\mathrm{A23})\cos(\beta\mathrm{A23})\sin^2(\beta\mathrm{A13})\sin(\beta\mathrm{A23})\sin^2(\beta\mathrm{A12}) +$ $0.707107\,\mathrm{A12}^2\,\mathrm{A23}\cos(2\,\alpha\mathrm{A12} - \alpha\mathrm{A23})\cos^2(\beta\mathrm{A12})\cos(\beta\mathrm{A23})\sin(\beta\mathrm{A23})\sin^2(\beta\mathrm{A12}) -$ $0.707107\,\mathrm{A12}^2\,\mathrm{A23}\cos(\alpha\mathrm{A23})\cos^2(\beta\mathrm{A12})\cos(\beta\mathrm{A23})\sin(\beta\mathrm{A23})\sin^2(\beta\mathrm{A12}) +$ $0.0625\,\mathrm{A12}\,\mathrm{A13}\,\mathrm{A23}\cos(2\,\alpha\mathrm{A12} - \alpha\mathrm{A13} - \alpha\mathrm{A23})\cos(\beta\mathrm{A13})\cos(\beta\mathrm{A23})\sin(\beta\mathrm{A13})\sin(\beta\mathrm{A23})\sin^2(\beta\mathrm{A12}) -$ $0.0625\,\mathrm{A12}\,\mathrm{A13}\,\mathrm{A23}\cos(2\,\alpha\mathrm{A12} + \alpha\mathrm{A13} - \alpha\mathrm{A23})\cos(\beta\mathrm{A13})\cos(\beta\mathrm{A23})\sin(\beta\mathrm{A13})\sin(\beta\mathrm{A23})\sin^2(\beta\mathrm{A12}) +$ $0.0625\,\mathrm{A12}\,\mathrm{A13}\,\mathrm{A23}\cos(2\,\alpha\mathrm{A12} - \alpha\mathrm{A13} + \alpha\mathrm{A23})\cos(\beta\mathrm{A13})\cos(\beta\mathrm{A23})\sin(\beta\mathrm{A13})\sin(\beta\mathrm{A23})\sin^2(\beta\mathrm{A12}) -$ $0.125\,\mathrm{A12}\,\mathrm{A23}^2\cos(\alpha\mathrm{A12} - \alpha\mathrm{A23})\cos(\beta\mathrm{A12})\cos(\beta\mathrm{A23})\sin^3(\beta\mathrm{A23})\sin(\beta\mathrm{A12}) +$ $0.125\,\mathrm{A12}\,\mathrm{A23}^2\cos(\alpha\mathrm{A12} + \alpha\mathrm{A23})\cos(\beta\mathrm{A12})\cos(\beta\mathrm{A23})\sin^3(\beta\mathrm{A23})\sin(\beta\mathrm{A12}) -$ $0.125\,\mathrm{A12}\,\mathrm{A23}^2\cos(\alpha\mathrm{A12} - 3\,\alpha\mathrm{A23})\cos(\beta\mathrm{A12})\cos(\beta\mathrm{A23})\sin^3(\beta\mathrm{A23})\sin(\beta\mathrm{A12}) -$ $0.707107\,\mathrm{A12}\,\mathrm{A23}^2\cos(\alpha\mathrm{A12})\cos(\beta\mathrm{A12})\cos^2(\beta\mathrm{A23})\sin^2(\beta\mathrm{A23})\sin(\beta\mathrm{A12}) +$ $0.707107\,\mathrm{A12}\,\mathrm{A23}^2\cos(\alpha\mathrm{A12} - 2\,\alpha\mathrm{A23})\cos(\beta\mathrm{A12})\cos^2(\beta\mathrm{A23})\sin^2(\beta\mathrm{A23})\sin(\beta\mathrm{A12}) -$ $0.0220971\,\mathrm{A12}\,\mathrm{A13}\,\mathrm{A23}\cos(\alpha\mathrm{A12} - 2\,\alpha\mathrm{A13} + 2\,\alpha\mathrm{A23})\cos(\beta\mathrm{A12})\sin^2(\beta\mathrm{A13})\sin^2(\beta\mathrm{A23})\sin(\beta\mathrm{A12}) +$ $0.0220971\,\mathrm{A12}\,\mathrm{A13}\,\mathrm{A23}\cos(\alpha\mathrm{A12} + 2\,\alpha\mathrm{A13} - 2\,\alpha\mathrm{A23})\cos(\beta\mathrm{A12})\sin^2(\beta\mathrm{A13})\sin^2(\beta\mathrm{A23})\sin(\beta\mathrm{A12}) +$ $0.0625\,\mathrm{A12}\,\mathrm{A13}\,\mathrm{A23}\cos(\alpha\mathrm{A12} - \alpha\mathrm{A13} + 2\,\alpha\mathrm{A23})\cos(\beta\mathrm{A12})\cos(\beta\mathrm{A13})\sin(\beta\mathrm{A13})\sin^2(\beta\mathrm{A23})\sin(\beta\mathrm{A12}) -$ $0.0625\,\mathrm{A12}\,\mathrm{A13}\,\mathrm{A23}\cos(\alpha\mathrm{A12} - \alpha\mathrm{A13} - 2\,\alpha\mathrm{A23})\cos(\beta\mathrm{A12})\cos(\beta\mathrm{A13})\sin(\beta\mathrm{A13})\sin^2(\beta\mathrm{A23})\sin(\beta\mathrm{A12}) +$ $0.0625\,\mathrm{A12}\,\mathrm{A13}\,\mathrm{A23}\cos(\alpha\mathrm{A12} + \alpha\mathrm{A13} - 2\,\alpha\mathrm{A23})\cos(\beta\mathrm{A12})\cos(\beta\mathrm{A13})\sin(\beta\mathrm{A13})\sin^2(\beta\mathrm{A23})\sin(\beta\mathrm{A12}) -$ $0.125\,\mathrm{A12}\,\mathrm{A13}\,\mathrm{A23}\cos(\alpha\mathrm{A12} - 2\,\alpha\mathrm{A13} + \alpha\mathrm{A23})\cos(\beta\mathrm{A12})\cos(\beta\mathrm{A23})\sin^2(\beta\mathrm{A13})\sin(\beta\mathrm{A23})\sin(\beta\mathrm{A12}) +$ $0.353553\,\mathrm{A12}\,\mathrm{A13}\,\mathrm{A23}\cos(\alpha\mathrm{A12} - \alpha\mathrm{A13} - \alpha\mathrm{A23})\cos(\beta\mathrm{A12})\cos(\beta\mathrm{A13})\cos(\beta\mathrm{A23})\sin(\beta\mathrm{A13})\sin(\beta\mathrm{A23})$ $\sin(\beta\mathrm{A12}) + 0.353553\,\mathrm{A12}\,\mathrm{A13}\,\mathrm{A23}\cos(\alpha\mathrm{A12} + \alpha\mathrm{A13} - \alpha\mathrm{A23})\cos(\beta\mathrm{A12})\cos(\beta\mathrm{A13})\cos(\beta\mathrm{A23})$ $\sin(\beta\mathrm{A13})\sin(\beta\mathrm{A23})\sin(\beta\mathrm{A12}) - 0.707107\,\mathrm{A12}\,\mathrm{A13}\,\mathrm{A23}\cos(\alpha\mathrm{A12} - \alpha\mathrm{A13} + \alpha\mathrm{A23})\cos(\beta\mathrm{A12})\cos(\beta\mathrm{A13})$ $\cos(\beta\mathrm{A23})\sin(\beta\mathrm{A13})\sin(\beta\mathrm{A23})\sin(\beta\mathrm{A12}) + 0.00976563\,\mathrm{A13}\,\mathrm{A23}^2\cos(2\,\alpha\mathrm{A13})\sin^2(\beta\mathrm{A13})\sin^4(\beta\mathrm{A23}) -$ $0.00976563\,\mathrm{A13}\,\mathrm{A23}^2\cos(2\,(\alpha\mathrm{A13} - 2\,\alpha\mathrm{A23}))\sin^2(\beta\mathrm{A13})\sin^4(\beta\mathrm{A23}) -$ $0.0552427\,\mathrm{A13}\,\mathrm{A23}^2\cos(2\,\alpha\mathrm{A13} - \alpha\mathrm{A23})\cos(\beta\mathrm{A23})\sin^2(\beta\mathrm{A13})\sin^3(\beta\mathrm{A23}) +$ $0.0552427\,\mathrm{A13}\,\mathrm{A23}^2\cos(2\,\alpha\mathrm{A13} - 3\,\alpha\mathrm{A23})\cos(\beta\mathrm{A23})\sin^2(\beta\mathrm{A13})\sin^3(\beta\mathrm{A23}) -$ $0.15625\,\mathrm{A13}\,\mathrm{A23}^2\cos(\alpha\mathrm{A13} - \alpha\mathrm{A23})\cos(\beta\mathrm{A13})\cos(\beta\mathrm{A23})\sin(\beta\mathrm{A13})\sin^3(\beta\mathrm{A23}) +$ $0.15625\,\mathrm{A13}\,\mathrm{A23}^2\cos(\alpha\mathrm{A13} + \alpha\mathrm{A23})\cos(\beta\mathrm{A13})\cos(\beta\mathrm{A23})\sin(\beta\mathrm{A13})\sin^3(\beta\mathrm{A23}) -$ $0.15625\,\mathrm{A13}\,\mathrm{A23}^2\cos(\alpha\mathrm{A13} - 3\,\alpha\mathrm{A23})\cos(\beta\mathrm{A13})\cos(\beta\mathrm{A23})\sin(\beta\mathrm{A13})\sin^3(\beta\mathrm{A23}) -$ $0.5\,\mathrm{A13}\,\Omega1^2\cos(2\,\alpha\mathrm{A13})\sin^2(\beta\mathrm{A13}) - 0.5\,\mathrm{A13}\,\Omega3^2\cos(2\,\alpha\mathrm{A13})\sin^2(\beta\mathrm{A13}) +$ $1.\,\mathrm{A13}\,\Omega1\,\Omega3\cos(2\,\alpha\mathrm{A13})\sin^2(\beta\mathrm{A13}) + 0.15625\,\mathrm{A13}\,\mathrm{A23}^2\cos(2\,(\alpha\mathrm{A13} - \alpha\mathrm{A23}))\cos^2(\beta\mathrm{A23})$ $\sin^2(\beta\mathrm{A13})\sin^2(\beta\mathrm{A23}) - 0.883883\,\mathrm{A13}\,\mathrm{A23}^2\cos(\alpha\mathrm{A13})\cos(\beta\mathrm{A13})\cos^2(\beta\mathrm{A23})\sin(\beta\mathrm{A13})\sin^2(\beta\mathrm{A23}) +$ $0.883883\,\mathrm{A13}\,\mathrm{A23}^2\cos(\alpha\mathrm{A13} - 2\,\alpha\mathrm{A23})\cos(\beta\mathrm{A13})\cos^2(\beta\mathrm{A23})\sin(\beta\mathrm{A13})\sin^2(\beta\mathrm{A23}) +$ $5.65685\,\mathrm{A13}\,\Omega1^2\cos(\alpha\mathrm{A13})\cos(\beta\mathrm{A13})\sin(\beta\mathrm{A13}) + 5.65685\,\mathrm{A13}\,\Omega3^2\cos(\alpha\mathrm{A13})\cos(\beta\mathrm{A13})\sin(\beta\mathrm{A13}) -$ $11.3137\,\mathrm{A13}\,\Omega1\,\Omega3\cos(\alpha\mathrm{A13})\cos(\beta\mathrm{A13})\sin(\beta\mathrm{A13})\big)$

$(I_2^- I_3^+ + I_2^+ I_3^-)$
$-\frac{1}{16\,\omega\mathrm{rot}^2}$
$\big(0.0078125\,\mathrm{A12}^2\,\mathrm{A13}\cos(2\,\alpha\mathrm{A13})\sin^2(\beta\mathrm{A13})\sin^4(\beta\mathrm{A12}) - 0.0078125\,\mathrm{A12}^2\,\mathrm{A13}\cos(4\,\alpha\mathrm{A12} - 2\,\alpha\mathrm{A13})\sin^2(\beta\mathrm{A13})$
$\sin^4(\beta\mathrm{A12}) + 0.00976563\,\mathrm{A12}^2\,\mathrm{A23}\cos(2\,\alpha\mathrm{A23})\sin^2(\beta\mathrm{A23})\sin^4(\beta\mathrm{A12}) -$
$0.00976563\,\mathrm{A12}^2\,\mathrm{A23}\cos(4\,\alpha\mathrm{A12} - 2\,\alpha\mathrm{A23})\sin^2(\beta\mathrm{A23})\sin^4(\beta\mathrm{A12}) -$
$0.0441942\,\mathrm{A12}^2\,\mathrm{A13}\cos(\alpha\mathrm{A12} - 2\,\alpha\mathrm{A13})\cos(\beta\mathrm{A12})\sin^2(\beta\mathrm{A13})\sin^3(\beta\mathrm{A12}) +$
$0.0441942\,\mathrm{A12}^2\,\mathrm{A13}\cos(3\,\alpha\mathrm{A12} - 2\,\alpha\mathrm{A13})\cos(\beta\mathrm{A12})\sin^2(\beta\mathrm{A13})\sin^3(\beta\mathrm{A12}) -$
$0.0552427\,\mathrm{A12}^2\,\mathrm{A23}\cos(\alpha\mathrm{A12} - 2\,\alpha\mathrm{A23})\cos(\beta\mathrm{A12})\sin^2(\beta\mathrm{A23})\sin^3(\beta\mathrm{A12}) +$
$0.0552427\,\mathrm{A12}^2\,\mathrm{A23}\cos(3\,\alpha\mathrm{A12} - 2\,\alpha\mathrm{A23})\cos(\beta\mathrm{A12})\sin^2(\beta\mathrm{A23})\sin^3(\beta\mathrm{A12}) -$
$0.125\,\mathrm{A12}^2\,\mathrm{A13}\cos(\alpha\mathrm{A12} - \alpha\mathrm{A13})\cos(\beta\mathrm{A12})\cos(\beta\mathrm{A13})\sin(\beta\mathrm{A13})\sin^3(\beta\mathrm{A12}) -$
$0.125\,\mathrm{A12}^2\,\mathrm{A13}\cos(3\,\alpha\mathrm{A12} - \alpha\mathrm{A13})\cos(\beta\mathrm{A12})\cos(\beta\mathrm{A13})\sin(\beta\mathrm{A13})\sin^3(\beta\mathrm{A12}) +$
$0.125\,\mathrm{A12}^2\,\mathrm{A13}\cos(\alpha\mathrm{A12} + \alpha\mathrm{A13})\cos(\beta\mathrm{A12})\cos(\beta\mathrm{A13})\sin(\beta\mathrm{A13})\sin^3(\beta\mathrm{A12}) -$
$0.15625\,\mathrm{A12}^2\,\mathrm{A23}\cos(\alpha\mathrm{A12} - \alpha\mathrm{A23})\cos(\beta\mathrm{A12})\cos(\beta\mathrm{A23})\sin(\beta\mathrm{A23})\sin^3(\beta\mathrm{A12}) -$
$0.15625\,\mathrm{A12}^2\,\mathrm{A23}\cos(3\,\alpha\mathrm{A12} - \alpha\mathrm{A23})\cos(\beta\mathrm{A12})\cos(\beta\mathrm{A23})\sin(\beta\mathrm{A23})\sin^3(\beta\mathrm{A12}) +$
$0.15625\,\mathrm{A12}^2\,\mathrm{A23}\cos(\alpha\mathrm{A12} + \alpha\mathrm{A23})\cos(\beta\mathrm{A12})\cos(\beta\mathrm{A23})\sin(\beta\mathrm{A23})\sin^3(\beta\mathrm{A12}) +$
$0.0078125\,\mathrm{A12}\,\mathrm{A13}^2\cos(2\,\alpha\mathrm{A12})\sin^4(\beta\mathrm{A13})\sin^2(\beta\mathrm{A12}) -$
$0.0078125\,\mathrm{A12}\,\mathrm{A13}^2\cos(2\,(\alpha\mathrm{A12} - 2\,\alpha\mathrm{A13}))\sin^4(\beta\mathrm{A13})\sin^2(\beta\mathrm{A12}) -$
$0.0441942\,\mathrm{A12}\,\mathrm{A13}^2\cos(2\,\alpha\mathrm{A12} - \alpha\mathrm{A13})\cos(\beta\mathrm{A13})\sin^3(\beta\mathrm{A13})\sin^2(\beta\mathrm{A12}) +$
$0.0441942\,\mathrm{A12}\,\mathrm{A13}^2\cos(2\,\alpha\mathrm{A12} - 3\,\alpha\mathrm{A13})\cos(\beta\mathrm{A13})\sin^3(\beta\mathrm{A13})\sin^2(\beta\mathrm{A12}) +$
$0.125\,\mathrm{A12}^2\,\mathrm{A13}\cos(2\,(\alpha\mathrm{A12} - \alpha\mathrm{A13}))\cos^2(\beta\mathrm{A12})\sin^2(\beta\mathrm{A13})\sin^2(\beta\mathrm{A12}) +$
$0.125\,\mathrm{A12}\,\mathrm{A13}^2\cos(2\,(\alpha\mathrm{A12} - \alpha\mathrm{A13}))\cos^2(\beta\mathrm{A13})\sin^2(\beta\mathrm{A13})\sin^2(\beta\mathrm{A12}) +$
$0.15625\,\mathrm{A12}^2\,\mathrm{A23}\cos(2\,(\alpha\mathrm{A12} - \alpha\mathrm{A23}))\cos^2(\beta\mathrm{A12})\sin^2(\beta\mathrm{A23})\sin^2(\beta\mathrm{A12}) -$
$0.00390625\,\mathrm{A12}\,\mathrm{A13}\,\mathrm{A23}\cos(2\,(\alpha\mathrm{A12} - \alpha\mathrm{A13} - \alpha\mathrm{A23}))\sin^2(\beta\mathrm{A13})\sin^2(\beta\mathrm{A23})\sin^2(\beta\mathrm{A12}) +$
$0.0078125\,\mathrm{A12}\,\mathrm{A13}\,\mathrm{A23}\cos(2\,(\alpha\mathrm{A12} + \alpha\mathrm{A13} - \alpha\mathrm{A23}))\sin^2(\beta\mathrm{A13})\sin^2(\beta\mathrm{A23})\sin^2(\beta\mathrm{A12}) -$
$0.00390625\,\mathrm{A12}\,\mathrm{A13}\,\mathrm{A23}\cos(2\,(\alpha\mathrm{A12} - \alpha\mathrm{A13} + \alpha\mathrm{A23}))\sin^2(\beta\mathrm{A13})\sin^2(\beta\mathrm{A23})\sin^2(\beta\mathrm{A12}) +$
$0.0220971\,\mathrm{A12}\,\mathrm{A13}\,\mathrm{A23}\cos(2\,\alpha\mathrm{A12} - \alpha\mathrm{A13} - 2\,\alpha\mathrm{A23})\cos(\beta\mathrm{A13})\sin(\beta\mathrm{A13})\sin^2(\beta\mathrm{A23})\sin^2(\beta\mathrm{A12}) -$
$0.0220971\,\mathrm{A12}\,\mathrm{A13}\,\mathrm{A23}\cos(2\,\alpha\mathrm{A12} + \alpha\mathrm{A13} - 2\,\alpha\mathrm{A23})\cos(\beta\mathrm{A13})\sin(\beta\mathrm{A13})\sin^2(\beta\mathrm{A23})\sin^2(\beta\mathrm{A12}) +$
$0.707107\,\mathrm{A12}^2\,\mathrm{A13}\cos(2\,\alpha\mathrm{A12} - \alpha\mathrm{A13})\cos^2(\beta\mathrm{A12})\cos(\beta\mathrm{A13})\sin(\beta\mathrm{A13})\sin^2(\beta\mathrm{A12}) -$
$0.707107\,\mathrm{A12}^2\,\mathrm{A13}\cos(\alpha\mathrm{A13})\cos^2(\beta\mathrm{A12})\cos(\beta\mathrm{A13})\sin(\beta\mathrm{A13})\sin^2(\beta\mathrm{A12}) +$
$0.883883\,\mathrm{A12}^2\,\mathrm{A23}\cos(2\,\alpha\mathrm{A12} - \alpha\mathrm{A23})\cos^2(\beta\mathrm{A12})\cos(\beta\mathrm{A23})\sin(\beta\mathrm{A23})\sin^2(\beta\mathrm{A12}) -$
$0.883883\,\mathrm{A12}^2\,\mathrm{A23}\cos(\alpha\mathrm{A23})\cos^2(\beta\mathrm{A12})\cos(\beta\mathrm{A23})\sin(\beta\mathrm{A23})\sin^2(\beta\mathrm{A12}) +$
$0.0625\,\mathrm{A12}\,\mathrm{A13}\,\mathrm{A23}\cos(2\,\alpha\mathrm{A12} - \alpha\mathrm{A13} - \alpha\mathrm{A23})\cos(\beta\mathrm{A13})\cos(\beta\mathrm{A23})\sin(\beta\mathrm{A13})\sin(\beta\mathrm{A23})\sin^2(\beta\mathrm{A12}) +$
$0.0625\,\mathrm{A12}\,\mathrm{A13}\,\mathrm{A23}\cos(2\,\alpha\mathrm{A12} + \alpha\mathrm{A13} - \alpha\mathrm{A23})\cos(\beta\mathrm{A13})\cos(\beta\mathrm{A23})\sin(\beta\mathrm{A13})\sin(\beta\mathrm{A23})\sin^2(\beta\mathrm{A12}) -$
$0.0625\,\mathrm{A12}\,\mathrm{A13}\,\mathrm{A23}\cos(2\,\alpha\mathrm{A12} - \alpha\mathrm{A13} + \alpha\mathrm{A23})\cos(\beta\mathrm{A13})\cos(\beta\mathrm{A23})\sin(\beta\mathrm{A13})\sin(\beta\mathrm{A23})\sin^2(\beta\mathrm{A12}) -$
$0.125\,\mathrm{A12}\,\mathrm{A13}^2\cos(\alpha\mathrm{A12} - \alpha\mathrm{A13})\cos(\beta\mathrm{A12})\cos(\beta\mathrm{A13})\sin^3(\beta\mathrm{A13})\sin(\beta\mathrm{A12}) +$
$0.125\,\mathrm{A12}\,\mathrm{A13}^2\cos(\alpha\mathrm{A12} + \alpha\mathrm{A13})\cos(\beta\mathrm{A12})\cos(\beta\mathrm{A13})\sin^3(\beta\mathrm{A13})\sin(\beta\mathrm{A12}) -$
$0.125\,\mathrm{A12}\,\mathrm{A13}^2\cos(\alpha\mathrm{A12} - 3\,\alpha\mathrm{A13})\cos(\beta\mathrm{A12})\cos(\beta\mathrm{A13})\sin^3(\beta\mathrm{A13})\sin(\beta\mathrm{A12}) -$
$0.707107\,\mathrm{A12}\,\mathrm{A13}^2\cos(\alpha\mathrm{A12})\cos(\beta\mathrm{A12})\cos^2(\beta\mathrm{A13})\sin^2(\beta\mathrm{A13})\sin(\beta\mathrm{A12}) +$
$0.707107\,\mathrm{A12}\,\mathrm{A13}^2\cos(\alpha\mathrm{A12} - 2\,\alpha\mathrm{A13})\cos(\beta\mathrm{A12})\cos^2(\beta\mathrm{A13})\sin^2(\beta\mathrm{A13})\sin(\beta\mathrm{A12}) +$
$0.0220971\,\mathrm{A12}\,\mathrm{A13}\,\mathrm{A23}\cos(\alpha\mathrm{A12} - 2\,\alpha\mathrm{A13} + 2\,\alpha\mathrm{A23})\cos(\beta\mathrm{A12})\sin^2(\beta\mathrm{A13})\sin^2(\beta\mathrm{A23})\sin(\beta\mathrm{A12}) -$
$0.0220971\,\mathrm{A12}\,\mathrm{A13}\,\mathrm{A23}\cos(\alpha\mathrm{A12} + 2\,\alpha\mathrm{A13} - 2\,\alpha\mathrm{A23})\cos(\beta\mathrm{A12})\sin^2(\beta\mathrm{A13})\sin^2(\beta\mathrm{A23})\sin(\beta\mathrm{A12}) -$
$0.125\,\mathrm{A12}\,\mathrm{A13}\,\mathrm{A23}\cos(\alpha\mathrm{A12} + \alpha\mathrm{A13} - 2\,\alpha\mathrm{A23})\cos(\beta\mathrm{A12})\cos(\beta\mathrm{A13})\sin(\beta\mathrm{A13})\sin^2(\beta\mathrm{A23})\sin(\beta\mathrm{A12}) +$
$0.0625\,\mathrm{A12}\,\mathrm{A13}\,\mathrm{A23}\cos(\alpha\mathrm{A12} + 2\,\alpha\mathrm{A13} - \alpha\mathrm{A23})\cos(\beta\mathrm{A12})\cos(\beta\mathrm{A23})\sin^2(\beta\mathrm{A13})\sin(\beta\mathrm{A23})\sin(\beta\mathrm{A12}) -$
$0.0625\,\mathrm{A12}\,\mathrm{A13}\,\mathrm{A23}\cos(\alpha\mathrm{A12} - 2\,\alpha\mathrm{A13} - \alpha\mathrm{A23})\cos(\beta\mathrm{A12})\cos(\beta\mathrm{A23})\sin^2(\beta\mathrm{A13})\sin(\beta\mathrm{A23})\sin(\beta\mathrm{A12}) +$
$0.0625\,\mathrm{A12}\,\mathrm{A13}\,\mathrm{A23}\cos(\alpha\mathrm{A12} - 2\,\alpha\mathrm{A13} + \alpha\mathrm{A23})\cos(\beta\mathrm{A12})\cos(\beta\mathrm{A23})\sin^2(\beta\mathrm{A13})\sin(\beta\mathrm{A23})\sin(\beta\mathrm{A12}) +$
$0.353553\,\mathrm{A12}\,\mathrm{A13}\,\mathrm{A23}\cos(\alpha\mathrm{A12} - \alpha\mathrm{A13} - \alpha\mathrm{A23})\cos(\beta\mathrm{A12})\cos(\beta\mathrm{A13})\cos(\beta\mathrm{A23})\sin(\beta\mathrm{A13})\sin(\beta\mathrm{A23})$
$\sin(\beta\mathrm{A12}) - 0.707107\,\mathrm{A12}\,\mathrm{A13}\,\mathrm{A23}\cos(\alpha\mathrm{A12} + \alpha\mathrm{A13} - \alpha\mathrm{A23})\cos(\beta\mathrm{A12})\cos(\beta\mathrm{A13})\cos(\beta\mathrm{A23})$
$\sin(\beta\mathrm{A13})\sin(\beta\mathrm{A23})\sin(\beta\mathrm{A12}) + 0.353553\,\mathrm{A12}\,\mathrm{A13}\,\mathrm{A23}\cos(\alpha\mathrm{A12} - \alpha\mathrm{A13} + \alpha\mathrm{A23})\cos(\beta\mathrm{A12})\cos(\beta\mathrm{A13})$
$\cos(\beta\mathrm{A23})\sin(\beta\mathrm{A13})\sin(\beta\mathrm{A23})\sin(\beta\mathrm{A12}) + 0.00976563\,\mathrm{A13}^2\,\mathrm{A23}\cos(2\,\alpha\mathrm{A23})\sin^4(\beta\mathrm{A13})\sin^2(\beta\mathrm{A23}) -$
$0.00976563\,\mathrm{A13}^2\,\mathrm{A23}\cos(4\,\alpha\mathrm{A13} - 2\,\alpha\mathrm{A23})\sin^4(\beta\mathrm{A13})\sin^2(\beta\mathrm{A23}) -$
$0.0552427\,\mathrm{A13}^2\,\mathrm{A23}\cos(\alpha\mathrm{A13} - 2\,\alpha\mathrm{A23})\cos(\beta\mathrm{A13})\sin^3(\beta\mathrm{A13})\sin^2(\beta\mathrm{A23}) +$
$0.0552427\,\mathrm{A13}^2\,\mathrm{A23}\cos(3\,\alpha\mathrm{A13} - 2\,\alpha\mathrm{A23})\cos(\beta\mathrm{A13})\sin^3(\beta\mathrm{A13})\sin^2(\beta\mathrm{A23}) +$
$0.15625\,\mathrm{A13}^2\,\mathrm{A23}\cos(2\,(\alpha\mathrm{A13} - \alpha\mathrm{A23}))\cos^2(\beta\mathrm{A13})\sin^2(\beta\mathrm{A13})\sin^2(\beta\mathrm{A23}) - 0.5\,\mathrm{A23}\,\Omega2^2\cos(2\,\alpha\mathrm{A23})$
$\sin^2(\beta\mathrm{A23}) - 0.5\,\mathrm{A23}\,\Omega3^2\cos(2\,\alpha\mathrm{A23})\sin^2(\beta\mathrm{A23}) + 1.\,\mathrm{A23}\,\Omega2\,\Omega3\cos(2\,\alpha\mathrm{A23})\sin^2(\beta\mathrm{A23}) -$
$0.15625\,\mathrm{A13}^2\,\mathrm{A23}\cos(\alpha\mathrm{A13} - \alpha\mathrm{A23})\cos(\beta\mathrm{A13})\cos(\beta\mathrm{A23})\sin^3(\beta\mathrm{A13})\sin(\beta\mathrm{A23}) -$
$0.15625\,\mathrm{A13}^2\,\mathrm{A23}\cos(3\,\alpha\mathrm{A13} - \alpha\mathrm{A23})\cos(\beta\mathrm{A13})\cos(\beta\mathrm{A23})\sin^3(\beta\mathrm{A13})\sin(\beta\mathrm{A23}) +$
$0.15625\,\mathrm{A13}^2\,\mathrm{A23}\cos(\alpha\mathrm{A13} + \alpha\mathrm{A23})\cos(\beta\mathrm{A13})\cos(\beta\mathrm{A23})\sin^3(\beta\mathrm{A13})\sin(\beta\mathrm{A23}) +$
$0.883883\,\mathrm{A13}^2\,\mathrm{A23}\cos(2\,\alpha\mathrm{A13} - \alpha\mathrm{A23})\cos^2(\beta\mathrm{A13})\cos(\beta\mathrm{A23})\sin^2(\beta\mathrm{A13})\sin(\beta\mathrm{A23}) -$
$0.883883\,\mathrm{A13}^2\,\mathrm{A23}\cos(\alpha\mathrm{A23})\cos^2(\beta\mathrm{A13})\cos(\beta\mathrm{A23})\sin^2(\beta\mathrm{A13})\sin(\beta\mathrm{A23}) +$
$5.65685\,\mathrm{A23}\,\Omega2^2\cos(\alpha\mathrm{A23})\cos(\beta\mathrm{A23})\sin(\beta\mathrm{A23}) + 5.65685\,\mathrm{A23}\,\Omega3^2\cos(\alpha\mathrm{A23})\cos(\beta\mathrm{A23})\sin(\beta\mathrm{A23}) -$
$11.3137\,\mathrm{A23}\,\Omega2\,\Omega3\cos(\alpha\mathrm{A23})\cos(\beta\mathrm{A23})\sin(\beta\mathrm{A23})\big)$

$(I_{1z}I_2^+I_3^- - I_{1z}I_2^-I_3^+)$
$-\frac{1}{24\,\omega\mathrm{rot}^2}$
$\big(0.1875\,\mathrm{A12\,A13}\,\Omega1\cos(2\,(\alpha\mathrm{A12}-\alpha\mathrm{A13}))\sin^2(\beta\mathrm{A13})\sin^2(\beta\mathrm{A12}) - 0.09375\,\mathrm{A12\,A13}\,\Omega2\cos(2\,(\alpha\mathrm{A12}-\alpha\mathrm{A13}))$
$\sin^2(\beta\mathrm{A13})\sin^2(\beta\mathrm{A12}) - 0.09375\,\mathrm{A12\,A13}\,\Omega3\cos(2\,(\alpha\mathrm{A12}-\alpha\mathrm{A13}))\sin^2(\beta\mathrm{A13})\sin^2(\beta\mathrm{A12}) -$
$0.09375\,\mathrm{A12\,A13}\,\Omega1\cos(2\,(\alpha\mathrm{A12}+\alpha\mathrm{A13}))\sin^2(\beta\mathrm{A13})\sin^2(\beta\mathrm{A12}) +$
$0.046875\,\mathrm{A12\,A13}\,\Omega2\cos(2\,(\alpha\mathrm{A12}+\alpha\mathrm{A13}))\sin^2(\beta\mathrm{A13})\sin^2(\beta\mathrm{A12}) +$
$0.046875\,\mathrm{A12\,A13}\,\Omega3\cos(2\,(\alpha\mathrm{A12}+\alpha\mathrm{A13}))\sin^2(\beta\mathrm{A13})\sin^2(\beta\mathrm{A12}) +$
$0.1875\,\mathrm{A12\,A23}\,\Omega2\cos(2\,(\alpha\mathrm{A12}-\alpha\mathrm{A23}))\sin^2(\beta\mathrm{A23})\sin^2(\beta\mathrm{A12}) -$
$0.1875\,\mathrm{A12\,A23}\,\Omega3\cos(2\,(\alpha\mathrm{A12}-\alpha\mathrm{A23}))\sin^2(\beta\mathrm{A23})\sin^2(\beta\mathrm{A12}) -$
$0.09375\,\mathrm{A12\,A23}\,\Omega2\cos(2\,(\alpha\mathrm{A12}+\alpha\mathrm{A23}))\sin^2(\beta\mathrm{A23})\sin^2(\beta\mathrm{A12}) +$
$0.09375\,\mathrm{A12\,A23}\,\Omega3\cos(2\,(\alpha\mathrm{A12}+\alpha\mathrm{A23}))\sin^2(\beta\mathrm{A23})\sin^2(\beta\mathrm{A12}) -$
$0.53033\,\mathrm{A12\,A13}\,\Omega1\cos(2\,\alpha\mathrm{A12}-\alpha\mathrm{A13})\cos(\beta\mathrm{A13})\sin(\beta\mathrm{A13})\sin^2(\beta\mathrm{A12}) -$
$0.53033\,\mathrm{A12\,A13}\,\Omega2\cos(2\,\alpha\mathrm{A12}-\alpha\mathrm{A13})\cos(\beta\mathrm{A13})\sin(\beta\mathrm{A13})\sin^2(\beta\mathrm{A12}) +$
$1.06066\,\mathrm{A12\,A13}\,\Omega3\cos(2\,\alpha\mathrm{A12}-\alpha\mathrm{A13})\cos(\beta\mathrm{A13})\sin(\beta\mathrm{A13})\sin^2(\beta\mathrm{A12}) +$
$0.53033\,\mathrm{A12\,A13}\,\Omega1\cos(2\,\alpha\mathrm{A12}+\alpha\mathrm{A13})\cos(\beta\mathrm{A13})\sin(\beta\mathrm{A13})\sin^2(\beta\mathrm{A12}) -$
$0.176777\,\mathrm{A12\,A13}\,\Omega2\cos(2\,\alpha\mathrm{A12}+\alpha\mathrm{A13})\cos(\beta\mathrm{A13})\sin(\beta\mathrm{A13})\sin^2(\beta\mathrm{A12}) -$
$0.353553\,\mathrm{A12\,A13}\,\Omega3\cos(2\,\alpha\mathrm{A12}+\alpha\mathrm{A13})\cos(\beta\mathrm{A13})\sin(\beta\mathrm{A13})\sin^2(\beta\mathrm{A12}) -$
$2.12132\,\mathrm{A12\,A23}\,\Omega2\cos(2\,\alpha\mathrm{A12}-\alpha\mathrm{A23})\cos(\beta\mathrm{A23})\sin(\beta\mathrm{A23})\sin^2(\beta\mathrm{A12}) +$
$2.12132\,\mathrm{A12\,A23}\,\Omega3\cos(2\,\alpha\mathrm{A12}-\alpha\mathrm{A23})\cos(\beta\mathrm{A23})\sin(\beta\mathrm{A23})\sin^2(\beta\mathrm{A12}) +$
$0.707107\,\mathrm{A12\,A23}\,\Omega2\cos(2\,\alpha\mathrm{A12}+\alpha\mathrm{A23})\cos(\beta\mathrm{A23})\sin(\beta\mathrm{A23})\sin^2(\beta\mathrm{A12}) -$
$0.707107\,\mathrm{A12\,A23}\,\Omega3\cos(2\,\alpha\mathrm{A12}+\alpha\mathrm{A23})\cos(\beta\mathrm{A23})\sin(\beta\mathrm{A23})\sin^2(\beta\mathrm{A12}) +$
$0.53033\,\mathrm{A12\,A13}\,\Omega1\cos(\alpha\mathrm{A12}+2\,\alpha\mathrm{A13})\cos(\beta\mathrm{A12})\sin^2(\beta\mathrm{A13})\sin(\beta\mathrm{A12}) -$
$0.353553\,\mathrm{A12\,A13}\,\Omega2\cos(\alpha\mathrm{A12}+2\,\alpha\mathrm{A13})\cos(\beta\mathrm{A12})\sin^2(\beta\mathrm{A13})\sin(\beta\mathrm{A12}) -$
$0.176777\,\mathrm{A12\,A13}\,\Omega3\cos(\alpha\mathrm{A12}+2\,\alpha\mathrm{A13})\cos(\beta\mathrm{A12})\sin^2(\beta\mathrm{A13})\sin(\beta\mathrm{A12}) -$
$0.53033\,\mathrm{A12\,A13}\,(\Omega1-2\,\Omega2+\Omega3)\cos(\alpha\mathrm{A12}-2\,\alpha\mathrm{A13})\cos(\beta\mathrm{A12})\sin^2(\beta\mathrm{A13})\sin(\beta\mathrm{A12}) +$
$0.353553\,\mathrm{A12\,A23}\,\Omega2\cos(\alpha\mathrm{A12}+2\,\alpha\mathrm{A23})\cos(\beta\mathrm{A12})\sin^2(\beta\mathrm{A23})\sin(\beta\mathrm{A12}) -$
$0.353553\,\mathrm{A12\,A23}\,\Omega3\cos(\alpha\mathrm{A12}+2\,\alpha\mathrm{A23})\cos(\beta\mathrm{A12})\sin^2(\beta\mathrm{A23})\sin(\beta\mathrm{A12}) +$
$1.06066\,\mathrm{A12\,A23}\,\Omega2\cos(\alpha\mathrm{A12}-2\,\alpha\mathrm{A23})\cos(\beta\mathrm{A12})\sin^2(\beta\mathrm{A23})\sin(\beta\mathrm{A12}) -$
$1.06066\,\mathrm{A12\,A23}\,\Omega3\cos(\alpha\mathrm{A12}-2\,\alpha\mathrm{A23})\cos(\beta\mathrm{A12})\sin^2(\beta\mathrm{A23})\sin(\beta\mathrm{A12}) +$
$3.\,\mathrm{A12\,A13}\,(2\,\Omega1-\Omega2-\Omega3)\cos(\alpha\mathrm{A12}-\alpha\mathrm{A13})\cos(\beta\mathrm{A12})\cos(\beta\mathrm{A13})\sin(\beta\mathrm{A13})\sin(\beta\mathrm{A12}) -$
$3.\,\mathrm{A12\,A13}\,\Omega1\cos(\alpha\mathrm{A12}+\alpha\mathrm{A13})\cos(\beta\mathrm{A12})\cos(\beta\mathrm{A13})\sin(\beta\mathrm{A13})\sin(\beta\mathrm{A12}) +$
$1.5\,\mathrm{A12\,A13}\,\Omega2\cos(\alpha\mathrm{A12}+\alpha\mathrm{A13})\cos(\beta\mathrm{A12})\cos(\beta\mathrm{A13})\sin(\beta\mathrm{A13})\sin(\beta\mathrm{A12}) +$
$1.5\,\mathrm{A12\,A13}\,\Omega3\cos(\alpha\mathrm{A12}+\alpha\mathrm{A13})\cos(\beta\mathrm{A12})\cos(\beta\mathrm{A13})\sin(\beta\mathrm{A13})\sin(\beta\mathrm{A12}) +$
$6.\,\mathrm{A12\,A23}\,\Omega2\cos(\alpha\mathrm{A12}-\alpha\mathrm{A23})\cos(\beta\mathrm{A12})\cos(\beta\mathrm{A23})\sin(\beta\mathrm{A23})\sin(\beta\mathrm{A12}) -$
$6.\,\mathrm{A12\,A23}\,\Omega3\cos(\alpha\mathrm{A12}-\alpha\mathrm{A23})\cos(\beta\mathrm{A12})\cos(\beta\mathrm{A23})\sin(\beta\mathrm{A23})\sin(\beta\mathrm{A12}) -$
$3.\,\mathrm{A12\,A23}\,\Omega2\cos(\alpha\mathrm{A12}+\alpha\mathrm{A23})\cos(\beta\mathrm{A12})\cos(\beta\mathrm{A23})\sin(\beta\mathrm{A23})\sin(\beta\mathrm{A12}) +$
$3.\,\mathrm{A12\,A23}\,\Omega3\cos(\alpha\mathrm{A12}+\alpha\mathrm{A23})\cos(\beta\mathrm{A12})\cos(\beta\mathrm{A23})\sin(\beta\mathrm{A23})\sin(\beta\mathrm{A12}) -$
$0.1875\,\mathrm{A13\,A23}\,\Omega2\cos(2\,(\alpha\mathrm{A13}-\alpha\mathrm{A23}))\sin^2(\beta\mathrm{A13})\sin^2(\beta\mathrm{A23}) +$
$0.1875\,\mathrm{A13\,A23}\,\Omega3\cos(2\,(\alpha\mathrm{A13}-\alpha\mathrm{A23}))\sin^2(\beta\mathrm{A13})\sin^2(\beta\mathrm{A23}) +$
$0.09375\,\mathrm{A13\,A23}\,\Omega2\cos(2\,(\alpha\mathrm{A13}+\alpha\mathrm{A23}))\sin^2(\beta\mathrm{A13})\sin^2(\beta\mathrm{A23}) -$
$0.09375\,\mathrm{A13\,A23}\,\Omega3\cos(2\,(\alpha\mathrm{A13}+\alpha\mathrm{A23}))\sin^2(\beta\mathrm{A13})\sin^2(\beta\mathrm{A23}) -$
$0.353553\,\mathrm{A13\,A23}\,\Omega2\cos(\alpha\mathrm{A13}+2\,\alpha\mathrm{A23})\cos(\beta\mathrm{A13})\sin(\beta\mathrm{A13})\sin^2(\beta\mathrm{A23}) +$
$0.353553\,\mathrm{A13\,A23}\,\Omega3\cos(\alpha\mathrm{A13}+2\,\alpha\mathrm{A23})\cos(\beta\mathrm{A13})\sin(\beta\mathrm{A13})\sin^2(\beta\mathrm{A23}) -$
$1.06066\,\mathrm{A13\,A23}\,\Omega2\cos(\alpha\mathrm{A13}-2\,\alpha\mathrm{A23})\cos(\beta\mathrm{A13})\sin(\beta\mathrm{A13})\sin^2(\beta\mathrm{A23}) +$
$1.06066\,\mathrm{A13\,A23}\,\Omega3\cos(\alpha\mathrm{A13}-2\,\alpha\mathrm{A23})\cos(\beta\mathrm{A13})\sin(\beta\mathrm{A13})\sin^2(\beta\mathrm{A23}) +$
$2.12132\,\mathrm{A13\,A23}\,\Omega2\cos(2\,\alpha\mathrm{A13}-\alpha\mathrm{A23})\cos(\beta\mathrm{A23})\sin^2(\beta\mathrm{A13})\sin(\beta\mathrm{A23}) -$
$2.12132\,\mathrm{A13\,A23}\,\Omega3\cos(2\,\alpha\mathrm{A13}-\alpha\mathrm{A23})\cos(\beta\mathrm{A23})\sin^2(\beta\mathrm{A13})\sin(\beta\mathrm{A23}) -$
$0.707107\,\mathrm{A13\,A23}\,\Omega2\cos(2\,\alpha\mathrm{A13}+\alpha\mathrm{A23})\cos(\beta\mathrm{A23})\sin^2(\beta\mathrm{A13})\sin(\beta\mathrm{A23}) +$
$0.707107\,\mathrm{A13\,A23}\,\Omega3\cos(2\,\alpha\mathrm{A13}+\alpha\mathrm{A23})\cos(\beta\mathrm{A23})\sin^2(\beta\mathrm{A13})\sin(\beta\mathrm{A23}) -$
$6.\,\mathrm{A13\,A23}\,\Omega2\cos(\alpha\mathrm{A13}-\alpha\mathrm{A23})\cos(\beta\mathrm{A13})\cos(\beta\mathrm{A23})\sin(\beta\mathrm{A13})\sin(\beta\mathrm{A23}) +$
$6.\,\mathrm{A13\,A23}\,\Omega3\cos(\alpha\mathrm{A13}-\alpha\mathrm{A23})\cos(\beta\mathrm{A13})\cos(\beta\mathrm{A23})\sin(\beta\mathrm{A13})\sin(\beta\mathrm{A23}) +$
$3.\,\mathrm{A13\,A23}\,\Omega2\cos(\alpha\mathrm{A13}+\alpha\mathrm{A23})\cos(\beta\mathrm{A13})\cos(\beta\mathrm{A23})\sin(\beta\mathrm{A13})\sin(\beta\mathrm{A23}) -$
$3.\,\mathrm{A13\,A23}\,\Omega3\cos(\alpha\mathrm{A13}+\alpha\mathrm{A23})\cos(\beta\mathrm{A13})\cos(\beta\mathrm{A23})\sin(\beta\mathrm{A13})\sin(\beta\mathrm{A23})\big)$

$(I_1^+ I_{2z} I_3^- - I_1^- I_{2z} I_3^+)$
$\frac{1}{24\,\omega\mathrm{rot}^2}\big(-0.1875\ \mathrm{A12\ A13}\ \Omega1 \cos(2\,(\alpha\mathrm{A12} - \alpha\mathrm{A13}))\sin^2(\beta\mathrm{A13})\sin^2(\beta\mathrm{A12}) +$ $0.1875\ \mathrm{A12\ A13}\ \Omega3 \cos(2\,(\alpha\mathrm{A12} - \alpha\mathrm{A13}))\sin^2(\beta\mathrm{A13})\sin^2(\beta\mathrm{A12}) +$ $0.09375\ \mathrm{A12\ A13}\ \Omega1 \cos(2\,(\alpha\mathrm{A12} + \alpha\mathrm{A13}))\sin^2(\beta\mathrm{A13})\sin^2(\beta\mathrm{A12}) -$ $0.09375\ \mathrm{A12\ A13}\ \Omega3 \cos(2\,(\alpha\mathrm{A12} + \alpha\mathrm{A13}))\sin^2(\beta\mathrm{A13})\sin^2(\beta\mathrm{A12}) +$ $0.09375\ \mathrm{A12\ A23}\ \Omega1 \cos(2\,(\alpha\mathrm{A12} - \alpha\mathrm{A23}))\sin^2(\beta\mathrm{A23})\sin^2(\beta\mathrm{A12}) -$ $0.1875\ \mathrm{A12\ A23}\ \Omega2 \cos(2\,(\alpha\mathrm{A12} - \alpha\mathrm{A23}))\sin^2(\beta\mathrm{A23})\sin^2(\beta\mathrm{A12}) +$ $0.09375\ \mathrm{A12\ A23}\ \Omega3 \cos(2\,(\alpha\mathrm{A12} - \alpha\mathrm{A23}))\sin^2(\beta\mathrm{A23})\sin^2(\beta\mathrm{A12}) -$ $0.046875\ \mathrm{A12\ A23}\ \Omega1 \cos(2\,(\alpha\mathrm{A12} + \alpha\mathrm{A23}))\sin^2(\beta\mathrm{A23})\sin^2(\beta\mathrm{A12}) +$ $0.09375\ \mathrm{A12\ A23}\ \Omega2 \cos(2\,(\alpha\mathrm{A12} + \alpha\mathrm{A23}))\sin^2(\beta\mathrm{A23})\sin^2(\beta\mathrm{A12}) -$ $0.046875\ \mathrm{A12\ A23}\ \Omega3 \cos(2\,(\alpha\mathrm{A12} + \alpha\mathrm{A23}))\sin^2(\beta\mathrm{A23})\sin^2(\beta\mathrm{A12}) +$ $2.12132\ \mathrm{A12\ A13}\ \Omega1 \cos(2\,\alpha\mathrm{A12} - \alpha\mathrm{A13})\cos(\beta\mathrm{A13})\sin(\beta\mathrm{A13})\sin^2(\beta\mathrm{A12}) -$ $2.12132\ \mathrm{A12\ A13}\ \Omega3 \cos(2\,\alpha\mathrm{A12} - \alpha\mathrm{A13})\cos(\beta\mathrm{A13})\sin(\beta\mathrm{A13})\sin^2(\beta\mathrm{A12}) -$ $0.707107\ \mathrm{A12\ A13}\ \Omega1 \cos(2\,\alpha\mathrm{A12} + \alpha\mathrm{A13})\cos(\beta\mathrm{A13})\sin(\beta\mathrm{A13})\sin^2(\beta\mathrm{A12}) +$ $0.707107\ \mathrm{A12\ A13}\ \Omega3 \cos(2\,\alpha\mathrm{A12} + \alpha\mathrm{A13})\cos(\beta\mathrm{A13})\sin(\beta\mathrm{A13})\sin^2(\beta\mathrm{A12}) +$ $0.53033\ \mathrm{A12\ A23}\ \Omega1 \cos(2\,\alpha\mathrm{A12} - \alpha\mathrm{A23})\cos(\beta\mathrm{A23})\sin(\beta\mathrm{A23})\sin^2(\beta\mathrm{A12}) +$ $0.53033\ \mathrm{A12\ A23}\ \Omega2 \cos(2\,\alpha\mathrm{A12} - \alpha\mathrm{A23})\cos(\beta\mathrm{A23})\sin(\beta\mathrm{A23})\sin^2(\beta\mathrm{A12}) -$ $1.06066\ \mathrm{A12\ A23}\ \Omega3 \cos(2\,\alpha\mathrm{A12} - \alpha\mathrm{A23})\cos(\beta\mathrm{A23})\sin(\beta\mathrm{A23})\sin^2(\beta\mathrm{A12}) +$ $0.176777\ \mathrm{A12\ A23}\ \Omega1 \cos(2\,\alpha\mathrm{A12} + \alpha\mathrm{A23})\cos(\beta\mathrm{A23})\sin(\beta\mathrm{A23})\sin^2(\beta\mathrm{A12}) -$ $0.53033\ \mathrm{A12\ A23}\ \Omega2 \cos(2\,\alpha\mathrm{A12} + \alpha\mathrm{A23})\cos(\beta\mathrm{A23})\sin(\beta\mathrm{A23})\sin^2(\beta\mathrm{A12}) +$ $0.353553\ \mathrm{A12\ A23}\ \Omega3 \cos(2\,\alpha\mathrm{A12} + \alpha\mathrm{A23})\cos(\beta\mathrm{A23})\sin(\beta\mathrm{A23})\sin^2(\beta\mathrm{A12}) -$ $0.353553\ \mathrm{A12\ A13}\ \Omega1 \cos(\alpha\mathrm{A12} + 2\,\alpha\mathrm{A13})\cos(\beta\mathrm{A12})\sin^2(\beta\mathrm{A13})\sin(\beta\mathrm{A12}) +$ $0.353553\ \mathrm{A12\ A13}\ \Omega3 \cos(\alpha\mathrm{A12} + 2\,\alpha\mathrm{A13})\cos(\beta\mathrm{A12})\sin^2(\beta\mathrm{A13})\sin(\beta\mathrm{A12}) -$ $1.06066\ \mathrm{A12\ A13}\ (\Omega1 - \Omega3) \cos(\alpha\mathrm{A12} - 2\,\alpha\mathrm{A13})\cos(\beta\mathrm{A12})\sin^2(\beta\mathrm{A13})\sin(\beta\mathrm{A12}) +$ $0.353553\ \mathrm{A12\ A23}\ \Omega1 \cos(\alpha\mathrm{A12} + 2\,\alpha\mathrm{A23})\cos(\beta\mathrm{A12})\sin^2(\beta\mathrm{A23})\sin(\beta\mathrm{A12}) -$ $0.53033\ \mathrm{A12\ A23}\ \Omega2 \cos(\alpha\mathrm{A12} + 2\,\alpha\mathrm{A23})\cos(\beta\mathrm{A12})\sin^2(\beta\mathrm{A23})\sin(\beta\mathrm{A12}) +$ $0.176777\ \mathrm{A12\ A23}\ \Omega3 \cos(\alpha\mathrm{A12} + 2\,\alpha\mathrm{A23})\cos(\beta\mathrm{A12})\sin^2(\beta\mathrm{A23})\sin(\beta\mathrm{A12}) -$ $1.06066\ \mathrm{A12\ A23}\ \Omega1 \cos(\alpha\mathrm{A12} - 2\,\alpha\mathrm{A23})\cos(\beta\mathrm{A12})\sin^2(\beta\mathrm{A23})\sin(\beta\mathrm{A12}) +$ $0.53033\ \mathrm{A12\ A23}\ \Omega2 \cos(\alpha\mathrm{A12} - 2\,\alpha\mathrm{A23})\cos(\beta\mathrm{A12})\sin^2(\beta\mathrm{A23})\sin(\beta\mathrm{A12}) +$ $0.53033\ \mathrm{A12\ A23}\ \Omega3 \cos(\alpha\mathrm{A12} - 2\,\alpha\mathrm{A23})\cos(\beta\mathrm{A12})\sin^2(\beta\mathrm{A23})\sin(\beta\mathrm{A12}) -$ $6.\ \mathrm{A12\ A13}\ (\Omega1 - \Omega3) \cos(\alpha\mathrm{A12} - \alpha\mathrm{A13})\cos(\beta\mathrm{A12})\cos(\beta\mathrm{A13})\sin(\beta\mathrm{A13})\sin(\beta\mathrm{A12}) +$ $3.\ \mathrm{A12\ A13}\ \Omega1 \cos(\alpha\mathrm{A12} + \alpha\mathrm{A13})\cos(\beta\mathrm{A12})\cos(\beta\mathrm{A13})\sin(\beta\mathrm{A13})\sin(\beta\mathrm{A12}) -$ $3.\ \mathrm{A12\ A13}\ \Omega3 \cos(\alpha\mathrm{A12} + \alpha\mathrm{A13})\cos(\beta\mathrm{A12})\cos(\beta\mathrm{A13})\sin(\beta\mathrm{A13})\sin(\beta\mathrm{A12}) +$ $3.\ \mathrm{A12\ A23}\ \Omega1 \cos(\alpha\mathrm{A12} - \alpha\mathrm{A23})\cos(\beta\mathrm{A12})\cos(\beta\mathrm{A23})\sin(\beta\mathrm{A23})\sin(\beta\mathrm{A12}) -$ $6.\ \mathrm{A12\ A23}\ \Omega2 \cos(\alpha\mathrm{A12} - \alpha\mathrm{A23})\cos(\beta\mathrm{A12})\cos(\beta\mathrm{A23})\sin(\beta\mathrm{A23})\sin(\beta\mathrm{A12}) +$ $3.\ \mathrm{A12\ A23}\ \Omega3 \cos(\alpha\mathrm{A12} - \alpha\mathrm{A23})\cos(\beta\mathrm{A12})\cos(\beta\mathrm{A23})\sin(\beta\mathrm{A23})\sin(\beta\mathrm{A12}) -$ $1.5\ \mathrm{A12\ A23}\ \Omega1 \cos(\alpha\mathrm{A12} + \alpha\mathrm{A23})\cos(\beta\mathrm{A12})\cos(\beta\mathrm{A23})\sin(\beta\mathrm{A23})\sin(\beta\mathrm{A12}) +$ $3.\ \mathrm{A12\ A23}\ \Omega2 \cos(\alpha\mathrm{A12} + \alpha\mathrm{A23})\cos(\beta\mathrm{A12})\cos(\beta\mathrm{A23})\sin(\beta\mathrm{A23})\sin(\beta\mathrm{A12}) -$ $1.5\ \mathrm{A12\ A23}\ \Omega3 \cos(\alpha\mathrm{A12} + \alpha\mathrm{A23})\cos(\beta\mathrm{A12})\cos(\beta\mathrm{A23})\sin(\beta\mathrm{A23})\sin(\beta\mathrm{A12}) +$ $0.1875\ \mathrm{A13\ A23}\ \Omega1 \cos(2\,(\alpha\mathrm{A13} - \alpha\mathrm{A23}))\sin^2(\beta\mathrm{A13})\sin^2(\beta\mathrm{A23}) -$ $0.1875\ \mathrm{A13\ A23}\ \Omega3 \cos(2\,(\alpha\mathrm{A13} - \alpha\mathrm{A23}))\sin^2(\beta\mathrm{A13})\sin^2(\beta\mathrm{A23}) -$ $0.09375\ \mathrm{A13\ A23}\ \Omega1 \cos(2\,(\alpha\mathrm{A13} + \alpha\mathrm{A23}))\sin^2(\beta\mathrm{A13})\sin^2(\beta\mathrm{A23}) +$ $0.09375\ \mathrm{A13\ A23}\ \Omega3 \cos(2\,(\alpha\mathrm{A13} + \alpha\mathrm{A23}))\sin^2(\beta\mathrm{A13})\sin^2(\beta\mathrm{A23}) +$ $0.707107\ \mathrm{A13\ A23}\ \Omega1 \cos(\alpha\mathrm{A13} + 2\,\alpha\mathrm{A23})\cos(\beta\mathrm{A13})\sin(\beta\mathrm{A13})\sin^2(\beta\mathrm{A23}) -$ $0.707107\ \mathrm{A13\ A23}\ \Omega3 \cos(\alpha\mathrm{A13} + 2\,\alpha\mathrm{A23})\cos(\beta\mathrm{A13})\sin(\beta\mathrm{A13})\sin^2(\beta\mathrm{A23}) -$ $2.12132\ \mathrm{A13\ A23}\ \Omega1 \cos(\alpha\mathrm{A13} - 2\,\alpha\mathrm{A23})\cos(\beta\mathrm{A13})\sin(\beta\mathrm{A13})\sin^2(\beta\mathrm{A23}) +$ $2.12132\ \mathrm{A13\ A23}\ \Omega3 \cos(\alpha\mathrm{A13} - 2\,\alpha\mathrm{A23})\cos(\beta\mathrm{A13})\sin(\beta\mathrm{A13})\sin^2(\beta\mathrm{A23}) +$ $1.06066\ \mathrm{A13\ A23}\ \Omega1 \cos(2\,\alpha\mathrm{A13} - \alpha\mathrm{A23})\cos(\beta\mathrm{A23})\sin^2(\beta\mathrm{A13})\sin(\beta\mathrm{A23}) -$ $1.06066\ \mathrm{A13\ A23}\ \Omega3 \cos(2\,\alpha\mathrm{A13} - \alpha\mathrm{A23})\cos(\beta\mathrm{A23})\sin^2(\beta\mathrm{A13})\sin(\beta\mathrm{A23}) +$ $0.353553\ \mathrm{A13\ A23}\ \Omega1 \cos(2\,\alpha\mathrm{A13} + \alpha\mathrm{A23})\cos(\beta\mathrm{A23})\sin^2(\beta\mathrm{A13})\sin(\beta\mathrm{A23}) -$ $0.353553\ \mathrm{A13\ A23}\ \Omega3 \cos(2\,\alpha\mathrm{A13} + \alpha\mathrm{A23})\cos(\beta\mathrm{A23})\sin^2(\beta\mathrm{A13})\sin(\beta\mathrm{A23}) +$ $6.\ \mathrm{A13\ A23}\ \Omega1 \cos(\alpha\mathrm{A13} - \alpha\mathrm{A23})\cos(\beta\mathrm{A13})\cos(\beta\mathrm{A23})\sin(\beta\mathrm{A13})\sin(\beta\mathrm{A23}) -$ $6.\ \mathrm{A13\ A23}\ \Omega3 \cos(\alpha\mathrm{A13} - \alpha\mathrm{A23})\cos(\beta\mathrm{A13})\cos(\beta\mathrm{A23})\sin(\beta\mathrm{A13})\sin(\beta\mathrm{A23}) -$ $3.\ \mathrm{A13\ A23}\ \Omega1 \cos(\alpha\mathrm{A13} + \alpha\mathrm{A23})\cos(\beta\mathrm{A13})\cos(\beta\mathrm{A23})\sin(\beta\mathrm{A13})\sin(\beta\mathrm{A23}) +$ $3.\ \mathrm{A13\ A23}\ \Omega3 \cos(\alpha\mathrm{A13} + \alpha\mathrm{A23})\cos(\beta\mathrm{A13})\cos(\beta\mathrm{A23})\sin(\beta\mathrm{A13})\sin(\beta\mathrm{A23})\big)$

$(I_1^+ I_2^- I_{3z} - I_1^- I_2^+ I_{3z})$
$-\frac{1}{24\,\omega\mathrm{rot}^2}$
$\big(0.1875\,\mathrm{A12\,A13}\,\Omega1\cos(2\,(\alpha\mathrm{A12}-\alpha\mathrm{A13}))\sin^2(\beta\mathrm{A13})\sin^2(\beta\mathrm{A12}) - 0.1875\,\mathrm{A12\,A13}\,\Omega2\cos(2\,(\alpha\mathrm{A12}-\alpha\mathrm{A13}))$
$\sin^2(\beta\mathrm{A13})\sin^2(\beta\mathrm{A12}) - 0.09375\,\mathrm{A12\,A13}\,\Omega1\cos(2\,(\alpha\mathrm{A12}+\alpha\mathrm{A13}))\sin^2(\beta\mathrm{A13})\sin^2(\beta\mathrm{A12}) +$
$0.09375\,\mathrm{A12\,A13}\,\Omega2\cos(2\,(\alpha\mathrm{A12}+\alpha\mathrm{A13}))\sin^2(\beta\mathrm{A13})\sin^2(\beta\mathrm{A12}) -$
$0.1875\,\mathrm{A12\,A23}\,\Omega1\cos(2\,(\alpha\mathrm{A12}-\alpha\mathrm{A23}))\sin^2(\beta\mathrm{A23})\sin^2(\beta\mathrm{A12}) +$
$0.1875\,\mathrm{A12\,A23}\,\Omega2\cos(2\,(\alpha\mathrm{A12}-\alpha\mathrm{A23}))\sin^2(\beta\mathrm{A23})\sin^2(\beta\mathrm{A12}) +$
$0.09375\,\mathrm{A12\,A23}\,\Omega1\cos(2\,(\alpha\mathrm{A12}+\alpha\mathrm{A23}))\sin^2(\beta\mathrm{A23})\sin^2(\beta\mathrm{A12}) -$
$0.09375\,\mathrm{A12\,A23}\,\Omega2\cos(2\,(\alpha\mathrm{A12}+\alpha\mathrm{A23}))\sin^2(\beta\mathrm{A23})\sin^2(\beta\mathrm{A12}) +$
$1.06066\,\mathrm{A12\,A13}\,\Omega1\cos(2\,\alpha\mathrm{A12}-\alpha\mathrm{A13})\cos(\beta\mathrm{A13})\sin(\beta\mathrm{A13})\sin^2(\beta\mathrm{A12}) -$
$1.06066\,\mathrm{A12\,A13}\,\Omega2\cos(2\,\alpha\mathrm{A12}-\alpha\mathrm{A13})\cos(\beta\mathrm{A13})\sin(\beta\mathrm{A13})\sin^2(\beta\mathrm{A12}) +$
$0.353553\,\mathrm{A12\,A13}\,\Omega1\cos(2\,\alpha\mathrm{A12}+\alpha\mathrm{A13})\cos(\beta\mathrm{A13})\sin(\beta\mathrm{A13})\sin^2(\beta\mathrm{A12}) -$
$0.353553\,\mathrm{A12\,A13}\,\Omega2\cos(2\,\alpha\mathrm{A12}+\alpha\mathrm{A13})\cos(\beta\mathrm{A13})\sin(\beta\mathrm{A13})\sin^2(\beta\mathrm{A12}) -$
$1.06066\,\mathrm{A12\,A23}\,\Omega1\cos(2\,\alpha\mathrm{A12}-\alpha\mathrm{A23})\cos(\beta\mathrm{A23})\sin(\beta\mathrm{A23})\sin^2(\beta\mathrm{A12}) +$
$1.06066\,\mathrm{A12\,A23}\,\Omega2\cos(2\,\alpha\mathrm{A12}-\alpha\mathrm{A23})\cos(\beta\mathrm{A23})\sin(\beta\mathrm{A23})\sin^2(\beta\mathrm{A12}) -$
$0.353553\,\mathrm{A12\,A23}\,\Omega1\cos(2\,\alpha\mathrm{A12}+\alpha\mathrm{A23})\cos(\beta\mathrm{A23})\sin(\beta\mathrm{A23})\sin^2(\beta\mathrm{A12}) +$
$0.353553\,\mathrm{A12\,A23}\,\Omega2\cos(2\,\alpha\mathrm{A12}+\alpha\mathrm{A23})\cos(\beta\mathrm{A23})\sin(\beta\mathrm{A23})\sin^2(\beta\mathrm{A12}) +$
$0.707107\,\mathrm{A12\,A13}\,\Omega1\cos(\alpha\mathrm{A12}+2\,\alpha\mathrm{A13})\cos(\beta\mathrm{A12})\sin^2(\beta\mathrm{A13})\sin(\beta\mathrm{A12}) -$
$0.707107\,\mathrm{A12\,A13}\,\Omega2\cos(\alpha\mathrm{A12}+2\,\alpha\mathrm{A13})\cos(\beta\mathrm{A12})\sin^2(\beta\mathrm{A13})\sin(\beta\mathrm{A12}) -$
$2.12132\,\mathrm{A12\,A13}\,(\Omega1-\Omega2)\cos(\alpha\mathrm{A12}-2\,\alpha\mathrm{A13})\cos(\beta\mathrm{A12})\sin^2(\beta\mathrm{A13})\sin(\beta\mathrm{A12}) -$
$0.707107\,\mathrm{A12\,A23}\,\Omega1\cos(\alpha\mathrm{A12}+2\,\alpha\mathrm{A23})\cos(\beta\mathrm{A12})\sin^2(\beta\mathrm{A23})\sin(\beta\mathrm{A12}) +$
$0.707107\,\mathrm{A12\,A23}\,\Omega2\cos(\alpha\mathrm{A12}+2\,\alpha\mathrm{A23})\cos(\beta\mathrm{A12})\sin^2(\beta\mathrm{A23})\sin(\beta\mathrm{A12}) +$
$2.12132\,\mathrm{A12\,A23}\,\Omega1\cos(\alpha\mathrm{A12}-2\,\alpha\mathrm{A23})\cos(\beta\mathrm{A12})\sin^2(\beta\mathrm{A23})\sin(\beta\mathrm{A12}) -$
$2.12132\,\mathrm{A12\,A23}\,\Omega2\cos(\alpha\mathrm{A12}-2\,\alpha\mathrm{A23})\cos(\beta\mathrm{A12})\sin^2(\beta\mathrm{A23})\sin(\beta\mathrm{A12}) +$
$6.\,\mathrm{A12\,A13}\,(\Omega1-\Omega2)\cos(\alpha\mathrm{A12}-\alpha\mathrm{A13})\cos(\beta\mathrm{A12})\cos(\beta\mathrm{A13})\sin(\beta\mathrm{A13})\sin(\beta\mathrm{A12}) -$
$3.\,\mathrm{A12\,A13}\,\Omega1\cos(\alpha\mathrm{A12}+\alpha\mathrm{A13})\cos(\beta\mathrm{A12})\cos(\beta\mathrm{A13})\sin(\beta\mathrm{A13})\sin(\beta\mathrm{A12}) +$
$3.\,\mathrm{A12\,A13}\,\Omega2\cos(\alpha\mathrm{A12}+\alpha\mathrm{A13})\cos(\beta\mathrm{A12})\cos(\beta\mathrm{A13})\sin(\beta\mathrm{A13})\sin(\beta\mathrm{A12}) -$
$6.\,\mathrm{A12\,A23}\,\Omega1\cos(\alpha\mathrm{A12}-\alpha\mathrm{A23})\cos(\beta\mathrm{A12})\cos(\beta\mathrm{A23})\sin(\beta\mathrm{A23})\sin(\beta\mathrm{A12}) +$
$6.\,\mathrm{A12\,A23}\,\Omega2\cos(\alpha\mathrm{A12}-\alpha\mathrm{A23})\cos(\beta\mathrm{A12})\cos(\beta\mathrm{A23})\sin(\beta\mathrm{A23})\sin(\beta\mathrm{A12}) +$
$3.\,\mathrm{A12\,A23}\,\Omega1\cos(\alpha\mathrm{A12}+\alpha\mathrm{A23})\cos(\beta\mathrm{A12})\cos(\beta\mathrm{A23})\sin(\beta\mathrm{A23})\sin(\beta\mathrm{A12}) -$
$3.\,\mathrm{A12\,A23}\,\Omega2\cos(\alpha\mathrm{A12}+\alpha\mathrm{A23})\cos(\beta\mathrm{A12})\cos(\beta\mathrm{A23})\sin(\beta\mathrm{A23})\sin(\beta\mathrm{A12}) -$
$0.09375\,\mathrm{A13\,A23}\,\Omega1\cos(2\,(\alpha\mathrm{A13}-\alpha\mathrm{A23}))\sin^2(\beta\mathrm{A13})\sin^2(\beta\mathrm{A23}) -$
$0.09375\,\mathrm{A13\,A23}\,\Omega2\cos(2\,(\alpha\mathrm{A13}-\alpha\mathrm{A23}))\sin^2(\beta\mathrm{A13})\sin^2(\beta\mathrm{A23}) +$
$0.1875\,\mathrm{A13\,A23}\,\Omega3\cos(2\,(\alpha\mathrm{A13}-\alpha\mathrm{A23}))\sin^2(\beta\mathrm{A13})\sin^2(\beta\mathrm{A23}) +$
$0.046875\,\mathrm{A13\,A23}\,\Omega1\cos(2\,(\alpha\mathrm{A13}+\alpha\mathrm{A23}))\sin^2(\beta\mathrm{A13})\sin^2(\beta\mathrm{A23}) +$
$0.046875\,\mathrm{A13\,A23}\,\Omega2\cos(2\,(\alpha\mathrm{A13}+\alpha\mathrm{A23}))\sin^2(\beta\mathrm{A13})\sin^2(\beta\mathrm{A23}) -$
$0.09375\,\mathrm{A13\,A23}\,\Omega3\cos(2\,(\alpha\mathrm{A13}+\alpha\mathrm{A23}))\sin^2(\beta\mathrm{A13})\sin^2(\beta\mathrm{A23}) -$
$0.353553\,\mathrm{A13\,A23}\,\Omega1\cos(\alpha\mathrm{A13}+2\,\alpha\mathrm{A23})\cos(\beta\mathrm{A13})\sin(\beta\mathrm{A13})\sin^2(\beta\mathrm{A23}) -$
$0.176777\,\mathrm{A13\,A23}\,\Omega2\cos(\alpha\mathrm{A13}+2\,\alpha\mathrm{A23})\cos(\beta\mathrm{A13})\sin(\beta\mathrm{A13})\sin^2(\beta\mathrm{A23}) +$
$0.53033\,\mathrm{A13\,A23}\,\Omega3\cos(\alpha\mathrm{A13}+2\,\alpha\mathrm{A23})\cos(\beta\mathrm{A13})\sin(\beta\mathrm{A13})\sin^2(\beta\mathrm{A23}) +$
$1.06066\,\mathrm{A13\,A23}\,\Omega1\cos(\alpha\mathrm{A13}-2\,\alpha\mathrm{A23})\cos(\beta\mathrm{A13})\sin(\beta\mathrm{A13})\sin^2(\beta\mathrm{A23}) -$
$0.53033\,\mathrm{A13\,A23}\,\Omega2\cos(\alpha\mathrm{A13}-2\,\alpha\mathrm{A23})\cos(\beta\mathrm{A13})\sin(\beta\mathrm{A13})\sin^2(\beta\mathrm{A23}) -$
$0.53033\,\mathrm{A13\,A23}\,\Omega3\cos(\alpha\mathrm{A13}-2\,\alpha\mathrm{A23})\cos(\beta\mathrm{A13})\sin(\beta\mathrm{A13})\sin^2(\beta\mathrm{A23}) -$
$0.53033\,\mathrm{A13\,A23}\,\Omega1\cos(2\,\alpha\mathrm{A13}-\alpha\mathrm{A23})\cos(\beta\mathrm{A23})\sin^2(\beta\mathrm{A13})\sin(\beta\mathrm{A23}) +$
$1.06066\,\mathrm{A13\,A23}\,\Omega2\cos(2\,\alpha\mathrm{A13}-\alpha\mathrm{A23})\cos(\beta\mathrm{A23})\sin^2(\beta\mathrm{A13})\sin(\beta\mathrm{A23}) -$
$0.53033\,\mathrm{A13\,A23}\,\Omega3\cos(2\,\alpha\mathrm{A13}-\alpha\mathrm{A23})\cos(\beta\mathrm{A23})\sin^2(\beta\mathrm{A13})\sin(\beta\mathrm{A23}) -$
$0.176777\,\mathrm{A13\,A23}\,\Omega1\cos(2\,\alpha\mathrm{A13}+\alpha\mathrm{A23})\cos(\beta\mathrm{A23})\sin^2(\beta\mathrm{A13})\sin(\beta\mathrm{A23}) -$
$0.353553\,\mathrm{A13\,A23}\,\Omega2\cos(2\,\alpha\mathrm{A13}+\alpha\mathrm{A23})\cos(\beta\mathrm{A23})\sin^2(\beta\mathrm{A13})\sin(\beta\mathrm{A23}) +$
$0.53033\,\mathrm{A13\,A23}\,\Omega3\cos(2\,\alpha\mathrm{A13}+\alpha\mathrm{A23})\cos(\beta\mathrm{A23})\sin^2(\beta\mathrm{A13})\sin(\beta\mathrm{A23}) -$
$3.\,\mathrm{A13\,A23}\,\Omega1\cos(\alpha\mathrm{A13}-\alpha\mathrm{A23})\cos(\beta\mathrm{A13})\cos(\beta\mathrm{A23})\sin(\beta\mathrm{A13})\sin(\beta\mathrm{A23}) -$
$3.\,\mathrm{A13\,A23}\,\Omega2\cos(\alpha\mathrm{A13}-\alpha\mathrm{A23})\cos(\beta\mathrm{A13})\cos(\beta\mathrm{A23})\sin(\beta\mathrm{A13})\sin(\beta\mathrm{A23}) +$
$6.\,\mathrm{A13\,A23}\,\Omega3\cos(\alpha\mathrm{A13}-\alpha\mathrm{A23})\cos(\beta\mathrm{A13})\cos(\beta\mathrm{A23})\sin(\beta\mathrm{A13})\sin(\beta\mathrm{A23}) +$
$1.5\,\mathrm{A13\,A23}\,\Omega1\cos(\alpha\mathrm{A13}+\alpha\mathrm{A23})\cos(\beta\mathrm{A13})\cos(\beta\mathrm{A23})\sin(\beta\mathrm{A13})\sin(\beta\mathrm{A23}) +$
$1.5\,\mathrm{A13\,A23}\,\Omega2\cos(\alpha\mathrm{A13}+\alpha\mathrm{A23})\cos(\beta\mathrm{A13})\cos(\beta\mathrm{A23})\sin(\beta\mathrm{A13})\sin(\beta\mathrm{A23}) -$
$3.\,\mathrm{A13\,A23}\,\Omega3\cos(\alpha\mathrm{A13}+\alpha\mathrm{A23})\cos(\beta\mathrm{A13})\cos(\beta\mathrm{A23})\sin(\beta\mathrm{A13})\sin(\beta\mathrm{A23})\big)$

Secular

I_{1z}	$\frac{1}{8\,\omega\mathrm{rot}^2}\Big(\mathrm{A12}^2\sin^2(\beta\mathrm{A12})\,(\Omega2-\Omega1)\,\big(-0.015625\,\mathrm{A12}^2\sin^2(\beta\mathrm{A12})\,\big(31.99\cos(2\,\alpha\mathrm{A12})\cos^2(\beta\mathrm{A12})+\sin(\beta\mathrm{A12})\,(11.31\cos(\alpha\mathrm{A12})\cos(\beta\mathrm{A12})-11.31\cos(3\,\alpha\mathrm{A12})\cos(\beta\mathrm{A12})+\cos(4\,\alpha\mathrm{A12})\sin(\beta\mathrm{A12}))\big)-0.031\,\mathrm{A12}^2\sin^2(\beta\mathrm{A12})+\cos^2(\beta\mathrm{A12})\big)+\mathrm{A13}^2\sin^2(\beta\mathrm{A13})\,(\Omega3-\Omega1)\,\big(-0.015625\,\mathrm{A13}^2\sin^2(\beta\mathrm{A13})\,\big(31.99\cos(2\,\alpha\mathrm{A13})\cos^2(\beta\mathrm{A13})+\sin(\beta\mathrm{A13})\,(11.31\cos(\alpha\mathrm{A13})\cos(\beta\mathrm{A13})-11.31\cos(3\,\alpha\mathrm{A13})\cos(\beta\mathrm{A13})+\cos(4\,\alpha\mathrm{A13})\sin(\beta\mathrm{A13}))\big)-0.031\,\mathrm{A13}^2\sin^2(\beta\mathrm{A13})+\cos^2(\beta\mathrm{A13})\big)\Big)$
I_{2z}	$\frac{1}{8\,\omega\mathrm{rot}^2}\Big(\mathrm{A23}^2\sin^2(\beta\mathrm{A23})\,(\Omega3-\Omega2)\,\big(-0.015625\,\mathrm{A23}^2\sin^2(\beta\mathrm{A23})\,\big(31.99\cos(2\,\alpha\mathrm{A23})\cos^2(\beta\mathrm{A23})+\sin(\beta\mathrm{A23})\,(11.31\cos(\alpha\mathrm{A23})\cos(\beta\mathrm{A23})-11.31\cos(3\,\alpha\mathrm{A23})\cos(\beta\mathrm{A23})+\cos(4\,\alpha\mathrm{A23})\sin(\beta\mathrm{A23}))\big)-0.031\,\mathrm{A23}^2\sin^2(\beta\mathrm{A23})+\cos^2(\beta\mathrm{A23})\big)-\mathrm{A12}^2\sin^2(\beta\mathrm{A12})\,(\Omega2-\Omega1)\,\big(-0.015625\,\mathrm{A12}^2\sin^2(\beta\mathrm{A12})\,\big(31.99\cos(2\,\alpha\mathrm{A12})\cos^2(\beta\mathrm{A12})+\sin(\beta\mathrm{A12})\,(11.31\cos(\alpha\mathrm{A12})\cos(\beta\mathrm{A12})-11.31\cos(3\,\alpha\mathrm{A12})\cos(\beta\mathrm{A12})+\cos(4\,\alpha\mathrm{A12})\sin(\beta\mathrm{A12}))\big)-0.031\,\mathrm{A12}^2\sin^2(\beta\mathrm{A12})+\cos^2(\beta\mathrm{A12})\big)\Big)$
I_{3z}	$\frac{1}{8\,\omega\mathrm{rot}^2}\big(-\mathrm{A13}^2\sin^2(\beta\mathrm{A13})\,(\Omega3-\Omega1)\,\big(-0.015625\,\mathrm{A13}^2\sin^2(\beta\mathrm{A13})\,\big(31.99\cos(2\,\alpha\mathrm{A13})\cos^2(\beta\mathrm{A13})+\sin(\beta\mathrm{A13})\,(11.31\cos(\alpha\mathrm{A13})\cos(\beta\mathrm{A13})-11.31\cos(3\,\alpha\mathrm{A13})\cos(\beta\mathrm{A13})+\cos(4\,\alpha\mathrm{A13})\sin(\beta\mathrm{A13}))\big)-0.031\,\mathrm{A13}^2\sin^2(\beta\mathrm{A13})+\cos^2(\beta\mathrm{A13})\big)-\mathrm{A23}^2\sin^2(\beta\mathrm{A23})\,(\Omega3-\Omega2)\,\big(-0.015625\,\mathrm{A23}^2\sin^2(\beta\mathrm{A23})\,\big(31.99\cos(2\,\alpha\mathrm{A23})\cos^2(\beta\mathrm{A23})+\sin(\beta\mathrm{A23})\,(11.31\cos(\alpha\mathrm{A23})\cos(\beta\mathrm{A23})-11.31\cos(3\,\alpha\mathrm{A23})\cos(\beta\mathrm{A23})+\cos(4\,\alpha\mathrm{A23})\sin(\beta\mathrm{A23}))\big)-0.031\,\mathrm{A23}^2\sin^2(\beta\mathrm{A23})+\cos^2(\beta\mathrm{A23})\big)\big)$

$I_{1z}I_{2z}$
$-\frac{1}{4\,\omega\mathrm{rot}^2}\big(0.00390625\,\mathrm{A12}\,\mathrm{A13}^2\cos(2\,(\alpha\mathrm{A12}-2\,\alpha\mathrm{A13}))\sin^2(\beta\mathrm{A12})\sin^4(\beta\mathrm{A13})+$ $0.00390625\,\mathrm{A13}^2\,\mathrm{A23}\cos(2\,\alpha\mathrm{A23})\sin^2(\beta\mathrm{A23})\sin^4(\beta\mathrm{A13})-$ $0.00390625\,\mathrm{A13}^2\,\mathrm{A23}\cos(4\,\alpha\mathrm{A13}-2\,\alpha\mathrm{A23})\sin^2(\beta\mathrm{A23})\sin^4(\beta\mathrm{A13})+$ $0.0220971\,\mathrm{A12}\,\mathrm{A13}^2\cos(2\,\alpha\mathrm{A12}-\alpha\mathrm{A13})\cos(\beta\mathrm{A13})\sin^2(\beta\mathrm{A12})\sin^3(\beta\mathrm{A13})-$ $0.0220971\,\mathrm{A12}\,\mathrm{A13}^2\cos(2\,\alpha\mathrm{A12}-3\,\alpha\mathrm{A13})\cos(\beta\mathrm{A13})\sin^2(\beta\mathrm{A12})\sin^3(\beta\mathrm{A13})-$ $0.0220971\,\mathrm{A13}^2\,\mathrm{A23}\cos(\alpha\mathrm{A13}-2\,\alpha\mathrm{A23})\cos(\beta\mathrm{A13})\sin^2(\beta\mathrm{A23})\sin^3(\beta\mathrm{A13})+$ $0.0220971\,\mathrm{A13}^2\,\mathrm{A23}\cos(3\,\alpha\mathrm{A13}-2\,\alpha\mathrm{A23})\cos(\beta\mathrm{A13})\sin^2(\beta\mathrm{A23})\sin^3(\beta\mathrm{A13})+$ $0.0625\,\mathrm{A12}\,\mathrm{A13}^2\cos(\alpha\mathrm{A12}-\alpha\mathrm{A13})\cos(\beta\mathrm{A12})\cos(\beta\mathrm{A13})\sin(\beta\mathrm{A12})\sin^3(\beta\mathrm{A13})-$ $0.0625\,\mathrm{A12}\,\mathrm{A13}^2\cos(\alpha\mathrm{A12}+\alpha\mathrm{A13})\cos(\beta\mathrm{A12})\cos(\beta\mathrm{A13})\sin(\beta\mathrm{A12})\sin^3(\beta\mathrm{A13})+$ $0.0625\,\mathrm{A12}\,\mathrm{A13}^2\cos(\alpha\mathrm{A12}-3\,\alpha\mathrm{A13})\cos(\beta\mathrm{A12})\cos(\beta\mathrm{A13})\sin(\beta\mathrm{A12})\sin^3(\beta\mathrm{A13})-$ $0.0625\,\mathrm{A13}^2\,\mathrm{A23}\cos(\alpha\mathrm{A13}-\alpha\mathrm{A23})\cos(\beta\mathrm{A13})\cos(\beta\mathrm{A23})\sin(\beta\mathrm{A23})\sin^3(\beta\mathrm{A13})-$ $0.0625\,\mathrm{A13}^2\,\mathrm{A23}\cos(3\,\alpha\mathrm{A13}-\alpha\mathrm{A23})\cos(\beta\mathrm{A13})\cos(\beta\mathrm{A23})\sin(\beta\mathrm{A23})\sin^3(\beta\mathrm{A13})+$ $0.0625\,\mathrm{A13}^2\,\mathrm{A23}\cos(\alpha\mathrm{A13}+\alpha\mathrm{A23})\cos(\beta\mathrm{A13})\cos(\beta\mathrm{A23})\sin(\beta\mathrm{A23})\sin^3(\beta\mathrm{A13})+$ $0.00390625\,\mathrm{A13}\,\mathrm{A23}^2\cos(2\,\alpha\mathrm{A13})\sin^4(\beta\mathrm{A23})\sin^2(\beta\mathrm{A13})-$ $0.00390625\,\mathrm{A13}\,\mathrm{A23}^2\cos(2\,(\alpha\mathrm{A13}-2\,\alpha\mathrm{A23}))\sin^4(\beta\mathrm{A23})\sin^2(\beta\mathrm{A13})-$ $0.0220971\,\mathrm{A13}\,\mathrm{A23}^2\cos(2\,\alpha\mathrm{A13}-\alpha\mathrm{A23})\cos(\beta\mathrm{A23})\sin^3(\beta\mathrm{A23})\sin^2(\beta\mathrm{A13})+$ $0.0220971\,\mathrm{A13}\,\mathrm{A23}^2\cos(2\,\alpha\mathrm{A13}-3\,\alpha\mathrm{A23})\cos(\beta\mathrm{A23})\sin^3(\beta\mathrm{A23})\sin^2(\beta\mathrm{A13})-$ $0.0625\,\mathrm{A12}\,\mathrm{A13}^2\cos(2\,(\alpha\mathrm{A12}-\alpha\mathrm{A13}))\cos^2(\beta\mathrm{A13})\sin^2(\beta\mathrm{A12})\sin^2(\beta\mathrm{A13})+$ $0.0625\,\mathrm{A13}^2\,\mathrm{A23}\cos(2\,(\alpha\mathrm{A13}-\alpha\mathrm{A23}))\cos^2(\beta\mathrm{A13})\sin^2(\beta\mathrm{A23})\sin^2(\beta\mathrm{A13})+$ $0.0625\,\mathrm{A13}\,\mathrm{A23}^2\cos(2\,(\alpha\mathrm{A13}-\alpha\mathrm{A23}))\cos^2(\beta\mathrm{A23})\sin^2(\beta\mathrm{A23})\sin^2(\beta\mathrm{A13})+$ $0.00390625\,\mathrm{A12}\,\mathrm{A13}\,\mathrm{A23}\cos(2\,(\alpha\mathrm{A12}-\alpha\mathrm{A13}-\alpha\mathrm{A23}))\sin^2(\beta\mathrm{A12})\sin^2(\beta\mathrm{A23})\sin^2(\beta\mathrm{A13})-$ $0.00195313\,\mathrm{A12}\,\mathrm{A13}\,\mathrm{A23}\cos(2\,(\alpha\mathrm{A12}+\alpha\mathrm{A13}-\alpha\mathrm{A23}))\sin^2(\beta\mathrm{A12})\sin^2(\beta\mathrm{A23})\sin^2(\beta\mathrm{A13})-$ $0.00195313\,\mathrm{A12}\,\mathrm{A13}\,\mathrm{A23}\cos(2\,(\alpha\mathrm{A12}-\alpha\mathrm{A13}+\alpha\mathrm{A23}))\sin^2(\beta\mathrm{A12})\sin^2(\beta\mathrm{A23})\sin^2(\beta\mathrm{A13})-$ $0.353553\,\mathrm{A12}\,\mathrm{A13}^2\cos(\alpha\mathrm{A12}-2\,\alpha\mathrm{A13})\cos(\beta\mathrm{A12})\cos^2(\beta\mathrm{A13})\sin(\beta\mathrm{A12})\sin^2(\beta\mathrm{A13})-$ $0.0110485\,\mathrm{A12}\,\mathrm{A13}\,\mathrm{A23}\cos(2\,\alpha\mathrm{A12}-2\,\alpha\mathrm{A13}-\alpha\mathrm{A23})\cos(\beta\mathrm{A23})\sin^2(\beta\mathrm{A12})\sin(\beta\mathrm{A23})\sin^2(\beta\mathrm{A13})+$ $0.0110485\,\mathrm{A12}\,\mathrm{A13}\,\mathrm{A23}\cos(2\,\alpha\mathrm{A12}-2\,\alpha\mathrm{A13}+\alpha\mathrm{A23})\cos(\beta\mathrm{A23})\sin^2(\beta\mathrm{A12})\sin(\beta\mathrm{A23})\sin^2(\beta\mathrm{A13})+$ $0.353553\,\mathrm{A13}^2\,\mathrm{A23}\cos(2\,\alpha\mathrm{A13}-\alpha\mathrm{A23})\cos^2(\beta\mathrm{A13})\cos(\beta\mathrm{A23})\sin(\beta\mathrm{A23})\sin^2(\beta\mathrm{A13})-$ $0.353553\,\mathrm{A13}^2\,\mathrm{A23}\cos(\alpha\mathrm{A23})\cos^2(\beta\mathrm{A13})\cos(\beta\mathrm{A23})\sin(\beta\mathrm{A23})\sin^2(\beta\mathrm{A13})-$ $0.03125\,\mathrm{A12}\,\mathrm{A13}\,\mathrm{A23}\cos(\alpha\mathrm{A12}+2\,\alpha\mathrm{A13}-\alpha\mathrm{A23})\cos(\beta\mathrm{A12})\cos(\beta\mathrm{A23})\sin(\beta\mathrm{A12})\sin(\beta\mathrm{A23})\sin^2(\beta\mathrm{A13})+$ $0.03125\,\mathrm{A12}\,\mathrm{A13}\,\mathrm{A23}\cos(\alpha\mathrm{A12}-2\,\alpha\mathrm{A13}-\alpha\mathrm{A23})\cos(\beta\mathrm{A12})\cos(\beta\mathrm{A23})\sin(\beta\mathrm{A12})\sin(\beta\mathrm{A23})\sin^2(\beta\mathrm{A13})+$ $0.03125\,\mathrm{A12}\,\mathrm{A13}\,\mathrm{A23}\cos(\alpha\mathrm{A12}-2\,\alpha\mathrm{A13}+\alpha\mathrm{A23})\cos(\beta\mathrm{A12})\cos(\beta\mathrm{A23})\sin(\beta\mathrm{A12})\sin(\beta\mathrm{A23})\sin^2(\beta\mathrm{A13})-$ $0.0625\,\mathrm{A13}\,\mathrm{A23}^2\cos(\alpha\mathrm{A13}-\alpha\mathrm{A23})\cos(\beta\mathrm{A13})\cos(\beta\mathrm{A23})\sin^3(\beta\mathrm{A23})\sin(\beta\mathrm{A13})+$ $0.0625\,\mathrm{A13}\,\mathrm{A23}^2\cos(\alpha\mathrm{A13}+\alpha\mathrm{A23})\cos(\beta\mathrm{A13})\cos(\beta\mathrm{A23})\sin^3(\beta\mathrm{A23})\sin(\beta\mathrm{A13})-$ $0.0625\,\mathrm{A13}\,\mathrm{A23}^2\cos(\alpha\mathrm{A13}-3\,\alpha\mathrm{A23})\cos(\beta\mathrm{A13})\cos(\beta\mathrm{A23})\sin^3(\beta\mathrm{A23})\sin(\beta\mathrm{A13})-$ $0.353553\,\mathrm{A13}\,\mathrm{A23}^2\cos(\alpha\mathrm{A13})\cos(\beta\mathrm{A13})\cos^2(\beta\mathrm{A23})\sin^2(\beta\mathrm{A23})\sin(\beta\mathrm{A13})+$ $0.353553\,\mathrm{A13}\,\mathrm{A23}^2\cos(\alpha\mathrm{A13}-2\,\alpha\mathrm{A23})\cos(\beta\mathrm{A13})\cos^2(\beta\mathrm{A23})\sin^2(\beta\mathrm{A23})\sin(\beta\mathrm{A13})-$ $0.0110485\,\mathrm{A12}\,\mathrm{A13}\,\mathrm{A23}\cos(2\,\alpha\mathrm{A12}-\alpha\mathrm{A13}-2\,\alpha\mathrm{A23})\cos(\beta\mathrm{A13})\sin^2(\beta\mathrm{A12})\sin^2(\beta\mathrm{A23})\sin(\beta\mathrm{A13})+$ $0.0110485\,\mathrm{A12}\,\mathrm{A13}\,\mathrm{A23}\cos(2\,\alpha\mathrm{A12}+\alpha\mathrm{A13}-2\,\alpha\mathrm{A23})\cos(\beta\mathrm{A13})\sin^2(\beta\mathrm{A12})\sin^2(\beta\mathrm{A23})\sin(\beta\mathrm{A13})-$ $0.03125\,\mathrm{A12}\,\mathrm{A13}\,\mathrm{A23}\cos(\alpha\mathrm{A12}-\alpha\mathrm{A13}+2\,\alpha\mathrm{A23})\cos(\beta\mathrm{A12})\cos(\beta\mathrm{A13})\sin(\beta\mathrm{A12})\sin^2(\beta\mathrm{A23})\sin(\beta\mathrm{A13})+$ $0.03125\,\mathrm{A12}\,\mathrm{A13}\,\mathrm{A23}\cos(\alpha\mathrm{A12}-\alpha\mathrm{A13}-2\,\alpha\mathrm{A23})\cos(\beta\mathrm{A12})\cos(\beta\mathrm{A13})\sin(\beta\mathrm{A12})\sin^2(\beta\mathrm{A23})\sin(\beta\mathrm{A13})+$ $0.03125\,\mathrm{A12}\,\mathrm{A13}\,\mathrm{A23}\cos(\alpha\mathrm{A12}+\alpha\mathrm{A13}-2\,\alpha\mathrm{A23})\cos(\beta\mathrm{A12})\cos(\beta\mathrm{A13})\sin(\beta\mathrm{A12})\sin^2(\beta\mathrm{A23})\sin(\beta\mathrm{A13})-$ $0.0625\,\mathrm{A12}\,\mathrm{A13}\,\mathrm{A23}\cos(2\,\alpha\mathrm{A12}-\alpha\mathrm{A13}-\alpha\mathrm{A23})\cos(\beta\mathrm{A13})\cos(\beta\mathrm{A23})\sin^2(\beta\mathrm{A12})\sin(\beta\mathrm{A23})\sin(\beta\mathrm{A13})-$ $0.353553\,\mathrm{A12}\,\mathrm{A13}\,\mathrm{A23}\cos(\alpha\mathrm{A12}-\alpha\mathrm{A13}-\alpha\mathrm{A23})\cos(\beta\mathrm{A12})\cos(\beta\mathrm{A13})\cos(\beta\mathrm{A23})\sin(\beta\mathrm{A12})\sin(\beta\mathrm{A23})$ $\sin(\beta\mathrm{A13})+0.176777\,\mathrm{A12}\,\mathrm{A13}\,\mathrm{A23}\cos(\alpha\mathrm{A12}+\alpha\mathrm{A13}-\alpha\mathrm{A23})\cos(\beta\mathrm{A12})\cos(\beta\mathrm{A13})\cos(\beta\mathrm{A23})\sin(\beta\mathrm{A12})$ $\sin(\beta\mathrm{A23})\sin(\beta\mathrm{A13})+0.176777\,\mathrm{A12}\,\mathrm{A13}\,\mathrm{A23}\cos(\alpha\mathrm{A12}-\alpha\mathrm{A13}+\alpha\mathrm{A23})\cos(\beta\mathrm{A12})\cos(\beta\mathrm{A13})\cos(\beta\mathrm{A23})$ $\sin(\beta\mathrm{A12})\sin(\beta\mathrm{A23})\sin(\beta\mathrm{A13})+0.00390625\,\mathrm{A12}\,\mathrm{A23}^2\cos(2\,(\alpha\mathrm{A12}-2\,\alpha\mathrm{A23}))\sin^2(\beta\mathrm{A12})\sin^4(\beta\mathrm{A23})+$ $0.0220971\,\mathrm{A12}\,\mathrm{A23}^2\cos(2\,\alpha\mathrm{A12}-\alpha\mathrm{A23})\cos(\beta\mathrm{A23})\sin^2(\beta\mathrm{A12})\sin^3(\beta\mathrm{A23})-$ $0.0220971\,\mathrm{A12}\,\mathrm{A23}^2\cos(2\,\alpha\mathrm{A12}-3\,\alpha\mathrm{A23})\cos(\beta\mathrm{A23})\sin^2(\beta\mathrm{A12})\sin^3(\beta\mathrm{A23})+$ $0.0625\,\mathrm{A12}\,\mathrm{A23}^2\cos(\alpha\mathrm{A12}-\alpha\mathrm{A23})\cos(\beta\mathrm{A12})\cos(\beta\mathrm{A23})\sin(\beta\mathrm{A12})\sin^3(\beta\mathrm{A23})-$ $0.0625\,\mathrm{A12}\,\mathrm{A23}^2\cos(\alpha\mathrm{A12}+\alpha\mathrm{A23})\cos(\beta\mathrm{A12})\cos(\beta\mathrm{A23})\sin(\beta\mathrm{A12})\sin^3(\beta\mathrm{A23})+$ $0.0625\,\mathrm{A12}\,\mathrm{A23}^2\cos(\alpha\mathrm{A12}-3\,\alpha\mathrm{A23})\cos(\beta\mathrm{A12})\cos(\beta\mathrm{A23})\sin(\beta\mathrm{A12})\sin^3(\beta\mathrm{A23})-$ $0.0625\,\mathrm{A12}\,\mathrm{A23}^2\cos(2\,(\alpha\mathrm{A12}-\alpha\mathrm{A23}))\cos^2(\beta\mathrm{A23})\sin^2(\beta\mathrm{A12})\sin^2(\beta\mathrm{A23})-$ $0.353553\,\mathrm{A12}\,\mathrm{A23}^2\cos(\alpha\mathrm{A12}-2\,\alpha\mathrm{A23})\cos(\beta\mathrm{A12})\cos^2(\beta\mathrm{A23})\sin(\beta\mathrm{A12})\sin^2(\beta\mathrm{A23})+2.82843\,\mathrm{A12}$ $\cos(\alpha\mathrm{A12})\cos(\beta\mathrm{A12})\sin(\beta\mathrm{A12})\big(0.125\,\mathrm{A13}^2\cos^2(\beta\mathrm{A13})\sin^2(\beta\mathrm{A13})+0.125\,\mathrm{A23}^2\cos^2(\beta\mathrm{A23})\sin^2(\beta\mathrm{A23})\big)-$ $0.25\,\mathrm{A12}\cos(2\,\alpha\mathrm{A12})\sin^2(\beta\mathrm{A12})\big(0.015625\,\mathrm{A13}^2\sin^4(\beta\mathrm{A13})+0.015625\,\mathrm{A23}^2\sin^4(\beta\mathrm{A23})\big)\big)$

$I_{1z}I_{3z}$
$-\frac{1}{4\,\omega\mathrm{rot}^2}\big(-0.00390625\,\mathrm{A12}^2\,\mathrm{A13}\cos(2\,\alpha\mathrm{A13})\sin^2(\beta\mathrm{A13})\sin^4(\beta\mathrm{A12})+$ $0.00390625\,\mathrm{A12}^2\,\mathrm{A13}\cos(4\,\alpha\mathrm{A12}-2\,\alpha\mathrm{A13})\sin^2(\beta\mathrm{A13})\sin^4(\beta\mathrm{A12})+$ $0.00390625\,\mathrm{A12}^2\,\mathrm{A23}\cos(2\,\alpha\mathrm{A23})\sin^2(\beta\mathrm{A23})\sin^4(\beta\mathrm{A12})-$ $0.00390625\,\mathrm{A12}^2\,\mathrm{A23}\cos(4\,\alpha\mathrm{A12}-2\,\alpha\mathrm{A23})\sin^2(\beta\mathrm{A23})\sin^4(\beta\mathrm{A12})+$ $0.0220971\,\mathrm{A12}^2\,\mathrm{A13}\cos(\alpha\mathrm{A12}-2\,\alpha\mathrm{A13})\cos(\beta\mathrm{A12})\sin^2(\beta\mathrm{A13})\sin^3(\beta\mathrm{A12})-$ $0.0220971\,\mathrm{A12}^2\,\mathrm{A13}\cos(3\,\alpha\mathrm{A12}-2\,\alpha\mathrm{A13})\cos(\beta\mathrm{A12})\sin^2(\beta\mathrm{A13})\sin^3(\beta\mathrm{A12})-$ $0.0220971\,\mathrm{A12}^2\,\mathrm{A23}\cos(\alpha\mathrm{A12}-2\,\alpha\mathrm{A23})\cos(\beta\mathrm{A12})\sin^2(\beta\mathrm{A23})\sin^3(\beta\mathrm{A12})+$ $0.0220971\,\mathrm{A12}^2\,\mathrm{A23}\cos(3\,\alpha\mathrm{A12}-2\,\alpha\mathrm{A23})\cos(\beta\mathrm{A12})\sin^2(\beta\mathrm{A23})\sin^3(\beta\mathrm{A12})+$ $0.0625\,\mathrm{A12}^2\,\mathrm{A13}\cos(\alpha\mathrm{A12}-\alpha\mathrm{A13})\cos(\beta\mathrm{A12})\cos(\beta\mathrm{A13})\sin(\beta\mathrm{A13})\sin^3(\beta\mathrm{A12})+$ $0.0625\,\mathrm{A12}^2\,\mathrm{A13}\cos(3\,\alpha\mathrm{A12}-\alpha\mathrm{A13})\cos(\beta\mathrm{A12})\cos(\beta\mathrm{A13})\sin(\beta\mathrm{A13})\sin^3(\beta\mathrm{A12})-$ $0.0625\,\mathrm{A12}^2\,\mathrm{A13}\cos(\alpha\mathrm{A12}+\alpha\mathrm{A13})\cos(\beta\mathrm{A12})\cos(\beta\mathrm{A13})\sin(\beta\mathrm{A13})\sin^3(\beta\mathrm{A12})-$ $0.0625\,\mathrm{A12}^2\,\mathrm{A23}\cos(\alpha\mathrm{A12}-\alpha\mathrm{A23})\cos(\beta\mathrm{A12})\cos(\beta\mathrm{A23})\sin(\beta\mathrm{A23})\sin^3(\beta\mathrm{A12})-$ $0.0625\,\mathrm{A12}^2\,\mathrm{A23}\cos(3\,\alpha\mathrm{A12}-\alpha\mathrm{A23})\cos(\beta\mathrm{A12})\cos(\beta\mathrm{A23})\sin(\beta\mathrm{A23})\sin^3(\beta\mathrm{A12})+$ $0.0625\,\mathrm{A12}^2\,\mathrm{A23}\cos(\alpha\mathrm{A12}+\alpha\mathrm{A23})\cos(\beta\mathrm{A12})\cos(\beta\mathrm{A23})\sin(\beta\mathrm{A23})\sin^3(\beta\mathrm{A12})+$ $0.00390625\,\mathrm{A12}\,\mathrm{A23}^2\cos(2\,\alpha\mathrm{A12})\sin^4(\beta\mathrm{A23})\sin^2(\beta\mathrm{A12})-$ $0.00390625\,\mathrm{A12}\,\mathrm{A23}^2\cos(2\,(\alpha\mathrm{A12}-2\,\alpha\mathrm{A23}))\sin^4(\beta\mathrm{A23})\sin^2(\beta\mathrm{A12})-$ $0.0220971\,\mathrm{A12}\,\mathrm{A23}^2\cos(2\,\alpha\mathrm{A12}-\alpha\mathrm{A23})\cos(\beta\mathrm{A23})\sin^3(\beta\mathrm{A23})\sin^2(\beta\mathrm{A12})+$ $0.0220971\,\mathrm{A12}\,\mathrm{A23}^2\cos(2\,\alpha\mathrm{A12}-3\,\alpha\mathrm{A23})\cos(\beta\mathrm{A23})\sin^3(\beta\mathrm{A23})\sin^2(\beta\mathrm{A12})-$ $0.0625\,\mathrm{A12}^2\,\mathrm{A13}\cos(2\,(\alpha\mathrm{A12}-\alpha\mathrm{A13}))\cos^2(\beta\mathrm{A12})\sin^2(\beta\mathrm{A13})\sin^2(\beta\mathrm{A12})+$ $0.0625\,\mathrm{A12}^2\,\mathrm{A23}\cos(2\,(\alpha\mathrm{A12}-\alpha\mathrm{A23}))\cos^2(\beta\mathrm{A12})\sin^2(\beta\mathrm{A23})\sin^2(\beta\mathrm{A12})+$ $0.0625\,\mathrm{A12}\,\mathrm{A23}^2\cos(2\,(\alpha\mathrm{A12}-\alpha\mathrm{A23}))\cos^2(\beta\mathrm{A23})\sin^2(\beta\mathrm{A23})\sin^2(\beta\mathrm{A12})-$ $0.00195313\,\mathrm{A12}\,\mathrm{A13}\,\mathrm{A23}\cos(2\,(\alpha\mathrm{A12}-\alpha\mathrm{A13}-\alpha\mathrm{A23}))\sin^2(\beta\mathrm{A13})\sin^2(\beta\mathrm{A23})\sin^2(\beta\mathrm{A12})-$ $0.00195313\,\mathrm{A12}\,\mathrm{A13}\,\mathrm{A23}\cos(2\,(\alpha\mathrm{A12}+\alpha\mathrm{A13}-\alpha\mathrm{A23}))\sin^2(\beta\mathrm{A13})\sin^2(\beta\mathrm{A23})\sin^2(\beta\mathrm{A12})+$ $0.00390625\,\mathrm{A12}\,\mathrm{A13}\,\mathrm{A23}\cos(2\,(\alpha\mathrm{A12}-\alpha\mathrm{A13}+\alpha\mathrm{A23}))\sin^2(\beta\mathrm{A13})\sin^2(\beta\mathrm{A23})\sin^2(\beta\mathrm{A12})-$ $0.353553\,\mathrm{A12}^2\,\mathrm{A13}\cos(2\,\alpha\mathrm{A12}-\alpha\mathrm{A13})\cos^2(\beta\mathrm{A12})\cos(\beta\mathrm{A13})\sin(\beta\mathrm{A13})\sin^2(\beta\mathrm{A12})+$ $0.353553\,\mathrm{A12}^2\,\mathrm{A13}\cos(\alpha\mathrm{A13})\cos^2(\beta\mathrm{A12})\cos(\beta\mathrm{A13})\sin(\beta\mathrm{A13})\sin^2(\beta\mathrm{A12})+$ $0.0110485\,\mathrm{A12}\,\mathrm{A13}\,\mathrm{A23}\cos(2\,\alpha\mathrm{A12}-2\,\alpha\mathrm{A13}-\alpha\mathrm{A23})\cos(\beta\mathrm{A23})\sin^2(\beta\mathrm{A13})\sin(\beta\mathrm{A23})\sin^2(\beta\mathrm{A12})-$ $0.0110485\,\mathrm{A12}\,\mathrm{A13}\,\mathrm{A23}\cos(2\,\alpha\mathrm{A12}-2\,\alpha\mathrm{A13}+\alpha\mathrm{A23})\cos(\beta\mathrm{A23})\sin^2(\beta\mathrm{A13})\sin(\beta\mathrm{A23})\sin^2(\beta\mathrm{A12})+$ $0.353553\,\mathrm{A12}^2\,\mathrm{A23}\cos(2\,\alpha\mathrm{A12}-\alpha\mathrm{A23})\cos^2(\beta\mathrm{A12})\cos(\beta\mathrm{A23})\sin(\beta\mathrm{A23})\sin^2(\beta\mathrm{A12})-$ $0.353553\,\mathrm{A12}^2\,\mathrm{A23}\cos(\alpha\mathrm{A23})\cos^2(\beta\mathrm{A12})\cos(\beta\mathrm{A23})\sin(\beta\mathrm{A23})\sin^2(\beta\mathrm{A12})+$ $0.03125\,\mathrm{A12}\,\mathrm{A13}\,\mathrm{A23}\cos(2\,\alpha\mathrm{A12}-\alpha\mathrm{A13}-\alpha\mathrm{A23})\cos(\beta\mathrm{A13})\cos(\beta\mathrm{A23})\sin(\beta\mathrm{A13})\sin(\beta\mathrm{A23})\sin^2(\beta\mathrm{A12})-$ $0.03125\,\mathrm{A12}\,\mathrm{A13}\,\mathrm{A23}\cos(2\,\alpha\mathrm{A12}+\alpha\mathrm{A13}-\alpha\mathrm{A23})\cos(\beta\mathrm{A13})\cos(\beta\mathrm{A23})\sin(\beta\mathrm{A13})\sin(\beta\mathrm{A23})\sin^2(\beta\mathrm{A12})+$ $0.03125\,\mathrm{A12}\,\mathrm{A13}\,\mathrm{A23}\cos(2\,\alpha\mathrm{A12}-\alpha\mathrm{A13}+\alpha\mathrm{A23})\cos(\beta\mathrm{A13})\cos(\beta\mathrm{A23})\sin(\beta\mathrm{A13})\sin(\beta\mathrm{A23})\sin^2(\beta\mathrm{A12})-$ $0.0625\,\mathrm{A12}\,\mathrm{A23}^2\cos(\alpha\mathrm{A12}-\alpha\mathrm{A23})\cos(\beta\mathrm{A12})\cos(\beta\mathrm{A23})\sin^3(\beta\mathrm{A23})\sin(\beta\mathrm{A12})+$ $0.0625\,\mathrm{A12}\,\mathrm{A23}^2\cos(\alpha\mathrm{A12}+\alpha\mathrm{A23})\cos(\beta\mathrm{A12})\cos(\beta\mathrm{A23})\sin^3(\beta\mathrm{A23})\sin(\beta\mathrm{A12})-$ $0.0625\,\mathrm{A12}\,\mathrm{A23}^2\cos(\alpha\mathrm{A12}-3\,\alpha\mathrm{A23})\cos(\beta\mathrm{A12})\cos(\beta\mathrm{A23})\sin^3(\beta\mathrm{A23})\sin(\beta\mathrm{A12})-$ $0.353553\,\mathrm{A12}\,\mathrm{A23}^2\cos(\alpha\mathrm{A12})\cos(\beta\mathrm{A12})\cos^2(\beta\mathrm{A23})\sin^2(\beta\mathrm{A23})\sin(\beta\mathrm{A12})+$ $0.353553\,\mathrm{A12}\,\mathrm{A23}^2\cos(\alpha\mathrm{A12}-2\,\alpha\mathrm{A23})\cos(\beta\mathrm{A12})\cos^2(\beta\mathrm{A23})\sin^2(\beta\mathrm{A23})\sin(\beta\mathrm{A12})-$ $0.0110485\,\mathrm{A12}\,\mathrm{A13}\,\mathrm{A23}\cos(\alpha\mathrm{A12}-2\,\alpha\mathrm{A13}+2\,\alpha\mathrm{A23})\cos(\beta\mathrm{A12})\sin^2(\beta\mathrm{A13})\sin^2(\beta\mathrm{A23})\sin(\beta\mathrm{A12})+$ $0.0110485\,\mathrm{A12}\,\mathrm{A13}\,\mathrm{A23}\cos(\alpha\mathrm{A12}+2\,\alpha\mathrm{A13}-2\,\alpha\mathrm{A23})\cos(\beta\mathrm{A12})\sin^2(\beta\mathrm{A13})\sin^2(\beta\mathrm{A23})\sin(\beta\mathrm{A12})+$ $0.03125\,\mathrm{A12}\,\mathrm{A13}\,\mathrm{A23}\cos(\alpha\mathrm{A12}-\alpha\mathrm{A13}+2\,\alpha\mathrm{A23})\cos(\beta\mathrm{A12})\cos(\beta\mathrm{A13})\sin(\beta\mathrm{A13})\sin^2(\beta\mathrm{A23})\sin(\beta\mathrm{A12})-$ $0.03125\,\mathrm{A12}\,\mathrm{A13}\,\mathrm{A23}\cos(\alpha\mathrm{A12}-\alpha\mathrm{A13}-2\,\alpha\mathrm{A23})\cos(\beta\mathrm{A12})\cos(\beta\mathrm{A13})\sin(\beta\mathrm{A13})\sin^2(\beta\mathrm{A23})\sin(\beta\mathrm{A12})+$ $0.03125\,\mathrm{A12}\,\mathrm{A13}\,\mathrm{A23}\cos(\alpha\mathrm{A12}+\alpha\mathrm{A13}-2\,\alpha\mathrm{A23})\cos(\beta\mathrm{A12})\cos(\beta\mathrm{A13})\sin(\beta\mathrm{A13})\sin^2(\beta\mathrm{A23})\sin(\beta\mathrm{A12})-$ $0.0625\,\mathrm{A12}\,\mathrm{A13}\,\mathrm{A23}\cos(\alpha\mathrm{A12}-2\,\alpha\mathrm{A13}+\alpha\mathrm{A23})\cos(\beta\mathrm{A12})\cos(\beta\mathrm{A23})\sin^2(\beta\mathrm{A13})\sin(\beta\mathrm{A23})\sin(\beta\mathrm{A12})+$ $0.176777\,\mathrm{A12}\,\mathrm{A13}\,\mathrm{A23}\cos(\alpha\mathrm{A12}-\alpha\mathrm{A13}-\alpha\mathrm{A23})\cos(\beta\mathrm{A12})\cos(\beta\mathrm{A13})\cos(\beta\mathrm{A23})\sin(\beta\mathrm{A13})\sin(\beta\mathrm{A23})$ $\sin(\beta\mathrm{A12})+0.176777\,\mathrm{A12}\,\mathrm{A13}\,\mathrm{A23}\cos(\alpha\mathrm{A12}+\alpha\mathrm{A13}-\alpha\mathrm{A23})\cos(\beta\mathrm{A12})\cos(\beta\mathrm{A13})\cos(\beta\mathrm{A23})$ $\sin(\beta\mathrm{A13})\sin(\beta\mathrm{A23})\sin(\beta\mathrm{A12})-0.353553\,\mathrm{A12}\,\mathrm{A13}\,\mathrm{A23}\cos(\alpha\mathrm{A12}-\alpha\mathrm{A13}+\alpha\mathrm{A23})\cos(\beta\mathrm{A12})\cos(\beta\mathrm{A13})$ $\cos(\beta\mathrm{A23})\sin(\beta\mathrm{A13})\sin(\beta\mathrm{A23})\sin(\beta\mathrm{A12})-0.00390625\,\mathrm{A13}\,\mathrm{A23}^2\cos(2\,\alpha\mathrm{A13})\sin^2(\beta\mathrm{A13})\sin^4(\beta\mathrm{A23})+$ $0.00390625\,\mathrm{A13}\,\mathrm{A23}^2\cos(2\,(\alpha\mathrm{A13}-2\,\alpha\mathrm{A23}))\sin^2(\beta\mathrm{A13})\sin^4(\beta\mathrm{A23})+$ $0.0220971\,\mathrm{A13}\,\mathrm{A23}^2\cos(2\,\alpha\mathrm{A13}-\alpha\mathrm{A23})\cos(\beta\mathrm{A23})\sin^2(\beta\mathrm{A13})\sin^3(\beta\mathrm{A23})-$ $0.0220971\,\mathrm{A13}\,\mathrm{A23}^2\cos(2\,\alpha\mathrm{A13}-3\,\alpha\mathrm{A23})\cos(\beta\mathrm{A23})\sin^2(\beta\mathrm{A13})\sin^3(\beta\mathrm{A23})+$ $0.0625\,\mathrm{A13}\,\mathrm{A23}^2\cos(\alpha\mathrm{A13}-\alpha\mathrm{A23})\cos(\beta\mathrm{A13})\cos(\beta\mathrm{A23})\sin(\beta\mathrm{A13})\sin^3(\beta\mathrm{A23})-$ $0.0625\,\mathrm{A13}\,\mathrm{A23}^2\cos(\alpha\mathrm{A13}+\alpha\mathrm{A23})\cos(\beta\mathrm{A13})\cos(\beta\mathrm{A23})\sin(\beta\mathrm{A13})\sin^3(\beta\mathrm{A23})+$ $0.0625\,\mathrm{A13}\,\mathrm{A23}^2\cos(\alpha\mathrm{A13}-3\,\alpha\mathrm{A23})\cos(\beta\mathrm{A13})\cos(\beta\mathrm{A23})\sin(\beta\mathrm{A13})\sin^3(\beta\mathrm{A23})-$ $0.0625\,\mathrm{A13}\,\mathrm{A23}^2\cos(2\,(\alpha\mathrm{A13}-\alpha\mathrm{A23}))\cos^2(\beta\mathrm{A23})\sin^2(\beta\mathrm{A13})\sin^2(\beta\mathrm{A23})+$ $0.353553\,\mathrm{A13}\,\mathrm{A23}^2\cos(\alpha\mathrm{A13})\cos(\beta\mathrm{A13})\cos^2(\beta\mathrm{A23})\sin(\beta\mathrm{A13})\sin^2(\beta\mathrm{A23})-$ $0.353553\,\mathrm{A13}\,\mathrm{A23}^2\cos(\alpha\mathrm{A13}-2\,\alpha\mathrm{A23})\cos(\beta\mathrm{A13})\cos^2(\beta\mathrm{A23})\sin(\beta\mathrm{A13})\sin^2(\beta\mathrm{A23})\big)$

$I_{2z}I_{3z}$
$-\frac{1}{4\,\omega\mathrm{rot}^2}\big(0.00390625\,\mathrm{A12}^2\,\mathrm{A13}\cos(2\,\alpha\mathrm{A13})\sin^2(\beta\mathrm{A13})\sin^4(\beta\mathrm{A12}) -$ $0.00390625\,\mathrm{A12}^2\,\mathrm{A13}\cos(4\,\alpha\mathrm{A12} - 2\,\alpha\mathrm{A13})\sin^2(\beta\mathrm{A13})\sin^4(\beta\mathrm{A12}) -$ $0.00390625\,\mathrm{A12}^2\,\mathrm{A23}\cos(2\,\alpha\mathrm{A23})\sin^2(\beta\mathrm{A23})\sin^4(\beta\mathrm{A12}) +$ $0.00390625\,\mathrm{A12}^2\,\mathrm{A23}\cos(4\,\alpha\mathrm{A12} - 2\,\alpha\mathrm{A23})\sin^2(\beta\mathrm{A23})\sin^4(\beta\mathrm{A12}) -$ $0.0220971\,\mathrm{A12}^2\,\mathrm{A13}\cos(\alpha\mathrm{A12} - 2\,\alpha\mathrm{A13})\cos(\beta\mathrm{A12})\sin^2(\beta\mathrm{A13})\sin^3(\beta\mathrm{A12}) +$ $0.0220971\,\mathrm{A12}^2\,\mathrm{A13}\cos(3\,\alpha\mathrm{A12} - 2\,\alpha\mathrm{A13})\cos(\beta\mathrm{A12})\sin^2(\beta\mathrm{A13})\sin^3(\beta\mathrm{A12}) +$ $0.0220971\,\mathrm{A12}^2\,\mathrm{A23}\cos(\alpha\mathrm{A12} - 2\,\alpha\mathrm{A23})\cos(\beta\mathrm{A12})\sin^2(\beta\mathrm{A23})\sin^3(\beta\mathrm{A12}) -$ $0.0220971\,\mathrm{A12}^2\,\mathrm{A23}\cos(3\,\alpha\mathrm{A12} - 2\,\alpha\mathrm{A23})\cos(\beta\mathrm{A12})\sin^2(\beta\mathrm{A23})\sin^3(\beta\mathrm{A12}) -$ $0.0625\,\mathrm{A12}^2\,\mathrm{A13}\cos(\alpha\mathrm{A12} - \alpha\mathrm{A13})\cos(\beta\mathrm{A12})\cos(\beta\mathrm{A13})\sin(\beta\mathrm{A13})\sin^3(\beta\mathrm{A12}) -$ $0.0625\,\mathrm{A12}^2\,\mathrm{A13}\cos(3\,\alpha\mathrm{A12} - \alpha\mathrm{A13})\cos(\beta\mathrm{A12})\cos(\beta\mathrm{A13})\sin(\beta\mathrm{A13})\sin^3(\beta\mathrm{A12}) +$ $0.0625\,\mathrm{A12}^2\,\mathrm{A13}\cos(\alpha\mathrm{A12} + \alpha\mathrm{A13})\cos(\beta\mathrm{A12})\cos(\beta\mathrm{A13})\sin(\beta\mathrm{A13})\sin^3(\beta\mathrm{A12}) +$ $0.0625\,\mathrm{A12}^2\,\mathrm{A23}\cos(\alpha\mathrm{A12} - \alpha\mathrm{A23})\cos(\beta\mathrm{A12})\cos(\beta\mathrm{A23})\sin(\beta\mathrm{A23})\sin^3(\beta\mathrm{A12}) +$ $0.0625\,\mathrm{A12}^2\,\mathrm{A23}\cos(3\,\alpha\mathrm{A12} - \alpha\mathrm{A23})\cos(\beta\mathrm{A12})\cos(\beta\mathrm{A23})\sin(\beta\mathrm{A23})\sin^3(\beta\mathrm{A12}) -$ $0.0625\,\mathrm{A12}^2\,\mathrm{A23}\cos(\alpha\mathrm{A12} + \alpha\mathrm{A23})\cos(\beta\mathrm{A12})\cos(\beta\mathrm{A23})\sin(\beta\mathrm{A23})\sin^3(\beta\mathrm{A12}) +$ $0.00390625\,\mathrm{A12}\,\mathrm{A13}^2\cos(2\,\alpha\mathrm{A12})\sin^4(\beta\mathrm{A13})\sin^2(\beta\mathrm{A12}) -$ $0.00390625\,\mathrm{A12}\,\mathrm{A13}^2\cos(2\,(\alpha\mathrm{A12} - 2\,\alpha\mathrm{A13}))\sin^4(\beta\mathrm{A13})\sin^2(\beta\mathrm{A12}) -$ $0.0220971\,\mathrm{A12}\,\mathrm{A13}^2\cos(2\,\alpha\mathrm{A12} - \alpha\mathrm{A13})\cos(\beta\mathrm{A13})\sin^3(\beta\mathrm{A13})\sin^2(\beta\mathrm{A12}) +$ $0.0220971\,\mathrm{A12}\,\mathrm{A13}^2\cos(2\,\alpha\mathrm{A12} - 3\,\alpha\mathrm{A13})\cos(\beta\mathrm{A13})\sin^3(\beta\mathrm{A13})\sin^2(\beta\mathrm{A12}) +$ $0.0625\,\mathrm{A12}^2\,\mathrm{A13}\cos(2\,(\alpha\mathrm{A12} - \alpha\mathrm{A13}))\cos^2(\beta\mathrm{A12})\sin^2(\beta\mathrm{A13})\sin^2(\beta\mathrm{A12}) +$ $0.0625\,\mathrm{A12}\,\mathrm{A13}^2\cos(2\,(\alpha\mathrm{A12} - \alpha\mathrm{A13}))\cos^2(\beta\mathrm{A13})\sin^2(\beta\mathrm{A13})\sin^2(\beta\mathrm{A12}) -$ $0.0625\,\mathrm{A12}^2\,\mathrm{A23}\cos(2\,(\alpha\mathrm{A12} - \alpha\mathrm{A23}))\cos^2(\beta\mathrm{A12})\sin^2(\beta\mathrm{A23})\sin^2(\beta\mathrm{A12}) -$ $0.00195313\,\mathrm{A12}\,\mathrm{A13}\,\mathrm{A23}\cos(2\,(\alpha\mathrm{A12} - \alpha\mathrm{A13} - \alpha\mathrm{A23}))\sin^2(\beta\mathrm{A13})\sin^2(\beta\mathrm{A23})\sin^2(\beta\mathrm{A12}) +$ $0.00390625\,\mathrm{A12}\,\mathrm{A13}\,\mathrm{A23}\cos(2\,(\alpha\mathrm{A12} + \alpha\mathrm{A13} - \alpha\mathrm{A23}))\sin^2(\beta\mathrm{A13})\sin^2(\beta\mathrm{A23})\sin^2(\beta\mathrm{A12}) -$ $0.00195313\,\mathrm{A12}\,\mathrm{A13}\,\mathrm{A23}\cos(2\,(\alpha\mathrm{A12} - \alpha\mathrm{A13} + \alpha\mathrm{A23}))\sin^2(\beta\mathrm{A13})\sin^2(\beta\mathrm{A23})\sin^2(\beta\mathrm{A12}) +$ $0.0110485\,\mathrm{A12}\,\mathrm{A13}\,\mathrm{A23}\cos(2\,\alpha\mathrm{A12} - \alpha\mathrm{A13} - 2\,\alpha\mathrm{A23})\cos(\beta\mathrm{A13})\sin(\beta\mathrm{A13})\sin^2(\beta\mathrm{A23})\sin^2(\beta\mathrm{A12}) -$ $0.0110485\,\mathrm{A12}\,\mathrm{A13}\,\mathrm{A23}\cos(2\,\alpha\mathrm{A12} + \alpha\mathrm{A13} - 2\,\alpha\mathrm{A23})\cos(\beta\mathrm{A13})\sin(\beta\mathrm{A13})\sin^2(\beta\mathrm{A23})\sin^2(\beta\mathrm{A12}) +$ $0.353553\,\mathrm{A12}^2\,\mathrm{A13}\cos(2\,\alpha\mathrm{A12} - \alpha\mathrm{A13})\cos^2(\beta\mathrm{A12})\cos(\beta\mathrm{A13})\sin(\beta\mathrm{A13})\sin^2(\beta\mathrm{A12}) -$ $0.353553\,\mathrm{A12}^2\,\mathrm{A13}\cos(\alpha\mathrm{A13})\cos^2(\beta\mathrm{A12})\cos(\beta\mathrm{A13})\sin(\beta\mathrm{A13})\sin^2(\beta\mathrm{A12}) -$ $0.353553\,\mathrm{A12}^2\,\mathrm{A23}\cos(2\,\alpha\mathrm{A12} - \alpha\mathrm{A23})\cos^2(\beta\mathrm{A12})\cos(\beta\mathrm{A23})\sin(\beta\mathrm{A23})\sin^2(\beta\mathrm{A12}) +$ $0.353553\,\mathrm{A12}^2\,\mathrm{A23}\cos(\alpha\mathrm{A23})\cos^2(\beta\mathrm{A12})\cos(\beta\mathrm{A23})\sin(\beta\mathrm{A23})\sin^2(\beta\mathrm{A12}) +$ $0.03125\,\mathrm{A12}\,\mathrm{A13}\,\mathrm{A23}\cos(2\,\alpha\mathrm{A12} - \alpha\mathrm{A13} - \alpha\mathrm{A23})\cos(\beta\mathrm{A13})\cos(\beta\mathrm{A23})\sin(\beta\mathrm{A13})\sin(\beta\mathrm{A23})\sin^2(\beta\mathrm{A12}) +$ $0.03125\,\mathrm{A12}\,\mathrm{A13}\,\mathrm{A23}\cos(2\,\alpha\mathrm{A12} + \alpha\mathrm{A13} - \alpha\mathrm{A23})\cos(\beta\mathrm{A13})\cos(\beta\mathrm{A23})\sin(\beta\mathrm{A13})\sin(\beta\mathrm{A23})\sin^2(\beta\mathrm{A12}) -$ $0.03125\,\mathrm{A12}\,\mathrm{A13}\,\mathrm{A23}\cos(2\,\alpha\mathrm{A12} - \alpha\mathrm{A13} + \alpha\mathrm{A23})\cos(\beta\mathrm{A13})\cos(\beta\mathrm{A23})\sin(\beta\mathrm{A13})\sin(\beta\mathrm{A23})\sin^2(\beta\mathrm{A12}) -$ $0.0625\,\mathrm{A12}\,\mathrm{A13}^2\cos(\alpha\mathrm{A12} - \alpha\mathrm{A13})\cos(\beta\mathrm{A12})\cos(\beta\mathrm{A13})\sin^3(\beta\mathrm{A13})\sin(\beta\mathrm{A12}) +$ $0.0625\,\mathrm{A12}\,\mathrm{A13}^2\cos(\alpha\mathrm{A12} + \alpha\mathrm{A13})\cos(\beta\mathrm{A12})\cos(\beta\mathrm{A13})\sin^3(\beta\mathrm{A13})\sin(\beta\mathrm{A12}) -$ $0.0625\,\mathrm{A12}\,\mathrm{A13}^2\cos(\alpha\mathrm{A12} - 3\,\alpha\mathrm{A13})\cos(\beta\mathrm{A12})\cos(\beta\mathrm{A13})\sin^3(\beta\mathrm{A13})\sin(\beta\mathrm{A12}) -$ $0.353553\,\mathrm{A12}\,\mathrm{A13}^2\cos(\alpha\mathrm{A12})\cos(\beta\mathrm{A12})\cos^2(\beta\mathrm{A13})\sin^2(\beta\mathrm{A13})\sin(\beta\mathrm{A12}) +$ $0.353553\,\mathrm{A12}\,\mathrm{A13}^2\cos(\alpha\mathrm{A12} - 2\,\alpha\mathrm{A13})\cos(\beta\mathrm{A12})\cos^2(\beta\mathrm{A13})\sin^2(\beta\mathrm{A13})\sin(\beta\mathrm{A12}) +$ $0.0110485\,\mathrm{A12}\,\mathrm{A13}\,\mathrm{A23}\cos(\alpha\mathrm{A12} - 2\,\alpha\mathrm{A13} + 2\,\alpha\mathrm{A23})\cos(\beta\mathrm{A12})\sin^2(\beta\mathrm{A13})\sin^2(\beta\mathrm{A23})\sin(\beta\mathrm{A12}) -$ $0.0110485\,\mathrm{A12}\,\mathrm{A13}\,\mathrm{A23}\cos(\alpha\mathrm{A12} + 2\,\alpha\mathrm{A13} - 2\,\alpha\mathrm{A23})\cos(\beta\mathrm{A12})\sin^2(\beta\mathrm{A13})\sin^2(\beta\mathrm{A23})\sin(\beta\mathrm{A12}) -$ $0.0625\,\mathrm{A12}\,\mathrm{A13}\,\mathrm{A23}\cos(\alpha\mathrm{A12} + \alpha\mathrm{A13} - 2\,\alpha\mathrm{A23})\cos(\beta\mathrm{A12})\cos(\beta\mathrm{A13})\sin(\beta\mathrm{A13})\sin^2(\beta\mathrm{A23})\sin(\beta\mathrm{A12}) +$ $0.03125\,\mathrm{A12}\,\mathrm{A13}\,\mathrm{A23}\cos(\alpha\mathrm{A12} + 2\,\alpha\mathrm{A13} - \alpha\mathrm{A23})\cos(\beta\mathrm{A12})\cos(\beta\mathrm{A23})\sin^2(\beta\mathrm{A13})\sin(\beta\mathrm{A23})\sin(\beta\mathrm{A12}) -$ $0.03125\,\mathrm{A12}\,\mathrm{A13}\,\mathrm{A23}\cos(\alpha\mathrm{A12} - 2\,\alpha\mathrm{A13} - \alpha\mathrm{A23})\cos(\beta\mathrm{A12})\cos(\beta\mathrm{A23})\sin^2(\beta\mathrm{A13})\sin(\beta\mathrm{A23})\sin(\beta\mathrm{A12}) +$ $0.03125\,\mathrm{A12}\,\mathrm{A13}\,\mathrm{A23}\cos(\alpha\mathrm{A12} - 2\,\alpha\mathrm{A13} + \alpha\mathrm{A23})\cos(\beta\mathrm{A12})\cos(\beta\mathrm{A23})\sin^2(\beta\mathrm{A13})\sin(\beta\mathrm{A23})\sin(\beta\mathrm{A12}) +$ $0.176777\,\mathrm{A12}\,\mathrm{A13}\,\mathrm{A23}\cos(\alpha\mathrm{A12} - \alpha\mathrm{A13} - \alpha\mathrm{A23})\cos(\beta\mathrm{A12})\cos(\beta\mathrm{A13})\cos(\beta\mathrm{A23})\sin(\beta\mathrm{A13})\sin(\beta\mathrm{A23})$ $\sin(\beta\mathrm{A12}) - 0.353553\,\mathrm{A12}\,\mathrm{A13}\,\mathrm{A23}\cos(\alpha\mathrm{A12} + \alpha\mathrm{A13} - \alpha\mathrm{A23})\cos(\beta\mathrm{A12})\cos(\beta\mathrm{A13})\cos(\beta\mathrm{A23})$ $\sin(\beta\mathrm{A13})\sin(\beta\mathrm{A23})\sin(\beta\mathrm{A12}) + 0.176777\,\mathrm{A12}\,\mathrm{A13}\,\mathrm{A23}\cos(\alpha\mathrm{A12} - \alpha\mathrm{A13} + \alpha\mathrm{A23})\cos(\beta\mathrm{A12})\cos(\beta\mathrm{A13})$ $\cos(\beta\mathrm{A23})\sin(\beta\mathrm{A13})\sin(\beta\mathrm{A23})\sin(\beta\mathrm{A12}) - 0.00390625\,\mathrm{A13}^2\,\mathrm{A23}\cos(2\,\alpha\mathrm{A23})\sin^4(\beta\mathrm{A13})\sin^2(\beta\mathrm{A23}) +$ $0.00390625\,\mathrm{A13}^2\,\mathrm{A23}\cos(4\,\alpha\mathrm{A13} - 2\,\alpha\mathrm{A23})\sin^4(\beta\mathrm{A13})\sin^2(\beta\mathrm{A23}) +$ $0.0220971\,\mathrm{A13}^2\,\mathrm{A23}\cos(\alpha\mathrm{A13} - 2\,\alpha\mathrm{A23})\cos(\beta\mathrm{A13})\sin^3(\beta\mathrm{A13})\sin^2(\beta\mathrm{A23}) -$ $0.0220971\,\mathrm{A13}^2\,\mathrm{A23}\cos(3\,\alpha\mathrm{A13} - 2\,\alpha\mathrm{A23})\cos(\beta\mathrm{A13})\sin^3(\beta\mathrm{A13})\sin^2(\beta\mathrm{A23}) -$ $0.0625\,\mathrm{A13}^2\,\mathrm{A23}\cos(2\,(\alpha\mathrm{A13} - \alpha\mathrm{A23}))\cos^2(\beta\mathrm{A13})\sin^2(\beta\mathrm{A13})\sin^2(\beta\mathrm{A23}) +$ $0.0625\,\mathrm{A13}^2\,\mathrm{A23}\cos(\alpha\mathrm{A13} - \alpha\mathrm{A23})\cos(\beta\mathrm{A13})\cos(\beta\mathrm{A23})\sin^3(\beta\mathrm{A13})\sin(\beta\mathrm{A23}) +$ $0.0625\,\mathrm{A13}^2\,\mathrm{A23}\cos(3\,\alpha\mathrm{A13} - \alpha\mathrm{A23})\cos(\beta\mathrm{A13})\cos(\beta\mathrm{A23})\sin^3(\beta\mathrm{A13})\sin(\beta\mathrm{A23}) -$ $0.0625\,\mathrm{A13}^2\,\mathrm{A23}\cos(\alpha\mathrm{A13} + \alpha\mathrm{A23})\cos(\beta\mathrm{A13})\cos(\beta\mathrm{A23})\sin^3(\beta\mathrm{A13})\sin(\beta\mathrm{A23}) -$ $0.353553\,\mathrm{A13}^2\,\mathrm{A23}\cos(2\,\alpha\mathrm{A13} - \alpha\mathrm{A23})\cos^2(\beta\mathrm{A13})\cos(\beta\mathrm{A23})\sin^2(\beta\mathrm{A13})\sin(\beta\mathrm{A23}) +$ $0.353553\,\mathrm{A13}^2\,\mathrm{A23}\cos(\alpha\mathrm{A23})\cos^2(\beta\mathrm{A13})\cos(\beta\mathrm{A23})\sin^2(\beta\mathrm{A13})\sin(\beta\mathrm{A23})\big)$

2.2.7.3 Fittings

MAS rate dependence in two spin systems

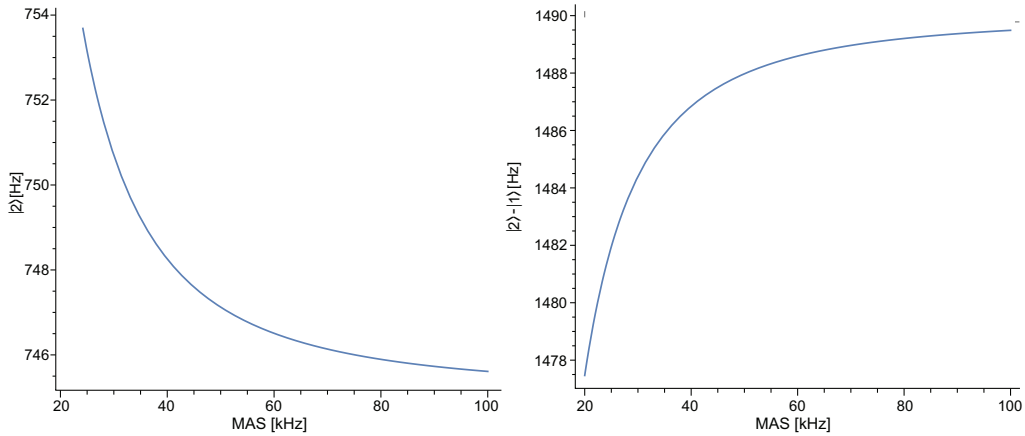

Figure 2.15 The eigenvalue |2⟩ (left) of equation 29 and the |2⟩-|1⟩ transition frequency (right)as a function of ω_r for the second-order truncated average Hamiltonian, for the two spin systems example in Figure 2.2. Ω_{iso1} = 1490 Hz, Ω_{iso2} = 2980 Hz. The coupling in the PAF was set to A_{12} = 30 kHz. The Euler angles for the crystal to rotor frame transformation are: $\{\alpha_{12}, \beta_{12}, \gamma_{12}\} = \{45°, 60°, 30°\}$

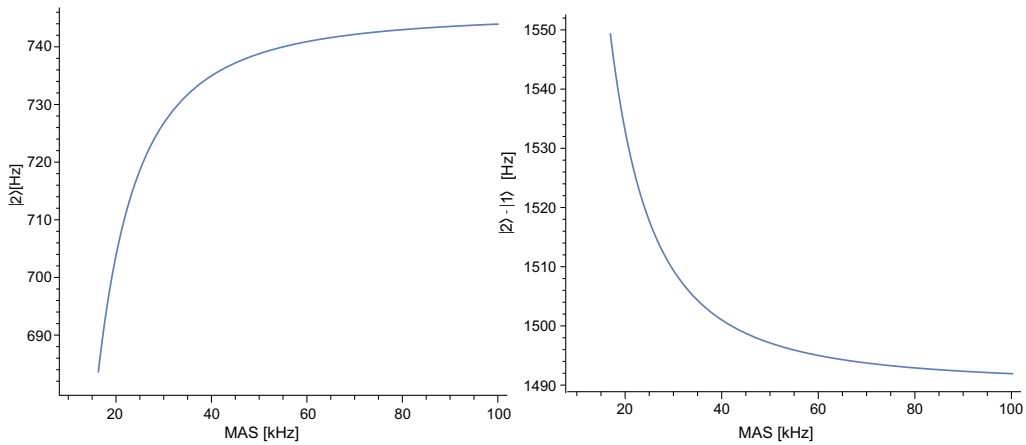

Figure 2.16 The eigenvalue |2⟩ (left) of equation 29 and the |2⟩-|1⟩ transition frequency (right)as a function of ω_r for the full to third order average Hamiltonian, for the two spin systems example in Figure 2.2. Ω_{iso1} = 1490 Hz, Ω_{iso2} = 2980 Hz. The coupling in the PAF was set to A_{12} = 30 kHz. The Euler angles for the crystal to rotor frame transformation are: $\{\alpha_{12}, \beta_{12}, \gamma_{12}\} = \{45°, 60°, 30°\}$

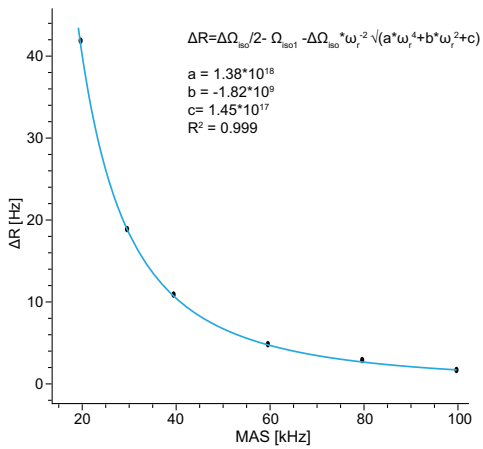

Figure 2.17 Fitting of the residual shifts as a function of the MAS for the spectra simulated in Figure 2.2, with numerical simulation (black dots). The fitting is done with the model obtained with the eigenvalues for the full average Hamiltonian.

MAS rate dependence in two spin systems

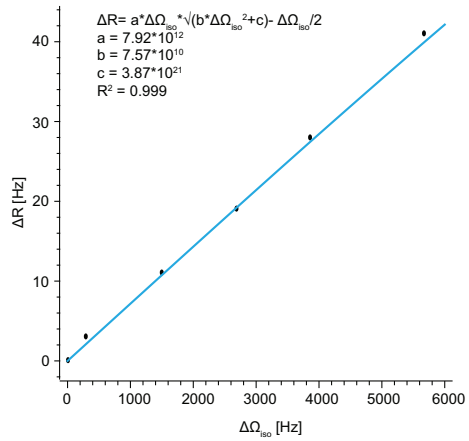

Figure 2.18 Fitting of the residual shifts as a function of the chemical shift difference obtained in Figure 2.5, with numerical simulation (black dots). The fitting is done with the model obtained with the eigenvalues for the full average Hamiltonian. The isotropic shift Ω_1 was set to 1490 Hz, while Ω_2 is varied. The residual shift evolution fits to a polynomial equation $\Delta R = ax^2 + bx$, with a R^2 of 0.999. The linear term is dominant as predicted by AHT.

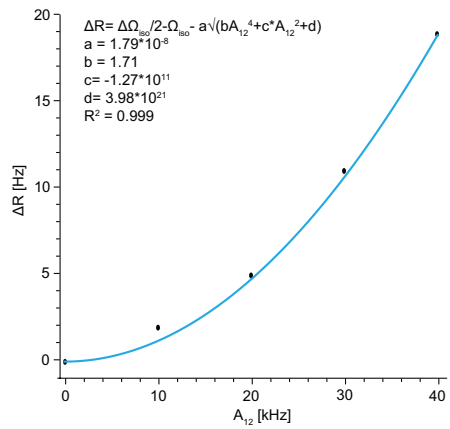

Figure 2.19 Fitting of the residual shifts as a function of the dipolar coupling obtained in Figure 2.6, with numerical simulation (black dots). The residual shift evolution (blue line) fits to the model obtained with the eigenvalues for the full average Hamiltonian, with a R^2 of 0.999.

ΔR in the slow to intermediate spinning regime

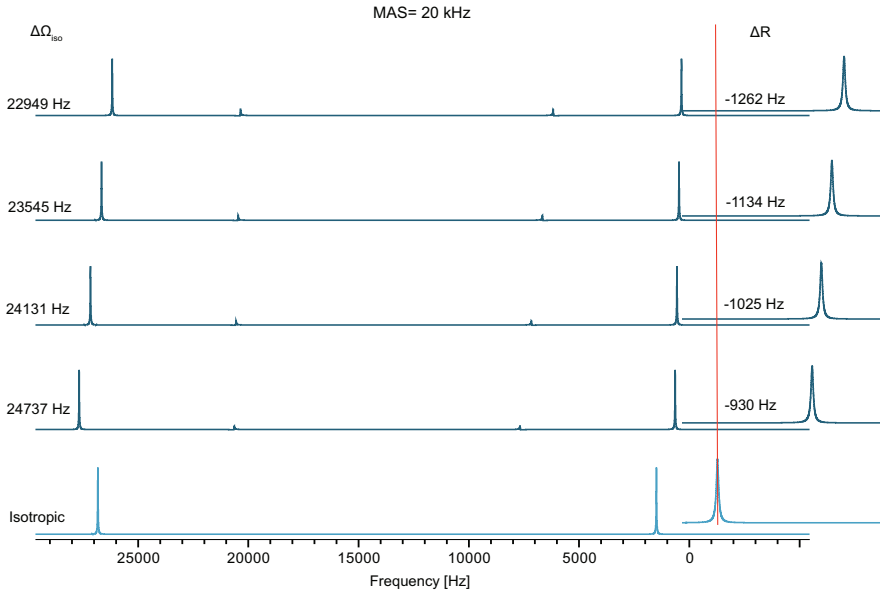

Figure 2.20 Residual shift evolution in the slow to intermediate spinning regime. The isotropic shift Ω_1 was set to 1490 Hz, while Ω_2 is initially set to 28823 Hz, in the isotropic spectrum (bottom). The Ω_2 is then decreased. The dipolar coupling A_{12} was set to 30 kHz and the Euler angles to $\{45°, 60°, 30°\}$. The Nakai parameter ϵ is equal to 28469 Hz. The spectra were simulated with SPINACH at 20 kHz MAS. The zoom on the right shows the Ω_1 region and the corresponding residual shift.

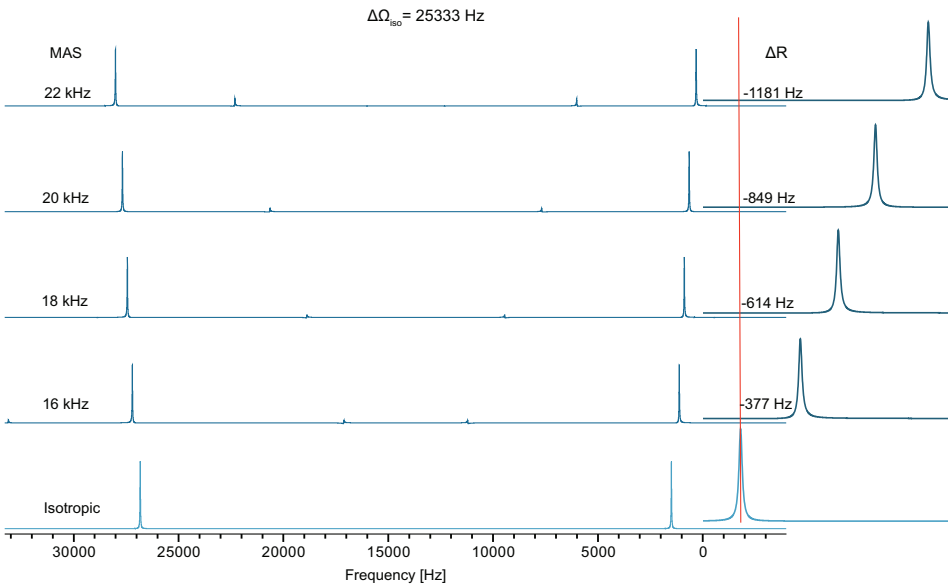

Figure 2.21 Residual shift evolution in the slow to intermediate spinning regime as a function of the MAS rate. The isotropic shift Ω_1 was set to 1490 Hz, while Ω_2 is set to 28823 Hz. The dipolar coupling A_{12} was set to 30 kHz and the Euler angles to $\{45°, 60°, 30°\}$. The Nakai parameter ϵ is equal to 28469 Hz. The spectra were simulated with SPINACH from 16 to 22 kHz MAS, with steps of 2 kHz. The zoom on the right shows the Ω_1 region and the corresponding residual shift.

MAS rate dependence in three spin systems

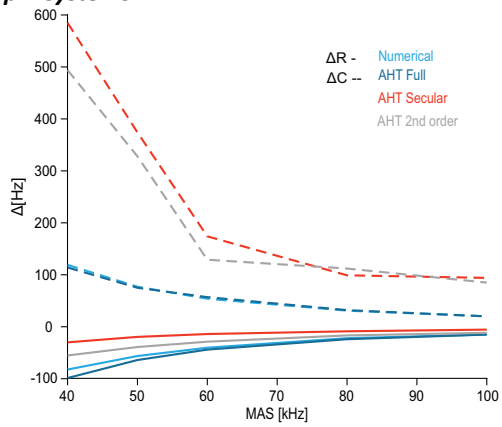

Figure 2.22 Residual shift (ΔR) and residual coupling (ΔC) evolution as function of the MAS rate of the peak in the Ω_{iso2} region of a three spin system in a single orientation, with the parameters given in Figure 2.7. The blue line is the exact numerical simulation, the red line represents the secular Hamiltonian until third order, the grey line represent the full Hamiltonian until second order and the dark blue lines are the full representation of the Hamiltonian until 3rd order, with the non-secular terms.

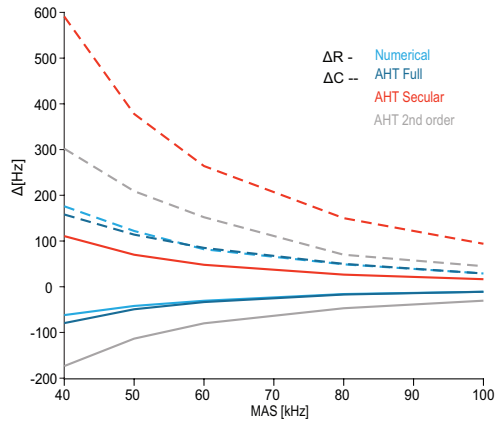

Figure 2.23 Residual shift (ΔR) and residual coupling (ΔC) evolution as function of the MAS rate of the peak in the Ω_{iso3} region of a three spin system in a single orientation, with the parameters given in Figure 2.7. The blue line is the exact numerical simulation, the red line represents the secular Hamiltonian until third order, the grey line represent the full Hamiltonian until second order and the dark blue lines are the full representation of the Hamiltonian until 3rd order, with the non-secular terms.

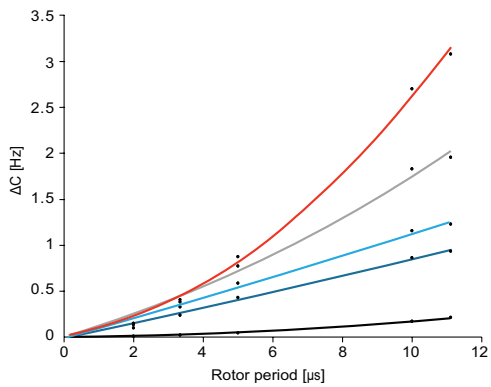

Figure 2.24 Residual coupling (ΔC) as function of the MAS period (2 to 12 μs, corresponding to 90-500 kHz MAS rates) for the Ω_2 region of three-spin systems in a single orientation. The three isotropic chemical shifts were: $\Omega_1 = \Omega_2 = \Omega_3 = 200$ Hz (black line); $\Omega_1 = \Omega_2 = 200$ Hz, $\Omega_3 = 150$ Hz (dark blue); $\Omega_1 = 200$ Hz, $\Omega_2 = 250$ Hz, $\Omega_3 = 150$ Hz (light blue); $\Omega_1 = 200$ Hz, $\Omega_2 = 300$ Hz, $\Omega_3 = 150$ Hz (grey); $\Omega_1 = 200$ Hz, $\Omega_2 = 400$ Hz, $\Omega_3 = 150$ Hz (red); The couplings remained unchanged at $A_{12} = 44.8$ kHz, $A_{13} = 8.9$ kHz and $A_{23} = 5.8$ kHz. The corresponding Euler angles for the crystal to rotor frame transformation are: $\{\alpha_{12}, \beta_{12}, \gamma_{12}\} = \{60°, 45°, 30°\}$;$\{\alpha_{13}, \beta_{13}, \gamma_{13}\} = \{45°, 60°, 60°\}$; $\{\alpha_{23}, \beta_{23}, \gamma_{23}\} = \{30°, 36°, 30°\}$. °}. In this orientation, in the lab frame, the couplings correspond to 19.4 kHz, 3.8 kHz and 2.5 kHz. The spectra were calculated with SpinDynamica as detailed in SI. ΔC is measured as the difference in eigenvalues between the outer single-quantum allowed transitions in the "doublet of doublets" structure, and the fit parameters are given in Table 2.1.

Table 2.1 Fitting parameters for ΔC as function of the rotor period (τ_r) of Figure 2.24

Ω_{iso}	ΔC	R^2
$\Omega_1=\Omega_2=\Omega_3$= 200 Hz	$2*10^9\,\tau_r^2+6.98*10^4\,\tau_r$	0.9974
$\Omega_1=\Omega_2$=200 Hz; Ω_3= 150 Hz	$7*10^9\,\tau_r^2+1.07*10^5\,\tau_r$	0.991
Ω_1=250 Hz;Ω_2=200 Hz; Ω_3= 150 Hz	$1*10^9\,\tau_r^2+1.01*10^5\,\tau_r$	0.9907
Ω_1=300 Hz;Ω_2=200 Hz; Ω_3= 150 Hz	$1*10^9\,\tau_r^2+7.2*10^4\,\tau_r$	0.9919
Ω_1=400 Hz;Ω_2=200 Hz; Ω_3= 150 Hz	$2*10^9\,\tau_r^2+151.45\,\tau_r$	1

Table 2.2 Fitting parameters for Δ as function of the rotor period (τ_r) of Figure 2.12

Ω_{iso}	Δ	R^2
Ω_1	$9*10^{10}\,\tau_r^2+2.00*10^6\,\tau_r+40$	0.9952
Ω_2	$1*10^{11}\,\tau_r^2+2.00*10^6\,\tau_r+40$	0.9987
Ω_3	$1*10^{11}\,\tau_r^2+8.70*10^5\,\tau_r+40$	0.9926

Table 2.3 second rank reduced Wigner matrix elements $d^{(2)}_{mm'}(-\beta)$

m	2	1	0	-1	-2
2	$\cos^4\left(\frac{\beta}{2}\right)$	$-\frac{1}{2}\sin(1+\cos\beta)$	$\sqrt{\frac{3}{8}}\sin^2\beta$	$\frac{1}{2}\sin(-1+\cos\beta)$	$\sin^4\left(\frac{\beta}{2}\right)$
1	$\frac{1}{2}\sin(1+\cos\beta)$	$\frac{1}{2}(\cos\beta-1)(\cos\beta+1)$	$-\sqrt{\frac{3}{2}}\sin\beta\cos\beta$	$\frac{1}{2}(2\cos\beta+1)(1-\cos\beta)$	$\frac{1}{2}\sin(-1+\cos\beta)$
0	$\sqrt{\frac{3}{8}}\sin^2\beta$	$\sqrt{\frac{3}{2}}\sin\beta\cos\beta$	$\frac{1}{2}(3\cos^2\beta-1)$	$-\sqrt{\frac{3}{2}}\sin\beta\cos\beta$	$\sqrt{\frac{3}{8}}\sin^2\beta$
-1	$\frac{1}{2}\sin(-1+\cos\beta)$	$\frac{1}{2}(2\cos\beta+1)(1-\cos\beta)$	$\sqrt{\frac{3}{2}}\sin\beta\cos\beta$	$\frac{1}{2}(\cos\beta-1)(\cos\beta+1)$	$=-\frac{1}{2}\sin(1+\cos\beta)$
-2	$\sin^4\left(\frac{\beta}{2}\right)$	$-\frac{1}{2}\sin(-1+\cos\beta)$	$\sqrt{\frac{3}{8}}\sin^2\beta$	$\frac{1}{2}\sin(1+\cos\beta)$	$\cos^4\left(\frac{\beta}{2}\right)$

2.3 Conclusion and Perspectives

In conclusion, we analytically integrated the average Hamiltonian up to third order of homonuclear two and three spin systems with different chemical shifts in rotating solids. The two spin systems have been extensively studied[103, 106, 108] (see **Section 2.2.1**) and our two spin simulations corroborate the previous findings, with a residual shift observed on the ^{1}H spectrum caused by the higher order terms.

For three spin, several studies have used AHT[104-105], Floquet Theory[107, 109, 111-112, 238] and numerical simulations [113, 219] for a second moment approach to study the linewidth under MAS. Although the first studies [104-105] found a linear dependence on the rotor period on the ^{1}H linewidth, recent publications[107, 112, 238] have found a polynomial behaviour which was supported by experiment.

The third order terms from our average Hamiltonian have a ω_r^{-2} dependence and they contribute to the description of the lineshape. The polynomial dependence is obtained when combined with the second order terms. The weight of the third order terms depends on the strength of the dipolar couplings and the chemical shift difference between the spins of the system.

At the high spinning regime, these terms will become less important due to the quadratic dependance and therefore a linear dependence will be more pronounced. This consideration was also demonstrated in the study by Chavez *et al..*[238] using Floquet Theory.

Although the average Hamiltonian analysis only considered a single orientation, the numerical simulations on powder lineshapes also presented a MAS dependent residual shift and linewidth, in line with the single orientation results.

These results considered the homonuclear dipolar couplings and the chemical shift as the main spin interactions in a three spin system to describe the ^{1}H lineshape. Stronger coupled systems with a chemical shift difference will have higher order terms with a greater magnitude which will translate in a larger linewidth. As the spinning rate increases these residual terms will get more diminished, and every spin system will have a particular spinning rate where its homogeneous contribution will be essentially zero, depending on the magnitude of its dipolar couplings.

However, there are still some routes worth exploring on the theoretical analysis as faster spinning rates are reached experimentally. The first one would be to include weaker spin interactions in the initial Hamiltonian, particularly homonuclear J couplings, to investigate its relevance at faster MAS rates. The effect on the lineshape caused by CSA in addition the homonuclear dipolar couplings was briefly studied with numerical simulations for both two and three spin systems. Early conclusions presented almost no effect on the residual shift for both two and three spins, and the residual splitting was only affected at very large values of CSA (> 40 ppm).

Another path would be to investigate the on the lineshape by including a larger number of spins in the analytical integration. This approach could provide a clearer insight on the MAS dependence on the linewidth and the multispin effect.[123]

Finally, it could be of interest to include the effect of inhomogeneous interactions, particularly anisotropic bulk magnetic susceptibility[239-240]. This source of broadening is already the main contribution to the linewidth for many samples (see **Chapter 5**) and will be more dominant with the increase of spinning rates.

Chapter 3 Improved ^{1}H resolution combining MAS and multiple pulse sequences

3.1 Introduction

The previous chapter presented the residual average Hamiltonian terms that contribute to the ^{1}H lineshape in the fast-spinning regime. They affect the spectral resolution and impede complete assignment with ^{1}H solid state NMR. Only at infinite MAS rate would the residuals be totally removed.

Today it is possible to spin at 100-150 kHz[110, 116-119], and at the laboratory level rates up to 200 kHz have been achieved[137, 241]. However, the field has always needed better ^{1}H resolution, even when spinning was much slower than the rates available today. Therefore, a lot of effort has been put into find alternatives that would achieve further homonuclear dipolar decoupling.

In principle, this is possible with methods that combine sample rotation and muti-pulse spectroscopy (CRAMPS). The simultaneous application of MAS and pulse sequences is designed to suppress homonuclear dipolar couplings while retaining isotropic chemical shifts. The seminal work by Gerstein *et. al.*[131] in 1977 introduced this idea with CaF_2 single crystal and since then many decoupling schemes were developed[242]. Up to 65 kHz MAS, these techniques can produce narrower linewidths than the ones obtained with conventional MAS spectra[132-134, 136, 243].

At faster MAS rates, no advantage has been reported so far with CRAMPS approaches, and the resolution obtained from conventional MAS experiments at 100 kHz is comparable to the ones obtained from CRAMPS at slower rates.

Other strategies using delayed acquisition[244-246] or constant-time approaches have been reported to remove homogeneous broadening, but they have attracted limited attention so far.

In **Chapter 3.2,** an alternative method is presented to obtain narrower ^{1}H spectra at 100 kHz MAS using the anti-z COSY pulse sequence. This sequence originally introduced by Oschkinat *et al.*.[247] was implemented later for broadband homonuclear J decoupling in liquid state[248]. In the context of MAS, it is applied to remove the secular third order two spin terms of the average Hamiltonian[249] ($\Delta C(3)_{secij} I_{iz}I_{jz}$, Eq. 2.35 and Eq. 2.37 in Chapter 2.2.3). These 'J-coupling like' terms result in residual splittings in the spectrum and therefore anti-z COSY can remove them, while retaining the residual third order shift ($\Delta R(3)_{seci}I_{iz}$, Eq. 2.35 and Eq. 2.36 in Chapter 2.2.3).

In **Chapter 3.3**, an adaptation of anti-z COSY, named TAZ-COSY, is presented. This version of the experiment is based on the same theoretical aspects but it tackles the main disadvantage of anti-z COSY: its experimental time. The pulse sequence is modified and combined with an affine transformation, the two-dimensional one pulse transformation (TOP) and it is able to achieve the same level of narrowing as the parent experiment. However instead of hours of experimental time with anti-z COSY, the TAZ COSY experiment is obtained in 20 min.

3.2 Homonuclear Decoupling in ^{1}H NMR of Solids by Remote Correlation

This chapter has been adapted with permission from: Moutzouri, P.; Paruzzo, F. M.; Simões de Almeida, B.; Stevanato, G.; Emsley, L., Homonuclear Decoupling in ^{1}H NMR of Solids by Remote Correlation. *Angew Chem Int Ed Engl* **2020,** *59* (15), 6235-6238. (post-print)

My contribution was to help in applying the method and obtaining the spectra, and to analysing results. I participated in the review and editing process of the manuscript.

3.2.1 Introduction

This chapter shows how narrower ^{1}H spectra are obtained from a simple 2D scheme that exclusively generates correlations in which the coupling partners have all flipped their spin states, i.e., correlations between so-called remote transitions. Specifically, we show that the residual broadening under MAS in a multi-spin system with different chemical shifts is due to a combination of second order shifts and splittings, and that these splittings will be removed in a 45° projection of an anti-z-COSY spectrum.

3.2.2 Methods

The anti-z-COSY pulse sequence (Figure 3.1) was first introduced by Oschkinat et al.[247] to probe correlations between connected and remote transitions, and then implemented by Pell et al.[248] for broadband homonuclear *J* decoupling in liquid state NMR. The experiment produces phase-sensitive COSY like 2D spectra in which, in the limit where the pulse angle β tends to zero, the fine structure of the diagonal peaks only contains correlations between the remote transitions, i.e., transitions in which the passive spins (the coupling partners) have inverted their spin state between t_1 and t_2. These transitions lead to peaks that lie along an anti-diagonal positioned at the center of gravity of the splitting.

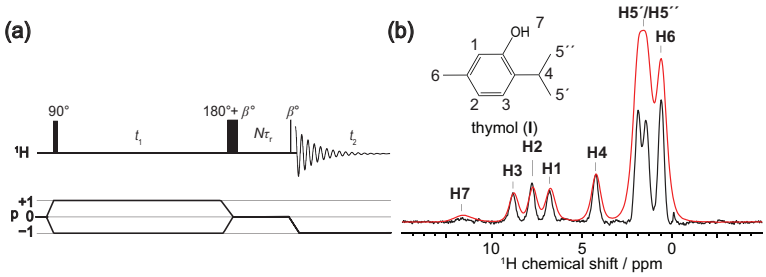

Figure 3.1 (a) Anti-*z*-COSY pulse sequence and coherence transfer pathway, where β indicates a low flip angle pulse. (b) Echo-detected spectrum (red) and a 45° projection of an anti-z-COSY spectrum with a flip angle of 5° (black) of thymol (**I**) acquired with 100 kHz MAS. Further details in Appendix II.

3.2.3 Results & Discussion

Figure 3.1 shows the one-dimensional ^{1}H spectrum obtained from a 45° projection across the diagonal peaks in an anti-z-COSY experiment [247-248] on a sample of powdered thymol (**I**), in comparison to the conventional echo-detected MAS experiment. Both spectra were obtained at 100 kHz MAS. The anti-z-COSY spectrum yields resonances that are narrower up to a factor two.

The effect of MAS on dipolar coupled nuclear spins has been the subject of many studies. A review is out of the scope here, but most pertinent to our work are the articles by Nakai and McDowell[108] and Levitt *et al.*.[106] who both treated the case of two inequivalent dipolar coupled spins in the AB regime. They showed that, to second order, MAS leads to removal of the splitting caused by the dipolar coupling, but that there will be a residual shift (ΔR) in the position of the resonances, away from the isotropic values. There are no residual splittings. The shift depends on both the chemical shift and coupling tensors. This is illustrated in Figure 3.2 (a).

The average Hamiltonian to third order for an arbitrary ABC spin system[229] (see Appendix II for details) shows (Eq. 3.6) that now both $\boldsymbol{I_z}$ and two-spin $\boldsymbol{I_z I_z}$ terms survive MAS. The resulting spectrum consists of resonances

that are also shifted from the isotropic value by a shift (ΔR), and which are additionally now split in general into a doublet of doublets, as illustrated in Figure 3.2 (b). Both the residual shifts and the splittings depend on all the spin system parameters, and they are predicted to decrease with $1/\omega_r^2$ as shown in Figure 3.2 (c).

The effect of the anti-z COSY pulse sequence on these spectra is to remove the residual splittings, but to retain the residual shifts, and this is the underlying cause of the narrowing observed experimentally in Figure 3.1. The above is supported by the numerical simulations for single orientations shown in Figure3.2 (d)-(f), and by the powder simulations for 4 and 5 spin systems in Figures 3.11 and 3.12. The ratio between the desired anti-diagonal peaks and the other peaks in the multiplet should increase as β decreases.[248] However, the overall intensity of the correlations also decreases with decreasing β. Usually an angle between 5° and 20° gives the best compromise between spectral resolution and sensitivity.

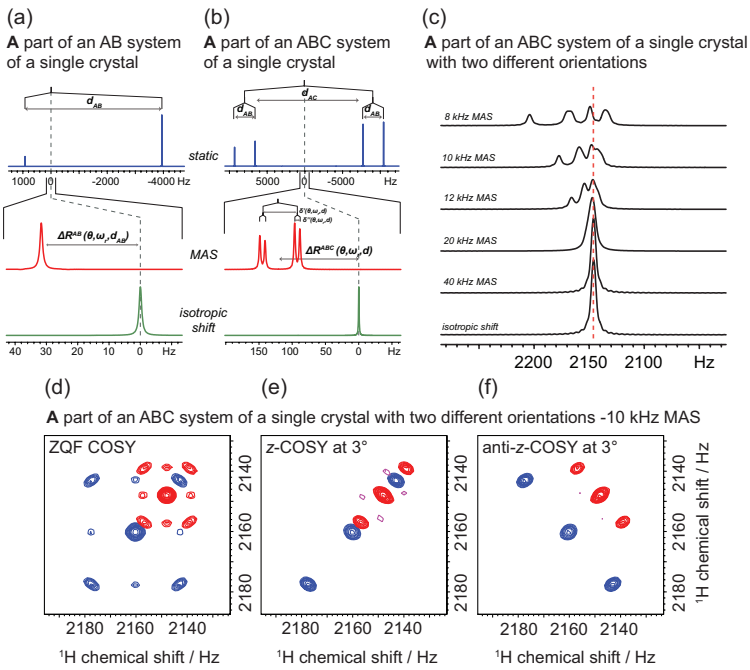

Figure 3.2 (a) The A part of the spectrum of an AB system, and (b) the A part of the spectrum of an ABC system, for a single orientation simulated using SPINACH[231] for (top) a static sample, (middle) under MAS, and (bottom) only the isotropic shift. (c) The A part of the spectrum of an ABC system for two orientations as a function of the MAS rate. (d-f) Contour plots of the A diagonal peak region in the 2D spectra of an ABC system, for two different orientations (red and blue) for (d) ZQF-COSY, (e) z-COSY and (f) anti-z-COSY experiments. All the simulation methods and parameters are detailed in the Appendix II.

Figure 3.3 (a)-(c) shows the difference in the 2D lineshapes observed experimentally for thymol in a ZQF-COSY (i.e. the 90° experiment), a z-COSY, and an anti-z-COSY experiment, and the strong flip-angle dependence is confirmed in Figure 3.3 (d)-(g) showing the linewidths for thymol for β angles from 90° to 3°. In the spectrum with β = 3° for H1, H2, H3, and H4 of thymol we measure linewidths of 208, 194, 245 and 218 Hz, as compared to 359, 336, 350, and 346 Hz in the β = 90° spectra. This corresponds to a factor of between 1.4 to 1.7 increase in resolution.

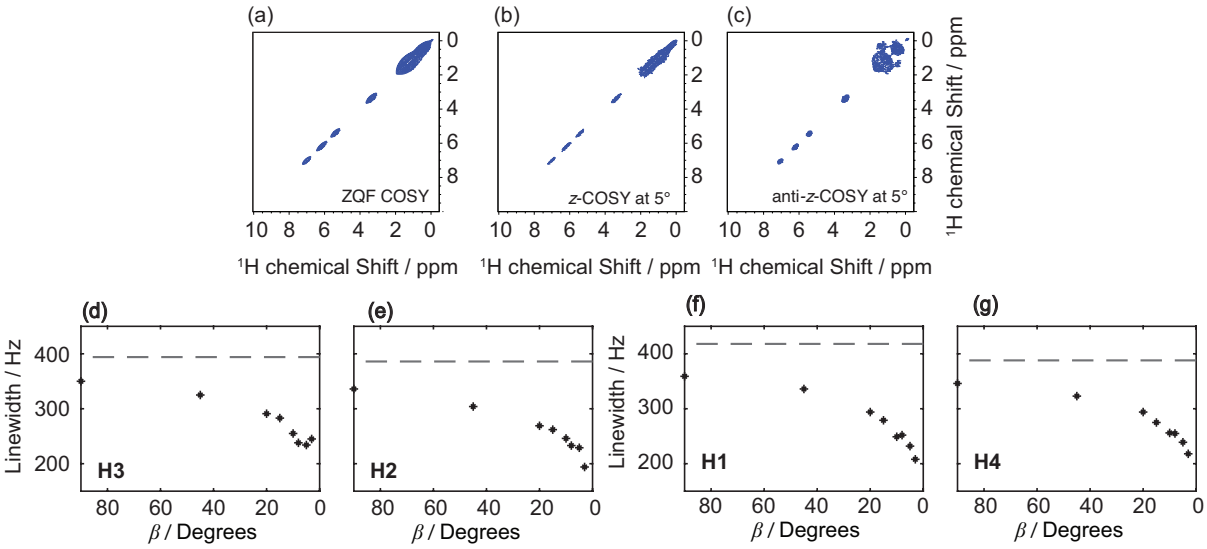

Figure 3.3 Contour plots of (a) ZQF COSY, (b) z-COSY, and (c) anti-z-COSY spectra of thymol acquired at a MAS rate of 100 kHz. (b) and (c) were obtained with β = 5°. (d-g) Measured full linewidths at half height of the resonances of protons H1-H4 from anti-z-COSY spectra of thymol as a function of β acquired at a MAS rate of 100 kHz. The dashed lines denote the proton linewidths measured in the conventional spin echo spectrum.

The method is also demonstrated for microcrystalline powder samples of β-AspAla (**II**) and strychnine (**III**). Figure 3.4 shows projections extracted from anti-z-COSY spectra of β-AspAla which show the same decoupling effect as observed for thymol above. Again, in this sample the linewidths are reduced by almost a factor of two for most of the protons. Figure 3.5 shows the 1D spectrum for strychnine extracted from the 2D anti-z-COSY spectrum acquired with an 8° flip angle, which is again significantly narrowed. The narrowing factor will depend on the strength of the residual coupling of each nucleus in each sample and the absolute remaining linewidth will still be broadened by residual homogenous shift and inhomogeneous contributions.

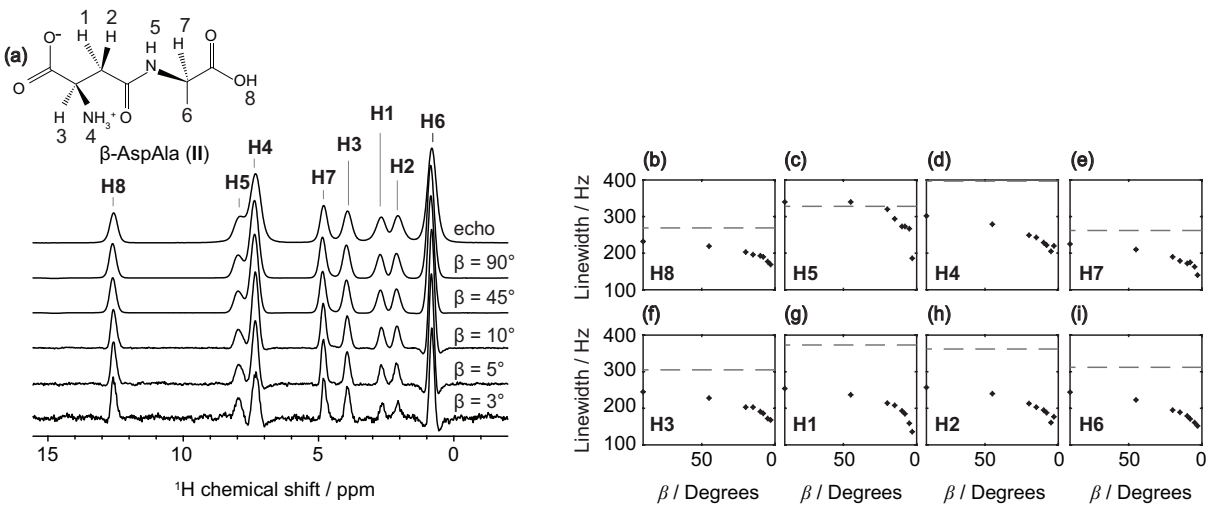

Figure 3.4 (a) Spectra of β-AspAla (**II**) obtained from integral projections of the 45° projection of the anti-z-COSY spectra acquired at 100 kHz MAS. The top spectrum was acquired with the conventional spin echo sequence at the same sample spinning rate. (b-i) Measured linewidth of protons H1-H8 as a function of β. The dashed lines denote the proton linewidths measured in the conventional spin echo spectrum.

All three samples used here yield clean anti-z-COSY spectra. In solution, these experiments can be compromised by artifacts due to the appearance of cross-peaks in the spectrum, as well as zero-quantum transfers within the diagonal peaks, and additional measures are required to actively suppress them.[248, 250] However, we note that such unwanted peaks appear in anti-phase with respect to the couplings, and have no net integral. The numerous

couplings and the comparatively broader lines expected in the solid-state mean that these unwanted peaks are likely to largely cancel themselves out, with no further action required. Additionally, the orientation distributions present in the powder leads to different sizes of the residual couplings, and might act in a similar manner to the active measures usually taken to suppress artifacts. Indeed, the cross-peaks we observe here are weak in intensity (see Figure 3.7).

We note that equivalent spins will behave differently. This is simulated for an A_2B system in Appendix II. We see in Figure 3.10 that the 2D lineshape has some negative intensity in the anti-z-COSY spectrum, that leads to small negative dips in the 45° projection. This might correspond to the origin of the dips observed for the CH_3 and NH_3^+ peaks in Figures 3.1 and 3.4 for small β values.

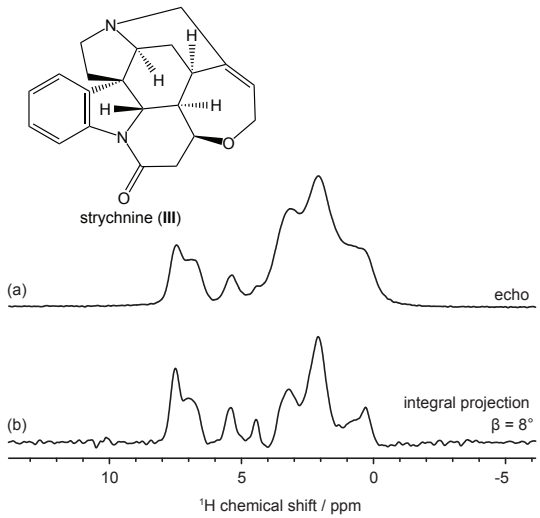

Figure 3.5 (a) Echo-detected 100 kHz MAS spectrum of strychnine (**III**). (b) 1D spectra extracted as an integral projection from a doubly sheared 2D anti-z-COSY spectrum acquired with a flip angle of β = 8° at 100 kHz MAS.

For the anti-*z*-COSY concept to work properly it is important that the *z* magnetization should remain unchanged during the z-filter period. Therefore, any effect that changes any of the spin states during the mixing scheme will lead to reduction in resolution. Notably, spin diffusion during this period will induce spin flip-flops. While the fast spinning rate slows down homonuclear spin diffusion, it is important to keep the delay as short as possible. Additionally, any dipolar recoupling effects caused by the mixing pulses will also induce spin flips. Here we use a mixing time equal to a single rotor period. These effects and others leading to limiting resolution will be explored further in the future. We finally note that we expect this strategy to also lead to better resolution at lower spinning speeds. This is confirmed in Figure 3.13, where we show the results for thymol at a MAS rate of 62.5 kHz. In this case we obtain a gain in resolution of a factor between 1.8 and 2.1.

3.2.4 Conclusion

In conclusion, the simple approach introduced here for achieving homonuclear decoupling in organic solids by generating exclusively remote correlations, yields up to a factor of two gain in resolution as compared to conventional echo-detected MAS experiments. Smaller flip angles produce spectra with higher resolution, at the expense of reduced sensitivity. The factor two gain in resolution achieved with the concept as introduced here in its most simple form is striking, with clear room for improvement through further development.

3.2.5 Appendix II

3.2.5.1 Experimental details

Bruker Avance Neo spectrometer equipped with a 0.7 mm triple resonance HCN CP-MAS probe. Data where acquired on three different samples. The powdered samples of thymol (2-Isopropyl-5-methylphenol), β-AspAla ((2S)-2-amino-3-{[(1S)-1-carboxyethyl]carbamoypropanoic acid), and strychnine were purchased from AppliChem, Bachem, and Signal-Aldrich respectively and were used without further recrystallization, after mild crushing with a mortar and a pestle.

All data were acquired with rotor synchronized delays, at a sample spinning speed of 100 kHz. Presaturation was applied on the ^{1}H channel. For the thymol and β-AspAla spectra, a proton pulse with amplitude ν_1=294 kHz was used, whereas for the strychnine data a ν_1=278 kHz was used.

All 2D spectra were acquired with the States-TPPI acquisition method. For the 2D ZQF COSY and z-COSY experiments a total of 256 t_1 points were acquired with t_2 acquisition times of 10.2 ms and with a maximum t_1 delay of 12.8 ms. The recycle delay was 5 s and for each t_1 increment 8 and 32 scans were acquired respectively. All anti-z-COSY spectra of thymol were acquired with 256 t_1 increments and a maximum t_1 delay of 10.2 ms, whereas the anti-z-COSY spectra of β-AspAla were acquired with 448 t_1 increments and a maximum t_1 delay of 20.1 ms. For thymol, the t_2 acquisition time was 10.2 ms and for β-AspAla 12.8 ms. When flip angles of 90°, 45°, 20°, 15° were used, 8 scans were acquired, while for flip angles of 8°, 5°, and 3°, 16, 32 and 64 scans were acquired respectively. The 2D anti-z-COSY experiment of strychnine was acquired with 180 t_1 points, a maximum t_1 delay of 8.1 ms and a t_2 acquisition time of 8 ms. The flip angle was set to 8°, 32 scans were acquired for each t_1 point, and the recycle delay was 50 s.

The 1D echo spectra of thymol and β-AspAla were acquired with 5 s recycle time, and 10 ms acquisition time. The spectrum of strychnine was acquired with 50 s recycle time, and 8 ms acquisition time.

All processing was done either using the Bruker software TopSpin 4.0.6, or with homemade MATLAB scripts. All 2D anti-z-COSY spectra were double Fourier transformed, and sheared twice, once parallel to F_1 with a shear factor of $\kappa_t = -1$ and once more parallel to the new F'_2 dimension with a new shear factor of $\kappa_t = +(1/2)$, where the shear factor κ_t is related to the shear angle θ according to the equation $tan\theta = \kappa_t$. This was done at TopSpin using the ajp_share "au" program.{Pell, 2007 #185} After double shearing, an integral projection onto F_2 of the F_1 range spanned by the lineshape of the signals was taken. ^{1}H chemical shifts were reference according to literature. [45, 135]

The experimental details are summarized in the following tables:

Table 3.1 Experimental details of experiments acquired on a powdered sample of thymol.

Experiment	(ω_r/2π) /kHz	(ω_{RF}/2π) /kHz	*Total exp. time*	t_2 acquisition time / ms	*Maximum* t_1 increment / ms	td_2 complex points	td_1 complex points	NS	d1 /s	τ_z / µs
echo detected	100	312.5	20 s	10.2 ms	-	2048	-	4	5	10
ZQF-COSY	100	294	2 h 52 min	10.2 ms	12.8	2048	128	8	5	10
z-COSY (5°)	100	294	11 h 31 min	10.2 ms	12.8	2048	128	32	5	10
anti-z-COSY (90°)	100	294	2 h 52 min	10.2 ms	12.8	2048	128	8	5	10
anti-z-COSY (45°)	100	294	2 h 52 min	10.2 ms	12.8	2048	128	8	5	10
anti-z-COSY (20°)	100	294	2 h 52 min	10.2 ms	12.8	2048	128	8	5	10
anti-z-COSY (15°)	100	294	2 h 52 min	10.2 ms	12.8	2048	128	8	5	10
anti-z-COSY (10°)	100	294	2 h 52 min	10.2 ms	12.8	2048	128	8	5	10
anti-z-COSY (8°)	100	294	5 h 45 min	10.2 ms	12.8	2048	128	16	5	10
anti-z-COSY (5°)	100	294	11 h 31 min	10.2 ms	12.8	2048	128	32	5	10
anti-z-COSY (3°)	100	294	23 h 2 min	10.2 ms	12.8	2048	128	64	5	10

Table 3.2 Experimental details of experiments acquired on a powdered sample of β-AspAla.

Experiment	(ω_r/2π) /kHz	(ω_{RF}/2π) /kHz	*Total exp. time*	t_2 acquisition time / ms	*Maximum* t_1 increment / ms	td_2 complex points	td_1 complex points	NS	d1 /s	τ_z / µs
echo detected	100	294	20 s	10	-	2048	-	4	5	10
anti-z-COSY (90°)	100	294	5 h 2 min	12.8	20.1	2560	224	8	5	10
anti-z-COSY (45°)	100	294	5 h 2 min	12.8	20.1	2560	224	8	5	10
anti-z-COSY (20°)	100	294	5 h 2 min	12.8	20.1	2560	224	8	5	10
anti-z-COSY (15°)	100	294	5 h 2 min	12.8	20.1	2560	224	8	5	10
anti-z-COSY (10°)	100	294	5 h 2 min	12.8	20.1	2560	224	8	5	10
anti-z-COSY (8°)	100	294	10 h 5 min	12.8	20.1	2560	224	16	5	10
anti-z-COSY (5°)	100	294	10 h 5 min	12.8	20.1	2560	224	16	5	10
anti-z-COSY (3°)	100	294	20 h 11 min	12.8	20.1	2560	224	32	5	10

Table 3.3 Experimental details of experiments acquired on a powdered sample of β-AspAla.

Experiment	(ω_r/2π) /kHz	(ω_{RF}/2π) /kHz	*Total exp. time*	t_2 acquisition time / ms	*Maximum* t_1 increment / ms	td_2 complex points	td_1 complex points	NS	d1 /s	τ_z / µs
echo detected	100	277.8	3 min 20 s	8	-	1600	-	4	50	10
anti-z-COSY (8°)	100	277.8	3d 8 h 12 min	8	8	1600	90	32	50	10

3.2.5.2 Processing of experimental data

1) All 2D anti-z-COSY spectra were double Fourier transformed, zero filled to 8k and 1k points in F_2 and F_1 respectively, and then sheared twice, once parallel to F_1 and once more parallel to the new F'_2 dimension using the ajp_share "au" program written by A. J. Pell.[248]
2) An integral projection onto F_2 of the F_1 range spanned by the lineshape of the signals was taken in order to avoid the addition of unnecessary noise in the extracted 1D spectrum. For thymol, H4 was chosen was a reference point, and for β-AspAla H7.
3) Peak widths at half height were measured using the *peakw* command in topspin 4.0.6.

3.2.5.3 Thymol data

Spectra at different angles

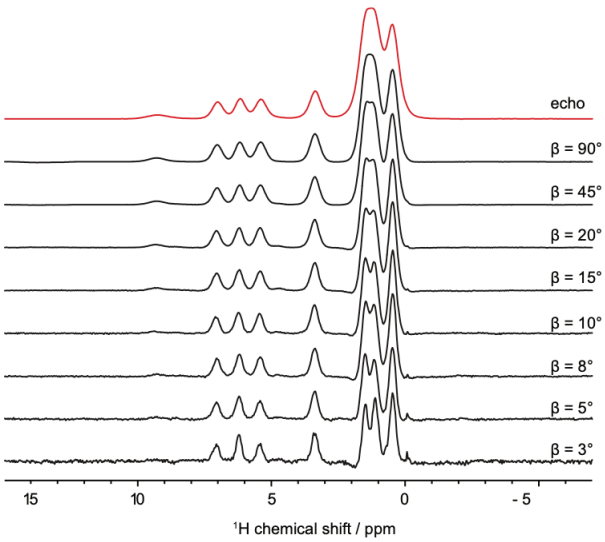

Figure 3.6 Spectra of thymol obtained as integral projections from 45° sheared 2D anti-*z*-COSY spectra acquired with flip angles, β, of 90° 45°, 20°, 15°, 10°, 8°, 5°, and 3° at 100 kHz MAS. The top spectrum shows the result of the echo-detected experiment at the same spin rate.

Linewidths at half height of thymol spectra

Table 3.4 Linewidths of thymol spectra measured at half height

Proton/β	echo	90	45	20	15	10	8	5	3
H1	418	359	336	294	279	249	252	232	208
H2	386	336	304	269	262	246	233	229	194
H3	394	350	325	291	283	255	238	234	245
H4	388	346	323	294	275	256	255	239	218
H5´*	752	649	627	564	533	524	521	516	501
H5´´*	752	649	627	564	533	524	521	516	501
H6	444	433	395	301	283	249	251	236	221

T_2' measurements of thymol

Table 3.5 T_2 relaxation measurements on a sample of thymol

Proton	Echo (measured linewidths in Hz)	T2´ (ms)	Δ (1/(π T2´) in Hz)
H1	417	2.71	121
H2	393	3.59	89
H3	409	2.64	118
H4	391	2.79	114

Linewidths at half height of echo-detected spectra acquired on the same day and at the same MAS rate were measured.

2D contour plots of anti-z-COSY spectra

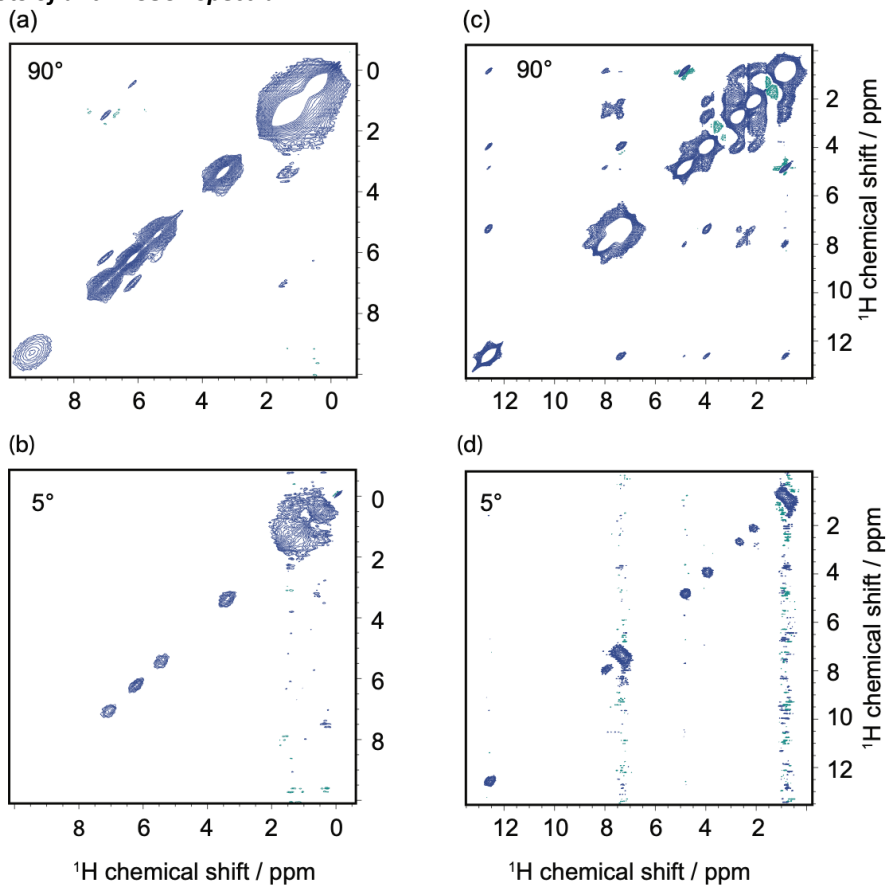

Figure 3.7 a) and b) anti-z-COSY spectra of thymol acquired with flip angles of 90° and 5° respectively. c) and d) anti-z-COSY spectra of β-AspAla acquired with flip angles of 90° and 5° respectively. The contour levels are plotted in a way that the peaks of H4 of thymol and H7 of β-AspAla have the same intensity in the 90° and 5° anti-z-COSY spectra.

3.2.5.4 β-AspAla data

Linewidths at half height of β -AspAla spectra

Table 3.6 Linewidths of β-AspAla spectra measured at half height.

Proton/β	echo	90	45	20	15	10	8	5	3
H8	269	232	219	203	196	193	190	177	169
H5	328	340	340	320	294	273	273	267	186
H4	397	302	279	249	243	229	222	205	220
H7	262	225	210	190	179	172	175	163	140
H3	305	245	228	203	203	191	186	172	168
H1	373	254	237	214	208	193	185	159	136
H2	362	257	240	213	203	195	188	161	177
H6	312	244	223	195	189	179	171	161	152

T_2' measurements on β-AspAla

Table 3.7 T_2 relaxation measurements on a sample of β-AspAla

Proton	Echo (measured linewidths in Hz)	T2´ (ms)	Δ (1/(π T2´) in Hz)
H8	227	5.41	59
H5	322	3.71	86
H4	342	2.5	127
H7	219	4.97	64
H3	267	3.07	104
H1	301	2.82	113
H2	303	2.92	109
H6	264	3.2	100

Linewidths at half height of echo-detected MAS spectra acquired on the same day and at the same MAS rate were measured.

3.2.5.5 SPINACH simulations – single crystal

Spectra were simulated using SPINACH[231] which runs inside the MATLAB framework, and were processed on Topspin 4.0.6 similarly to the experimental data. The transfer of the data from MATLAB to Topspin was done using a homemade script written by M. Foroozandeh.

Spin systems in Figure 3.2:

For the 3 spins simulations, the three chemical shifts were all different and isotropic, and all spins were dipolar coupled. No scalar couplings were included in the spin system. All simulations were performed invoking magic angle sample spinning, and using a single crystal with a single orientation in figure 3.2b, and two different orientations with the same weight in Figure 3.2c-f. A Gaussian line broadening of 8 Hz was applied in both dimensions of the 2D plots prior to Fourier transformation.

Table 3.8 Spin system parameters for the spin system illustrated in Fig. 3.2.

	Zeeman Eigenvalues (ppm)	**Dipolar Coupling Eigenvalues (Hz)**	**Dipolar Coupling Euler Angles**
Figure 2a	Ω_1 = 9.0 Ω_2 = 15.0	D_{12} = 18000 Hz	E_{12} = (π/5 π/7 π/20)
Figure 2b	Ω_1 = 2.5 Ω_2 = 45.0 Ω_3 = 40.0	D_{12} = 3600 Hz D_{13} = -24000 Hz D_{23} = -12500 Hz	E_{12} = π*(0.0 170 0.0)/180 E_{13} = π*(0.0 190 0.0)/180 E_{23} = π*(0.0 100 0.0)/180
Figure 2c-f	Ω_1 = 4.0 Ω_2 = 3.6 Ω_3 = 12.0	D_{12} = 4000 Hz D_{13} = 6600 Hz D_{23} = 4400 Hz	E_{12} = (π/6 π/2 π/20) E_{13} = (π/4 π/2 π/3) E_{23} = (π/3 π/3 π/2)

Orientations File :

α = [0 0.3142]
β = [0 1.0472]
γ = [0 3.491]
weights = [1 1]

Simulation parameters :

Table 3.9 Simulation parameters for the spin system illustrated in Fig. 3.2.

Magnetic field	14.0 T
Spectral Width in F_1	10000 Hz
Spectral Width in F_2	10000 Hz
Number of complex points in F_1	4096
Number of complex points in F_2	4096
Spectral Offset	4801.04 Hz
β angle	3°
MAS rate	variable

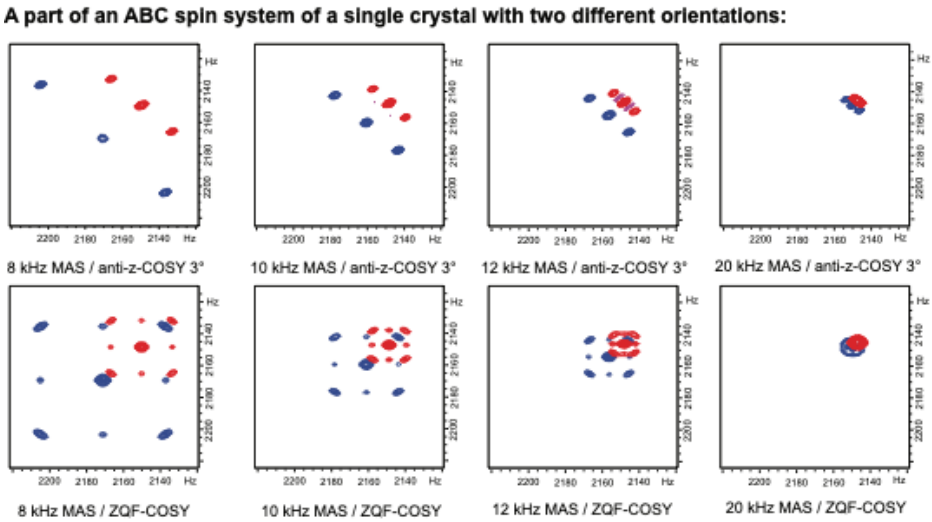

Figure 3.8 A part of an ABC spin system for a single crystal with two different orientations. ZQF and anti-z-COSY (β of 3°) simulations were performed at different MAS rates: 8, 10,12, and 20 kHz.

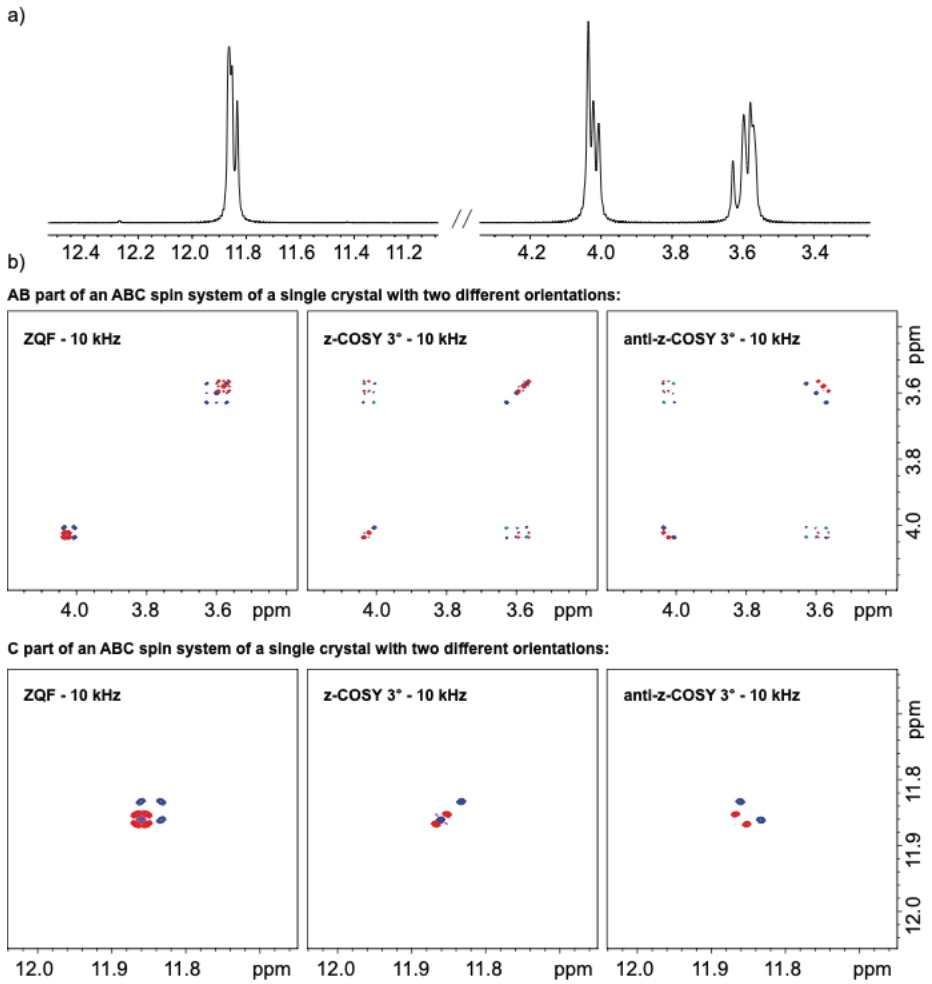

Figure 3.9 a) One-dimensional ^{1}H spectrum simulated with SPINACH for an ABC spin system of a single crystal with two different orientations. b) ZQF, z-COSY (β of 3°), and anti-z-COSY (β of 3°) simulations of the same system performed at 10 kHz MAS rate.

A_2B Equivalent spin system:

A spin system of 2 equivalent and of an additional non-equivalent spin was used. The chemical shifts were isotropic and all spins shared dipolar couplings with one another. No scalar couplings were included in the spin system. All simulations were performed invoking magic angle sample spinning, and using a single crystal with a single orientation. A Gaussian line broadening of 8.5 Hz was applied in both dimensions of the 2D plots prior to Fourier transformation.

Table 3.10 Spin system parameters for the the A_2B spin system.

	Zeeman Eigenvalues (ppm)	**Dipolar Coupling Eigenvalues (Hz)**	**Dipolar Coupling Euler Angles**
Figure S5	$\Omega_1 = 2.6$ $\Omega_2 = 4.0$ $\Omega_3 = 4.0$	$D_{12} = 4000$ Hz $D_{13} = 10000$ Hz $D_{23} = 10000$ Hz	$E_{12} = (\pi/6\ \pi/2\ \pi/20)$ $E_{13} = (\pi/4\ \pi/2\ \pi/3)$ $E_{23} = (\pi/3\ \pi/3\ \pi/2)$

<u>Simulation parameters:</u>

Table 3.11 Simulation parameters for the A_2B spin system.

Magnetic field	14.0 T
Spectral Width in F_1	2500 Hz
Spectral Width in F_2	2500 Hz
Number of complex points in F_1	512
Number of complex points in F_2	512
Spectral Offset	2000 Hz
β angle	3°
MAS rate	20000

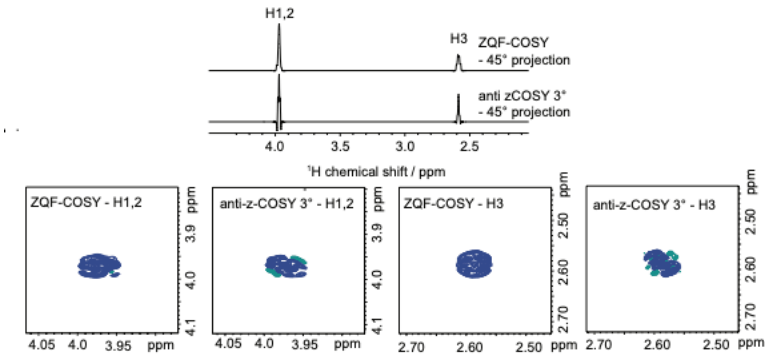

Figure 3.10 The top part of the figure shows the 45° projections extracted from the ZQF COSY and anti-z-COSY (3°) simulations of the spin system described above. The lower part shows the diagonal peak regions of the 2D COSY spectra.

3.2.5.6 SPINACH simulations – powder pattern of 4 and 5 spins

A spin system of 4 or 5 inequivalent spins was used. The chemical shifts included chemical shift anisotropy, and all spins shared dipolar couplings with one another. Scalar couplings were also included (or not) in the spin system. All simulations were performed with magic angle spinning using either 42 (5 spins simulations) or 162 (4 spins simulations) orientations on an icosahedral grid. No line broadening was applied in the 2D plots.

4 spin simulations

Simulation parameters:

Table 3.12 Simulation parameters for the 4 spins powder average.

Magnetic field	14.0 T
Spectral Width in F_1	10000 Hz
Spectral Width in F_2	10000 Hz
Number of complex points in F_1	256
Number of complex points in F_2	256
Spectral Offset	3500 Hz
β angle	3°
MAS rate	60000

Table 3.13 Simulation parameters for the 4 spins powder average.

	Zeeman Eigenvalues (ppm)	**Zeeman Euler Angles**	**Dipolar Coupling Eigenvalues (Hz)**	**Dipolar Coupling Euler Angles**	**Scalar Coupling (Hz)**
Figure S6	Ω_1 = (1.6 2.6 0.6) Ω_2 = (6.0 4.0 2.0) Ω_3 = (7.5 6.5 8.0) Ω_4 = (10.0 10.0 10.0)	ZE_1 = (π/7 π/6 π/11) ZE_2 = (π/3 π/4 π/2) ZE_3 = (π/20 π/10 π/7) ZE_4 = (π/4 π/2 π/9)	D_{12} = 32000 D_{13} = 16600 D_{14} = 56000 D_{23} = 67200 D_{24} = 24000 D_{34} = 36800	E_{12} = π*(0 130 0)/180 E_{13} = π* (0 120 0) /180 E_{14} = π* (0 140 0) /180 E_{23} = π* (0 150 0) /180 E_{24} = π* (0 160 0) /180 E_{34} = π* (0 135 0) /180	J_{12} = 10 J_{13} = 9 J_{14} = -5 J_{23} =5 J_{24} = 4 J_{34} = 7

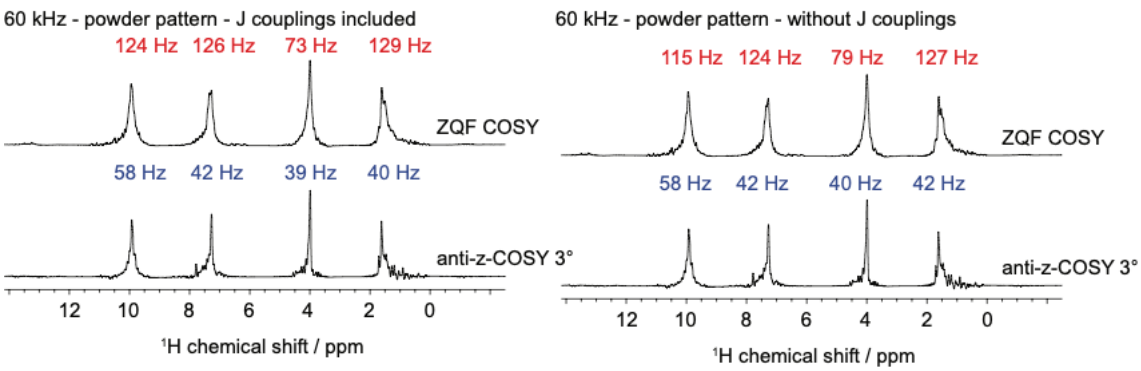

Figure 3.11 45° projections extracted from the ZQF COSY and anti-z-COSY (3°) simulations of the 4 spin system described above simulated at a 60 kHz MAS rate. In the top part of the figure J couplings are included and in the bottom part they are omitted. We note that the choice of Euler angles has a fairly strong effect on the overall lineshape and line broadening observed in the simulations for limited numbers of spins. We do not expect them to reproduce the experimental spectra quantitatively. The parameter dependencies of these simulations will be explored more extensively in future work.

5 spin simulations

Simulation parameters:

Table 3.14 Simulation parameters for the 5 spin powder average.

Magnetic field	14.0 T
Spectral Width in F_1	12000 Hz
Spectral Width in F_2	12000 Hz
Number of complex points in F_1	256
Number of complex points in F_2	256
Spectral Offset	3500 Hz
β angle	3°
MAS rate	60000

Table 3.15 Spin system parameters for the 5 spins powder average.

	Zeeman Eigenvalues (ppm)	**Zeeman Euler Angles**	**Dipolar Coupling Eigenvalues (Hz)**	**Dipolar Coupling Euler Angles**	**Scalar Coupling (Hz)**
Figure S6	Ω_1 = (1.6 2.6 0.6) Ω_2 = (6.0 4.0 2.0) Ω_3 = (7.5 6.5 8.0) Ω_4 = (10.0 10.0 10.0) Ω_5 = (12.2 12.1 12.3)	ZE_1 = (π/7 π/6 π/11) ZE_2 = (π/3 π/4 π/2) ZE_3 = (π/20 π/10 π/7) ZE_4 = (π/4 π/2 π/9) ZE_5 = (π/3 π/2 π/6)	D_{12} = 32000 D_{13} = 16600 D_{14} = 56000 D_{15} = 48000 D_{23} = 67200 D_{24} = 24000 D_{25} = 14400 D_{34} = 36800 D_{35} = 46400 D_{45} = 19200	E_{12} = π*(0 130 0)/180 E_{13} = π* (0 120 0) /180 E_{14} = π* (0 140 0) /180 E_{15} = π* (0 125 0) /180 E_{23} = π* (0 150 0) /180 E_{24} = π* (0 160 0) /180 E_{25} = π* (0 170 0) /180 E_{34} = π* (0 135 0) /180 E_{35} = π* (0 145 0) /180 E_{45} = π* (0 150 0) /180	J_{12} = 10 J_{13} = 9 J_{14} = -5 J_{15} = -3 J_{23} =5 J_{24} = 4 J_{25} = 6 J_{34} = 7 J_{35} = 11 J_{45} = 2

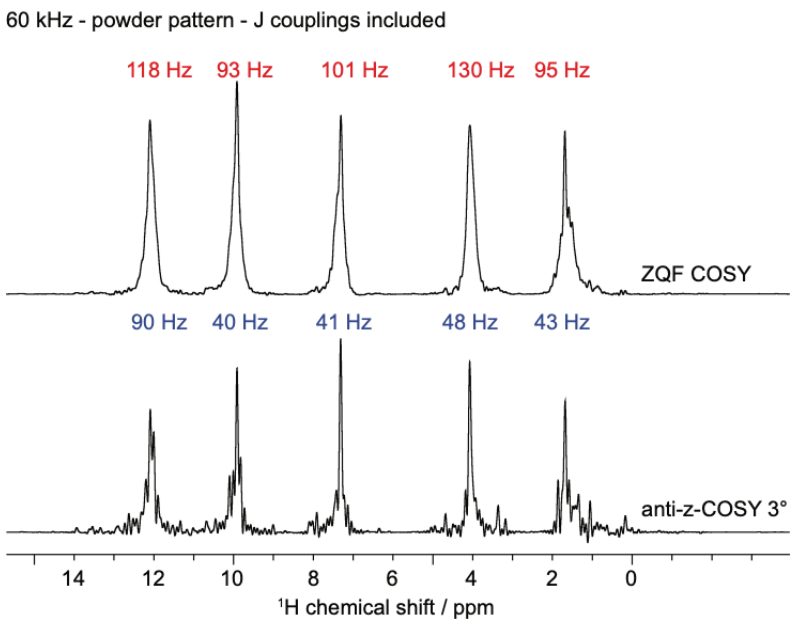

Figure 3.12 45° projections extracted from the ZQF COSY and anti-z-COSY (3°) simulations of the 5 spin system described above simulated at a 60 kHz MAS rate. We again note that the choice of Euler angles has a fairly strong effect on the overall lineshape and line broadening observed in the simulations for limited numbers of spins.

3.2.5.7 Average Hamiltonians under MAS

The effect of MAS on dipolar coupled nuclear spins has been the subject of many studies, both relating to observed lineshapes[70 112 107] and to spin diffusion[103 251 222 252 253 226]. A review is out of the scope here, but most pertinent to our work are the articles by Nakai and McDowell[108] and Levitt *et al.*.[106] who both treated the case of two inequivalent dipolar coupled spins. Both papers provide expression for the lineshapes to second order that predict that MAS leads to removal of the splitting caused by the dipolar coupling, but that there will be a residual shift (ΔR) in the position of the resonances, away from the isotropic values, due to higher order $\boldsymbol{I_z}$ terms, and this shift will depend on both the chemical shift and coupling tensors. The higher-order shift is predicted to decrease as the spinning rate increases as $1/\omega^2_{rot}$. This is illustrated in Figure 3.2 (a).

The case of three inequivalent spins has been treated by Scholz *et al.*.[229], who presented the average Hamiltonian but who did not discuss the result in terms of spectral properties (since that article was focused on formalism and not applications). Malär *et al.*.[107] and Grommek *et al.*.[226] have presented the case of three equivalent spins. They also considered the inclusion of the effect of chemical shift differences on the lineshape invoking a weak coupling approximation.

Here, we have reproduced the average Hamiltonian to third order for an arbitrary ABC spin system. The result (obtained using the symbolic package SpinDynamica[230] within Mathematica) is given below. (An example Mathematica notebook is also included.)

We see that in an ABC system both $\boldsymbol{I_z}$ and two-spin $\boldsymbol{I_z}\,\boldsymbol{I_z}$ terms survive MAS at third order, and that the resulting spectrum consists of resonances for each spin that are again shifted from the isotropic value by a shift (ΔR), and which are also split into a doublet of doublets. Both the shift and the residual splittings depend on all the spin system parameters. This is illustrated in Figure 3.2 (b). The higher-order shifts and splittings are predicted to decrease as the spinning speed is increased as $1/\omega^2_{rot}$. The exact functional dependence of the higher-order shifts and splittings on the spin system parameters is beyond the current scope and will be presented and explored in further work.

The effect of the anti-z COSY pulse sequence on these spectra is to remove the residual splittings, but to retain the residual shifts. This is illustrated in the SPINACH simulations shown in Figure 3.2 (d)-(f).

<u>Second Order Average Hamiltonian in an AB spin system under MAS:</u>

$$\bar{\boldsymbol{H}}^{\boldsymbol{AB}} = \bar{\boldsymbol{H}}^{\boldsymbol{AB}}_{(1)} + \bar{\boldsymbol{H}}^{\boldsymbol{AB}}_{(2)} + \bar{\boldsymbol{H}}^{\boldsymbol{AB}}_{(3)} \tag{3.1}$$

$$\bar{H}^{AB}_{(1)} = \omega_1 \boldsymbol{I_{1z}} + \omega_2 \boldsymbol{I_{2z}} \tag{3.2}$$

$$\bar{H}^{AB}_{(2)} = 0 \tag{3.3}$$

$$\bar{H}^{AB}_{(3)} = \frac{1}{\omega_{rot}{}^2} C1\,(\boldsymbol{I_{2z}} - \boldsymbol{I_{1z}}) \tag{3.4}$$

where ω_1 and ω_2 are the isotropic chemical shifts of spin 1 and spin 2 and C1 is a function of ω_1, ω_2, and d_{12} which is the dipolar interaction between spin 1 and spin 2, $d_{12} = -\left(\frac{\mu_0}{4\pi}\right)\frac{\hbar\gamma_1\gamma_2}{r_{12}^3} \times \frac{1}{2}\,(3\cos\theta_{12}{}^2 - 1)$.

<u>Second Order Average Hamiltonian in an ABC spin system under MAS:</u>

$$\bar{\boldsymbol{H}}^{\boldsymbol{ABC}} = \bar{\boldsymbol{H}}^{\boldsymbol{ABC}}_{(1)} + \bar{\boldsymbol{H}}^{\boldsymbol{ABC}}_{(2)} + \bar{\boldsymbol{H}}^{\boldsymbol{ABC}}_{(3)} \tag{3.5}$$

$$\bar{H}^{ABC}_{(1)} = \omega_1 \boldsymbol{I_{1z}} + \omega_2 \boldsymbol{I_{2z}} + \omega_3 \boldsymbol{I_{3z}} \tag{3.6}$$

where ω_1, ω_2, and ω_3 are the isotropic chemical shifts of spins 1, 2, and 3 respectively.

$$\bar{H}^{ABC}_{(2)} = 0 \tag{3.7}$$

$$\bar{H}^{ABC}_{(3)} = \frac{1}{\omega_{rot}{}^2}(C1\,\boldsymbol{I_{1z}} + C2\,\boldsymbol{I_{2z}} + C3\,\boldsymbol{I_{3z}} + C4\,\boldsymbol{I_{1z}}\cdot\boldsymbol{I_{2z}} + C5\,\boldsymbol{I_{1z}}\cdot\boldsymbol{I_{3z}} + C6\,\boldsymbol{I_{2z}}\cdot\boldsymbol{I_{3z}}) \tag{3.8}$$

where C1-6 are functions of ω_1, ω_2, ω_3, d_{12}, d_{13}, and d_{23}, and where d_{ab} is the dipolar coupling constant between spins a and b, $d_{ab} = -\left(\frac{\mu_0}{4\pi}\right)\frac{\hbar\gamma_a\gamma_b}{r_{ab}^3} \times \frac{1}{2}\,(3\cos\theta_{ab}{}^2 - 1)$.

The average Hamiltonians of equations 3.3, 3.4, 3.7, and 3.8, show only the parts that are secular with respect to differences in the chemical shifts.

3.2.5.8 Anti-z-COSY at 62.5 kHz MAS

Experimental Details:

Table 3.16 Experimental parameters for experiments acquired on a sample of thymol at 62.5 kHz MAS.

Experiment	(ω_r/2π) /kHz	(ω_{RF}/2π) /kHz	*Total exp. time*	t_2 acquisition time / ms	*Maximum* t_1 increment / ms	td_2 complex points	td_1 complex points	NS	d1 /s	τ_z / µs
ZQF COSY	62.5	444	2 h 29 min	10.2	24.6	2048	128	8	4.3	16
anti-z-COSY (5°)_1	62.5	444	9 h 58 min	10.2	24.6	2048	128	32	4.3	2
anti-z-COSY (5°)_2	62.5	444	9 h 58 min	10.2	24.6	2048	128	32	4.3	16
anti-z-COSY (5°)_3	62.5	444	9 h 58 min	10.2	24.6	2048	128	32	4.3	80
anti-z-COSY (5°)_4	62.5	444	9 h 58 min	10.2	24.6	2048	128	32	4.3	160

Spectra:

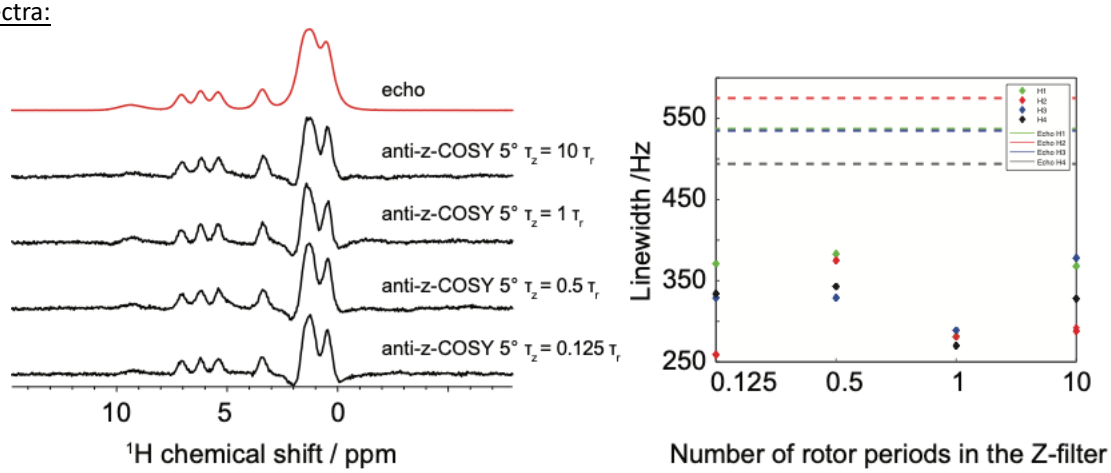

Figure 3.13 Spectra of thymol at 62.5 kHz obtained as integral projections from 45° sheared 2D ZQF and anti-z-COSY spectra (β of 5°) acquired with different multiples of the rotor period for the *z*-filter delay. On the right, the linewidths of H1, H2, H3, and H4 are plotted as a function of the *z*-filter delay.

3.3 Fast Remote Correlation Experiments for ^{1}H Homonuclear Decoupling in Solids

This chapter has been adapted with permission from: Moutzouri, P.; Simões de Almeida, B.; Emsley, L., Fast remote correlation experiments for ^{1}H homonuclear decoupling in solids. *J Magn Reson* **2020,** *321*, 106856. (post-print).

My contribution was to help in developing and applying the method, obtaining the spectra, and analysing results. I participated in the writing, review and editing process of the manuscript.

3.3.1 Introduction

The main drawback of Anti-z-COSY is the need to record a two-dimensional spectrum with high resolution in both dimensions, which more often than not can be quite time-consuming. Typically, hundreds of points are required in t_1, leading to acquisition times of hours. Here, we show how a modification of the pulse sequence and the acquisition scheme can offer identical results in terms of spectral resolution but in a few minutes. We combine the anti-*z*-COSY experiment with an affine transformation[254 255 256 257]. This enables the remapping of the data to allow narrow spectral widths to be acquired in the indirect dimension. This approach speeds up the acquisition times of the anti-*z*-COSY experiment by a factor of 15 or more, while maintaining here peaks up to a factor 2.3 narrower than in the conventional one-pulse one-dimensional experiment at the same MAS rate.

3.3.2 Methods

3.3.2.1 Modification of the anti-z-COSY pulse sequence

As described in detail previously,[213 247-248] the anti-*z*-COSY pulse sequence consists of an initial excitation 90° pulse followed by an evolution period t_1 and a mixing element of the form, 180°+β — τ_z — β, where β denotes a small flip angle, as shown in Figure 3.14 (a). The sequence of Figure 3.14 (b) is modified in order to maintain the criteria needed for the application of the affine transformation and to allow whole echo acquisition in t_1. [258 259-261] The affine transformation which consists in a series of shearing transformations will allow under-sampled spectra in t_1 to inherit the spectral properties in t_2 after transformation. This was first used in NMR in the context of Two-dimensional One Pulse (TOP) experiments. [262] In the experiment of Figure 3.14 (b), the 180° pulse and the low flip angle *z*-filter, β - τ_z - β, are placed in the middle of the evolution period, t_1. At this position this element allows the pure chemical shift evolution to be sampled in the indirect dimension independently of the effects of homonuclear coupling.

In the experiment of Figure 3.14 (b), the 180° pulse and the low flip angle *z*-filter, β - τ_z - β, are placed in the middle of the evolution period, t_1. At this position this element allows the pure chemical shift evolution to be sampled in the indirect dimension independently of the effects of homonuclear coupling. In analogy with approaches to pure shift spectroscopy in solution NMR,[263] the small flip angle building block together with the 180° pulse thus only yields correlations between remote transitions since any splittings caused by homonuclear coupling to other spins are suppressed through the inversion of the spin state of their coupling partners by the 180° pulse.

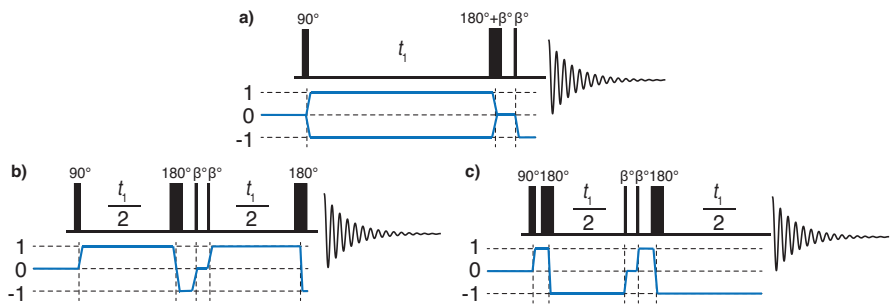

Figure 3.14 (a) Anti-*z*-COSY pulse sequence and coherence pathway. (b,c) TAZ-COSY pulse sequence and coherence-transfer pathways for the acquisition of (a) the echo and (b) the anti-echo part of the signal. Here, β indicates a low-flip-angle pulse.

As illustrated in Figure 3.15 (a), the time domain of this experiment consists in pure chemical shifts along t_1 and the sum of shifts and residual couplings in t_2. Compared to the anti-*z*-COSY experiment, the shape of the diagonal peaks is no longer perpendicular to the diagonal of the spectrum but is now parallel to the direct dimension. A further modification lies in the 2D scheme used for the acquisition of the two-dimensional absorptive phase-sensitive spectrum. For the parent anti-*z*-COSY experiment a States-TPPI hypercomplex acquisition [264] is typically used, for which two different data sets with quadrature phases for the initial excitation pulse are acquired.

In the TAZ-COSY sequence, pure absorption mode lineshapes can be achieved simply by collecting the first half of the indirect increments with the sequence shown in Figure 3.14 (b), that records a positive sense of evolution for the chemical shift interaction, and the second half with the sequence shown in Figure 3.14 (c), that records respectively a negative sense of evolution. This leads to whole echo acquisition in t_1,[258 259 260 261] and upon 2D Fourier transformation, absorption mode data are acquired without the necessity of an additional *z*-filter at the end of the sequence scheme.

3.3.2.1 Data processing: shearing and symmetrization

This data structure allows the affine transformation to be applied in a similar way as in the 2D TOP-PASS experiment described by Davis et. al., [255] since the dataset as acquired separates the chemical shift evolution, which evolves along t_1 from the evolution due to homonuclear couplings, which proceeds along the negative diagonal, $\varepsilon = -t_1 / t_2$. This is illustrated in Figure 3.15 (a). The affine transformation remaps the data such that the two interactions, chemical shift and homonuclear couplings, lie along the horizontal and vertical axis respectively while simultaneously inheriting the sampling properties of the axis onto which they are transformed. [255] Through this approach, it is possible to record data that are heavily under-sampled in the indirect dimension. This allows us to reduce the spectral width and number of increments in the indirect dimension, since it will only contain the residual dipolar broadening in the final spectrum. As a result, the peaks will be folded along t_1 in the raw spectrum, and the affine transformation here consists in applying two sequential active shearing transformations as shown in Figure 3.15 (b-e):

$$\begin{bmatrix} t_1' \\ t_2' \end{bmatrix} = \underbrace{\begin{bmatrix} 1 & 0 \\ -1 & 1 \end{bmatrix}}_{\kappa_2} \underbrace{\begin{bmatrix} 1 & +1 \\ 0 & 1 \end{bmatrix}}_{\kappa_1} \begin{bmatrix} t_1 \\ t_2 \end{bmatrix} \qquad (3.9)$$

The scheme presented allows us to reduce the experimental time here by a factor of 16.5. Note that a similar shearing based approach was used in the initial anti-*z*-COSY article.

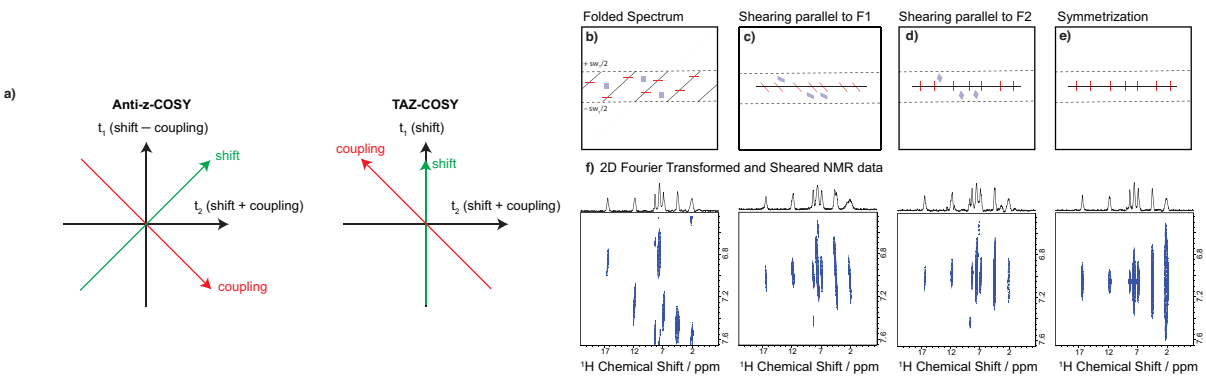

Figure 3.15 (a) Representation of the time-domain data structure for an anti-*z*-COSY and a TAZ-COSY experiment. (b) Schematic representation of a folded spectrum between the $+sw_1/2$ and $-sw_1/2$ limits, where diagonal peaks are represented as solid red lines and cross peaks as blue boxes. (c) First shear parallel to F1 with a shearing rate of -1. (d) Second shear parallel to F2 with a shearing rate of +1. (e) Symmetrization of the spectrum shown in (d). (f) Exemplification of the shearing process and of the symmetrization with NMR data acquired with the sequences shown in Figure 3.14 (b) and (c) for L-Histidine monohydrochloride monohydrate. The processing scripts used here are provided in the Appendix III

As shown in Figure 3.15 (b), when the spectral width of the indirect dimension is reduced, the diagonal folds into parallel sections, which remain tilted at a 45˚ with respect to both of the axes of the 2D plot. The diagonal peak shapes all remain parallel to the direct axis. In the frequency domain the first shear, which is parallel to F1 and has a shearing factor of -1, leads to the spectrum shown in Figure 3.15 (c). Any sections that ended up outside the original spectral window during the first shearing process have been wrapped back inside. Finally, in Figure 3.15 (d), the second shear, which is parallel to the F2 dimension and has a shearing factor of +1, aligns the multiplets to be parallel to F1. At this point a sum projection about the cross section F1 = 0 can be taken and the extracted 1D spectrum is free from any broadening due to homonuclear couplings. Folding of the spectrum does not affect the diagonal peaks in the final spectrum, since in the 2D double-sheared spectrum they will be symmetrically distributed about the cross section and centered at F1=0. However, as shown in Figure 3.15 (d), this will not be the case for the cross peaks, or anything else that is not a diagonal peak. (Weak cross peaks are sometimes observed in anti-z-COSY spectra of solids, as discussed in reference).[213] In most cases, they will be folded/wrapped in positions that are no longer symmetric with respect to their partners. We can therefore exploit this characteristic to remove them from the final 2D spectrum by applying a symmetrization procedure perpendicular to ω_2. This will remove all the cross peaks, unless by chance they have folded in symmetrical positions. In cases where their final position in the doubly-sheared spectrum coincides with a diagonal peak, symmetrization can perturb the intensity of the diagonal peak.

(Note that the approach described above can be also applied for the acquisition of homonuclear *J* decoupled proton spectra in the liquid state. A sequence and some examples can be found in the Appendix III.)

3.3.3 Results and Discussion

Figure 3.16 shows the linewidths achieved with the pulse sequences of Figure 3.14 (b) and (c) and the processing described in Figure 3.15 for a powdered sample of L-Histidine monohydrochloride monohydrate, acquired at 298 K and with a 100 kHz MAS rate. The pulse flip angles β tested range from 90° to 5°, and the bar chart of Figure 3.16 (f) clearly shows the expected dependence of the ^{1}H homonuclear decoupling efficiency on the β angle. At β = 5° we measured linewidths of 269, 164, 174, 189, 163, and 214 Hz for protons H1, H5, H6, H7, H8, and H9 respectively as compared to 563, 380, 346, 408, 376, and 682 Hz in the 1D spectrum acquired with the conventional spin-echo experiment. The spectra were acquired with a highly reduced spectral window in F1, specifically a width of 2000 Hz was used and only 16 increments were acquired in the indirect dimension. As a result, the amount of experimental time needed to acquire the spectrum was reduced by a factor 8.25 compared to a conventional full anti-z-COSY spectrum. The span of the integral projection was taken according to the width of the narrowest peak in ω_1.

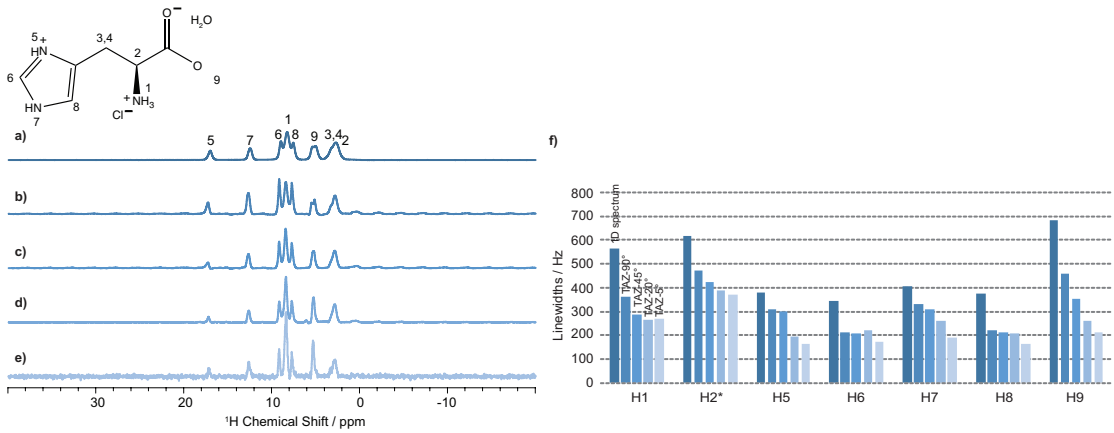

Figure 3.16 (a) Echo-detected 100 kHz MAS spectrum of powdered microcrystalline L-Histidine monohydrochloride monohydrate. (b-e) Spectra obtained from integral projections of the TAZ-COSY spectrum acquired at 100 kHz MAS, with β angle of 90°, 45°, 20°, and 5°. (f) Measured linewidths of the spin-echo experiment and of the TAZ-COSY projections as a function of β. The asterisks on H2 denotes overlapping resonance peaks. See Appendix III for full details.

In Figure 3.17 the spectra measured with the new TAZ-COSY sequence and the previously reported anti-*z*-COSY sequence (with a full spectral width in the indirect dimension) are compared. The comparison was performed for two different MAS spinning rates, at 50 and at 100 kHz. The 50 kHz MAS data were recorded with an indirect spectral width of 16.6 kHz, with 128 increments, 16 scans and a recycle delay of 5 s for the unfolded full anti-*z*-COSY spectrum, and with an indirect spectral width of 1.0 kHz, 16 increments, 16 scans and a recycle delay of 5 s for the TAZ-COSY spectrum. The 100 kHz MAS data were recorded with an indirect spectral width of 16.6 kHz, 122 increments, 32 scans and a recycle delay of 5 s for the unfolded full anti-*z*-COSY spectrum and with an indirect spectral width of 1.0 kHz, 8 increments, 32 scans and a recycle delay of 5 s for the TAZ-COSY spectrum.

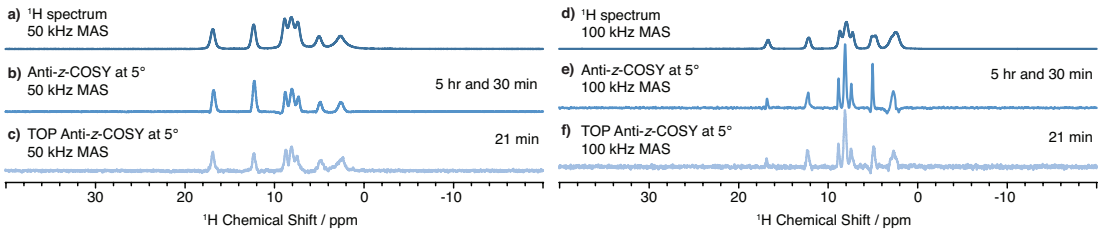

Figure 3.17 (a) and (d) echo-detected 50 and 100 kHz MAS spectra of powdered microcrystalline L-Histidine monohydrochloride monohydrate. (b) and (e) 1D spectra obtained as integral projections of an anti-z-COSY spectrum acquired with a full spectral with in the indirect dimension and with a β of 5°. (c) and (f) 1D spectra obtained as integral projections from a TAZ-COSY spectrum acquired with an indirect spectral width of 1000 Hz and with a β of 5°. See Appendix III for full details.

In both cases, the spectra extracted from the data acquired with either a full or a folded indirect spectral width look essentially identical. The resolution enhancement obtained from anti-z-COSY is fully preserved in the TAZ-COSY spectrum. (Table 3.20 provides a numerical comparison of the measured linewidths for each peak in the spectrum.) The key difference lies in the experimental time. With the TAZ-COSY we can acquire a high-resolution spectrum in only twenty minutes, which is 16.5 times faster than the full anti-z-COSY which took nearly 6 hours. We note that the water and aliphatic resonances in Fig. 3.17 (e) and (f) show minor lineshape distortions that we have previously seen in the anti-z-COSY experiments and which we attribute to strong coupling effects. [213]

Practical aspects concerning the set-up of a TAZ-COSY experiment include the selection of the correct indirect spectral width and the correct number of points to be recorded in the indirect dimension. The spectral width in t_1 should be wide enough in order to fit the untruncated residual dipolar broadening. In most cases a spectral width between 500 and 2000 Hz should suffice. The number of increments should be sufficient to yield a t_{1max} that avoids truncation of the residual dipolar broadening. Depending on the choice of indirect spectral width, a number of t_1 increments between 4 and 16 should be appropriate. Finally, it should be noted that a reduced signal to noise ratio is obtained in the rapid TAZ-COSY projections, as compared to the full anti-*z*-COSY projections, which simply due to the reduced time-averaging. The signal to noise ratio per unit time should be equivalent (more details can be found in Table 3.21).

3.3.4 Conclusion

In summary, we have introduced a modified anti-*z*-COSY sequence that is compatible with the TOP transform and whole echo acquisition and which here results in a factor of 16.5 reduction in the experimental time required to obtain ^{1}H remote correlation spectra in solids. We use the resulting TAZ-COSY sequence to obtain spectra from powdered microcrystalline L-Histidine monohydrochloride monohydrate at both 50 and 100 kHz MAS rates, where we confirm that the method provides the highest ^{1}H resolution available today in ^{1}H MAS NMR of solids. We have also shown the application of this methodology to liquid-state data with a suitably adapted sequence.

3.3.5 Appendix III

3.3.5.1 Experimental details

Room temperature solid-state NMR experiments were performed at room temperature on an 18.8 T Bruker Avance Neo spectrometer equipped with a 0.7 mm triple resonance HCN CP-MAS probe and on a 21.15 T Bruker Avance Neo spectrometer equipped with a 1.3 mm triple resonance HCN CP-MAS probe. Data where acquired on a powdered sample of L-histidine monohydrochloride monohydrate purchased from Signal-Aldrich and used without further recrystallization, after mild crushing with a mortar and a pestle.

Table 3.17 Experimental parameters of the spectra displayed in Figure 3.16.

Pulse Sequence	**TAZ**	**1D-Echo**
Recycle delay (s)	5	2
MAS rate (kHz)	100	100
Acquisition length (ms)	20.5	10.25
Number of t2 points	4096	2048
1H 90° pulse (µs)	0.865	0.865
1H pulse power (W)	48.52	48.52
z-filter delay (µs)	10	-
F1 spectral width (Hz)	2000	-
F2 spectral width (Hz)	100000	100000
Number of t1 increments	16	-
Cnst4 (sets pch1 in F1)	2521	-
β angle* (cnst2)	90°,45°,20°,5°	-

* 8 scans were acquired for the 90°, 45°, and 20° experiments, and 32 scans for the 5° experiment.

** 4 scans were acquired for the echo-detected experiment

*** All data were acquired with pre-saturation on the ^{1}H channel (33 loops with an inter-pulse delay of 1.1 ms)

Table 3.18 Experimental parameters of the spectra displayed in Figure 3.17.

Pulse Sequence	**TAZ-5°**	**Antiz-5°**	**1D-Echo**	**TAZ-5°**	**Antiz-5°**	**1D-Echo**
Recycle delay (s)	5	5	5	5	5	10
MAS rate (kHz)	100	100	100	50	50	50
Acquisition length (ms)	20.5	20.5	10.25	20.5	20.5	22.7
Number of t2 points	4096	4096	2048	4096	4096	4544
1H 90° pulse (µs)	0.865	0.865	0.865	2.2	2.2	2.2
1H pulse power (W)	48.52	48.52	48.52	48.52	48.52	48.52
z-filter delay (µs)	10	10	-	20	20	-
F1 spectral width (Hz)	1000	16666	-	1000	16666	-
F2 spectral width (kHz)	100	100	100	100	100	100
Number of t1 increments	8	122	-	16	128	-
Cnst4 (sets pch1 in F1)	1080	-	-	2520	-	-
β angle (cnst2)	5°	5°	-	5°	5°	-
Number of scans	32	32	4	16	16	

* All data were acquired with pre-saturation on the ^{1}H channel (33 loops with an inter-pulse delay of 1.1 ms)

3.3.5.2 Linewidth Measurements

Table 3.19 Measured linewidths (in Hz) of proton peaks in Figure 3.16.

Proton / β pulse	90°	45°	10°	5°	1D-Echo
H1	364	287	266	269	563
H2*	474	425	389	369	616
H3,4*	-	-	-	-	-
H5	308	301	196	164	380
H6	211	208	220	174	346
H7	330	311	263	189	408
H8	223	214	209	163	376
H9	461	355	259	214	682

* The asterisks indicate overlapping resonance peaks.

Table 3.20 Measured linewidths (in Hz) of proton peaks in Figure 3.17.

Proton / β pulse	TAZ-5° 100kHz	Antiz-5° 100kHz	1D-Echo 100 kHz	TAZ-8° 50 kHz	Antiz-8° 50 kHz	1D-Echo 50 kHz
H1	252	211	563	456	458	753
H2*	333	348	616	593	546	1042
H3,4*	-	-	-	-	-	-
H5	125	141	380	320	367	507
H6	152	136	346	332	321	544
H7	252	244	408	335	356	485
H8	213	158	376	375	368	547
H9	246	127	682	574	414	664

3.3.5.3 Processing

All data we processed using TopSpin 4.0.6 using the following protocol:

1. Set PHC1 in F1 equal to ***cnst4*** calculated by the sequence. (The whole-echo acquisition shifts the signal maximum in t_1, and therefore a first order phase correction in the indirect dimension is needed.)
2. Perform double FT (XFB command in topspin) and correct the zero-order phase in the direct dimension.
3. Apply the au program: shearing_taz
4. Apply the au program: ajp_sym
5. Extract a sum projection of rows with the command “proj”

3.3.5.4 Liquid-State pulse sequence and example

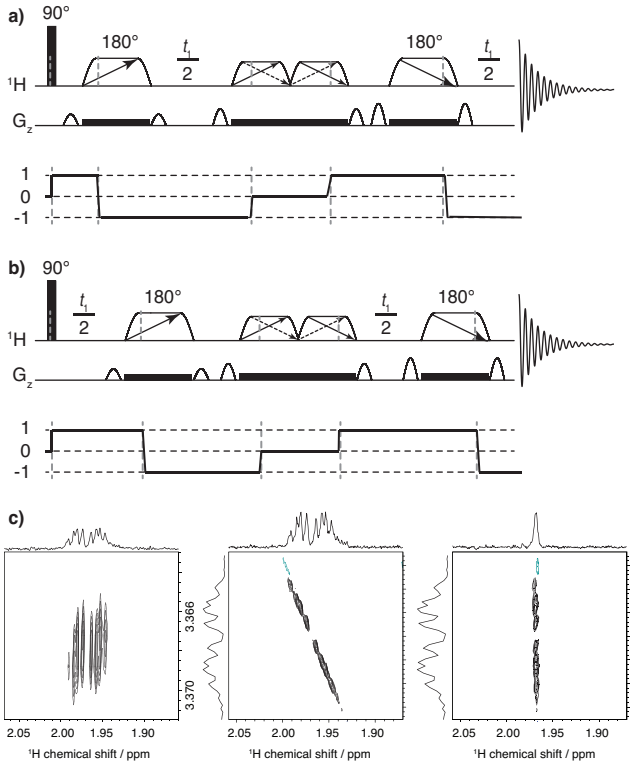

Figure 3.18 Pulse sequence and coherence transfer pathway for TOP-TSE-PSYCHE, to acquire (a) the echo and (b) the anti-echo pathway. Narrow rectangles are hard 90° pulses, trapezoids with single arrows denote unidirectional chirp pulses and trapezoids with double arrows are low-power saltire chirp pulses of flip angle β. Half sine shapes indicate coherence transfer pathway gradient pulses, whereas all rectangular gradient pulses are weak and are applied during the frequency swept pulses. (c) Affine transformation performed as two consecutive active shear transformations is depicted in 2D Fourier transformed liquid-state NMR data.

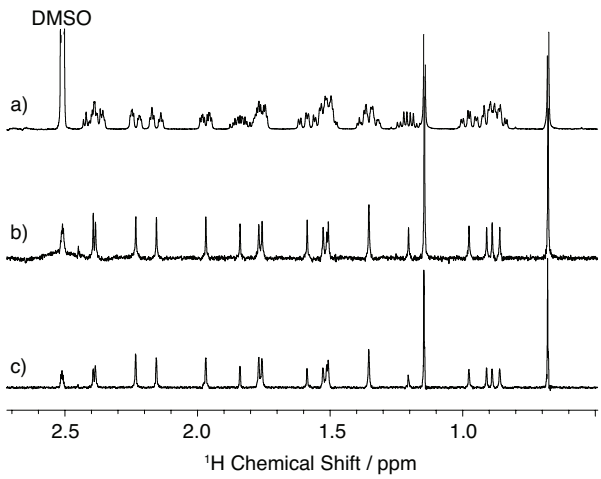

Figure 3.19 (a) Proton liquid-state NMR spectrum of testosterone in DMSO-d_6 (b) TSE-PSYCHE[265] and (c) TOP-TSE-PSYCHE spectra acquired with an indirect spectral width of 100 Hz, 82 chunks/increments, 2 scans, β angle of 20°, and 2 s recycle delay.

3.4 Conclusion and Perspectives

In conclusion, two new pulse sequences based on a previous liquid-state experiment designed for homonuclear J decoupling[247-248] were presented to further improve the homonuclear dipolar coupling in the context of rotating solids. After acquisition, the obtained 2D generates correlations between remote transitions. After applying a shearing process, the 45° projection is extracted and the resolution can be up to a factor of two narrower than the conventional 1D spectrum. These methods were tested on four different organic solids.

The resolution improves with smaller flip angle pulse, but the gain in the resolution is at the expense of reduced sensitivity. Due to the necessity of high resolution acquisition of the indirect dimension for the anti-z COSY sequence, the TAZ COSY experiment combines a modified pulse sequence of the anti-z with the TOP[262] transformation. The same level of resolution is obtained but with a greatly reduced experimental time.

These results presented the highest resolution in ^{1}H spectrum of organic solids at the time. In contrast to CRAMPS, the anti-z COSY is applicable at faster MAS rates (> 65 kHz). The residual coupling removed in this experiment is supported by theory and simulation (See **Chapter 2**).

However, the residual shift term is still present, therefore there is still room for improvement and development of methods that are able to remove all second and third order terms caused by homonuclear dipolar coupling.

All these terms being scaled by the spinning rate, the future availability of faster MAS rates will eventually reduce their contribution to a very small percentage on the lineshape.

In the meantime, one way to expand the utility of anti-z COSY would be to insert it in higher order experiments where ^{1}H resolution is needed, for instance homonuclear or heteronuclear correlation experiments.

Alternatively, the path to follow is to develop other experiments that could remove all source of homogeneous broadening in the ^{1}H spectrum. The following chapter describes a few attempts on that strategy.

Chapter 4 Improved ^{1}H resolution exploiting error mapping

4.1 Introduction

The present chapter presents an alternative strategy on the quest for higher resolution, which is different from the approaches described in the previous sections. This chapter presents a strategy to extract the pure isotropic spectrum, free of any homogeneous broadening, by measuring the spectrum as a function of the MAS rate and parametrizing out the residual broadening. The previous strategies aim to remove as much broadening as possible in. a single experiment, such as the anti-z COSY experiment. However, the anti-z COSY experiment only removes part of the higher order terms (the coupling-like terms) from the average Hamiltonian, whereas Chapter 2 showed that in the average Hamiltonian for three spins still produce both residual shift and splitting and currently there is no single experiment that is able to remove both residual homogeneous shift and splitting. Therefore, the optimal method should be able to remove all residual homogeneous sources of broadening, leaving only the first order terms, *i.e*. the isotropic chemical shifts.

All the higher order terms are scaled by the MAS rate, therefore the corresponding residual homogeneous broadening in the ^{1}H spectrum has a precise MAS rate dependence which is dependent on the strength of spin interactions (chemical shift and homonuclear dipolar coupling). The parametrization of the residual broadening is the foundation of the approach in the next sections. The whole strategy is based on mapping the residual broadening and the isotropic shift interaction in a 2D grid.

The development of this mapping strategy has produced three outcomes with a different focus and perspective on the ^{1}H resolution improvement goal.

In **Chapter 4.2**, the parametric mapping approach is explained to show how the isotropic spectrum can be retrieved from variable MAS data. Experimentally, a series of MAS spectra at increasing spinning rates are recorded and mapped into the 2D grid. The model to describe the general ^{1}H lineshape is defined by the isotropic amplitudes and the linearly MAS dependent broadening and shift parameters. By fitting the experimental MAS spectra series to these parameters, the isotropic spectrum (as well as the broadening and shift terms) is obtained for six organic solids, with a resolution improvement factor of up to 20.

In **Chapter 4.3,** a deep learning approach to extract the isotropic spectrum from the same k-space is described. Deep learning overcomes the assumptions and restrictions inherent to a fitting approach and provides an enhanced performance on the same experimental data as shown in **4.2.** The architecture of the neural network is described and the results present the narrowest ^{1}H resolution to date.

In **Chapter 4.4,** the deep learning approach is extended to 2D ^{1}H-^{1}H correlation experiments, which can also greatly benefit from improved resolution. Again, experimental 2D spectra are recorded as a function of spinning rate, before applying the neural network to obtain the isotropic spectrum. The method is demonstrated on two different samples, on both DQ/SQ and spin-diffusion experiments. Narrower linewidths are obtained in both dimensions, and the pure isotropic 2D dimensional spectrum is obtained.

4.2 Pure Isotropic Proton Solid State NMR (PIP)

This chapter has been adapted with permission from: Moutzouri, P.; Simões de Almeida, B.; Torodii, D.; Emsley, L., Pure Isotropic Proton Solid State NMR. *J Am Chem Soc* **2021,** *143* (26), 9834-9841. (post-print).

My contribution was to be part of the development and application of the method, acquisition of the data, and results analysis. I was part of the writing, review and editing process of the manuscript.

4.2.1 Introduction

The alternative approach of pure isotropic proton (PIP) strategies consists of putting aside any attempts to design a single experiment with a coherent averaging scheme, and instead parametrically mapping the broadening in such a way they can be removed in a multi-dimensional correlation experiment. A series of MAS spectra recorded at different spinning rates can be mapped (at least in an abstract sense) into *k*-space by a comparison of the expected parametric behaviour of the intrinsic pure isotropic shift terms to the parametric behaviour of the residual broadening terms according to the predictions of Average Hamiltonian Theory. By mapping the spectra in *k*-space in this way we should then be able to extract the pure isotropic signal.

We illustrate the approach on a series of organic solids where the model we use produces pure isotropic spectra that are significantly narrower than the fastest MAS spectrum we can record (100 kHz). In most cases the isotropic spectra extracted from a series of up to 40 MAS spectra recorded at rates between 20 and 100 kHz are typically a factor of 7 narrower than those observed in the 100 kHz MAS spectra.

4.2.2 Methods

4.2.2.1 Theory

Any NMR spectrum can always be represented in a one- or multi-dimensional reciprocal space, usually referred to as *k*-space. Indeed, most NMR experiments are today actually recorded in time domain, and the frequency domain spectrum is obtained by Fourier transformation.

$$S(\omega_x, \omega_y) = \int\int_{-\infty}^{\infty} s(k_x, k_y)\, e^{-ik_x\omega_x} e^{-ik_y\omega_y} dk_x dk_y \qquad (4.1)$$

where for example $k_x = t_2$ and $k_y = t_1$.

In two-dimensional NMR spectroscopy experiments, there are usually two time periods that are independently sampled, and which are represented as two orthogonal directions in *k*-space. They are usually sampled on a cartesian grid, and methods have been developed to sample the whole of *k*-space[264] as shown schematically in Figure 4.1 (a).

More generally, the *k*-vector can contain other terms, for example in magnetic resonance imaging experiments, where for example $k_x = G_x t_x$ with G_x being the amplitude of the field gradient applied along the *X* direction and t_x being the length of gradient pulse. By varying either *t* or the gradient directions, other sampling schemes can be developed, for example the radial sampling scheme shown in Figure 4.1 (b). This kind of approach has led to single-shot 2D J-experiments in solution,[266] experiments that correlate isotropic shifts with chemical shift anisotropies in solids,[267] two-dimensional one pulse (TOP) experiments in solids,[262] or even to the single shot multi-dimensional encoding schemes used in solution.[268]

Here we suggest a potential *k*-space representation where one axis (e.g. k_y), corresponds to the evolution of the desired pure interaction in a coherent averaging experiment, and the other axis (or axes) (e.g. k_x) corresponds to the evolution of the error terms, where the definition of an error term includes any errors generated by the imperfect coherent averaging of MAS. Errors generated from other sources, such as poor shimming or RF inhomogeneities, will probably translate into broader isotropic distributions. If the effective Hamiltonian is time-

independent, a given FID would then lie along a straight line in this two-dimensional *k*-space, at an angle φ to k_y, where φ depends on the scaling factor of the error terms.

$$S(\omega_{error}, \omega_{pure}) = \int\int_{-\infty}^{\infty} s(k_x, k_y)\, e^{-ik_x\omega_{error}} e^{-ik_y\omega_{pure}} dk_x dk_y \qquad (4.2)$$

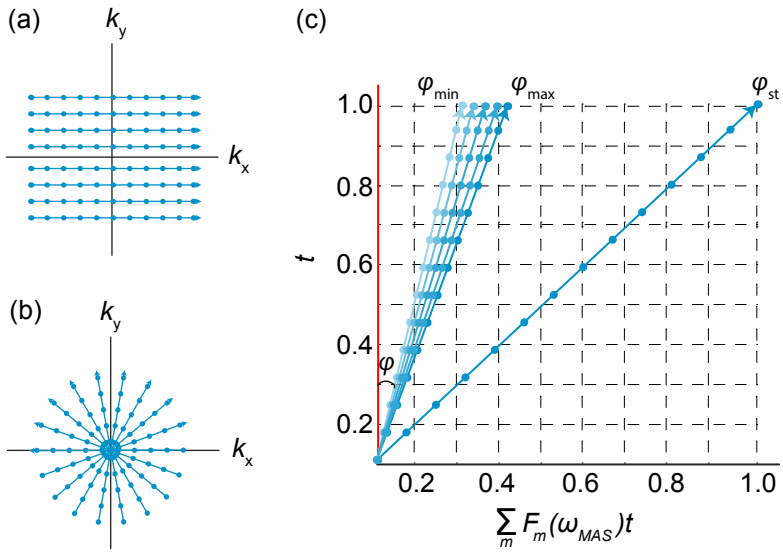

Figure 4.1 General approaches to mapping time-domain NMR data in *k*-space for Cartesian (a) and radial (b) sampling schemes. Lines represent individual FIDs, and dots show sampling points. (c) Schematic representation of a series of NMR data acquired at different MAS rates in a *k*-space where $k_x = \sum_m F_m(\omega_{MAS})t$ and $k_y = t$. The angles ϕ_{max} and ϕ_{min} indicate the maximum and minimum angle between the acquired FID and the pure shift term axis, k_y. The FID at $\varphi_{st} = 45°$ corresponds to a static sample. As the MAS rate increases, φ decreases. A pure isotropic FID lies along the vertical axes, shown in red.

To illustrate this, consider a set of ^{1}H MAS spectra acquired at different magic angle spinning rates ω_{MAS}. The average Hamiltonian for the system at any given spinning rate can be simplified to:

$$\bar{H}_{mas}(\omega_{MAS}) = H_{iso} + \sum_m F_m(\omega_{MAS})\ \bar{H}_{error,m} \qquad (4.3)$$

where H_{iso} and $\bar{H}_{error,m}$ are the Hamiltonians describing the pure isotropic shift and the error terms respectively, and the F_m are MAS rate dependent pre-factors. In an approximation where this Hamiltonian were to be secular, then the reciprocal space of Eq. 4.2 can be directly given using:

$$k_x = \sum_m F_m(\omega_{MAS})t \text{ and } k_y = t \qquad (4.4)$$

The FIDs would then be distributed in this *k*-space as shown schematically in Figure 4.1 (c), with angles varying from φ_{min} for the fastest MAS rate, to φ_{max} for the slowest MAS rate. The angle φ is given by the ratio between the pre-factor of the error terms (including residual couplings and shifts, due to imperfect averaging of dipolar couplings and chemical shift anisotropies that are responsible for the broadening in the spectra),[103 106, 108, 221, 249] and the pure isotropic terms (isotropic chemical shifts). For a static sample $\varphi_{st} = 45°$ since $\sum_m F_m(\omega_{MAS}) = 1$. As the spinning speed is increased φ will decrease, since the error terms will be progressively reduced while the isotropic term is constant. Most importantly, we can, by definition, never actually acquire an experiment with $\varphi = 0°$, which would require $\omega_{MAS} = \infty$.

In this case, the angles should be available from the parametric dependence of the error terms on the spinning rate from theory. According to Average Hamiltonian Theory (AHT), in the fast-spinning regime for a three-spin dipolar coupled system up to third order, only the pure isotropic chemical shift terms lack any MAS dependence, whereas the rest of the terms describing the system have a dependence of the following sort:[233 103 105-106, 108-109, 111-113, 234, 249]

$$\bar{H}_{mas}(\omega_{MAS}) = H_{iso} + \sum_{m=1}^{2} \frac{1}{\omega_{MAS}^{m}} \bar{H}_{error,m} \qquad (4.5)$$

Full expressions of the average Hamiltonian in different cases are given in references 103, 224, 225 and 239. For simplicity, if we assume that $\bar{H}_{error,1} >> \bar{H}_{error,2}$ that the m = 2 term in Eq. 4.5 can be neglected, and neglecting any non-secular correction to the frequencies as a function of MAS, (these assumptions are discussed further below), we can now choose $k_x = \frac{1}{\omega_{MAS}} t$ and the angle φ is then defined as (in the fast-spinning regime):

$$\varphi = tan^{-1}\left(\frac{1}{\omega_{MAS}}\right) \qquad (4.6)$$

We note that at spinning rates of 20 to 100 kHz, and with the spinning rate expressed in Hz, this yields angles of 0.00045° to 0.000092°. These apparently very small angles highlight the fact that fast MAS spinning spectra are "nearly isotropic," with linewidths of 200-300 Hz, compared to about 20 kHz linewidths in the static spectrum. However, this does not change the fact that the missing fraction of a degree cannot be neglected as it encodes all the residual broadening.

Because the *k*-space cannot be completely sampled (if we could sample along k_y, there would be no need for this strategy), data processing is not as straightforward as a simple 2D FT as normally applied in NMR. There has been intense research into transforming incomplete and non-uniformly sampled data, in particular because of the importance of MRI and CT scanning, where this is often the case, but also in high-resolution NMR applications, where reducing acquisition times is important.[269-273] We also note that corrections to the frequencies due to non-secular terms in Eq. (4.5) will make ω_{error} dependent on k_x, which will introduce an error in the mapping (though this will be small in the fast MAS regime). It is possible that higher order expansions of the k-space could be used to take this into account.

There are probably many ways to approach the detailed mapping and transformation of the data to obtain the pure isotropic spectrum, and we expect this to be the subject of detailed future study. Here we demonstrate the method with a parametric fitting approach informed by Average Hamiltonian Theory. [233 103 105-106, 108-109, 111-113, 234, 249]

4.2.2.2 Model

So far, we have made no assumptions about the nature of the spectra. Since we cannot yet see a way to simply map the data into the conceptual *k*-space described above, nor to do the data transformation on the truncated data set, in the following we will use a model in which we make no assumptions about the shape of the isotropic spectrum, but we will assume that in MAS spectra of powders the error terms lead to a MAS rate dependent broadening, with a shape that is a sum of Gaussian and Lorentzian components, and that they also lead to a MAS rate dependent shift in the peak positions. These properties are all predicted by average Hamiltonian analysis and numerical simulations.[103-109, 111-113, 219, 234, 249, 274]. This leads to the following model:

$$S(\omega_{MAS}) = \sum_{1}^{n} \int A_n e^{i\omega_{n,iso}t} e^{i\omega_{shift}t} e^{-\lambda_G t^2} e^{-\lambda_L t}\, dt \qquad (4.7)$$

with

$$\lambda_{G,L} = \frac{\gamma_{G,L}}{\omega_{MAS}} \tag{4.8}$$

and

$$\omega_{shift} = \frac{\gamma_{shift}}{\omega_{MAS}} \tag{4.9}$$

where S is the frequency-domain signal of each MAS spectrum, n is the number of points in the spectrum and where the $\omega_{n,iso}$ is the isotropic frequency of the nth point,

$$\omega_{n,iso} = \frac{n\,\Delta\omega}{N} \tag{4.10}$$

where $\Delta\omega$ is the spectral width and N is the total number of points in the spectrum, and $\gamma_{G,L}$ are the widths of the Gaussian and Lorentzian broadening. γ_{shift} defines a MAS dependent shift from the isotropic position.

A corresponds to the vector of amplitudes of the pure isotropic spectrum. The model is summarized schematically in Figure 4.2 (a).

In order to extract the pure isotropic spectrum ***A***, we can fit the set of MAS spectra acquired at different spinning speeds (that we refer to as VS data) to [A_n], the two broadening parameters and the shift. This is demonstrated in Figure 4.2 (b) with a synthetic VS dataset generated by convolution of the arbitrary isotropic spectrum shown in red in Figure 4.2 (a) with the broadening function shown in orange. Here we fit 128 points for the spectral amplitudes [A_n], and the process extracts the pure isotropic spectrum shown in Figure 4.2 (b), which accurately reproduces the original input function shown in Figure 4.2 (a).

It should be noted that there is no assumption made about the nature of the isotropic profile, neither in terms of isotropic peak positions, the number of isotropic shifts, or the intrinsic distributions or lineshapes. In principle ***A*** can have any shape, and the example in Figure 4.2 includes narrow and broad, Gaussian, triangular and square isotropic distributions as examples. Some other examples of distributions are shown in Figures 4.10-4.12.

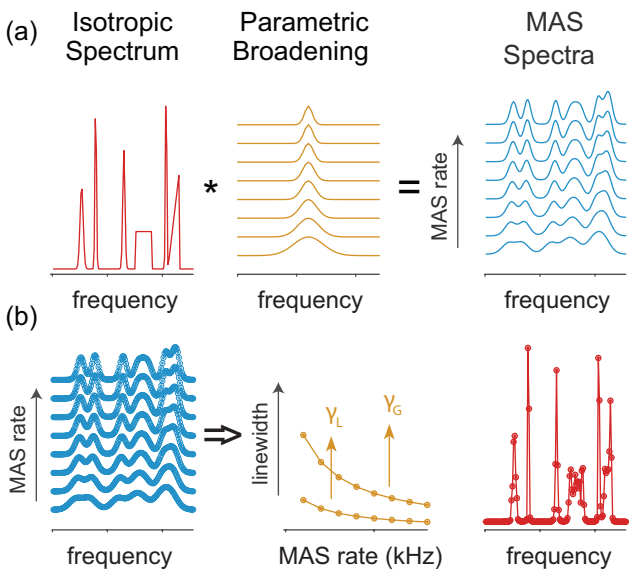

Figure 4.2 (a) Schematic representation of the model described in Eq.s 4.7-4.10 according to which each MAS spectrum (blue) can be described by the convolution of a constant pure isotropic spectrum (red) with a MAS rate dependent broadening function (orange) (b) Performance of the model in fitting synthetic VS data, where the pure isotropic spectrum shown in red on the right is obtained, together with the broadening factors γ_G, and γ_L, that lead to the linewidths shown in orange. The shift factor, γ_{shift}, is also extracted by the model fitting (not shown).

4.2.3 Results and Discussion

4.2.3.1 Samples and Data Acquisition

This new approach is applied to six different micro-crystalline organic solids: L-tyrosine hydrochloride, β-AspAla, L-histidine hydrochloride monohydrate, thymol, flutamide, and ampicillin (Figure 4.3). The ^{1}H MAS spectra recorded at 100 kHz were assigned either according to literature[135 46, 54, 275-277] or by two-dimensional ^{1}H-^{13}C correlation experiments (see Appendix IV for details). For each sample a set of spectra was acquired at MAS rates ranging from 20 to 100 kHz, in steps of 2 kHz, using a Bruker 0.7 mm room temperature HCN CP-MAS probe at a magnetic field of 18.8 T corresponding to a ^{1}H frequency of 800 MHz. The choice of 2 kHz was made in order to balance between experimental time efficiency and a high-density sampling scheme. The magic angle was set for each sample by maximizing the T_2' of the proton signals at the fastest MAS rate, the 90° pulse width was optimized, and the data were acquired with active temperature regulation to maintain the sample temperature at about 295 K across the range of spinning rates and to avoid any spectral changes related to mobile protons or strongly temperature dependent chemical shifts. The thymol data were acquired at a constant VT temperature of 275 K because of its low melting point. A simple one rotor period rotor-synchronised spin echo for background suppression was used for acquisition.

4.2.3.2 Fitting procedure and results

To both reduce the computational requirements associated with multi-parameter fitting of the *N* points in the spectrum, the fitting was done by subregions containing one or more peaks, chosen for each sample according to the proximity and linewidths of the resonances in the fastest MAS spectrum. The subregions each contained between *N* = 27 and 121 points. For each region, a single shift parameter, a single Gaussian and a single Lorentzian broadening are determined together with the pure isotropic spectrum. To avoid any amplitude variations due to experimental imperfections or due to signal losses from centerbands to sidebands at the lowest rates, prior to fitting the spectral regions are inverse Fourier transformed and scaled in order to give spectra with constant integrals after back Fourier transformation.

The fitting of each region was repeated ten times using random starting points for the broadening and shift parameters. The 100 kHz MAS spectrum is used as the initial guess for ***A***, but the same results are obtained with ***A*** = 0 as the starting point (in more time). The χ^2 residual for each fit is calculated as a percentage per point. Typical good fits here yield χ^2 of 1.5-3% per point. (The fits for each of the six samples are shown in Figures 4.13-4.18). Outliers were excluded using the following condition:

$$\chi^2 < \bar{\chi}^2 + 0.25 * \sigma(\chi^2) \qquad (4.11)$$

More details of the fitting process and the MATLAB scripts are given in Appendix IV.

Figure 4.3(a-f) shows the pure isotropic spectra obtained with this process in comparison to the fastest MAS spectrum, acquired at 100 kHz MAS, for each sample.

The resulting pure isotropic spectra are spectacular, with all the spectra showing exceptionally high resolution. Not only do we see narrow resonances for many peaks, but we also clearly resolve peaks where the 100 kHz MAS spectrum is broad.

For all the micro-crystalline samples studied here the narrowing effect leads to linewidths being reduced by factors estimated between 1.2 and 20, with an average of a factor of 7. The narrowest lines in the spectra, seen repeatedly across the samples, are 48 Hz broad. This corresponds to the digital resolution limit here. (Tables 4.8-4.13 gives the full linewidths at half-height for all the observed resonances).

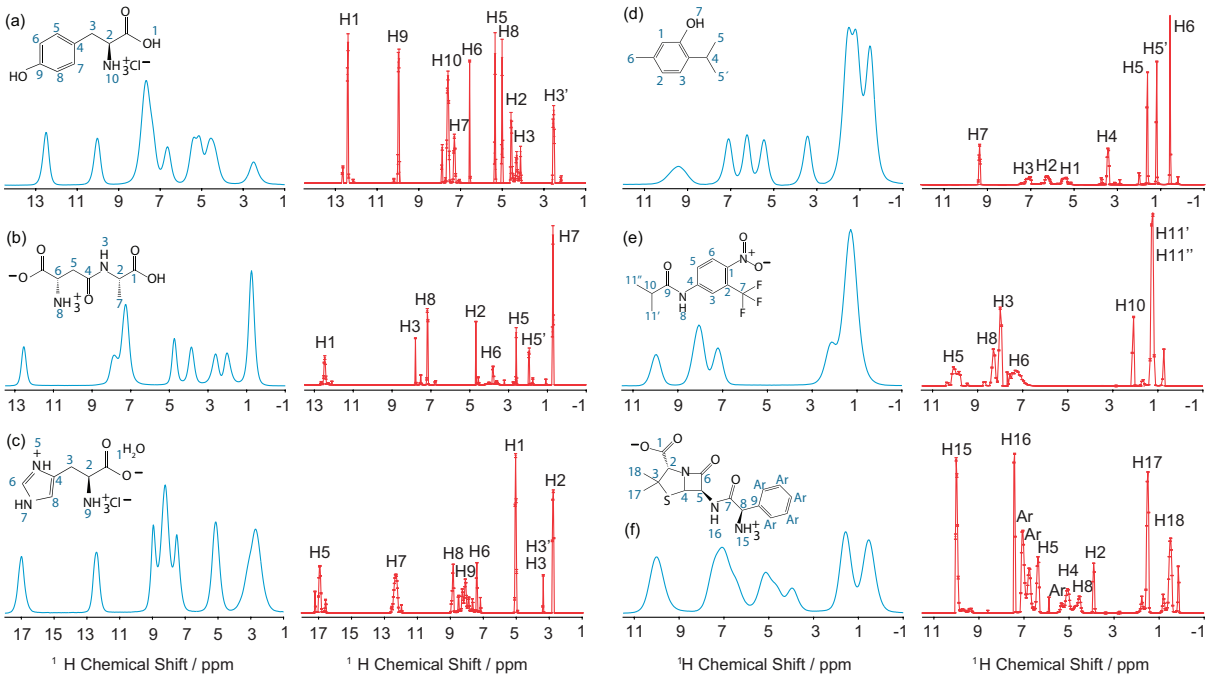

Figure 4.3 100 kHz MAS spectra (blue) and the average pure isotropic proton spectra (red) extracted from VS data using the model of equations 7-10 for powdered samples of (a) L-tyrosine hydrochloride, (b) β-AspAla, (c) L-histidine hydrochloride monohydrate, (d) thymol, (e) flutamide, and (f) ampicillin. The assignments of the spectra are also indicated. Each point is the average of ten fits, and the error-bars correspond to the standard deviation of the ten different fits. Signal referencing was done according to literature.

The resolving power is apparent when we look at, for example, the region of the spectrum of thymol between 0 and 3 ppm, where pure isotropic spectra reveal very clearly the presence of signals from the three methyl groups, H5, H5', and H6. A similar effect is seen for the region between 4 and 6 ppm in the spectrum of L-tyrosine hydrochloride, and perhaps most dramtically in the region between 3 to 8 ppm in the spectrum of ampicillin. All of the resolved peaks in these spectra correspond to the expectations from ^{1}H-^{13}C HETCOR spectra (shown in Appendix IV).

Importantly, that this process is not just fitting the data to narrow lines is apparent when we consider the distribution of lineshapes in some of the pure isotropic spectra. For example, in L-histidine hydrochloride monohydrate the region containing protons H6, H8, and H9 was fit as one section and leads to narrow lines for protons H6 and H8, but to a broader distribution for H9. This may be explained by the fact that H9 belongs to an amino-proton, and the isotropic peak is motionally broadened. A similar effect is seen for the H10 proton in L-tyrosine hydrochloride, which is also in an NH_3^+ group. For flutamide the pure isotropic spectrum shows very narrow lines in the aliphatic region, and relatively broader lines in the aromatic part of the spectrum, which might again reflect some degree of motion or static disorder in the structure. Finally, we have previously noted that the isotropic shifts are not necessarily at the center of gravity of the peaks in the fast-MAS spectrum, since there is a MAS rate dependent shift contained in the error terms. [278] This effect is small but noticeable here for several of the peaks in the pure-isotropic spectra. These shifts are clearly visible in some of the datasets here as shown in Table 4.8. It is important to note that the shifts seen in the experimental spectra might also be due to temperature effects, although we have taken care to try to maintain a constant temperature across all the spinning speeds. We note that the resolution of the narrowest peaks (48 Hz) is limited by the digital resolution we achieve here. The determination of the isotropic profile is computationally demanding, since we are fitting up to 124 independent variables, and fitting a given region from a spectrum with a total of 4k points typically takes ~2 h on a desktop computer using our current unoptimized code. We see that for some peaks the resolution plateaus as the number of points in increased from 1k to 2k to 4k points in the spectrum (e.g. H9 in L-histidine hydrochloride monohydrate), but that for others the resolution continues to increase with the digitization in the fit. A detailed exploration of the limiting resolution will be the subject of further study.

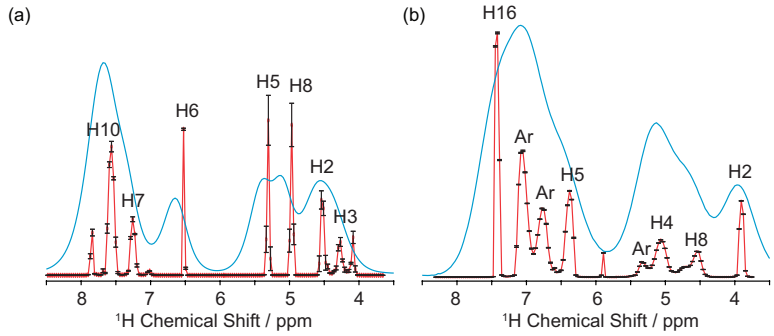

Figure 4.4 Expansions of selected regions of the 100 kHz MAS spectra (blue) and the average pure isotropic proton spectra (red) extracted from VS data for powdered samples of (a) L-tyrosine and (b) ampicillin. The regions between 4 and 9 ppm and 3.5 and 8.5 ppm are shown respectively for the two samples to provide a clearer view of the resolved peaks and of the error-bars that correspond to the standard deviation of the ten different fits, and which indicate the uncertainty of the fit for each point.

Figure 4.4 shows an expansion of the most interesting spectral regions for the samples of L-tyrosine hydrochloride and ampicillin. Notably, the figure allows a clearer view of the highly resolved peaks, but also of the variance in the peak intensities between the ten different fits.

Although it is difficult to assess the fidelity of the chemical shifts in the pure isotropic spectra, since they are unknown and since the peak positions in the 100 kHz MAS spectra are not necessarily at the isotropic chemical shifts, [108 249] Figures 4.5 and 4.6 show the correlation between the proton shifts measured from 100 kHz MAS or HETCOR spectra and the proton shifts from the pure isotropic proton spectra. We see that the correlation has an RMSE of 0.11 ppm with an R^2 of 0.9992.

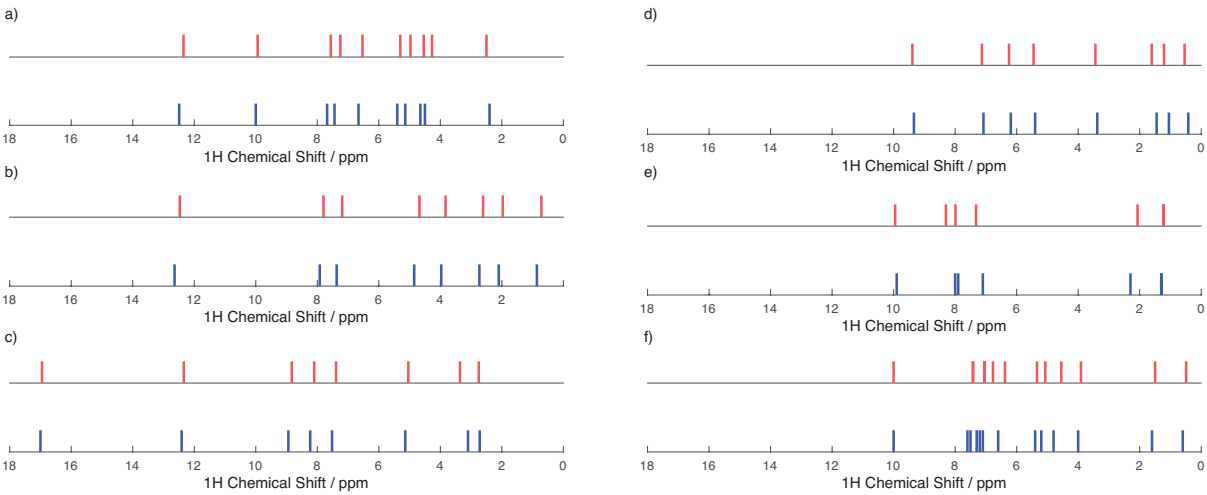

Figure 4.5 Pure isotropic proton shifts (red) and the experimentally measured shifts (blue) at 100 kHz MAS reported in the tables above for samples of (a) L-tyrosine hydrochloride, (b) β-AspAla, 8c) L-histidine hydrochloride monohydrate, (d) thymol, (e) flutamide, and (f) ampicillin. Note that we do not expect the spectra to be completely coincident, because of the MAS dependent frequency shift present in the 100 kHz MAS spectra.

In addition to the expected peaks, there are a small number of minor peaks that are probably artifacts. These are seen at 0.95 ppm in the spectrum of flutamide, 4.1 and 7.9 ppm in the spectrum of L-tyrosine hydrochloride, and in the 0-1 ppm region and at 5.9 ppm in the spectrum of ampicillin. These are most likely caused by the approximations in the model failing slightly to fully explain the data. While broad lines are not unexpected, an alternative explanation for the broader lines discussed above could in some cases also be that the model is failing for these peaks. Notably, if the lineshapes are not fully symmetric, if the MAS dependence of the broadening is not purely $1/\omega_{MAS}$, or if within a given fit region the peak positions shift with different MAS dependencies, all of which might happen according to the prediction of AHT, [108 249] then artifacts might appear. An example of this is shown in Figure 4.33 for an asymmetric lineshape, producing minor peaks that look similar to some of those observed in the spectra of Figure 4.3. Artifacts could also potentially be introduced by baseline or phasing errors

since these could also translate into lineshape asymmetries or amplitude variations. AHT predicts error terms with both $1/\omega_{MAS}$ and $1/\omega_{MAS}^2$ dependence. We have tried to include a second $1/\omega_{MAS}^2$ term in the model, but this has not so far led to any statistically significant improvement in the fit, or to any changes in the fitted spectra. The apparent dominance of the first term in the series observed here is also in line with previous observations for proton linewidths.[104, 107, 109-111, 113, 274] The model used here can probably be improved in the future, for example in order to include effects where motion could interfere with MAS leading to broader spectra at higher MAS rates, and this will be a topic of further investigation and development.

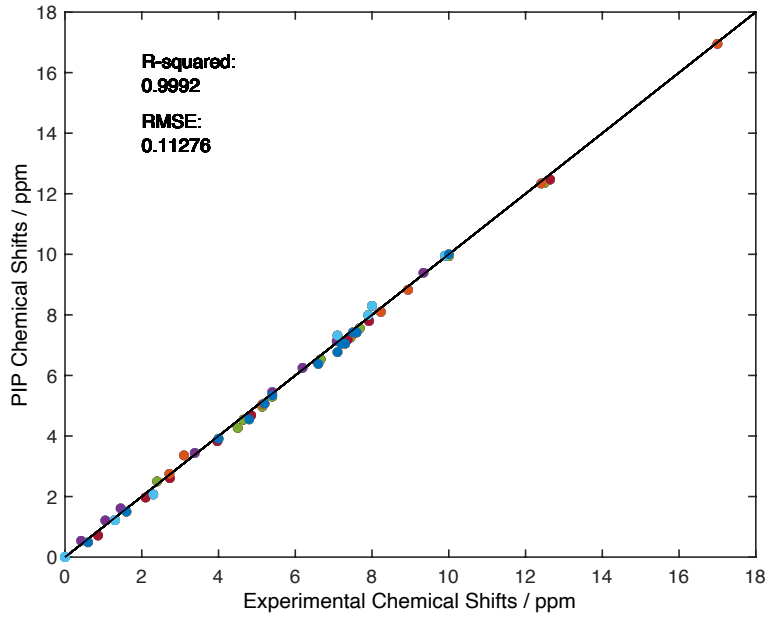

Figure 4.6. Correlation plot of PIP shifts versus experimentally measured shifts at 100 kHz MAS for all samples. The R-squared and RMSE values are also given. It is important to note, as discussed in the text, that the peak positions in the 100 kHz MAS spectra are not necessarily exactly at the isotropic shifts, and the errors due to shift effects that are not included in the model (e.g., a parasitic temperature dependence of the intrinsic chemical shift) could lead to infidelities in the PIP shifts. Therefore, the source of the RMSE observed here can originate on both axes.

4.2.4 Conclusions

In conclusion we have introduced a new approach to error reduction in NMR spectroscopy based on a *k*-space description, in which the error terms are separated from the desired pure interactions by exploiting differences in the parametric dependence of the errors and the pure interactions in a multi-dimensional dataset.

Here we have illustrated the approach by addressing the residual broadening due to incomplete coherent averaging in fast ^{1}H MAS spectra. By exploiting the variation of the errors in a set of spectra recorded at different MAS rates, we were here able to determine pure isotropic ^{1}H spectra with linewidths down to 48 Hz. The results shown for six different organic samples show on average 7-fold increase in resolution, and up to a factor of 20, as compared with spectra acquired at 100 kHz MAS.

The resolution and chemical shift fidelity that can be obtained in the pure isotropic spectra may now be limited by several factors. As discussed above, some are intrinsic to the samples and their structures or chemistry, such as any degree of structural disorder or intermediate dynamics, or magnetic susceptibility broadening. Others are due to the experimental parameters, such as MAS rate instabilities, that might lead to imperfect removal of the errors, which could lead to shifts or line shape distortions. These also include the digital resolution that we can obtain in the fitting procedure, the accuracy of the assumptions made in the model, the quality of the spectra and any experimental imperfections, baseline or phase errors introduced by processing, the size of the VS data set, or the maximum spinning speed attainable. It should be noted that the maximum spinning speed used here is not a prerequisite and similar results can be attained with lower maximum speeds, as showin in Figure S30 for a sample of L-tyrosine hydrochloride extracted by using rates between 30 and 64 kHz.

One additional limitation to address from this first PIP approach is assuming a common linear MAS dependent broadening and shift factors for all points within the same sub region of the spectrum. The overlap of different resonances does not mean that they have the same residual broadening and shift. Therefore, the PIP linewidths and shifts in regions with overlap are associated with greater uncertainty than the regions with a single isolated peak.

These factors will all be investigated in the future, and, in principle at least, the experimental factors can all be addressed through improved approaches to extracting the pure isotropic spectrum from the *k*-space representations, improved fitting models, or simply more computational power.

Even given these current limitations, the particular model used here as a first example can efficiently extract the pure isotropic spectra in all the samples without any prior knowledge. We expect that further developments will lead to even better ^{1}H resolution in the future, and we anticipate that the same underlying principle for removing errors introduced here can be extended to multi-dimensional experiments and also applied to other problems in NMR spectroscopy.

4.2.5 Appendix IV

4.2.5.1 Experimental

All solid state NMR experiments were performed with a 18.8 T Bruker Avance Neo spectrometer equipped with a 0.7 mm triple resonance HCN CP-MAS probe. All spectra were acquired using a rotor synchronized spin echo sequence and were processed in TopSpin 4.0.6 where they were zero-filled once and carefully phase and baseline corrected. No weighting function was applied prior to Fourier transformation. The samples of β-AspAla, L-histidine hydrochloride monohydrate, ampicillin, and L-tyrosine hydrochloride were purchased from Sigma Aldrich. The samples of thymol and flutamide were purchased from Carl Roth and Tokyo Chemical Industry respectively. All the samples were used without further recrystallization, after mild crushing with a mortar and a pestle.

Table 4.1 Experimental details of all VS datasets used in this study.

Sample	MAS range (kHz)	Step Size (kHz)	VT (K)	90° RF amplitude (kHz)	d1(s)	Number of FID points	SW (kHz)	Size of real spectrum used in the fits
L-tyrosine hydrochloride	100 -30	2000	275-295	294	5	2048	100	4096
β-AspAla	100 -26	2000	275-295	277	6	2048	100	4096
L-histidine hydrochloride monohydrate	100 -20	2000	275-295	289	30	2048	100	4096
Thymol	100 -42	2000	275	277	6	1024	100	4096
Flutamide	100 -20	2000	275-295	286	18	2048	100	2048
Ampicillin	100 -20	2000	275-295	286	3	4096	100	4096

4.2.5.2 Spectral Assignment and Referencing

<u>L-tyrosine hydrochloride</u>

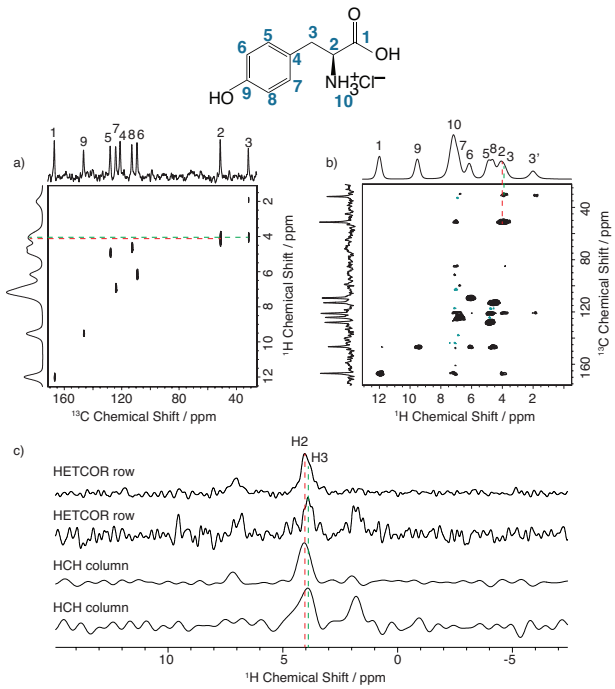

Figure 4.7 (a) One-bond 1H/13C HETCOR and b) long range $^{1}H/^{13}C$ HCH for a sample of L-tyrosine hydrochloride. (c) Rows and columns extracted from HETCOR and HCH at the cross sections indicated by the red and green dotted lines.

Table 4.2 Proton experimental chemical shifts of L-tyrosine hydrochloride measured from the HETCOR experiment of Figure 4.5 and referenced according to reference[275]

Nuclei	δ (ppm)
H1	12.49
H2	4.65
H3	4.50, 2.40
H5	5.40
H6	6.66
H7	7.44
H8	5.14
H9	10.0
H10	7.68

<u>β-Aspala</u>

Table 4.3 Proton experimental chemical shifts of β-AspAla according to reference[135]

Nuclei	δ (ppm)
H1	12.64
H2	4.85
H3	7.92
H5	2.73
H5’	2.10
H6	3.97
H7	0.86
H8	7.37

<u>L-Histidine hydrochloride monohydrate</u>

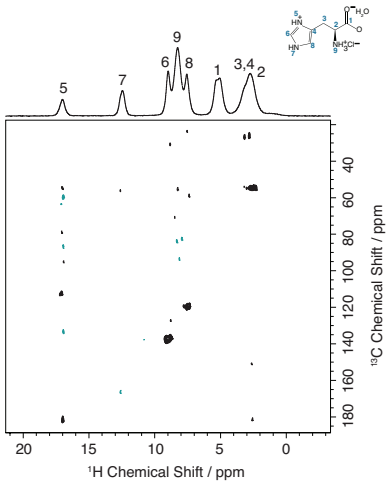

Figure 4.8 (a) One-bond $^{1}H/^{13}C$ HCH for a sample of L-histidine hydrochloride monohydrate.

Table 4.4 Proton experimental chemical shifts of L-histidine hydrochloride monohydrate measured from the HETCOR experiment of Figure 4.6 and referenced according to references[276-277]

Nuclei	δ (ppm)
H1	5.14
H2	2.72
H3	3.10
H5	17.0
H6	7.52
H7	12.41
H8	8.94
H9	8.23

Thymol

Table 4.5 : Proton experimental chemical shifts of thymol according to reference[54]

Nuclei	δ (ppm)
H1	5.40
H2	6.19
H3	7.08
H4	3.38
H5	1.45
H5’	1.05
H6	0.42
H7	9.34

Flutamide

Table 4.6 Proton experimental chemical shifts of flutamide according to reference[46]

Nuclei	δ (ppm)
H3	7.9
H5	9.9
H6	7.1
H8	8.0
H10	2.3
H11	1.3
H11’	1.3

Ampicillin

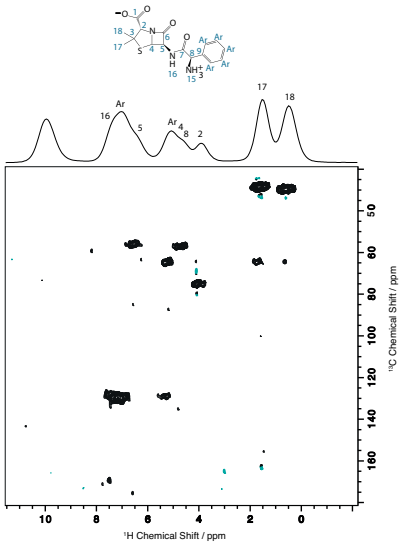

Figure 4.9 (a) One-bond $^{1}H/^{13}C$ one-bond HCH for a sample of ampicillin at 100 kHz MAS.

Table 4.7 Proton experimental chemical shifts of ampicillin according to reference[46]

Nuclei	δ (ppm)
H2	4.0
H4	5.2
H5	6.6
H8	4.8
Ar	5.4, ~7.1-7.3, 7.6
H15	10.0
H16	7.5
H17	0.6
H18	1.6

4.2.5.3 RAW VS DATA SETS

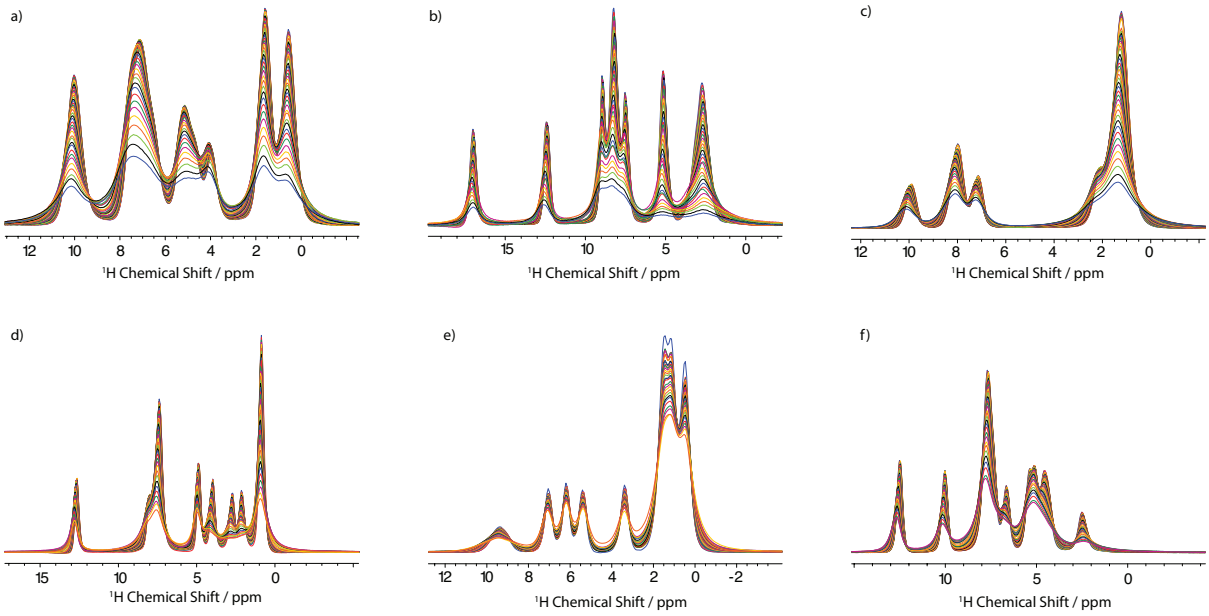

Figure 4.10 Raw VS datasets for the samples of (a) ampicillin, (b) L-histidine hydrochloride monohydrate, (c) flutamide, (d) β-AspAla, (e) thymol, and (f) L-tyrosine hydrochloride acquired at variable MAS rates with the parameters and spinning rates described above.

4.2.5.4 MODEL FITTING PROCEDURE

The fitting was performed in Matlab R2021a using homemade scripts. The following procedure was applied:

Data were Fourier transformed in TopSpin 4.0.6 and zero filled as stated in table 4.1. This yields a digital resolution in all the spectra of 49 Hz. All spectra were carefully phase and baseline corrected. This step is important, as the pure isotropic spectra are constrained to positive values.

The VS spectra were then imported into Matlab R2021a using homemade scripts.

To reduce the computational requirements, the fits for each spectrum were done region by region (this also allows each region to have different shift and broadening properties). Each spectrum was broken down as shown into the distinct spectral regions shown in Figure 4.9, containing between 27 and 121 points (as specified in the caption to Figure 4.11). Each region was then first normalized to a maximum intensity of 2500 and then inverse Fourier transformed and scaled in order to give a set of spectra with constant integrals over all spinning rates after back Fourier transformation.

A set of predicted VS data were then generated from a trial ***A***, where ***A*** corresponds to the vector of amplitudes of the pure isotropic spectrum, broadened by a trial Gaussian MAS rate dependent component, γ_G, and a trial Lorentzian MAS rate dependent component, γ_L. The synthetic data were also given a trial MAS dependent shift component, γ_{shift}, from the isotropic position. Here, the fastest MAS spectrum was chosen as the initial trial ***A***. The same results are obtained, but in more computational time if the initial trial ***A*** is set to zero everywhere.

Then, the difference between the predicted VS data and the set of experimental spectra was minimized by varying the individual elements of ***A*** together with γ_G, γ_L and γ_{shift}, using the *fmincon* routine in Matlab R2021a. The algorithm of *interior-point* was used and 10.000 iterations were allowed.

Lower and upper bounds were set for the minimization. The extracted pure isotropic spectrum, ***A***, and the $\gamma_{L,G}$ were restricted to positive amplitudes whereas the γ_{shift} was allowed to vary between -150 and 150.

Definition of χ^2:

$$\chi^2 = 100\,\frac{\sum_{j=1}^{N}\sum_{i=1}^{n} abs(VSexp_{j,i} - VSpre_{j,i})}{n\,N\,\max\,(S_{100kHz})} \qquad (4.12)$$

where ***N*** is the number of experimental spectra in the VS dataset and ***n*** is the number of points in each spectrum. As *VSexp* we define the experimental dataset and as *VSpre* the VS dataset predicted by the model. The χ^2 is normalized by the maximum intensity of the *VSexp* data set (which by definition depends on the maximum intensity of the spectrum recorded at the highest MAS rate) and is given as a percentage per point.

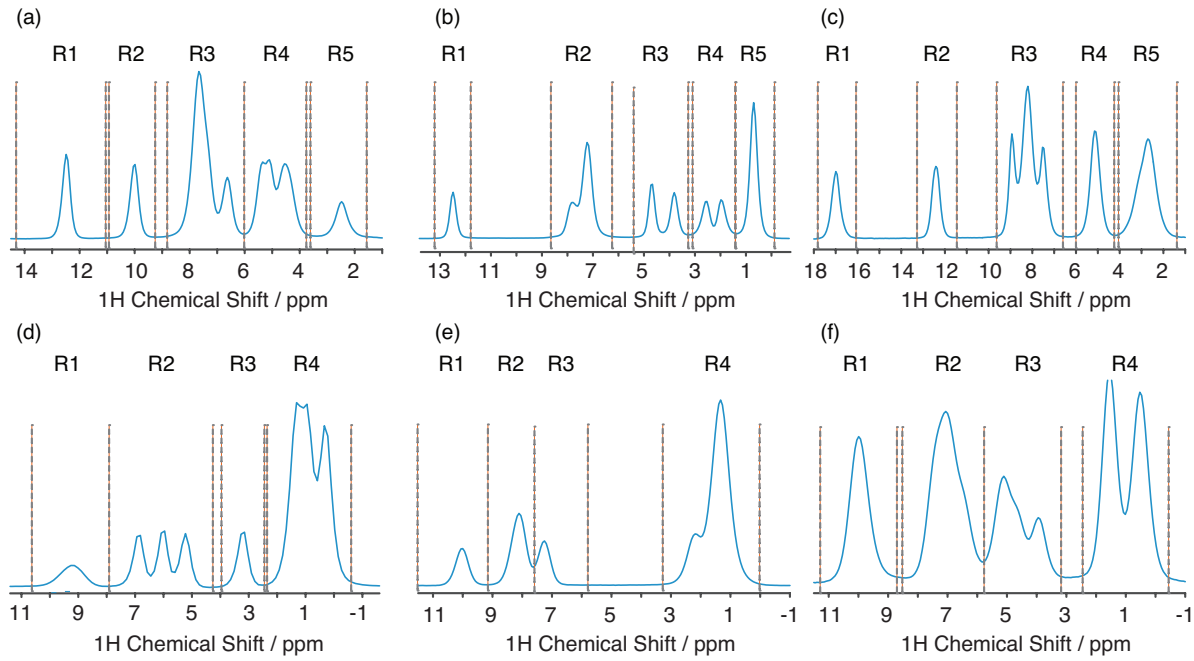

Figure 4.11 Display of the spectral regions used for the fitting for L-tyrosine hydrochloride (a), β-AspAla (b), L-histidine hydrochloride monohydrate (c), thymol (d), flutamide (e), and ampicillin (f). For L-tyrosine hydrochloride the spectral regions R1-R5 consist of 51, 51, 101, 76, and 56 points, respectively. For β-AspAla the spectral regions R1-R5 consist of 41, 76, 71, 59, and 49 points, respectively. For L-histidine hydrochloride monohydrate the spectral regions R1-R5 consist of 46, 39, 101, 46, and 81 points, respectively. For thymol the spectral regions R1-R4 consist of 81, 121, 61, and 121 points, respectively. For flutamide the spectral regions R1-R4 consist of 35, 27, 31, and 51 points, respectively. For ampicillin the spectral regions R1-R4 consist of 101, 86, 74, and 111 points, respectively.

4.2.5.5 FITS TO SYNTHETIC ISOTROPIC PROFILES

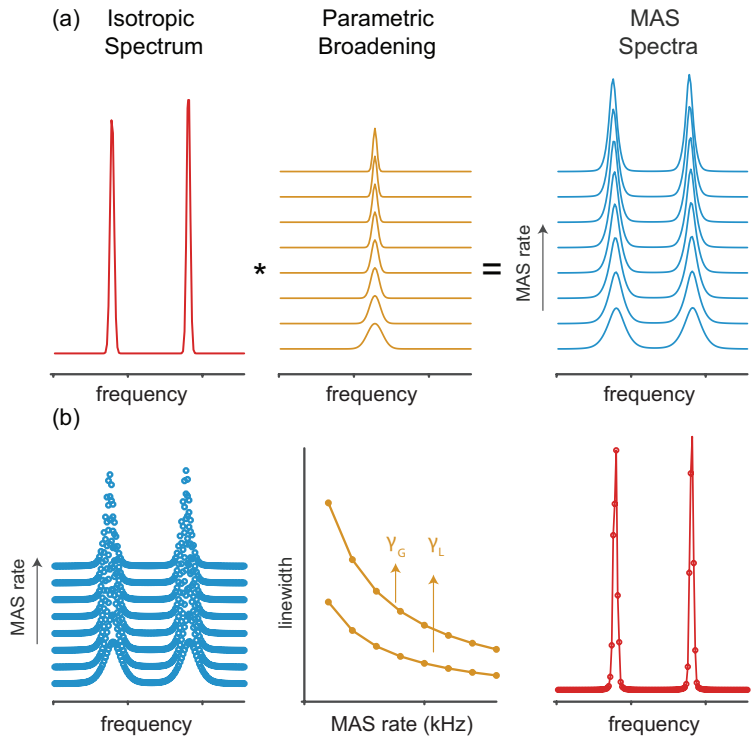

Figure 4.12 (a) Schematic representation of the model described in Eq. 4.7-4.10 of the manuscript according to which each MAS spectrum (blue) can be described by the convolution of a constant pure isotropic spectrum (red) with a MAS rate dependent broadening function (yellow). In this case the isotropic spectrum (128 points) consists of two narrow lines with lineshapes that are a mix of Gaussian and Lorentzian components. (b) Performance of the model in fitting synthetic VS data, where the pure isotropic spectrum shown on the right is obtained, together the broadening factors γ_G, and γ_L, that lead to the linewidths shown in yellow. The shift parameter γ_{shift} is also extracted.

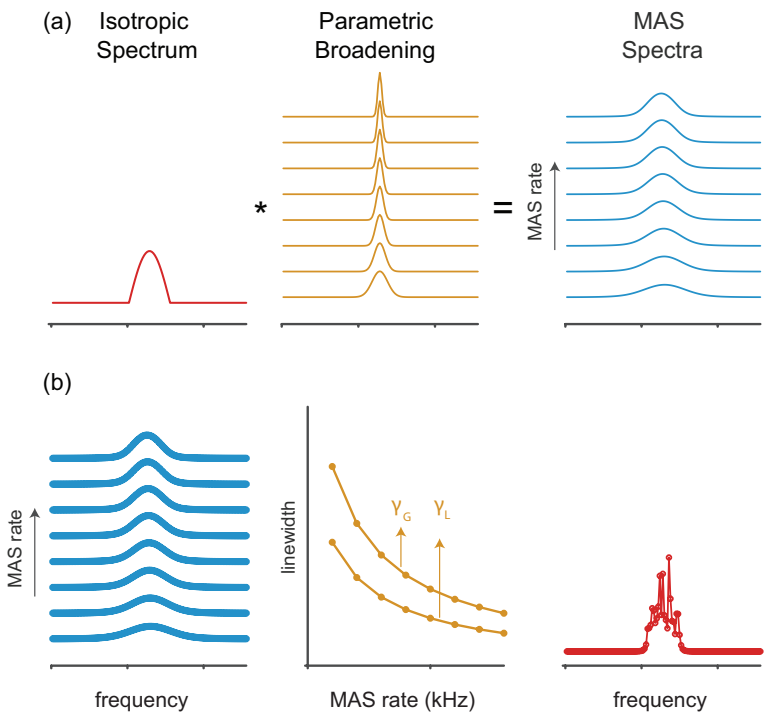

Figure 4.13 (a) Schematic representation of the model described in Eq. 4.7-4.10 of the manuscript according to which each MAS spectrum (blue) can be described by the convolution of a constant pure isotropic spectrum (red) with a MAS rate

dependent broadening function (yellow). In this case the isotropic spectrum (128 points) consists of a single broad shape that mimics the case of chemical shift distribution. (b) Performance of the model in fitting synthetic VS data, where the pure isotropic spectrum shown on the right is obtained, together with the broadening factors γ_G, and γ_L, that lead to the linewidths shown in yellow. The shift parameter γ_{shift} is also extracted.

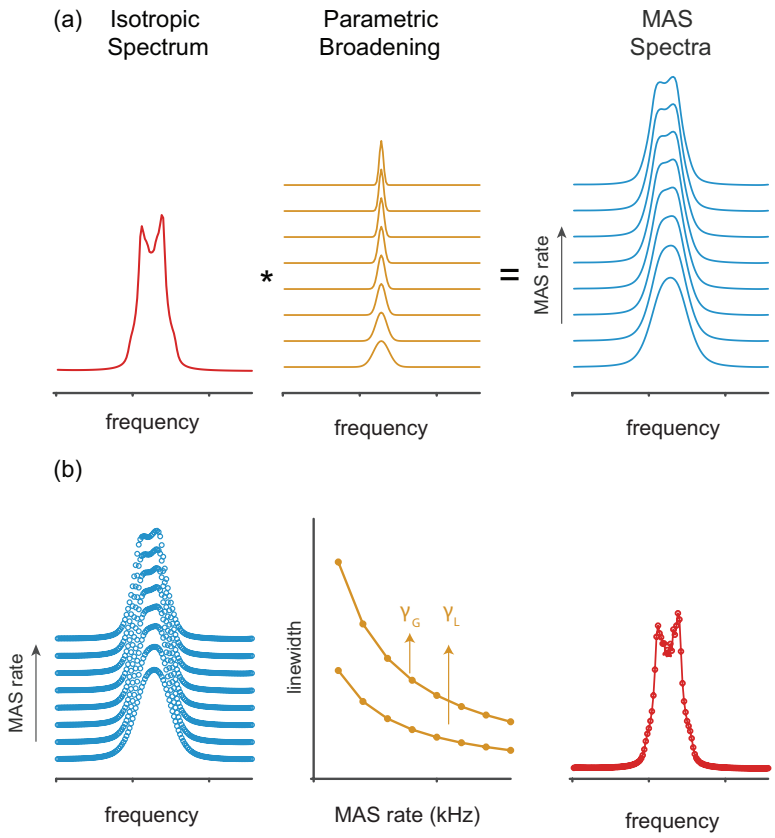

Figure 4.14 (a) Schematic representation of the model described in Eq. 4.7-4.10 of the manuscript according to which each MAS spectrum (blue) can be described by the convolution of a constant pure isotropic spectrum (red) with a MAS rate dependent broadening function (yellow). In this case the isotropic spectrum (128 points) consists of a single pake shape. (b) Performance of the model in fitting synthetic VS data, where the pure isotropic spectrum shown on the right is obtained, together with the broadening factors γ_G, and γ_L, that lead to the linewidths shown in yellow. The shift parameter γ_{shift} is also extracted.

4.2.5.6 FITS

The fitting of each region was repeated ten times using random starting points for the broadening and shift parameters. The 100 kHz MAS spectrum is used as the initial guess for ***A***.

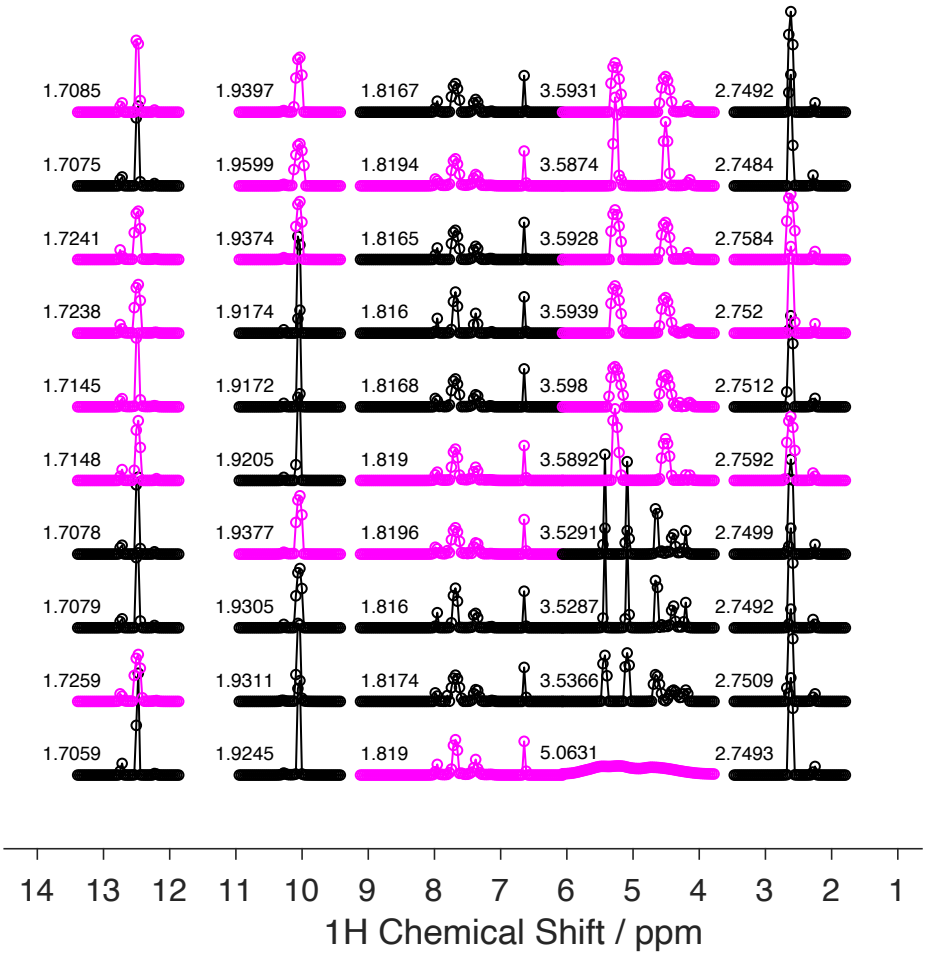

Figure 4.15 The results for the pure isotropic spectra obtained for ten fits of the five separate regions of a sample of L-tyrosine hydrochloride varying randomly the starting values for γ_G, γ_L, and γ_{shift}. The χ^2 values are also listed. The hits are depicted in black and the outliers are in magenta.

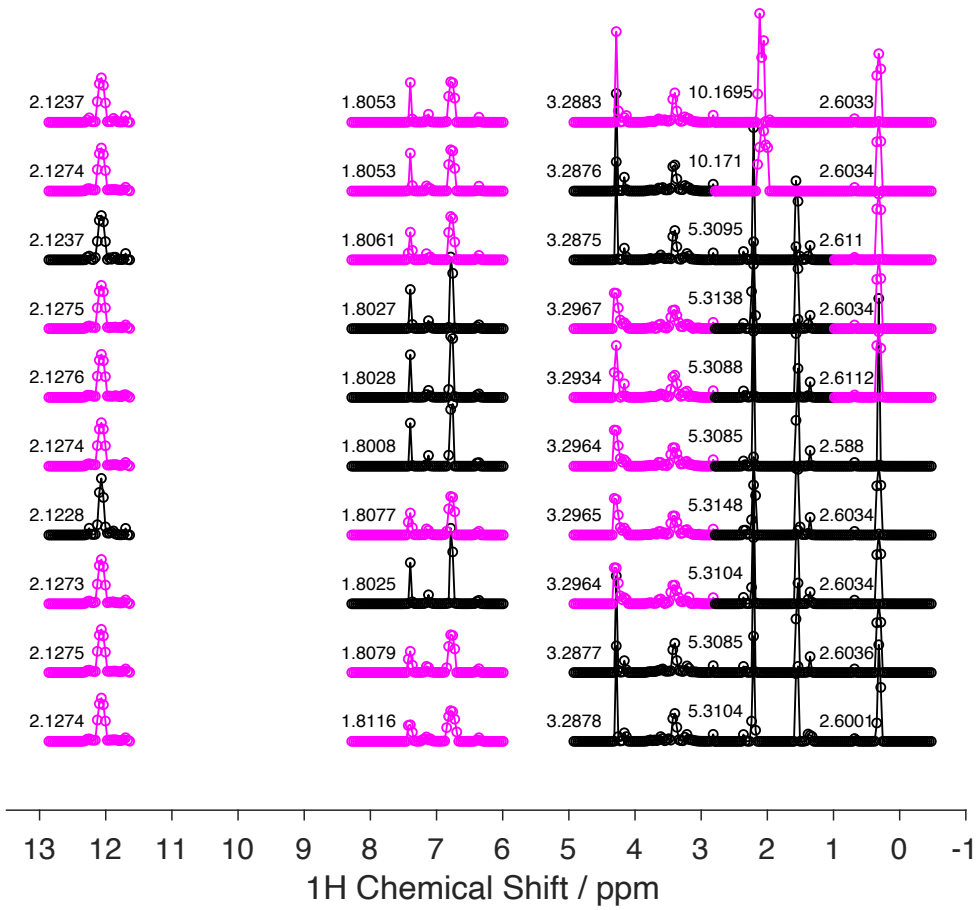

Figure 4.16 Ten fitting attempts of the five separate regions of a sample of β-AspAla varying randomly γ_G, γ_L, and γ_{shift}. The χ^2 values are also listed. The hits are depicted in black and the outliers are in magenta.

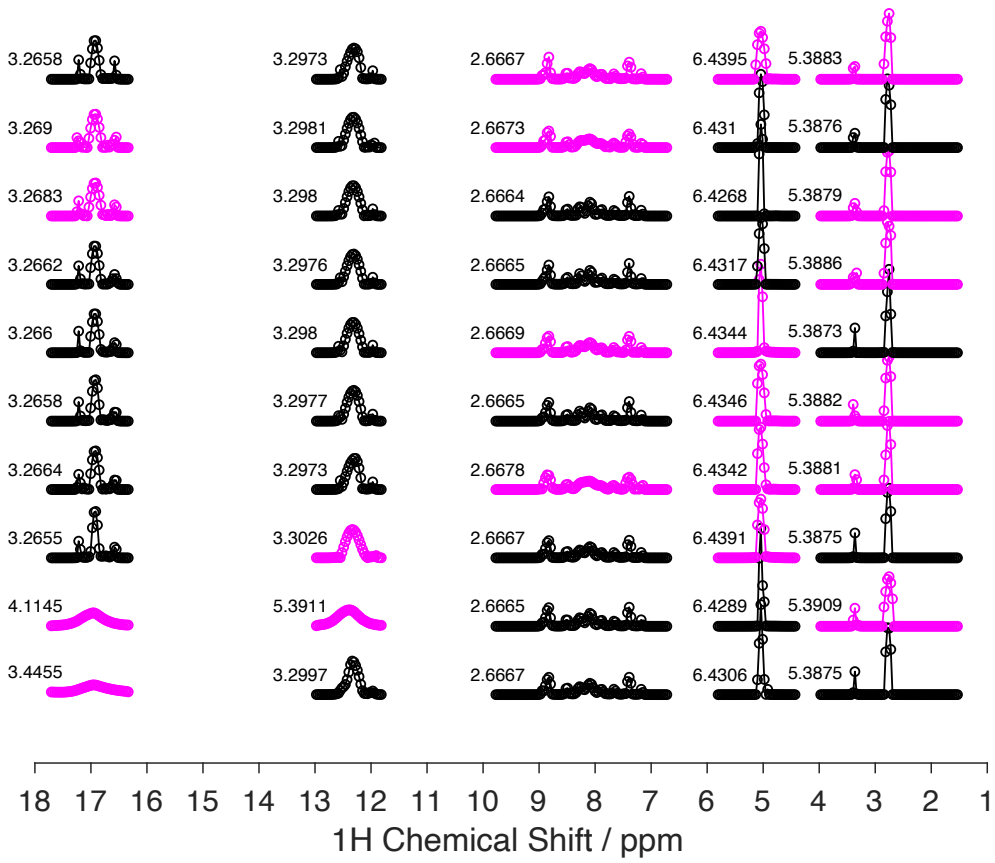

Figure 4.17 Ten fitting attempts of the five separate regions of a sample of L-histidine hydrochloride monohydrate varying randomly γ_G, γ_L, and γ_{shift}. The χ^2 values are also listed. The hits are depicted in black and the outliers are in magenta.

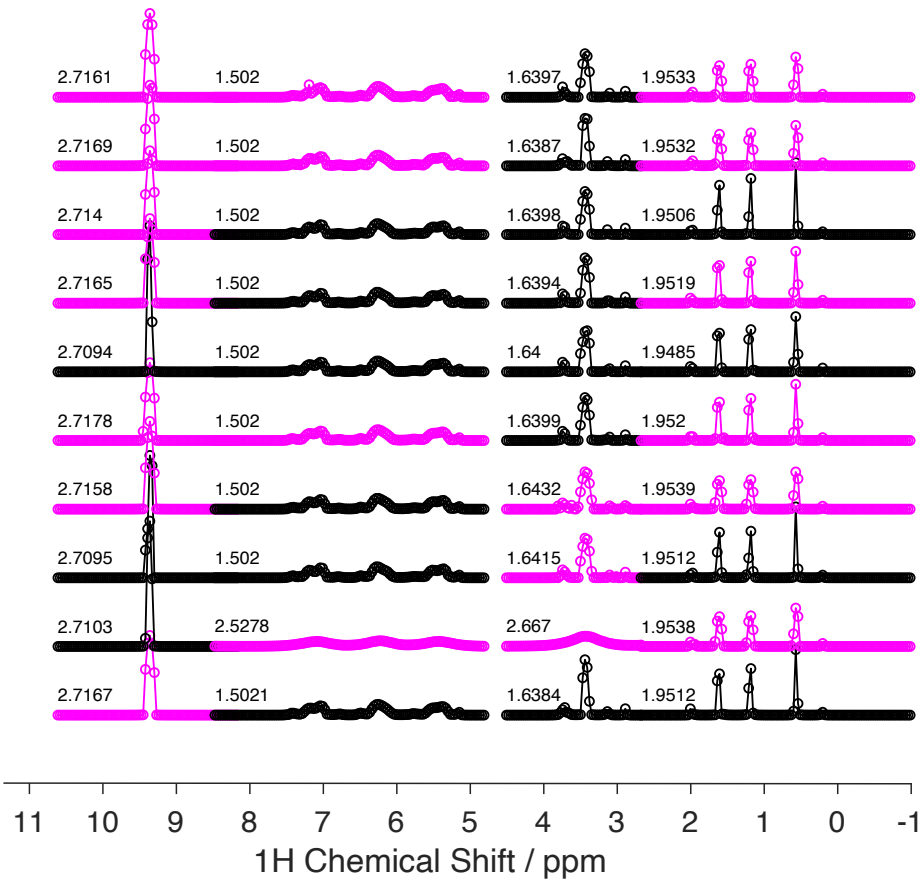

Figure 4.18 Ten fitting attempts of the four separate regions of a sample of thymol varying randomly γ_G, γ_L, and γ_{shift}. The χ^2 values are also listed. The hits are depicted in black and the outliers are in magenta.

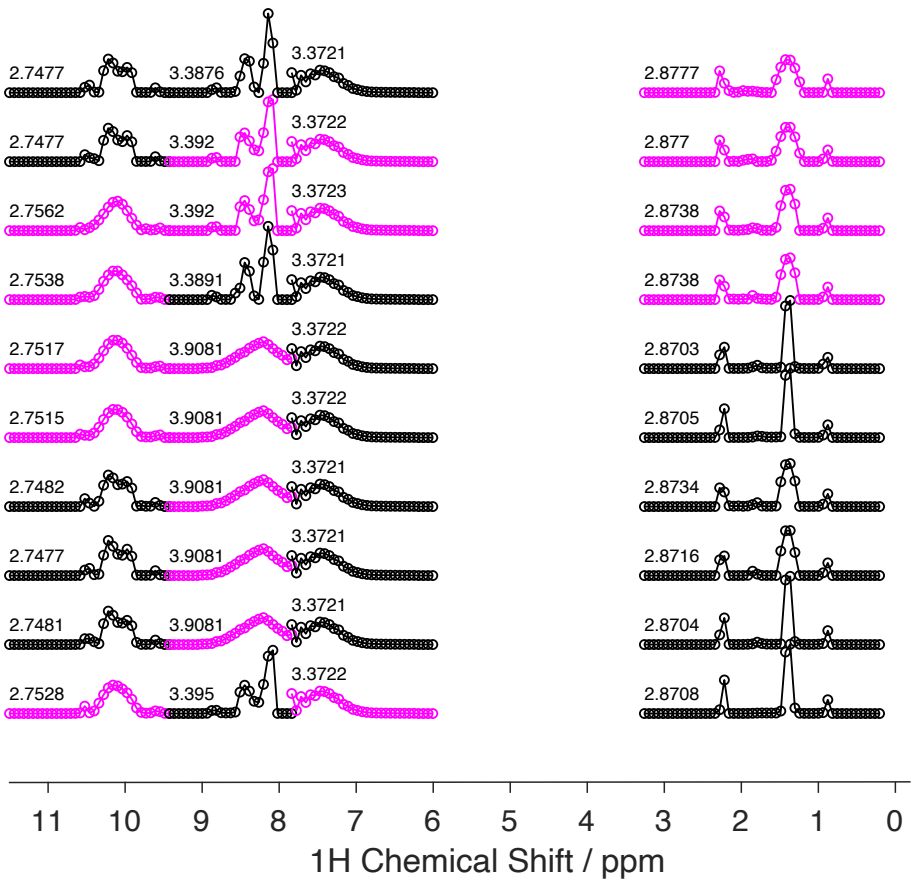

Figure 4.19 Ten fitting attempts of the four separate regions of a sample of flutamide varying randomly γ_G, γ_L, and γ_{shift}. The χ^2 values are also listed. The hits are depicted in black and the outliers are in magenta.

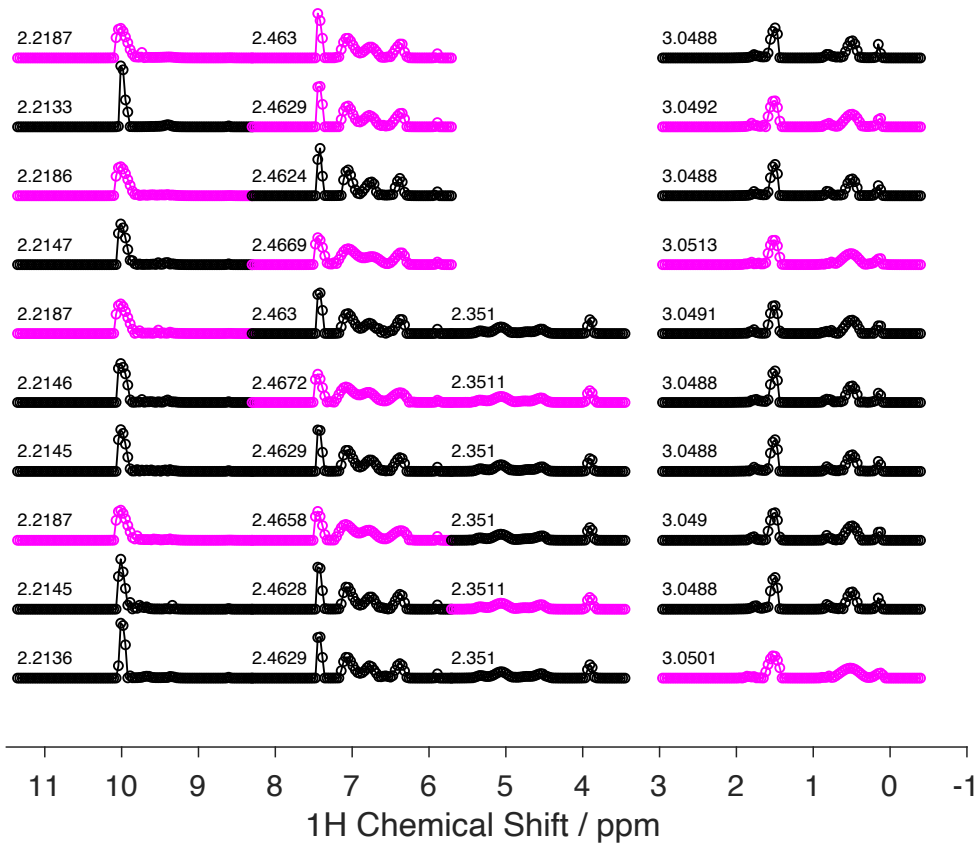

Figure 4.20 Ten fitting attempts of the four separate regions of a sample of ampicillin varying randomly γ_G, γ_L, and γ_{shift}. The χ^2 values are also listed. The hits are depicted in black and the outliers are in magenta.

4.2.5.7 QUALITY OF FITTING FOR THE AVERAGE OF THE SUCCESSFUL HITS

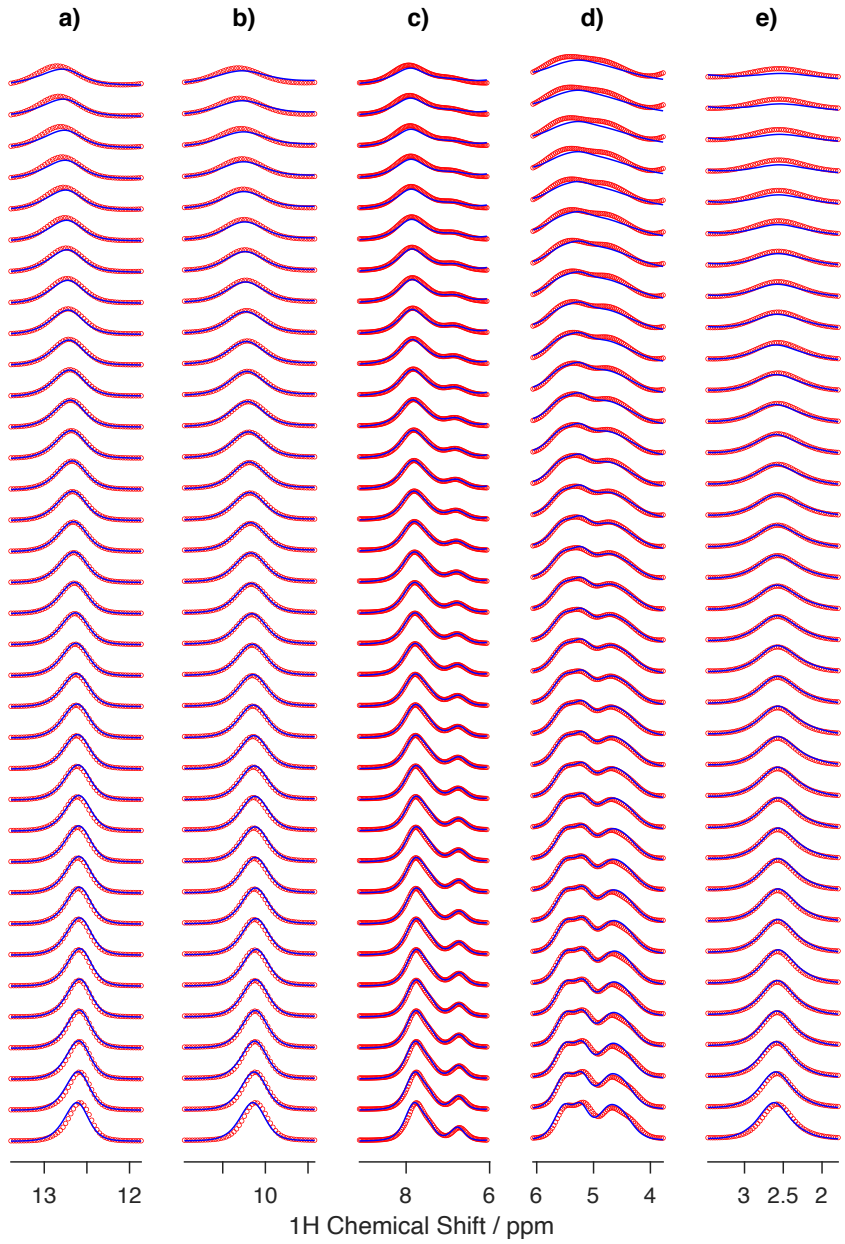

Figure 4.21 Experimental VS data (in solid blue lines) and predicted VS data (in red dotted lines) for the five separate fitting regions of a sample of L-tyrosine hydrochloride. (a)-(e) depict the regions R1-R5 shown in Figure 4.9

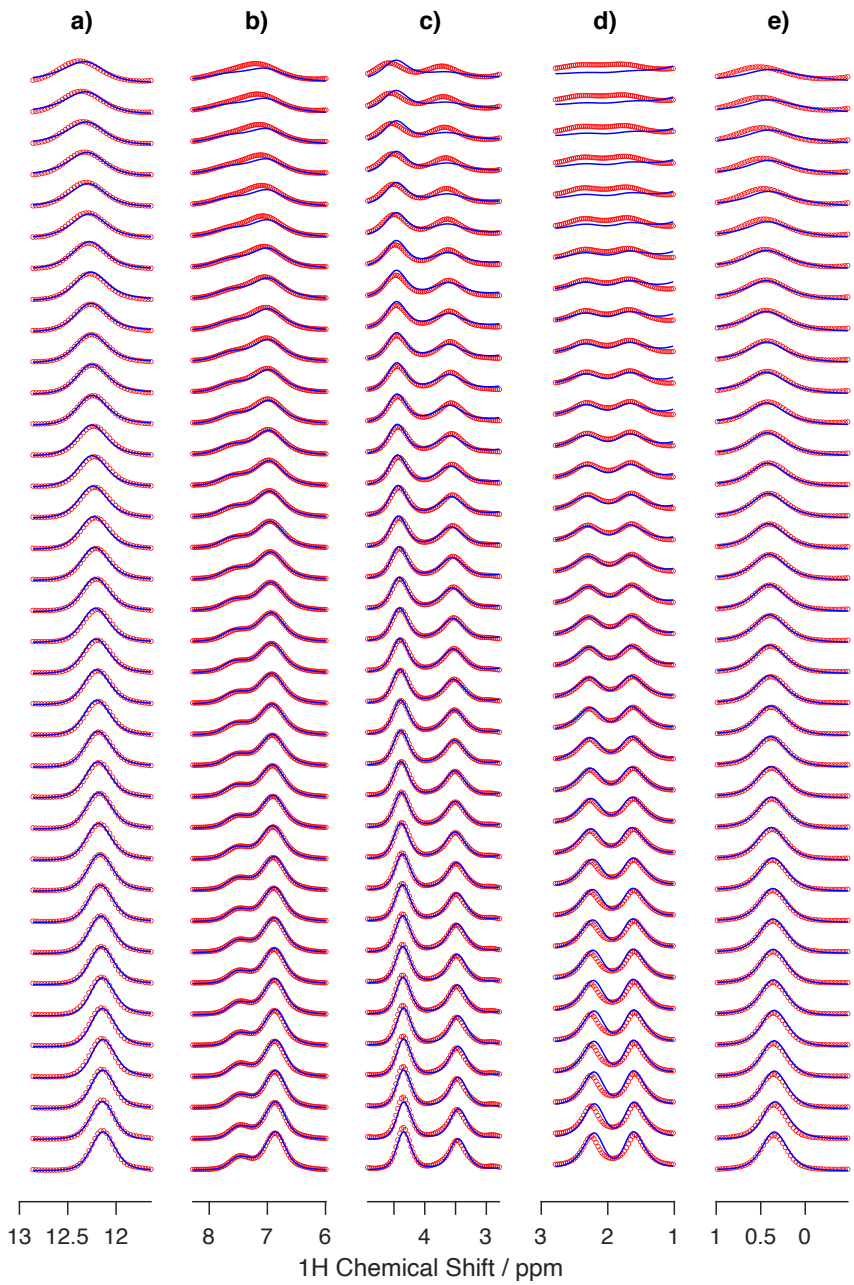

Figure 4.22 Experimental VS data (in solid blue lines) and predicted VS data (in red dotted lines) for the five separate fitting regions of a sample of β-AspAla. (a)-(e) depict the regions R1-R5 shown in Figure 4.9.

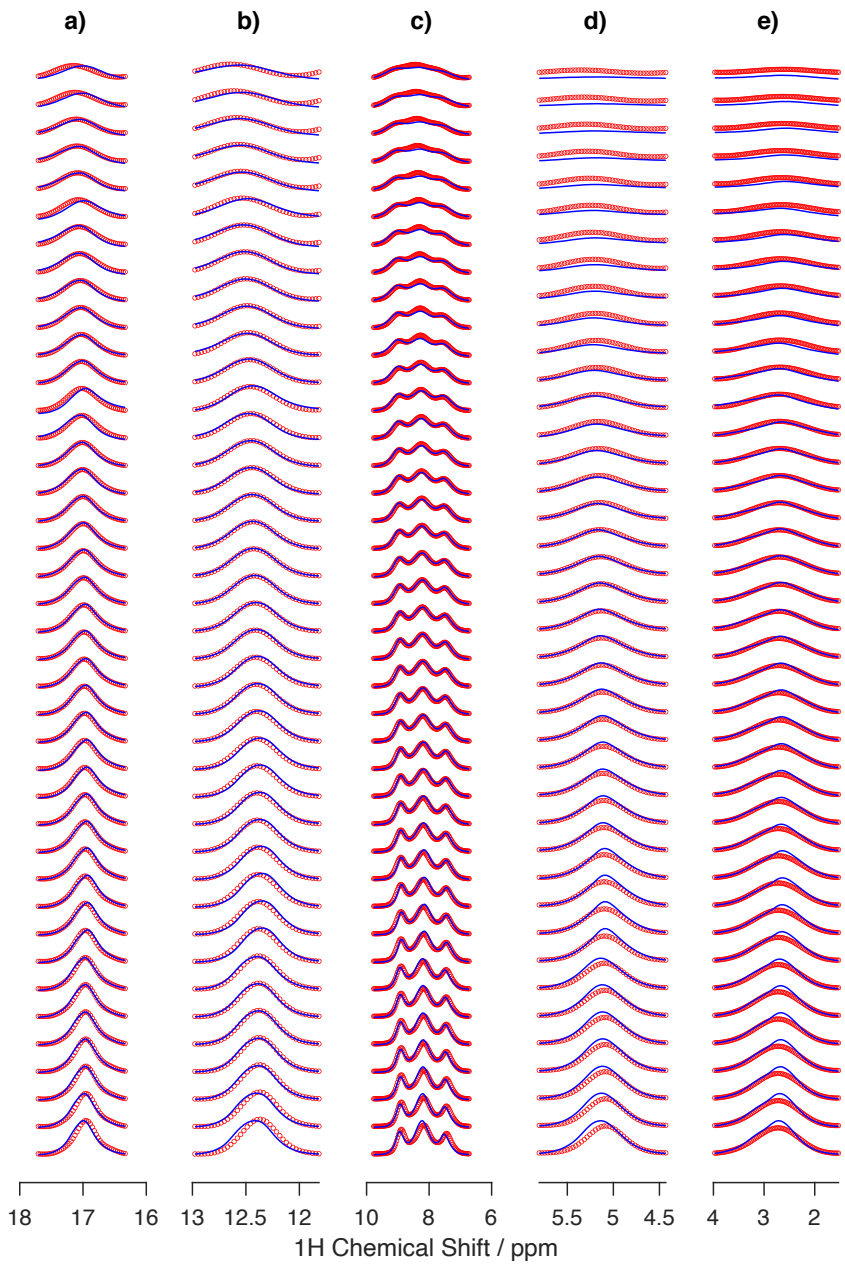

Figure 4.23 Experimental VS data (in solid blue lines) and predicted VS data (in red dotted lines) for the five separate fitting regions of a sample of L-histidine hydrochloride monohydrate. a)-e) depict the regions R1-R5 shown in Figure 4.9.

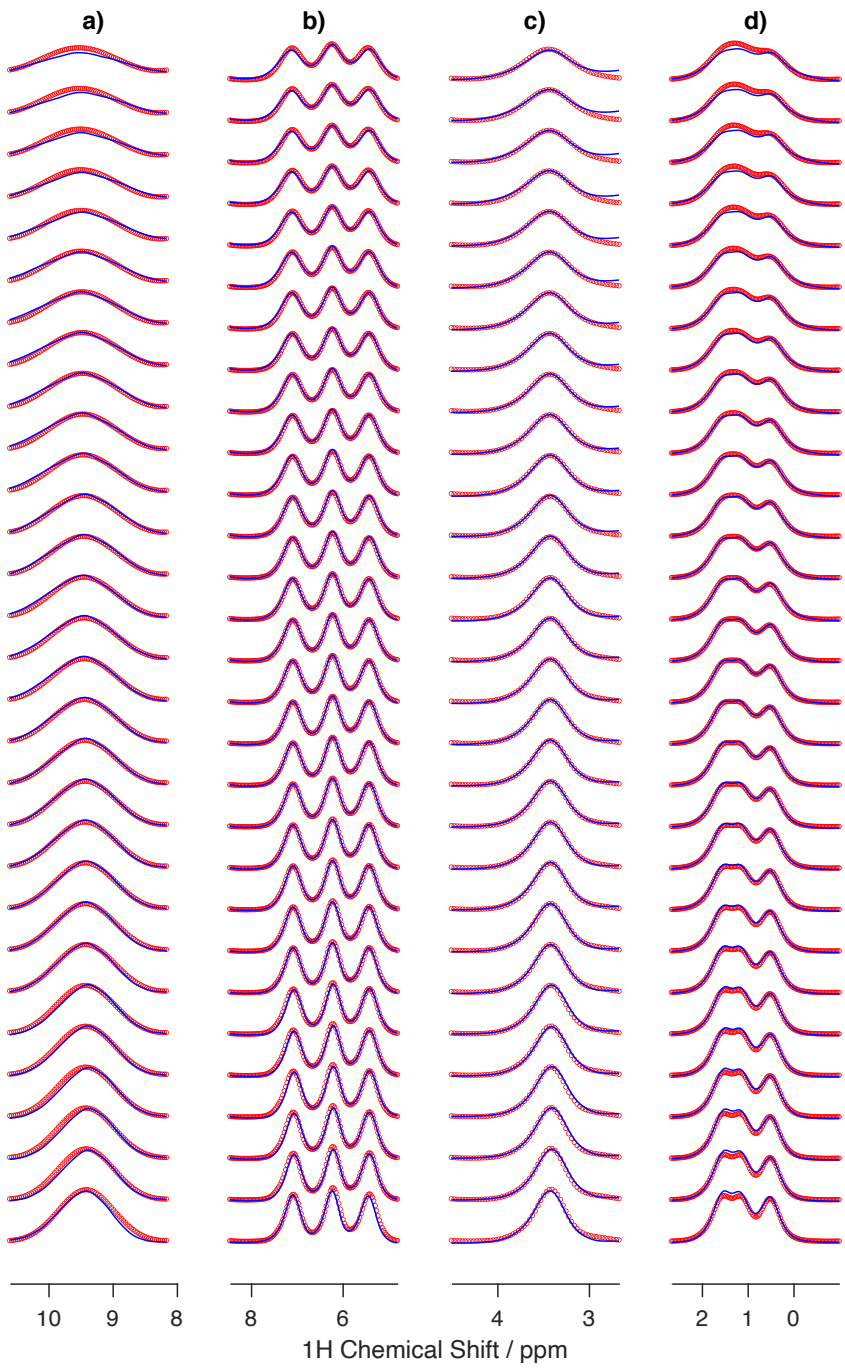

Figure 4.24 Experimental VS data (in solid blue lines) and predicted VS data (in red dotted lines) for the five separate fitting regions of a sample of thymol. a)-d) depict the regions R1-R4 shown in Figure 4.9.

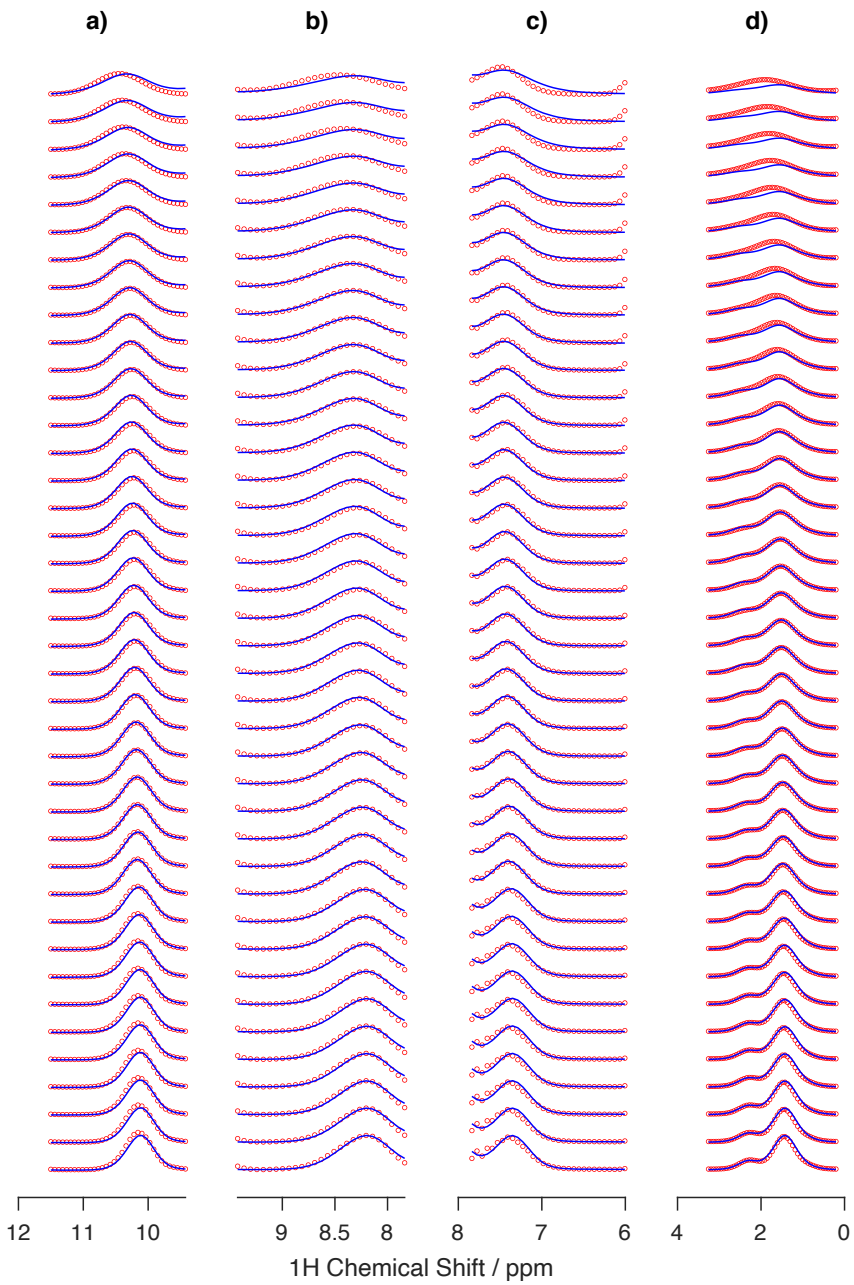

Figure 4.25 Experimental VS data (in solid blue lines) and predicted VS data (in red dotted lines) for the five separate fitting regions of a sample of **flutamide**. a)-d) depict the regions R1-R4 shown in Figure 4.9.

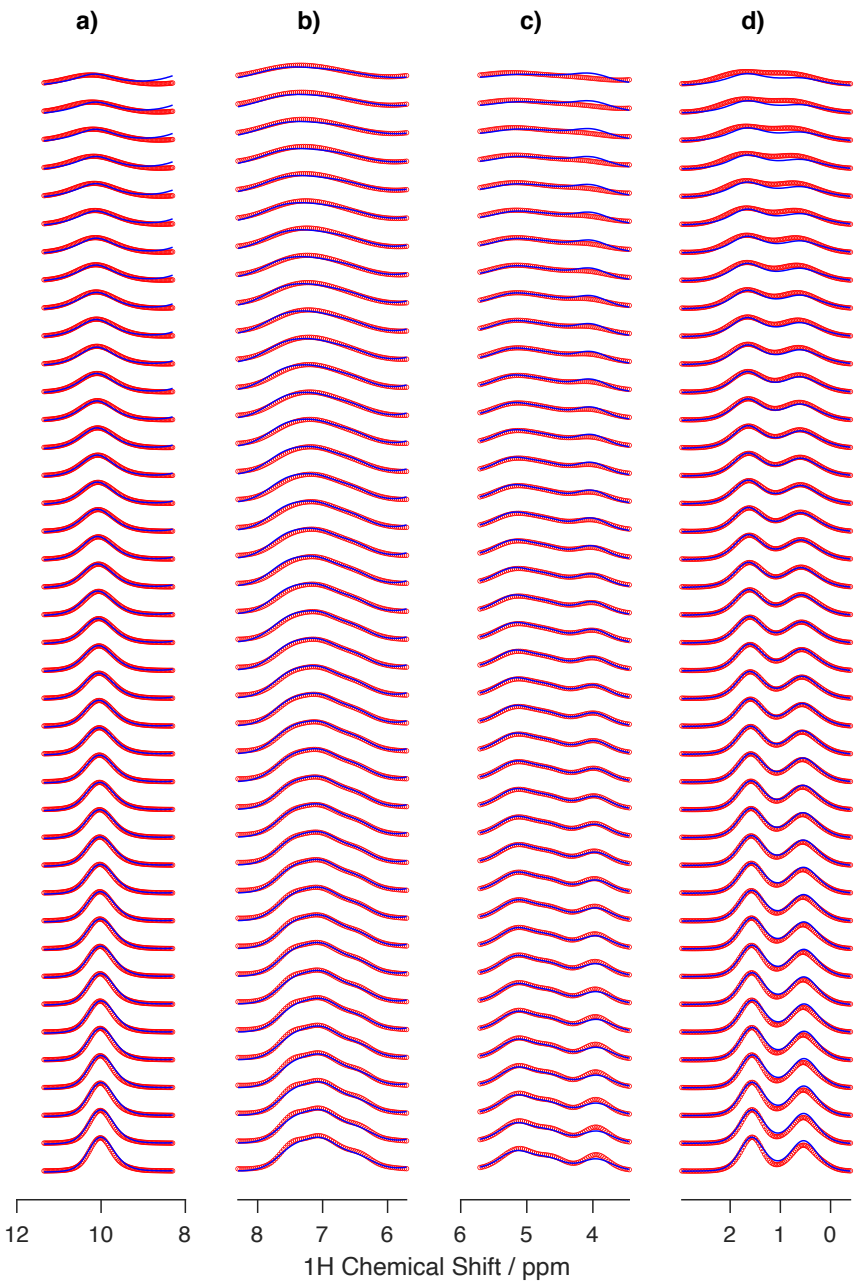

Figure 4.26 Experimental VS data (in solid blue lines) and predicted VS data (in red dotted lines) for the five separate fitting regions of a sample of **ampicillin**. a)-d) depict the regions R1-R4 shown in Figure 4.9.

4.2.5.8 PREDICTED GAMMAS AND SHIFTS

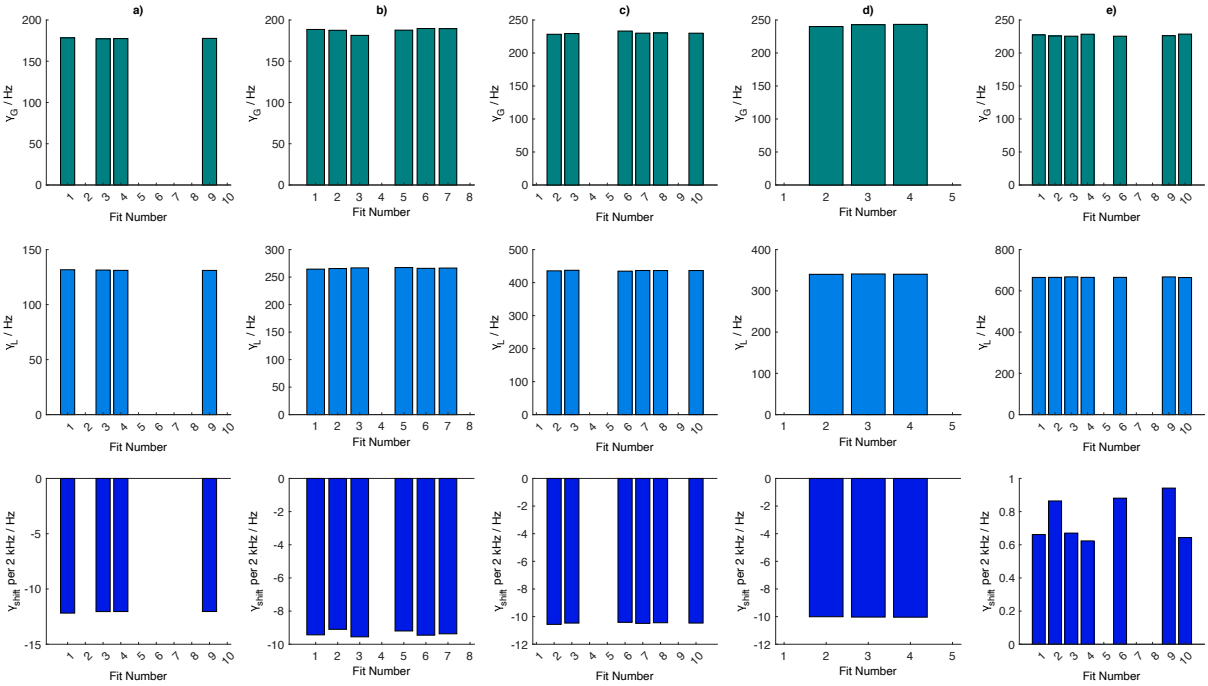

Figure 4.27 Predicted γ_G, γ_L, and γ_{shift} for the successful fits of the five separate fitting regions (a-e) of a sample of L-tyrosine hydrochloride.

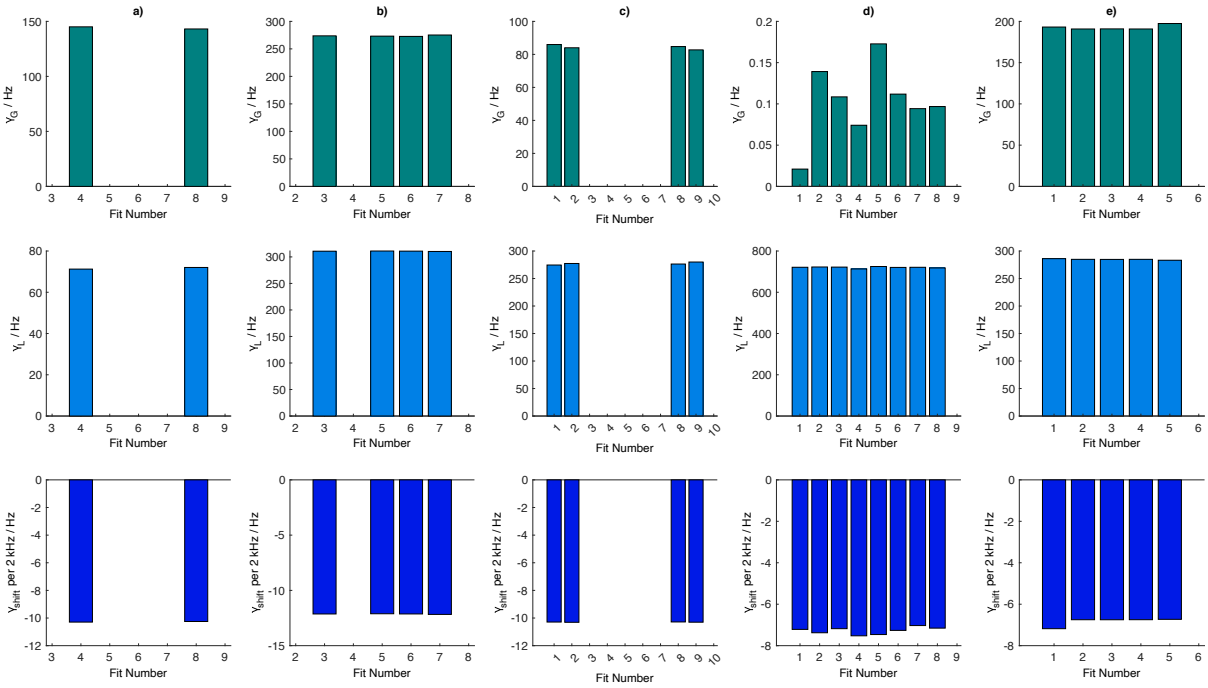

Figure 4.28 Predicted γ_G, γ_L, and γ_{shift} for the successful fits of the five separate fitting regions (a-e) of β-AspAla.

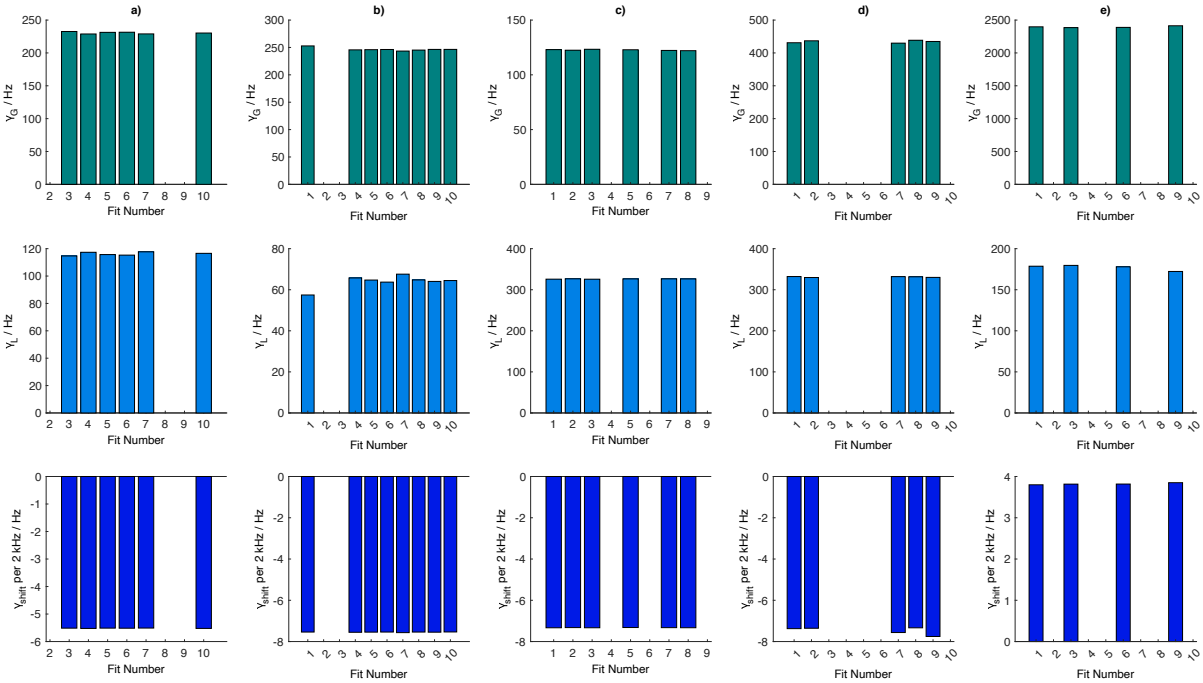

Figure 4.29 Predicted γ_G, γ_L, and γ_{shift} for the successful fits of the five separate fitting regions (a-e) of L-histidine hydrochloride monohydrate.

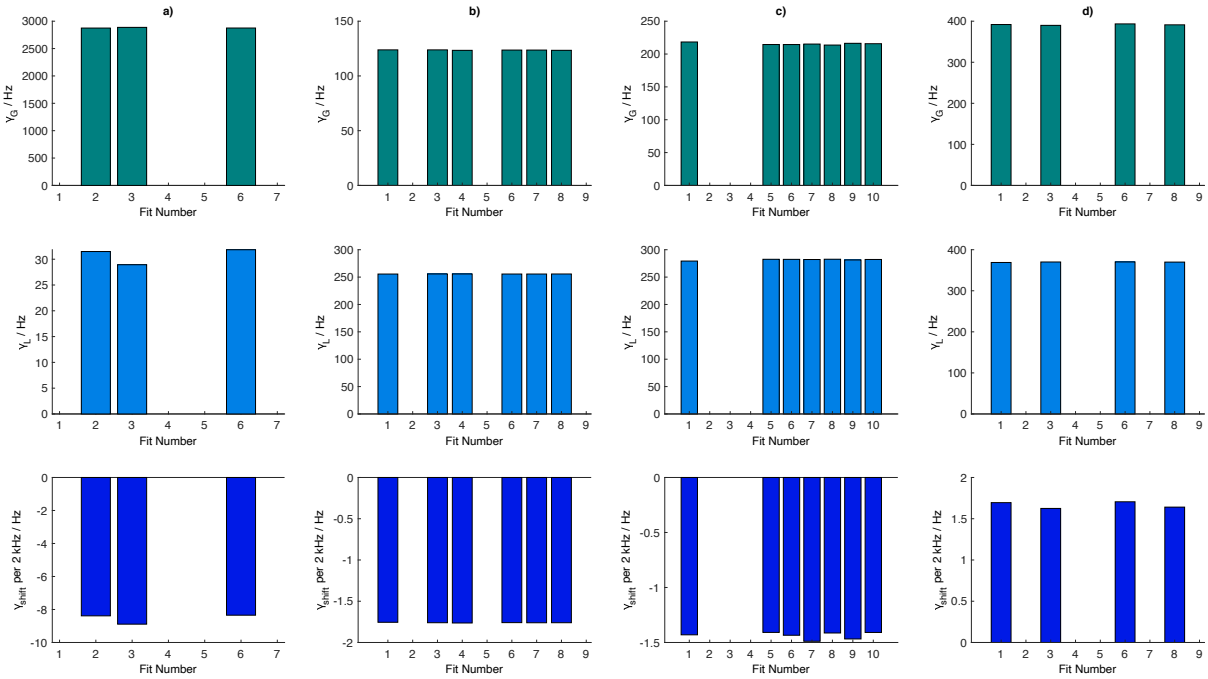

Figure 4.30 Predicted γ_G, γ_L, and γ_{shift} for the successful fits of the four separate fitting regions (a-d) of thymol.

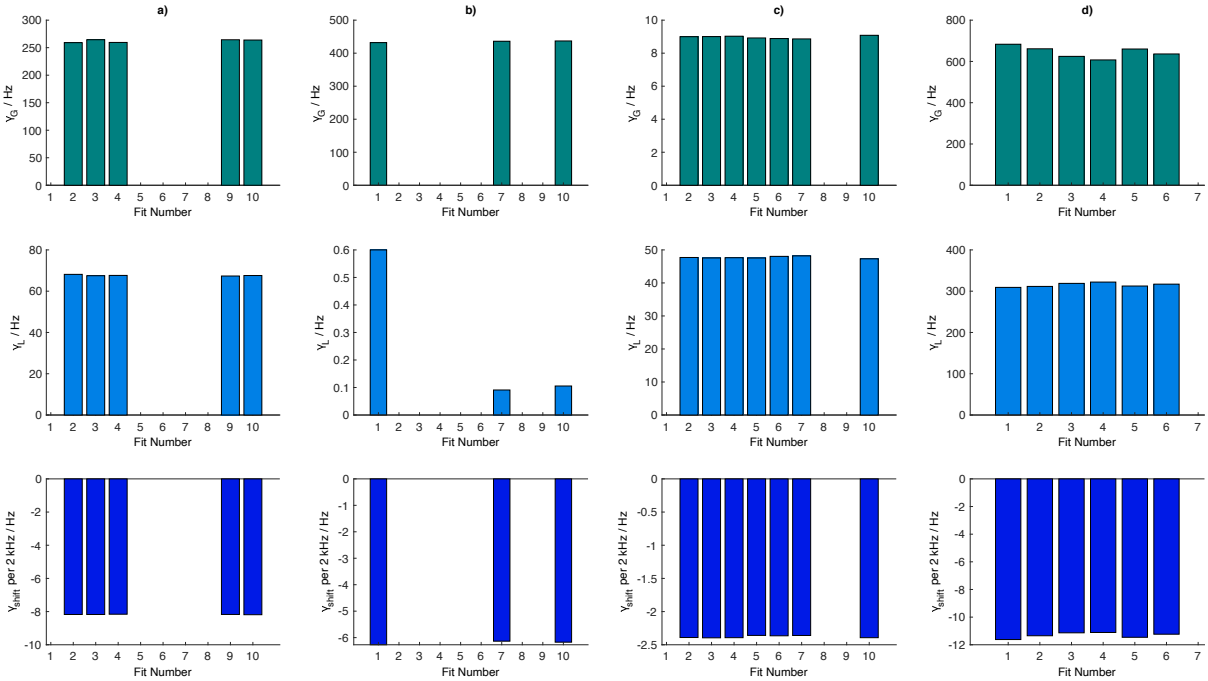

Figure 4.31 Predicted γ_G, γ_L, and γ_{shift} for the successful fits of the four separate fitting regions (a-d) of flutamide.

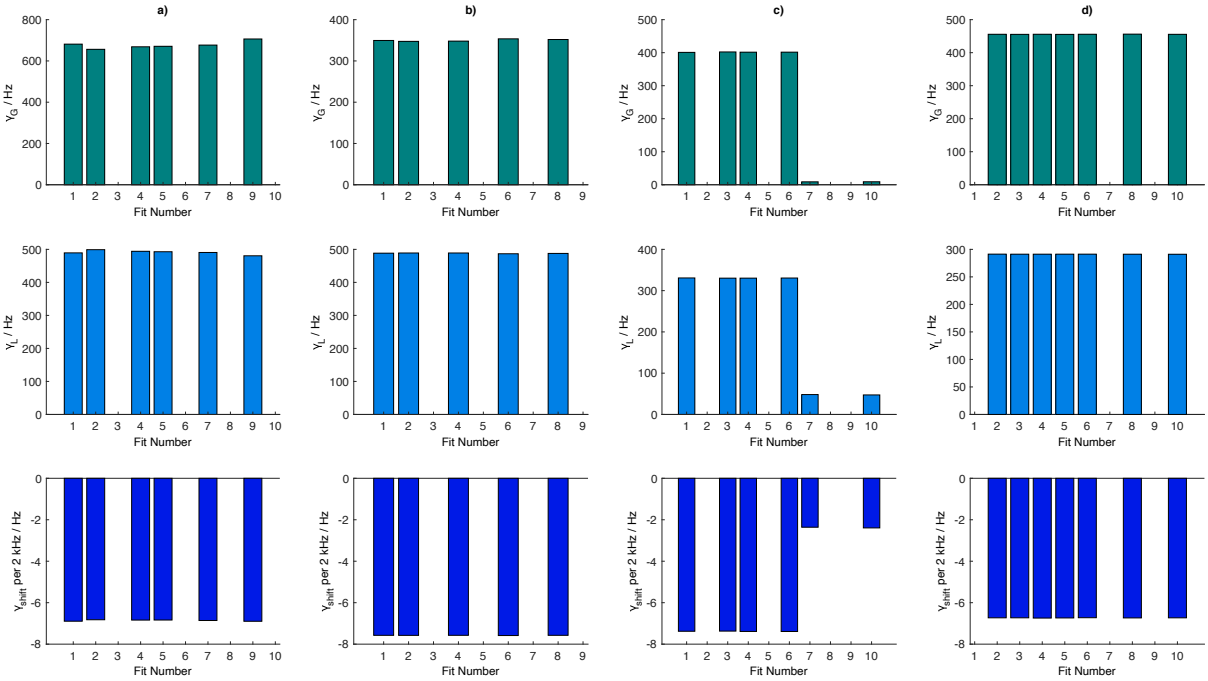

Figure 4.32 Predicted γ_G, γ_L, and γ_{shift} for the successful fits of the four separate fitting regions (a-d) of ampicillin.

4.2.5.9 ORIGIN OF ARTEFACTS

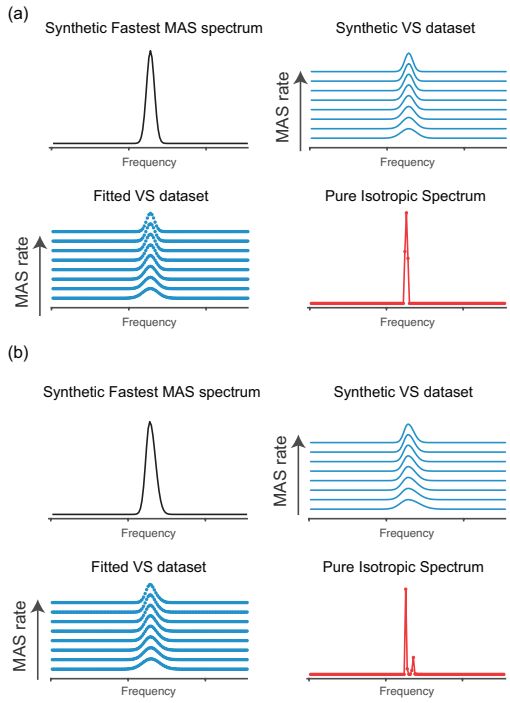

Figure 4.33 Performance of the model in fitting synthetic VS data (128 points) of (a) a single, symmetric Gaussian lineshape and of (b) a single asymmetric Gaussian lineshape. In both cases the isotropic spectrum should be represented by a delta function. However, in case (b) the model predicts the presence of a minor peak that looks similar to some of those observed in the spectra of Figure 5.3.

4.2.5.10 RATES UP TO 64 KHZ

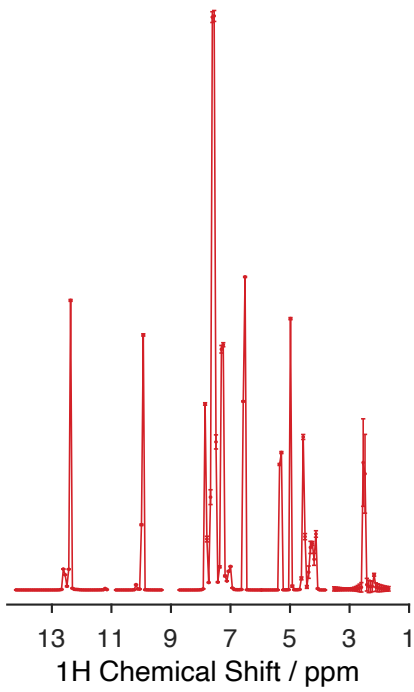

Figure 4.34 Performance of the model in fitting VS data of a sample of L-tyrosine hydrochloride (2k real points) using only MAS rates between 30 and 64 kHz.

4.2.5.11 MEASURED LINEWIDTHS

All linewidths measured are considered to be estimates and therefore do not possess error bars, which are estimated to be at the order of ± 50 Hz.

Table 4.8 Peak widths of L-tyrosine hydrochloride measured for the spectrum acquired at 100 kHz MAS and for the pure isotropic spectrum. Asterisks indicate signal overlap.

Nuclei	Δexp (FWHM Hz)	Δiso (FWHM Hz)
H1	270	48
H2	455*	48
H3	455*, 400	48,48
H5	575*	48
H6	358	48
H7	513*	48
H8	575*	48
H9	285	73
H10	513*	48

Table 4.9 Peak widths of β-AspAla measured for the spectrum acquired at 100 kHz MAS and for the pure isotropic spectrum. Asterisks indicate signal overlap.

Nuclei	Δexp (FWHM Hz)	Δiso (FWHM Hz)
H1	240	98
H2	230	48
H3	330	48
H5	332	48
H5’	326	48
H6	278	48
H7	287	48
H8	377	48

Table 4.10 Peak widths of L-histidine hydrochloride monohydrate measured for the spectrum acquired at 100 kHz MAS and for the pure isotropic spectrum. Asterisks indicate signal overlap.

Nuclei	Δexp (FWHM Hz)	Δiso (FWHM Hz)
H1	408	48
H2	743*	73
H3	743*	48
H5	341	122
H6	363	48
H7	339	219
H8	318	73
H9	468	-

Table 4.11 Peak widths of thymol measured for the spectrum acquired at 100 kHz MAS and for the pure isotropic spectrum. Asterisks indicate signal overlap.

Nuclei	**Δexp (FWHM Hz)**	**Δiso (FWHM Hz)**
H1 H2	337 326	122 146
H3	335	122
H4	323	73
H5	764*	48
H5’	764*	48
H6	440	48
H7	770	48

Table 4.12 Peak widths of flutamide measured for the spectrum acquired at 100 kHz MAS and for the pure isotropic spectrum. Asterisks indicate signal overlap.

Nuclei	Δexp (FWHM Hz)	Δiso (FWHM Hz)
H3 H5	471* 396	98 98
H6	408	341
H8	471*	98
H10	431	98
H11	559*	98
H11’	599*	98

Table 4.13 Peak widths of ampicillin measured for the spectrum acquired at 100 kHz MAS and for the pure isotropic spectrum. Asterisks indicate signal overlap.

Nuclei	Δexp (FWHM Hz)	Δiso (FWHM Hz)
H2 H4	474 805*	48 98
H5	972*	98
H8	805*	98
Ar	805*, 972*	98, 98,98
H15	580	73
H16	972*	48
H17	488	73
H18	527	98

4.3 Pure Isotropic Proton NMR Spectra in Solids using Deep Learning

This chapter has been adapted with permission from: Cordova, M.; Moutzouri, P.; Simões de Almeida, B.; Torodii, D.; Emsley, L., Pure Isotropic Proton NMR Spectra in Solids using Deep Learning. *Angew Chem Int Ed Engl* **2023,** *62* (8), e202216607. (post-print)

My contribution was to be part of the application of the method, data acquisition, and results analysis. Concerning the manuscript, I was part of the review and editing process.

4.3.1 Introduction

Although the PIP concept was built on a parameter fitting approach, the PIP concept can also be constructed with a deep learning (DL) approach. Deep learning (DL) has made significant advances in many areas of science and technology over the last decade, thanks to the ability of deep neural networks (NNs) to learn complex functions in an automated manner.[279-280] In particular, convolutional neural networks (CNNs) are popular models to extract information from images or spectral data[281-283] and have been used in the context of NMR to denoise or deconvolute spectra, to reconstruct under-sampled spectra, to virtually decouple spectra, and to perform automated peak picking.[284 285-289] Recurrent neural networks (RNNs) are a class of neural network developed to process time series data. The "long short-term memory" (LSTM) architecture has been shown to outperform other types of RNNs in many applications, including language modelling. [290-293 294]In NMR, models based on the LSTM architecture have been used to reconstruct under-sampled free induction decays (FIDs).[294]

Here, by encoding two-dimensional dataset of MAS spectra recorded at different spinning rates as a series, we infer the isotropic ^{1}H NMR spectrum (i.e., the spectrum that would be obtained at infinite rate) using a modified convolutional LSTM neural network trained on millions of synthetic datasets. The model, dubbed PIPNet, yields isotropic spectra that display linewidths in the 50 – 400 Hz range, in line with expectations, from experimental sets of MAS spectra for eight molecular solids, β-aspartylalanine (β-AspAla), flutamide, thymol, L-tyrosine hydrochloride, ampicillin, L-histidine hydrochloride monohydrate, ±-N,α,-Dimethyl-3,4-methylenedioxyphenethylamine hydrochloride (MDMA) hydrochloride and molnupiravir. The model bypasses assumptions about the MAS-dependent broadening and shift parameters of neighboring peaks, suppresses artifacts arising from inconsistencies between spectra acquired at different MAS rates, and inferences of full spectra can be performed in seconds.

4.3.2 Results and Discussion

Training deep neural networks requires substantial amounts of data. Given the relatively low number of available experimental datasets of ^{1}H MAS spectra recorded at different spinning rates, and the lack of any method to independently acquire the target isotropic spectra, synthetic data were used to train the model. Figure 4.35 shows an example set of eight synthetic MAS spectra and the associated isotropic spectrum, allowing the training of the model on millions of sets of synthetic variable MAS spectra that include all the possible parameter variations in peaks positions, peak shapes, MAS dependences, phase and intensity errors, and noise as described in detail in the Experimental section of Appendix V.

The architecture of the LSTM cell used here is described in Fig. 4.35 (B) (and is described in detail in the Experimental section of Appendix V). The two main differences compared to the original description of LSTM[290] are the use of CNN layers to process the inputs and the removal of the output gate. The former allows the processing of spectral data without the need for fixed input size and independently of the particular frequencies of peaks observed, while presence of the latter was found to be unnecessary since the isotropic spectrum is directly encoded into the memory of the LSTM network C_t and H_t, and does not require decoding that depends on the last MAS spectrum fed to the network (see Fig. 4.43).

Figure 4.35 (C) shows the complete processing pipeline performed by PIPNet in order to obtain the predicted isotropic spectrum from the set of MAS spectra shown in Fig. 4.35 (A). At each step, another MAS spectrum from the set with a different rate is used as input to the network to update the state vectors of the LSTM cells. The spectra are fed into the process in order of increasing MAS rate, until all the spectra in the set (8 in Fig. 4.35 A,

but 24 in the actual model training process) have been input. After each step, the state vector H_t of the final layer is processed by a final CNN layer to yield the predicted isotropic spectrum.

In order to obtain the uncertainty of the predicted isotropic spectra, PIPNet is a committee model made up of 16 neural networks with identical architectures, but each trained on completely independent synthetic data. At inference, the mean over the 16 predictions yields the predicted isotropic spectrum, and the standard deviation gives an indication of the uncertainty associated to the prediction at each point in the spectrum. Notably, uncertainty on the order of the predicted intensity highlights regions where the predicted spectrum is unreliable.

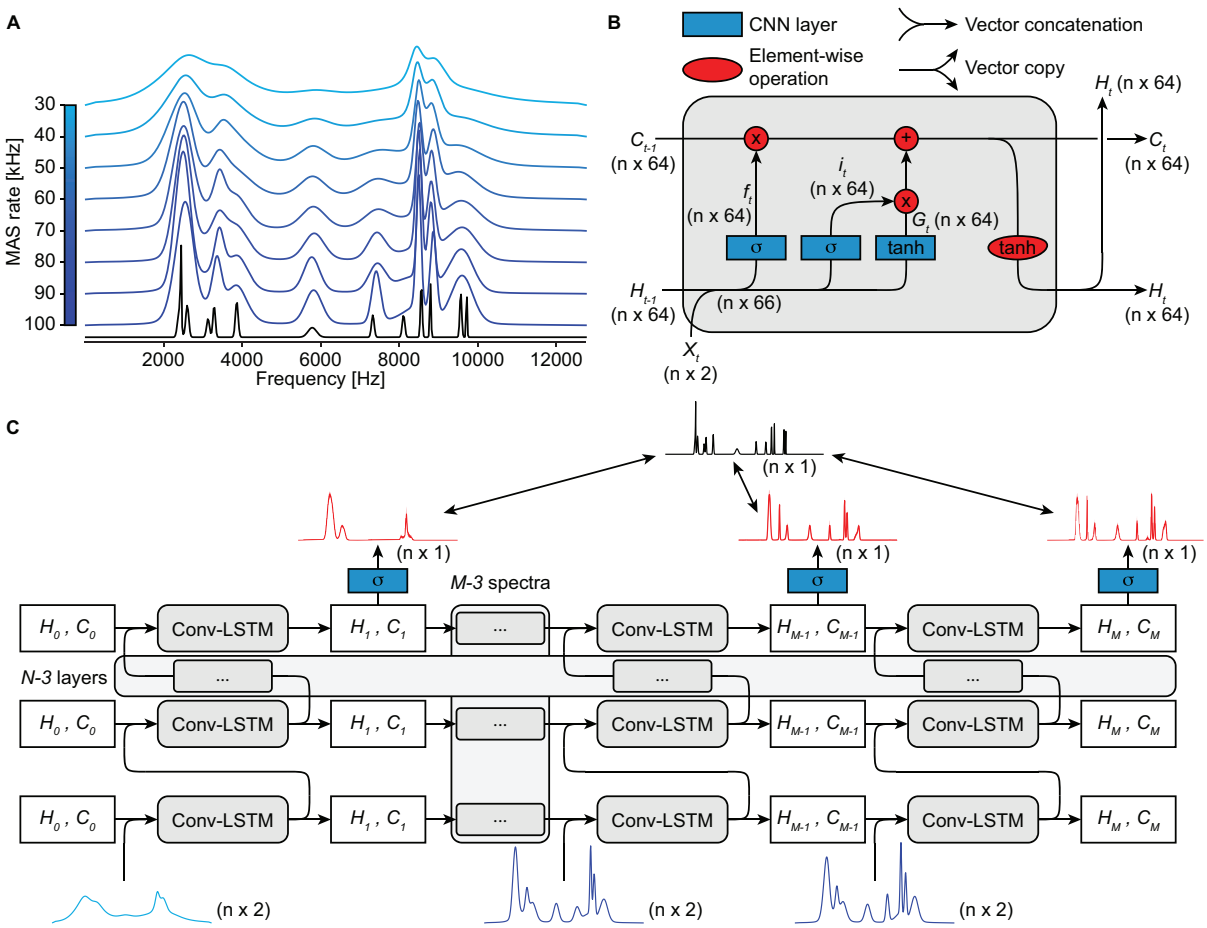

Figure 4.35 Data generation and signal processing. (A) Example of generated isotropic (black) and variable-rate MAS (blue) spectra. Here the top and bottom-most MAS spectra correspond to MAS rates of 30 and 100 kHz, respectively. (B) Convolutional LSTM cell used to process a spectrum, according to the overall scheme shown in (C) which describes the complete processing of the M = 8 MAS spectra each containing n points in (A) with N LSTM layers to obtain predicted isotropic spectra. The initial cell state vectors H_0 and C_0 are described in the text. MAS spectra are encoded as vectors with two channels, the first one being the real part of the spectrum and the second one containing the MAS rate at each point. After the last layer, the hidden state H_t is processed with a CNN with sigmoidal activation function (blue square) to produce the prediction at each step (red spectra). When training, the predictions at each step are compared with the target isotropic spectrum (black spectrum), as indicated by the double arrow lines.

Figure 4.36 (A) shows the evolution of the loss function, corresponding to the mean absolute error (MAE) between the predicted and ground-truth isotropic spectra, during the model training. The significant changes of scale in the loss after 320,000 and 800,000 training samples per model reflects the change in the weighting of the loss function (see Methods section in Appendix V). This was performed in order to promote the detection of peaks at the beginning of the training by decreasing the importance of the prediction in empty regions of the isotropic spectra. Figure 4.36 (B) shows the comparison of the predictions obtained after training each model on 16,000, 800,000, 1,600,000, 2,400,000, 3,200,000 and 4,000,000 sets of MAS spectra. Significant improvement of the predictions can be seen until 1,600,000 training samples, after which the model was considered to have converged. This is reflected both by the plateau in the loss function in Fig. .4.36 (A) and by the obtained predictions for the example shown in Fig. 4.36 (B), where the five peaks between 3500 and 5000 Hz were found to be captured by the model only after 1,600,000 training samples (although with different intensities). After

that point, the isotropic spectra obtained did not display any significant change with increased amounts of training data. Nonetheless, we selected the final model at the end of the full training process, i.e., after 4,000,000 training samples per model.

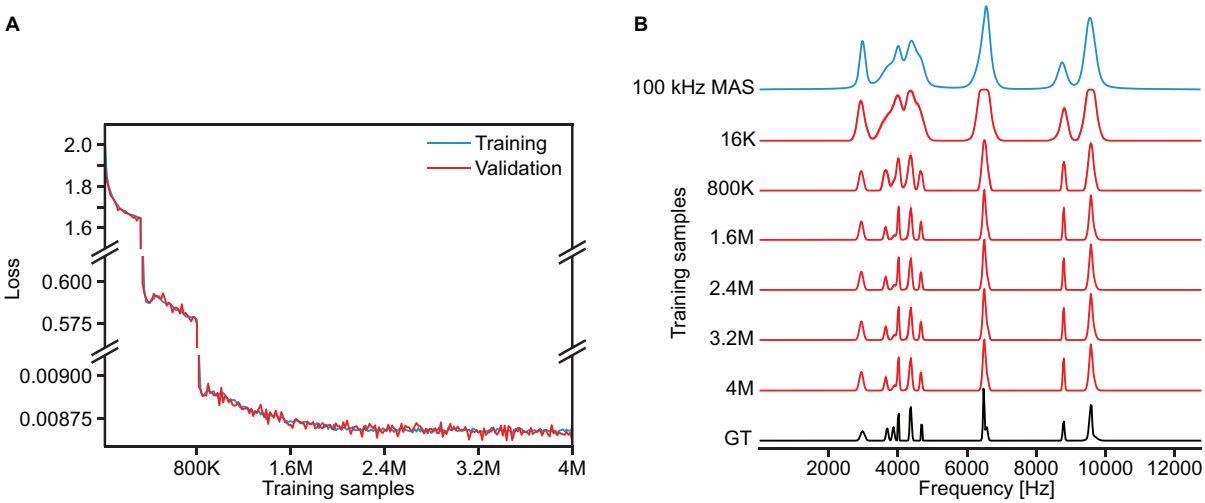

Figure 4.36 Model training. (A) Evolution of the loss function during model training. The large changes after 320,000 and 800,000 training samples per model correspond to the changes in loss function applied as described in the methods section. (B) Synthetic 100 kHz MAS spectrum (blue) and its associated ground-truth (GT) isotropic spectrum (black) compared to predictions of the model trained on 16,000, 800,000, 1,600,000, 2,400,000, 3,200,000 and 4,000,000 samples (red). The shaded areas in the predicted spectra indicates the standard deviation between the 16 neural networks making up the committee model.

Figure 4.37 displays the behavior of the model with different numbers of isotropic peaks, MAS dependences and levels of noise. The model was found to be robust to the number of peaks, with each peak resulting in a similar increase of the MAE between predicted and ground-truth isotropic spectra (see Fig. 4.37 (A)). As seen in Fig. 4.37 (D), the number of peaks is generally correctly captured both for sparse and more crowded spectra. In instances where different peaks are not captured, they are typically found to coalesce into a single, broader peak. Figures 4.37 (B) and 4.37 (E) highlight the ability of the model to capture both first- and second-order MAS dependence of linewidths and shifts in MAS spectra, as well as combined first- and second-order dependence. A purely second-order MAS dependence was found to slightly raise the error between inferred and ground-truth isotropic spectra. In addition, using a set of identical spectra with different MAS rates (no MAS dependence) was found to result in only very marginal amounts of unexpected sharpening of peaks arising from overfitting of the model, seen in the region around 8000 Hz in Fig. 4.37 (E). This indicates that PIPNet is robust to different MAS dependences. Figures 4.37 (C) and 4.37 (F) show the robustness with respect to the level of noise in the MAS spectra. The MAE between inferred and ground-truth isotropic spectra was found to increase with noise levels of 10^{-3} and above, corresponding to a signal-to-noise ratio (SNR) of 1,000 and below in 100 kHz MAS spectra. We find that the predicted spectra visually display no significant perturbations down to a SNR of 100, below which some noise and uncertainties start to appear in the inferred spectra. Importantly, the model is still able to correctly identify the regions containing signals from pure noise down to a SNR of 10. Experimental fast MAS spectra of pure organic solids typically have SNR ~1000. Artifacts are thus expected to appear only with low signal-to-noise ratio spectra, and would typically be associated with a high uncertainty (see Fig. 4.37 (F). We found that the false positive rate in predicted spectra was under 1% up to a noise level of 10-3 (SNR down to 100), and was found to be 22% with a noise level of 10^{-2} (SNR of 10) (see Figure 4.44).

The model was also found to be robust to perturbations in the MAS-dependent linewidth, shift, number of MAS spectra and range of MAS rates selected (see Fig. 4.44 and 4.45).

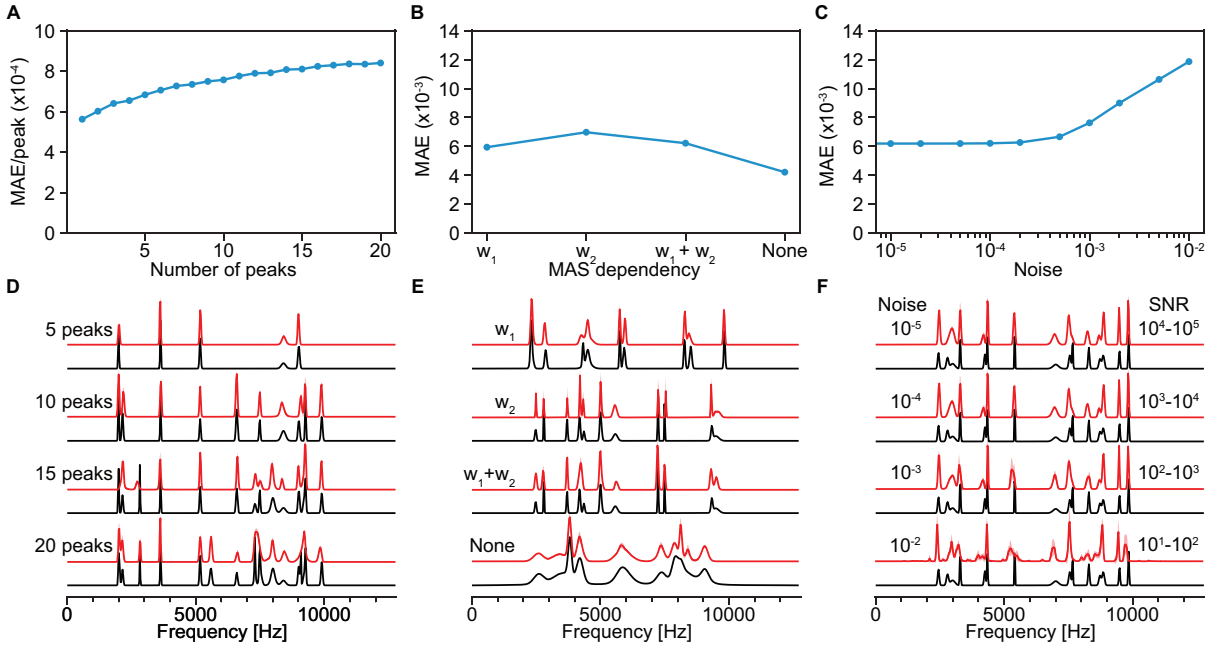

Figure 4.37 Model evaluation. (A), (B), (C) MAE between predictions and ground-truth isotropic spectra for 1,024 samples and (D), (E), (F), illustrative comparisons of predicted (red) and ground-truth (black) isotropic spectra with various (A), (D) number of peaks, (B), (E) MAS dependences (w_1: first-order, w_2: second-order), and (C), (F) noise levels. The MAE in (A) is normalized by the number of peaks. The typical range of signal-to-noise ratio (SNR) in 100 kHz MAS spectra corresponding to each level of noise is indicated in (F).

Figure 4.38 shows the isotropic spectra obtained from eight experimental sets of variable rate MAS spectra recorded on different compounds (detailed in the Experimental in Appendix V) in comparison to the corresponding 100 kHz MAS spectra. We note that the spectra obtained using PIPNet from these two-dimensional datasets were found to be similar to the parametrically fitted isotropic spectra, while notably displaying fewer artifacts (see Fig. 4.46).

The samples are microcrystalline forms of β-AspAla, flutamide, thymol, L-tyrosine hydrochloride, ampicillin, L-histidine hydrochloride monohydrate, MDMA hydrochloride and molnupiravir. The assignment and MAS datasets of β-AspAla, flutamide, thymol, L-tyrosine hydrochloride and ampicillin have already been reported previously.[46, 54, 135, 275, 295-296]

The ^{1}H and ^{13}C assignment of MDMA hydrochloride and molnupiravir are done here as described in the Experimental, based on the acquisition of 100 kHz 0.7 mm 1D ^{13}C CPMAS and ^{1}H MAS spectra, 2D ^{1}H-^{13}C hCH[175] and ^{13}C-^{13}C INADEQUATE spectra, [297-298] DFT chemical shift calculations for MDMA and the probabilistic assignment approach of Cordova et al.{Cordova, 2021 #261} (see Fig. 4.41). A DNP enhanced INADEQUATE spectrum[297-298] was recoded for MDMA (Fig. 4.41) at 9.4 T in a 3.2 mm DNP probe at 100 K.

If we look at the case of L-tyrosine hydrochloride (Fig. 4.38 D) as a representative example, the expected number of peaks is retrieved and the peak positions match expectations from assignments carried out using 2D methods (see Experimental in Appendix V). The observed linewidths in the isotropic spectrum are very significantly narrower than the 100 kHz MAS spectrum, with full widths at half maximum (FWHM) between 62 and 250 Hz (0.08 and 0.32 ppm).

We note that while the obtained isotropic spectra generally display sharper lineshapes than those measured at the highest MAS rates, finite linewidths are still anticipated, as we expect distributions of the isotropic shifts due to the presence of more or less structural disorder in the sample. Isotropic shift distributions will also be caused by anisotropic bulk magnetic susceptibility (ABMS) effects, [239-240] or as a result of imperfect B_0 homogeneity.

Importantly, no significant artifacts are seen in the isotropic spectra obtained. This behavior is seen in general across all eight samples in Fig. 4.38. The linewidths observed in the isotopic spectrum are in line with expectations from a previous analysis of the MAS dependence of the measured linewidths of the resolved peaks (1 and 3') given in Fig. 2.14[249]. It is especially notable that the isotropic spectrum predicted from the variable MAS dataset correctly identifies the 7 peaks present in the crowded spectral between 3 and 9 ppm, that are not resolved in the 100 kHz MAS spectrum.

It is important to note that PIPNet is not just identifying potential peaks and replacing them with uniformly narrow lines. We notably see in the cases of flutamide (Fig. 4.38 (B)) that there is only minor narrowing in the isotropic spectrum as compared to the 100 kHz MAS spectrum (see Table 4.18 for a list of resolved linewidths measured in both the 100 kHz MAS spectra and the isotropic spectra, for all eight compounds). Similar behavior was also observed using the parametric fitting approach (Fig. 4.46), and we thus conclude that these peaks are dominated by chemical shift broadening and not MAS dependent dipolar broadening. We note that for ampicillin we also see only limited narrowing in the isotropic spectrum from PIPNet. In this case this in contrast with the parametric fitting approach, which produced narrower lines (Fig. 4.46, Table 4.18). Here we suspect that the parametric fitting approach might be overfitting, and this is a good example of the more general and robust nature of the PIPNet model.

In addition to the six compounds previously reported,[295] here we have obtained isotropic spectra for two additional molecular solids, MDMA hydrochloride and molnupiravir (Fig. 4.38 F and 4.38 G, respectively). For MDMA hydrochloride, the expected peaks were clearly identified, except potentially for one in the aromatic (protons 7-12) regions of the spectrum. However, as seen in the HETCOR spectrum of the compound (Fig. 4.41 and dashed vertical lines in Fig. 4.38 (G)), protons 10 and 11 display very similar chemical shifts, suggesting that the peaks might overlap in the isotropic spectrum. The isotropic spectrum of molnupiravir displayed all expected peaks. In particular, the two peaks in the region between 2 and 3 ppm are clearly identified from the PIPNet spectrum, while the fitted isotropic spectrum predicts only one broader peak (Fig. 4.46). This highlights one limitation of the fitted model, as the presence of two isotropic peaks can be seen from the increasing asymmetry of the corresponding peak in the set of MAS spectra with increasing rate (Fig. 4.42 (H)), which corresponds to the two underlying isotropic peaks having different MAS-dependent shifts and/or broadenings. Considering multiple different MAS-dependent shifts in a single spectral region is thus critical here in order to correctly describe the experimental spectra as a function of MAS rate. While this is not captured by the fitted model due to the assumption that only one MAS-dependent shift is assigned to each fitted region, PIPNet makes no such assumption and thus is able to identify the two distinct resonances.

In summary, the isotropic spectra inferred by PIPNet from the experimental variable rate MAS datasets were found to display the expected number of peaks, without any prior information given about the sample measured. No significant artifacts were identified in the inferred spectra, highlighting the increased generality and robustness of the deep learning model compared to the previous fitted approach.

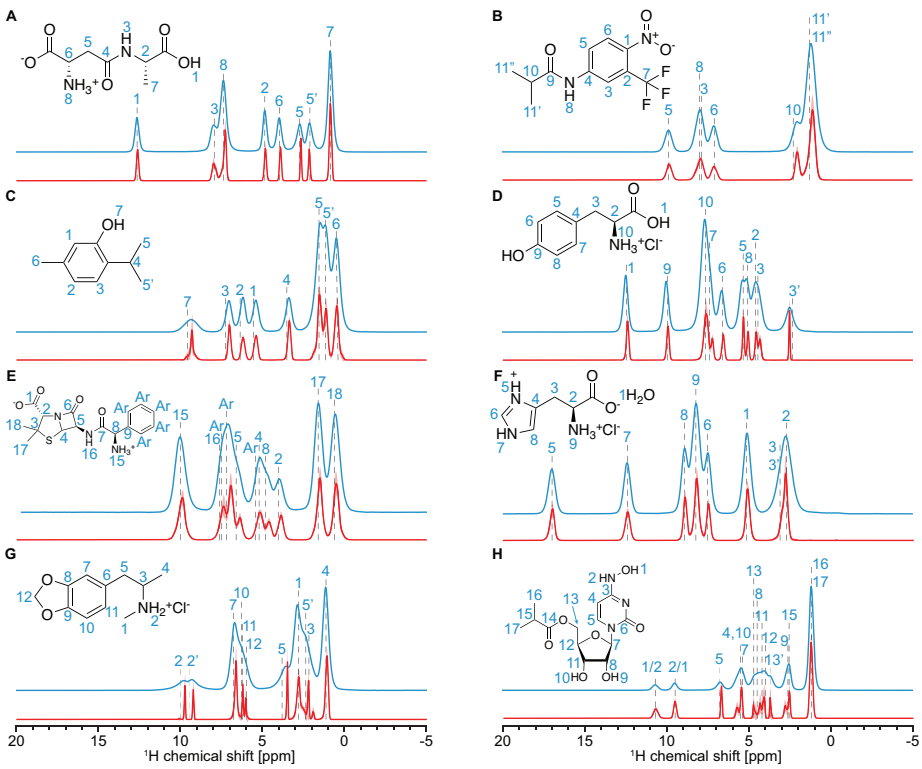

Figure 4.38 Predictions on experimental data. Experimental 100 kHz MAS spectra (blue) and isotropic spectra (red) of (A) b-AspAla, (B) flutamide, (C) thymol, (D) L-tyrosine hydrochloride, (E) ampicillin, (F) L-histidine hydrochloride monohydrate, (G)

MDMA hydrochloride and (H) molnupiravir. The isotropic spectra were obtained for each compound from a set of between 31 and 41 MAS spectra recorded at rates between 20 and 100 kHz (as detailed in the Methods in Appendix V) using the model presented here. The assignment of the 100 kHz spectra, based on two-dimensional experiments (see Experimental in Appendix V), is indicated with vertical dashed black lines and blue numbers. In (H), the assignment of protons 1 and 2 is ambiguous.

Figure 4.39 shows the comparison between the chemical shifts of 32 selected peaks from the compounds studied here, and Fig. 4.47 compares the linewidths obtained, using the deep learning approach presented here with the positions observed at 100 kHz MAS, and with the fitted approach. We find strong correlations between the observed peak positions with the three methods, with a root-mean-square error of 0.060 ppm (~50 Hz) and a R^2 coefficient above 0.999. We note that this is not a direct metric of the accuracy of our model, as the 100 kHz MAS peak positions are not at exactly the isotropic shifts,[106, 108, 213, 238, 249] and the fitting approach also suffers from shortcomings as mentioned above. The consistency between the three results does however strongly suggest that the method allows measurement of resolved isotropic shifts to within an error of 0.060 ppm. In Fig. 4.39 B, differences appear at discrete values in steps of ~0.03 ppm, corresponding to the spectral resolution. If needed, more accurate peak maxima could be obtained or by increasing the spectral resolution through zero-padding before running the prediction, or by applying more peak picking approaches to the isotropic spectrum.[289]

Figure 4.47 and Table 4.18 suggests that linewidths are generally predicted to be broader using PIPNet than with the fitting approach. Because the model was found able to predict linewidths as low as 57 Hz (0.07 ppm)(see Table 4.19), we expect these differences to arise from approximations present in the fitted approach leading to a degree of overfitting, and not from incomplete removal of MAS-dependent broadening by the machine learning model.

As seen in Fig. 4.48, the relative integrals of different spectral regions are retained in the predicted isotropic spectra compared to the experimental 100 kHz MAS spectra, with a deviation of less than ~5% of the total integral for all compounds. [289]

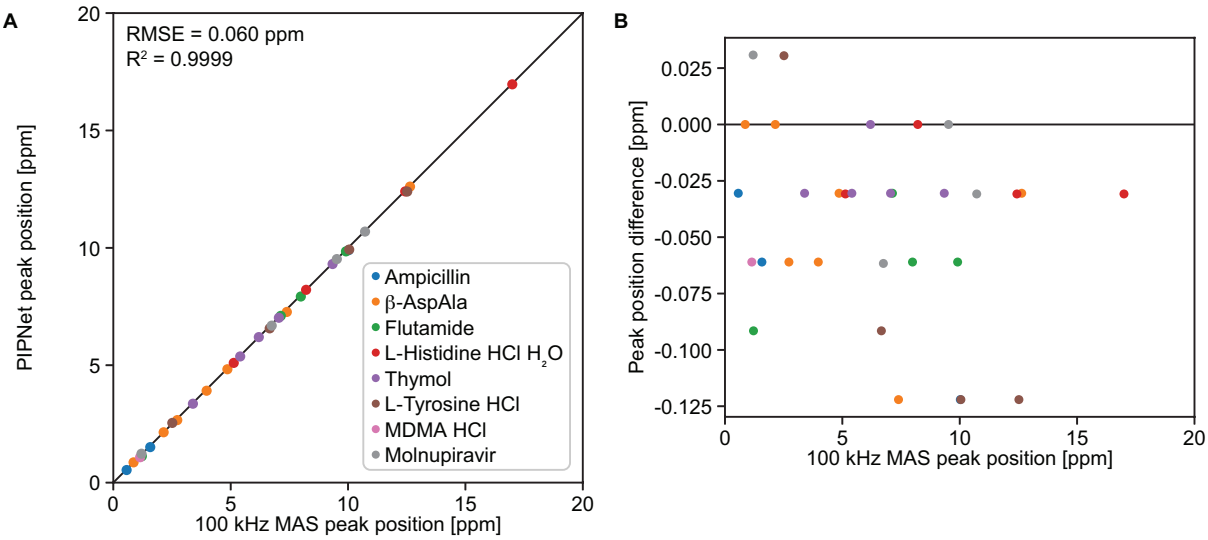

Figure 4.39 Predicted peak positions. (A) Comparison of the position of selected isolated peaks in the 100 kHz MAS and those in the isotropic spectra. (B) Difference in position of the peaks shown in (A). The black lines indicate perfect correlation.

An additional useful feature of the model presented here is the ability to predict spectra with linewidths comparable to high MAS rates (above 100 kHz) using only the lower MAS rate experimental spectra recorded. As shown in Fig. 4.40, using only experimental spectra measured between 30 and 40-50 kHz, the model was found to generate a spectrum that is sharper than the experimental 100 kHz MAS spectra of L-tyrosine hydrochloride and b-AspAla. Similar examples for the other 6 compounds are shown in Fig. 4.49. This highlights an alternative use of the model to obtain resolved spectra without the hardware needed to perform experiments at the highest MAS rates. In particular, this opens up the possibility to combine higher sensitivity of NMR experiments performed on samples prepared in, e.g., 1.3 mm or 1.9 mm diameter rotors with resolution corresponding to

100 kHz MAS, which is only currently attainable using smaller 0.7 mm diameter rotors. An example for L-histidine hydrochloride monohydrate obtained on a 1.3 mm MAS probe with 16 rates from 30 to 60 kHz is shown in Fig. 4.50. Figure 4.40 shows that adding faster MAS spectra consistently leads to increased resolution of the predicted isotropic spectra until 80 kHz, after which the predictions were generally found to converge here. (It will be interesting to see what happens at even higher experimental MAS rates in the future).

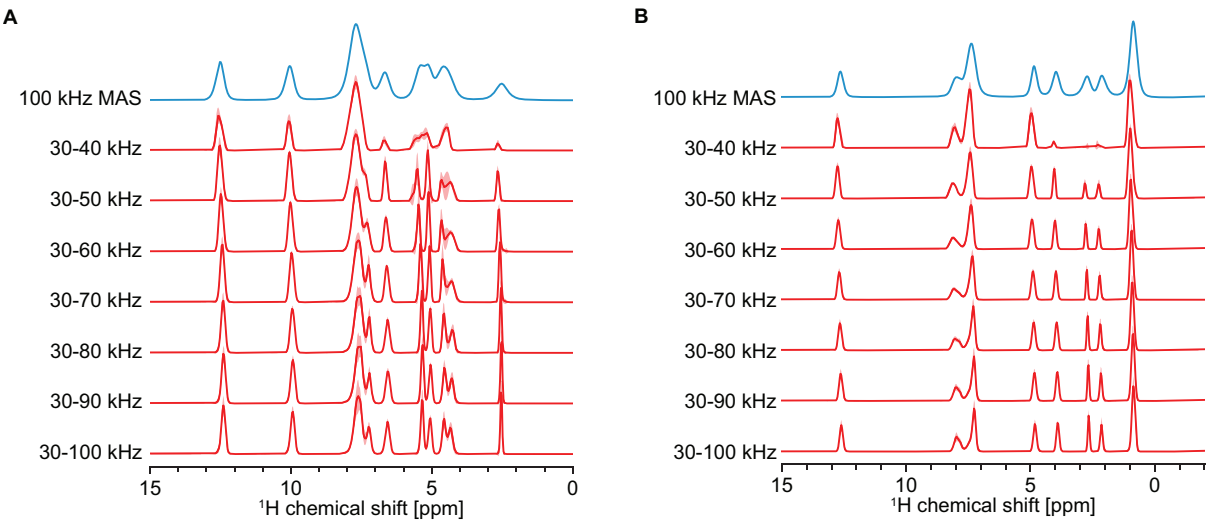

Figure 4.40 Isotropic spectra from different ranges of experimental MAS rates collected in 2 kHz increments. 100 kHz MAS spectra (blue) and isotropic spectra (red) obtained from different ranges of MAS rates for (A) L-tyrosine hydrochloride and (B) b-AspAla. The range of MAS rates used is indicated next to each isotropic spectrum.

Figure 4.51 suggests that using a lower number of experimental spectra while retaining the range of MAS rates used (40 to 100 kHz in Fig. 4.51) leads to only marginal changes in the isotropic spectra obtained, up to increments of 10 kHz between measured MAS spectra. In light of this result and those shown in Fig. 4.40 and Fig. 4.49, we consider that converged isotropic spectra can typically be obtained using spectra from 30 to at least 80 kHz MAS rate, in increments of up to 10 kHz. We note that, in general, a minimum of 5 spectra are typically required to obtain meaningful isotropic spectra (see Fig. 4.43). The quality of the isotropic spectra obtained is nonetheless expected to be higher using a larger range of MAS rates and a higher number of MAS spectra.

4.3.3 Conclusion

Here we have developed PIPNet, a deep learning approach to predict isotropic ^{1}H NMR spectra of solids from a two-dimensional dataset of variable rate MAS spectra, using a convolutional recurrent deep neural network with modified convolutional LSTM layers. The model is able to reliably predict linewidths on par with a previously introduced fitting approach, while bypassing several limitations of the latter approach and at a fraction of the computational cost, leading to faster and improved predictions. The model was applied to sets of MAS spectra for eight molecular solids and showed marked resolution improvements compared to the highest MAS rates available, with linewidths down to 57 Hz. In addition, even using only relatively low MAS rates (30-50 kHz) as input for the model led to predictions with linewidths comparable to fast MAS (>100 kHz), which opens up the possibility to obtain well-resolved ^{1}H spectra for molecular solids from experimental data recorded at spinning rates accessible on less specialized hardware, such as, e.g., 1.3 mm MAS probes.

The spectra obtained using the PIPNet model from complete sets of variable rate MAS data up to 100 kHz MAS yield the best resolved ^{1}H spectra of molecular solids recorded to date, and we anticipate that access to even faster spinning rates in the future will further improve the robustness of this method. The model is freely available at https://github.com/manucordova/PIPNet.

4.3.4 Appendix V

4.3.4.1 Experimental: Theory and Methods

Previous approach

Moutzouri *et al.*.[236] proposed a method to obtain the isotropic spectrum from a two-dimensional dataset of MAS spectra measured at different rates. To transform these data they assumed, based on predictions from average Hamiltonian theory,[103, 111, 233, 238, 249] that the lineshape of a peak in a ^{1}H MAS spectrum can be described as a convolution of the intrinsic (isotropic) lineshape of the peak, subject to a MAS-dependent frequency shift, with a MAS-dependent broadening function. Assuming an inverse linear MAS dependence of the shift and broadening, they optimized a vector of amplitudes (the isotropic spectrum), as well as the MAS-dependent shift and widths of Lorentzian and Gaussian broadening functions, such that the difference between the resulting simulated MAS spectra and experiment was minimized.

This approach to transforming the data involves assumptions and restrictions that limit its performance. Notably, there is an assumption that the MAS dependent part of the lineshape is the same across the whole spectrum. Because of this, the spectrum is broken down into a series of resolved regions, in order to minimize its impact. Further, the number of variables to fit (the amplitude vector and the MAS-dependent broadening and shift), usually ranges between 50 and 300 for each separate region, resulting in intensive computations to obtain the isotropic spectrum, typically taking several CPU hours. Separating the spectra into regions can introduce artifacts in the isotropic spectra arising from inconsistent integrals between the spectra recorded at different MAS speeds due to truncation of the spectra within the selected regions at low MAS rates. Finally, with the large number of points used, convergence can be an issue, which thus requires to perform several fits with different starting guesses, which increases the robustness of the method but at the cost of performing the fitting several times.

Data generation

Due to the substantial amount of data required to train deep neural networks and the impossibility to record isotropic spectra of solids experimentally to use as targets for the predictions, synthetic isotropic and variable MAS rate spectra were generated according to a theoretical description of the dependence of the spectra on the MAS rate. Here, to maintain the highest level of generality, a MAS spectrum is composed of a sum of peaks, where each peak $I_{\omega_r}(\nu)$ is described as a convolution between the corresponding (Gaussian) peak in the isotropic spectrum $I_\infty(\nu)$ and a Gaussian-Lorentzian sum (GLS) function: [299]

$$GLS(\nu; w, p, m) = (1-m)\exp\left[-\frac{4\ln(2)\,(\nu-p)^2}{w^2}\right] + \frac{m}{1+4\frac{(\nu-p)^2}{w^2}} \qquad (4.13)$$

where *w* is the width of the GLS function, *p* is the peak position of the GLS, here always set to the middle of the spectrum, such that convoluting the GLS with the isotropic spectrum does not affect the position of the peak, and *m* is the mixing factor describing the lineshape of the function. A mixing of 0 corresponds to a pure Gaussian function, while a mixing of 1 corresponds to a pure Lorentzian function. The ranges of possible mixing and width of the GLS were set based on observed MAS dependence of the lineshape. This function is particularly well suited to describe ^{1}H MAS broadening, where the expectation is that the lineshape is a mixture of Gaussian and Lorentzian components, and where the mixture for each spin is a function of both the MAS rate and the local dipolar coupling network.[70, 109]

In addition, a MAS-dependent shift of the frequency of the peak s_{ω_r} was added to capture the residual shift observed in MAS spectra.[106, 108, 213, 238, 249] The generation of a peak in an MAS spectrum is thus described as:

$$I_{\omega_r}(\nu) = \mathrm{FT}\left[I_\infty(t)\cdot e^{i2\pi s_{\omega_r}}\right] * GLS\left(\nu; w_{\omega_r}, p, m_{\omega_r}\right) \qquad (4.14)$$

where FT[·] is the Fourier transform and $*$ denotes the convolution operation. The multiplication of the isotropic FID $I_\infty(t)$ with a complex exponential shifts the frequency of the corresponding peak after the Fourier transform, which is then convoluted with the MAS-dependent GLS function. Spectra made up of 512 points with a time-domain sampling frequency of 12.8 kHz were generated, corresponding to a frequency domain resolution of 25 Hz.

Isotropic spectra were generated as the sum of between 1 and 15 peaks made up of one Gaussian function each, with a linewidth sampled from a uniform distribution between 50 and 200 Hz (70% probability), between 100 and 500 Hz (20% probability), or between 100 and 1000 Hz (10% probability). This was done to ensure the representation of both sharp and broad isotropic peaks in the training spectra. The sharpest linewidth (50 Hz) was selected to be twice the frequency domain resolution (25 Hz), as we observed that sharper linewidths led to artifacts seen as negative points in the isotropic spectra. To ensure all isotropic spectra are positive, we set any points of negative intensity to zero. In order to allow different intrinsic intensities to be represented, we rescaled each isotropic peak by a random factor sampled from a uniform distribution in the range [0.5, 1]. The intensity of the obtained isotropic spectra was then divided by 256 in order to obtain peak intensities roughly between 0.1 and 1. Generating spectra in this way by summing a series of Gaussian peaks with different isotropic widths and frequencies, we can include both well resolved spectra and more complex isotropic lineshapes that result from superpositions.

Twenty-four MAS rates were then selected randomly between 30 and 100 kHz, and the corresponding MAS spectra were constructed by shifting and convoluting each peak with a GLS function with parameters s_{ω_r}, w_{ω_r} and m_{ω_r} following a second-order inverse MAS dependence subject to noise.

$$w_{\omega_r} = \frac{w_1}{\omega_r} + \frac{w_2}{\omega_r^2} + \Delta w \tag{4.15}$$

$$s_{\omega_r} = \frac{s_1}{\omega_r} + \frac{s_2}{\omega_r^2} + \Delta s \tag{4.16}$$

$$m_{\omega_r} = \frac{m_1}{\omega_r} + \frac{m_2}{\omega_r^2} \tag{4.17}$$

For each peak, the value of w_1 in Eq. 3 was drawn from a uniform distribution in the range [10^7, $5{\cdot}10^7$] Hz^2 with 80% probability, and in the range [$5{\cdot}10^7$, 10^8] Hz^2 otherwise (corresponding to a contribution of 100 to 1,000 Hz to the width of the GLS at an MAS rate of 100 kHz), w_2 was set to be either 0 with a 50% probability, or a random value between 10^{11} and $5{\cdot}10^{11}$ Hz^3 (contributing to the width of the GLS by 10 to 50 Hz at an MAS rate of 100 kHz). In addition, for each MAS rate the GLS width w_{ω_r} was randomly perturbed by a value drawn from a normal distribution $\Delta w \sim \mathcal{N}(0, \sigma_w)$ Hz where σ_w was set to be 5% of the range of widths generated between the lowest and highest MAS rates with the selected values of w_1 and w_2. The value of s_1 in Eq. 4.16 was randomly sampled between -10^7 and 10^7 Hz^2 (introducing a shift contribution between -100 and 100 Hz at 100 kHz MAS), and s_2 was set to zero with an 80% probability, or to a random value between -$2{\cdot}10^{10}$ and $2{\cdot}10^{10}$ Hz^3 (corresponding to a shift between -2 and 2 Hz at 100 kHz MAS). Δs was randomly drawn from a normal distribution $\Delta s \sim \mathcal{N}(0, 25)$ Hz for each peak and each MAS rate. The GLS width and frequency shift applied to a peak in an MAS rate is described in Eqs. 4.15-4.16. The mixing m_{ω_r} was set to follow the inverse MAS dependence described in Eq. 4.17 with a probability of 50% and with the value of m_1 set to zero with a 10% probability or randomly sampled from a uniform distribution in the range [0, 10^4] Hz with 10% probability, or in the range [10^4, $5{\cdot}10^4$] Hz, and with m_2 set to zero with an 80% probability or randomly sampled between 10^8 and $5{\cdot}10^8$ Hz^2. Resulting values of m_{ω_r} above one were capped to one. Otherwise, the mixing m_{ω_r} was set to be either constant, monotonously increasing with random values between 0 and 1, or monotonously decreasing with random values between 0 and 1 with increasing MAS rate. These three dependences were considered with equal probabilities.

For each peak and each MAS rate, a random phase is drawn from a normal distribution $\mathcal{N}(0, 0.05)$ and used to distort that peak in the corresponding MAS spectrum with a probability of 50%. Additionally, each isotropic peak was assigned a 10% chance to have a decreasing intensity in MAS spectra with increasing rate by multiplying the intensity of the corresponding peak in each MAS spectrum by a value linearly decreasing between 1 and a final value sampled uniformly in the range [0.3, 0.7].

After generating the MAS spectra as described in Eq. 4.14, the intensity of the spectra was divided by 64 in order to obtain peak intensities roughly between 0.1 and 1. The ten leftmost and rightmost points of the obtained spectra were linearly smoothed to a value of zero

Deep convolutional LSTM model

The model used to encode isotropic spectra from the set of variable rate MAS spectra is a recurrent neural network with six convolutional LSTM layers adapted from a model used for precipitation nowcasting.[300] In particular, the output gate was found to be unnecessary and was removed from the LSTM cells. The vectors C_0 and H_0 describing the initial state of the cell are initialized as zero-filled vectors of the length of the spectra and with 64 channels. In each layer and for each step in the recurrent process, the previous hidden state H_{t-1} of the LSTM cell is combined with the input X_t, which is the next MAS spectrum in the series, and fed into two one-dimensional CNN layers with a sigmoidal (σ) activation function to yield the forget and input gates f_t and i_t, respectively, as well as into a CNN layer with a hyperbolic tangent (tanh) activation function to yield the vector of new candidate values G_t to add to the state. The previous state vector C_{t-1} is first weighted element-wise by f_t before the vector of candidate values G_t, weighted element-wise by i_t, is added to form the updated cell state C_t. Taking the hyperbolic tangent of C_t then yields H_t, which is used as the input for the next LSTM layer. The process is summarized in Eq. 4.18 where $*$ and $\circ$ indicate convolutions and element-wise multiplication, respectively.

$$\begin{gathered} i_t = \sigma(W_{xi} * X_t + W_{hi} * H_{t-1} + b_i) \\ f_t = \sigma\big(W_{xf} * X_t + W_{hf} * H_{t-1} + b_f\big) \\ G_t = \tanh\big(W_{xg} * X_t + W_{hg} * H_{t-1} + b_g\big) \quad C_t = f_t \circ C_{t-1} + i_t \circ G_t \\ H_t = \tanh(C_t) \end{gathered} \tag{4.18}$$

Each CNN layer corresponds to convoluting a matrix of weights *W* with the input and the previous hidden state, adding a bias *b*, and applying the activation function. We used a kernel size of 5 for all convolutional layers. After the final layer, the resulting hidden cell state H_t after each step is fed into a CNN layer with a kernel size of 5 and a sigmoidal activation function to yield the prediction of the isotropic spectrum.

MAS spectra are encoded as vectors with two channels, the first being the real part of the spectrum and the second being a constant pseudo-spectrum containing the MAS rate divided by 100 kHz in each element. At each step, a new spectrum X_t is fed into the network, in order of increasing MAS rate.

Model training

We trained a committee of 16 models with the same architecture on different generated data in order to evaluate the confidence of predictions. Each model was trained for a total of 250,000 batches of 16 different samples, each comprising one isotropic spectrum and 24 corresponding MAS spectra at different simulated MAS rates. After every 1,000 batches (16,000 training samples), the model was evaluated on 200 batches of 16 isotropic spectra. The model was trained by minimizing the mean absolute error (MAE) between the output of the model $\hat{I}_\infty(\nu)$ and the ground-truth isotropic spectrum $I_\infty(\nu)$.

Due to the sparsity of isotropic spectra, we initially convoluted the whole of each target isotropic spectrum with a Gaussian function ($G_\mathcal{L}$) in order to increase the proportion of spectra containing signal and prevent the network from initially predicting spectra containing no signal. In addition, we introduced a weight to the loss function for each frequency ν_i in the isotropic spectrum to be the maximum between 1 and *k* times the value at frequency ν_i in the isotropic spectrum (after convolution with the Gaussian function) in order to bias the training towards correctly predicting regions that contain signal. The resulting loss function is:

$$\mathcal{L} = \frac{1}{N}\sum_i \left|\hat{I}_\infty(\nu_i) - (I_\infty * G_\mathcal{L})(\nu_i)\right| \cdot \max\big(1, k \cdot (I_\infty * G_\mathcal{L})(\nu_i)\big) \tag{4.19}$$

We set the width of $G_{\mathcal{L}}$ to 75 Hz and k to 100 during the first 320,000 training samples, then reduced the width of $G_{\mathcal{L}}$ to 25 Hz and k to 10 for 480,000 additional training samples, before removing the convolution with $G_{\mathcal{L}}$ completely and setting k to zero for the rest of the training.

Random noise was introduced in the generated MAS spectra such as to match the typical signal to noise ratio observed in experimental ^{1}H MAS spectra (between 100 and 1,000 for the most intense peak at 100 kHz). The predictions were compared to the generated isotropic spectra after each step. The final predictions were obtained as the mean over the 16 models, and the uncertainties were estimated as the standard deviation of the prediction of each model.

Model evaluation

The model was evaluated by computing the MAE between synthetic ground-truth and predicted isotropic spectra for batches of 1,024 samples generated with different parameters. We investigated the effect of the number of peaks in the isotropic spectra, different MAS dependences (first-order only, first- and second-order, second-order only, or independent) of the linewidth and MAS-dependent shift, the range of MAS rates generated, the number of MAS spectra used, as well as the amount of noise introduced in the spectra themselves and in the linewidth and shift dependences.

The propensity of PIPNet to produce false positive signals was evaluated for the spectra generated with different noise levels by computing the false positive rate, defined here as the percentage of points containing signal in the inferred isotropic spectra but not containing signal in the corresponding ground-truth spectra, among all the points in the predicted isotropic spectra identified as containing signal (Figure 4.44). A point is considered to contain signal if its value is at least 1% of the maximum intensity in the whole spectrum. False positives are thus the points containing signal in the predicted isotropic spectrum but not in the ground-truth. In practice, to prevent considering lineshapes that are predicted to be broader or at a slightly different frequency with respect to the ground-truth as false positives, we only consider points containing signal in the predicted isotropic spectra as false positives if they are further than 250 Hz away from any point containing signal in the ground-truth.

Application to experimental spectra

The digital resolution of all experimental spectra (acquired as described below) was set to about 25 Hz by zero-padding the end of the FID to match the spectral resolution of the training spectra. After phasing and correcting the baseline of the recorded spectra, the spectral range between 20 and -5 ppm was extracted. All spectra were normalized by integral and scaled to a maximum amplitude of the most intense spectrum set to 0.5 in order to reproduce intensities present in the generated training spectra. Spectra with MAS rates of 30 kHz and above were used. Predictions were subsequently performed in the same manner as for synthetic spectra.

NMR experiments

The method was applied to eight different microcrystalline organic solids: β-AspAla, flutamide, thymol, L-tyrosine hydrochloride, ampicillin, L-histidine hydrochloride monohydrate, MDMA hydrochloride and molnupiravir. The assignment and MAS datasets of β-AspAla, flutamide, thymol, L-tyrosine hydrochloride and ampicillin have already been reported previously.[46, 54, 135, 236, 275, 296] The samples of MDMA hydrochloride and molnupiravir were purchased from Lipomed AG and MedChemExpress, respectively.

Assignment

Here we report the ^{1}H and ^{13}C assignment of MDMA hydrochloride and molnupiravir based on the acquisition of 100 kHz 0.7 mm 1D ^{13}C CPMAS and ^{1}H MAS spectra, 2D ^{1}H-^{13}C hCH[175] and ^{1}H-^{13}C INADEQUATE spectra, [297] DFT chemical shift calculations for MDMA and the probabilistic assignment approach of Cordova et al.{Cordova, 2021 #261} (see Fig. 4.41). The assignments of β-AspAla, flutamide, thymol, L-tyrosine hydrochloride, ampicillin and L-histidine hydrochloride monohydrate have been previously reported. }[46, 54, 135, 275, 296] A DNP enhanced INADEQUATE spectrum, [297] was recoded for MDMA (Fig. 4.41) at 9.4 T in a 3.2 mm DNP probe at 100 K. The spectra of MDMA hydrochloride were referenced by setting the ^{1}H chemical shift of proton 17 of ampicillin to 0.6 ppm and the ^{13}C chemical shifts of MDMA hydrochloride according to ref.[301]. The spectra of molnupiravir

were referenced by setting the ^{1}H chemical shift of proton 1 of L-tyrosine hydrochloride to 12.4 ppm and the ^{13}C chemical shift of carbon 6 of ampicillin to 175 ppm.

For MDMA, quaternary carbons were first identified by their absence in the short range hCH spectrum, and then further assigned by comparison to predictions of DFT shifts (Table 4.20). This led to no significant ambiguity, except for carbons labelled 8 and 9 in MDMA hydrochloride. The INADEQUATE spectrum shown in Fig. 4.41 E was used to fully assign the aromatic carbons of MDMA hydrochloride without ambiguity. The aliphatic carbon-proton pairs in MDMA hydrochloride were then assigned by comparison of the observed joint ^{1}H and ^{13}C shifts to DFT shifts (Table 4.20). The remaining protons were assigned using the ^{1}H-^{13}C hCH spectrum (Fig. 4.41 C).

For molnupiravir, quaternary carbons were first identified by their absence in the short range hCH spectrum, and then further assigned by comparison to probabilistic distributions (Fig. 4.41 F-G) {Cordova, 2021 #261} without ambiguity. Carbon 13 was assigned based on its correlation with two distinct protons (Fig. 4.41 D). The remaining carbon-proton pairs were assigned based on the most probable assignment given by Fig. 4.41 G. Protons 9 and 10 were assigned based on long-range correlations to carbons 8 and 11, respectively, observed in the hCH spectrum (Fig. 4.41 D, inset). The assignment of protons 1 and 2 was not resolved.

Variable rate MAS spectra

For each sample, spectra were acquired with a Bruker 0.7 mm room temperature HCN CP-MAS probe on an 18.81 T Bruker Avance Neo spectrometer corresponding to a ^{1}H frequency of 800 MHz, except for L-histidine hydrochloride monohydrate and molnupiravir which were acquired on a 21.14 T Bruker Avance Neo spectrometer (900 MHz ^{1}H frequency). The spectra of ampicillin, flutamide, L-histidine hydrochloride monohydrate, β-AspAla, L-tyrosine hydrochloride and thymol were recorded at MAS rates between 30 and 100 kHz. The spectra of MDMA hydrochloride and molnupiravir were measured from 40 to 100 kHz MAS rates. All spectra were measured in steps of 2 kHz. The magic angle was set for each sample by maximizing the T_2' of the proton signal at 100 kHz, the 90° pulse width was optimized, and the data was recorded with active temperature regulation to keep the sample temperature at about 295 K across the range of MAS rates. The thymol and molnupiravir data were acquired at a constant VT temperature of 275 K. The pulse sequence used was a rotor synchronized spin echo for background suppression. The echo delay was equal to one rotor period for all samples except for molnupiravir, for which two rotor periods were used. For L-histidine hydrochloride monohydrate, an additional dataset of ^{1}H MAS spectra was recorded using a Bruker 1.3 mm room temperature HDCN CP-MAS probe on a 21.14 T Bruker Avance Neo spectrometer (900 MHz ^{1}H frequency). All the acquisition parameters and raw NMR data are available in Tables S1-S4. The spectra of ampicillin, flutamide, β-AspAla, L-tyrosine hydrochloride and thymol used are those already reported in ref. [236]. The two-dimensional datasets of MAS spectra recorded at different MAS rates for all compounds are shown in Fig. 4.42.

GIPAW DFT computation of chemical shifts of MDMA hydrochloride

All DFT computations were performed using the plane-wave DFT software Quantum ESPRESSO version 6.5.[302-303] Atomic positions of the crystal structure of MDMA (Refcode: NEDMIS)[304] were first optimized at the PBE[305] level of theory using Grimme D2 dispersion correction[306] and ultrasoft pseudopotentials obtained from the PSLibrary version 1.0.0.[307] Wavefunction and charge density energy cutoffs were set to 160 and 1,280 Rydberg, respectively. A 2x2x1 Monkhorst-pack grid of k-points was used.[308] Shielding computation was subsequently performed using the GIPAW method. [309-310] The computed shieldings were converted to chemical shift by linear regression against experimentally measured shifts.

4.3.4.2 Supplementary Tables

Table 4.14 Experimental details of all spectra datasets used in this study. Raw data is available at the link given above. The data for β-AspAla, flutamide, thymol, L-tyrosine hydrochloride and ampicillin are the same as previously reported.[236]

Sample	MAS range (kHz)	Step Size (kHz)	VT (K)	90° RF amplitude (kHz)	d1(s)	Number of FID points	SW (kHz)
β-AspAla	100 -30	2	275-295	277	6	2048	100
Flutamide	100 -30	2	275-295	286	18	2048	100
Thymol	100 -30	2	275	277	6	1024	100
L-tyrosine hydrochloride	100 -30	2	275-295	294	5	2048	100
Ampicillin	100 -30	2	275-295	286	3	4096	100
L-histidine hydrochloride monohydrate	100 -30	2	285-295	305	16	4096	227
MDMA hydrochloride	100 -40	2	275-295	277	7	2048	100
Molnupiravir	100 -40	2	275	333	30	4096	227
L-histidine hydrochloride monohydrate (1.3mm probe)	60 -30	2	265-290	114	13.5	2048	100

Table 4.15 Experimental details of ^{13}C CP spectra of MDMA hydrochloride and molnupiravir. Exponential line broadening of 100 Hz was applied prior to Fourier transform of MDMA hydrochloride ^{13}C CP spectrum.

Sample	B0 field (MHz)	MAS rate (kHz)	VT (K)	d1(s)	Number of FID points	^{1}H-^{13}C CP contact time (ms)	Acquisition time (ms)	^{1}H decoupling during acquisition	Size of real spectrum
MDMA hydrochloride	900	100	295	8	2776	3	10	Waltz16 (10 kHz)	16384
Molnupiravir	900	100	275	15	2776	3	10	Waltz16 (10 kHz)	16384

Table 4.16 Experimental details of hCH spectra of MDMA hydrochloride and molnupiravir. Exponential line broadening of 50 Hz was applied in the direct dimension prior to Fourier transform of MDMA hydrochloride hCH. Exponential line broadening of 50 and 500 Hz was applied in the direct and indirect dimension, respectively, prior to Fourier transform of molnupiravir hCH.

Sample	B0 field (MHz)	MAS rate (kHz)	VT (K)	d1(s)	Number of FID points (F2; F1)	^{1}H-^{13}C CP contact time (ms)	^{1}H-^{13}C back CP contact time (ms)	^{1}H decoupling during t_1	^{13}C decoupling during t_2	Size of real spectrum	Acquisition time (ms)
MDMA hydrochloride	800	100	275	7	1638/128	2.5	0.5	Waltz16 (10 kHz)	-	8192/512	1 in F2 10 in F1
Molnupiravir	900	100	275	15	4096/128	3	1.5	Waltz16 (10 kHz)	Waltz16 (6 kHz)	8192/256	1 in F2 22.5 in F1

Table 4.17 Experimental details of ^{13}C INADEQUATE spectrum of MDMA hydrochloride impregnated with AMUPOL in DNP juice. Exponential line broadening of 300 Hz was applied both in the direct and indirect dimension prior to Fourier transform.

Sample	B0 field (MHz)	MAS rate (kHz)	VT (K)	d1(s)	Number of FID points	^{1}H-^{13}C CP contact time (ms)	^{1}H decoupling during t_1 and t_2	Acquisition time (ms)	Size of real spectrum
MDMA hydrochloride	400	10	100	2.2	1024/50	2	Spinal64 (100 kHz)	5 in F2 0.75 in F1	8192 /1024

Table 4.18 Measured frequencies and linewidths of selected isolated peaks. Comparison of the position and linewidth (FWHM) of selected isolated peaks in experimentally measured 100 kHz MAS spectra, PIPNet predicted isotropic spectra, and spectra predicted using the previous fitting approach (PIP). The 100 kHz spectra for β-AspAla, flutamide, thymol, L-tyrosine hydrochloride and ampicillin are the same as previously reported[236]

Compound	Label	Peak position [ppm]			Linewidth (FWHM) [ppm / Hz]		
		100 kHz MAS	PIPNet	PIP	100 kHz MAS	PIPNet	PIP
Ampicillin	18	0.57	0.54	0.46	0.66 / 529	0.38 / 307	0.16 / 128
	17	1.57	1.51	1.47	0.60 / 480	0.34 / 275	0.11 / 92
	15	10.03	9.90	9.98	0.72 / 579	0.44 / 355	0.11 / 90
β-AspAla	7	0.86	0.86	0.79	0.34 / 268	0.16 / 129	0.07 / 52
	5’	2.14	2.14	2.01	0.39 / 308	0.11 / 90	0.06 / 48
	5	2.72	2.66	2.68	0.39 / 309	0.09 / 73	0.03 / 27
	6	3.97	3.91	3.87	0.34 / 270	0.14 / 110	0.08 / 66
	2	4.86	4.83	4.75	0.28 / 224	0.15 / 122	0.04 / 31
	8	7.39	7.27	7.26	0.44 / 355	0.17 / 135	0.07 / 59
	1	12.64	12.61	12.54	0.29 / 229	0.15 / 123	0.11 / 89
Flutamide	11’/11”	1.21	1.12	1.11	0.70 / 559	0.38 / 301	0.11 / 90
	6	7.13	7.10	7.17	0.51 / 407	0.41 / 326	0.08 / 67
	3/8	7.99	7.93	7.84	0.58 / 461	0.46 / 368	0.08 / 62
	5	9.91	9.85	9.91	0.49 / 393	0.37 / 295	0.40 / 319
L-histidine hydrochloride monohydrate	1	5.13	5.10	5.10	0.52 / 472	0.29 / 256	0.07 / 65
	9	8.21	8.21	8.21	0.65 / 588	0.30 / 270	0.23 / 210
	7	12.44	12.40	12.40	0.46 / 412	0.34 / 308	0.35 / 316
	5	17.00	16.97	16.97	0.49 / 444	0.31 / 278	0.32 / 287
Thymol	4	3.39	3.36	3.31	0.42 / 333	0.20 / 161	0.15 / 122
	1	5.41	5.37	5.23	0.43 / 340	0.27 / 216	0.27 / 215
	2	6.20	6.20	6.11	0.39 / 315	0.27 / 212	0.23 / 183
	3	7.05	7.02	6.91	0.41 / 330	0.20 / 159	0.26 / 211
	7	9.34	9.31	9.29	0.94 / 749	0.14 / 112	0.08 / 62
L-tyrosine hydrochloride	3’	2.51	2.54	2.47	0.50 / 396	0.08 / 62	0.08 / 68
	6	6.66	6.57	6.49	0.44 / 353	0.18 / 147	0.03 / 25
	9	10.05	9.93	9.88	0.35 / 282	0.17 / 139	0.07 / 58
	1	12.52	12.40	12.32	0.33 / 264	0.17 / 132	0.07 / 53
MDMA hydrochloride	4	1.14	1.08	1.04	0.43 / 341	0.19 / 151	0.07 / 59
Molnupiravir	13/14	1.20	1.23	1.18	0.31 / 277	0.20 / 180	0.04 / 36
	4	6.75	6.69	6.64	0.43 / 387	0.10 / 89	0.07 / 63
	1/2	9.52	9.52	9.51	0.35 / 318	0.19 / 173	0.20 / 179
	2/1	10.72	10.69	10.65	0.42 / 380	0.33 / 295	0.46 / 414

Table 4.19 Additional frequencies and linewidths of selected isolated peaks in isotropic spectra. Position and linewidth (FWHM) of selected isolated peaks in PIPNet predicted isotropic spectra, excluding peaks already present in Table 4.18.

Compound	Label	Peak position [ppm]	Linewidth (FWHM) [ppm / Hz]
Ampicillin	2	3.89	0.36 / 290
β-AspAla	3	7.97	0.30 / 238
Flutamide	10	2.04	0.28 / 226
L-histidine hydrochloride monohydrate	6	7.50	0.25 / 203
	8	8.92	0.25 / 201
Thymol	6	0.46	0.28 / 225
L-tyrosine hydrochloride	8	5.05	0.09 / 71
	5	5.35	0.12 / 98
	10	7.61	0.32 / 252
MDMA hydrochloride	3	1.94	0.12 / 98
	5’	2.21	0.10 / 76
	1	2.82	0.22 / 173
	5	3.49	0.07 / 58
	12	6.02	0.07 / 57
	10/11	6.21	0.08 / 61
	7	6.64	0.14 / 112
	2’	9.23	0.08 / 65
	2	9.75	0.08 / 62
Molnupiravir	13’	3.73	0.09 / 71
	7	5.48	0.14 / 109

Table 4.20 Chemical shift assignment of MDMA hydrochloride. Assignment of ^{1}H and ^{13}C chemical shifts of MDMA hydrochloride.

Label	^{1}H exp. [ppm]	^{13}C exp. [ppm]	^{1}H DFT [ppm]	^{13}C DFT [ppm]
1	2.8	34	3.1	28
2	9.5, 10.0	-	9.9, 10.6	-
3	2.2	60	2.2	59
4	1.1	21	1.2	14
5	2.4, 3.8	38	2.5, 3.8	32
6	-	132	-	129
7	6.8	112	7.2	109
8	-	149	-	151
9	-	148	-	149
10	6.3	110	7.4	106
11	6.2	125	6.5	122
12	6.0	105	7.3, 7.9	110

Table 4.21 Chemical shift assignment of MDMA hydrochloride. Assignment of ^{1}H and ^{13}C chemical shifts of molnupiravir. A slash "/" indicates ambiguous assignments.

Label	^{1}H chemical shift [ppm]	^{13}C chemical shift [ppm]
1	9.5 / 10.7	-
2	10.7 / 9.5	-
3	-	140
4	5.5	104
5	6.8	128
6	-	154
7	5.4	86
8	4.5	70
9	2.7	-
10	5.4	-
11	4.2	68
12	10.0	80
13	3.7, 4.7	63
14	-	176
15	2.6	34
16	1.2	19 / 20
17	1.2	20 / 19

4.3.4.3 Supplementary Figures

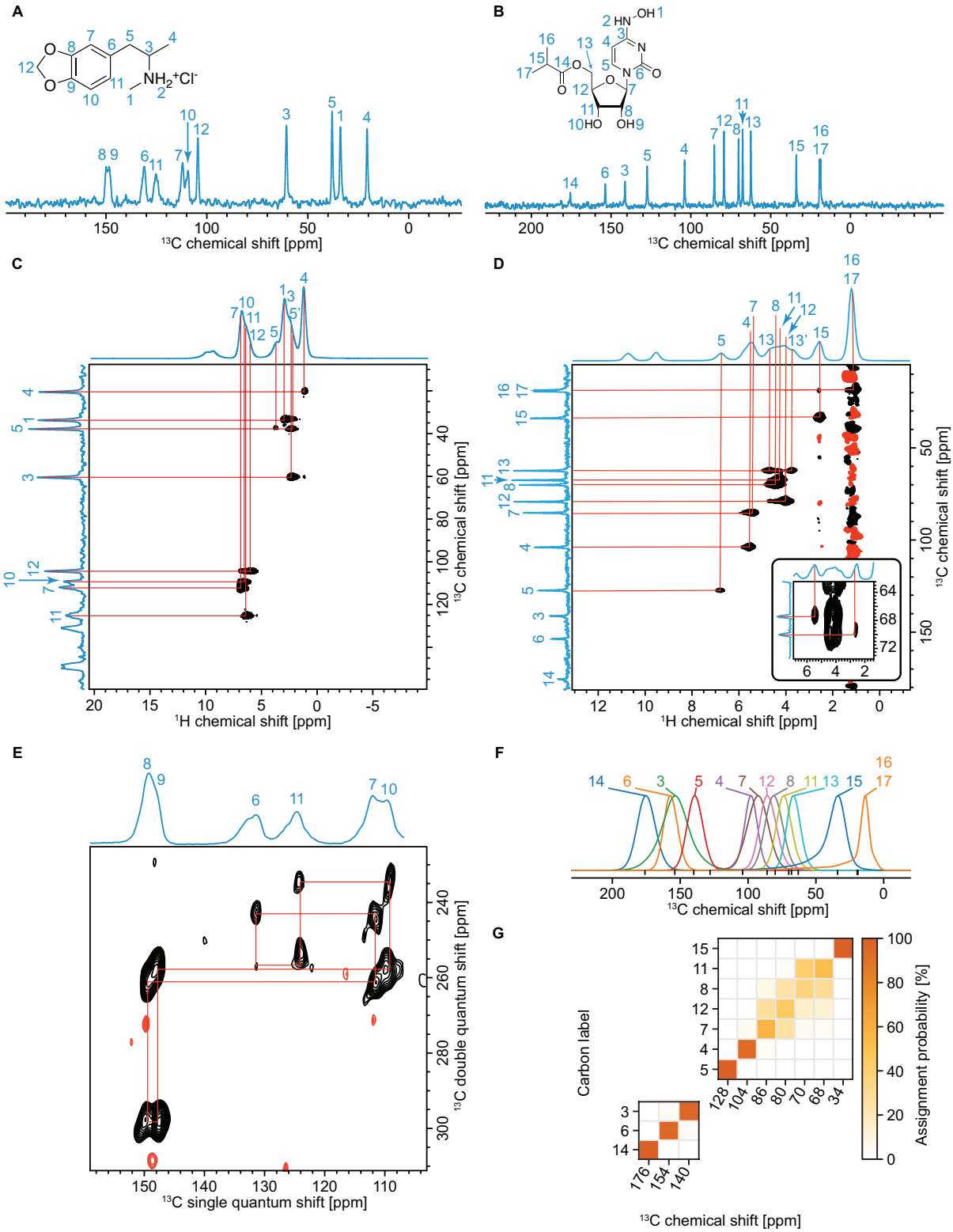

Figure 4.41 NMR experiments used for assignment. 100 kHz MAS (A), (B) ^{13}C CPMAS and (C), (D) ^{1}H-^{13}C hCH spectra of (A), (C) MDMA hydrochloride (18.8 T) and (B), (D) molnupiravir (21.1 T). (E) 13C-13C INADEQUATE spectrum of the aromatic region of MDMA hydrochloride. (F) Statistical distributions of ^{13}C chemical shifts obtained from the bonding environment of each carbon in molnupiravir and compared to the experimentally measured shifts (black vertical lines). (G) Probabilistic assignment of ^{13}C chemical shifts of quaternary and CH carbons of molnupiravir. Complete parameter sets and pulse sequences used to obtain the spectra are available with the raw data at the link given above. Blue numbers and red lines indicate the assignments obtained.

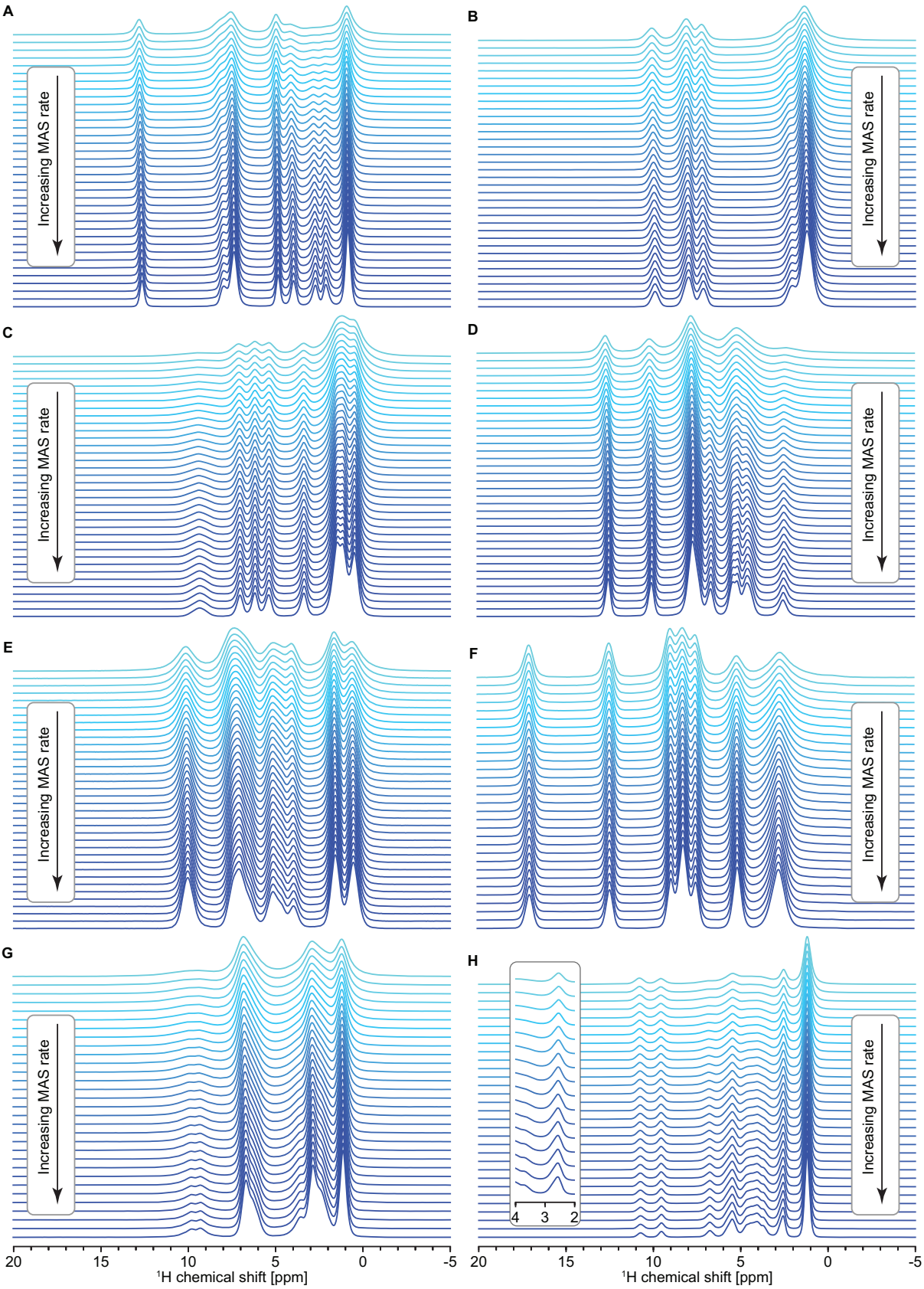

Figure 4.42 Experimental sets of variable-rate MAS spectra recorded for (A) b -AspAla, (B) flutamide, (C) thymol, (D) L-tyrosine hydrochloride, (E) ampicillin, (F) L-histidine hydrochloride monohydrate, (G) MDMA hydrochloride and (H) molnupiravir. The insert in (H) shows the 2-4 ppm region of every other spectrum recorded for molnupiravir, displaying the increasing asymmetry of the peak observed with increasing MAS rate. The data for (A-E) are the same as previously reported.

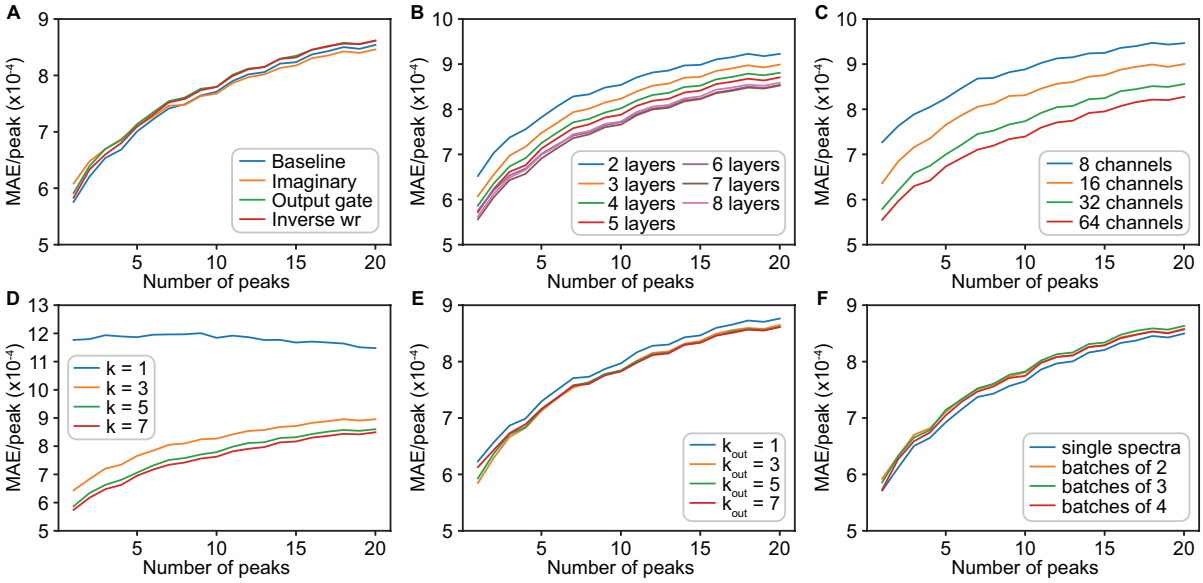

Figure 4.43 Model optimization. MAE between predictions and ground-truth isotropic spectra for 1,024 samples with various numbers of peaks obtained with models trained with different (A) encoding of MAS spectra and with LSTM cells containing the output gate (green line), (B) number of layers, (C) number of hidden channels, (D) kernel sizes in the LSTM cells, (E) kernel sizes to convert the state vector of the last layer to the inferred isotropic spectra, and (F) numbers of spectra fed to the network at each step. In (A), "baseline" (blue line) corresponds to the encoding described in the Experimental. "Imaginary" (orange line) corresponds to the addition of the imaginary part of the MAS spectra as an additional channel to the input vector. "Output gate" (green line) corresponds to the original convolutional LSTM cell with an output gate. "Inverse wr" (red line) corresponds to encoding the inverse of the MAS rate instead of the (normalized) MAS rate as described in the methods section.

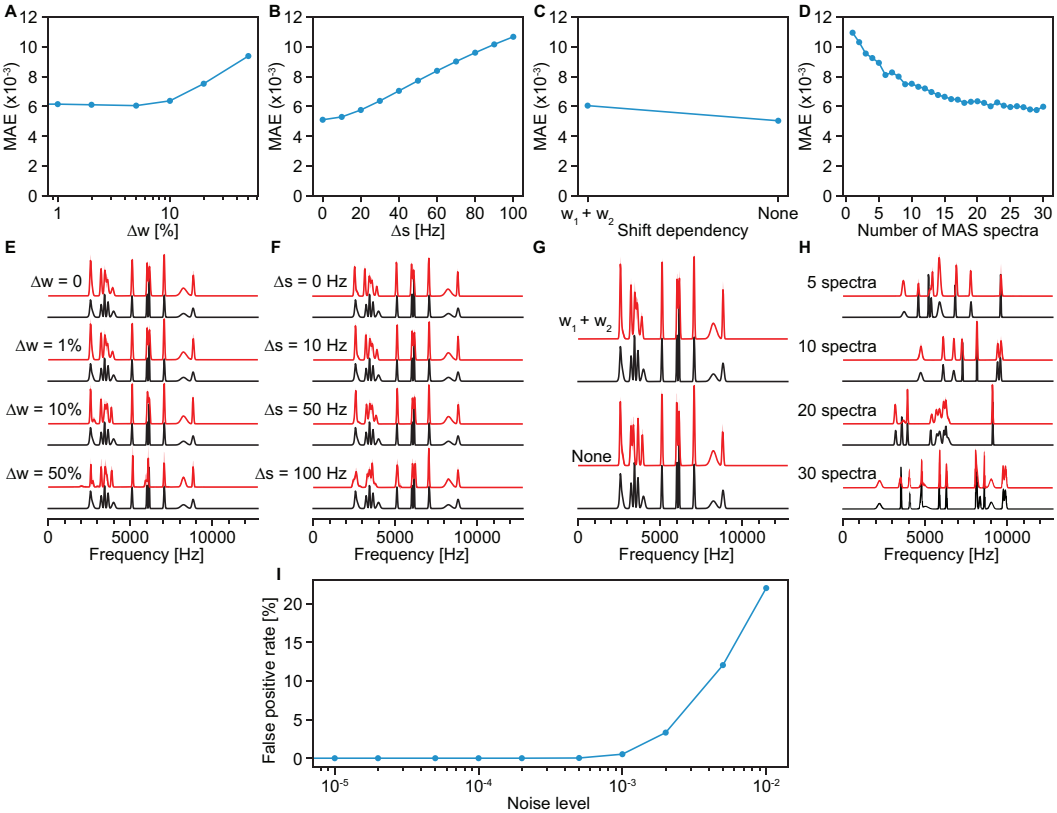

Figure 4.44 Model evaluation: MAS dependencies, number of spectra and false positive rate. (A), (B), (C), (D) MAE between predictions and ground-truth isotropic spectra for 1,024 samples and (E), (F), (G), (H) illustrative comparisons of predicted (red) and ground-truth (black) isotropic spectra with various (A), (E) levels of noise in the MAS-dependent width (see Eq. 3), (B), (F) levels of noise in the MAS-dependent shift parameter (see Eq. 4), (C), (G) shift dependences and (D), (H) numbers of MAS

spectra fed to the network. (I) False positive signal rate (as defined above) observed in the isotropic spectra predicted from synthetic MAS spectra as a function of the noise level.

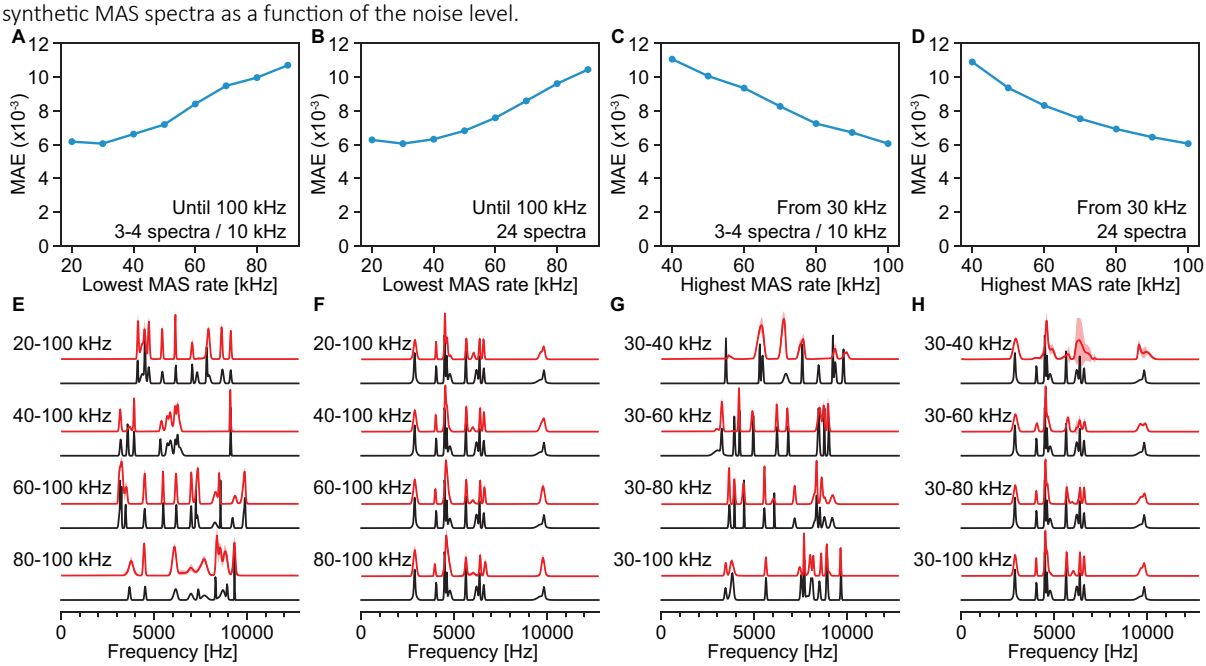

Figure 4.45 Model evaluation: MAS rate ranges. (A), (B), (C), (D) MAE between predictions and ground-truth isotropic spectra for 1,024 samples and (E), (F), (G), (H) illustrative comparisons of predicted (red) and ground-truth (black) isotropic spectra obtained from MAS datasets containing various (A), (B), (E), (F) lower bounds for the MAS rate while keeping the higher bound to 100 kHz and (C), (D), (G), (H) higher bounds for the MAS rate while keeping the lower bound to 30 kHz. In (A), (C), (E) and (G) the number of MAS spectra generated was set such that there are on average between 3 and 4 spectra per 10 kHz MAS rate range. In (B), (D), (F) and (H), the number of MAS spectra generated was set to 24 regardless of the range of MAS rates considered.

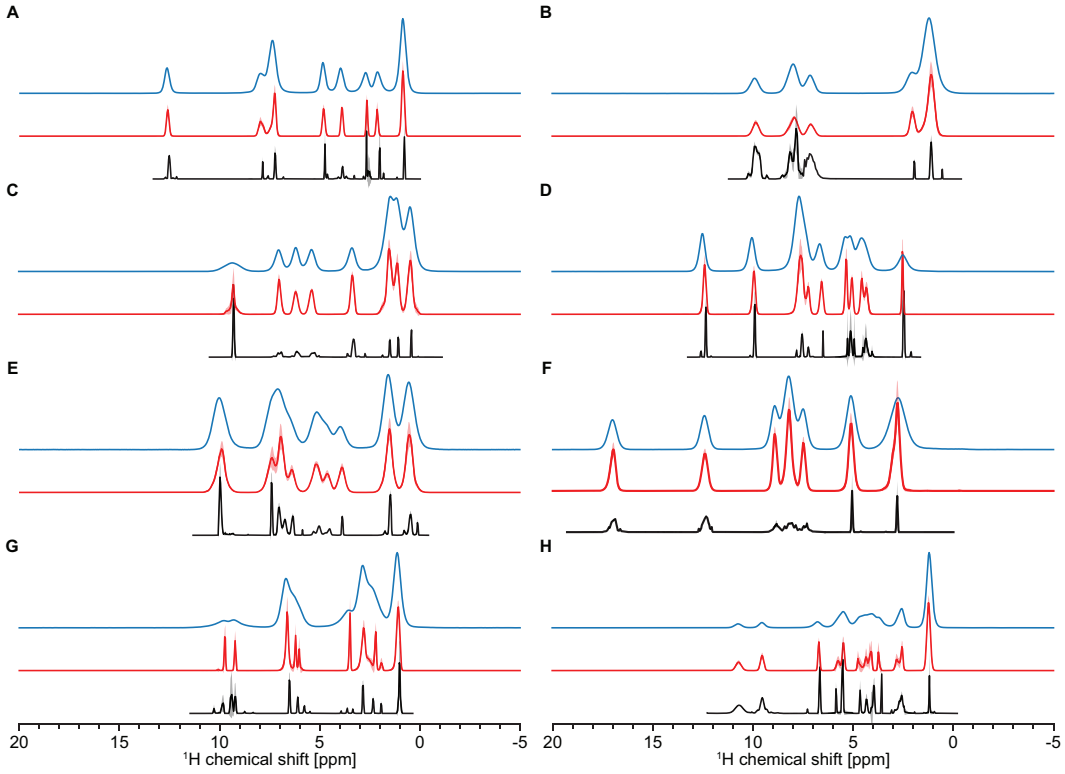

Figure 4.46 Comparison with the previous approach. 100 kHz MAS spectra (blue) and isotropic spectra of (A) b-AspAla, (B) flutamide, (C) thymol, (D) L-tyrosine hydrochloride, (E) ampicillin, (F) L-histidine hydrochloride monohydrate, (G) MDMA hydrochloride and (H) molnupiravir obtained using PIPNet (red) and the previous approach (black).

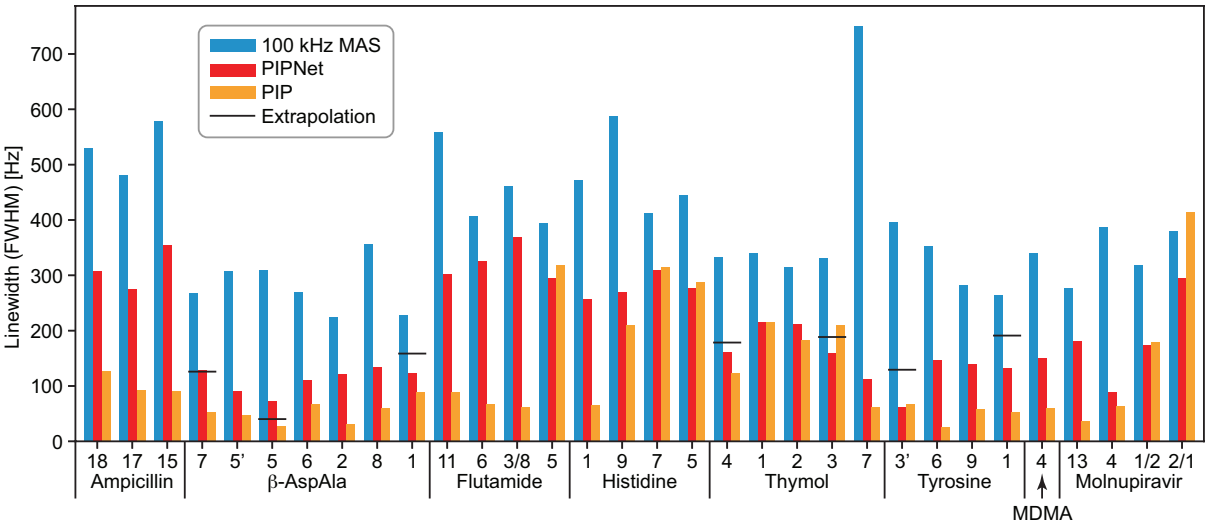

Figure 4.47 Linewidth comparison. Comparison of the linewidth of selected isolated peaks in 100 kHz MAS spectra (blue) and isotropic spectra obtained using PIPNet (red) and the previous fitting approach (orange). Black lines indicate the linewidths obtained from extrapolation of the linewidths in MAS spectra, assuming a first-order inverse MAS dependence .

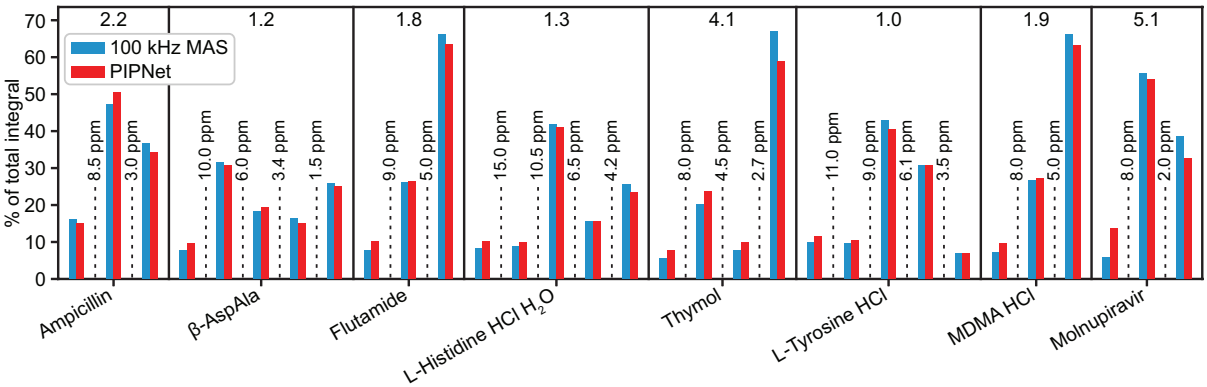

Figure 4.48 . Relative integrals. Comparison of the integral of separate regions from the 100 kHz MAS spectra (blue) and predicted isotropic spectra (red). The mean absolute error on the percentage of total integral of regions for each compound is indicated at the top of each panel.

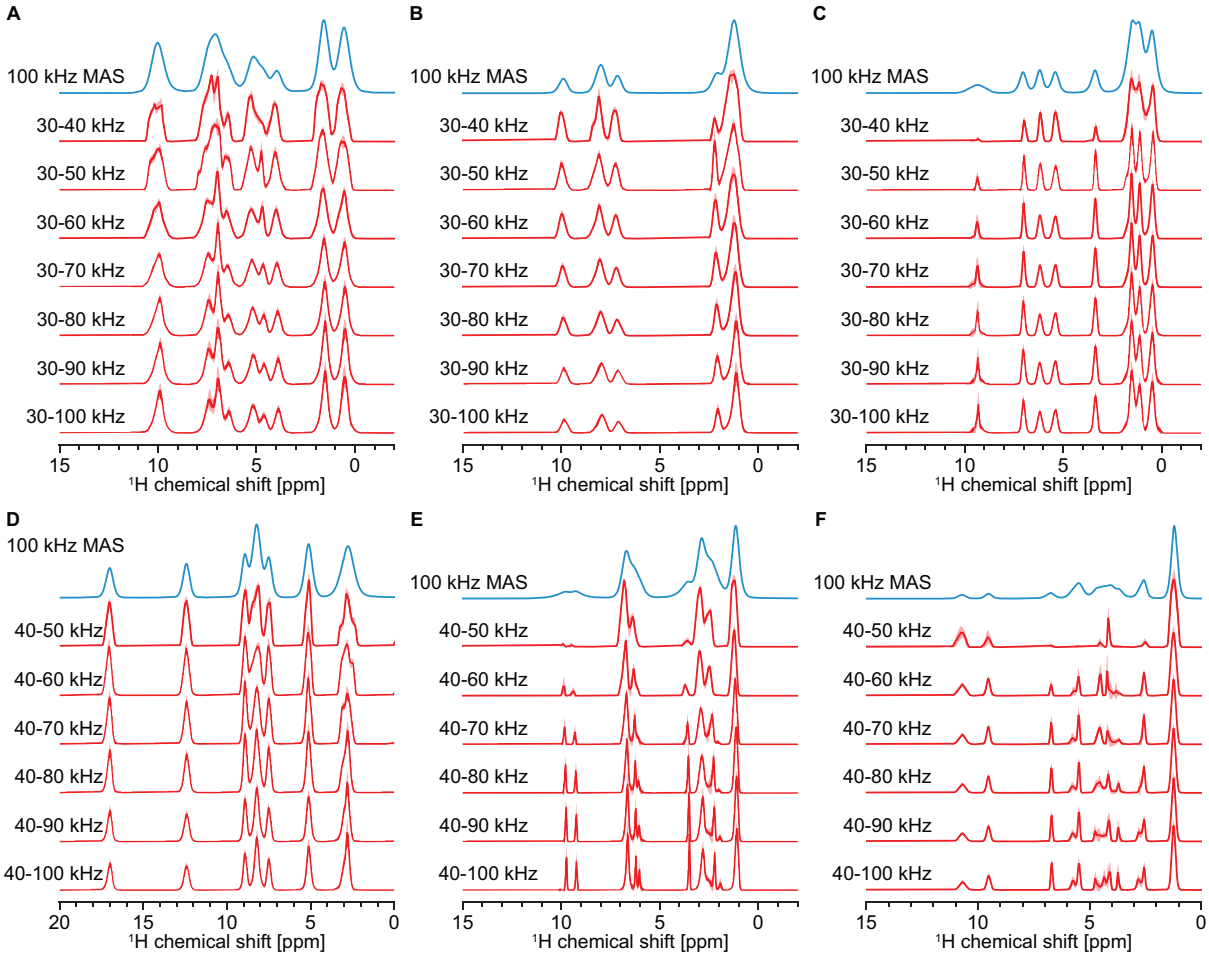

Figure 4.49 Isotropic spectra from different ranges of experimental MAS rates collected in 2 kHz increments. 100 kHz MAS spectra (blue) and isotropic spectra (red) obtained from different ranges of MAS rates for (A) ampicillin, (B) flutamide, (C) thymol, (D) L-histidine hydrochloride monohydrate, (E) MDMA hydrochloride and (F) molnupiravir. The range of MAS rates used is indicated next to each isotropic spectrum.

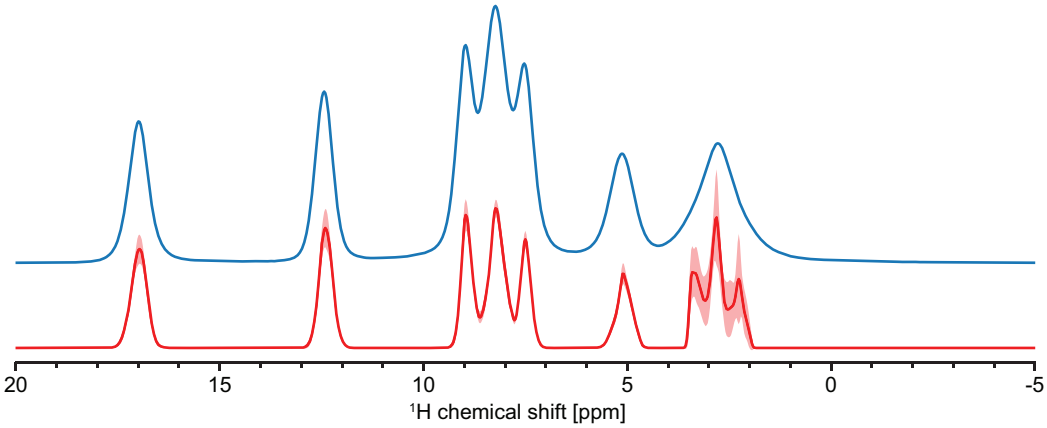

Figure 4.50 60 kHz MAS spectrum (blue) and isotropic spectrum (red) obtained from a dataset of 16 MAS spectra of L-histidine hydrochloride obtained using a 1.3 mm rotor.

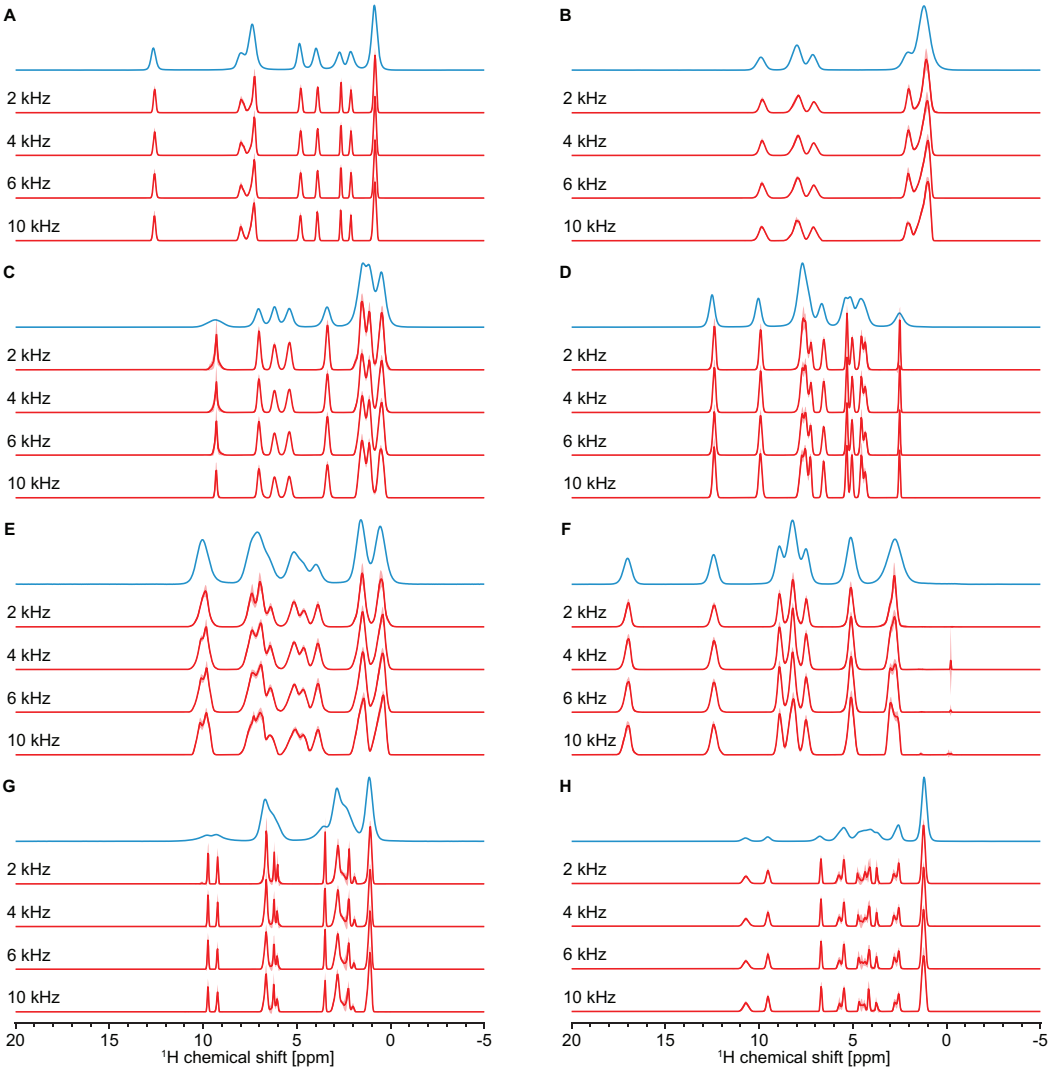

Figure 4.51 Isotropic spectra from different increments of experimental MAS rates measured between 40 and 100 kHz. 100 kHz MAS spectra (blue) and isotropic spectra (red) obtained from different MAS rate increments for (A) b-AspAla, (B) flutamide, (C) thymol, (D) L-tyrosine hydrochloride, (E) ampicillin, (F) L-histidine hydrochloride monohydrate, (G) MDMA hydrochloride and (H) molnupiravir. The MAS rate increment used is indicated next to each isotropic spectrum.

4.4 Two-dimensional Pure Isotropic Proton Solid State NMR

This chapter has been adapted with permission from: Moutzouri, P.; Cordova, M.; Simões de Almeida, B.; Torodii, D.; Emsley, L., Two-dimensional Pure Isotropic Proton Solid State NMR. *Angew Chem Int Ed Engl* **2023,** *62* (21), e202301963. (post-print)

My contribution was to be part of the application of the method, data acquisition, and results analysis. Concerning the manuscript, I was part of the review and editing process.

4.4.1 Introduction

Although high-resolution one-dimensional spectra are useful, most applications of NMR spectroscopy today require two-dimensional correlation experiments. In this respect, the possibility of measuring ultrahigh-resolution ^{1}H–^{1}H correlations is especially attractive, as it enables both structure determination and assignment.

Here, we extend the PIP approach to a second dimension in order to obtain ultra-high resolution ^{1}H–^{1}H double-quantum/single-quantum[192] (DQ/SQ) dipolar correlation spectra and ^{1}H–^{1}H spin-diffusion[311] (PSD) spectra. We illustrate the method on L-tyrosine hydrochloride and ampicillin, where we obtain two-dimensional spectra with significantly higher resolution as compared to corresponding spectra acquired at 100 kHz MAS. The spectral resolution is very significantly increased in both dimensions, allowing the identification of resolved isotropic correlation peaks that were overlapped in the 100 kHz MAS spectra.

In the previous sections, the PIP strategy was applied on one-dimensional spectra from a two-dimensional set of MAS spectra recorded at variable spinning rates (VMAS), either using a parameter fitting or a deep learning approach. [215, 236] Both approaches, yield isotropic spectra that display linewidths in the 50 – 400 Hz range for crystalline molecular solids. The robustness of the deep learning method opens the possibility to expand the PIP strategy to higher order spectra that could also benefit from improved resolution.

Here, we use three-dimensional datasets made up of two-dimensional DQ/SQ or spin-diffusion spectra acquired at different MAS rates to obtain two-dimensional ^{1}H-^{1}H DQ/SQ or ^{1}H-^{1}H PSD correlation spectra with pure isotropic lineshapes in both dimensions by transforming the data with a suitable deep learning prediction network, dubbed PIPNet2D.

4.4.2 Results and Discussion

In the absence of any extensive experimental databases of NMR spectra, training machine learning models on synthetic datasets (of shifts or spectra) has been to shown to be an efficient way forward.[286, 294, 312-317 318 319 320-322 323 289 284-285, 287-288, 324] Here, the generation of synthetic three-dimensional datasets used to train a LSTM neural network was based on a protocol analogous to that used previously for two-dimensional VMAS datasets.[215] The overall approach is illustrated schematically in Figure 4.52. Specifically, synthetic two-dimensional pure isotropic spectra (ground truth) were generated as the outer product of two randomly generated one-dimensional isotropic spectra. The component one- dimensional isotropic spectra and associated VMAS spectra were generated assuming that the dipolar couplings lead to a MAS rate dependent broadening, with a shape that is a sum of Gaussian and Lorentzian components, and that they also lead to a MAS rate dependent shift in the peak positions.[249 236] We also include random parameter variations in peak positions, peak shapes, MAS dependences, phase and intensity errors, and noise, as described previously in reference[215] but with an increased probability to generate broad isotropic peaks in order to promote diversity in the two-dimensional isotropic lineshapes.

The corresponding synthetic three-dimensional datasets of two-dimensional spectra at variable MAS rates were generated by the outer product of the 2D VMAS datasets. To mimic varying degrees of correlation in the 2D lineshapes, the sets of isotropic and associated MAS spectra were then rotated with a probability of 50% by a random angle uniformly sampled between 0 and 90°, in order to produce lineshapes with elongated shapes along different orientations in the 2D spectra. (Examples are shown in Figure 4.41). Each three-dimensional dataset generated contained 12 MAS spectra, each of which generated with a random MAS rate sampled from a uniform distribution between 50 and 100 kHz. Complete details about the data generation are given in Appendix

VI. An example of a synthetic MAS dataset and its isotropic counterpart typically used for the training of the model is shown in Figure 4.52.

Note that the synthetic spectra generated here do not actually make any assumptions or follow any particular rules associated with a type of experimental 2D correlation spectrum. That is, they do not correspond to, e.g., COSY, or DQ/SQ spectra, with diagonal and/or cross peaks in well-defined positions. The synthetic spectra only consist of a set of two-dimensional peaks in randomized positions in the spectra, and with lineshapes that obey the rules described above. As such, the model could be applied to any 2D correlation spectrum.

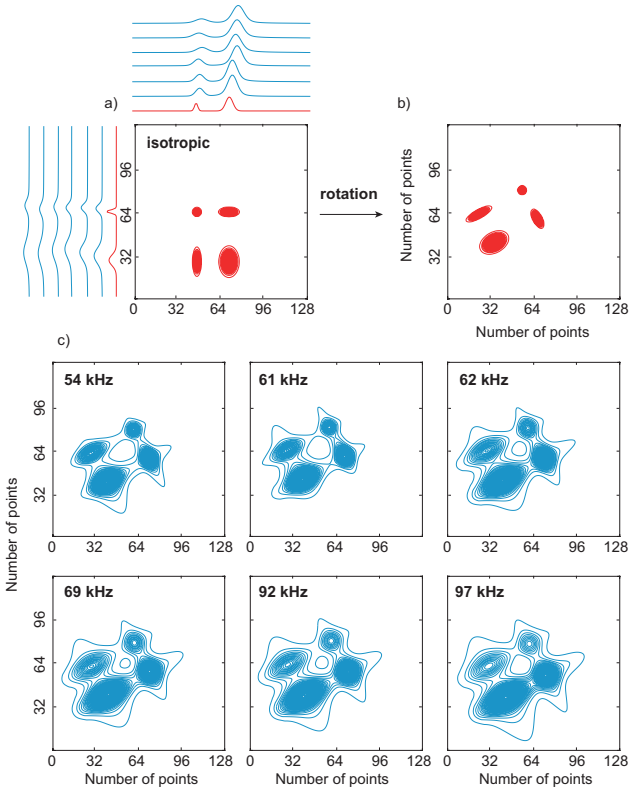

Figure 4.52 Representative example of a synthetic isotropic (red) two-dimensional spectrum (a) before and (b) after rotation and (c) a three-dimensional dataset (blue) that consists of two-dimensional spectra at different MAS rates. In (a) the one-dimensional isotropic spectra whose outer product leads to this two-dimensional isotropic spectrum and their corresponding variable MAS rate spectra are also shown. Here the full dataset contains 12 spectra at different MAS rates but only six selected spectra are shown. The rotation angle applied here during the data generation process was 61.5°.

Several approaches to using machine learning in NMR related problems have been proposed recently. [215, 286, 294, 312-317, 318, 319, 320-322, 323, 289, 280, 284-285, 287-288, 324-325] These range from deep and convolutional neural networks to predict chemical shifts in liquids,[320-322] to CNN models for reconstruction of two-dimensional spectra from undersampled data,[286-287, 294, 323] denoising of low signal-to-noise spectra,[313] performing deconvolution and deep learning-based peak picking[289, 312] and virtual decoupling.[284, 288] In the problem at hand, the LSTM type of network appears suitable since it has been shown to outperform other recurrent neural networks in processing time series,[290] and since it was shown to work well to predict 1D isotropic spectra.[215] The only changes used here with respect to the model to predict 1D spectra is the use of two-dimensional convolutional layers, using 4 layers instead of 6, and the use of only one model instead of a committee of 16 models. The latter being done in order to reduce the computational requirement at inference. The model was trained on a total of 1,000,000 datasets, corresponding to 12,000,000 spectra. To process each three-dimensional dataset of MAS spectra in order to obtain the isotropic 2D spectrum, the network is incrementally given the next MAS spectrum in the series in order of increasing MAS rate, and produces an output after each step, as described previously.[215] The model was trained by minimizing the mean absolute error (MAE) between the prediction after each step and the ground-truth two-dimensional isotropic spectrum.

As before, due to the sparsity of signal in the two-dimensional isotropic spectra, we initially convoluted the entire target isotropic spectrum with a 2D Gaussian function with a width of 25 Hz and weighted the loss function by the maximum between 1 and 10 times the value of the target isotropic spectrum (after convolution with the

Gaussian) in order to promote the identification of signal in the spectra. After 200,000 sets of spectra, this convolution and weighting were removed for the rest of the training. Random noise was also introduced into the generated MAS two-dimensional spectra following the typical signal-to-noise ratios observed in experimental ^{1}H-^{1}H correlation spectra (between 10 and 100 for the most intense peak at 100 kHz). Figure 4.53 (a) shows the evolution of the loss function during the model training.

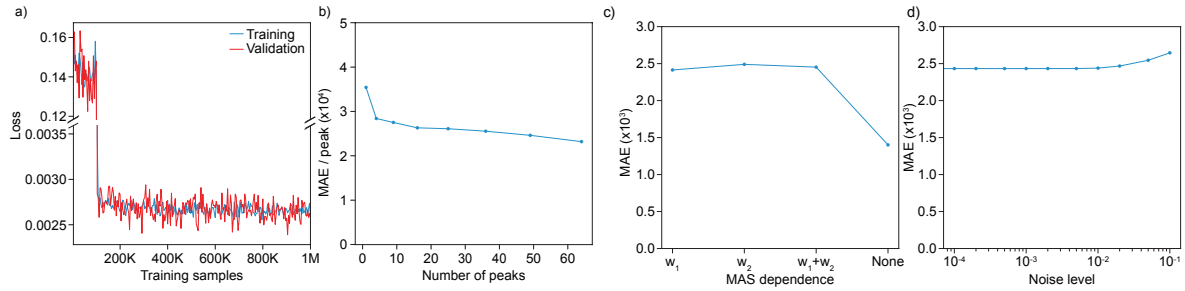

Figure 4.53 (a) Evolution of the loss function during model training. (b)-(d) MAE between predictions and ground-truth isotropic spectra for 1024 samples of isotropic spectra with various (b) numbers of peaks, (c) MAS dependence (w_1: first-order, w_2: second-order), and (d) noise levels.

The model was evaluated by computing the MAE between the synthetic ground truth and the predicted isotropic spectra for samples generated with different parameters. We investigated the effect of (i) the number of peaks in the two-dimensional isotropic spectra, (ii) different MAS dependencies of the linewidths and MAS-dependent shift (first-order, second-order, mixed first- and second-order, or MAS independent), the range of MAS rates generated, the number of MAS spectra used, as well as the amount of noise introduced into the spectra themselves and into the linewidth and shift dependences. Mean absolute errors between predictions and ground-truth isotropic spectra for 1024 samples of isotropic spectra with various numbers of peaks, MAS dependences (first order, second order, combined, or constant), and noise levels are shown in Figure 4.53 (b-d) and some selected examples are shown in Figure 4.54 (more details and examples (Figure 4.58) are given in the Appendix VI) in order to provide a more visual appreciation of the expected changes in the spectra corresponding to the changes in MAE in Figure 4.53.

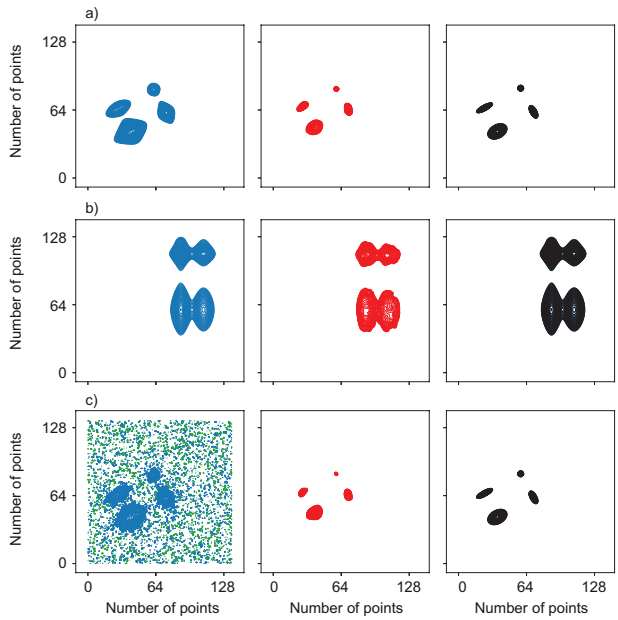

Figure 4.54 (a)-(c) Illustrative comparisons of synthetic highest MAS rate spectra (blue), predicted isotropic (red), and ground-truth isotropic (black) spectra with (a) the example of the synthetic dataset shown in Figure 1, (b) a MAS independent synthetic dataset, and (c) a synthetic dataset with a high noise level. In this example the spectra

are made up of 128 x 128 points, that would correspond to a frequency range of 3 kHz with about 24 Hz/point digital resolution.

Figure 4.55 shows the 1D and 2D isotropic spectra obtained from two experimental sets of variable MAS 1D and 2D spectra recorded on two small organic micro-crystalline samples of L-tyrosine hydrochloride and ampicillin The isotropic spectra of ritonavir are presented in Fig 4.56, but without spectral assignment. Figures 4.55 (a) and 4.55 (b) show the performance of the PIPNet2D model on sheared three-dimensional VMAS datasets for both compounds, consisting of two-dimensional BABA spectra recorded at 9 (ampicillin) and 11 (L-tyrosine hydrochloride) rates between 50 and 100 kHz MAS. The sheared SQ/SQ representation is exactly equivalent to the DQ/SQ but gives an easier to visualize rendition of the two-dimensional lineshapes.[326] Full details are given in the Appendix VI.

In Figures 4.55 (c) and 4.55 (d) and 4.56 (b), the marked increase in resolution achieved in both dimensions of the pure isotropic 2D spectra, as compared with that obtained in the corresponding spectra at 100 kHz MAS, is clearly visible. This increase is most prominent in the crowded spectral regions between 4 and 8 ppm both for L-tyrosine hydrochloride and ampicillin (expansions of these regions in both the pure isotropic and corresponding 100 kHz MAS 2D spectra are shown in Figures 4.55 (e) to 4.55 (h)).

We note in particular that, as discussed above, the model was not specifically trained to recognize sheared DQ/SQ spectra, so that, for example, the inferred spectra are not constrained to have any particular symmetry. Furthermore, the model can be equally well applied to the unsheared DQ/SQ spectra, and very similar results are obtained as shown in Figures 4.64 and 4.65. Rows from the pure-isotropic and the 100 kHz MAS spectra are also shown in Figure 4.64 for comparison.

The two-dimensional pure isotropic spectra were found to retain the expected number of peaks from the known assignments, without displaying any significant artifacts or any additional peaks in unexpected regions of the spectra. This is impressive, especially if we consider the reduced quality of the datasets used here as compared to typical 1D MAS spectra. Compared with the one-dimensional data used before, here the 2D spectra have much lower signal-to-noise ratios and display t_1 noise, and baseline and cross-peak intensity distortions across the range of MAS rates. (Note for example that since the BABA mixing time is rotor synchronized, the mixing time systematically decreases as the MAS rate increases, which will lead to variations in cross-peak intensities.) Another important point is that the isotropic two-dimensional peaks in the inferred spectra seem to retain the lineshape characteristics present in the 100 kHz MAS spectra, arising possibly from inhomogeneous contributions, correlated two-dimensional lineshapes,[327-333] or magnetic susceptibility effects.[239-240, 334-335]

PIPNet2D is therefore not simply identifying potential peaks and replacing them with uniformly narrow shapes. This can be clearly seen for protons H2 and H17/H18 of ampicillin as well as the labile protons of L-tyrosine hydrochloride. The MAS independent inhomogeneous sources of broadening are dominant for some samples at fast MAS. For this reason, PIPNET2D was as applied to two additional samples: hexamethylbenzene (HMB), known to have an important contribution to the linewidth from anisotropic bulk magnetic susceptibility (ABMS), and polystyrene (PS) in the form of beads, which is an amorphous sample and therefore its corresponding spectrum has severe broadening due to chemical shift disorder. The spectra are presented in Figure 4.57 and the experimental details are found in the Appendix of Chapter 5, where the inhomogeneous contributions to the linewidth are detailed. For HMB (Figure 4.57(a),(c) and (e)), the 100 kHz MAS and isotropic projection have essentially the same linewidth. The DQ/SQ peak is tilted along the diagonal, which is characteristic of ABMS. The isotropic row is slightly narrower than the 100 kHz row. Concerning polystyrene, the isotropic linewidths are narrower than the 100 kHz, but the remaining linewidth is still several hundred of Hz broad due to the disorder of the sample. The difference in linewidth between row and projections and the detail of the inhomogeneous contribution is detailed in Chapter 5.

Overall, the spectra obtained using the 1D PIPNet model and PIPNet2D were found to be coherent, with good agreement between the 1D isotropic spectra obtained from a set of 1D MAS spectra using PIPNet and the projection of the 2D isotropic spectra obtained here for L-tyrosine hydrochloride and ampicillin, respectively. We do note that the 2D model does not yield the same degree of line narrowing in the projections of Figures 4.64 and 4.65 as compared to the 1D model. This is not surprising given the increased sources of errors discussed above in the 2D datasets, and it clearly indicates that further progress can be made in the future.

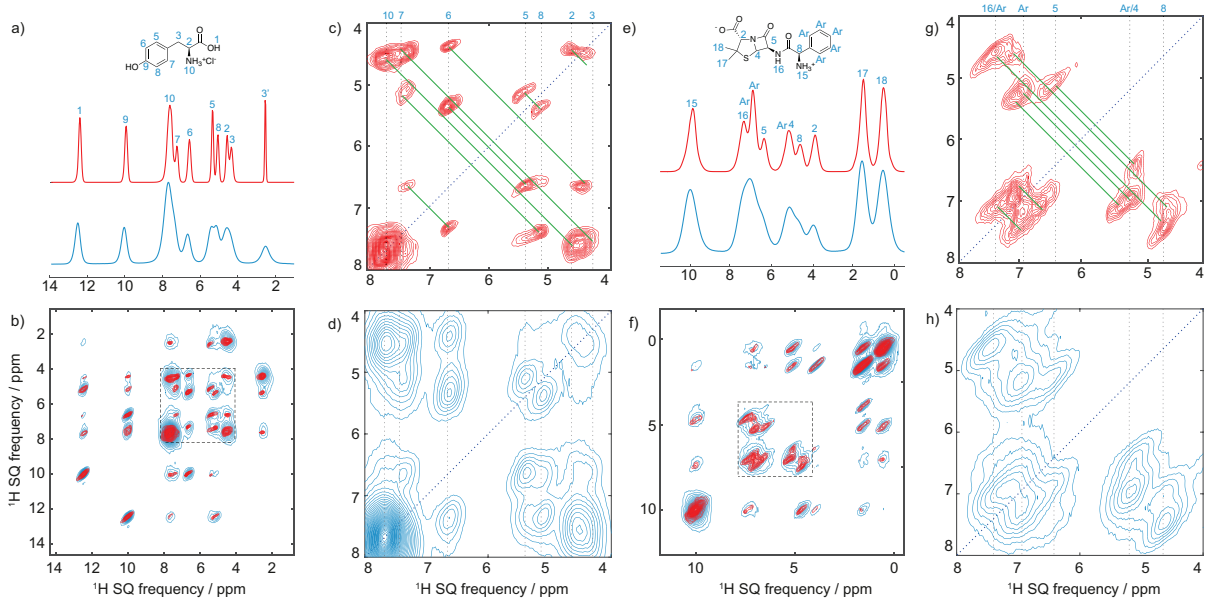

Figure 4.55 Spectra obtained from microcrystalline powdered samples of L-tyrosine hydrochloride (left) and ampicillin (right). (a) and (b) 100 kHz MAS spectra (blue) and isotropic spectra (red) inferred with the PIPNet model from a VMAS dataset of 1D spectra recorded at 36 rates between 30 and 100 kHz. (c) and (d) corresponding 100 kHz MAS 2D ^{1}H-^{1}H DQ/SQ BABA spectra (blue) and pure isotropic 2D ^{1}H-^{1}H DQ/SQ BABA spectra (red) inferred with the PINet2D model from a VMAS dataset of 11 and 9 2D spectra recorded at the MAS rates between 50 and 100 kHz, both after shearing to an SQ/SQ representation, for samples of L-tyrosine hydrochloride and ampicillin, respectively, and acquired with one rotor period of DQ recoupling. (e) and (f) expansions of the pure isotropic 2D spectra, and (g) and (h) expansions of the 100 kHz 2D spectra. In (e) to (h) the vertical dotted lines indicate the previously assigned proton shifts at 100 kHz MAS, the blue dotted line the diagonal of the spectrum, and the green solid lines the observed double quantum correlations.

Figures 4.58 shows the performance of the PIPNet2D model on a three-dimensional PSD VMAS dataset for L-tyrosine hydrochloride (Figure 4.63), consisting of two-dimensional ^{1}H-^{1}H spin-diffusion spectra recorded at 6 MAS rates between 50 and 100 kHz MAS. In Figure 4.58 (d) the resolution achieved in both dimensions of the pure isotropic 2D spectrum is evident and allows the clear identification of correlations between, for example, H6 and H10 or H2 and H5, that were difficult to clearly observe in the corresponding PSD spectrum at 100 kHz MAS, shown in Figure 4.58 (c).

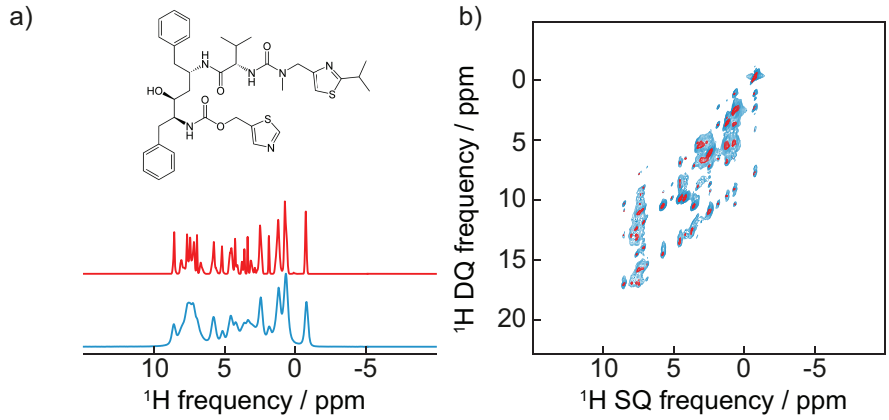

Figure 4.56 Spectra obtained from ritonavir form II. (a) 100 kHz MAS spectrum (blue) and isotropic spectrum (red) inferred with the PIPNet model from a VMAS dataset of 1D spectra recorded at 8 rates between 40 and 100 kHz. (b) 100 kHz MAS 2D ^{1}H-^{1}H DQ/SQ BABA spectrum (blue) and pure isotropic 2D ^{1}H-^{1}H DQ/SQ BABA spectra (red) inferred with the PINet2D model from a VMAS dataset of 8 2D spectra recorded at the MAS rates between 40 and 100 kHz, acquired with one rotor period of DQ recoupling.

The horizontal cross sections shown in Figure 4.58 (e-h) are an additional direct illustration of the enhanced resolution of the pure isotropic 2D spectrum over the corresponding 100 kHz MAS 2D spectrum. PIPNet2D is

expected to perform best for the cross peaks, as compared to the diagonal peaks, since the integral normalization of the 3D dataset was done with respect to a selected cross peak intensity.

In the VMAS experiments, the PSD mixing time was varied from 5 to 10 ms as the spinning rate was increased in order to compensate for slower spin diffusion at faster MAS rates and to maintain similar cross-peak intensities across the dataset (as described in Appendix VI). Since the spin diffusion rates between different spin pairs will have slightly different MAS rate dependencies,[224] this procedure cannot be perfect and will introduce a source of error.

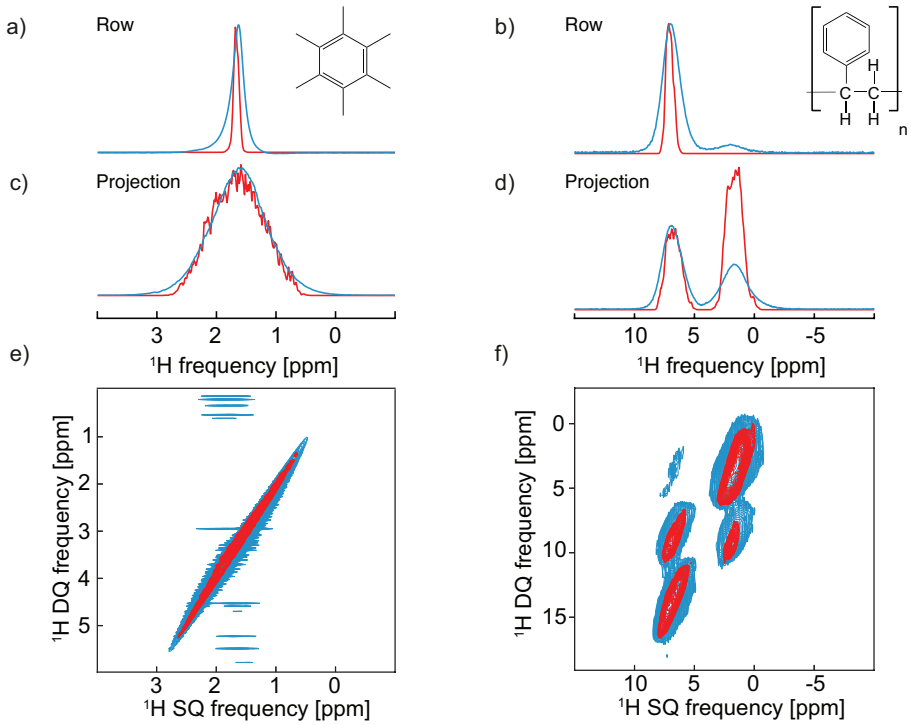

Figure 4.57 Spectra obtained from HMB and PS. (a,c) HMB 100 kHz MAS row and projection (blue) and isotropic spectrum (red) inferred with the PIPNet2D model; (e) HMB 100 kHz MAS 2D ^{1}H-^{1}H DQ/SQ BABA spectrum (blue) and pure isotropic 2D ^{1}H-^{1}H DQ/SQ BABA spectra (red) inferred with the PINet2D model from a VMAS dataset of 14 2D spectra recorded at the MAS rates between 40 and 100 kHz, acquired with one rotor period of DQ recoupling. (b,d) PS 100 kHz MAS row and projection (blue) and isotropic spectrum (red) inferred with the PIPNet2D model; (f) PS 100 kHz MAS 2D ^{1}H-^{1}H DQ/SQ BABA spectrum (blue) and pure isotropic 2D ^{1}H-^{1}H DQ/SQ BABA spectra (red) inferred with the PINet2D model from a VMAS dataset of 6 2D spectra recorded at the MAS rates between 50 and 100 kHz, acquired with one rotor period of DQ recoupling.

That the model can be successfully directly applied to DQ/SQ (whether sheared or not) or to PSD datasets illustrates that the PIPNet2D model is quite robust and can be used quite generally to obtain two-dimensional ^{1}H-^{1}H correlation spectra with higher resolution in both dimensions from 3D VMAS datasets, and that it is not restricted to inferences for a specific type of two-dimensional spectra.

Across the three sets of 2D spectra shown here, PIPNet2D reduced observed linewidths by a factor of 3.33 ± 0.10 in both dimensions compared to 100 kHz MAS spectra (see Table 4.25).

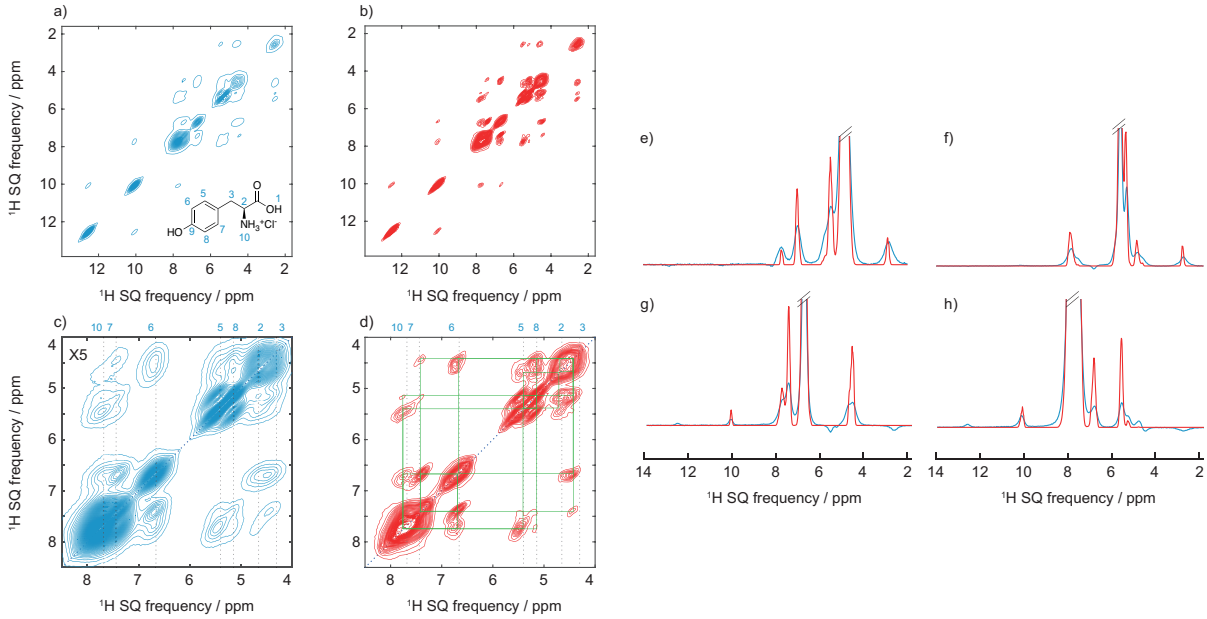

Figure 4.58 Spectra obtained from microcrystalline powdered samples of L-tyrosine hydrochloride. (a) and (b) 100 kHz MAS 2D ^{1}H-^{1}H spin-diffusion spectra (blue) and pure isotropic 2D ^{1}H-^{1}H spin-diffusion spectra (red) inferred with the PINet2D model from a VMAS dataset of 6 2D spectra recorded at the MAS rates between 50 and 100 kHz. In the VMAS experiments, the PSD mixing time was varied from 5 to 10 ms as the spinning rate was increased to maintain similar cross-peak intensities across the dataset (as described in Appendix VI). (c) and (d) expansions of the 100 kHz and pure isotropic 2D spectra. (e) to (f) horizontal cross sections extracted for F_1 SQ frequencies of 4.5, 5.5, 6.7, and 7.7 ppm. In (c) to (d) the vertical dotted lines indicate the previously assigned proton shifts at 100 kHz MAS, the blue dotted line the diagonal of the spectrum, and the green squares the observed spin-diffusion correlations.

4.4.3 Conclusion

We have introduced PIPNet2D, a deep learning model to increase resolution in two-dimensional NMR spectroscopy by predicting pure isotopic two-dimensional correlation spectra of solids from three-dimensional datasets of 2D spectra acquired at variable MAS rates. We have illustrated the method by obtaining isotropic spectra from experimental datasets on two different microcrystalline organic solids. The resolution obtained is very significantly improved compared with the 100 kHz MAS spectra. The residual linewidths or the quantitative character of the inferred spectra can in principle be limited by several factors. Some are intrinsic to the samples, such as structural disorder or magnetic susceptibility broadening, and others might be due to experimental imperfections such as MAS instabilities or poor shimming, or limitations in the model, such as incomplete descriptions of the lineshape and MAS-dependence. All these factors will be the subject of future study.

For example, we expect that the use of more robust pulse sequences for DQ/SQ type experiments, that might better remove some of the experimental imperfections, should potentially improve the robustness of the model [212, 336]. Further improved results might also be obtained by training models specifically on a given type of correlation experiment.

In conclusion, the model presented here provides significant improvement in the resolution of 2D ^{1}H-^{1}H DQ/SQ and spin-diffusion spectra, and we expect that the approach can be used to develop models for other two-dimensional correlation experiments in the future.

4.4.4 Appendix VI

4.4.4.1 Experimental Details

The pure isotropic 2D approach is applied here to experimental datasets from two micro-crystalline organic solids: L-tyrosine hydrochloride and ampicillin. For each sample a set of 2D BABA (Figure 4.59 and 4.60) or spin-diffusion[311] spectra (Figure 4.61) was acquired at MAS rates ranging from 50 to 100 kHz, using a Bruker 0.7 mm room temperature HCN CP-MAS probe at a magnetic field of 21.1 T corresponding to a ^{1}H frequency of 900 MHz. For each sample, prior to acquisition the magic angle was set by maximizing the T_2' of the proton signals at the fastest MAS rate, and the 90° pulse width was optimized. All the data were acquired with active temperature regulation to maintain the sample temperature at about 295 K across the range of spinning rates. For each MAS rate, the BABA 2D experiments were rotor-synchronized in the indirect dimension and the number or increments was adjusted to achieve a t_1^{max} of 2.5 and 2.4 ms for L-tyrosine hydrochloride and ampicillin, respectively. For L-tyrosine hydrochloride the spin-diffusion 2D experiments were acquired with a t_1^{max} of 14.6 ms and with a mixing time chosen to produce cross peaks with similar intensities throughout the series. More specifically, as the spinning rate was increased, the PSD mixing time was varied was also increased in order to compensate for slower spin diffusion at faster MAS rates. A States-TPPI acquisition scheme was used to obtain phase-sensitive two-dimensional spectra. A 16-step phase cycling was used for BABA and EXSY experiments.

All spectra were phased, baseline corrected, their full integrals were normalized (either with respect to the total integral, for the DQ/SQ spectra, or with respect to a selected cross peak intensity, for the PSD spectra), and the spectra were scaled to the maximum amplitude of the 100 kHz spectrum at 1 in order to match the typical amplitudes of the generated training spectra. The experimental DQ/SQ MAS spectra were sheared to an SQ/SQ representation prior to processing. The SQ/SQ representation is exactly equivalent to the DQ/SQ but gives an easier to visualize rendition of the two-dimensional lineshapes.[326] No weighting function was applied prior to Fourier transformation.

Table 4.22 Experimental details of the BABA VMAS 3D dataset acquired for L-tyrosine hydrochloride.

L-tyrosine hydrochloride	VT (K)	90° RF amplitude (kHz)	d1(s)	Number of co-added transients	Number of FID points: F2/F1	SW (kHz): F2/F1	Size of real spectrum: F2/F1	DQ recoupling time (µs)	Experimental time
100 kHz	285	294	2	16	4096/100	90.9/20	4096/1024	10	57 min
96 kHz	285	294	2	16	4096/96	90.9/19.2	4096/1024	10.42	54 min
94 kHz	285	294	2	16	4096/94	90.9/18.8	4096/1024	10.64	54 min
90 kHz	285	294	2	16	4096/90	90.9/18	4096/1024	11.11	51 min
88 kHz	285	294	2	16	4096/110	90.9/22	4096/1024	11.36	1h2min
80 kHz	290	294	2	16	4096/100	90.9/20	4096/1024	12.5	57 min
78 kHz	290	294	2	16	4096/130	90.9/26	4096/1024	12.82	1h14min
72 kHz	290	294	2	16	4096/120	90.9/24	4096/1024	13.89	1h8min
66 kHz	290	294	2	16	4096/110	90.9/22	4096/1024	15.15	1h2min
60 kHz	295	294	2	16	4096/100	90.9/20	4096/1024	16.67	57 min
52 kHz	295	294	2	16	4096/130	90.9/26	4096/1024	19.23	1h14min

Table 4.23 Experimental details of the BABA VMAS 3D dataset acquired for ampicillin.

Ampicillin	VT (K)	90° RF amplitude (kHz)	d1(s)	Number of co-added transients	Number of FID points: F2/F1	SW (kHz): F2/F1	Size of real spectrum: F2/F1	DQ recoupling time (µs)	Experimental time
100 kHz	285	294	2	16	4096/160	90.9/33.3	4096/1024	10	1h31min
90 kHz	285	294	2	16	4096/144	90.9/30	4096/1024	11.1	1h22min
85 kHz	290	294	2	16	4096/136	90.9/28.3	4096/1024	11.76	1h17min
80 kHz	290	294	2	16	4096/128	90.9/26.6	4096/1024	12.5	1h13min
75 kHz	290	294	2	16	4096/120	90.9/25	4096/1024	13.3	1h2min
70 kHz	290	294	2	16	4096/168	90.9/35	4096/1024	14.28	1h35 min
60 kHz	290	294	2	16	4096/144	90.9/30	4096/1024	16.67	1h22min
55 kHz	290	294	2	16	4096/132	90.9/27.5	4096/1024	18.18	1h15min
50 kHz	290	294	2	16	4096/120	90.9/25	4096/1024	20	1h8min

Table 4.24 : Experimental details of the PSD VMAS 3D dataset acquired for L-tyrosine hydrochloride.

L-tyrosine hydrochloride	VT (K)	90° RF amplitude (kHz)	d1(s)	Number of co-added transients	Number of FID points: F2/F1	SW (kHz): F2/F1	Size of real spectrum: F2/F1	DQ recoupling time (ms)	Experimental time
100 kHz	285	294	3	8	8192/366	227.3/12.5	16384/1024	10	2h31 min
90 kHz	290	294	3	8	8192/366	227.3/12.5	16384/1024	9	2h31 min
80 kHz	290	294	3	8	8192/366	227.3/12.5	16384/1024	6	2h31 min
70 kHz	290	294	3	8	8192/366	227.3/12.5	16384/1024	6	2h31 min
60 kHz	290	294	3	8	8192/366	227.3/12.5	16384/1024	6	2h31min
50 kHz	290	294	3	8	8192/366	227.3/12.5	16384/1024	5	2h31 min

4.4.4.2 DATA GENERATION

As described previously,[215] we generate synthetic isotropic and variable MAS rate 1D spectra according to a theoretical description of the dependence of the spectra on the MAS rate. A MAS spectrum is composed of a sum of peaks $I_{\omega_r}(\nu)$, each resulting from the convolution between the corresponding Gaussian peak in the isotropic spectrum $I_\infty(\nu)$ and a Gaussian-Lorentzian sum (GLS) function:

$$GLS(\nu; w, p, m) = (1-m)\exp\left[-\frac{4\ln(2)\,(\nu-p)^2}{w^2}\right] + \frac{m}{1+\frac{4(\nu-p)^2}{w^2}} \qquad (4.20)$$

where *w* and *p* are the width and position of the GLS function, respectively, and *m* is the mixing factor describing the lineshape of the function (purely Gaussian with *m* = 0, and purely Lorentzian with *m* = 1). We set *p* to be in the middle of the generated spectrum, such that convoluting the GLS with the isotropic peak does not affect the position after convolution. After the convolution, a MAS-dependent shift of the frequency of the peak s_{ω_r} was added to capture the residual shift observed in MAS spectra. The generation of a peak in an MAS spectrum is thus described as:

$$I_{\omega_r} = \mathrm{FT}\left[I_\infty(t)\cdot e^{i2\pi s_{\omega_r}}\right] * GLS\left(\nu; w_{\omega_r}, p, m_{\omega_r}\right) \qquad (4.21)$$

Where $\mathrm{FT}[\cdot]$ is the Fourier transform and $*$ denotes the convolution operation.

Here, we generated spectra made up of 128 points with a time-domain sampling frequency of 3.2 kHz, corresponding to a frequency domain resolution of 25 Hz.

1D isotropic spectra were generated as the sum of between 1 and 5 Gaussian peaks, with a linewidth sampled from a uniform distribution between 50 and 200 Hz (60% probability), between 100 and 500 Hz (20% probability), or between 100 and 1000 Hz (20% probability). Potential negative points in the isotropic spectra generated were set to zero. In order to randomize peak intensities, we rescaled the height of each isotropic peak to a random value between 0.1 and 1.

For each pair of 1D isotropic spectra, 12 MAS rates were selected randomly between 50 and 100 kHz, and the corresponding MAS spectra were constructed as described in Eq. 4.21, using a GLS function with parameters s_{ω_r}, w_{ω_r} and m_{ω_r} following a second-order MAS dependence subject to noise.

$$w_{\omega_r} = \frac{w_1}{\omega_r} + \frac{w_2}{\omega_r^2} + \Delta w \tag{4.22}$$

$$s_{\omega_r} = \frac{s_1}{\omega_r} + \frac{w_2}{\omega_r^2} + \Delta s \tag{4.23}$$

$$m_{\omega_r} = \frac{m_1}{\omega_r} + \frac{m_2}{\omega_r^2} \tag{4.24}$$

For each peak, the value of w_1 in Eq. 4.22 was drawn from a uniform distribution in the range [10^7, $2{\cdot}10^7$] Hz^2 with 60% probability, in the range [10^7, $5{\cdot}10^7$] Hz^2 with 20% probability, and in the range [$5{\cdot}10^7$, 10^8] Hz^2 otherwise. w_2 was set to be 0 with 50% probability, or a random value between 10^{11} and $5{\cdot}10^{11}$ Hz^3. In addition, for each MAS rate the GLS width w_{ω_r} was randomly perturbed by a value drawn from a normal distribution $\Delta w \sim \mathcal{N}(0, \sigma_w)$ Hz where σ_w was set to be 5% of the range of width generated between the lowest and highest MAS rates with the selected values of w_1 and w_2. The value of s_1 in Eq. 4.23 was randomly sampled between -10^7 and 10^7 Hz^2, and s_2 was set to zero with a 50% probability, or randomly sampled between -$2{\cdot}10^{10}$ and $2{\cdot}10^{10}$ Hz^3. Δs was randomly drawn from a normal distribution $\Delta s \sim \mathcal{N}(0{,}25)$ Hz for each peak and each MAS rate. The GLS mixing was set to follow the inverse MAS dependence described in Eq. 4.24 with a probability of 50% and with the value of m_1 set to zero with a 20% probability, drawn from a uniform distribution in the range [0, 10^4] Hz with 20% probability, or drawn from a uniform distribution in the range [10^4, $5{\cdot}10^4$] Hz, and with m_2 set to zero with a 50% probability, or drawn from a uniform distribution in the range [10^8, $5{\cdot}10^8$] Hz^2. Resulting values of m_{ω_r} above one were capped to one. Otherwise, the mixing m_{ω_r} was set to be either constant, monotonously increasing with random values between 0 and 1, or monotonously decreasing with random values between 0 and 1 with increasing MAS rate. These three dependences were considered with equal probability.

In addition, each peak in each 1D MAS spectrum was subject to phase distortion drawn from a normal distribution $\mathcal{N}(0, 0.05)$ with a 50% probability, and each isotropic peak was assigned a 30% chance to have a decreasing intensity in MAS spectra with increasing rate by multiplying the intensity of the corresponding peak in each MAS spectrum by a value linearly decreasing between 1 and a final value sampled uniformly in the range [0.3, 0.7].

After generating the pairs of isotropic and MAS spectra for each rate, convolution and rotation yields the final 2D isotropic and sets of MAS spectra.

4.4.4.3 EXAMPLES OF SYNTHETIC DATA

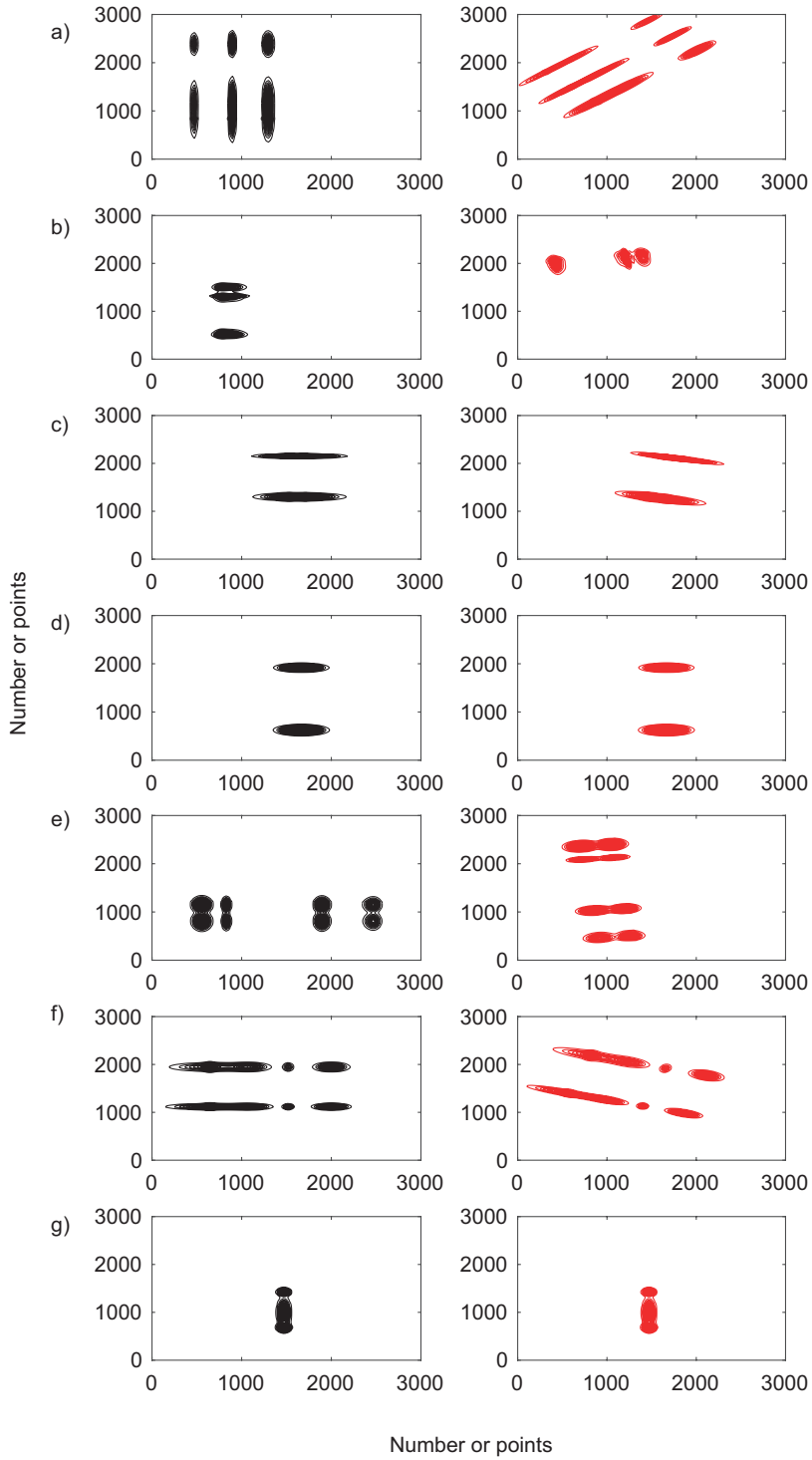

Figure 4.59 Representative examples of synthetic isotropic two-dimensional spectra (a) before (black) and (b) after (red) rotation. The rotation angles applied here during the data generation process were 47°, 80.7°, 12.8°, 0°, 21.3°, 17.9°, and 0°.

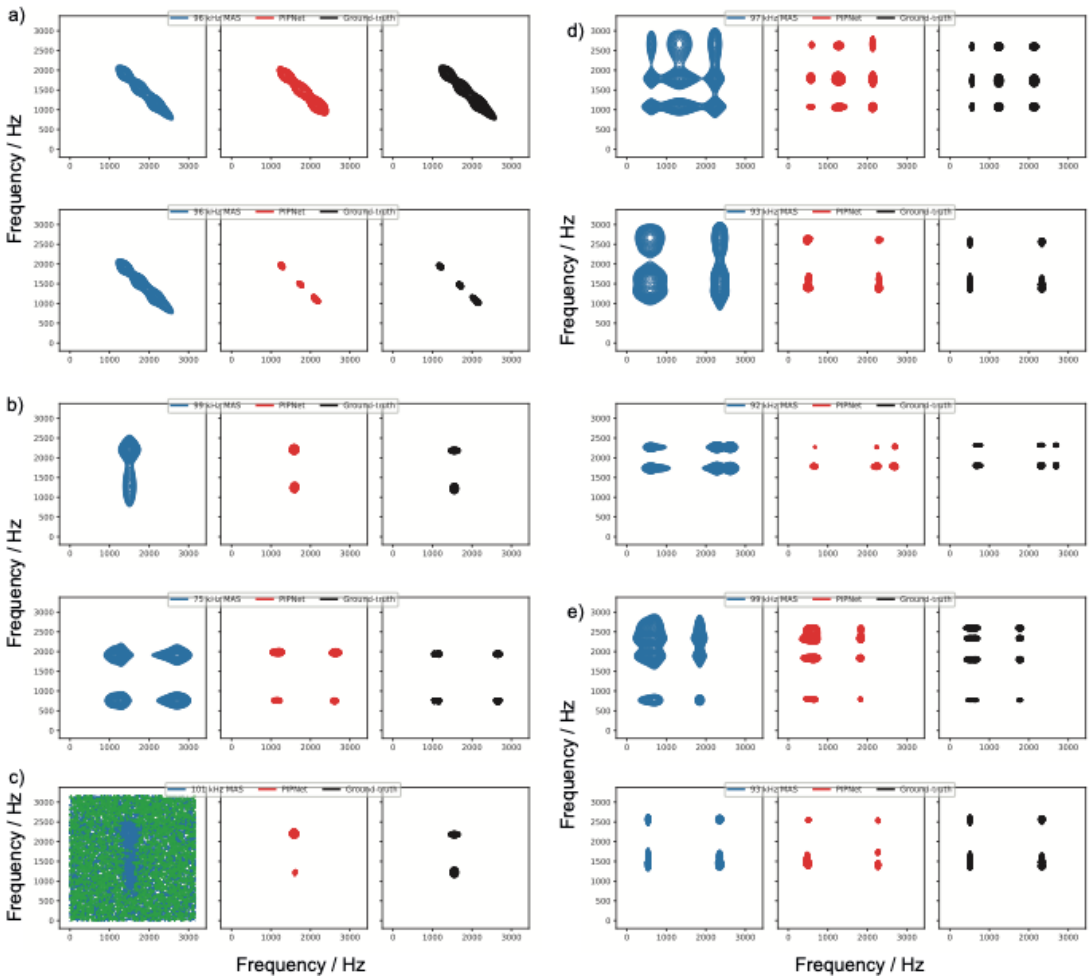

Figure 4.60 Representative sets of examples of synthetic isotropic two-dimensional spectra where the fastest 2D spectrum used in the series is indicated in blue, the PIPNet2D inferred spectrum is shown in red, and the ground truth is shown in black. (a) Example of synthetic data without (top) and with (bottom) MAS-dependent broadening. (b). Example of synthetic data in which the highest MAS 2D spectrum used in the series is 99 kHz (top) and 75 kHz (bottom). (c) Example of synthetic data with a high level of noise. (d) Example of synthetic data in which 16 (top), 12 (middle), and 6 (bottom) 2D spectra are used in the series. (e) Example of synthetic data with a first order MAS-dependence (top) and a second order MAS-dependence (bottom).

4.4.4.4 CONTOUR PLOTS OF THE RAW 3D DATASETS

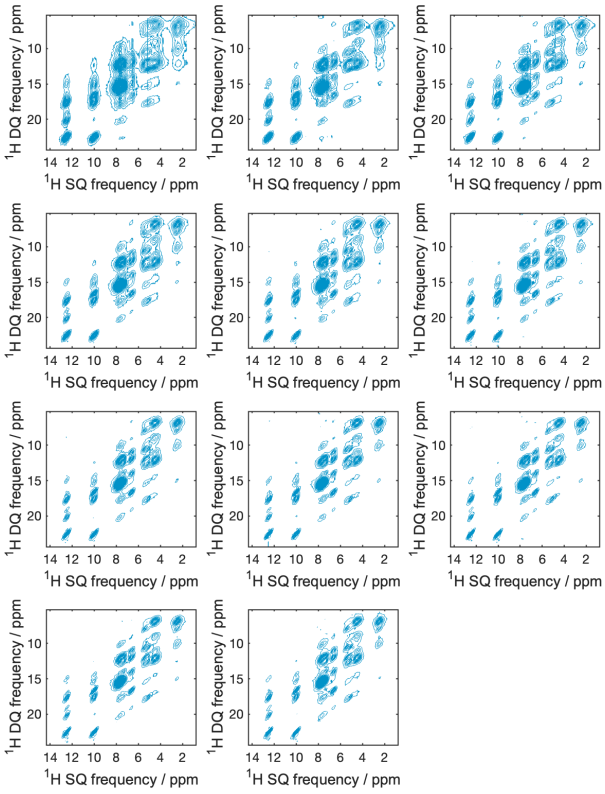

Figure 4.61 3D dataset of L-tyrosine hydrochloride consisting of 11 unsheared 2D 1H-1H DQ/SQ BABA spectra acquired at MAS rates of 50, 62, 66, 72, 78, 80, 88, 90, 94, 96, and 100 kHz (top to bottom).

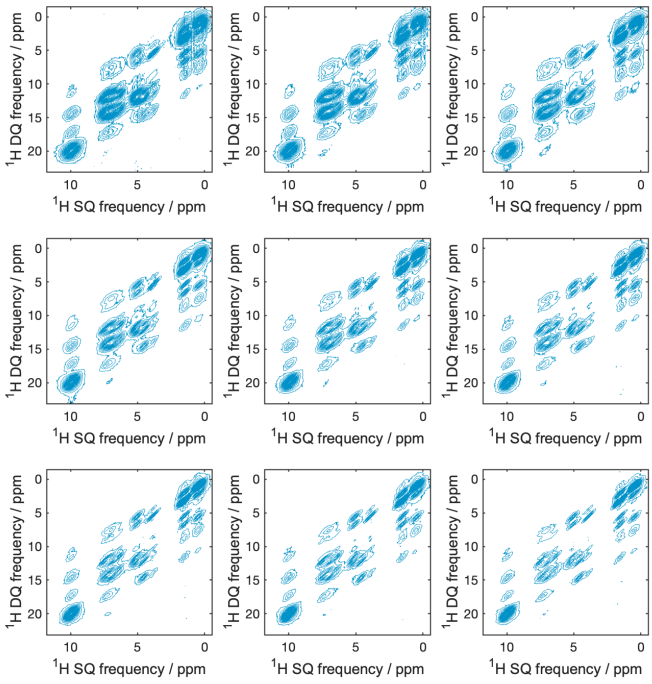

Figure 4.62 3D dataset of ampicillin consisting of 9 unsheared 2D 1H-1H DQ/SQ BABA spectra acquired at MAS rates of 50, 55, 60, 70, 75, 80, 85, 90, and 100 kHz (top to bottom).

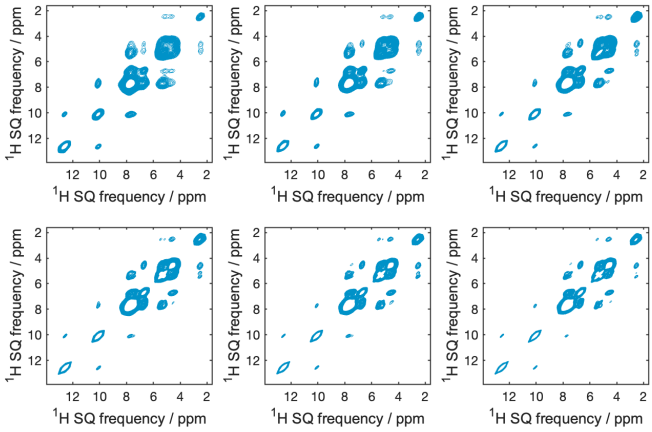

Figure 4.63 3D dataset of L-tyrosine hydrochloride consisting of 6 unsheared 2D 1H-1H spin-diffusion spectra acquired at MAS rates of 50, 60, 70, 80, 90, and 100 kHz (top to bottom).

4.4.4.5 RESULTS ON UNSHEARED 2D SPECTRA

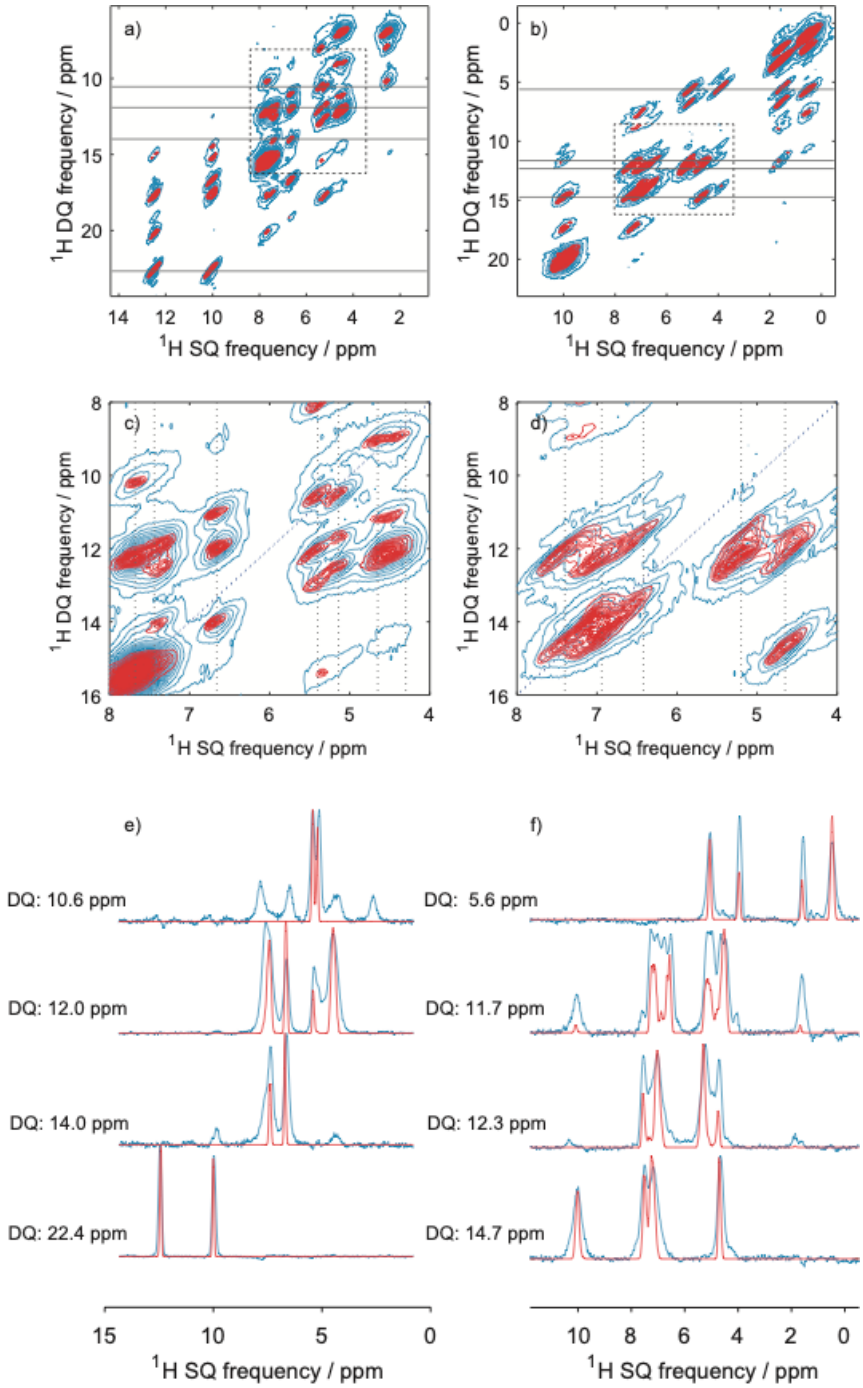

Figure 4.64 (a) and (b) 100 kHz MAS 2D ^{1}H-^{1}H DQ/SQ BABA spectra (blue) and pure isotropic 2D ^{1}H-^{1}H DQ/SQ BABA spectra (red) inferred with the PINet2D model from a VMAS dataset of 11 and 9 2D spectra recorded at the MAS rates between 50 and 100 kHz, both before shearing to an SQ/SQ representation, for samples of L-tyrosine hydrochloride and ampicillin, respectively. (c) and (d) expansions of the pure isotropic 2D spectra and 100 kHz 2D spectra. In (c) to (d) the vertical dotted lines indicate the previously assigned proton shifts at 100 kHz MAS and the blue dotted line the diagonal of the spectrum. In (a) and (b) the horizontal lines indicate the cross sections plotted in (e) and (f).

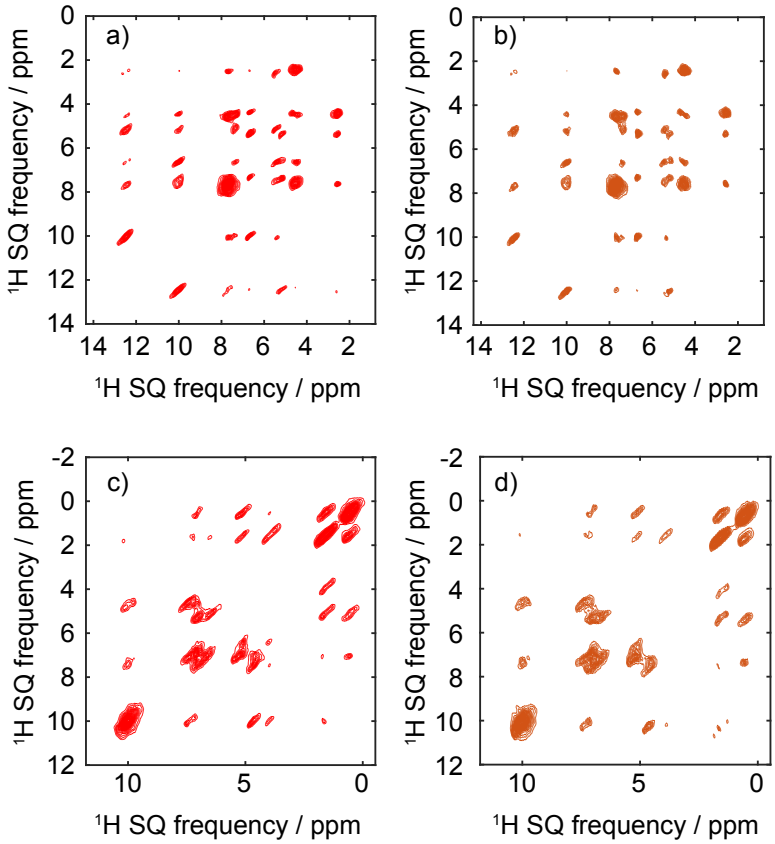

Figure 4.65 Pure isotropic 2D ^{1}H-^{1}H DQ/SQ BABA spectra inferred with the PINet2D model from a VMAS dataset of 11 and 9 2D spectra recorded at the MAS rates between 50 and 100 kHz, (a) and (c) after shearing to an SQ/SQ representation and (b) and (d) before shearing to an SQ/SQ representation, for samples of L-tyrosine hydrochloride and ampicillin, respectively. (b) and (d) are sheared to an SQ/SQ representation after inference.

4.4.4.6 Comparisons with inferences from 2D VMAS datasets

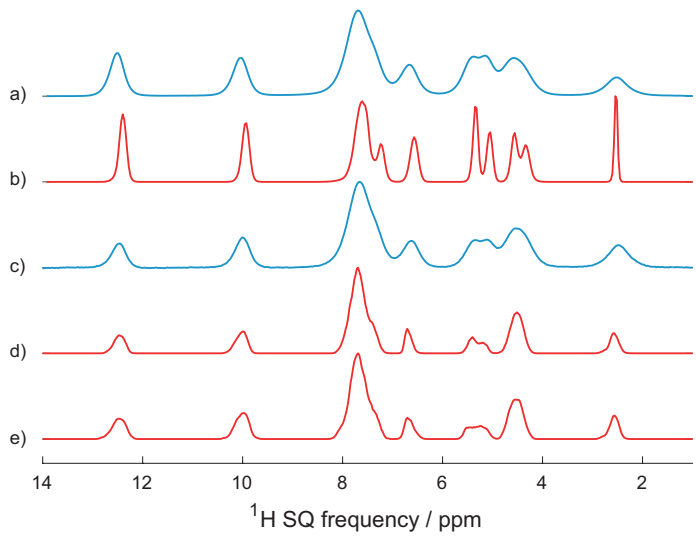

Figure 4.66 Spectra obtained from microcrystalline powdered samples of L-tyrosine hydrochloride. (a) and (b) 100 kHz MAS spectra (blue) and isotropic spectra (red) inferred with the PIPNet model from a VMAS dataset of 1D spectra recorded at 36 rates between 30 and 100 kHz. (c) Sum projection along F1 of the unsheared 100 kHz MAS 2D ^{1}H-^{1}H DQ/SQ BABA spectrum (blue), and sum projections along F1 of the pure isotropic 2D ^{1}H-^{1}H DQ/SQ BABA spectra inferred with the PINet2D model from a VMAS dataset of 11 2D spectra recorded at the MAS rates between 50 and 100 kHz, (d) before and (e) after shearing to an SQ/SQ representation.

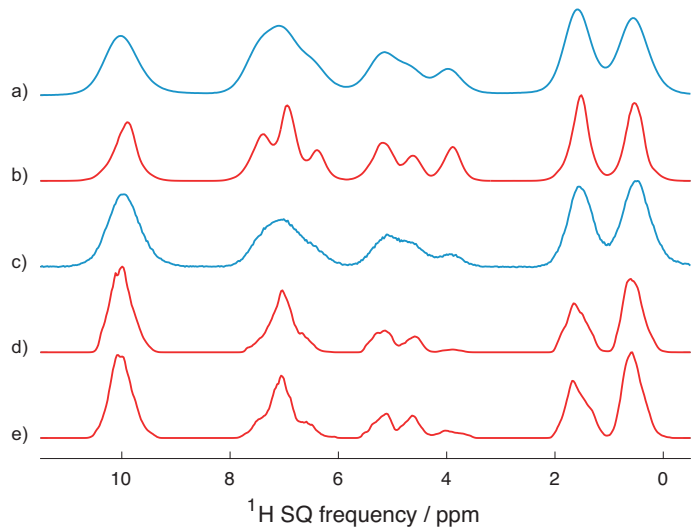

Figure 4.67 Spectra obtained from microcrystalline powdered samples of ampicillin. (a) and (b) 100 kHz MAS spectra (blue) and isotropic spectra (red) inferred with the PIPNet model from a VMAS dataset of 1D spectra recorded at 36 rates between 30 and 100 kHz. (c) Sum projection along F1 of the unsheared 100 kHz MAS 2D ^{1}H-^{1}H DQ/SQ BABA spectrum (blue), and sum projections along F1 of the pure isotropic 2D ^{1}H-^{1}H DQ/SQ BABA spectra inferred with the PINet2D model from a VMAS dataset of 11 2D spectra recorded at the MAS rates between 50 and 100 kHz, (d) before and (e) after shearing to an SQ/SQ representation.

4.4.4.7 Evaluation of integrals

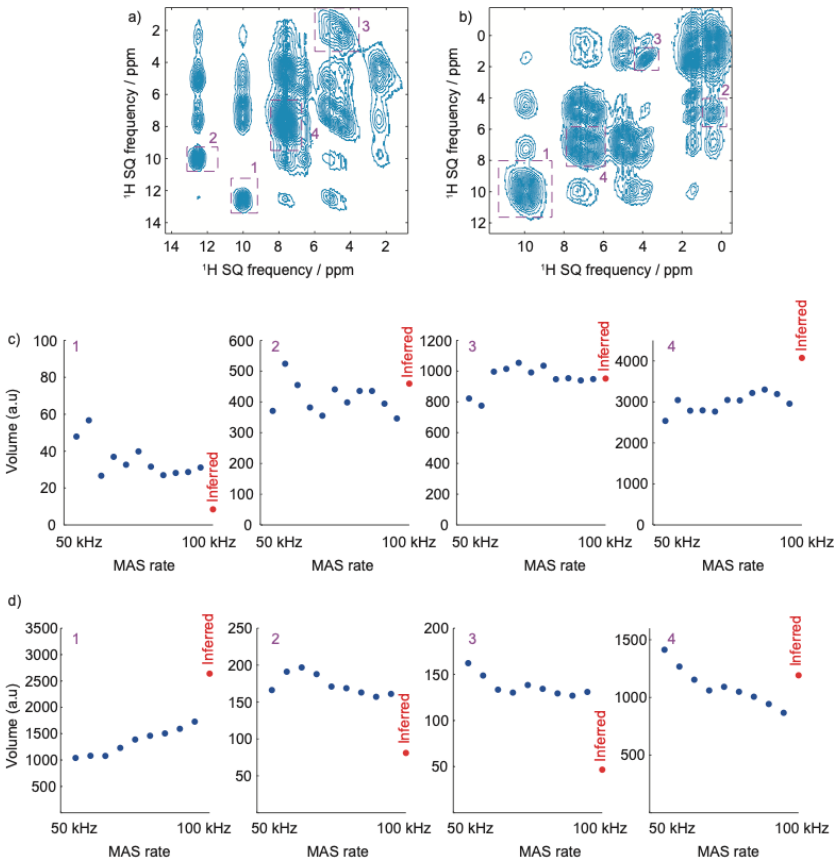

Figure 4.68 (a) and (b) corresponding 50 kHz MAS 2D ^{1}H-^{1}H DQ/SQ BABA spectra after shearing to an SQ/SQ representation, for samples of L-tyrosine hydrochloride and ampicillin. (c) and (d) 2D peak volumes measured from the 2D ^{1}H-^{1}H DQ/SQ BABA spectra as a faction of the MAS rate (blue) and from the inferred pure isotropic 2D spectra (red). In (a) to (b) the 2D peaks chosen for volume measurements are indicated with purple dotted boxes.

4.4.4.8 Evaluation of linewidths

Table 4.25 Full width at half maximum (FWHM) values of selected peaks in 100 kHz MAS and isotropic (PIP) spectra. The values were obtained by fitting Gaussian functions to selected rows or columns in the spectra.

L-tyrosine hydrochloride BABA				Ampicillin BABA				L-tyrosine hydrochloride PSD			
F1 (ppm)	F2 (ppm)	FWHM F1 100kHz / PIP (ppm)	FWHM F2 100kHz / PIP (ppm)	F1 (ppm)	F2 (ppm)	FWHM F1 100kHz / PIP (ppm)	FWHM F2 100kHz / PIP (ppm)	F1 (ppm)	F2 (ppm)	FWHM F1 100kHz / PIP (ppm)	FWHM F2 100kHz / PIP (ppm)
2.5	12.5	0.56/0.09	0.36/0.14	1.8	10.2	0.52/0.11	0.48/0.09	10.0	12.5	0.19/0.09	0.18/0.10
6.6	12.5	0.34/0.08	0.27/0.10	10.1	10.1	0.79/0.43	0.58/0.30	12.4	9.9	0.17/0.09	0.18/0.07
10.0	12.4	0.35/0.19	0.28/0.18	4.8	10.1	0.61/0.27	0.52/0.24	7.6	9.9	0.35/0.17	0.28/0.14
5.1	12.4	0.47/0.20	0.28/0.24	7.5	10.0	0.57/0.29	0.44/0.21	7.3	9.9	0.33/0.10	0.26/0.08
4.4	12.3	0.43/0.16	0.29/0.09	10.1	7.5	0.67/0.16	0.48/0.14	6.5	9.9	0.25/0.06	0.23/0.07
2.4	12.3	0.36/0.08	0.31/0.12	4.6	7.4	0.54/0.24	0.50/0.31	10.0	7.7	0.26/0.12	0.37/0.14
6.6	9.9	0.49/0.11	0.29/0.19	6.9	7.1	0.76/0.23	1.22/0.35	5.4	7.6	0.31/0.12	0.37/0.14
5.1	9.9	0.39/0.11	0.30/0.19	0.6	7.1	0.86/0.17	0.72/0.17	6.6	7.6	0.38/0.14	0.53/0.17
4.4	9.9	0.44/0.13	0.31/0.17	5.2	7.0	0.74/0.31	0.64/0.26	5.0	7.6	0.50/0.11	0.48/0.15
7.5	9.9	0.80/0.10	0.32/0.29	4.0	6.5	0.47/0.14	0.44/0.13	4.6	7.6	0.39/0.06	0.47/0.12
2.4	9.9	0.76/0.30	0.18/0.06	5.2	6.5	0.50/0.23	0.61/0.25	5.1	7.3	0.31/0.11	0.35/0.10
12.3	9.9	0.40/0.07	0.28/0.17	1.7	6.5	0.42/0.12	0.39/0.13	6.6	7.3	0.29/0.12	0.34/0.12
9.9	9.9	0.36/0.15	0.26/0.05	7.0	5.2	0.75/0.29	0.51/0.26	4.3	7.3	0.35/0.08	0.33/0.07
12.3	7.6	0.25/0.06	0.45/0.10	0.6	5.2	0.49/0.17	0.41/0.21	9.9	7.3	0.23/0.07	0.40/0.07
7.6	7.6	0.51/0.17	0.46/0.33	1.5	5.0	0.40/0.15	0.38/0.12	7.6	6.6	0.56/0.12	0.39/0.14
4.4	7.6	0.73/0.41	0.51/0.36	10.1	4.7	0.54/0.19	0.43/0.16	4.4	6.6	0.58/0.17	0.34/0.12
2.4	7.6	0.59/0.11	0.47/0.17	7.4	4.6	0.61/0.38	0.45/0.17	7.3	6.6	0.29/0.12	0.28/0.13
10.0	7.5	0.52/0.12	0.60/0.24	1.8	4.2	0.34/0.19	0.30/0.14	9.9	6.5	0.20/0.05	0.23/0.05
6.5	7.2	0.53/0.11	0.46/0.17	10.1	4.1	0.45/0.18	0.54/0.12	2.6	5.5	0.34/0.08	0.32/0.05
4.9	7.2	1.23/0.22	0.55/0.19	6.4	4.1	0.38/0.14	0.42/0.14	7.6	5.4	0.35/0.15	0.29/0.10
4.4	7.2	0.70/0.19	0.64/0.34	0.6	4.0	0.32/0.11	0.25/0.10	4.6	5.4	0.48/0.12	0.45/0.12
10.0	6.7	0.45/0.12	0.35/0.10	1.4	3.8	0.33/0.22	0.29/0.21	2.5	5.1	0.42/0.10	0.77/0.11
12.3	6.6	0.39/0.09	0.29/0.07	7.1	1.7	0.49/0.18	0.51/0.08	7.3	5.1	0.29/0.09	0.36/0.09
7.2	6.6	0.48/0.12	0.38/0.11	10.0	1.7	0.53/0.15	0.38/0.11	4.5	5.1	0.83/0.35	0.61/0.20
4.3	6.6	0.54/0.09	0.39/0.15	5.2	1.7	0.41/0.22	0.34/0.17	7.6	4.6	0.39/0.06	0.29/0.05
2.4	6.6	0.59/0.07	0.34/0.08	4.0	1.7	0.34/0.22	0.31/0.14	5.3	4.6	0.41/0.18	0.43/0.16
5.2	6.6	0.59/0.16	0.35/0.18	1.6	1.7	0.46/0.28	0.40/0.25	2.5	4.5	0.45/0.13	0.53/0.14
5.1	5.4	0.50/0.13	0.35/0.12	0.6	1.7	0.52/0.25	0.39/0.22	5.1	4.4	0.40/0.16	0.58/0.22
2.5	5.4	0.50/0.15	0.36/0.14	3.8	1.4	0.33/0.19	0.31/0.18	6.6	4.3	0.30/0.12	0.44/0.17
10.0	5.3	0.57/0.11	0.52/0.13	1.6	0.7	0.60/0.25	0.49/0.27	7.3	4.3	0.28/0.06	0.30/0.07
4.3	5.3	0.60/0.07	0.49/0.16	0.6	0.7	0.61/0.35	0.48/0.29	5.4	2.5	0.29/0.07	0.32/0.09
6.5	5.2	0.53/0.13	0.47/0.23	2.7	0.6	0.77/0.16	0.45/0.14	5.1	2.5	0.38/0.08	0.35/0.10
12.4	5.2	0.50/0.13	0.76/0.14	7.0	0.6	0.66/0.14	0.44/0.17	4.5	2.5	0.52/0.12	0.42/0.14
5.3	5.1	0.70/0.15	0.62/0.15	5.1	0.6	0.52/0.27	0.41/0.21				
7.3	5.1	0.53/0.13	0.55/0.19								
4.3	4.5	0.67/0.11	0.56/0.29								
7.5	4.5	0.90/0.30	0.56/0.31								
12.2	4.4	0.53/0.08	0.84/0.08								
2.4	4.4	0.68/0.22	0.60/0.33								
6.5	4.4	0.71/0.13	0.55/0.22								
12.4	2.5	0.45/0.10	0.51/0.07								
4.4	2.5	0.67/0.22	0.45/0.23								
7.5	2.4	0.72/0.12	0.40/0.17								
5.3	2.4	0.57/0.14	0.38/0.17								

4.5 Conclusion and Perspectives

In conclusion, the error mapping strategy described in this chapter provided narrower linewidths than those obtained in **Chapter 3**, and the best ^{1}H resolution to date. The main difference between the two approaches is that PIP strategies are able to remove all higher order terms from the Average Hamiltonian, whereas anti-z COSY only removes the residual coupling terms. Starting with a parameter fitting method, the deep learning methodologies were able to optimize performance and extend the resolution improvement to 2D correlation spectra. The PIP spectra obtained for the different eight different organic solids were consistent to the previous attributed assignments and the most of the linewidths were reduced to a few tens of Hz.

One main advantage of the PIP approaches is the simplicity of the experimental data. To obtain the isotropic signal, one only needs conventional 1D or 2D ^{1}H-^{1}H correlation spectra recorded at different spinning rates (eight different rates should be enough to describe the linewidth evolution). Plus, acquiring at the fastest MAS rates is not necessarily essential as the deep learning model is still able to predict a narrow isotropic spectrum with data up to 60 kHz MAS.

In PIPNET, it is worthy to note that the similar levels of performance were obtained for samples of different complexity, for example between β-AspAla and Molnupiravir. If the 1D isotropic spectrum still presents some overlap due to inhomogeneous contributions, the 2D isotropic spectrum obtained with PIPNET2D helps to disentangle the overlapped peaks, due to the addition of a second dimension on the spectrum, as demonstrated for L-tyrosine hydrochloride and ampicillin. In microcrystalline organic solids, the inhomogeneous contributions in 2D spectra (disorder and/or ABMS) will result most of the time in elongated and tilted lineshapes, facilitating the peak assignment.

The robustness of PIPNET enables the applicability to be expanded to other correlation experiments and other nuclei, that can benefit from greater resolution. The only necessary condition is to have the residual broadening that can be parametrized and mapped onto a different dimension from the desired isotropic signal.

Regarding ^{1}H linewidths, although most signals can be reduced to less than 100 Hz linewidth with the PIP strategy for some specific peaks in certain samples, the homogeneous broadening is no longer the dominating contribution to the ^{1}H lineshape. The isotropic spectra still present some ^{1}H signals with linewidths of several tens or hundreds of Hz. **Chapter 5** focuses on identifying and quantifying the different limiting contributions to ^{1}H lineshapes at the fastest MAS rates, which still prevent us from obtaining solid state ^{1}H linewidths that are comparable to those obtained in the liquid state.

Chapter 5 Remaining Barriers

This chapter has been adapted with permission from: Simões de Almeida, B.; Torodii, D.; Moutzouri, P.; Emsley, L., Barriers to Resolution in ^{1}H NMR of Rotating Solids, *J Magn Reson*, **2023**, 233, 107557.

My contribution was to acquire the data, process it and to analyse the results obtained. I also wrote the manuscript, with contributions of all authors.

5.1 Introduction

The ^{1}H resolution methods described in the previous chapters were focused on the removal of the residual homogeneous broadening. However, ^{1}H resolution of solids is also hampered by various inhomogeneous contributions, such as those caused by anisotropic bulk magnetic susceptibility (ABMS)[239-240, 334-335, 337], Δ_{ABMS}, chemical shift dispersion due to any degree of structural disorder[338], $\Delta_{disorder}$, and B_0 field inhomogeneity.[339] If we assume that B_0 field inhomogeneity is negligible in a properly shimmed magnetic field, the total ^{1}H linewidth under MAS can then be defined as follows:

$$\Delta_{total} = \Delta_{dipolar}^{MAS} + \Delta_{ABMS} + \Delta_{disorder} \qquad (5.1)$$

where $\Delta_{dipolar}^{MAS}$ is the residual homogeneous broadening caused by the higher order terms from the average Hamiltonian, as seen in Chapter 2. Among these higher order terms, up to third order half of them are refocused in a spin-echo experiment.[249] For this reason, we decompose $\Delta_{dipolar}^{MAS}$ into two components corresponding to the refocusable and non-refocusable parts:

$$\Delta_{dipolar}^{MAS} = \Delta_{dipolar}^{refocusable} + \Delta_{dipolar}^{non-refocusable} \qquad (5.2)$$

The PIP and PIPNET approaches are able to remove $\Delta_{dipolar}^{MAS}$ while retaining the isotropic signal. The PIP spectra obtained (see Chapter 4) yield linewidths between 50-400 Hz in crystalline compounds. There is now high interest in understanding both what these linewidths might correspond to, and if they are under- or over-estimated by the current PIPNet models, but also, more generally, to understand what the limiting linewidths in crystalline solids are. This would also be valuable to independently assess the robustness of PIP spectra. In principle, with the use of such methods and the development of new instrumentation capable of reaching even faster MAS rates, the inhomogeneous contributions might become the main limitation for high spectral resolution in ^{1}H solid-state NMR.

In **Chapter 5.2**, the distribution of the different contributions to the ^{1}H linewidth is quantified for five different samples. There is a particular focus on the ABMS broadening, with dilution experiments and DQ/SQ spectra. This source of broadening plus any correlated disorder broadening can be effectively removed by extracting the antidiagonal of a selected DQ/SQ peak, leading to substantially narrower linewidths. The evolution of the linewidth and of the lineshape as a function of the MAS rate is studied by fitting the different peaks to a Gaussian Lorentzian Sum (GLS) function.

5.2 Barriers to Resolution in ^{1}H of Rotating Solids

This chapter has been adapted with permission from: Simões de Almeida, B.; Torodii, D.; Moutzouri, P.; Emsley, L., Barriers to Resolution in ^{1}H NMR of Rotating Solids, J. Magn. Reson, in revision, **2023**.

My contribution was to develop and apply the method, acquire the data, and to analyse the results obtained. I also wrote the manuscript, with contributions of all authors.

5.2.1 Introduction

Faster MAS rates will improve ^{1}H resolution but it will only remove the homogeneous contributions to the linewidth. Here we aim to add to the existing literature by determining experimentally the weight of the different contributions to the linewidths in fast ^{1}H MAS spectra (up to 100 kHz) in a series of five compounds. We disentangle the different contributions through one- and two-dimensional experiments: by using dilution to identify the contribution of ABMS; by using extensive deuteration to identify the dipolar contributions; and by using variable MAS rates to determine the ratio between homogeneous and inhomogeneous components. We use five samples to illustrate key cases and limits: hexamethylbenzene (HMB) and 2-methyl-imidazole (2-MeIm) which have a significant ABMS contribution but different dipolar contributions, a zeolitic-imidazolate framework (ZIF-8) which has negligible ABMS and a high level of crystallinity, polystyrene (PS) which has a high level of structural disorder, and L-tyrosine hydrochloride which is a typical molecular organic compound. The findings are discussed in the context of limiting factors on ^{1}H resolution.

5.2.2 Theory

5.2.2.1 Linewidths

Bulk magnetic susceptibility (BMS), which originates from the interaction of a particle with the static magnetic field and results in the distortion of the local magnetic field, is an inhomogeneous interaction that can often broaden proton linewidths.[239-240, 334, 337, 340] For a given crystallite, BMS contains contributions both from the particle itself (the internal field) and its neighboring crystallites, which depends on their shape, orientation and distribution.[337] According to Alla and Lippmaa[240], under MAS, the isotropic part of the BMS is averaged out completely, and the only term that contributes to the MAS lineshape depends on the anisotropic part of the BMS, known as ABMS, leading to a shift of the form:[240]

$$\langle \Delta B_k' \rangle = \frac{1}{9} B_0 \Delta\chi_k \Delta D_k (3cos^2\gamma_k - 1) \qquad (5.3)$$

where for each crystallite, k, in the sample, B_0 is the applied magnetic field, $\Delta\chi_k$ is the anisotropy of the axially symmetric susceptibility tensor, ΔD_k is the anisotropy of the dipolar field tensor due to the neighboring particles, and γ_k is the angle between the principal axes of the susceptibility and dipolar field tensors. Samoson et al. also detailed the ABMS broadening.[340]

Alternatively, in the absence of MAS, the isotropic part of BMS can also be removed by impregnating a powder with a liquid of identical susceptibility, a method known as susceptibility matching.[341-342 343]

On the other hand, the ABMS broadening (Δ_{ABMS}) under MAS can be reduced by strategies that involve dilution of the sample of interest in a matrix that has purely isotropic BMS,[239] such as adamantane[240], NaCl[335] and KBr[334]. Surrounding the sample crystallites with crystallites with no ABMS reduces the effect of the local field induced by the neighboring crystallites.[104, 239]

ABMS produces a spread of chemical shifts, similarly to the effect of structural disorder, and the two effects cannot be immediately distinguished (i.e., they are both refocused by a 180° pulse). However, if ABMS is responsible for shift broadening (Δ_{ABMS}), the shift caused by ABMS will necessarily be the same for every nucleus

of a given molecule in a given crystallite. In a 2D shift correlation experiment, the ABMS shift broadening will be perfectly 1:1 correlated, creating an elongated lineshape parallel to the spectrum diagonal. This is not necessarily the case for shifts due to structural disorder ($\Delta_{disorder}$), which can take any shape and orientation/tilt angle, [328, 331, 344-347] [327] which here will be dubbed as uncorrelated disorder broadening ($\Delta_{disorder}^{uncorrelated}$). The total broadening due to structural disorder is decomposed as

$$\Delta_{disorder} = \Delta_{disorder}^{correlated} + \Delta_{disorder}^{uncorrelated} \quad (5.4)$$

Therefore, ABMS can be distinguished from uncorrelated broadening due to disorder by inspection of lineshapes in 2D correlation spectra.[328, 334, 344-345]

The contribution to the linewidth from $\Delta_{dipolar}^{non-refocusable}$ can be determined directly by the measurement of T_2' from a spin-echo decay[242, 348-349]:

$$\Delta_{dipolar}^{non-refocusable} = \Delta' = \frac{1}{\pi T_2'} \quad (5.5)$$

We note that the effect of broadening in ^{1}H MAS spectra due dipole-dipole couplings ($\Delta_{dipolar}^{MAS}$) can be reduced or removed by extensive deuteration of the sample, resulting in signals from isolated ^{1}H nuclei.

In a 2D correlation spectrum, the projection ($\Delta_{projection}$) over all the rows of the direct dimension should contain the same terms as Δ_{total}. On the other hand, the linewidth of the antidiagonal (i.e., a cross section through the 2D spectrum along a direction perpendicular to the diagonal) crossing through a given peak ($\Delta_{antidiag}$) will be free of broadening that is correlated along the diagonal.

With these experimental linewidths in hand the correlated and uncorrelated inhomogeneous broadening can be disentangled as

$$\Delta_{inhomogeneous}^{correlated} = \Delta_{ABMS} + \Delta_{disorder}^{correlated} = \Delta_{projection} - \Delta_{antidiag} \quad (5.6)$$

$$\Delta_{inhomogeneous}^{uncorrelated} = \Delta_{antidiag} - \Delta' \quad (5.7)$$

5.2.2.2 Lineshapes

In order to identify the limits of ^{1}H resolution, and the evolution of the linewidths with dilution and as a function of the MAS rate, an appropriate fitting function that accurately describes the experimental ^{1}H lineshapes must be chosen.

Spectral lineshapes are commonly described with the aid of Lorentzian and Gaussian functions. Typically, Lorentzian lineshapes are associated with isolated I = 1/2 spins, which are broadened by homogeneous mechanisms. [110, 350] On the other hand, Gaussian lineshapes are often found in rigid systems with distributions of isotropic chemical shifts. [110, 350] As a result, in many micro-crystalline organic powdered solids under MAS, the experimental lineshapes are characterized by a combination of both Lorentzian and Gaussian components. The most complete way to treat such a lineshape would be the use of a Voigt function,[299, 351] which is a convolution of a Gaussian (G) and a Lorentzian (L) function:

$$\mathrm{G}(\nu; w_G, p) = exp\left[-\frac{4\,ln(2)\,(\nu - p)^2}{{w_G}^2}\right] \quad (5.8)$$

$$\mathrm{L}(v; w_L, p) = \frac{1}{1 + 4\frac{(v-p)^2}{{w_L}^2}} \tag{5.9}$$

$$\mathrm{Voigt}(v; w_G, w_L, p) = G * L \tag{5.10}$$

where *w* is the full width at half maximum (FWHM) of the function, and *p* is the peak position.

Historically, the repeated convolution required during a fitting process was time consuming,[351] and an analytical approximation was introduced which consisted of a linear combination of Gaussian and Lorentzian lines. Wertheim *et al.*. introduced the Gaussian-Lorentzian Sum (GLS) (Eq. 5.11) [299, 351-352] to fit any experimental lineshape:

$$\mathrm{GLS}(v; w, p, m) = (1-m)\, exp\left[-\frac{4\, ln(2)\,(v-p)^2}{w^2}\right] + \frac{m}{1 + 4\frac{(v-p)^2}{w^2}} \tag{5.11}$$

where *m* is the mixing factor describing the lineshape, with *m* = 1 being purely Lorentzian, and *m* = 0 being purely Gaussian. Unlike Voigt, in GLS the same width is used for the Gaussian and Lorentzian components, and the components are weighted by the mixing factor. It has been shown with simulations that the GLS function accurately determines peak areas created by different Voigt profiles, down 0.72% error.[352] The GLS function has long been used for lineshape fitting for NMR spectral quantification[353], with GLS, also sometimes referred to as GALORE, still being used in recently developed software for NMR spectral analysis or peak deconvolution.[354-356]

In the following, all reported FWHM are from fitting to a GLS function, unless specified otherwise. In sections 5.2.4.3 and 5.2.4.4, *m* and *w* are studied as a function of the MAS rate, and fits to the Voigt function are similarly analyzed to serve as a complementary tool to aid our understanding of proton lineshape behavior with increasing spinning speeds.

5.2.3 Experimental

Zinc 2-methylimidazole metal-organic framework (ZIF-8) and natural abundance 2-methylimidazole (2-MeIm) were purchased from abcr GmbH. HMB, L-tyrosine hydrochloride and KBr were purchased from Thermo Fisher Scientific, Combi-Blocks and Sigma Aldrich, respectively. 98% deuterated 2-MeIm-d6 was purchased from Cambridge Isotope Laboratories Inc. Polystyrene (PS) beads with a mean particle size of 1.1 µm size were purchased from Sigma Aldrich as an aqueous suspension and lyophilized. All samples were used without further recrystallization and were crushed with a mortar and pestle prior to packing into the NMR sample rotors.

All spectra were acquired on a 21.14 T Bruker Avance Neo spectrometer corresponding to 900 MHz ^{1}H frequency. The sets of spectra at variable MAS rates ranging from 40 to 100 kHz were acquired using a Bruker 0.7 mm room temperature HCN CP-MAS probe with active temperature control in order to maintain the sample temperature at approximately 295 K across all spinning rates so as to minimize any spectral changes related to temperature effects. The magic angle was optimized directly on each sample by maximizing the T_2'.[357] The following experiments were acquired at every MAS rate: an 1D ^{1}H spectrum, acquired using a rotor-synchronized spin echo sequence for background suppression; a pseudo 2D echo experiment with increasing rotor-synchronized delays to measure T_2'; and a 2D Double Quantum – Single Quantum (DQ/SQ) ^{1}H-^{1}H spectrum using the $BABA_{xy16}$ pulse sequence.[203] (Details are given in Appendix VII)

Spectra of HMB and 2-MeIm diluted in KBr were acquired using a Bruker 1.3 mm room temperature HDCN CP-MAS probe. The temperature was kept constant using a VT flow at 295K for 2-MeIm and 265K for HMB. The ^{1}H chemical shifts of L-tyrosine hydrochloride at 100 kHz MAS and the ^{1}H and ^{13}C chemical shifts of HMB were referenced and assigned according to literature.[214,334] L-tyrosine hydrochloride and HMB were then used as external references for the referencing of the proton chemical shifts of 2-MeIm, ZIF-8 and Polystyrene. All experiments and raw data are detailed in the Supplementary Information.

Both 0.7 and 1.3 mm probes were shimmed using a rotor filled with adamantane (also used as an external reference) and yielding 3 and 14 Hz for the ^{13}C linewidth, respectively, measured through a ^{13}C cross-polarization

(CP) experiment. (Note the shimming was not explicitly evaluated with single pulse ^{13}C NMR to confirm the quality of shimming on the whole sample, and it is assumed that the B_0 field inhomogeneity in the adamantane rotor is comparable to that in the other samples.) For all compounds, $\Delta\chi$ was predicted from the bulk magnetic susceptibility tensor, calculated from DFT computations using Quantum ESPRESSO (section 5.2.5.4 in Appendix VII). All the lineshapes presented in this work were fitted to both Voigt and GLS functions using a home-written script in MATLAB (available in Supplementary Information. All fitting parameters of the linewidth evolution as a function of the rotor period are detailed in section 5.2.5.2 of Appendix VII.

5.2.4 Results & Discussion

5.2.4.1 Removal of correlated inhomogeneous broadening

HMB is a reference sample for the investigation of ABMS[113, 239-240, 334], since with a predicted $\Delta\chi$ of 1.34 ppm (Table 5.64), it presents significant broadening due to susceptibility. The effect of dilution of HMB with KBr on its ^{1}H and ^{13}C linewidths at 60 kHz MAS is depicted in Figure 5.1, where spectra of undiluted HMB are shown in blue, and those of diluted HMB in KBr (20:80% w/w) are shown in red. From a series of dilution experiments[335] (Table 5.65), this ratio was found to give the best narrowing effect while retaining sufficient sensitivity. As shown in Figure 5.1 (a) and (b), dilution results in approximately 0.6 ppm of line narrowing to both ^{1}H 1D and ^{13}C CP linewidths, due to the partial suppression of ABMS. The susceptibility broadening is proportional to B_0, so it is expected to be the same for different nuclei when expressed in ppm. Another effect of ABMS is an overall shift[239, 358-360] for all ^{1}H and ^{13}C resonances observed in the spectra, and dilution reduces this shift by 0.46 ppm in Figure 5.1. This experiment confirms that at least 45% of the residual ^{1}H linewidth in HMB at 60 kHz MAS is due to ABMS. The remaining 55% (669 Hz) can be due to residual ABMS, dipolar broadening, and structural disorder.

Figure 5.1 (c) depicts ^{1}H-^{1}H DQ/SQ spectra of HMB with and without dilution. We note that the lineshape in both samples is elongated along the diagonal. This indicates that the broadening is highly correlated. To estimate the degree of correlation, we compare the linewidth in the skyline/positive projection ($\Delta_{projection}$) of the spectrum to the linewidth of the antidiagonal perpendicular to the DQ diagonal of the DQ/SQ spectrum ($\Delta_{antidiag}$). (Note that in principle, the sum projections should be identical to the 1D spectra. The small differences in the linewidths measured here for the 1D spectra and the projections are related to the selection of crystallites with longer relaxation times which occurs whenever t_1 evolution is present.[213, 349] Thus, it is most appropriate here to compare the individual horizontal cross sections to the projections.) Notably, in the undiluted sample, the antidiagonal shows a ^{1}H line narrowing of 1.04 ppm compared to the projection. The reduction we see here is due to the removal of residual ABMS and any broadening due to correlated structural disorder.[328] The remaining 160 Hz ($\Delta_{antidiag}$) can be due to dipolar broadening and/or to uncorrelated structural disorder. For both undiluted and diluted HMB samples the narrowing effect in the 2D spectra is due to suppression of ABMS and any correlated disorder.

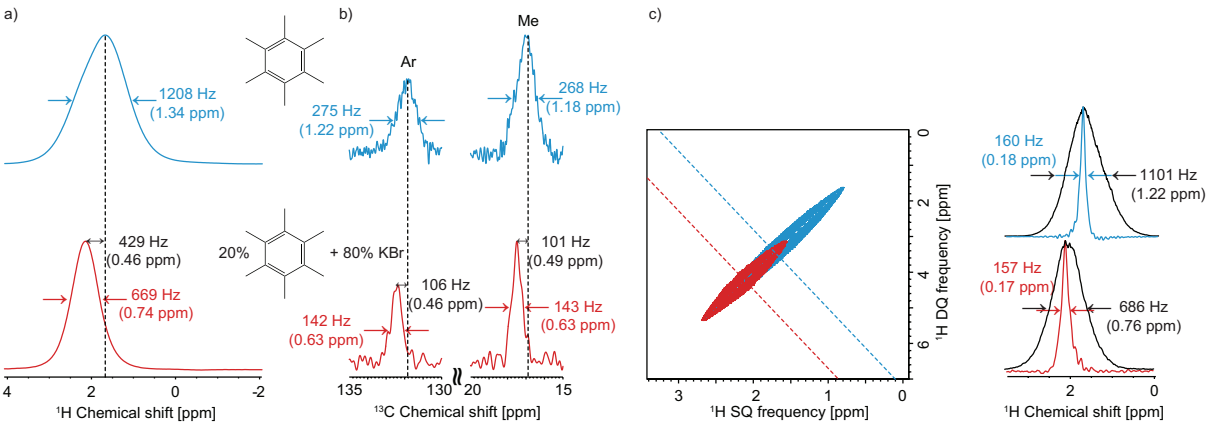

Figure 5.1 The effect of dilution in KBr on ^{1}H spectra of HMB: (a) ^{1}H 1D, (b) ^{13}C CP, (c) ^{1}H-^{1}H DQ/SQ BABA for a sample of HMB with (red) and without (blue) dilution in 80% of KBr. The tilted dashed lines in the 2D spectrum represent the antidiagonals extracted from 2D spectra. The vertical dashed lines highlight the ^{1}H and ^{13}C chemical shift of the undiluted sample and the shift induced by KBr dilution is given in Hz and ppm for each peak in the diluted spectra. In (c), the projections of the two-dimensional experiments are shown in black, overlaid with the antidiagonals. The full width at half maximum (FWHM) of each peak is indicated.

5.2.4.2 Removal of correlated inhomogeneous broadening $\Delta_{dipolar}^{MAS}$

To probe the total homogeneous contributions ($\Delta_{dipolar}^{MAS}$) to the residual linewidths, we propose to use extensive deuteration to remove ^{1}H-^{1}H dipolar couplings. To this end we studied four samples of 2-MeIm ($\Delta\chi$ = 2.69 ppm), shown in Figure 5.2: natural abundance undiluted (blue), 98% deuterated undiluted (purple), and their variants diluted with KBr to 95% (protonated in red and deuterated in orange). In both protonated and deuterated 2-MeIm, KBr dilution results in line narrowing of 0.17 ppm for H1 and approximately 0.1 ppm for H4, as depicted in Figure 5.2 (a) In the protonated 2-MeIm, the line narrowing for C4 was 0.15 ppm (Figure 5.2 (b)). KBr dilution in both cases reduces (but does not completely remove) the contribution due to ABMS. (Note also that, as expected,[239, 358-360] and as observed above for HMB, dilution with KBr also reduces the ABMS induced shift).

Deuteration of 2-MeIm, on the other hand, also results in 0.09 and 0.18 ppm line narrowing for H1 and H4, respectively, but this time due to the removal of residual ^{1}H homonuclear dipolar couplings. As expected, the spectrum with the narrowest lines is the one acquired for the 98% deuterated 95% diluted 2-MeIm sample (Figure 5.2 (a)), due to the simultaneous partial suppression of ABMS and essentially complete suppression of residual dipolar coupling, yielding linewidths of 0.53 ppm (475 ± 24 Hz) (H1) and 0.52 ppm (466 ± 24 Hz) (H4). Figure 5.2 (c) shows the region of the DQ/SQ spectra for H1-H4 correlation peaks. Again, the linewidths measured from the antidiagonals are almost the same for undiluted and diluted 98% deuterated 2-MeIm. Small differences in the measured linewidths are assumed to be due to the low sensitivity of the fully deuterated diluted 2-MeIm sample. The linewidths in the antidiagonals are 106 ± 27 and 110 ± 27 Hz for H1 and H4, respectively, as opposed to 687 ± 27 and 702 ± 27 Hz in the ordinary, fully protonated, undiluted projections.

As with HMB, the narrowest linewidths are found with the antidiagonal of the DQ/SQ experiment for both HMB and 2-MeIm, since they are free from any correlated inhomogeneous broadening ($\Delta_{inhomogeneous}^{correlated}$). The linewidth will therefore be limited by the homogeneous broadening. Here we clearly see that 98% deuteration, which removes the remaining homogeneous broadening ($\Delta_{dipolar}^{MAS}$), leads to a reduction in linewidth, down to 103 Hz. This remaining linewidth is thus attributed to $\Delta_{disorder}^{uncorrelated}$.

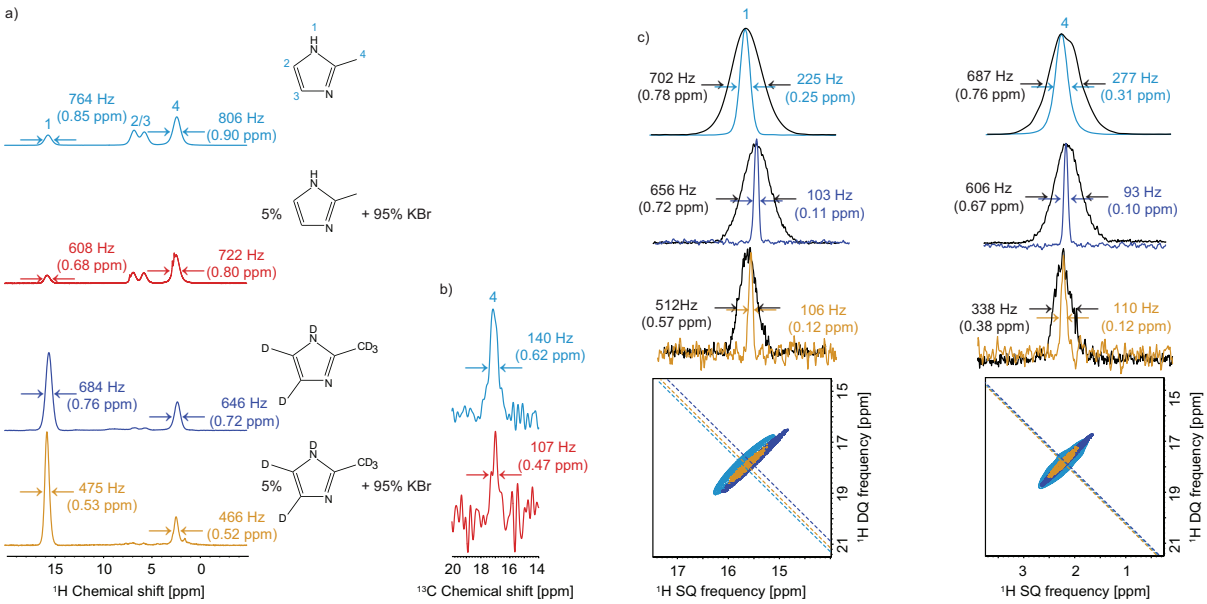

Figure 5.2 The effect of dilution with KBr and deuteration on the spectra of 2-MeIm: a) ^{1}H 1D, b) ^{13}C CP, c) ^{1}H-^{1}H DQ/SQ BABA regions of the H1/H4 cross peaks of pure natural abundance (blue), pure 98% deuterated (purple), and diluted in 95% w/w KBr for the fully protonated (red) and 98% deuterated 2-MeIm (orange) samples. The tilted dashed lines in the 2D spectra represent the antidiagonals extracted from the DQ/SQ spectra. The projections of the two-dimensional spectra are shown in black, overlaid with the antidiagonals, extracted from the same 2D spectra. The linewidths are represented as FWHM in each case.

5.2.4.3 Linewidths and lineshapes as a function of the MAS rate

Proton lineshapes were studied over a range of MAS rates between 40 and 100 kHz. The one-dimensional ^{1}H spectrum of HMB acquired at 100 kHz MAS (Figure 5.3 (a), shows a linewidth of 969 ± 27.6 Hz. The corresponding DQ/SQ spectrum (Figure 5.3 (b)) acquired for the same sample shows, as expected, a highly correlated 2D lineshape, similar to the one acquired at 60 kHz MAS (Figure 5.1 (c)), characteristic of ABMS and correlated structural disorder. Notably, in this spectrum, the projection ($\Delta_{projection}$) of the two-dimensional peak has a linewidth of 926 ± 27.6 Hz, whereas the linewidth of the antidiagonal ($\Delta_{antidiag}$), which as discussed above lacks contributions of ABMS or correlated structural disorder, is reduced to 111 ± 27.6 Hz, as shown in Figure 5.3 (c). At 100 kHz MAS, the T_2' measured for the HMB proton resonance is 5.73 ± 0.01 ms, corresponding to a homogeneous contribution Δ′of 55 ± 1 Hz, which corresponds to 6% of the linewidth of the projection.

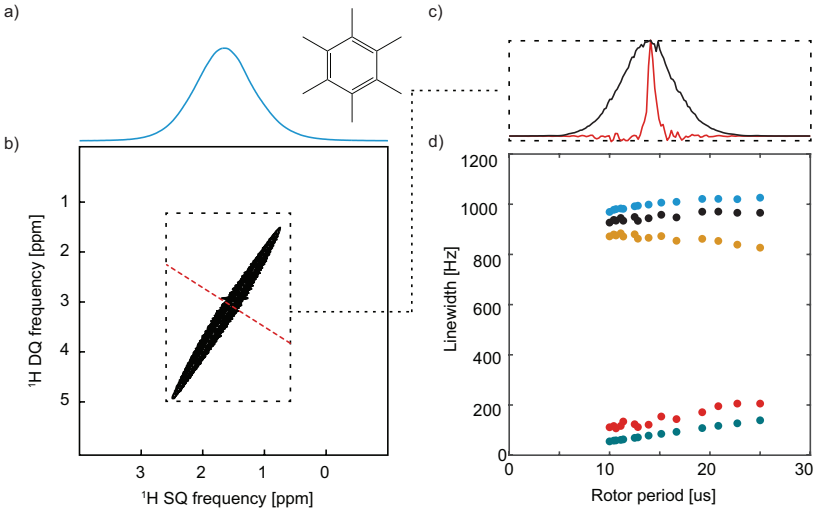

Figure 5.3 HMB: (a) Chemical structure and 1D ^{1}H spectrum and (b) 2D ^{1}H-^{1}H DQ/SQ spectrum of HMB at 100 kHz MAS. The tilted dashed line in the 2D spectrum represents the antidiagonal extracted. (c) Skyline projection $\Delta_{projection}$ (black) and antidiagonal $\Delta_{antidiag}$ (red) from the ^{1}H-^{1}H DQ/SQ spectrum in (b). (d) Measured linewidths as a function of the rotor period: 1D ^{1}H (blue), Δ′ (blue lagoon) (from the measurement of T_2', see Appendix VII for details), the DQ/SQ projection (black), DQ/SQ antidiagonal (red), and the total inhomogeneous contribution (orange), calculated as $\Delta_{projection} - \Delta'$

In Figure 5.3 (d), the dependence of these different linewidths fitted to the GLS lineshape function, as a function of the rotor period, are shown. (Note that the Voigt linewidths are given in Figure 5.12 and Table 5.30, and the quality of the lineshape fits with both functions is summarized in Figure 5.11. The GLS fits are slightly better than for Voigt, but the difference is negligible. Overall, the RMSE for all the lineshape fits at all MAS rates is small (a maximum of 0.04) yielding accurate fitting to both functions.) All the linewidths shown in Figure 5.3 (d) were fitted to both a linear and a quadratic dependence on the rotor period, in order to assess what is the MAS dependence of the linewidth of every studied resonance here. The level of the MAS dependence is linked to the preponderance of the higher order terms of the average Hamiltonian. All fitting parameters are detailed in Table 5.23. The root-mean square error (RMSE) values and the linewidths predicted at an infinite MAS rate for the linear fitting are summarized in Table 5.1. The linewidth corresponding to the inverse of T_2', $\Delta' = 1/(\pi T_2')$, decreases linearly with MAS and is completely eliminated at infinite MAS rate. This linear dependence is characteristic of the fact that only the second order terms of the average Hamiltonian, which have an inverse linear dependence on the MAS rate, are relevant, and higher order terms are negligible in this case.[249] The one-dimensional ^{1}H linewidth (blue dots) has an overall decrease of just 45 Hz over the range of MAS rates recorded here, showcasing again a rather small homogeneous contribution. (Which is expected since the HMB molecules rotate rapidly in the plane of the ring, and the methyl groups rotate rapidly around their C3 axes, leading to a significant reduction In the intramolecular dipolar couplings.[361]) If Δ′ is subtracted from the projection, the total inhomogeneous linewidth (orange dots) is obtained. As would be expected, since only the terms arising from dipolar couplings should vary with MAS rate, the inhomogeneous linewidth is seen to be almost constant over the whole range of MAS rates. Additionally, in the Voigt fittings (Figure 5.12), the w_G of both the projection and the antidiagonal are constant, in agreement with the GLS linewidths.

Table 5.1 HMB: Predicted linewidth at infinite MAS rate Δ_∞ of the different ^{1}H contributions, obtained by fitting the data in Figure 3 to a linear function of the rotor period, together with the standard errors (95 % confidence) and the RMSE *values for* the fits.

	HMB H1	
	Linear	
	Δ_∞	RMSE
1D	917 ± 13	3.01
Δ'	0 ± 0	0.59
$\Delta_{projection}$	911 ± 16	8.18
$\Delta_{antidiag}$	31 ± 19	9.91

Concerning the DQ/SQ spectra, the linewidths of the projections of the two-dimensional lineshapes (black dots) follows a similar dependence as the inhomogeneous linewidth, showing that the dominant contribution to the linewidth is ABMS and/or correlated disorder. In the antidiagonal extracted from the 100 kHz spectrum, the homogeneous contribution Δ' = 55 Hz measured through T_2' represents 49% of the total linewidth of the antidiagonal ($\Delta_{antidiag}$ = 111.0 ± 27.7 Hz). $\Delta_{antidiag}$ decreases linearly as a function of the rotor period, and has an intercept at 31 ± 19 Hz, which in principle corresponds to the uncorrelated inhomogeneous linewidth ($\Delta_{inhomogeneous}^{uncorrelated}$). In summary, we find that the overall lineshapes in HMB is dominated by ABMS and/or correlated disorder. However, if the antidiagonal is extracted from a 2D correlation experiment, the linewidth is much narrower and the removal of residual homogeneous contributions at faster rates is still beneficial.

The second sample studied here is ZIF-8. Due to its cubic crystal structure (Figure 5.4), ABMS is predicted to be zero. In addition, the highly ordered crystalline environment should translate to only a small contribution from structural disorder.

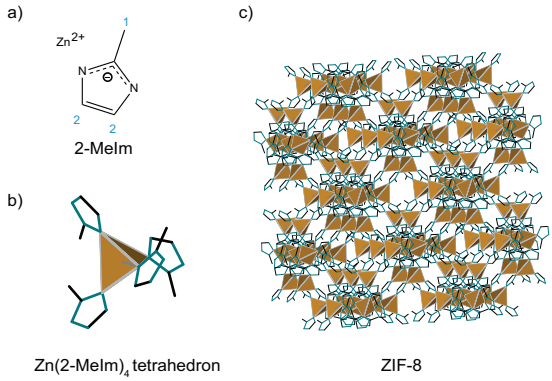

Figure 5.4 ZIF-8 structure: (a) 2D structure of Zn^{2+} and 2-methylimidazole (2MeIm); (b) 3D structure of Zn(2-MeIm) tetrahedron; (c) Zeolitic imidazolate framework ZIF-8. The structure is taken from CSD entry FAWCEN04. [362]

In Figure 5.5 (a), the 1D ^{1}H spectrum at 100 kHz MAS shows linewidths of 200 ± 7 Hz (H2) and 245 ± 7 Hz (H1). In the same figure, the corresponding DQ/SQ spectrum shows two auto correlation peaks and cross peaks between H1 and H2. The projection $\Delta_{projection}$ (black) and the antidiagonals $\Delta_{antidiag}$ (red) have almost identical linewidths, indicating that, in direct contrast to HMB, correlated broadening is negligible in this sample.

The T_2' measured at this rate are 3.43 ± 0.02 ms for H2 and 2.46 ± 0.02 ms for H1 corresponding to linewidths of Δ' = 92 ± 1 and 129 ± 1 Hz, respectively. The homogeneous contributions represent therefore 57 % of the projection for H2, and 95 % for H1.

Table 5.2 shows the predicted linewidth at infinite MAS rate, Δ_∞. For H2, the linewidths fit best to a quadratic depenence. From Average Hamiltonian Theory, a quadratic dependence is symptomatic of third order terms contributing to the linewidth.[249] For H2, the total inhomogeneous contribution (orange dots) is nearly constant across the MAS rate range with an average value of 56 ± 7 Hz. The spectra exctracted from DQ/SQ projections and antidiagonals show very similar linewidths over all MAS rates, indicating the absence of any correlated inhomogeneous distributions. Therefore, the ^{1}H spectrum will still benefit from faster spinning, allowing the more complete removal of residual homogeneous contributions.

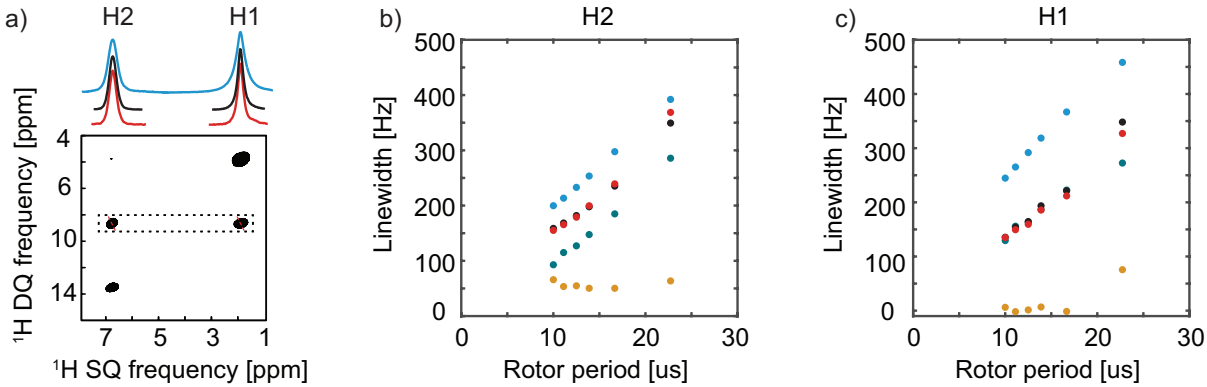

Figure 5.5 ZIF-8: (a) 2D ^{1}H-^{1}H DQ/SQ spectra of ZIF-8 at 100 kHz MAS and 1D ^{1}H (blue), $\Delta_{antidiag}$ single row (red) and positive projection $\Delta_{projection}$ (black) extracted from the region delimited by the dashed rectangle. The tilted dashed lines in the 2D spectrum represent the antidiagonals extracted. (b) and (c) evolution of the measured linewidths as a function of the rotor period for (c) H2 and c) H1: 1D ^{1}H (blue), Δ' contribution (blue lagoon), ^{1}H-^{1}H DQ/SQ projection (black), ^{1}H-^{1}H DQ/SQ antidiagonal (red), and the inhomogeneous contribution (orange), calculated as " $\Delta_{projection} - \Delta'$"

For the methyl peak (H1) in Figure 5.5 (c), the linewidths fit best to a linear regression. The linewidths measured in the $\Delta_{projection}$ and $\Delta_{antidiag}$ have similar values to those calculated from the T_2' measurements, appearing to be purely homogeneous. The 1D linewidths presents an intercept at 81 ± 20 Hz, respectively, showing the presence of small inhomogeneous contributions.

Note that for the methyl peak, fitting with the Voigt function (Figure 5.14) yields a purely Lorentzian lineshape that is equal to Δ', symptomatic of pure dipolar broadening. [110, 350]

This high crystallinity of ZIF-8 allows to illustrate briefly the effect of B_0 inhomogeneity. In Figure 5.24, the DQ/SQ spectrum at 100 kHz MAS of ZIF-8 was acquired with deliberately bad shims. The peak from H2 is no longer round, but is elongated and tilted. The transformation of the peak shape shows how B_0 inhomogeneity induces the same kind of correlated broadening as ABMS.

Table 5.2 ZIF-8: Predicted linewidth at infinite MAS rate Δ_∞ of the different ^{1}H contributions, obtained by fitting the data in Figure 5 to a quadratic function of the rotor period for H2, and linear function for H1, together with the standard errors (95 % confidence) and the RMSE values for the fits.

	ZIF-8 H2		ZIF-8 H1	
	Quadratic		Linear	
	Δ_∞	RMSE	Δ_∞	RMSE
1D	69 ± 30	1.44	81 ± 20	4.93
Δ'	0	3.21	0	4.72
$\Delta_{projection}$	139 ± 8	0.37	0 ± 5	4.61
$\Delta_{antidiag}$	138 ± 30	1.45	0 ± 5	5.14

The third compound studied is L-tyrosine hydrochloride ($\Delta\chi$ = 0.62 ppm), which has 10 different resonances, some of them overlapping even at 100 kHz MAS, as seen in Figure 5.6. Linewidths were measured only for protons H1, H9 and H3', which are well-resolved peaks.

The DQ/SQ spectrum shows markedly correlated lineshapes for the double quantum pair between H1 and H9, whereas the H3' 2D peak in the H2/H3-H3' double quantum correlation pair has a rounder shape.

In Figure 5.7, the antidiagonal linewidths in red are compared to the respective projection, in black. For all three protons, $\Delta_{antidiag}$ is again narrower (141 ± 6 Hz, 149 ± 6 Hz, and 314 ± 6 Hz for H1, H9, and H3' respectively) than $\Delta_{projection}$ (289, 298, and 394 Hz for H1, H9, and H3' respectively). The T_2' measured at 100 kHz are 5.33 ± 0.02 ms (60 ± 1 Hz) for H1, 4.08 ± 0.02 ms (78 ± 1 Hz) for H9, and 1.74 ± 0.02 ms (182 ± 1 Hz) for H3', corresponding to homogeneous linewidths of 20%, 26% and 46% with respect to the projection.

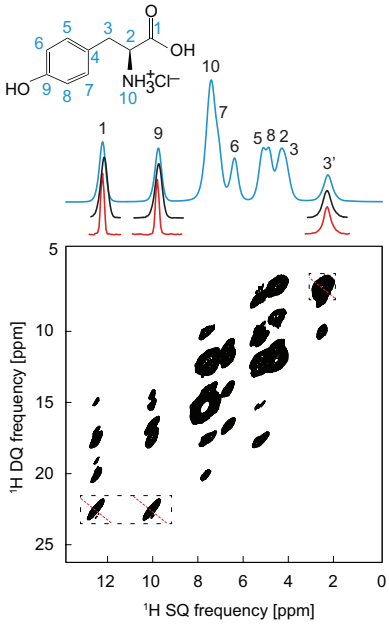

Figure 5.6 L-tyrosine.HCl: 2D ^{1}H-^{1}H DQ/SQ at 100 kHz MAS, 1D ^{1}H spectrum (blue), positive projections (black) extracted between 22.8 ppm - 25.5 ppm and 7.20 ppm - 9.12 ppm and antidiagonals (red). The tilted dashed lines in the 2D spectrum represent the antidiagonals extracted from the DQ/SQ spectrum.

The linewidths at infinite MAS rate extrapolated from the MAS dependence for L-tyrosine hydrochloride (Figure 5.7 (a), (b) and (c)) are summarized in Table 5.3.

For H1 in Figure 5.7 (a), all linewidths fit best to a quadratic dependence on the MAS rate (Table 5.3). $\Delta_{projection}$ (black dots) intercepts at 277 ± 21 Hz and $\Delta_{antidiag}$ intercepts at 37 ± 25 Hz, highlighting the considerable correlated inhomogeneous contribution to the linewidth. H9 also fits best to a quadratic MAS dependence, with similar values as the ones from H1.

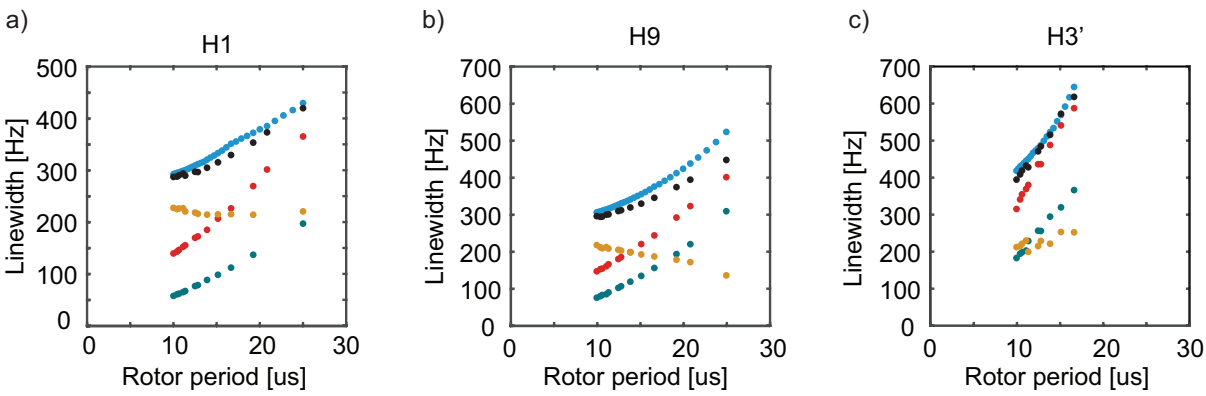

Figure 5.7 L-Tyrosine HCl: Evolution of the measured linewidths as a function of the rotor period for (a) H1, (b) H9 and (c) H3': 1D ^{1}H (blue), Δ' contribution (blue lagoon), $\Delta_{projection}$ (black), $\Delta_{antidiagonal}$ (red), and the inhomogeneous contribution (orange), calculated as $\Delta_{projection} - \Delta'$

For H3', in Figure 5.7 (c), the T_2' follows a quadratic dependence between 60-100 kHz MAS. $\Delta_{antidiag}$ intercepts at zero, but the RMSE is higher than for the other sites. This would mean that there is no uncorrelated inhomogeneous contribution, and this was not observed for the other protons. For this to be the case, $\Delta_{antidiag}$ should align with the Δ' values, as was shown in ZIF-8.

Table 5.3. L-Tyrosine hydrochloride: Predicted linewidth at infinite MAS rate Δ_∞ of the different ^{1}H contributions, obtained by fitting the data in Figure *5* to a *quadratic* function of the rotor period *for H1, H9 and H3',* together with the standard errors (95 % confidence) and the RMSE *values for* the fits.

	Tyr H1		Tyr H9		Tyr H3'	
	Quadratic		Quadratic		Quadratic	
	Δ_∞	RMSE	Δ_∞	RMSE	Δ_∞	RMSE
1D	219 ± 10	1.76	288 ± 5	0.74	348 ± 71	1.15
Δ'	0	1.28	0	0.86	0	6.61
$\Delta_{projection}$	277 ± 21	2.47	284 ± 48	1.48	181 ± 176	5.41
$\Delta_{antidiag}$	37 ± 25	2.77	55 ± 32	0.99	0 ± 10	14.3

The final sample studied here is lyophilized polystyrene. The aromatic peak at 7 ppm in the 1D spectrum has a linewidth of 1613 ± 222 Hz. The autocorrelation peak for the aromatic protons in the DQ/SQ spectrum shown in Figure 5.8 (b) and (c) presents a linewidth of 1538 ± 111 Hz for the projection and 948 ± 111 Hz for the antidiagonal. The T_2' measured at 100 kHz MAS is 1.97 ± 0.02 ms, (161 ± 1 Hz). This peak is mainly inhomogeneously broadened since the homogeneous contribution accounts for only 10% of the total linewidth.

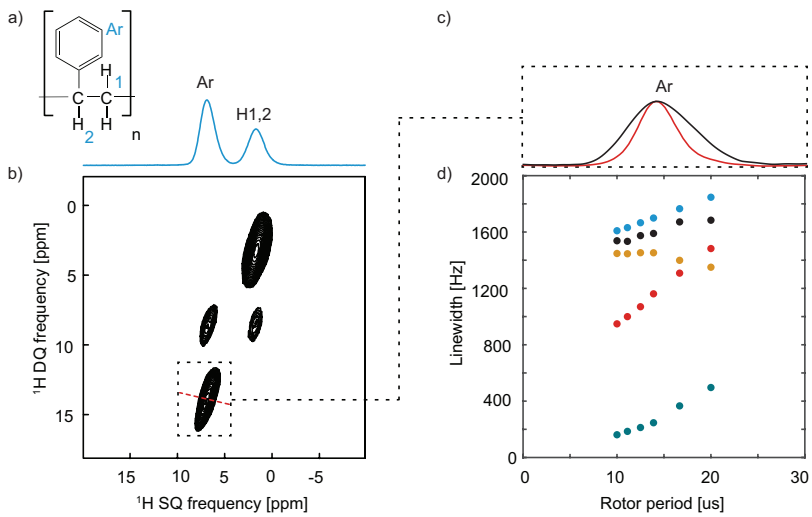

Figure 5.8 Polystyrene: (a) chemical structure, 1D ^{1}H spectrum, and (b) 2D ^{1}H-^{1}H DQ/SQ spectrum acquired at 100 kHz MAS. The tilted dashed lines in the 2D spectrum represent the antidiagonals extracted from DQ/SQ. (c) Positive projection (black) extracted between 9.90 ppm – 18.78 ppm overlayed with antidiagonal (red) for the Ar and (d) evolution of the measured linewidths as a function of the rotor period: 1D ^{1}H (blue), Δ' contribution (blue lagoon), ^{1}H-^{1}H DQ/SQ projection (black), ^{1}H-^{1}H DQ/SQ antidiagonal (red), and the inhomogeneous contribution (orange), calculated as $\Delta_{projection} - \Delta'$.

The linewidths fit best to a linear regression. The Δ_∞ for the projection is 1363 ± 90 Hz and 402 ± 32 Hz for the antidiagonal. For polystyrene, the resolution improvement from the DQ antidiagonal will be less important as compared to the other samples, since uncorrelated inhomogeneous broadening is the main contribution to the linewidth, due to structural disorder.

Table 5.4 Polystyrene: Predicted linewidth at infinite MAS rate Δ_∞ of the different ^{1}H contributions, obtained by fitting the data in Figure *8* to a *linear* function of the rotor period *for Ar,* together with the standard errors (95 % confidence) and the RMSE *values for* the fits.

	PS Ar	
	Linear	
	Δ_∞	RMSE
1D	1367 ± 8	1.74
Δ′	0	8.04
$\Delta_{projection}$	1363 ± 90	18.68
$\Delta_{antidiag}$	402 ± 32	6.94

5.2.4.4 Summary of the contributions to the linewidth

The individual contributions to the total linewidth for each resonance studied here is shown in Figure 5.9 for two different MAS rates, 60 kHz and 100 kHz (90, 80 and 72 kHz MAS are presented in Figure 5.23). The uncorrelated inhomogeneous contribution can be calculated as the difference between the antidiagonal from the DQ spectrum and Δ′. The correlated inhomogeneous linewidth is the difference between the total linewidth (projection) and the antidiagonal. The decomposition of the linewidths shows how each molecule can have a different distribution of contributions. The HMB linewidth is mainly composed of correlated inhomogeneous interactions and the removal of the remaining homogeneous contribution will only slightly improve the resolution.

Often, the biggest gain in resolution is here obtained by recording a 2D spectrum, which will result in characteristic elongated lineshapes in the 2D space, with a much narrower linewidth across the antidiagonal.

Different distributions of contributions can even be observed within the same molecule. The linewidths in L-tyrosine hydrochloride are certainly uniformly much narrower than those in HMB, but H1 and H9 present similar levels of the different contributions, with 147 ± 22 and 148 ± 22 Hz of correlated inhomogeneous broadening, respectively, while H3' has a significantly larger homogeneous and uncorrelated inhomogeneous contribution than H1 and H9. However, it only has 79 ± 22 Hz of correlated inhomogeneous contributions.

ZIF-8 shows the narrowest linewidths among the four samples, with for H1, the linewidth being essentially entirely homogeneous, with only 5 ± 13 Hz of uncorrelated inhomogeneous broadening.

Note that we used cross peaks in the analysis because they were generally better resolved in most of the samples (and autocorrelation peaks are not always present). In the cases where both cross peaks and autocorrelation peaks are present and resolved we do see differences between the widths of the cross- and auto-peaks, of between 10 to 50 Hz). This is not unexpected, but in most cases, this is within the overall error of the analysis, and we have not pursued this any further. The linewidths of all the observable peaks are given in the Tables in the Appendix VII.

Only ABMS is common to all peaks, and the homogeneous contribution is common to all 2D peaks of the same site. Notably, in previous work by Cadars et al.[327, 345], DQ/SQ spectra presented different shapes and tilt angles for cross peaks corresponding to the same spin, but for different correlations.

PS has the largest linewidth. Although it also has a large homogeneous contribution (160 Hz) when compared to other samples, it is only a small contribution to the total linewidth. The uncorrelated inhomogeneous linewidth is the largest contribution (786 ± 110 Hz), when compared to correlated one (589 ± 110 Hz). This is most striking in the DQ/SQ spectrum where, unlike HMB, the spectrum presents a rounder lineshape, a clear indication of the uncorrelated contribution. Note that the uncorrelated inhomogneous linewidth includes both the contribution from $\Delta_{dipolar}^{refocusable}$ and the contribution due to structural disorder. Since $\Delta_{dipolar}^{refocusable}$ is likely to be of the same order in magnitude as Δ', when the uncorrelated inhomogeneous linewidth ($\Delta_{inhomogeneous}^{uncorrelated}$) is much larger than Δ', as is the case for PS, then it can be ascribed to the effect of structural disorder.

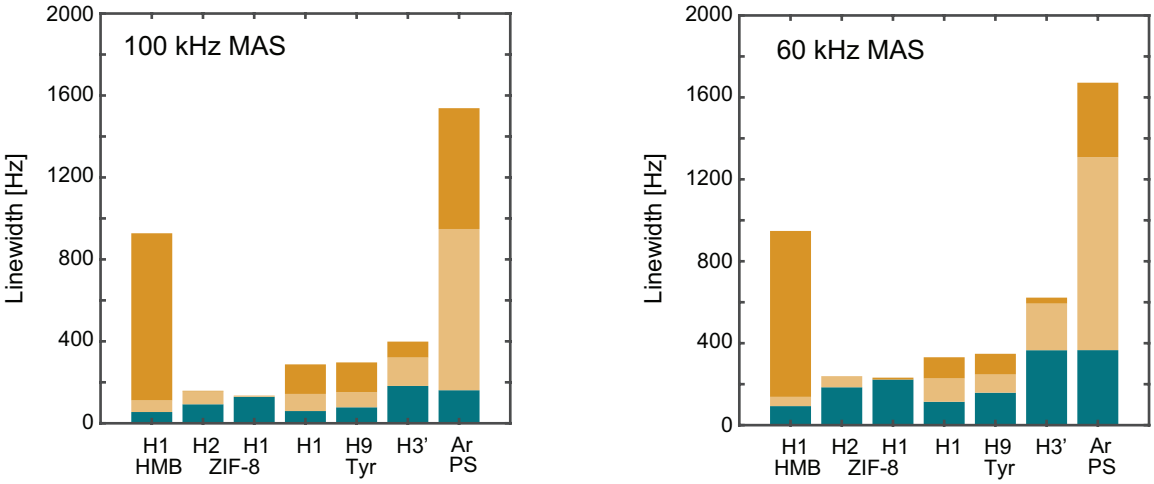

Figure 5.9 The different contributions to linewidth at 100 kHz MAS (a) and 60 kHz MAS (b): For all the different resonances, the homogeneous contribution (green), the uncorrelated inhomogeneous contribution (fade yellow) and the correlated inhomogeneous contribution (yellow) are shown.

Although the total inhomogeneous contribution is essentially constant with increasing MAS rates in all the samples, as expected, it is interesting to note that, for both PS and tyrosine, the correlated inhomogeneous contribution appears to increase between 60 and 100 kHz, while the uncorrelated contribution appears to be reduced (The evolution of the correlated and uncorrelated inhomogeneous broadenings as a function of the MAS rate for every peak is shown in Figures 5.13, 5.15, 5.16, 5.18, 5.19, 5.20 and 5.22). We ascribe this to an artifact in the fitting due to the fact that overall 2D lineshapes of these peaks is changing from a rounded lineshape at lower MAS rates, dominated by the homogeneous contribution, to the resolved tilted peaks at faster MAS, where the correlated and ABMS contributions dominate. It is the convolution of the homogeneous and the inhomogeneous lineshapes that determine the correlated and uncorrelated contributions. We note from simulations (Figures 5.25-S28) with different convolutions of Lorentzian and Gaussian components that the fits to the GLS (or Voigt) lineshapes do not always fit best to the input parameters for the mixed lineshapes, and that this has also been observed previously[353], and that this can lead to the type of variation seen here for L-Tyrosine.HCl and PS. The true proportions of the components within the inhomogeneous contributions should be invariant to MAS rate, as seen for example with HMB and ZIF-8. In the cases where they vary with MAS, we believe that the proportions measured at the fastest rates (*i.e.* with the least contribution from homogeneous (Lorentzian) terms, are likely to be the most reliable.

In all the samples studied here, the antidiagonals extracted from DQ/SQ experiments give the narrowest linewidths.

5.2.4.5 Lineshapes

In addition to the linewidths, the lineshapes of all the resonances were determined using the GLS function of Eq. 5.11. In each panel, the mixing factor obtained at 60 and 100 kHz MAS rate are shown, (fitted values for all the rates are given in Tables 5.30-63).

For HMB Figure 5.10 (a), the mixing factor *m* of the DQ projection is 0.15 at 100 kHz and *m* = 0.15 at 60 kHz. The lineshape character does not alter much across the MAS rates and it remains mostly Gaussian. On the other hand, the DQ/SQ antidiagonal has a significant Lorentzian character (*m* = 0.52) at 100 kHz. There is a major difference in the lineshape character between the DQ-SQ projection (Gaussian) and the DQ/SQ antidiagonal (Lorentzian).

For H2 of ZIF-8, The DQ/SQ projection (Figure 5.10 (b)) shows at 60 kHz MAS a Lorentzian lineshape (m = 0.52) but at 100 kHz the lineshape has Gaussian characteristics (*m* = 0.33). The corresponding DQ-SQ antidiagonal is mostly Gaussian (at 100 kHz, *m* = 0.25, and at 60 kHz, *m* = 0.35). The fact that the Lorentzian character is more pronounced at slower MAS rates indicates that it is correlated with homogeneous contributions to the linewidth.

Concerning the methyl peak (H1) of ZIF-8 (Figure 5.10 (c)), the lineshape is purely Lorentzian across all MAS rates for the DQ projection and antidiagonal. This correlates with the fact that the major contribution to the linewidth of this peak is homogeneous.

Concerning the DQ-SQ antidiagonals of Tyr H1 and H9, the lineshapes are mostly Gaussian at 100 kHz (m = 0.01). In Figure 5.10 (f), the mixing factor for the projection and antidiagonal of H3' is mostly Lorentzian at 60 kHz MAS and is reduced to 0.5 at 100 kHz MAS.

The last panel (Figure 5.10 (g)) shows the character for the aromatic proton of PS. The linewidth is Gaussian at 100 kHz for the DQ-SQ projection and the antidiagonal, with m=0.31 and 0.29, respectively. The character is almost unchanged for all MAS rates, showing that the homogenous contribution affects only slightly the lineshape character of a compound that is dominated by inhomogeneous broadening

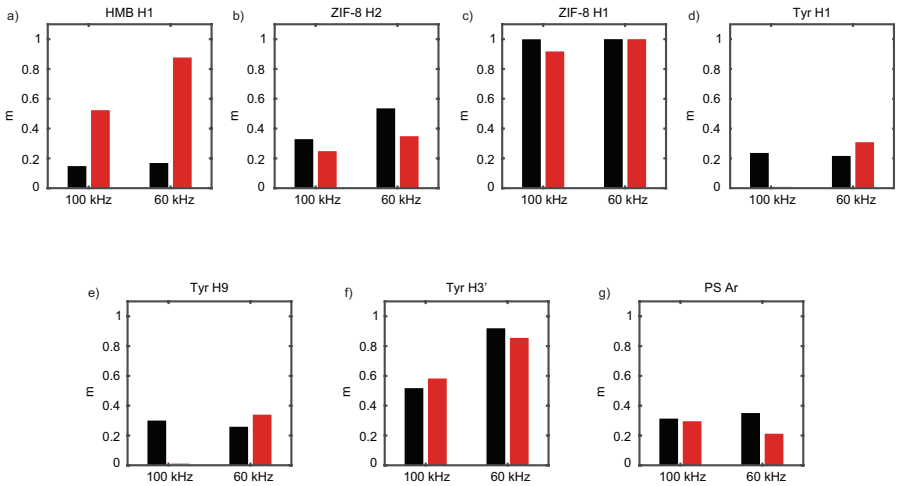

Figure 5.10 GLS lineshape mixing factors: (a) H1 of HMB, (b) H2 of ZIF-8; (c) H1 of ZIF-8, (d) H1 of L-tyrosine hydrochloride; (e) H9 of L-tyrosine hydrochloride, (f) H3' of L-tyrosine hydrochloride and (g) H Ar of polystyrene. A mixing factor of m = 1 represents a purely Lorentzian lineshape, whereas m = 0 represents a pure Gaussian. The mixing factor is presented for the DQ/SQ projection (black) and the antidiagonal from DQ/SQ experiment (red). The mixing factor is presented at the fastest MAS rate recorded (100 kHz), and at the slowest (40, 44, 50 or 60 kHz).

These results show that for compounds with a strong inhomogeneous contribution, the lineshapes tend to have a Gaussian character. However, the DQ/SQ antidiagonals contain only the homogeneous and uncorrelated inhomogeneous contributions. If the former is dominant, then the lineshape will have a Lorentzian character. For compounds with cubic symmetry that do not experience ABMS, there will be no correlated inhomogeneous contribution. The Lorentzian character of the lineshape will depend on the contribution of the homogenous broadening. It is important to note that the lineshape character is unique to each resonance in the spectrum, since each one experiences a unique set of homogeneous and inhomogeneous broadenings (cf. H2 and H1 of ZIF-8 in Figure 5.9).

For compounds with a relatively more complicated chemical structure, such as L-Tyrosine hydrochloride, there will be resonances (H1 and H9), which have a large correlated inhomogeneous contribution, therefore a more Gaussian character. On the other hand, H3' has a more Lorentzian lineshape, even at 100 kHz MAS, showcasing homogeneous broadening as the main contribution.

5.2.5 Conclusion

In summary, here we have investigated the different contributions to ^{1}H linewidths in MAS NMR spectra. We find that in a set of typical molecular solids the overall widths, and the nature of the different contributions to the linewidths, can vary very considerably.

The different contributions to the ^{1}H lineshape were studied at MAS rates up to 100 kHz in different organic solids and one metal-organic framework. It is important to first remark that, quite simply, faster spinning always yields narrower lines and longer coherence lifetimes.

For ZIF-8 and the methylene protons in L-tyrosine hydrochloride, the dipolar contribution was significant even at the fastest MAS rate. Therefore, here we expect considerable further narrowing at faster MAS rates.

However, we also find that at the fastest rates the dipolar contribution can become less critical than the inhomogeneous one. This is observed in HMB, some resonances of L-tyrosine hydrochloride, and the aromatic protons of polystyrene.

Our analysis of the lineshapes confirms the expectation that resonances dominated by dipolar broadening will have a more pronounced Lorentzian character, which will decrease with faster MAS rates, and that inhomogeneous contributions are associated with Gaussian characters.

We believe that in most cases today the highest ^{1}H resolution achievable with 100 kHz MAS alone is obtained in two-dimensional shift correlation spectra (like the ^{1}H-^{1}H DQ/SQ spectra used here), since they will often lead to elongated lineshapes where the anti-diagonal will be free of any correlated broadening. The resolution of these two-dimensional spectra should increase with increasing MAS rate.

We hope that our work will serve to inform methods to further increase ^{1}H resolution. A key open question now is how to remove the different (undesirable) remaining contributions. Faster MAS, or the PIP type experiments discussed in the introduction, can potentially reduce or eliminate the (MAS dependent) dipolar contribution, but they will not remove the inhomogeneous contributions from ABMS or disorder. (We note that in many cases the chemical shift distribution induced by disorder is a desirable feature, that should be measured rather than removed).

In a proof of principle demonstration, we show that in 2-MeIm dipolar contributions to the ^{1}H linewidth can be completely removed using a 98% deuterated sample, and that ^{1}H ABMS can be partially suppressed by sample dilution in an ABMS free matrix. [239-240, 334] This reduced the 1D linewidth by a factor ~2. However, we note that this is not likely to be a practical approach to line narrowing in ^{1}H MAS, due to the difficulty in preparing highly deuterated samples, and due to the very dramatic accompanying reduction (here a factor > 1 000) in ^{1}H sensitivity.

Our results suggest that while further suppressing dipolar contributions would be beneficial, a general approach to removing the contribution of ABMS would be a very significant step forward for ^{1}H resolution MAS NMR spectra of molecular solids.

5.2.5 Appendix VII

5.2.5.1 Experimental details

The experiments on ABMS dilution were applied to three micro-crystalline organic solids: hexamethylbenzene (HMB), 2-methyl-imidazole (2MeIm) and 2-methyl-imidazole-d6 98% deuterated (2MeIm-d6). For HMB, the ^{1}H 1D, the 2D ^{1}H-^{1}H DQ/SQ BABA and the ^{1}H-^{13}C HETCOR experiments were acquired. For 2MeIm and 2MeIm-d6, only ^{1}H 1D, the 2D ^{1}H -^{1}H DQ/SQ BABA. All the experiments were acquired at 60 kHz MAS for the natural abundance sample and also for a mixture of 5% of sample and 95% of KBr. A Bruker 1.3 mm room temperature HDCN CP-MAS probe at a magnetic field of 21.1 T corresponding to a ^{1}H frequency of 900 MHz. The temperature was kept constant using a VT flow of 295 K for 2-MeIm and 2-meIm-d6 and 265 K for HMB. For each sample, prior to acquisition the magic angle was set by maximizing the T_2' of the proton signals at the fastest MAS rate, and the 90° pulse width was optimized. A States-TPPI acquisition scheme was used to obtain phase-sensitive two-dimensional spectra. All spectra were phased and baseline corrected. No weighting function was applied prior to Fourier transformation.

Table 5.5. 1D ^{1}H experimental details for HMB and HMB diluted with KBr

Sample	MAS rate (kHz)	VT (K)	90° RF amplitude (kHz)	recycle delay(s)	Number of FID points	SW (kHz)	Size of real spectrum:	Number of scans
HMB	60	265	119	3	2048	100	4096	4
20% HMB 80% KBr	60	265	119	3	2048	100	4096	4

Table 5.6. ^{1}H-^{13}C HETCOR experimental details for HMB and HMB diluted with KBr

Sample	MAS rate (kHz)	VT (K)	90° RF amplitude (kHz)	Contact time ^{1}H-^{13}C (ms)	recycle delay(s)	Number of FID points: F2/F1	SW (kHz): F2/F1	Size of real spectrum: F2/F1	Number of scans
HMB	60	265	119	3.5	2	8192/200	100/3	16384/512	32
20% HMB 80% KBr	60	265	119	3.5	2	8192/200	100/3	16384/512	384

Table 5.7. ^{1}H-^{1}H DQ/SQ BABA experimental details for HMB and HMB diluted with KBr

Sample	MAS rate (kHz)	VT (K)	90° RF amplitude (kHz)	recycle delay(s)	Number of FID points: F2/F1	SW (kHz): F2/F1	Size of real spectrum: F2/F1	DQ recoupling time (µs)	Number of scans
HMB	60	265	119	3	4096/600	82/12	8192/1024	41.6	16
20% HMB 80% KBr	60	265	119	3	4096/600	82/12	8192/1024	41.6	16

Table 5.8. 1D ^{1}H experimental details for 2MeIm, 2MeIm-d6, 2MeIm diluted with KBr, and 2MeIm-d6 diluted with KBr

Sample	MAS rate (kHz)	VT (K)	90° RF amplitude (kHz)	recycle delay(s)	Number of FID points	SW (kHz)	Size of real spectrum	Number of scans
2MeIm	60	295	119	250	2048	100	4096	4
5% 2MeIm 95 % KBr	60	295	119	250	16384	100	32768	4
2MeIm-d6	60	295	119	500	2048	100	4096	4
5% 2MeIm-d6 95 % KBr	60	295	119	500	8192	100	16384	128

Table 5.9. ^{13}C CP experimental details for 2MeIm and 2MeIm diluted with KBr

Sample	MAS rate (kHz)	VT (K)	90° RF amplitude (kHz)	Contact time ^{1}H-^{13}C (ms)	recycle delay(s)	Number of FID points	SW (kHz)	Size of real spectrum
2MeIm	60	295	119	2.5	10	9090	113	16384
5% 2MeIm 95 % KBr	60	295	119	2.5	10	16384	100	32768

Table 5.10. ^{1}H-^{1}H DQ/SQ BABA experimental details for 2MeIm, 2MeIm-d6, and 2MeIm-d6 diluted with KBr

Sample	MAS rate (kHz)	VT (K)	90° RF amplitude (kHz)	recycle delay(s)	Number of FID points: F2/F1	SW (kHz): F2/F1	Size of real spectrum: F2/F1	DQ recoupling time (µs)	Number of scans
2MeIm	60	285	305	50	4096/180	227/20	8192/512	25	16
2MeIm-d6	60	295	119	50	8192/200	82/3	8192/1024	166.6	16
5% 2MeIm-d6 95 % KBr	60	295	119	50	8192/200	82/3	8192/1024	166.6	16

The experiments on the linewidth evolution as a function of the MAS were done for the following solids: HMB, L-tyrosine.HCl, amorphous polystyrene (PS), and ZIF-8. For all samples, the ^{1}H 1D, the 2D ^{1}H -^{1}H DQ/SQ BABA. The T_2' were also measured with a pseudo 2D-Hahn echo experiment. The experiments were acquired at different MAS rates, from 40 to 100 kHz. A Bruker 0.7 mm room temperature HCN CP-MAS probe at a magnetic field of 21.1 T corresponding to a ^{1}H frequency of 900 MHz. The temperature was kept constant using a VT flow of 295 K. For each sample, prior to acquisition the magic angle was set by maximizing the T_2' of the proton signals at the fastest MAS rate, and the 90° pulse width was optimized. A States-TPPI acquisition scheme was used to obtain phase-sensitive two-dimensional spectra. All spectra were phase- and baseline-corrected. No weighting function was applied prior to Fourier transform.

Table 5.11. Experimental details of the 1D VMAS ^{1}H datasets acquired for HMB with the 0.7 mm probe

MAS rate (kHz)	VT (K)	90° RF amplitude (kHz)	recycle delay(s)	Number of FID points	SW (kHz)	Size of real spectrum:	Number of scans
100	285	299	3.8	6144	227	16384	8
96	285	299	3.8	6144	227	16384	8
94	285	299	3.8	6144	227	16384	8
90	290	299	3.8	6144	227	16384	8
88	290	299	3.8	6144	227	16384	8
80	290	299	3.8	6144	227	16384	8
78	290	299	3.8	6144	227	16384	8
72	290	299	3.8	6144	227	16384	8
66	290	299	3.8	6144	227	16384	8
60	290	299	3.8	6144	227	16384	8
52	290	299	3.8	6144	227	16384	8
48	290	299	3.8	6144	227	16384	8
44	290	299	3.8	6144	227	16384	8
40	290	299	3.8	6144	227	16384	8

Table 5.12. Experimental details of the 1D VMAS ^{1}H datasets acquired for ZIF-8 with the 0.7 mm probe

MAS rate (kHz)	VT (K)	90° RF amplitude (kHz)	recycle delay(s)	Number of FID points	SW (kHz)	Size of real spectrum	Number of scans
100	285	304	7	16384	227	32768	4
90	290	304	7	16384	227	32768	4
80	290	304	7	16384	227	32768	4
72	290	304	7	16384	227	32768	4
60	290	304	7	16384	227	32768	4
44	295	304	7	16384	227	32768	4

Table 5.13. Experimental details of the 1D VMAS ^{1}H datasets acquired for L-tyrosine hydrochloride with the 0.7 mm probe

MAS rate (kHz)	VT (K)	90° RF amplitude (kHz)	recycle delay(s)	Number of FID points:	SW (kHz)	Size of real spectrum	Number of scans
100	280	290	6	6144	227	16384	8
98	280	290	6	6144	227	16384	8
96	280	290	6	6144	227	16384	8
94	280	290	6	6144	227	16384	8
90	280	290	6	6144	227	16384	8
88	280	290	6	6144	227	16384	8
86	280	290	6	6144	227	16384	8
84	280	290	6	6144	227	16384	8
82	280	290	6	6144	227	16384	8
80	285	290	6	6144	227	16384	8
78	285	290	6	6144	227	16384	8
76	285	290	6	6144	227	16384	8
74	285	290	6	6144	227	16384	8
72	285	290	6	6144	227	16384	8
70	290	290	6	6144	227	16384	8
68	290	290	6	6144	227	16384	8
66	290	290	6	6144	227	16384	8
64	290	290	6	6144	227	16384	8
62	290	290	6	6144	227	16384	8
60	290	290	6	6144	227	16384	8
58	295	290	6	6144	227	16384	8
54	295	290	6	6144	227	16384	8
52	295	290	6	6144	227	16384	8
50	295	290	6	6144	227	16384	8
48	295	290	6	6144	227	16384	8
44	295	290	6	6144	227	16384	8
42	295	290	6	6144	227	16384	8
40	295	290	6	6144	227	16384	8

Table 5.14. Experimental details of the 1D VMAS ^{1}H datasets acquired for polystyrene beads with the 0.7 mm probe

MAS rate (kHz)	VT (K)	90° RF amplitude (kHz)	recycle delay(s)	Number of FID points:	SW (kHz)	Size of real spectrum	Number of scans
100	285	333	50	4096	227	8192	4
90	290	333	50	4096	227	8192	4
80	290	333	50	4096	227	8192	4
72	290	333	50	4096	227	8192	4
60	290	333	50	4096	227	8192	4
50	290	333	50	4096	227	8192	4

Table 5.15. Experimental details of the BABA VMAS ^{1}H datasets acquired for HMB with the 0.7 mm probe

MAS rate (kHz)	VT (K)	90° RF amplitude (kHz)	recycle delay(s)	Number of FID points: F2/F1	SW (kHz): F2/F1	Size of real spectrum: F2/F1	DQ recoupling time (µs)	Number of scans
100	285	294	3	6144/250	227/5.55	16384/512	180	16
96	285	294	3	6144/250	227/5.65	16384/512	177.14	16
94	285	294	3	6144/250	227/5.53	16384/512	180.88	16
90	290	294	3	6144/250	227/5.62	16384/512	177.76	16
88	290	294	3	6144/250	227/5.50	16384/512	181.76	16
80	290	294	3	6144/250	227/5.71	16384/512	175	16
78	290	294	3	6144/250	227/5.57	16384/512	179.48	16
72	290	294	3	6144/250	227/5.54	16384/512	180.57	16
66	290	294	3	6144/250	227/5.50	16384/512	181.80	16
60	290	294	3	6144/250	227/5.45	16384/512	183.37	16
52	290	294	3	6144/250	227/5.78	16384/512	173.07	16
48	295	294	3	6144/250	227/6.66	16384/512	166.64	16
44	295	294	3	6144/250	227/6.11	16384/512	181.84	16
40	295	294	3	6144/250	227/5.71	16384/512	175	16

Table 5.16. Experimental details of the BABA VMAS ^{1}H datasets acquired for ZIF-8 with the 0.7 mm probe

MAS rate (kHz)	VT (K)	90° RF amplitude (kHz)	recycle delay(s)	Number of FID points: F2/F1	SW (kHz): F2/F1	Size of real spectrum: F2/F1	DQ recoupling time (µs)	Number of scans
100	285	294	7	16384/100	227/5.55	32768/256	200	16
90	290	294	7	16384/100	227/5.55	32768/256	199.98	16
80	290	294	7	16384/100	227/5.55	32768/256	200	16
72	290	294	7	16384/100	227/5.33	32768/256	208.35	16
60	290	294	7	16384/100	227/5.55	32768/256	200.04	16
44	295	294	7	16384/100	227/5.43	32768/256	204.57	16

Table 5.17. Experimental details of the BABA VMAS 1H datasets acquired for L-Tyrosine hydrochloride with the 0.7 mm probe

MAS rate (kHz)	VT (K)	90° RF amplitude (kHz)	recycle delay(s)	Number of FID points: F2/F1	SW (kHz): F2/F1	Size of real spectrum: F2/F1	DQ recoupling time (µs)	Number of scans
100	285	294	2	4096/100	90.9/20	16384/256	10	16
96	285	294	2	4096/96	90.9/19.2	16384/256	10.42	16
94	285	294	2	4096/94	90.9/18.8	16384/256	10.64	16
90	285	294	2	4096/90	90.9/18	16384/256	11.11	16
88	285	294	2	4096/110	90.9/22	16384/256	11.36	16
80	290	294	2	4096/100	90.9/20	16384/256	12.5	16
78	290	294	2	4096/130	90.9/26	16384/256	12.82	16
72	290	294	2	4096/120	90.9/24	16384/256	13.89	16
66	290	294	2	4096/110	90.9/22	16384/256	15.15	16
60	295	294	2	4096/100	90.9/20	16384/256	16.67	16
52	295	294	2	4096/130	90.9/26	16384/256	19.23	16
48	295	294	2	4096/120	90.9/24	16384/256	20.83	16
40	295	294	2	4096/100	90.9/20	16384/256	25	16

Table 5.18. Experimental details of the BABA VMAS 1H datasets acquired for polystyrene with the 0.7 mm probe

MAS rate (kHz)	VT (K)	90° RF amplitude (kHz)	recycle delay(s)	Number of FID points: F2/F1	SW (kHz): F2/F1	Size of real spectrum: F2/F1	DQ recoupling time (µs)	Number of scans
100	285	333	50	4096/30	227/20	8192/64	25	16
90	290	333	50	4096/90	227/18	8192/256	28	16
80	290	333	50	4096/100	227/20	8192/256	25	16
72	290	333	50	4096/120	227/18	8192/256	28	16
60	290	333	50	4096/100	227/20	8192/256	25	16
50	290	333	50	4096/130	227/17	8192/256	30	16

Table 5.19. Experimental details of the pseudo 2D-Hahn echo datasets for HMB with the 0.7 mm probe

MAS rate, kHz	VT (K)	90° RF amplitude (kHz)	recycle delay(s)	Number of FID points: F2/F1	SW (kHz) in F2	Size of real spectrum in F2	Total t_1 increment (ms)	Number of scans
100	285	305	3	6144/22	227	16384	1500	4
96	285	305	3	6144/22	227	16384	1500	4
94	285	305	3	6144/22	227	16384	1489	4
88	290	305	3	6144/22	227	16384	1500	4
80	290	305	3	6144/22	227	16384	1500	4
78	290	305	3	6144/22	227	16384	1487	4
72	290	305	3	6144/22	227	16384	1500	4
66	290	305	3	6144/22	227	16384	1485	4
60	290	305	3	6144/22	227	16384	1500	4
52	290	305	3	6144/22	227	16384	1500	4
48	295	305	3	6144/22	227	16384	1500	4
44	295	305	3	6144/22	227	16384	1500	4
40	295	305	3	6144/22	227	16384	1500	4

Table 5.20. Experimental details of the pseudo 2D-Hahn echo datasets for ZIF-8 with the 0.7 mm probe

MAS rate, kHz	VT (K)	90° RF amplitude (kHz)	recycle delay(s)	Number of FID points: F2/F1	SW (kHz) in F2	Size of real spectrum in F2	Total t_1 increment (ms)	Number of scans
100	285	305	7	16384/22	227	32768	1000	4
90	290	305	7	16384/22	227	32768	1111	4
80	290	305	7	16384/22	227	32768	250	4
72	290	305	7	16384/22	227	32768	500	4
60	290	305	7	16384/22	227	32768	500	4
44	295	305	7	16384/22	227	32768	500	4

Table 5.21. Experimental details of the pseudo 2D-Hahn echo datasets for L-tyrosine.HCl with the 0.7 mm probe

MAS rate, kHz	VT (K)	90° RF amplitude (kHz)	recycle delay(s)	Number of FID points: F2/F1	SW (kHz) in F2	Size of real spectrum in F2	Total t_1 increment (ms)	Number of scans
100	285	291	3	4096/40	227	8192	500	4
96	285	291	3	4096/40	227	8192	521	4
94	285	291	3	4096/40	227	8192	532	4
90	285	291	3	4096/40	227	8192	511	4
88	285	291	3	4096/40	227	8192	523	4
80	290	291	3	4096/40	227	8192	575	4
78	290	291	3	4096/40	227	8192	513	4
72	290	291	3	4096/40	227	8192	500	4
66	290	291	3	4096/40	227	8192	515	4
60	295	291	3	4096/40	227	8192	500	4
52	295	291	3	4096/40	227	8192	500	4
48	295	291	3	4096/40	227	8192	542	4
40	295	291	3	4096/40	227	8192	500	4

Table 5.22. Experimental details of the pseudo 2D-Hahn echo datasets for polystyrene with the 0.7 mm probe

MAS rate, kHz	VT (K)	90° RF amplitude (kHz)	recycle delay(s)	Number of FID points: F2/F1	SW (kHz) in F2	Size of real spectrum in F2	Total t_1 increment (ms)	Number of scans
100	285	333	12	4096/40	227	16384	200	4
90	290	333	12	4096/40	227	16384	222	4
80	290	333	12	4096/40	227	16384	200	4
72	290	333	12	4096/40	227	16384	222	4
60	290	333	12	4096/40	227	16384	200	4
50	290	333	12	4096/40	227	16384	200	4

5.2.5.2 Fitting parameters

The width w for the 1D ^{1}H, 2D DQ/SQ antidiagonal and 2D DQ/SQ projection and the T2' was fitted to the following polynomial functions:

$$w = w_1\tau_r + w_2\tau_r^2 + \Delta\infty \qquad (5.12)$$

$$w = w_1\tau_r + \Delta\infty \qquad (5.13)$$

Where w represents the linewidth in Hz, w_1 and w_2 are the coefficients of the polynomial, τ_r represents the rotor period in seconds. And $\Delta\infty$ the residual linewidth at infinite MAS rate. The goodness of the linewidth evolution fitting to these functions is represented by the coefficient of determination R^2. These fitting parameters w_1, w_2 and $\Delta\infty$, but also R^2 are summarized in the following tables for each selected resonance.

Table 5.23. Fitting parameters for HMB H1 linewidths as a function of the rotor period

	HMB H1								
	$\mathbf{w = w_1\tau_r + \Delta\infty}$				$\mathbf{w_1\tau_r + w_2\tau_r^2 + \Delta\infty}$				
	w_1	Δ_∞	R^2	RMSE	w_1	w_2	Δ_∞	R^2	RMSE
1D	5.76 ± 0.21*10^6	917 ± 13	0.95	3.01	3.58 ± 6.92*10^6	2.60*10^7 ± 2.0210^11	944 ± 55	0.90	6.35
Δ'*	5.58 ± 0.02*10^6	0	0.99	0.59	5.59 ± 0.11*10^6	1.00 ± 4.24*10^9	0	0.99	0.59
$\Delta_{projection}$	2.43 ± 1.02*10^6	911 ± 17	0.70	3.012	1.04 ± 0.76*10^7	-2.36 ± 2.23*10^11	849 ± 60	0.80	6.98
$\Delta_{antidiag}$	7.49 ± 1.20*10^6	31 ± 19	0.94	9.91	0..12 ± 1.04*10^7	1.86 ± 3.06*10^11	80 ± 82	0.95	1.60

*The linear fitting was done in the range 60-100 kHz

Table 5.24. Fitting parameters for ZIF-8 H2 linewidths as a function of the rotor period

	ZIF-8 H2								
	$\mathbf{w = w_1\tau_r + \Delta\infty}$				$\mathbf{w_1\tau_r + w_2\tau_r^2 + \Delta\infty}$				
	w_1	Δ_∞	R^2	RMSE	w_1	w_2	Δ_∞	R^2	RMSE
1D	1.53 ± 0.06*10^7	44 ± 10	0.99	2.32	1.20 ± 0.39*10^7	1.01 ± 0.84*10^11	69 ± 31	0.99	1.44
Δ'*	1.055 ± 0.15*10^7	0	0.90	21.81	7.39 ± 0.89*10^6	2.27 ± 5.07*10^11	0	0.99	3.21
$\Delta_{projection}$	1.49 ± 0.07*10^7	0	0.98	9.88	-3.67 ± 1.02*10^6	5.69 ± 0.31*10^11	139 ± 8	0.99	0.37
$\Delta_{antidiag}$	1.51 ± 0.09*10^7	0	0.97	14.20	-4.88 ± 3.96*10^6	5.42 ± 1.19*10^11	138 ± 31	0.99	1.45

*The linear fitting was done in the range 72-100 kHz

Table 5.25. Fitting parameters for ZIF-8 H1 linewidths as a function of the rotor period

	ZIF-8 H1								
	$\mathbf{w = w_1\tau_r + \Delta\infty}$				$\mathbf{w_1\tau_r + w_2\tau_r^2 + \Delta\infty}$				
	w_1	Δ_∞	R^2	RMSE	w_1	w_2	Δ_∞	R^2	RMSE
1D*	1.68 ± 0.13*10^7	81 ± 20	0.99	4.93	1.56 ± 1.73*10^7	1.42*10^7 ± 7.24*10^11	74 ± 102	1	0.19
Δ'	1.33 ± 0.05*10^7	0	0.98	4.72	1.20 ± 0.44*10^7	1.00 ± 3.09*10^11	0	0.97	6.79
$\Delta_{projection}$*	1.35 ± 0.04*10^7	0	0.98	4.61	1.35 ± 0.34*10^7	1.10 ± 0.12*10^11	0	0.98	7.99
$\Delta_{antidiag}$*	1.31 ± 0.05*10^7	0	0.97	5.14	1.35 ± 0.34*10^7	1.10 ± 0.12*10^11	0	0.93	5.32

*The linear and quadratic fitting was done in the range 60-100 kHz

Table 5.26. Fitting parameters for Tyr H1 linewidths as a function of the rotor period

	Tyr H1								
	$\mathbf{w = w_1\tau_r + \Delta\infty}$				$\mathbf{w_1\tau_r + w_2\tau_r^2 + \Delta\infty}$				
	w_1	Δ_∞	R^2	RMSE	w_1	w_2	Δ_∞	R^2	RMSE
1D	9.20 ± 0.92*10^6	198 ± 3	0.99	2.25	6.48 ± 1.26*10^6	8.11 ± 3.73*10^10	219 ± 10	0.99	1.76
Δ'*	6.27 ± 0.30*10^6	0	0.91	5.39	5.05 ± 0.44*10^6	1.36 ± 0.33*10^11	0	0.99	1.28
$\Delta_{projection}$	8.66 ± 0.97*10^6	194 ± 15	0.97	7.05	-2.18 ± 2.73*10^6	3.21 ± 0.81*10^11	277 ± 21	0.99	2.47
$\Delta_{antidiag}$	1.40 ± 0.03*10^7	0	0.99	6.77	8.30 ± 3.06*10^6	2.01 ± 0.90*10^11	37 ± 25	0.99	2.77

*The linear fitting was done in the range 66-100 kHz

Table 5.27. Fitting parameters for Tyr H9 linewidths as a function of the rotor period

	Tyr H9								
	$\mathbf{w = w_1\tau_r + \Delta\infty}$				$\mathbf{w_1\tau_r + w_2\tau_r^2 + \Delta\infty}$				
	w_1	Δ_∞	R^2	RMSE	w_1	w_2	Δ_∞	R^2	RMSE
1D	1.37 ± 0.08*10^7	159 ± 12	0.98	8.82	-2.8 ± 0.5*10^6	4.90 ± 0.16*10^11	288 ± 5	0.99	0.74
Δ'*1	8.23 ± 0.52*10^6	0	0.91	9.01	5.18 ± 0.29*10^6	2.57 ± 0.22*10^11	0	0.99	0.86
$\Delta_{projection}$*2	7.67 ± 0.22*10^6	206	0.98	2.23	-2.81 ± 7.42*10^6	3.98 ± 2.81*10^11	284 ± 48	0.99	1.48
$\Delta_{antidiag}$*2	1.45 ± 0.06*10^7	0	0.99	1.65	6.33 ± 4.99*10^6	3.58 ± 1.39*10^11	55 ± 32	0.99	0.99

*1 The linear fitting was done in the range 80-100 kHz
*2 The linear fitting was done in the range 60-100 kHz
*3 The linear fitting was done in the range 52-100 kHz

Table 5.28. Fitting parameters for Tyr H3' linewidths as a function of the rotor period

	Tyr H3								
	$\mathbf{w = w_1\tau_r + \Delta\infty}$				$\mathbf{w_1\tau_r + w_2\tau_r^2 + \Delta\infty}$				
	w_1	Δ_∞	R^2	RMSE	w_1	w_2	Δ_∞	R^2	RMSE
1D*1	2.61 ± 0.09*10^7	156 ± 13	0.99	2.18	-6.51*10^6 ± 1.09*10^7	1.37 ± 0.51*10^12	348 ± 71	0.99	1.15
Δ'*2	2.02 ± 0.09*10^7	0	0.92	17.2	1.31 ± 0.23*10^7	5.39 ± 1.07*10^11	0	0.99	6.62
$\Delta_{projection}$*3	3.36 ± 0.21*10^7	55 ± 27	0.99	6.03	1.40 ± 2.71*10^7	7.44*10^11 ± 1.02*10^12	181 ± 176	0.99	5.41
$\Delta_{antidiag}$*3	3.34 ± 0.09*10^7	0	0.96	16	3.29 ± 4.93*10^7	1.00 ± 3.68*10^11	0	0.93	14.3

Table 5.29. Fitting parameters for polystyrene (PS) Ar linewidths as a function of the rotor period

	Polystyrene Ar								
	$\mathbf{w = w_1\tau_r + \Delta\infty}$				$\mathbf{w_1\tau_r + w_2\tau_r^2 + \Delta\infty}$				
	w_1	Δ_∞	R^2	RMSE	w_1	w_2	Δ_∞	R^2	RMSE
1D	2.39 ± 0.60*10^7	1367 ± 8	0.99	1.74	2.13 ± 0.63*10^7	8.29*10^10 ± 2.09*10^11	1386 ± 45	0.99	1.585
Δ'	2.00 ± 0.11*10^7	0	0.95	8.04	5.02 ± 3.86*10^6	9.651 ± 2.39*10^11	0	0.99	10.82
$\Delta_{projection}$	1.68 ±0.62*10^7	1363 ± 90	0.94	18.68	3.54 ± 7.89*10^7	-6.19*10^11 ± 2.61*10^12	1231 ± 678	0.94	19.78
$\Delta_{antidiag}$	5.42 ± 0.23*10^7	402 ± 33	0.99	6.94	5.63 ± 3.17*10^7	-7.21 ±2.71*10^10	387 ± 228	0.99	7.95

5.2.5.3 Voigt Fitting Results and Comparison with GLS

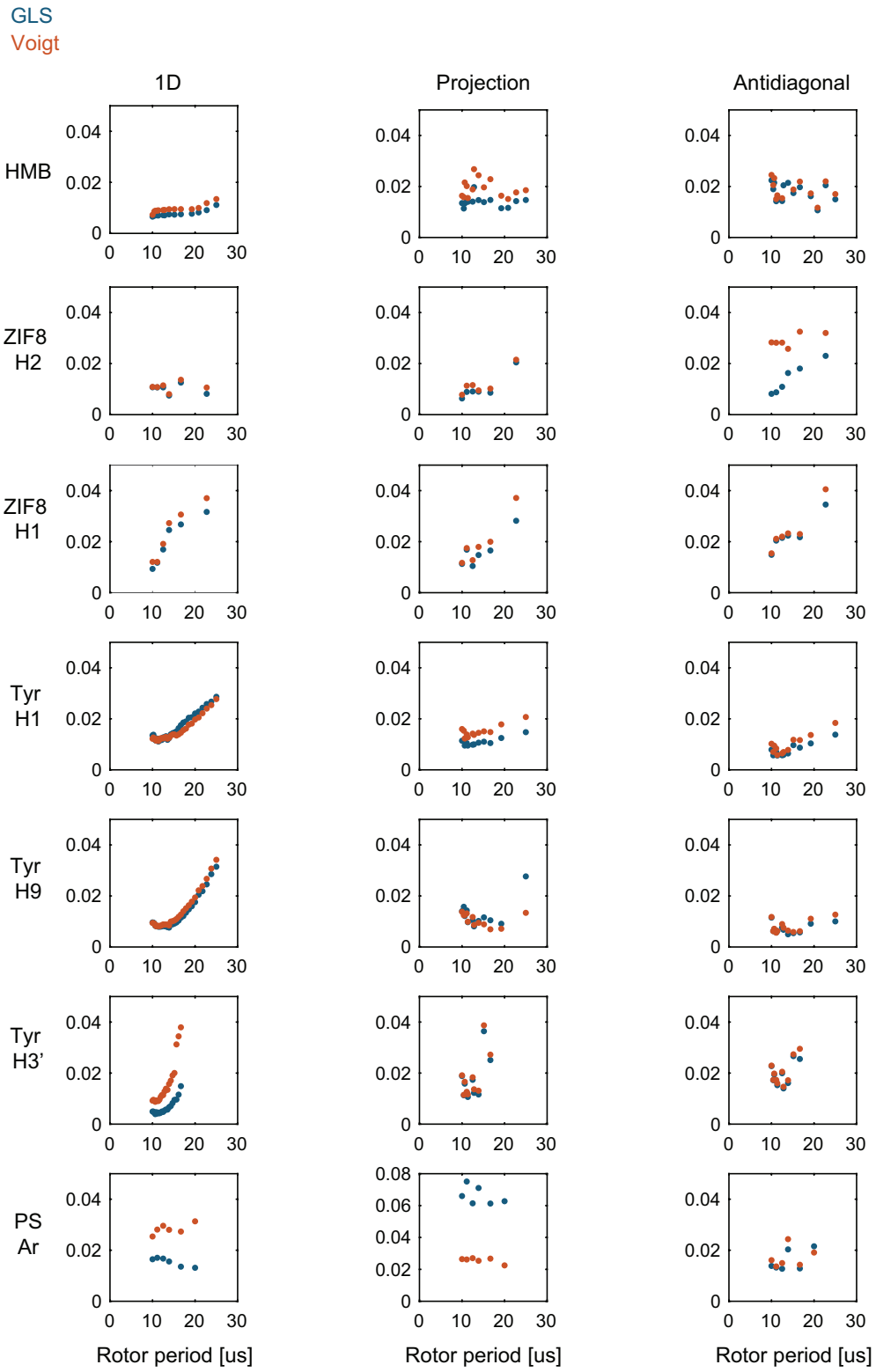

Figure 5.11. Quality of the Fittings. Root-mean square error (RMSE) evaluation for the GLS (green) and Voigt(orange) fitting as a function of the rotor period. The RMSE was calculated for every experimental lineshape (1D, DQ/SQ projection and DQ/SQ antidiagonal) of every sample: HMB, ZIF-8 (H2 and H1), L-tyrosine hydrochloride (Tyr H1, H9 and H3') and PS (Ar).

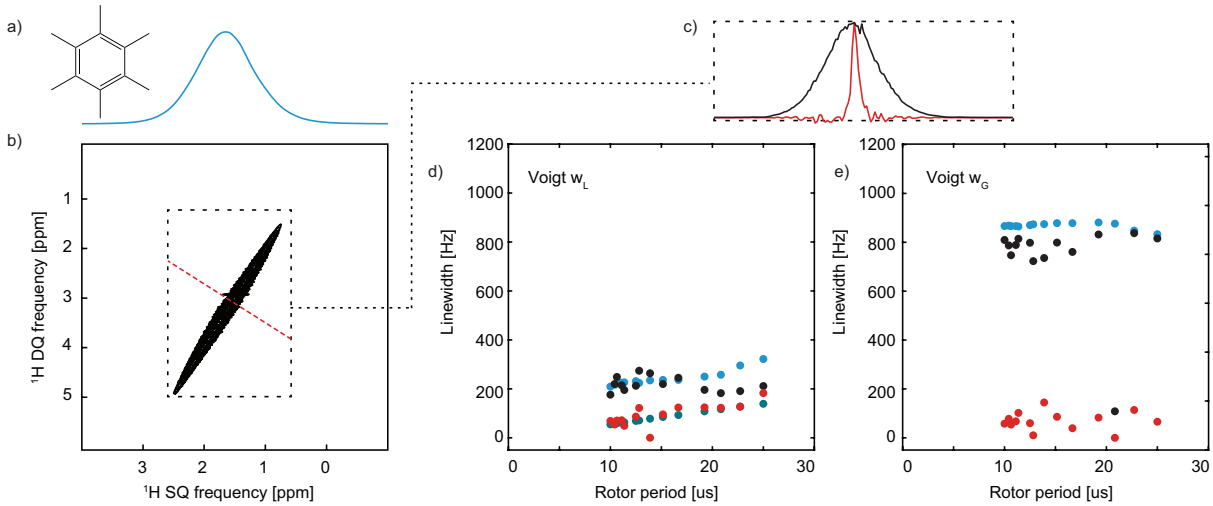

Figure 5.12. HMB. (a) Chemical structure and 1D ^{1}H spectrum and (b) 2D ^{1}H-^{1}H DQ/SQ spectrum of hexamethylbenzene (HMB) at 100 kHz MAS. The tilted dashed line in the 2D spectrum represent the antidiagonals extracted. (c) Skyline projection $\Delta_{projection}$ (black) and single row $\Delta_{antidiag}$ (red) extrated at a DQ frequency of 3.3 ppm from the ^{1}H-^{1}H DQ/SQ spectrum in (b). (d-e) Voigt measured linewidths as a function of the rotor period: d) Lorentzian linewidths (w_L): 1D ^{1}H (blue), Δ' (green)(from the measurement of T_2', see SI for details), the DQ/SQ projection (black) and DQ/SQ antidiagonal (red) and e) Gaussian linewidths(w_G): 1D ^{1}H (blue), the DQ/SQ projection (black) and DQ/SQ antidiagonal (red).

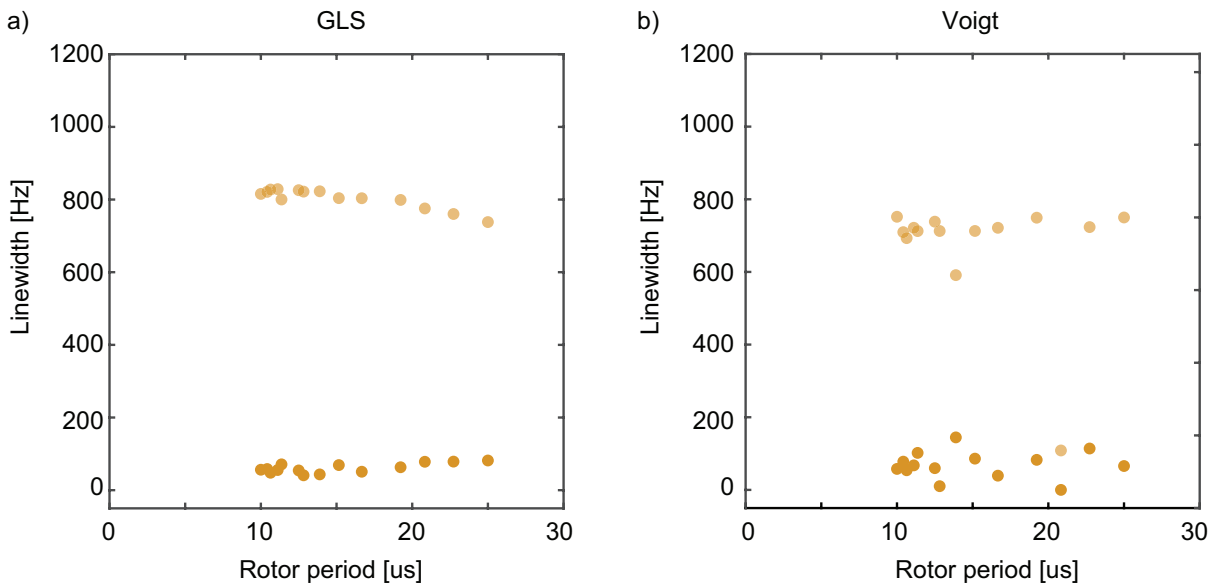

Figure 5.13. HMB. $\Delta_{inhomogeneous}^{correlated}$ (black) and $\Delta_{disorder}^{uncorrelated}$ (red) inhomogeneous linewidths as a function of the MAS rate. (a) For the GLS results, is calculated as $\Delta_{inhomogeneous}^{correlated} = \Delta_{projection} - \Delta_{antidiag}$ and $\Delta_{disorder}^{uncorrelated} = \Delta_{antidiag} - \Delta'$. (b) For the Voigt results, $\Delta_{inhomogeneous}^{correlated} = \Delta_{projection} - \Delta_{antidiag}$ and $\Delta_{disorder}^{uncorrelated} = \Delta_{antidiag}$, using the measured Gaussian linewidths (w_G).

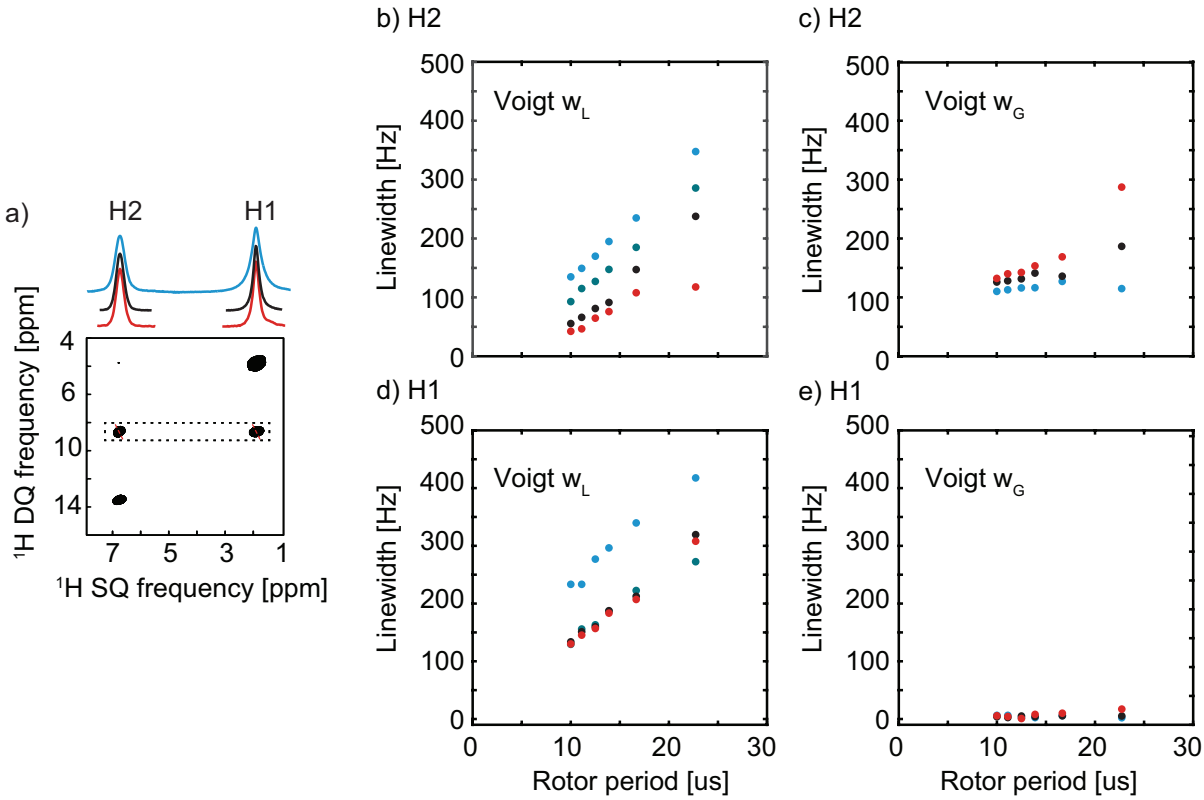

Figure 5.14. ZIF-8. (a) 2D ^{1}H-^{1}H DQ/SQ spectra of ZIF-8 at 100 kHz MAS and 1D ^{1}H (blue), $\Delta_{antidiag}$ single row (red) and positive projection $\Delta_{projection}$ (black) extracted from the region delimited by the dashed rectangle. The tilted dashed lines in the 2D spectrum represent the antidiagonals extracted. (b,e) Voigt measured Lorentzian (w_L) and Gaussian (w_G) linewidths as a function of the rotor period b,c) H2 and d,e)H1. The following linewidths are presented: 1D 1H (blue), Δ' contribution (green), ^{1}H-^{1}H DQ/SQ projection (black) and ^{1}H-^{1}H DQ/SQ antidiagonal (red).

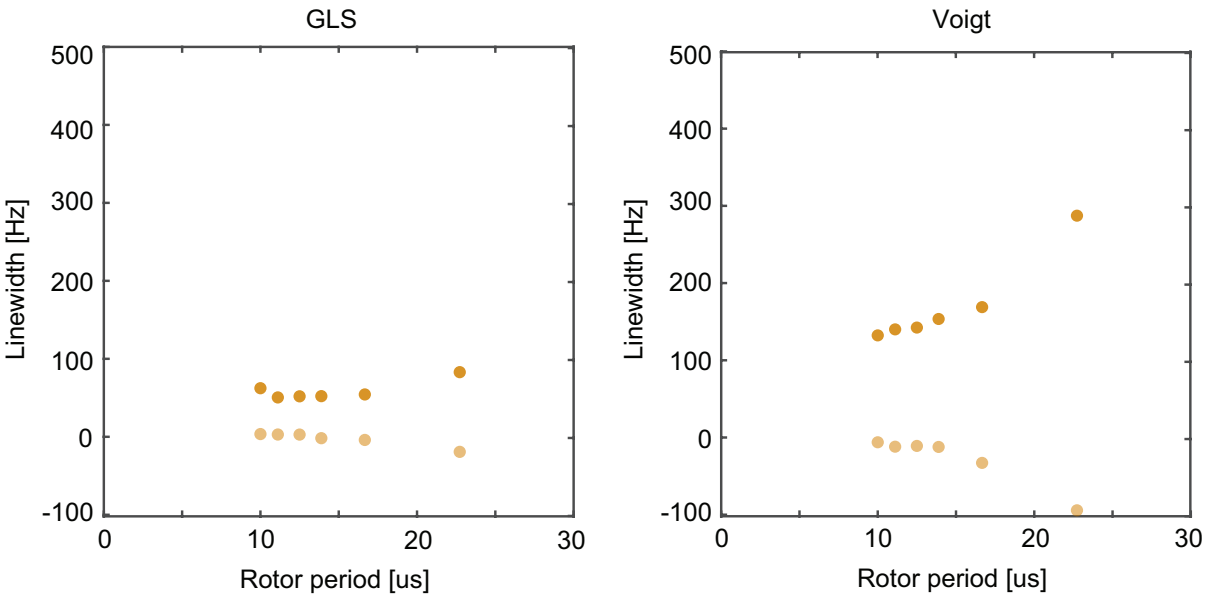

Figure 5.15. ZIF-8 H2. $\Delta_{inhomogeneous}^{correlated}$ (black) and $\Delta_{disorder}^{uncorrelated}$ (red) inhomogeneous linewidths as a function of the MAS rate. (a) For the GLS results, is calculated as $\Delta_{inhomogeneous}^{correlated} = \Delta_{projection} - \Delta_{antidiag}$ and $\Delta_{disorder}^{uncorrelated} = \Delta_{antidiag} - \Delta'$. (b) For the Voigt results, $\Delta_{inhomogeneous}^{correlated} = \Delta_{projection} - \Delta_{antidiag}$ and $\Delta_{disorder}^{uncorrelated} = \Delta_{antidiag}$, using the measured Gaussian linewidths (w_G).

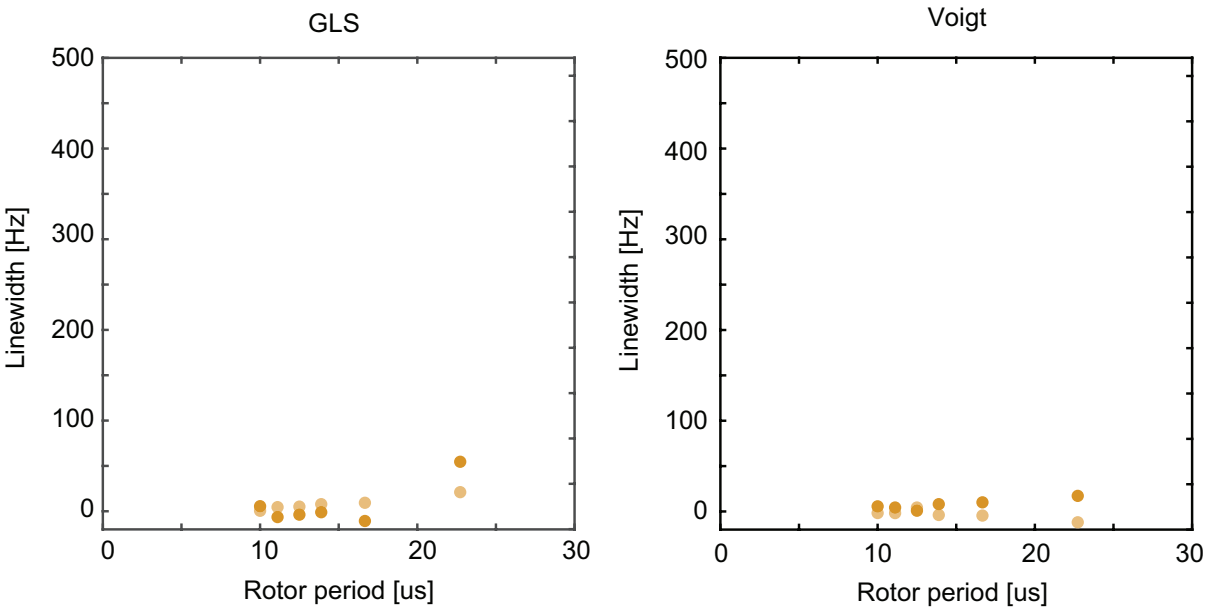

Figure 5.16. ZIF-8 H1. $\Delta_{inhomogeneous}^{correlated}$ (black) and $\Delta_{disorder}^{uncorrelated}$ (red) inhomogeneous linewidths as a function of the MAS rate. (a) For the GLS results, is calculated as $\Delta_{inhomogeneous}^{correlated} = \Delta_{projection} - \Delta_{antidiag}$ and $\Delta_{disorder}^{uncorrelated} = \Delta_{antidiag} - \Delta'$. (b) For the Voigt results, $\Delta_{inhomogeneous}^{correlated} = \Delta_{projection} - \Delta_{antidiag}$ and $\Delta_{disorder}^{uncorrelated} = \Delta_{antidiag}$, using the measured Gaussian linewidths (w_G).

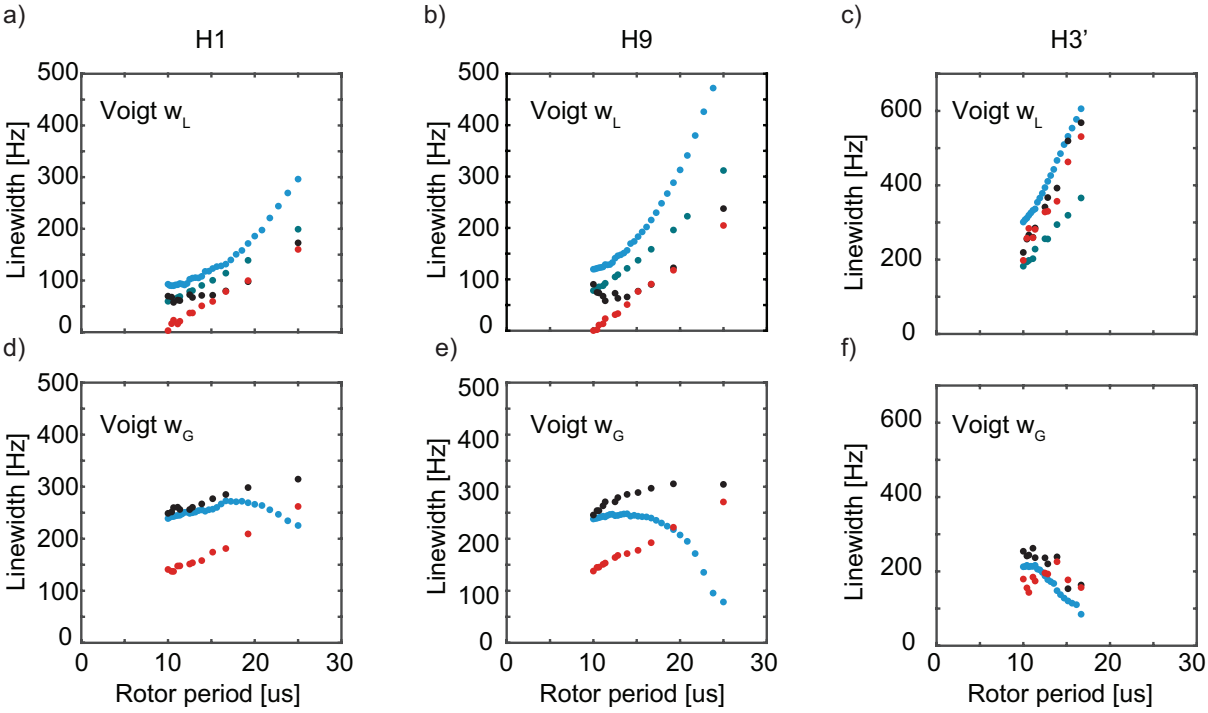

Figure 5.17. L-tyrosine.HCl. Evolution of the Voigt measured Lorentzian (w_L) and Gaussian (w_G)as a function of the rotor period for (a,d) H1, (b,e) H9 and (c,f) H3': 1D ^{1}H (blue), Δ'' contribution (green), $\Delta_{projection}$ (black), $\Delta_{antidiagonal}$ (red).

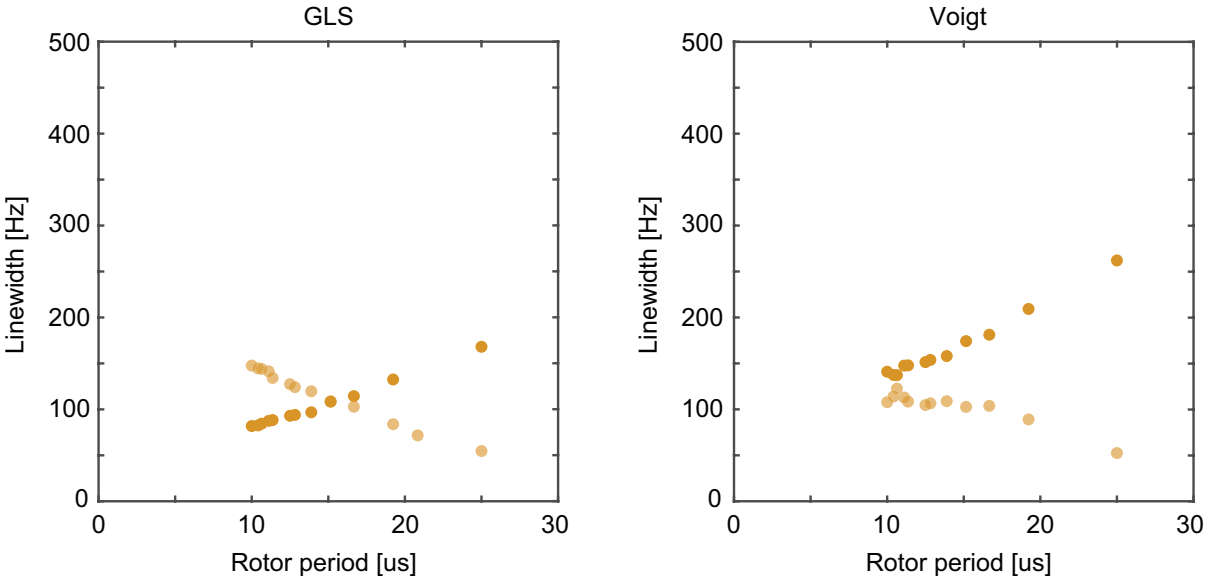

Figure 5.18. L-Tyrosine hydrochloride H1. $\Delta_{inhomogeneous}^{correlated}$ (black) and $\Delta_{disorder}^{uncorrelated}$ (red) inhomogeneous linewidths as a function of the MAS rate. (a) For the GLS results, is calculated as $\Delta_{inhomogeneous}^{correlated} = \Delta_{projection} - \Delta_{antidiag}$ and $\Delta_{disorder}^{uncorrelated} = \Delta_{antidiag} - \Delta'$. (b) For the Voigt results, $\Delta_{inhomogeneous}^{correlated} = \Delta_{projection} - \Delta_{antidiag}$ and $\Delta_{disorder}^{uncorrelated} = \Delta_{antidiag}$, using the measured Gaussian linewidths (w_G).

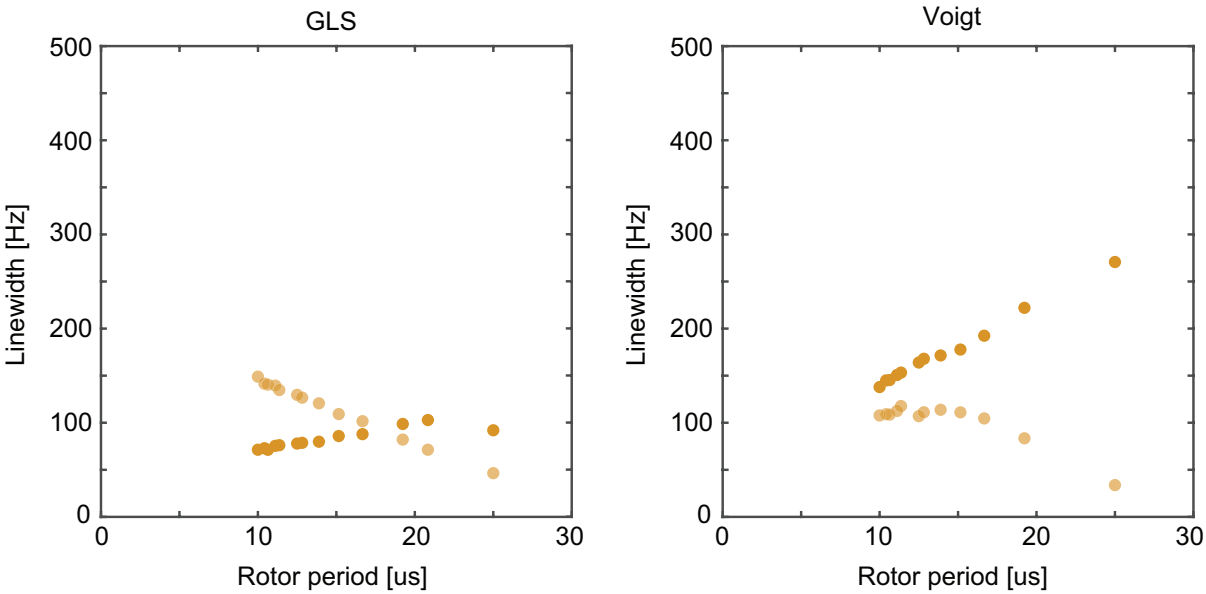

Figure 5.19. L-Tyrosine hydrochloride H9. $\Delta_{inhomogeneous}^{correlated}$ (black) and $\Delta_{disorder}^{uncorrelated}$ (red) inhomogeneous linewidths as a function of the MAS rate. (a) For the GLS results, is calculated as $\Delta_{inhomogeneous}^{correlated} = \Delta_{projection} - \Delta_{antidiag}$ and $\Delta_{disorder}^{uncorrelated} = \Delta_{antidiag} - \Delta'$. (b) For the Voigt results, $\Delta_{inhomogeneous}^{correlated} = \Delta_{projection} - \Delta_{antidiag}$ and $\Delta_{disorder}^{uncorrelated} = \Delta_{antidiag}$, using the measured Gaussian linewidths (w_G).

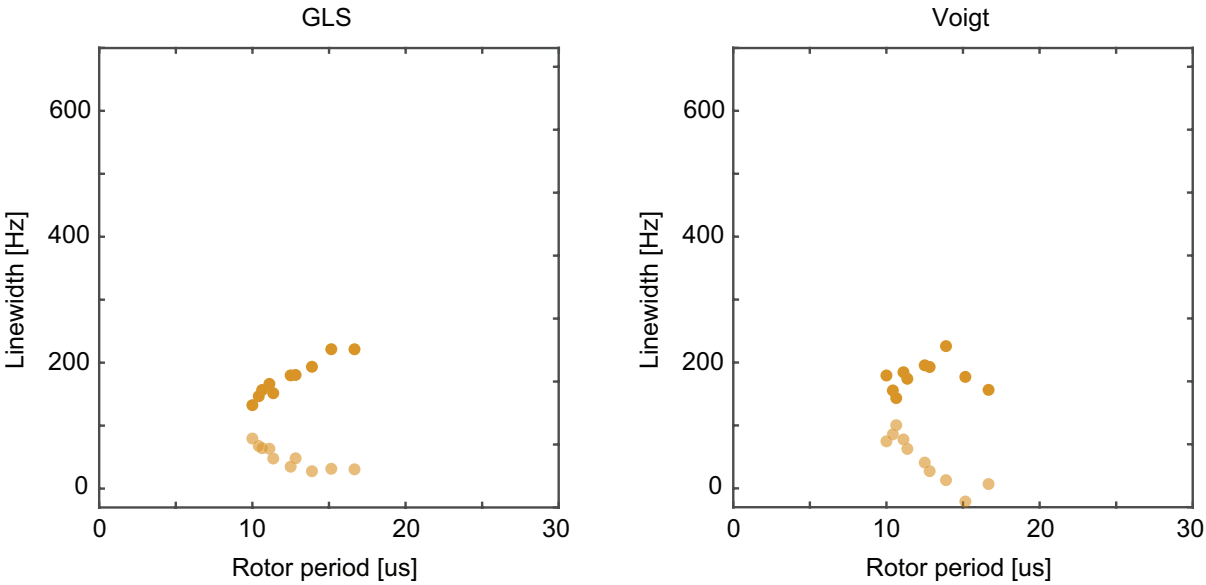

Figure 5.20. L-Tyrosine hydrochloride H3'. $\Delta_{inhomogeneous}^{correlated}$ (black) and $\Delta_{disorder}^{uncorrelated}$ (red) inhomogeneous linewidths as a function of the MAS rate. (a) For the GLS results, is calculated as $\Delta_{inhomogeneous}^{correlated} = \Delta_{projection} - \Delta_{antidiag}$ and $\Delta_{disorder}^{uncorrelated} = \Delta_{antidiag} - \Delta'$. (b) For the Voigt results, $\Delta_{inhomogeneous}^{correlated} = \Delta_{projection} - \Delta_{antidiag}$ and $\Delta_{disorder}^{uncorrelated} = \Delta_{antidiag}$, using the measured Gaussian linewidths (w_G).

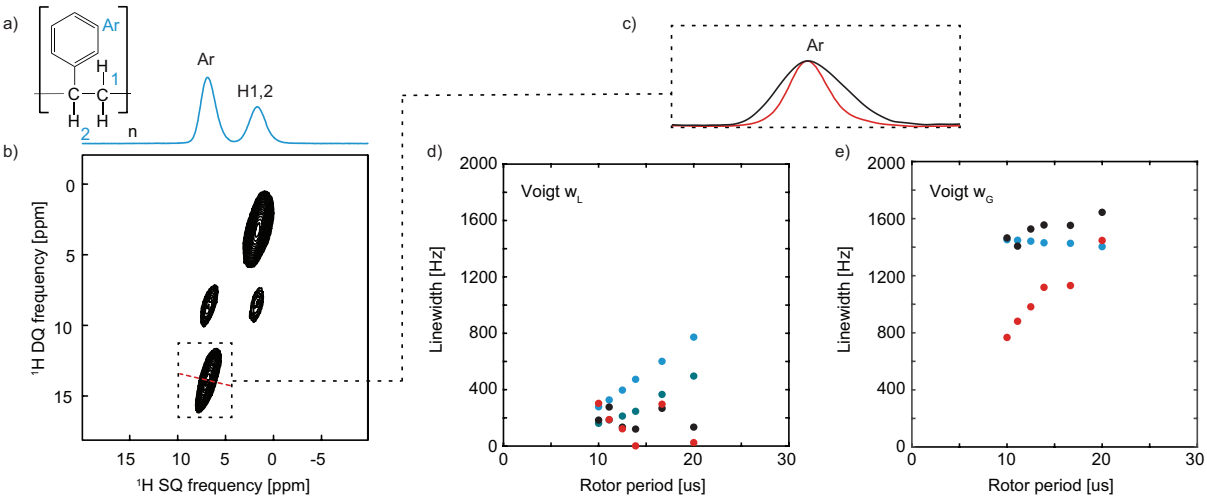

Figure 5.21. Polystyrene. (a) chemical structure, 1D ^{1}H spectrum, and (b) 2D ^{1}H-^{1}H DQ/SQ of polystyrene at 100 kHz MAS. The tilted dashed lines in the 2D spectrum represent the antidiagonals extracted. 8c) Positive projection (black) extracted between 9.90 ppm – 18.78 ppm overlayed with antidiagonal (red) for the Ar and (d,e) Evolution of the Voigt measured Lorentzian (w_L) and Gaussian (w_G)as a function of the rotor period: 1D 1H (blue), Δ' contribution (green), ^{1}H-^{1}H DQ/SQ projection (black), ^{1}H-^{1}H DQ/SQ antidiagonal (red).

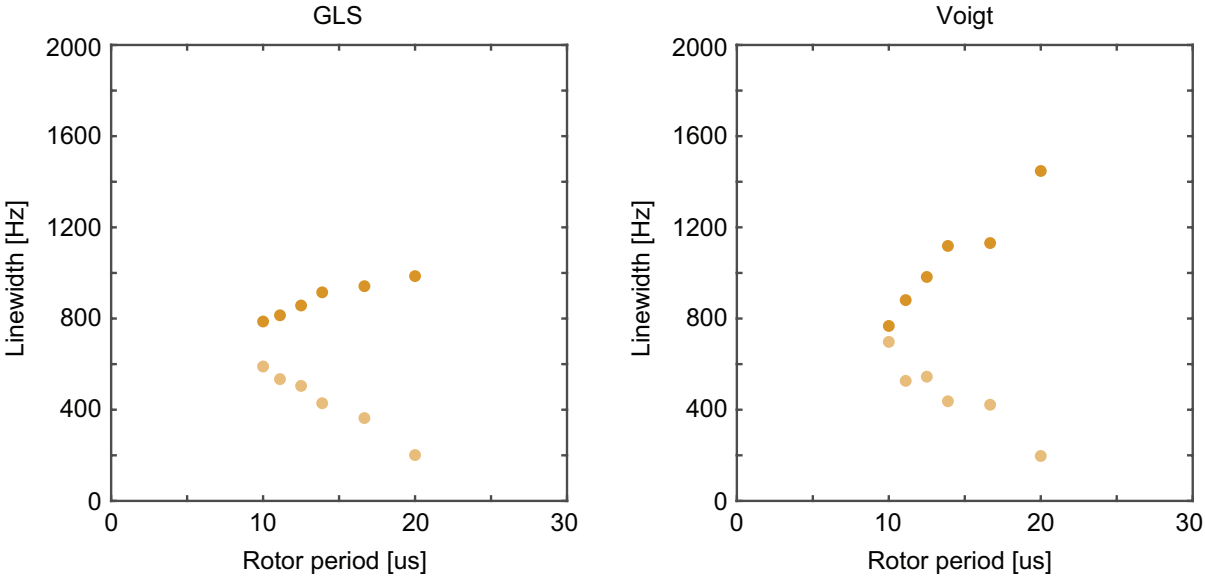

Figure 5.22. Polystyrene Ar. $\Delta_{inhomogeneous}^{correlated}$ (black) and $\Delta_{disorder}^{uncorrelated}$ (red) inhomogeneous linewidths as a function of the MAS rate. a) For the GLS results, is calculated as $\Delta_{inhomogeneous}^{correlated} = \Delta_{projection} - \Delta_{antidiag}$ and $\Delta_{disorder}^{uncorrelated} = \Delta_{antidiag} - \Delta'$. b) For the Voigt results, $\Delta_{inhomogeneous}^{correlated} = \Delta_{projection} - \Delta_{antidiag}$ and $\Delta_{disorder}^{uncorrelated} = \Delta_{antidiag}$, using the measured Gaussian linewidths (w_G).

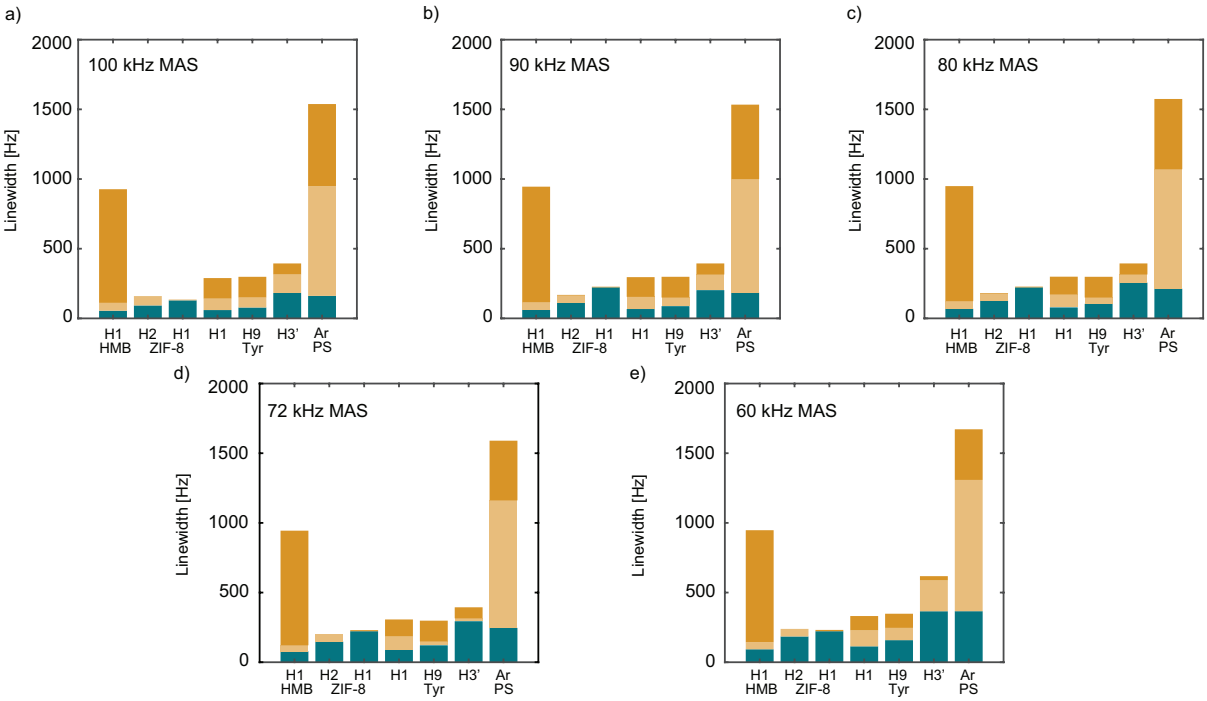

Figure 5.23. The different contributions to linewidth at 100 kHz (a), (b) 90 kHz, (c) 80 kHz, (d) 72 kHz and (e) 60 kHz MAS : For all the different resonances, the homogeneous contribution (blue lagoon), the uncorrelated inhomogeneous contribution (yellow) and the correlated inhomogeneous contribution (orange) are shown.

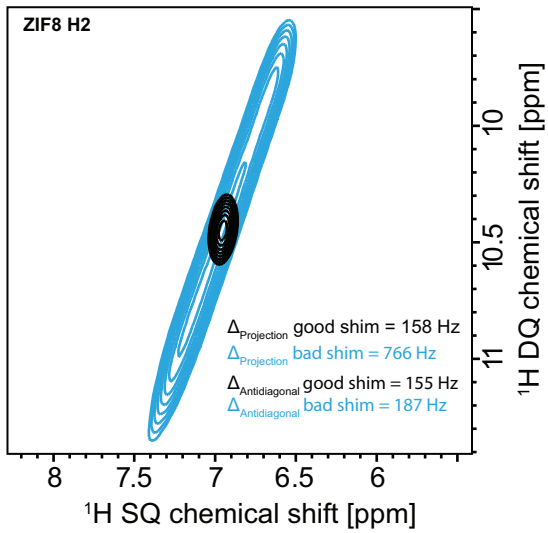

Figure 5.24. B_0 inhomogeneity effect on the spectrum. 2D ^{1}H-^{1}H DQ/SQ spectra of ZIF-8 at 100 kHz MAS. The Spectra are zoomed on H2 peak from the H2-H1 correlation. In black, the peak is the same from Figure S4, after shimming on adamantane. In blue, the spectrum was acquired with bad shimming values that lead to considerable B_0 inhomogeneity. The projection and the antidiagonal linewidths are presented for both spectra.

Table 5.30. HMB 1D GLS and Voigt results

MAS rate [kHz]	GLS w [Hz]	GLS m	Voigt w_G [Hz]	Voigt w_L [Hz]
100	969.3 ± 27.8	0.191	866.4 ± 27.8	209.0 ± 27.8
96	977.7 ± 27.8	0.184	868.0 ± 27.8	216.8 ± 27.8
94	980.5 ± 27.8	0.186	866.4 ± 27.8	221.4 ± 27.8
90	983.0 ± 27.8	0.189	866.3 ± 27.8	225.1 ± 27.8
88	981.7 ± 27.8	0.189	864.8 ± 27.8	226.3 ± 27.8
80	991.8 ± 27.8	0.192	870.1 ± 27.8	231.4 ± 27.8
78	994.1 ± 27.8	0.185	873.7 ± 27.8	224.2 ± 27.8
72	998.5 ± 27.8	0.193	874.4 ± 27.8	234.6 ± 27.8
66	1006.3 ± 27.8	0.193	878.4 ± 27.8	236.6 ± 27.8
60	1009.5 ± 27.8	0.196	878.4 ± 27.8	236.6 ± 27.8
52	1021.2 ± 27.8	0.206	881.1 ± 27.8	250.1 ± 27.8
48	1021.4 ± 27.8	0.213	876.2 ± 27.8	257.5 ± 27.8
44	1020.1 ± 27.8	0.236	847.7 ± 27.8	295.5 ± 27.8
40	1026.0 ± 27.8	0.262	833.2 ± 27.8	321.8 ± 27.8

Table 5.31. HMB DQ/SQ Projection GLS and Voigt results

MAS rate [kHz]	GLS w [Hz]	GLS m	Voigt w_G [Hz]	Voigt w_L [Hz]
100	926.8 ± 55.4	0.148	809.6 ± 55.4	176.2 ± 55.4
96	937.4 ± 55.4	0.179	787.2 ± 55.4	219.8 ± 55.4
94	934.6 ± 55.4	0.179	747.1 ± 55.4	248.6 ± 55.4
90	945.2 ± 55.4	0.157	789.0 ± 55.4	214.6 ± 55.4
88	934.3 ± 55.4	0.177	814.3 ± 55.4	195.3 ± 55.4
80	949.2 ± 55.4	0.161	798.2 ± 55.4	212.5 ± 55.4
78	933.8 ± 55.4	0.194	722.9 ± 55.4	274.0 ± 55.4
72	944.2 ± 55.4	0.175	735.7 ± 55.4	263.7 ± 55.4
66	958.0 ± 55.4	0.162	798.8 ± 55.4	219.7 ± 55.4
60	947.4 ± 55.4	0.169	760.6 ± 55.4	245.1 ± 55.4
52	970.1 ± 55.4	0.145	832.0 ± 55.4	195.9 ± 55.4
48	970.7 ± 55.4	0.141	108.6 ± 55.4	182.4 ± 55.4
44	965.9 ± 55.4	0.153	837.3 ± 55.4	190.8 ± 55.4
40	958.7 ± 55.4	0.169	815.6 ± 55.4	211.5 ± 55.4

Table 5.32. HMB DQ/SQ Antidiagonal GLS and Voigt results

MAS rate [kHz]	GLS w [Hz]	GLS m	Voigt w_G [Hz]	Voigt w_L [Hz]
100	111.3 ± 55.4	0.523	57.76 ± 55.4	68.81 ± 55.4
96	116.2 ± 55.4	0.396	77.75 ± 55.4	54.31 ± 55.4
94	107.0 ± 55.4	0.588	54.07 ± 55.4	70.44 ± 55.4
90	116.5 ± 55.4	0.574	67.53 ± 55.4	71.68 ± 55.4
88	134.1 ± 55.4	0.321	101.88 ± 55.4	49.03 ± 55.4
80	123.3 ± 55.4	0.639	59.84 ± 55.4	86.45 ± 55.4
78	111.9 ± 55.4	0.919	10.24 ± 55.4	121.90 ± 55.4
72	121.4 ± 55.4	0.834	144.52 ± 55.4	0.29 ± 55.4
66	154.1 ± 55.4	0.553	86.06 ± 55.4	95.52 ± 55.4
60	143.8 ± 55.4	0.877	39.19 ± 55.4	123.84 ± 55.4
52	171.1 ± 55.4	0.691	82.71 ± 55.4	124.20 ± 55.4
48	195.2 ± 55.4	0.573	0.00 ± 55.4	122.80 ± 55.4
44	205.6 ± 55.4	0.553	113.94 ± 55.4	127.46 ± 55.4
40	220.7 ± 55.4	0.735	65.72 ± 55.4	182.50 ± 55.4

Table 5.33. HMB T_2' measured at every MAS rate

MAS rate [kHz]	Δ' [Hz]	T_2' [ms]
100	56	5.634 ± 0.008
96	58	5.488 ± 0.008
94	59	5.395 ± 0.008
90	61	5.218 ± 0.008
88	63	5.053 ± 0.008
80	69	4.613 ± 0.008
78	71	4.483 ± 0.008
72	78	4.081 ± 0.008
66	85	3.745 ± 0.008
60	93	3.423 ± 0.008
52	108	2.947 ± 0.008
48	117	2.721 ± 0.008
44	127	2.506 ± 0.008
40	139	2.290 ± 0.008

Table 5.34. ZIF-8 H2 1D GLS and Voigt results

MAS rate [kHz]	GLS w [Hz]	GLS m	Voigt w_G [Hz]	Voigt w_L [Hz]
100	199.8 ± 13.8	0.657	110.2 ± 13.8	134.8 ± 13.8
90	213.4 ± 13.8	0.682	112.9 ± 13.8	149.3 ± 13.8
80	233.0 ± 13.8	0.710	116.1 ± 13.8	169.9 ± 13.8
72	253.5 ± 13.8	0.751	116.4 ± 13.8	194.9 ± 13.8
60	297.5 ± 13.8	0.768	127.1 ± 13.8	234.9 ± 13.8
44	392.1 ± 13.8	0.848	114.9 ± 13.8	347.7 ± 13.8

Table 5.35. ZIF-8 H2 DQ/SQ Projection GLS and Voigt results

MAS rate [kHz]	GLS w [Hz]	GLS m	Voigt w_G [Hz]	Voigt w_L [Hz]
100	158.7 ± 27.6	0.329	126.1 ± 27.6	55.5 ± 27.6
90	168.4 ± 27.6	0.363	128.1 ± 27.6	66.1 ± 27.6
80	181.9 ± 27.6	0.409	131.5 ± 27.6	81.1 ± 27.6
72	197.9 ± 27.6	0.442	141.3 ± 27.6	91.4 ± 27.6
60	235.2 ± 27.6	0.536	136.0 ± 27.6	147.2 ± 27.6
44	349.3 ± 27.6	0.670	186.7 ± 27.6	237.6 ± 27.6

Table 5.36. ZIF-8 H2 DQ/SQ Antidiagonal GLS and Voigt results

MAS rate [kHz]	GLS w [Hz]	GLS m	Voigt w_G [Hz]	Voigt w_L [Hz]
100	155.1 ± 27.6	0.248	132.2 ± 27.6	42.3 ± 27.6
90	165.5 ± 27.6	0.258	140.0 ± 27.6	46.6 ± 27.6
80	179.0 ± 27.6	0.318	142.4 ± 27.6	64.7 ± 27.6
72	199.6 ± 27.6	0.320	153.5 ± 27.6	75.9 ± 27.6
60	239.3 ± 27.6	0.349	168.8 ± 27.6	107.9 ± 27.6
44	368.6 ± 27.6	0.264	287.3 ± 27.6	117.7 ± 27.6

Table 5.37. ZIF-8 H2 DQ/SQ auto-correlation peak Projection GLS and Voigt results

MAS rate [kHz]	GLS w [Hz]	GLS m
100	180.7 ± 27.6	0.176
90	193.4 ± 27.6	0.249
80	205.7 ± 27.6	0.303
72	224.4 ± 27.6	0.331
60	259.5 ± 27.6	0.498
44	346.3 ± 27.6	0.792

Table 5.38. ZIF-8 H2 DQ/SQ auto-correlation peak Antidiagonal GLS and Voigt results

MAS rate [kHz]	GLS w [Hz]	GLS m
100	169.7 ± 27.6	0.109
90	185.9 ± 27.6	0.139
80	197.7 ± 27.6	0.189
72	219.4 ± 27.6	0.201
60	259.1 ± 27.6	0.288
44	364.2 ± 27.6	0.364

Table 5.39. ZIF-8 H2 T_2' measured at every MAS rate

MAS rate [kHz]	Δ' [Hz]	T_2' [ms]
100	92.83	3.429 ± 0.01
90	115.00	2.768 ± 0.01
80	127.12	2.504 ± 0.01
72	147.50	2.158 ± 0.01
60	184.96	1.721 ± 0.01
44	285.74	1.114 ± 0.01

Table 5.40. ZIF-8 H1 1D GLS and Voigt results

MAS rate [kHz]	GLS w [Hz]	GLS m	Voigt w_G [Hz]	Voigt w_L [Hz]
100	244.7 ± 13.8	1.00	6.35 ± 13.8	233.3 ± 13.8
90	265.2 ± 13.8	1.00	6.35 ± 13.8	233.3 ± 13.8
80	291.8 ± 13.8	1.00	2.21 ± 13.8	277.0 ± 13.8
72	318.6 ± 13.8	1.00	2.42 ± 13.8	296.4 ± 13.8
60	366.8 ± 13.8	1.00	5.95 ± 13.8	339.7 ± 13.8
44	458.3 ± 13.8	1.00	2.17 ± 13.8	417.7 ± 13.8

Table 5.41. ZIF-8 H1 DQ/SQ Projection GLS and Voigt results

MAS rate [kHz]	GLS w [Hz]	GLS m	Voigt w_G [Hz]	Voigt w_L [Hz]
100	135.5 ± 27.6	0.999	3.88 ± 27.6	133.7 ± 27.6
90	154.0 ± 27.6	1.000	2.53 ± 27.6	151.1 ± 27.6
80	164.5 ± 27.6	1.000	5.15 ± 27.6	159.7 ± 27.6
72	193.6 ± 27.6	1.000	4.15 ± 27.6	187.6 ± 27.6
60	221.2 ± 27.6	1.000	5.52 ± 27.6	212.6 ± 27.6
44	348.2 ± 27.6	1.000	5.23 ± 27.6	319.4 ± 27.6

Table 5.42. ZIF-8 H1 DQ/SQ Antidiagonal GLS and Voigt results

MAS rate [kHz]	GLS w [Hz]	GLS m	Voigt w_G [Hz]	Voigt w_L [Hz]
100	135.0 ± 27.6	0.918	5.63 ± 27.6	130.0 ± 27.6
90	149.5 ± 27.6	0.940	4.35 ± 27.6	145.3 ± 27.6
80	159.4 ± 27.6	1.000	0.83 ± 27.6	156.8 ± 27.6
72	185.7 ± 27.6	1.000	8.03 ± 27.6	183.4 ± 27.6
60	211.9 ± 27.6	1.000	10.06 ± 27.6	207.1 ± 27.6
44	327.1 ± 27.6	1.000	17.18 ± 27.6	308.0 ± 27.6

Table 5.43. ZIF-8 H1 DQ/SQ auto-correlation peak Projection GLS and Voigt results

MAS rate [kHz]	GLS w [Hz]	GLS m
100	189.6 ± 27.6	0.825
90	203.6 ± 27.6	0.852
80	207.1 ± 27.6	0.961
72	224 ± 27.6	1.000
60	265.5 ± 27.6	1.000
44	371.9 ± 27.6	1.000

Table 5.44. ZIF-8 H1 DQ/SQ auto-correlation peak Antidiagonal GLS and Voigt results

MAS rate [kHz]	GLS w [Hz]	GLS m
100	187.5 ± 27.6	0.793
90	205.6 ± 27.6	0.663
80	207.4 ± 27.6	0.849
72	223.7 ± 27.6	0.947
60	260.2 ± 27.6	1.000
44	341.9 ± 27.6	1.000

Table 5.45. ZIF-8 H1 T_2' measured at every MAS rate

MAS rate [kHz]	Δ' [Hz]	T_2' [ms]
100	129.4	2.460 ± 0.01
90	155.9	2.042 ± 0.01
80	163.2	1.951 ± 0.01
72	186.8	1.704 ± 0.01
60	222.6	1.430 ± 0.01
44	272.5	1.168 ± 0.01

Table 5.46. L-Tyrosine HCl H1 1D GLS and Voigt results

MAS rate [kHz]	GLS w [Hz]	GLS m	Voigt w_G [Hz]	Voigt w_L [Hz]
100	294.7 ± 27.6	0.307	238.9 ± 27.6	92.8 ± 27.6
98	295.8 ± 27.6	0.298	241.1 ± 27.6	90.3 ± 27.6
96	297.1 ± 27.6	0.298	242.7 ± 27.6	90.0 ± 27.6
94	297.8 ± 27.6	0.303	242.7 ± 27.6	90.0 ± 27.6
92	299.4 ± 27.6	0.303	244.1 ± 27.6	91.5 ± 27.6
90	300.9 ± 27.6	0.297	244.8 ± 27.6	91.9 ± 27.6
88	302.4 ± 27.6	0.305	245.2 ± 27.6	94.2 ± 27.6
86	304.4 ± 27.6	0.300	247.7 ± 27.6	93.0 ± 27.6
84	306.6 ± 27.6	0.290	250.6 ± 27.6	91.4 ± 27.6
82	308.8 ± 27.6	0.298	251.2 ± 27.6	94.2 ± 27.6
80	311.3 ± 27.6	0.313	248.8 ± 27.6	102.4 ± 27.6
78	314.0 ± 27.6	0.320	250.0 ± 27.6	104.7 ± 27.6
76	316.2 ± 27.6	0.315	251.2 ± 27.6	105.5 ± 27.6
74	318.5 ± 27.6	0.316	254.1 ± 27.6	105.0 ± 27.6
72	322.6 ± 27.6	0.315	255.4 ± 27.6	108.1 ± 27.6
70	326.7 ± 27.6	0.334	252.9 ± 27.6	117.7 ± 27.6
68	330.5 ± 27.6	0.326	255.7 ± 27.6	118.0 ± 27.6
66	335.3 ± 27.6	0.333	256.8 ± 27.6	123.2 ± 27.6
64	340.1 ± 27.6	0.338	260.2 ± 27.6	126.9 ± 27.6
62	346.3 ± 27.6	0.335	266.8 ± 27.6	128.2 ± 27.6
60	353.3 ± 27.6	0.335	272.8 ± 27.6	131.7 ± 27.6
58	357.7 ± 27.6	0.347	271.9 ± 27.6	139.8 ± 27.6
56	363.3 ± 27.6	0.376	271.1 ± 27.6	150.7 ± 27.6
54	368.4 ± 27.6	0.389	272.0 ± 27.6	158.1 ± 27.6
52	374.4 ± 27.6	0.414	269.2 ± 27.6	171.7 ± 27.6
50	381.2 ± 27.6	0.437	266.1 ± 27.6	185.9 ± 27.6
48	387.4 ± 27.6	0.454	263.9 ± 27.6	197.6 ± 27.6
46	397.3 ± 27.6	0.488	255.7 ± 27.6	220.9 ± 27.6
44	407.9 ± 27.6	0.513	246.9 ± 27.6	243.9 ± 27.6
42	418.2 ± 27.6	0.546	234.5 ± 27.6	269.4 ± 27.6
40	431.9 ± 27.6	0.567	225.4 ± 27.6	296.2 ± 27.6

Table 5.47. L-Tyrosine HCl H1 DQ/SQ Projection GLS and Voigt results

MAS rate [kHz]	GLS w [Hz]	GLS m	Voigt w_G [Hz]	Voigt w_L [Hz]
100	289.2 ± 22.18	0.236	248.8 ± 22.18	69.8 ± 22.18
96	289.9 ± 22.18	0.222	251.5 ± 22.18	67.9 ± 22.18
94	292.4 ± 22.18	0.190	259.8 ± 22.18	57.6 ± 22.18
90	295.9 ± 22.18	0.205	260.5 ± 22.18	62.2 ± 22.18
88	291.7 ± 22.18	0.192	256.3 ± 22.18	61.2 ± 22.18
80	299.2 ± 22.18	0.219	256.1 ± 22.18	72.4 ± 22.18
78	298.7 ± 22.18	0.213	260.4 ± 22.18	67.2 ± 22.18
72	306.9 ± 22.18	0.223	266.9 ± 22.18	71.1 ± 22.18
66	317.5 ± 22.18	0.211	276.9 ± 22.18	71.5 ± 22.18
60	331.6 ± 22.18	0.216	285.0 ± 22.18	79.8 ± 22.18
52	355.4 ± 22.18	0.239	298.3 ± 22.18	97.8 ± 22.18
40	421.9 ± 22.18	0.340	314.5 ± 22.18	172.8 ± 22.18

Table 5.48. L-Tyrosine HCl H1 DQ/SQ Antidiagonal GLS and Voigt results

MAS rate [kHz]	GLS w [Hz]	GLS m	Voigt w_G [Hz]	Voigt w_L [Hz]
100	141.6 ± 22.18	0.002	141.0 ± 22.18	3.1 ± 22.18
96	145.3 ± 22.18	0.085	137.4 ± 22.18	16.5 ± 22.18
94	148.4 ± 22.18	0.125	137.2 ± 22.18	23.2 ± 22.18
90	154.5 ± 22.18	0.066	147.7 ± 22.18	15.9 ± 22.18
88	157.4 ± 22.18	0.102	147.9 ± 22.18	21.1 ± 22.18
80	171.8 ± 22.18	0.187	151.4 ± 22.18	37.0 ± 22.18
78	174.5 ± 22.18	0.185	153.8 ± 22.18	37.3 ± 22.18
72	187.2 ± 22.18	0.253	158.0 ± 22.18	51.0 ± 22.18
66	208.8 ± 22.18	0.260	174.2 ± 22.18	59.5 ± 22.18
60	228.6 ± 22.18	0.308	181.2 ± 22.18	78.7 ± 22.18
52	271.6 ± 22.18	0.316	209.3 ± 22.18	99.8 ± 22.18
40	367.3 ± 22.18	0.351	262.0 ± 22.18	160.1 ± 22.18

Table 5.49. L-Tyrosine HCl H1 cross peak correlated with H10 DQ/SQ Projection GLS and Voigt results

MAS rate [kHz]	GLS w [Hz]	GLS m
100	288.9 ± 22.18	0.315
96	282.2 ± 22.18	0.459
94	273.2 ± 22.18	0.468
90	283.6 ± 22.18	0.387
88	288.4 ± 22.18	0.401
80	293.3 ± 22.18	0.342
78	273.1 ± 22.18	0.467
72	301.3 ± 22.18	0.305
66	309.0 ± 22.18	0.411
60	322.7 ± 22.18	0.338
52	344.6 ± 22.18	0.351
40	408.0 ± 22.18	0.39

Table 5.50. L-Tyrosine HCl H1 cross peak correlated with H10 DQ/SQ Antidiagonal GLS and Voigt results

MAS rate [kHz]	GLS w [Hz]	GLS m
100	167.5 ± 22.18	0.358
96	174.5 ± 22.18	0.111
94	178.1 ± 22.18	0.419
90	179.5 ± 22.18	0.523
88	183.4 ± 22.18	0.363
80	214.8 ± 22.18	0.343
78	208.7 ± 22.18	0.517
72	232.2 ± 22.18	0.388
66	238.3 ± 22.18	0.428
60	260.2 ± 22.18	0.272
52	294.0 ± 22.18	0.388
40	362.5 ± 22.18	0.548

Table 5.51. L-Tyrosine HCl H1 T_2' measured at every MAS rate

MAS rate [kHz]	Δ' [Hz]	T_2' [ms]
100	59.8	5.326 ± 0.02
96	62.7	5.076 ± 0.02
94	64.0	4.972 ± 0.02
90	67.0	4.750 ± 0.02
88	69.1	4.608 ± 0.02
80	78.7	4.044 ± 0.02
78	80.5	3.953 ± 0.02
72	90.4	3.520 ± 0.02
66	100.4	3.170 ± 0.02
60	114.2	2.787 ± 0.02
52	139.1	2.289 ± 0.02
40	199.2	1.598 ± 0.02

Table 5.52. L-Tyrosine HCl H9 1D GLS and Voigt results

MAS rate [kHz]	GLS w [Hz]	GLS m	Voigt w_G [Hz]	Voigt w_L [Hz]
100	308.7 ± 27.6	0.361	119.7 ± 27.6	238.0 ± 27.6
98	309.9 ± 27.6	0.362	120.3 ± 27.6	238.9 ± 27.6
96	311.1 ± 27.6	0.365	121.5 ± 27.6	239.4 ± 27.6
94	313.0 ± 27.6	0.367	122.6 ± 27.6	240.6 ± 27.6
92	314.6 ± 27.6	0.368	123.2 ± 27.6	241.8 ± 27.6
90	316.6 ± 27.6	0.368	124.2 ± 27.6	243.2 ± 27.6
88	318.5 ± 27.6	0.380	128.8 ± 27.6	242.0 ± 27.6
86	320.8 ± 27.6	0.375	128.1 ± 27.6	244.7 ± 27.6
84	323.3 ± 27.6	0.373	128.8 ± 27.6	246.7 ± 27.6
82	326.3 ± 27.6	0.382	132.7 ± 27.6	247.2 ± 27.6
80	329.3 ± 27.6	0.402	141.2 ± 27.6	244.4 ± 27.6
78	332.9 ± 27.6	0.411	145.9 ± 27.6	244.7 ± 27.6
76	335.9 ± 27.6	0.412	147.8 ± 27.6	246.4 ± 27.6
74	339.4 ± 27.6	0.417	151.1 ± 27.6	247.6 ± 27.6
72	343.5 ± 27.6	0.426	156.4 ± 27.6	248.0 ± 27.6
70	348.2 ± 27.6	0.455	169.6 ± 27.6	243.4 ± 27.6
68	352.8 ± 27.6	0.460	173.8 ± 27.6	245.0 ± 27.6
66	357.8 ± 27.6	0.478	183.1 ± 27.6	243.3 ± 27.6
64	363.7 ± 27.6	0.493	192.3 ± 27.6	242.4 ± 27.6
62	370.4 ± 27.6	0.507	201.9 ± 27.6	241.9 ± 27.6
60	378.4 ± 27.6	0.531	215.4 ± 27.6	239.8 ± 27.6
58	384.9 ± 27.6	0.554	229.7 ± 27.6	235.4 ± 27.6
56	394.0 ± 27.6	0.586	247.9 ± 27.6	230.2 ± 27.6
54	403.7 ± 27.6	0.616	266.9 ± 27.6	224.2 ± 27.6
52	414.7 ± 27.6	0.648	288.0 ± 27.6	217.6 ± 27.6
50	426.5 ± 27.6	0.684	312.9 ± 27.6	207.2 ± 27.6
48	440.6 ± 27.6	0.723	341.0 ± 27.6	195.0 ± 27.6
46	456.9 ± 27.6	0.777	379.8 ± 27.6	171.5 ± 27.6
44	476.2 ± 27.6	0.836	426.1 ± 27.6	135.4 ± 27.6
42	498.7 ± 27.6	0.901	472.2 ± 27.6	95.5 ± 27.6
40	526.0 ± 27.6	0.968	511.2 ± 27.6	78.5 ± 27.6

Table 5.53. L-Tyrosine HCl H9 DQ/SQ Projection GLS and Voigt results

MAS rate [kHz]	GLS w [Hz]	GLS m	Voigt w_G [Hz]	Voigt w_L [Hz]
100	298.4 ± 22.18	0.300	245.7 ± 22.18	90.4 ± 22.18
96	296.7 ± 22.18	0.251	254.1 ± 22.18	74.6 ± 22.18
94	297.2 ± 22.18	0.238	254.0 ± 22.18	73.6 ± 22.18
90	302.5 ± 22.18	0.221	263.3 ± 22.18	67.2 ± 22.18
88	303.3 ± 22.18	0.190	271.0 ± 22.18	58.3 ± 22.18
80	312.2 ± 22.18	0.226	271.0 ± 22.18	73.0 ± 22.18
78	314.4 ± 22.18	0.195	279.1 ± 22.18	63.1 ± 22.18
72	321.9 ± 22.18	0.201	285.2 ± 22.18	65.8 ± 22.18
66	332.2 ± 22.18	0.232	288.8 ± 22.18	77.0 ± 22.18
60	348.1 ± 22.18	0.259	297.0 ± 22.18	90.0 ± 22.18
52	376.8 ± 22.18	0.322	305.5 ± 22.18	122.5 ± 22.18
40	450.2 ± 22.18	0.566	304.5 ± 22.18	237.7 ± 22.18

Table 5.54. L-Tyrosine HCl H9 DQ/SQ Antidiagonal GLS and Voigt results

MAS rate [kHz]	GLS w [Hz]	GLS m	Voigt w_G [Hz]	Voigt w_L [Hz]
100	141.6 ± 22.18	0.002 ± 22.18	137.9 ± 22.18	0.2 ± 22.18
96	145.3 ± 22.18	0.085 ± 22.18	145.0 ± 22.18	2.0 ± 22.18
94	148.4 ± 22.18	0.125 ± 22.18	145.3 ± 22.18	11.1 ± 22.18
90	154.5 ± 22.18	0.066 ± 22.18	150.8 ± 22.18	13.5 ± 22.18
88	157.4 ± 22.18	0.102 ± 22.18	153.3 ± 22.18	23.5 ± 22.18
80	171.8 ± 22.18	0.187 ± 22.18	164.0 ± 22.18	31.2 ± 22.18
78	174.5 ± 22.18	0.185 ± 22.18	168.0 ± 22.18	33.4 ± 22.18
72	187.2 ± 22.18	0.253 ± 22.18	171.5 ± 22.18	50.9 ± 22.18
66	208.8 ± 22.18	0.260 ± 22.18	177.7 ± 22.18	76.4 ± 22.18
60	228.6 ± 22.18	0.308 ± 22.18	192.4 ± 22.18	90.8 ± 22.18
52	271.6 ± 22.18	0.316 ± 22.18	222.1 ± 22.18	117.7 ± 22.18
40	367.3 ± 22.18	0.351 ± 22.18	270.7 ± 22.18	204.8 ± 22.18

Table 5.55. L-Tyrosine HCl H9 T_2' measured at every MAS rate

MAS rate [kHz]	Δ' [Hz]	T_2' [ms]
100	78.1	4.075 ± 0.02
96	82.2	3.871 ± 0.02
94	85.4	3.726 ± 0.02
90	87.6	3.635 ± 0.02
88	92.4	3.445 ± 0.02
80	104.7	3.040 ± 0.02
78	109.1	2.918 ± 0.02
72	121.4	2.622 ± 0.02
66	137.1	2.322 ± 0.02
60	158.5	2.008 ± 0.02
52	196.0	1.624 ± 0.02
40	311.8	1.021 ± 0.02

Table 5.56. L-Tyrosine HCl H3' 1D GLS and Voigt results

MAS rate [kHz]	GLS w [Hz]	GLS m	Voigt w_G [Hz]	Voigt w_L [Hz]
100	418.3 ± 27.6	0.691	212.5 ± 27.6	301.1 ± 27.6
98	423.5 ± 27.6	0.714	213.0 ± 27.6	307.3 ± 27.6
96	429.7 ± 27.6	0.708	216.2 ± 27.6	311.7 ± 27.6
94	433.6 ± 27.6	0.713	212.5 ± 27.6	319.2 ± 27.6
92	439.2 ± 27.6	0.725	213.8 ± 27.6	325.8 ± 27.6
90	444.9 ± 27.6	0.748	213.6 ± 27.6	332.5 ± 27.6
88	450.2 ± 27.6	0.718	216.3 ± 27.6	336.4 ± 27.6
86	457.3 ± 27.6	0.772	206.1 ± 27.6	354.3 ± 27.6
84	466.3 ± 27.6	0.805	204.1 ± 27.6	365.6 ± 27.6
82	472.3 ± 27.6	0.825	197.4 ± 27.6	378.3 ± 27.6
80	479.1 ± 27.6	0.846	187.9 ± 27.6	393.9 ± 27.6
78	487.2 ± 27.6	0.881	177.7 ± 27.6	410.5 ± 27.6
76	498.8 ± 27.6	0.908	172.4 ± 27.6	426.3 ± 27.6
74	510.7 ± 27.6	0.911	167.6 ± 27.6	442.7 ± 27.6
72	522.5 ± 27.6	0.956	148.2 ± 27.6	466.9 ± 27.6
70	533.5 ± 27.6	0.990	137.4 ± 27.6	485.2 ± 27.6
68	551.8 ± 27.6	1.000	128.2 ± 27.6	509.5 ± 27.6
66	568.6 ± 27.6	1.000	120.5 ± 27.6	531.6 ± 27.6
64	591.5 ± 27.6	1.000	114.5 ± 27.6	553.8 ± 27.6
62	616.5 ± 27.6	1.000	110.4 ± 27.6	577.4 ± 27.6
60	644.5 ± 27.6	1.000	84.7 ± 27.6	605.9 ± 27.6

Table 5.57. L-Tyrosine HCl H3' Projection GLS and Voigt results

MAS rate [kHz]	GLS w [Hz]	GLS m	Voigt w_G [Hz]	Voigt w_L [Hz]
100	394.2 ± 22.18	0.518	254.1 ± 22.18	219.3 ± 22.18
96	408.3 ± 22.18	0.587	241.4 ± 22.18	255.2 ± 22.18
94	418.7 ± 22.18	0.597	243.8 ± 22.18	266.1 ± 22.18
90	432.1 ± 22.18	0.565	262.3 ± 22.18	260.1 ± 22.18
88	427.5 ± 22.18	0.633	236.9 ± 22.18	285.1 ± 22.18
80	470.6 ± 22.18	0.700	236.5 ± 22.18	341.5 ± 22.18
78	484.0 ± 22.18	0.714	220.2 ± 22.18	367.0 ± 22.18
72	515.2 ± 22.18	0.730	239.1 ± 22.18	392.4 ± 22.18
66	572.1 ± 22.18	0.908	153.4 ± 22.18	519.4 ± 22.18
60	617.7 ± 22.18	0.919	163.4 ± 22.18	568.4 ± 22.18

Table 5.58. L-Tyrosine HCl H3' Antidiagonal GLS and Voigt results

MAS rate [kHz]	GLS w [Hz]	GLS m	Voigt w_G [Hz]	Voigt w_L [Hz]
100	314.2 ± 22.18	0.518	254.1 ± 22.18	219.3 ± 22.18
96	408.3 ± 22.18	0.587	241.4 ± 22.18	255.2 ± 22.18
94	418.7 ± 22.18	0.597	243.8 ± 22.18	266.1 ± 22.18
90	432.1 ± 22.18	0.565	262.3 ± 22.18	260.1 ± 22.18
88	427.5 ± 22.18	0.633	236.9 ± 22.18	285.1 ± 22.18
80	470.6 ± 22.18	0.700	236.5 ± 22.18	341.5 ± 22.18
78	484.0 ± 22.18	0.714	220.2 ± 22.18	367.0 ± 22.18
72	515.2 ± 22.18	0.730	239.1 ± 22.18	392.4 ± 22.18
66	572.1 ± 22.18	0.908	153.4 ± 22.18	519.4 ± 22.18
60	617.7 ± 22.18	0.919	163.4 ± 22.18	568.4 ± 22.18

Table 5.59. L-Tyrosine HCl H3' T_2' measured at every MAS rate

MAS rate [kHz]	Δ' [Hz]	T_2' [ms]
100	182.3	1.746 ± 0.02
96	194.0	1.641 ± 0.02
94	197.8	1.609 ± 0.02
90	202.5	1.572 ± 0.02
88	228.3	1.394 ± 0.02
80	256.1	1.243 ± 0.02
78	255.5	1.246 ± 0.02
72	294.2	1.082 ± 0.02
66	319.3	0.997 ± 0.02
60	365.9	0.870 ± 0.02

Table 5.60. Polystyrene Aromatic 1D GLS and Voigt results

MAS rate [kHz]	GLS w [Hz]	GLS m	Voigt w_G [Hz]	Voigt w_L [Hz]
100	1609 ± 221.8	0.05	1452 ± 221.8	278.4 ± 221.8
90	1631 ± 221.8	0.06	1449 ± 221.8	327.4 ± 221.8
80	1666 ± 221.8	0.06	1442 ± 221.8	396.8 ± 221.8
72	1699 ± 221.8	0.10	1431 ± 221.8	473.4 ± 221.8
60	1765 ± 221.8	0.13	1427 ± 221.8	601.1 ± 221.8
50	1847 ± 221.8	0.14	1404 ± 221.8	772.6 ± 221.8

Table 5.61. Polystyrene Aromatic Projection GLS and Voigt results

MAS rate [kHz]	GLS w [Hz]	GLS m	Voigt w_G [Hz]	Voigt w_L [Hz]
100	1538 ± 110.9	0.31	1465 ± 110.9	184 ± 110.9
90	1534 ± 110.9	0.38	1408 ± 110.9	277 ± 110.9
80	1574 ± 110.9	0.26	1527 ± 110.9	134 ± 110.9
72	1590 ± 110.9	0.29	1556 ± 110.9	121 ± 110.9
60	1672 ± 110.9	0.35	1553 ± 110.9	268 ± 110.9
50	1684 ± 110.9	0.29	1644 ± 110.9	134 ± 110.9

Table 5.62. Polystyrene Aromatic Antidiagonal GLS and Voigt results

MAS rate [kHz]	GLS w [Hz]	GLS m	Voigt w_G [Hz]	Voigt w_L [Hz]
100	948 ± 110.9	0.30	767 ± 110.9	303 ± 110.9
90	1000 ± 110.9	0.15	881 ± 110.9	188 ± 110.9
80	1070 ± 110.9	0.07	982 ± 110.9	122 ± 110.9
72	1161 ± 110.9	0.00	1118 ± 110.9	1 ± 110.9
60	1308 ± 110.9	0.21	1131 ± 110.9	297 ± 110.9
50	1684 ± 110.9	0.29	1447 ± 110.9	24 ± 110.9

Table 5.63. Polystyrene Aromatic T_2' measured at every MAS rate

MAS rate [kHz]	Δ' [Hz]	T_2' [ms]
100	161.4	1.972 ± 0.03
90	185.4	1.717 ± 0.03
80	212.8	1.496 ± 0.03
72	246.6	1.291 ± 0.03
60	366.3	0.869 ± 0.03
50	496.6	0.641 ± 0.03

5.2.5.4 Computation of Magnetic Susceptibility Tensors with DFT

All DFT computations were performed using the plane-wave DFT software Quantum ESPRESSO version 6.5.[302-303] Atomic positions of the crystal structures were first optimized at the PBE[363] level of theory using Grimme D2 dispersion correction[306] and ultrasoft pseudopotentials obtained from the PSLibrary version 1.0.0.[307] Wavefunction and charge density energy cutoffs were set to 160 and 1,280 Rydberg, respectively. A 2x2x1 Monkhorst-pack grid of k-points was used. [308] Shielding computation was subsequently performed using the GIPAW method.[309-310] After obtaining the macroscopic shape contribution tensor (the magnetic susceptibility tensor), the $\Delta\chi$ is estimated as the largest absolute difference between the principal values of the tensor. Every tensor and $\Delta\chi$ is presented in Table. The refcode of the used crystal structures are the following: HMB (HMBENZ05)[364], 2-MeIm (XOJXUR)[365], ZIF-8 (FAWCEN04)[362] and L-Tyrosine Hydrochloride (LTYRHC10)[366].

Table 5.64. Computed Magnetic Susceptibility Tensors

Sample	χ_{11} [ppm]	χ_{22} [ppm]	χ_{33} [ppm]	$\Delta\chi$
HMB	7.45	7.49	6.14	1.35
2-MeIm	6.97	7.69	5.01	2.68
ZIF-8	-7.77	-7.77	-7.77	0
L-Tyr HCl	6.77	7.39	7.01	0.62

5.2.5.5 Dilution of HMB with KBr

Table 5.65. Linewidth and SNR of HMB as a function of the dilution factor with KBr

HMB:KBr ratio (w/w)	LW, Hz	SNR (4 scans)
100:0	1209	6930
20:80	670	1573
10:90	715	1193
5:95	747	1143

5.2.5.6 Fitted LW from the simulated 2D convolution of a Gaussian and Lorentzian

The tilted Gaussian 2D has a mean of zero and a constant standard deviation of 0.01 and 0.3 The Lorentzian distribution has its standard deviation varied to mimic an inhomogeneous distribution with a homogeneous contribution that is reduced with increasing MAS rate. The projection and the diagonal of the 2D convoluted distribution are extracted and fitted to both GLS and Voigt.

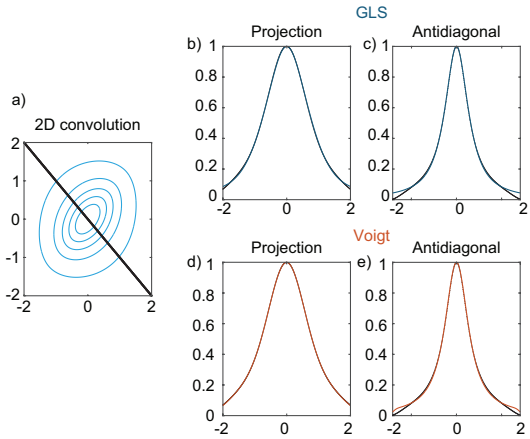

Figure 5.25. (a) 2D Convolution of a tilted Gaussian and a Lorentzian of standard deviation of 0.5; (b-c) Extracted Projection and Antidiagonal (black dots) fitted to the GLS function (green); (d-e) Extracted Projection and Antidiagonal (black dots) fitted to the Voigt function (orange)

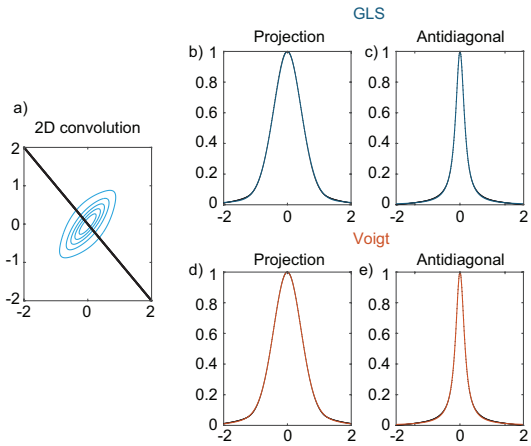

Figure 5.26. (a) 2D Convolution of a tilted Gaussian and a Lorentzian of standard deviation of 0.1; (b-c) Extracted Projection and Antidiagonal (black dots) fitted to the GLS function (green); (d-e) Extracted Projection and Antidiagonal (black dots) fitted to the Voigt function (orange)

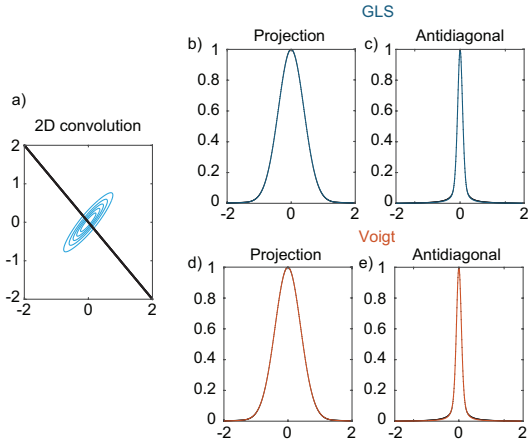

Figure 5.27. (a) 2D Convolution of a tilted Gaussian and a Lorentzian of standard deviation of 0.00001; (b-c) Extracted Projection and Antidiagonal (black dots) fitted to the GLS function (green); (d-e) Extracted Projection and Antidiagonal (black dots) fitted to the Voigt function (orange)

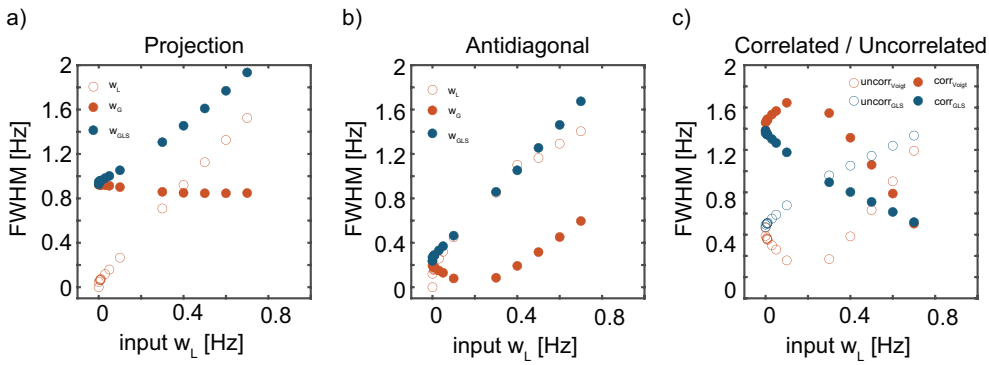

Figure 5.28. Measured linewidths with GLS (green dots) and Voigt (orange dots) as a function of the Lorentzian standard deviation input for the 2D convolution of a Gaussian and Lorentzian. The projections (a) and antidiagonals (b) are fitted with GLS (w_{GLS}) and Voigt (w_G and w_L). In c), the correlated (filled dots) and uncorrelated (hollow dots) linewidths are calculated according to Eq.s 5.5 and 5.6 in the main text.

5.3 Conclusion and Perspectives

In conclusion, this final topic detailed the different contributions to the ^{1}H linewidth. The importance of each source of broadening can vary between different samples and even between different resonances of the sample (see Figure 5.9 with L-tyrosine hydrochloride and ZIF-8).
The homogeneous contribution can be removed with faster spinning and/or PIP strategies. However, for many cases, the inhomogeneous contribution is already dominant at 100 kHz MAS and it can be hundreds of Hz broad. The investigation of the lineshapes from 2D DQ/SQ spectra by extracting projections and antidiagonals showed that ABMS and correlated disorder are particularly relevant inhomogeneous broadening sources.
ABMS broadens and shifts every nucleus in the same crystallite by the same amount, and for that reason it would ideally be the next contribution to suppress from ^{1}H spectra, after the reduction of homogeneous broadening. Dilution experiments with an ABMS free matrix only partially reduce the broadening but also reduce greatly the signal intensity. In the future, the development of methods that effectively and consistently remove ABMS broadening will be of great importance in order to further improve ^{1}H resolution.
One way could consist of developing pulse sequences able to disentangle the particular chemical shift from each nucleus from the ABMS shift through DQ or ZQ evolution. The extraction of the antidiagonal of any peak in a DQ/SQ spectrum leads to a lineshape free of any correlated inhomogeneous broadening. Therefore, a pulse sequence or shearing process able to consistently retrieve full spectra composed of these antidiagonal line shape would be of great interest.
Alternatively, if the ABMS broadening can be modulated separately to the chemical shift (with dilution experiments), as homogeneous broadening is with variable MAS rates, one could design a PIP type strategy to remove the ABMS contribution. The effectiveness of the removal of ABMS with dilution experiments depends on the percentage of the ABMS free matrix content[335], which could act as the variable parameter in a PIP method.

Chapter 6 Conclusion

6.1 Results Achieved

In conclusion, we have extensively studied the causes of broadening in ^{1}H solid state MAS NMR and developed new methods to improve the spectral resolution.

Firstly, the focus was on the homogeneous residual broadening caused by homonuclear dipolar couplings. The higher order terms of the average Hamiltonian cause both residual shifts and splittings in the spectrum and have a linear or polynomial MAS dependence, according to the strength of the nuclear spin interactions.

Then, all new methods for resolution improvement proposed here focused on removing the residual homogeneous broadening. Demonstrated on four different organic solids, Anti-Z COSY and TAZ COSY remove the residual coupling terms and can have a narrowing factor up to 2.

On the other hand, PIP is able to remove both residual shift and splitting, and the narrowing factor is greater when compared to Anti-Z COSY. The method was applied to six different samples.

However, PIPNET and PIPNET 2D are the most robust methods proposed in this work, because their machine learning framework is able to overcome some of the PIP original limitations and assumptions.

All these works were based on spinning the sample at a fast rate (100 kHz), which acts as the workhorse for coherent averaging.

These new methods are at a very early stage. Much more work is needed to validate the lineshapes and linewidths produced by these new approaches.

For example, the linewidths obtained in conventional 1D and 2D experiments, in addition to the T_2' measurements, show that the sources of inhomogeneous broadening are increasingly relevant at fast MAS, and in some cases, more important than the homogeneous broadening.

These conventional experiments are great tools to investigate the lineshapes and our studies on five different samples (HMB, 2-MeIM, ZIF-8, L-tyrosine HCl and polystyrene) and showed that every resonance has a particular distribution of the different contributions to the linewidth. However, in the more typical organic solids examples (HMB, 2-MeIm and L-tyrosine HCl), it is found that correlated inhomogeneous broadening, and particularly ABMS, has a significant role in the total linewidth. This was demonstrated by dilution and experiments and DQ/SQ spectra, by extracting the antidiagonal of the peaks.

A highly symmetric compound like ZIF-8 does not experience any ABMS or correlated disorder, so one is expecting infinitely narrow linewidths at infinite MAS rate. On the other hand, an amorphous compound such as polystyrene, in the form of beads, can have a substantial contribution from residual dipolar coupling and ABMS, however the total linewidth is still largely dominated by the uncorrelated disorder of the sample. Faster MAS or any strategy to remove ABMS will have a smaller effect on the linewidth compared to the crystalline compounds.

However, it is important to reiterate the necessity of faster spinning rates (>100-200 kHz MAS) to obtain higher ^{1}H resolution. Particularly in more complex crystalline compounds, where the overlap is still significant and the DQ/SQ spectra have a lot of rounded shaped and Lorentzian peaks, the residual homogeneous broadening is still dominant and hides the underlying correlated and uncorrelated inhomogeneous contributions.

6.2 Future Developments

Possible future developments for each research topic have already been discussed in the previous chapters.
The resolution enhancement methods developed here open up many new avenues, from improving the experiments themselves to thinking about what comes next for ^{1}H resolution?
The last chapter of the thesis body assessed the current barriers to the ^{1}H linewidth. Employing the word “barriers” might be a stretch, but in our lab experience, in the context of organic solids, no structural characterization problem has been solved so far by using ^{1}H as the only or the central nucleus for assignment: one would always resort to ^{13}C, particularly if the compound is amorphous. With the help of 1D CP, 2D

INADEQUATE and HETCOR experiments, molecules such as Molnupiravir and MDMA were assigned almost with no ambiguities (see Chapter 4).
Concerning relatively simpler molecules such as L-tyrosine hydrochloride or other amino acids, ^{1}H fast MAS can be the central nucleus of assignment, with the limited number of resonances being quite spread across the spectrum.
We have seen with the examples in Chapters 4 and 5, that 2D DQ/SQ methods are very rich in information and overlap can be significantly disentangled with the second dimension. For more complex molecules (see ritonavir in Chapter 1, 4 and 5), 1D 100 kHz MAS alone will not be enough, and even faster rates may probably have limited effect, due to the inhomogeneous broadening. However, 2D DQ/SQ spectra at faster rates can greatly improve resolution: if the residual homogeneous broadening is only small, most peaks will be elongated and tilted but significantly narrower (as seen with HMB and L-Tyrosine HCl).
If the spectra start to resemble in shape to those obtained with ^{13}C INADEQUATE, then assignment with ^{1}H will be very insightful.
The elongated and tilted shape observed in these experiments is due to correlated inhomogeneous broadening, particularly ABMS. As discussed in Chapter 5, ABMS broadening would be the next target to eliminate from ^{1}H spectra, along with the reduction of homogeneous broadening as faster MAS rates become available, or as PIP type methods become more and more robust.
Spinning faster implies smaller rotor sizes (< 0.7 mm) and therefore dilution experiments with an ABMS free matrix would be less practical due to the restricted volume and reduced signal intensity. This reasoning shifts our direction of thought to new pulse sequence methods or PIP strategies to consistently separate effects from ABMS from the desired chemical shift interaction.

Supplementary Information

Homonuclear Decoupling in ^{1}H NMR of Solids by Remote Correlation

Pulse sequences

```
;Anti-z-cosy experiment
;PM&FMP 2019
;Reference: Magn. Reson. Chem., 45, 296-316 (2007) and http://www-keeler.ch.cam.ac.uk/utilities/index.html
;Tested on Avance Neo

;PARAMETERS:

;pl1 : power level for 90°/180° and small flip angle pulse
;pl20 : power level for 1H saturation pulses

;p1 : 1H 90 degree pulse at pl1
;p2 : 1H beta+180degree pulse at pl1
;p3 : 1H beta pulse at pl1
;p20 : 1H 90 degree saturation pulse at pl20

;d0 : t1 delay
;d1 : recycle delay
;d51 : delay for Z-filter
;d50 : delay for Z-filter after subtraction of pulse duration
;
;cnst1  : multiplication factor for beta angle calculation
;cnst2  : beta angle (in degrees)
;cnst31 : spinning rate for rotor period calculation

;o1 : 1H offset
;l6 : number of rotor periods incremented for each t1 point
;ns=n*8

;FnMODE : States-TPPI

;$CLASS=Solids
;$DIM=2D
;$TYPE=homonuclear decoupling
;$SUBTYPE=anti-z-cosy
;$COMMENT=
;

#include <Avance.incl>
#include <Delay.incl>

define delay t_rot
"t_rot=1/cnst31"

"cnst1=cnst2/90"
"p2=p1*cnst1+2*p1"
"p3=p1*cnst1"

"d50=d51-p3/2-p2/2"
```

```
"d0=0"
"in0=l6*t_rot"
"inf1=in0"

1 ze
2 10m
#ifdef sat
  3u pl20:f1  ;saturate 1H channel
20 d20
  p20:f1 ph20^
  lo to 20 times l20
#endif
 d1 pl1:f1
3 p1:f1 ph1
 d0                                                    ; t1 increment

 p2:f1  ph25    ; 180 + beta pulse
 d50                                                   ; z filter
 p3:f1 ph26                          ; beta pulse

4 go=2 ph31
          10m mc #0 to 2 F1PH(ip1,id0)
exit                          ;end

ph1  = 0 0 0 0 2 2 2 2
ph20= 0 1
ph25= 0
ph26= 0 1 2 3
ph31= 0 1 2 3 2 3 0 1
```

Scripts

Anti-z COSY Sequence

```
% AntizCOSY sequence
% parameters.beta: sets the beta angle
% parametes.antiz: when 0 a ZQF or zCOSY is simulated, when 1 an antizCOSY
is simulated
% by LE, PM, BS from EPFL

function fid=pm_antizcosy_solids(spin_system,parameters,H,R,K)

% Compose Liouvillian
L=H+1i*R+1i*K;

% Coherent evolution timestep
timestep2=1/parameters.sweep;
timestep1=1/parameters.sweep;

% Get the pulse operator
Lp=operator(spin_system,'L+','1H');
Lx=(Lp+Lp')/2;
Ly=(Lp-Lp')/2i;

Lx=kron(speye(parameters.spc_dim),Lx);
Ly=kron(speye(parameters.spc_dim),Ly);

p1= pi/2;
```

```
cnst1=parameters.beta/90;
cnst2=parameters.antiz;

p2=p1*cnst1+2*p1*cnst2;
p3=p1*cnst1;


% Apply the first pulse (States hypercomplex)
rho1_sin=step(spin_system,Lx,parameters.rho0,pi/2);
rho1_cos=step(spin_system,Ly,parameters.rho0,pi/2);

% Run the F1 evolution
rho2_sin=evolution(spin_system,L,[],rho1_sin,timestep1,parameters.npoints(1
)-1,'trajectory');
rho2_cos=evolution(spin_system,L,[],rho1_cos,timestep1,parameters.npoints(1
)-1,'trajectory');


% Apply the second pulse
rho4_sin=step(spin_system,Lx,rho2_sin,p2);
rho4_cos=step(spin_system,Lx,rho2_cos,p2);

% Select "0" coherence
rho4_sin=coherence(spin_system,rho4_sin,{{'1H',0}});
rho4_cos=coherence(spin_system,rho4_cos,{{'1H',0}});


% Apply the second pulse
rho5_sin=step(spin_system,Lx,rho4_sin,p3);
rho5_cos=step(spin_system,Lx,rho4_cos,p3);


% Run the F2 evolution
fid.sin=evolution(spin_system,L,parameters.coil,rho5_sin,timestep2,parameter
s.npoints(2)-1,'observable');
fid.cos=evolution(spin_system,L,parameters.coil,rho5_cos,timestep2,parameter
s.npoints(2)-1,'observable');

end
```

AB Spin System (Fig. 3.2 a))

```
% 1H MAS spectrum of a single crystal
% computed using the FP formalism.
% 2 spins simulation
% Calculation time: depends on spin system. Seconds for 2 spins.
%
% from i.kuprov@soton.ac.uk
% by LE, PM, BS form EPFL

function mas_1H_1D_2spins_Xtal ();

% Spin system properties
sys.enable={'greedy','gpu'};

sys.isotopes={'1H','1H'};

inter.coupling.eigs=cell(2,2);
inter.coupling.euler=cell(2,2);
inter.coupling.scalar=cell(2,2);
```

```
cscal=1.0;
inter.zeeman.eigs{1}=[15.0 15.0 15.0]*cscal;
inter.zeeman.eigs{2}=[9.0 9.0 9.0]*cscal;

inter.zeeman.euler{1}=[pi/7 pi/6 pi/11];
inter.zeeman.euler{2}=[pi/3 pi/13 pi/2];

dscal=1.0;
inter.coupling.eigs{1,2}=[18.0 -9.0 -9.0]*dscal*1e3;

inter.coupling.euler{1,2}=[pi/5 pi/7 pi/20];

jscal=0.0;
inter.coupling.scalar{1,2}=10*jscal;

% Magnet field
sys.magnet=14;

% Basis set
bas.formalism='sphten-liouv';
bas.approximation='none';
bas.projections=+1;

% Algorithmic options
sys.tols.inter_cutoff=1.0;
sys.tols.prox_cutoff=100.0;
sys.disable={'trajlevel'};

% Spinach housekeeping
spin_system=create(sys,inter);
spin_system=basis(spin_system,bas);

% Experiment setup
parameters.rate=20000;
parameters.axis=[1 1 1];
parameters.max_rank=5;
parameters.sweep=20000;
parameters.npoints=32*1024;
parameters.zerofill=64*1024;
parameters.offset=7250;
parameters.spins={'1H'};
parameters.decouple={};
parameters.axis_units='Hz';
parameters.invert_axis=1;
parameters.grid='single_crystal';
parameters.rho0=state(spin_system,'L+','1H','cheap');
parameters.coil=state(spin_system,'L+','1H','cheap');
parameters.verbose=0;

% Simulation
fid=singlerot(spin_system,@acquire,parameters,'nmr');

% Apodization
fida=apodization(fid,'exp-1d',4);

% Fourier transform
spectruma=fftshift(fft(fida,parameters.zerofill));

% Plotting
figure(1); plot_1d(spin_system,real(spectruma),parameters);

end
```

ABC Spin System (Fig. 3.2 b))

```
% 1H MAS spectrum of a single crystal
% computed using the FP formalism.
% 3 spin simulation
% Calculation time: Seconds for 3 spins.
%
% by LE, PM, BS form EPFL

function mas_1H_1D_3spins_Xtal ();

% Spin system properties
sys.enable={'greedy','gpu'};
sys.isotopes={'1H','1H','1H'};

inter.coupling.eigs=cell(3,3);
inter.coupling.euler=cell(3,3);
inter.coupling.scalar=cell(3,3);

cscal=1.0;
inter.zeeman.eigs{1}=[45.0 45.0 45.0]*cscal;
inter.zeeman.eigs{2}=[40.0 40.0 40.0]*cscal;
inter.zeeman.eigs{3}=[2.5 2.5 2.5]*cscal;

inter.zeeman.euler{1}=[0 0 0];
inter.zeeman.euler{2}=[pi/7 pi/3 pi/5];
inter.zeeman.euler{3}=[pi/8 pi/6 pi/10];

dscal=0.2; dscal1=3.0; dscal2=2.5;
inter.coupling.eigs{1,2}=[18.0 -9.0 -9.0]*dscal*1e3;
inter.coupling.eigs{1,3}=[-8 4 4]*dscal1*1e3;
inter.coupling.eigs{2,3}=[-5 2.5 2.5]*dscal2*1e3;

inter.coupling.euler{1,2}=pi*[0.00 170 0.00]/180;
inter.coupling.euler{1,3}=pi*[0.00 190 0.00]/180;
inter.coupling.euler{2,3}=pi*[0.00 100 0.00]/180;

jscal=0.0;
inter.coupling.scalar{1,2}=10*jscal;
inter.coupling.scalar{1,3}=9*jscal;
inter.coupling.scalar{2,3}=5*jscal;

% Magnet field
sys.magnet=14;

% Basis set
bas.formalism='sphten-liouv';
bas.approximation='none';
bas.projections=+1;

% Algorithmic options
sys.tols.inter_cutoff=1.0;
sys.tols.prox_cutoff=100.0;
sys.disable={'trajlevel'};

% Spinach housekeeping
spin_system=create(sys,inter);
spin_system=basis(spin_system,bas);

% Experiment setup;
parameters.rate=20000;
parameters.axis=[1 1 1];
parameters.max_rank=8;
```

```
parameters.sweep=80000;
parameters.npoints=32*1024;
parameters.zerofill=128*1024;
parameters.offset=8000;
parameters.spins={'1H'};
parameters.decouple={};
parameters.axis_units='Hz';
parameters.invert_axis=1;
parameters.grid='single_crystal';
parameters.rho0=state(spin_system,'L+','1H','cheap');
parameters.coil=state(spin_system,'L+','1H','cheap');
parameters.verbose=0;

% Simulation
fid=singlerot(spin_system,@acquire,parameters,'nmr');

% Apodization
fida=apodization(fid,'exp-1d',4);

% Fourier transform
spectruma=fftshift(fft(fida,parameters.zerofill));

% Plotting
figure(1); plot_1d(spin_system,real(spectruma),parameters);

end
```

ABC Spin System (Fig. 3.2 c))

```
% 1H MAS spectrum of a single crystal with two different orientations
% computed using the FP formalism.
% 3 spins simulation
% Calculation time: Seconds for 3 spins.
%
%
% by LE, PM, BS from EPFL

function mas_1H_1D_3spins_2o();

% Spin system properties
sys.enable={'greedy','gpu'};
sys.isotopes={'1H','1H','1H'};


inter.coupling.eigs=cell(3,3);
inter.coupling.euler=cell(3,3);
inter.coupling.scalar=cell(3,3);

cscal=1.0;
inter.zeeman.eigs{1}=[4.0 4.0 4.0]*cscal;
inter.zeeman.eigs{2}=[3.6 3.6 3.6]*cscal;
inter.zeeman.eigs{3}=[12 12 12]*cscal;

inter.zeeman.euler{1}=[pi/7 pi/6 pi/11];
inter.zeeman.euler{2}=[pi/3 pi/13 pi/2];
inter.zeeman.euler{3}=[pi/3 pi/10 pi/2];

dscal=1.0;
inter.coupling.eigs{1,2}=[4 -2 -2]*dscal*1e3;
inter.coupling.eigs{1,3}=[6.6 -3.3 -3.3]*dscal*1e3;
inter.coupling.eigs{2,3}=[4.4 -2.2 -2.2]*dscal*1e3;
```

```
inter.coupling.euler{1,2}=[pi/6 pi/2 pi/20];
inter.coupling.euler{1,3}=[pi/4 pi/2 pi/3];
inter.coupling.euler{2,3}=[pi/3 pi/3 pi/2];

jscal=0.0;
inter.coupling.scalar{1,2}=10*jscal;
inter.coupling.scalar{1,3}=9*jscal;
inter.coupling.scalar{2,3}=5*jscal;

% Magnet field
sys.magnet=14;

% Basis set
bas.formalism='sphten-liouv';
bas.approximation='none';
bas.projections=+1;

% Algorithmic options
sys.tols.inter_cutoff=1.0;
sys.tols.prox_cutoff=100.0;
sys.disable={'trajlevel'};

% Spinach housekeeping
spin_system=create(sys,inter);
spin_system=basis(spin_system,bas);

% Experiment setup;
parameters.rate=8000;
parameters.axis=[1 1 1];
parameters.max_rank=5;
parameters.sweep=10000;
parameters.npoints=2*1024;
parameters.zerofill=4*1024;
parameters.offset=4801.04;
parameters.spins={'1H'};
parameters.decouple={};
parameters.axis_units='Hz';
parameters.invert_axis=1;
parameters.grid='LE2orientations+1+1';
parameters.rho0=state(spin_system,'L+','1H','cheap');
parameters.coil=state(spin_system,'L+','1H','cheap');
parameters.verbose=0;

% Simulation
fid=singlerot(spin_system,@acquire,parameters,'nmr');

% Apodization
fida=apodization(fid,'exp-1d',2);

% Fourier transform
spectruma=fftshift(fft(fida,parameters.zerofill));

% Plotting
figure(1); plot_1d(spin_system,real(spectruma),parameters);

end
```

ABC Spin System (Fig. 3.2 e)-f))

```
% 2D 1H MAS z-COSY or anti-z-COSY spectra of a single crystal with two
different orientations
% computed using the FP formalism.
%
```

```
% Calculation time: depends on spin system.
%
% by LE, PM, BS from EPFL

function [fid]=mas_3spins_COSY()

sys.enable={'greedy','gpu'};
sys.isotopes={'1H','1H','1H'};

inter.coupling.eigs=cell(3,3);
inter.coupling.euler=cell(3,3);
inter.coupling.scalar=cell(3,3);

cscal=1.0;
inter.zeeman.eigs{1}=[4.0 4.0 4.0]*cscal;
inter.zeeman.eigs{2}=[3.6 3.6 3.6]*cscal;
inter.zeeman.eigs{3}=[12 12 12]*cscal;

inter.zeeman.euler{1}=[pi/7 pi/6 pi/11];
inter.zeeman.euler{2}=[pi/3 pi/13 pi/2];
inter.zeeman.euler{3}=[pi/3 pi/10 pi/2];

dscal=1.0;
inter.coupling.eigs{1,2}=[4 -2 -2]*dscal*1e3;
inter.coupling.eigs{1,3}=[6.6 -3.3 -3.3]*dscal*1e3;
inter.coupling.eigs{2,3}=[4.4 -2.2 -2.2]*dscal*1e3;

inter.coupling.euler{1,2}=[pi/6 pi/2 pi/20];
inter.coupling.euler{1,3}=[pi/4 pi/2 pi/3];
inter.coupling.euler{2,3}=[pi/3 pi/3 pi/2];

jscal=0.0;
inter.coupling.scalar{1,2}=10*jscal;
inter.coupling.scalar{1,3}=9*jscal;
inter.coupling.scalar{2,3}=5*jscal;

% Magnet field
sys.magnet=14;

% Basis set
bas.formalism='sphten-liouv';
bas.approximation='none';

% Algorithmic options
sys.tols.inter_cutoff=1.0;
sys.tols.prox_cutoff=100.0;

% Spinach housekeeping
spin_system=create(sys,inter);
spin_system=basis(spin_system,bas);

% Experiment setup
parameters.rate=20000;
parameters.axis=[1 1 1];
parameters.max_rank=5;
parameters.sweep=2500;
parameters.npoints=[256 256];
parameters.offset=2000;
parameters.spins={'1H'};
parameters.decouple={};
parameters.axis_units='Hz';
parameters.rho0=state(spin_system,'Lz','1H');
parameters.coil=state(spin_system,'L+','1H');
```

```
parameters.grid='2orientations';
parameters.verbose=0;
parameters.beta=3; %beta angle
parameters.antiz=1; %when 0 a ZQF or zCOSY is simulated, when 1 an antizCOSY
is simulated

% Simulation
fid=singlerot(spin_system,@pm_antizcosy_solids,parameters,'nmr');

end
```

Orientations File ('2orientations')

α = [0 0.3142]
β = [0 1.0472]
γ = [0 3.491]
weights = [1 1]

Average Hamiltonian

```
$Path =
  Append[$Path, "..../Mathematica/SDv3.3.2/SpinDynamica"];
Needs["SpinDynamica`"];
```

Two-spin system

```
In[239]:= SetSpinSystem[3];
```

Parameters;

```
In[4]:= Ω1 = 2 π 82.0; Ω2 = 2 π 12.0; Ω3 = 2 π 127.0;
A2,-2 = 0; A2,-1 = 0; A2,1 = 0; A2,2 = 0; A2,0 = 2000.0;
B2,-2 = 0; B2,-1 = 0; B2,1 = 0; B2,2 = 0; B2,0 = 4000.0;
C2,-2 = 0; C2,-1 = 0; C2,1 = 0; C2,2 = 0; C2,0 = 6000.0;
αMR1 = π / 20; βMR1 = π / 13; γMR1 = π / 7;
αMR2 = π / 7; βMR2 = π / 3; γMR2 = π / 5;
αMR3 = π / 8; βMR3 = π / 6; γMR3 = π / 10;
Htot[t_] := Ω1 opT[1, {1, 0}] + Ω2 opT[2, {1, 0}] +
   Ω3 opT[3, {1, 0}] + Sum[A2,m WignerD[2, {m, m1}][{αMR1, βMR1, γMR1}] ×
     WignerD[2, {m1, 0}][{ωRot t, ArcTan[Sqrt[2]], 0}] × opT[{1, 2}, {2, 0}],
    {m, -2, 2}, {m1, -2, 2}] + Sum[B2,m WignerD[2, {m, m1}][{αMR2, βMR2, γMR2}] ×
     WignerD[2, {m1, 0}][{ωRot t, ArcTan[Sqrt[2]], 0}] × opT[{1, 3}, {2, 0}],
    {m, -2, 2}, {m1, -2, 2}] + Sum[C2,m WignerD[2, {m, m1}][{αMR3, βMR3, γMR3}] ×
     WignerD[2, {m1, 0}][{ωRot t, ArcTan[Sqrt[2]], 0}] ×
     opT[{2, 3}, {2, 0}], {m, -2, 2}, {m1, -2, 2}] // Chop
```

First order

```
In[56]:= Ham1st[ωRot_] := ωRot/(2 π) Integrate[Htot[t], {t, 0, 2 π/ωRot}]
ExpressOperator[Operator@Ham1st[ωRot]]
```

Second order

```
commut2[t1_, t2_] :=
  MatrixRepresentation[Htot[t2]].MatrixRepresentation[Htot[t1]] -
   MatrixRepresentation[Htot[t1]].MatrixRepresentation[Htot[t2]];

Ham2nd[ωRot_] :=
 ωRot/(2 I 2 π) Integrate[Integrate[commut2[t1, t2], {t1, 0, t2}], {t2, 0, 2 π/ωRot}]
ExpressOperator[Operator@Ham2nd[ωRot], CartesianProductOperatorBasis[]] //
  Chop // FullSimplify


secularization1 = Secularize[ExpressOperator[Operator@Ham2nd[ωRot]],
  2 π 82.0 opI[1, "z"] + 2 π 12.0 opI[2, "z"] + 2 π 127.0 opI[3, "z"], 2 π 44.0 ]
```

Third order

```
In[203]:= commut12[t1_, t2_] :=
    MatrixRepresentation[Htot[t2]].MatrixRepresentation[Htot[t1]] -
     MatrixRepresentation[Htot[t1]].MatrixRepresentation[Htot[t2]]; // Chop
commut23[t2_, t3_] := MatrixRepresentation[Htot[t3]].
     MatrixRepresentation[Htot[t2]] -
    MatrixRepresentation[Htot[t2]].MatrixRepresentation[Htot[t3]]; // Chop
commut123[t1_, t2_, t3_] := MatrixRepresentation[Htot[t3]].commut12[t1, t2] -
    commut12[t1, t2].MatrixRepresentation[Htot[t3]]; // Chop
commut231[t1_, t2_, t3_] := commut23[t2, t3].MatrixRepresentation[Htot[t1]] -
    MatrixRepresentation[Htot[t1]].commut23[t2, t3]; // Chop
commut3[t1_, t2_, t3_] := commut123[t1, t2, t3] + commut231[t1, t2, t3] // Chop

In[209]:=
Ham3rd[ωRot_] := -ωRot/(6 * 2 π) Integrate[Integrate[
    Integrate[commut3[t1, t2, t3], {t1, 0, t2}], {t2, 0, t3}], {t3, 0, 2 π/ωRot}]
ExpressOperator[Operator@Ham3rd[ωRot], CartesianProductOperatorBasis[]]


In[211]:= secularization2 = Secularize[%,
  2 π 82.0 opI[1, "z"] + 2 π 12.0 opI[2, "z"] + 2 π 127.0 opI[3, "z"], 2 π 44.0 ]
```

Fast Remote Correlation Experiments for ^{1}H Homonuclear Decoupling in Solids

Pulse sequences

TAZ-COSY

```
;TOP-Anti-z-cosy experiment with QF acquisition mode
;PM 2020, LRM EPFL Lausanne
; Please cite XXX

;Disclaimer: please note our pulse sequences are provided free of charge and come with no warranty. They are
used at your own risk. In particular, mis-setting the parameters can potentially lead to damage.

; Any pulse sequences derived from this code must include this whole header.

;parameters:
;pl1 : power level for 90 degree and beta pulses
;pl20 : power level for 1H saturation pulses
;
;p1 : 1H 90 degree pulse at pl1
;p2 : 1H 180 degree pulse at pl1
;p3 : 1H beta degree pulse at pl1
;p20 : 1H 90 degree saturation pulse at pl20
;
;d0 : t1/2 delay (set by the seq) - decremented
;d10 : t1/2 delay   (set by the seq) - incremented
;d1 : recycle delay
;d2 : tau delay flanking hard 180°
;d50 : delay for Z-filter
;d20 : presaturation delay
;
;cnst1  : multiplication factor to calculate beta angles
;cnst2  : beta angle (in degree)
;cnst31 : current spin rate for rotor period calculation
;cnst4  : first order phase correction to be applied in F1
;cnst5  : calculations for cnst4

;l6: sets (inf1)/2
;l7: sets zfilter delay, integer to be multiplied with the rotor period [1]
;l8: sets short tau delay, integer to be multiplied with the rotor period [1]
;l20: sets presaturation loop
;ns=n*8


;FnMODE: QF
;$CLASS=Solids
;$DIM=2D
;$TYPE=DD coupling
;$SUBTYPE=fast anti z-cosy
;$COMMENT=
;


#include <Avance.incl>
#include <Delay.incl>
```

```
define delay rot_per
"rot_per=1/cnst31"


;Beta pulse calculations
"cnst1=cnst2/90"
"p2=2*p1"
"p3=p1*cnst1"

;zfilter calculations
"d50=l7*rot_per-p3"

;tau delay calculations
"d2=l8*rot_per"


;TOP calculations
"cnst3=td1/2"
"l0=1"
"in0=l6*rot_per"
"in10=l6*rot_per"
"inf1=2*in0"

define delay maxT
"maxT= (td1*inf1)/4-in0+1us"
"d0=maxT"
"cnst5=(2/(0.000001*inf1))"
"cnst4=(cnst5*2*3.14*maxT*360)/(2*3.14)"
"cnst4=cnst4+d10-d10"
"cnst5=cnst5+d10-d10"


1 ze
2 10m


#ifdef sat
  3u pl20:f1  ;saturate 1H
20 d20
  p20:f1 ph20^
  lo to 20 times l20
#endif


 d1 pl1:f1

                    if "l0 <= cnst3"
                              {
                               lab11, goto lab6
                              }
                    else
                              {
                              "d10=(l0-cnst3)*in0"
                               lab12, goto lab7
                              }
```

```
lab6, p1:f1 ph1                                  ;first 90

            d2
  p2:f1  ph2     ;first 180
            d2

            d0

  p3:f1  ph3     ; beta z filter
  d50
  p3:f1 ph4

  p2:f1  ph5     ;second 180

  d0

lab16,goto lab4


lab7, p1:f1 ph1                                  ;first 90

            d10

  p2:f1  ph2     ;first 180

  p3:f1  ph3     ; beta z filter
  d50
  p3:f1 ph4

  d10

            d2
  p2:f1  ph5     ;second 180
            d2


lab17,goto lab4


lab4, go=2 ph31
            10m mc #0 to 2
  F1QF(caldel(d0,-in0)& calclc(l0,1))




exit

ph1 = 0 2
ph2 = 0 0 1 1
ph3 = 0 0 0 0 1 1 1 1
ph4 = 0 0 0 0 1 1 1 1
ph5 = 0 0 0 0 0 0 0 0 1 1 1 1 1 1 1 1
ph20= 0 1
ph31= 0 2 2 0 2 0 0 2 2 0 0 2 0 2 2 0
```

TOP-TSE-PSYCHE

```
;TOP-TSE-PSYCHE with QF acquisition mode
;PM 2020, LRM EPFL Lausanne
;Please cite XXX

;Disclaimer: please note our pulse sequences are provided free of charge and come with no warranty. They are used at your own risk. In particular, mis-setting the parameters can potentially lead to damage.

; Any pulse sequences derived from this code must include this whole header.

;(Based on:
;TSE-PSYCHE
;Pure Shift Yielded by Chirp Excitation
;Using triple spin echo for suppression of strong coupling artefacts
;By Mohammadali Foroozandeh:
;(1)  Foroozandeh, M.; Adams, R. W.; Meharry, N. J.; Jeannerat, D.; Nilsson, M.; Morris, G. A. Angew. Chem. Int. Ed. 2014, 53, 6990.
;(2)  Foroozandeh, M.; Adams, R. W.; Nilsson, M.; Morris, G. A. J. Am. Chem. Soc. 2014, 136, 11867.
;(3)  Foroozandeh, M.; Adams, R. W.; Kiraly, P.; Nilsson, M.; Morris, G. A. Chem. Commun., 2015)


;$CLASS=HighRes
;$DIM=2D
;$TYPE=
;$SUBTYPE=
;$COMMENT=

#include <Avance.incl>
#include <Delay.incl>
#include <Grad.incl>

define delay tauA
define delay tauB

"in0=inf1/2"
"p2=p1*2"


"cnst50=(cnst20/360)*sqrt((2*cnst21)/(p40/2000000))"
"p30=1000000.0/(cnst50*4)"
"cnst31= (p30/p1) * (p30/p1)"
"spw40=plw1/cnst31"
"d12=20u"

"p31=1000000.0/(cnst51*4)"
"cnst32= (p31/p1) * (p31/p1)"
"spw41=plw1/cnst32"
"spw42=spw41"

"p20=p40"
"p21=p41"
"p22=p42"


"cnst3=td1/2"

define delay maxT
```

```
"maxT= (td1*inf1)/4-in0+1us"

"cnst5=(2/(0.000001*inf1))"
"cnst4=(cnst5*2*3.14*maxT*360)/(2*3.14)"
"cnst4=cnst4+d10-d10"
"cnst5=cnst5+d10-d10"


1 ze
2 d12 pl9:f1
  d1 cw:f1 ph29
  4u do:f1
  d12 pl1:f1

                    if "l0 <= cnst3"
                              {

          "d0=maxT-((l0-1)*in0)"

 10u pl1:f1

  p1 ph1
  50u UNBLKGRAD
  p16:gp1
  d16
  10u pl0:f1
  d16
  ( center (p41:sp41 ph2):f1 (p21:gp11) )
  d16
  60u
  p16:gp1
  d16
  d0
  p16:gp2
  d16
  10u
  d16
  ( center (p40:sp40 ph3):f1 (p20:gp10) )
  d16
  10u
  p16:gp2
  d16
  p16:gp3
  d16
  60u
  d16
  ( center (p42:sp42 ph4):f1 (p22:gp12) )
  d16
  10u pl1:f1
  p16:gp3
  d16
  d0
  50u BLKGRAD


lab16, goto lab4
```

```
                    }
          else
                    {
                    "d10=(l0-cnst3)*in0"

10u pl1:f1

 p1 ph1

 d10

 50u UNBLKGRAD
 p16:gp1
 d16
 10u pl0:f1
 d16
 ( center (p41:sp41 ph2):f1 (p21:gp11) )
 d16
 60u
 p16:gp1
 d16
 p16:gp2
 d16
 10u
 d16
 ( center (p40:sp40 ph3):f1 (p20:gp10) )
 d16
 10u
 p16:gp2
 d16
 d10
 p16:gp3
 d16
 60u
 d16
 ( center (p42:sp42 ph4):f1 (p22:gp12) )
 d16
 10u pl1:f1
 p16:gp3
 d16
 50u BLKGRAD

lab17,goto lab4

          }


lab4, go=2 ph31
     d12 mc #0 to 2 F1QF(calclc(l0,1))

exit

ph1= 0 2 0 2 0 2 0 2                    ; Hard_90
ph2= 0 0 0 0 1 1 1 1                    ; sweep-180
ph3= 0 0 1 1 0 0 1 1                    ; beta
ph4= 0 0 0 0 0 0 0 0                    ; sweep-180
ph29 = 0
```

```
ph31=0 2 2 0 2 0 0 2                                    ; Receiver

;pl0 : zero power
;pl1 : high power
;pl9 : f1 channel - power level for presaturation
;p1  : 90 degree high power pulse
;p16 : duration of CTP gradients (1m)
;p20 : duration of weak gradient during PSYCHE pulse element
;p21 : duration of weak gradient during 1st 180-degree swept-frequency pulse
;p22 : duration of weak gradient during 2nd 180-degree swept-frequency pulse
;p40 : duration of double-chirp PSYCHE pulse element
;p41 : duration of 1st 180-degree swept-frequency pulse
;p42 : duration of 2nd 180-degree swept-frequency pulse
;d0 : t1/2 delay (set by the seq) - decremented
;d10 : t1/2 delay   (set by the seq) – incremented
;d1  : relaxation delay
;d12: delay for power switching
;d16 : recovery delay for gradients
;spw40 : RF power of double-chirp PSYCHE pulse element
;spw41 : RF power of 1st 180-degree swept-frequency pulse
;spw42 : RF power of 2nd 180-degree swept-frequency pulse
;spnam40: file name for PSYCHE pulse element
;spnam41: file name for 1st 180-degree swept-frequency pulse
;spnam42: file name for 2nd 180-degree swept-frequency pulse
;gpz1: CTP gradient (35%)
;gpz2: CTP gradient (49%)
;gpz3: CTP gradient (77%)
;gpz10: weak gradient during PSYCHE element (1-3%)
;gpz11: weak gradient during 1st 180-degree chirp (1-3%)
;gpz12: weak gradient during 2nd 180-degree chirp (1-3%)
;gpnam1: SINE.100
;gpnam2: SINE.100
;gpnam3: SINE.100
;gpnam10: RECT.1
;gpnam11: RECT.1
;gpnam12: RECT.1
;cnst20: desired flip angle for PSYCHE pulse element (degree) (normally 10-25)
;cnst21: bandwidth of each chirp in PSYCHE pulse element (Hz) (normally 10000)
;cnst51: RF amplitude for 180-degree chirp pulses (Hz)
;cnst4  : first order phase correction to be applied in F1
;cnst5  : calculations for cnst4
;in0 : 1/(2 * SW) = DW
;nd0 : 2
;td1 : number of t1 increments
;MC2 : QF
```

Scripts

SHEARING_TAZ:

```
/*****************************************************************/
/*        LRM EPFL Lausanne                                      */

/*        Short Description :                                    */
/*        Program for shearing an TAZ-COSY spectrum          */
/*  Carry out XFB first.
```

```
  Apply the 1rst phase correction needed in F1 (given by cnst4)                    */
/*****************************************************************/
/*        Description :                                          */
/*        There are two stages to the program:                   */
/*        1. Shear parallel to F1      with linear interpolation   */
/*        2. Shear parallel to F2      with linear interpolation   */
/* Based on ajp_shear found at: http://www-keeler.ch.cam.ac.uk/utilities/index.html */



#define PAR2D    1          //         2D spectrum


int       i,
          row,
          col,
          parmode,
          si2,
          si1,
          first,
          second,
          *buffer,
          *backup;

float     actual,
          new,
          u,                 //
          t,                 //         Used for the interpolation during shearing
          shift;

double    sw2,
          sw1,
          ratioSI,
          ratioSW;

char      filename2d[PATH_LENGTH];

FILE      *spectrum;


//        Collect important parameters

GETCURDATA;
FETCHPARS("PARMODE", &parmode);
FETCHPARS("SI", &si2);
FETCHPAR1S("SI", &si1);
FETCHPARS("SW", &sw2);
FETCHPAR1S("SW", &sw1);



//        Is it a 2D spectrum?

if (parmode != PAR2D ) {STOPMSG( "Not a 2D dataset");
}
```

```
//          First shear (parallel to F1)


(void)sprintf(filename2d,"%s/%s/%d/pdata/%d/2rr",disk,name,expno,procno);

// Open the file 2rr

if ((spectrum=fopen(filename2d,"rb")) == NULL)
{
      (void)sprintf(text,"Cannot read 2rr file:\n%s ",filename2d);
      STOPMSG(text);
}

            buffer=(int *) malloc((size_t)(si2*si1*sizeof(int)));
            if (!buffer) STOPMSG("Could not allocate enough memory (buffer)");

            backup=(int *) malloc((size_t)(si2*si1*sizeof(int)));
            if (!backup) STOPMSG("Could not allocate enough memory (buffer)");


//          Read the 2rr file into the buffer

i = fread(buffer, sizeof(int), si2*si1, spectrum);


ratioSI = (si1*1.0)/(si2*1.0);
ratioSW = sw2/sw1;


/*  Now try to shear it
The first loop cycles through the rows
The second loop cycles through the data points in the present row
*/

for (row=0; row<si1; row++) {
for (col=0; col<si2; col++) {


shift = ratioSI*ratioSW*(col - si2/2.0);

new = row + shift;

while (new > si1 - 1)
{
actual = new - si1;
new = actual;
}

while (new < 0)
{
actual = new + si1;
new = actual;
}

first = new;

if (first < si1 - 1)
```

```
{
second = first + 1;
}
else second = first + 1 - si1;

u = new - first;
backup[row*si2 + col] = (1 - u)*buffer[first*si2 + col] + u*buffer[second*si2 + col];
}
}

spectrum=fopen(filename2d,"wb");
fwrite(backup, sizeof(int), si2*si1, spectrum);
fclose(spectrum);


VIEWDATA;
ssleep(5);


//          Second shear (parallel to F2)


(void)sprintf(filename2d,"%s/%s/%d/pdata/%d/2rr",disk,name,expno,procno);

// Open the file 2rr

if ((spectrum=fopen(filename2d,"rb")) == NULL)
{
      (void)sprintf(text,"Cannot read 2rr file:\n%s ",filename2d);
      STOPMSG(text);
}

            buffer=(int *) malloc((size_t)(si2*si1*sizeof(int)));
            if (!buffer) STOPMSG("Could not allocate enough memory (buffer)");

            backup=(int *) malloc((size_t)(si2*si1*sizeof(int)));
            if (!backup) STOPMSG("Could not allocate enough memory (buffer)");

//          Read the 2rr file into the buffer

i = fread(buffer, sizeof(int), si2*si1, spectrum);

ratioSI = (si2*1.0)/(si1*1.0);
ratioSW = sw1/sw2;




/*  Now try to shear it
The first loop cycles through the rows
The second loop cycles through the data points in the present row
*/


for (row=0; row<si1; row++) {
for (col=0; col<si2; col++) {
```

```
shift = -ratioSI*ratioSW*(row - si1/2.0);
new = col + shift;

while (new > si2 - 1)
{
actual = new - si2;
new = actual;
}

while (new < 0)
{
actual = new + si2;
new = actual;
}

first = new;

if (first < si2 - 1)
{
second = first + 1;
}
else second = first + 1 - si2;

t = new - first;
backup[row*si2 + col] = (1 - t)*buffer[row*si2 + first] + t*buffer[row*si2 + second];
}
}

spectrum=fopen(filename2d,"wb");
fwrite(backup, sizeof(int), si2*si1, spectrum);
fclose(spectrum);


free(buffer);
free(backup);

VIEWDATA;
ssleep(5);



QUITMSG("Processing finished");
```

AJP_SHEAR:

```
/*********************************************************/
/*      ajp_sym         26/09/2006                      */
/*********************************************************/
/*      Description :                                   */
/*      Symmetrizes the spectrum about F1 = 0           */
/*********************************************************/
/*      Author(s)       :                               */
/*      Name            : Andrew J. Pell            */
/*      Organisation    : University of Cambridge   */
/*********************************************************/
```

```
#define  PAR2D    1          //          2D spectrum


int         i,
            row,
            col,
            parmode,
            si2,
            si1,
            *buffer;


char        filename2d[PATH_LENGTH];

FILE        *spectrum;


// Collect important parameters

GETCURDATA;
FETCHPARS("PARMODE", &parmode);
FETCHPARS("SI", &si2);
FETCHPAR1S("SI", &si1);

// Is it a 2D spectrum?

if (parmode != PAR2D ) {STOPMSG( "Not a 2D dataset");
}



(void)sprintf(filename2d,"%s/%s/%d/pdata/%d/2rr",disk,name,expno,procno);

//(void)sprintf(filename2d,"%s/data/%s/nmr/%s/%d/pdata/%d/2rr",disk,user,name,expno,procno);

// Try to open the file

if ((spectrum=fopen(filename2d,"rb")) == NULL)
{
        (void)sprintf(text,"Cannot read 2rr file:\n%s ",filename2d);
        STOPMSG(text);
}

        buffer=(int *) malloc((size_t)(si2*si1*sizeof(int)));

        if (!buffer) STOPMSG("Could not allocate enough memory (buffer)");
              i = fread(buffer,sizeof(int),si2*si1,spectrum);

        if (si2*si1 != i)   { STOPMSG("Read Error1:  SI != Number of Points Read"); }

/* Now, let's play with the thing */
for (row=0; row<si1; row++) {
for (col=0; col<si2; col++) {

              if (abs(buffer[row*si2 + col]) < abs(buffer[si1*si2 -si2 - row*si2 + col]))

              buffer[row*si2 + col] = buffer[row*si2 + col];
```

```
            else buffer[row*si2 + col] = buffer[si1*si2 - si2 - row*si2 + col];
}}

spectrum=fopen(filename2d,"wb");
fwrite(buffer,sizeof(int),si2*si1,spectrum);
fclose(spectrum);

free(buffer);

VIEWDATA;

QUIT;
```

Barriers to Resolution in ^{1}H of Rotating Solids

Scripts

Matlab function to fit lineshapes to GLS function

```
function rmsefit = rmsevalconv_1pe(x,ltd,specs)
a1 = x(1);
idx1=x(2);
g1=x(3);
l1=x(4);


lshape=a1./(1+4*((ltd'-idx1)./l1).^2); % Lorentzian

gshape=a1.*exp(-4*log(2)*((ltd'-idx1)./(g1)).^2); % Gaussian

fitres=conv(lshape, gshape, 'same');

fitres=fitres./max(fitres);

rmsefit =sqrt(mean((specs - fitres').^2));  % Root Mean Squared Error

end
```

Matlab function to fit lineshapes to Voigt function (convolution Gaussian with a Lorentzian)

```
function rmsefit = rmsevalgls_1pe(x,ltd,specs)
a1 = x(1);
q1= x(2);
idx1=x(3);
c1=x(4);

fitres= a1.*(1-q1).*exp(-4.*log(2).*((ltd'-idx1)./c1).^2)+a1.*q1./(1+4.*((ltd'-idx1)./c1).^2);


rmsefit =sqrt(mean((specs - fitres).^2));  % Root Mean Squared Error

end
```

Matlab Script to extract the antidiagonal of a 2D peak

```
% Set the angle of the line in degrees
theta_line = 45;

theta_lineanti=theta_line+90

% Convert the angle to radians
theta_line_rad = deg2rad(theta_line);

theta_lineanti_rad = deg2rad(theta_lineanti);

% Calculate the slope of the line
m = tan(theta_line_rad);
manti=tan(theta_lineanti_rad);

% Calculate the corresponding y coordinates of the line, giving the x
% coordinates as input
y_line = m*(xar);
y_lineanti=manti*(xar);


%comparison coordinates of y coordinates and constructed y coordinates

diffs = yar - y_lineanti.';

% set a threshold for the differences
threshold=sry/2

% find the indices where the differences are below the threshold

[col_idy, row_idy] = find(diffs < threshold & diffs > -threshold);
```

```
yantidiag=yar(row_idy); %row is for the index of y, true for other angles

%corresponding antidiagonal x coordiantes
x_lineanti=yar(row_idy)/(manti);

diffsx= xar + x_lineanti.';

thresholdx=(srx/2);

[col_idx, row_idx] = find(diffsx < thresholdx & diffsx > -thresholdx);

xantidiag=fliplr(xar(row_idx));

row_idxflip=flipud(row_idx);



%INTENSITIES FROM ANTIDIAGONAL
for i=1:length(row_idy)

row_idy(i);
row_idxflip(i);
antidiag(i)=Z(row_idy(i),row_idxflip(i));

end

%scaling the antidiagonal x coordinates by trigonometry
tantilt=theta_lineanti_rad;


 %antidiagflipcos=xantidiag.*(cos(tantilt));
 xantidiagflipcos=xantidiag./(cos(tantilt));
```

Script to simulate a 2D convolution of a tilted Gaussian and a Lorentzian

```
% Define the x and y vectors


swx=2; %x spectral width
swy=2; %y spectral width

tdx=500; %td in x dimension
tdy=601; % td in y dimension


%definition of grid
xar = linspace(-swx, swx, tdx);

yar = linspace(-swy, swy, tdy);



%  meshgrid
[X, Y] = meshgrid(xar, yar);
XY = [X(:) Y(:)];

%  mean and std of  Gaussian
mu = [0, 0];
sigma = diag([0.01, 0.3]); % diagonal matrix


% Rotate the covariance matrix by an angle

theta = -45; % angle of tilt of gaussian
thetarad=deg2rad(theta);
R = [cos(thetarad) -sin(thetarad); sin(thetarad) cos(thetarad)];
sigma = R * sigma * R';

xpt = linspace(1, tdx, tdx);
ypt = linspace(1, tdy, tdy);
[Xpt,Ypt] = meshgrid(xpt, ypt);
XYpt = [Xpt(:) Ypt(:)];

%sr
srx=(xar(end)-xar(1))/tdx;
sry=(yar(end)-yar(1))/tdy;
```

```
% values of the Gaussian  at each point in the meshgrid
Zg = mvnpdf([Y(:) X(:)], mu, sigma);
Zg = reshape(Zg, length(yar), length(xar));
Zg=Zg./max(max(Zg));
 % Lorentzian
 gamma_x = 0.1;   % gamma in x direction
gamma_y = 0.1;   % gamma in y direction
x0 = 0;          % center in x direction
y0 = 0;          % center in y direction


xar = linspace(-swx, swx, tdx);
yar = linspace(-swy, swy, tdy);
[X, Y] = meshgrid(xar, yar);
 % Lorentzian at each point on the grid
Zl = 1./ ((X - x0).^2 / gamma_x^2 + (Y - y0).^2 / gamma_y^2 + 1);
 %Convolution of tilt gaussian and Lorentzian
Z=conv2(Zl,Zg,'same');
```

Bibliography

1. Bragg, W. L., The structure of some crystals as indicated by their diffraction of X-rays. *Proceedings of the Royal Society of London. Series A, Containing Papers of a Mathematical and Physical Character*, **1913,** *89* (610), 248-277.
2. Dickinson, R. G.; ; Raymond, A. L., The crystal structure of hexamethylene-tetramine. *J. Am. Chem. Soc.*, **1923,** *45* (1), 22-29.
3. Kendrew, J. C.; ; Bodo, G.; ; Dintzis, H. M.; ; Parrish, R. G.; ; Wyckoff, H.; ; Phillips, D. C., A Three-Dimensional Model of the Myoglobin Molecule Obtained by X-Ray Analysis. *Nature*, **1958,** *181* (4610), 662-666.
4. Smyth, M. S.; ; Martin, J. H. J., x Ray crystallography. *Mol. Pathol.*, **2000,** *53* (1), 8-14.
5. Ma, T.; ; Kapustin, E. A.; ; Yin, S. X.; ; Liang, L.; ; Zhou, Z.; ; Niu, J.; Li, L.-H.; Wang, Y.; Su, J.; Li, J.; Wang, X.; Wang, W. D.; Wang, W.; Sun, J.; Yaghi, O. M., Single-crystal x-ray diffraction structures of covalent organic frameworks. *Science*, **2018,** *361* (6397), 48-52.
6. Dubochet, J.; McDowall, A. W., Vitrification of Pure Water for Electron Microscopy. *J. Microsc.*, **1981,** *124* (3), 3-4.
7. Nakane, T.; Kotecha, A.; Sente, A.; McMullan, G.; Masiulis, S.; Brown, Pmge; Grigoras, I. T.; Malinauskaite, L.; Malinauskas, T.; Miehling, J.; Uchanski, T.; Yu, L.; Karia, D.; Pechnikova, E. V.; de Jong, E.; Keizer, J.; Bischoff, M.; McCormack, J.; Tiemeijer, P.; Hardwick, S. W.; Chirgadze, D. Y.; Murshudov, G.; Aricescu, A. R.; Scheres, S. H. W., Single-particle cryo-EM at atomic resolution. *Nature*, **2020,** *587* (7832), 152-156.
8. Yip, K. M.; Fischer, N.; Paknia, E.; Chari, A.; Stark, H., Atomic-resolution protein structure determination by cryo-EM. *Nature*, **2020,** *587* (7832), 157-161.
9. Jones, C. G.; Martynowycz, M. W.; Hattne, J.; Fulton, T. J.; Stoltz, B. M.; Rodriguez, J. A.; Nelson, H. M.; Gonen, T., The CryoEM Method MicroED as a Powerful Tool for Small Molecule Structure Determination. *ACS Cent. Sci.*, **2018,** *4* (11), 1587-1592.
10. Benjin, X.; Ling, L., Developments, applications, and prospects of cryo-electron microscopy. *Protein Sci.*, **2020,** *29* (4), 872-882.
11. Rabi, I. I.; Zacharias, J. R.; Millman, S.; Kusch, P., A New Method of Measuring Nuclear Magnetic Moment. *Phys. Rev.*, **1938,** *53* (4), 318-318.
12. Bloch, F., Nuclear Induction. *Phys. Rev.*, **1946,** *70* (7-8), 460-474.
13. Purcell, E. M.; Torrey, H. C.; Pound, R. V., Resonance Absorption by Nuclear Magnetic Moments in a Solid. *Phys. Rev.*, **1946,** *69* (1-2), 37-38.
14. Rietveld, H. M., A profile refinement method for nuclear and magnetic structures. *J. Appl. Crystallogr.*, **1969,** *2* (2), 65-71.
15. Marti-Rujas, J., Structural elucidation of microcrystalline MOFs from powder X-ray diffraction. *Dalton. Trans.*, **2020,** *49* (40), 13897-13916.
16. Meden, Anton; Radosavljevic Evans, Ivana, Structure determination from powder diffraction data: past, present and future challenges. *Cryst. Res. Technol.*, **2015,** *50* (9-10), 747-758.
17. Belik, A.; ; Iikubo, S.; Kodama, K.; Igawa, N.; Shamoto, S.-i.; Niitaka, S.; Azuma, M.; Shimakawa, Y.; Takano, M.; Izumi, F.; Takayama-Muromachi, E., Neutron Powder Diffraction Study on the Crystal and Magnetic Structures of BiCoO3. *Chem. Mater.*, **2006,** *18* (3), 798-803.
18. Lutterotti, L.; Matthies, S.; Wenk, H. R.; Schultz, A. S.; Richardson, J. W., Combined texture and structure analysis of deformed limestone from time-of-flight neutron diffraction spectra. *J. Appl. Phys.*, **1997,** *81* (2), 594-600.
19. Choi, C. S.; ; Boutin, H. P., A study of the crystal structure β-cyclotetramethylene tetranitramine by neutron diffraction. *Acta Crystallographica Section B Structural Crystallography and Crystal Chemistry*, **1970,** *26* (9), 1235-1240.
20. Soper, A. K., The Radial Distribution Functions of Water as Derived from Radiation Total Scattering Experiments: Is There Anything We Can Say for Sure? *ISRN Phys. Chem.*, **2013,** *2013*, 1-67.
21. Billinge, S. J.; Kanatzidis, M. G., Beyond crystallography: the study of disorder, nanocrystallinity and crystallographically challenged materials with pair distribution functions. *Chem. Commun. (Camb.)*, **2004,** (7), 749-60.
22. Billinge, Simon J. L.; Dykhne, Timur; Juhás, Pavol; Božin, Emil; Taylor, Ryan; Florence, Alastair J.; Shankland, Kenneth, Characterisation of amorphous and nanocrystalline molecular materials by total scattering. *CrystEngComm*, **2010,** *12* (5), 1366-1368.
23. Finney, J. L.; Hallbrucker, A.; Kohl, I.; Soper, A. K.; Bowron, D. T., Structures of high and low density amorphous ice by neutron diffraction. *Phys. Rev. Lett.*, **2002,** *88* (22), 225503.
24. Cavanagh, J.; ; Fairbrother, W. J.; Palmer III, A. G.; Skelton, N. J.; Rance, M., *Protein NMR Spectroscopy principles and practice*. 2nd edn ed.; Academic Press: 2006.
25. Breton, R. C.; Reynolds, W. F., Using NMR to identify and characterize natural products. *Natural Product Reports*, **2013,** *30* (4), 501-24.
26. Schmidt-Rohr, K.; ; Spiess, H. W., *Multidimensional Solid-State NMR and Polymers*. Elsevier: 2012.
27. Separovic, F. ; ; Sani, M., *A.Solid-State NMR: Applications in Biomembrane Structure*. IOP Publishing: 2020.
28. Damman, R.; Schutz, S.; Luo, Y.; Weingarth, M.; Sprangers, R.; Baldus, M., Atomic-level insight into mRNA processing bodies by combining solid and solution-state NMR spectroscopy. *Nat. Commun.*, **2019,** *10* (1), 4536.

29. Mandala, V. S.; Loftis, A. R.; Shcherbakov, A. A.; Pentelute, B. L.; Hong, M., Atomic structures of closed and open influenza B M2 proton channel reveal the conduction mechanism. *Nat. Struct. Mol. Biol.*, **2020,** *27* (2), 160-167.
30. Bamine, T.; Boivin, E.; Boucher, F.; Messinger, R. J.; Salager, E.; Deschamps, M.; Masquelier, C.; Croguennec, L.; Ménétrier, M.; Carlier, D., Understanding Local Defects in Li-Ion Battery Electrodes through Combined DFT/NMR Studies: Application to LiVPO4F. *J. Phys. Chem. C*, **2017,** *121* (6), 3219-3227.
31. Hope, M. A.; Rinkel, B. L. D.; Gunnarsdottir, A. B.; Marker, K.; Menkin, S.; Paul, S.; Sergeyev, I. V.; Grey, C. P., Selective NMR observation of the SEI-metal interface by dynamic nuclear polarisation from lithium metal. *Nat. Commun.*, **2020,** *11* (1), 2224.
32. Kumar, Abhishek; Walder, Brennan J.; Kunhi Mohamed, Aslam; Hofstetter, Albert; Srinivasan, Bhuvanesh; Rossini, Aaron J.; Scrivener, Karen; Emsley, Lyndon; Bowen, Paul, The Atomic-Level Structure of Cementitious Calcium Silicate Hydrate. *J. Phys. Chem. C*, **2017,** *121* (32), 17188-17196.
33. Kunhi Mohamed, A.; Moutzouri, P.; Berruyer, P.; Walder, B. J.; Siramanont, J.; Harris, M.; Negroni, M.; Galmarini, S. C.; Parker, S. C.; Scrivener, K. L.; Emsley, L.; Bowen, P., The Atomic-Level Structure of Cementitious Calcium Aluminate Silicate Hydrate. *J. Am. Chem. Soc.*, **2020,** *142* (25), 11060-11071.
34. Datta, K.; Caiazzo, A.; Hope, M. A.; Li, J.; Mishra, A.; Cordova, M.; Chen, Z.; Emsley, L.; Wienk, M. M.; Janssen, R. A. J., Light-Induced Halide Segregation in 2D and Quasi-2D Mixed-Halide Perovskites. *ACS Energy Lett.*, **2023,** *8* (4), 1662-1670.
35. Mishra, A.; Hope, M. A.; Gratzel, M.; Emsley, L., A Complete Picture of Cation Dynamics in Hybrid Perovskite Materials from Solid-State NMR Spectroscopy. *J. Am. Chem. Soc.*, **2023,** *145* (2), 978-990.
36. Damron, J. T.; Kersten, K. M.; Pandey, M. K.; Nishiyama, Y.; Matzger, A.; Ramamoorthy, A., Role of Anomalous Water Constraints in the Efficacy of Pharmaceuticals Probed by (1)H Solid-State NMR. *ChemistrySelect*, **2017,** *2* (23), 6797-6800.
37. Tatton, Andrew S.; Pham, Tran N.; Vogt, Frederick G.; Iuga, Dinu; Edwards, Andrew J.; Brown, Steven P., Probing intermolecular interactions and nitrogen protonation in pharmaceuticals by novel 15N-edited and 2D 14N-1H solid-state NMR. *CrystEngComm*, **2012,** *14* (8).
38. Hirsh, D. A.; Wijesekara, A. V.; Carnahan, S. L.; Hung, I.; Lubach, J. W.; Nagapudi, K.; Rossini, A. J., Rapid Characterization of Formulated Pharmaceuticals Using Fast MAS (1)H Solid-State NMR Spectroscopy. *Mol. Pharm.*, **2019,** *16* (7), 3121-3132.
39. Lu, X.; Tsutsumi, Y.; Huang, C.; Xu, W.; Byrn, S. R.; Templeton, A. C.; Buevich, A. V.; Amoureux, J. P.; Su, Y., Molecular packing of pharmaceuticals analyzed with paramagnetic relaxation enhancement and ultrafast magic angle pinning NMR. *Phys. Chem. Chem. Phys.*, **2020,** *22* (23), 13160-13170.
40. Zhou, D. H.; Shah, G.; Mullen, C.; Sandoz, D.; Rienstra, C. M., Proton-detected solid-state NMR spectroscopy of natural-abundance peptide and protein pharmaceuticals. *Angew. Chem. Int. Ed. Engl.*, **2009,** *48* (7), 1253-6.
41. Southern, S. A.; ; Bryce, D. L., Chapter One - Recent advances in NMR crystallography and polymorphism. *Annu. Rep. NMR Spectrosc.*, **2021,** *102*, 1-80.
42. Baias, M.; Dumez, J. N.; Svensson, P. H.; Schantz, S.; Day, G. M.; Emsley, L., De novo determination of the crystal structure of a large drug molecule by crystal structure prediction-based powder NMR crystallography. *J. Am. Chem. Soc.*, **2013,** *135* (46), 17501-7.
43. Li, M.; Meng, F.; Tsutsumi, Y.; Amoureux, J. P.; Xu, W.; Lu, X.; Zhang, F.; Su, Y., Understanding Molecular Interactions in Rafoxanide-Povidone Amorphous Solid Dispersions from Ultrafast Magic Angle Spinning NMR. *Mol. Pharm.*, **2020,** *17* (6), 2196-2207.
44. Brown, S. P.; Schaller, T.; Seelbach, U. P.; Koziol, F.; Ochsenfeld, C.; Klarner, F. G.; Spiess, H. W., Structure and Dynamics of the Host-Guest Complex of a Molecular Tweezer: Coupling Synthesis, Solid-State NMR, and Quantum-Chemical Calculations *Angew. Chem. Int. Ed. Engl.*, **2001,** *40* (4), 717-720.
45. Salager, E.; ; Stein, R.S.; Pickard, C.J.; Elena, B.; Emsley, L, Powder NMR crystallography of thymol. *Phys. Chem. Chem. Phys.*, **2009,** *11*, 2610-2621.
46. Hofstetter, A.; Balodis, M.; Paruzzo, F. M.; Widdifield, C. M.; Stevanato, G.; Pinon, A. C.; Bygrave, P. J.; Day, G. M.; Emsley, L., Rapid Structure Determination of Molecular Solids Using Chemical Shifts Directed by Unambiguous Prior Constraints. *J. Am. Chem. Soc.*, **2019,** *141* (42), 16624-16634.
47. Heider, E. M.; Harper, J. K.; Grant, D. M., Structural characterization of an anhydrous polymorph of paclitaxel by solid-state NMR. *Phys. Chem. Chem. Phys.*, **2007,** *9* (46), 6083-97.
48. Dudenko, D.; Kiersnowski, A.; Shu, J.; Pisula, W.; Sebastiani, D.; Spiess, H. W.; Hansen, M. R., A strategy for revealing the packing in semicrystalline pi-conjugated polymers: crystal structure of bulk poly-3-hexyl-thiophene (P3HT). *Angew. Chem. Int. Ed. Engl.*, **2012,** *51* (44), 11068-72.
49. Goward, G. R.; ; Sebastiani, D.; Schnell, I.; Spiess, H. W.; Kim, H.-D.; Ishida, H., Benzoxazine Oligomers: Evidence for a Helical Structure from Solid-State NMR Spectroscopy and DFT-Baed Dynamics and Chemical Shift Calculations. *J. Am. Chem. Soc.*, **2003,** *125* (19), 5792-5800.
50. Brown, S. P.; Spiess, H. W., Advanced Solid-State NMR Methods for the Elucidation of Structure and Dynamics of Molecular, Macromolecular, and Supramolecular Systems. *Chem. Rev.*, **2001,** *101* (12), 4125-4156.
51. Rapp, A.; ; Schnell, I.; Sebastiani, D.; Brown, S. P.; Percec, V.; Spiess, H. W., Supramolecular Assembly of Dendritic Polymers Elucidated by 1H and 13C Solid-State MAS NMR Spectroscopy. *J. Am. Chem. Soc.*, **2003,** *125* (43), 13284-13297.
52. Elena, B.; Pintacuda, G.; Mifsud, N.; Emsley, L., Molecular Structure Determination in Powders by NMR Crystallography from Proton Spin Diffusion. *J. Am. Chem. Soc.*, **2006,** *128* (29), 9555-9560.

53. Pickard, C. J.; Salager, E.; Pintacuda, G.; Elena, B.; Emsley, L., Resolving Structures from Powders by NMR Crystallography Using Combined Proton Spin Diffusion and Plane Wave DFT Calculations. *J. Am. Chem. Soc.*, **2007,** *129* (29), 8932-8933.
54. Salager, E.; Day, G. M.; Stein, R. S.; Pickard, C. J.; Elena, B.; Emsley, L., Powder Crystallography by Combined Crystal Structure Prediction and High-Resolution 1H Solid-State NMR Spectroscopy. *Journal of the American Chemical Society*, **2010,** *132* (8), 2564-2566.
55. Schaller, T.; Büchele, U. P.; Klärner, F—G.; Bläser, D.; Boese, R.; Brown, S. P.; Spiess, H. W.; Koziol, F.; Kussmann, J.; Ochsenfeld, C., Structure of Molecular Tweezer Complexes in the Solid State: NMR Experiments, X-ray Investigations, and Quantum Chemical Calculations. *J. Am. Chem. Soc.*, **2007,** *129* (5), 1293-1303.
56. Harper, J. K.; Grant, D.M., Enhancing Crystal-Structure Prediction with NMR Tensor Data. *Cryst. Growth Des.*, **2006,** *6* (10), 2315-2321.
57. Harper, J. K.; Barich, D. H.; Heider, E. M.; Grant, D. M.; Franke, R. R.; Johnson, J. H.; Zhang, Y.; Lee, P.; Von Dreele, R. B.; Scott, B.; Williams, D.; Ansell, G. B., A Combined Solid-State NMR and X-ray Powder Diffraction Study of a Stable Polymorph of Paclitaxel. *Cryst. Growth Des.*, **2005,** *5* (5), 1737-1742.
58. Elena, B.; Emsley, L., Powder Crystallography by Proton Solid-State NMR Spectroscopy. **2005,** *127* (25), 9140-9146.
59. Cavalli, A.; Salvatella, X.; Dobson, C. M.; Vendruscolo, M., Protein structure determination from NMR chemical shifts. *Proc. Natl. Acad. Sci. U S A*, **2007,** *104* (23), 9615-20.
60. Kay, L. E., NMR studies of protein structure and dynamics - a look backwards and forwards. *J. Magn. Reson.*, **2011,** *213* (2), 492-4.
61. Klein, A.; Rovo, P.; Sakhrani, V. V.; Wang, Y.; Holmes, J. B.; Liu, V.; Skowronek, P.; Kukuk, L.; Vasa, S. K.; Guntert, P.; Mueller, L. J.; Linser, R., Atomic-resolution chemical characterization of (2x)72-kDa tryptophan synthase via four- and five-dimensional (1)H-detected solid-state NMR. *Proc. Natl. Acad. Sci. U S A*, **2022,** *119* (4).
62. Maruyoshi, K.; Iuga, D.; Antzutkin, O. N.; Alhalaweh, A.; Velaga, S. P.; Brown, S. P., Identifying the intermolecular hydrogen-bonding supramolecular synthons in an indomethacin-nicotinamide cocrystal by solid-state NMR. *Chem. Commun. (Camb.)*, **2012,** *48* (88), 10844-6.
63. Duan, P.; Lamm, M. S.; Yang, F.; Xu, W.; Skomski, D.; Su, Y.; Schmidt-Rohr, K., Quantifying Molecular Mixing and Heterogeneity in Pharmaceutical Dispersions at Sub-100 nm Resolution by Spin Diffusion NMR. *Mol. Pharm.*, **2020,** *17* (9), 3567-3580.
64. Song, Y.; Yang, X.; Chen, X.; Nie, H.; Byrn, S.; Lubach, J. W., Investigation of drug-excipient interactions in lapatinib amorphous solid dispersions using solid-state NMR spectroscopy. *Mol. Pharm.*, **2015,** *12* (3), 857-66.
65. Lu, X.; Huang, C.; Lowinger, M. B.; Yang, F.; Xu, W.; Brown, C. D.; Hesk, D.; Koynov, A.; Schenck, L.; Su, Y., Molecular Interactions in Posaconazole Amorphous Solid Dispersions from Two-Dimensional Solid-State NMR Spectroscopy. *Mol. Pharm.*, **2019,** *16* (6), 2579-2589.
66. Lu, X.; Huang, C.; Li, M.; Skomski, D.; Xu, W.; Yu, L.; Byrn, S. R.; Templeton, A. C.; Su, Y., Molecular Mechanism of Crystalline-to-Amorphous Conversion of Pharmaceutical Solids from (19)F Magic Angle Spinning NMR. *J. Phys. Chem. B*, **2020,** *124* (25), 5271-5283.
67. Fernandes, José A.; Sardo, Mariana; Mafra, Luís; Choquesillo-Lazarte, Duane; Masciocchi, Norberto, X-ray and NMR Crystallography Studies of Novel Theophylline Cocrystals Prepared by Liquid Assisted Grinding. *Cryst. Growth Des.*, **2015,** *15* (8), 3674-3683.
68. Io, T.; Fukami, T.; Yamamoto, K.; Suzuki, T.; Xu, J.; Tomono, K.; Ramamoorthy, A., Homogeneous Nanoparticles to Enhance the Efficiency of a Hydrophobic Drug, Antihyperlipidemic Probucol, Characterized by Solid-State NMR. *Mol. Pharm.*, **2010,** *7*, 299-305.
69. Abragam, A. & Abragam, A., *The principles of nuclear magnetism*. Oxford university press: 1961.
70. Mehring, M., *Principles of High Resolution NMR in Solids*. 2md ed.; 1983.
71. Ernst, R. R.; Bodenhausen, G.; Wokaun, A., *Principles of nuclear magnetic resonance in one and two dimensions*. Clarendon Press: Oxford, 1987.
72. Levitt, M. H., *Spin Dynamics: Basics of Nuclear Magnetic Resonance*. 2nd ed.; John Wiley & Sons, Ltd: 2008.
73. Keeler, J., *Understanding NMR spectroscopy*. John Wiley & Sons: 2010.
74. Hore, P. J., *Nuclear magnetic resonance*. Oxford University Press: USA, 2015.
75. Jeener, J. Ampere International Summer School, Basko Polje, Yugoslavia, Basko Polje, Yugoslavia, 1971.
76. Aue, W. P.; Bartholdi, E.; Ernst, R. R., Two-dimensional spectroscopy. Application to nuclear magnetic resonance. *J. Chem. Phys.*, **1976,** *64* (1), 2229-2246.
77. Bodenhausen, G.; Ruben, D. J., Natural Abundance Nitrogen-15 NMR by Enhanced Heteronuclear Spectroscopy. *Chem. Phys. Lett.*, **1980,** *69* (1), 185-189.
78. Bax, A.; Freeman, R., Inverstigation of Complex Networks of Spin-Spin Coupling by Two-Dimensional NMR. *J. Magn. Reson.*, **1981,** *44*, 542-561.
79. Bax, A.; Freeman, R.; Frenkiel, T. A., An NMR Technique for Tracing Out the Carbon Skeleton of an Organic Molecule. *J. Am. Chem. Soc.*, **1981,** *103*, 2102-2104.
80. Braunschweiler, L.; Ernst, R. R., Coherence Transfer by Isotropic Mixing: Application to Proton Correlation Spectroscopy. *J. Magn. Reson.*, **1983,** *53*, 521-528.
81. Bax, A.; Summers, M. F., 1H and 13C Assignments from Sensitivity-Enhanced Detection of Heteronuclear Multiple-Bond Connectivity by 2D Multiple Quantum NMR. *J. Am. Chem. Soc.*, **1986,** *108*, 2093-2094.

82. Lerner, L.; Bax, A., Sensitivity-Enhanced Two-Dimensional Heteronuclear Relayed Coherence Transfer NMR Spectroscopy. *J. Magn. Reson.*, **1986,** *69*, 375-380.
83. Morris, Gareth A., Diffusion-Ordered Spectroscopy. In *Encyclopedia of Magnetic Resonance*, 2009.
84. Pausak, S.; Pines, A.; Waugh, J. S., Carbon-13 chemical shielding tensors in single-crystal durene. *J. Chem. Phys.*, **1973,** *59* (2), 591-595.
85. Freeman, R., Spin Decoupling In High Resolution Proton Magnetic Resonance. *Mol. Phys.*, **1960,** *3* (5), 435-439.
86. Waugh, J. S., Theory of broadband spin decoupling. *J. Magn. Reson.*, **1982,** *50* (1), 30-49.
87. Waugh, J. S., Systematic Procedure for Constructing Broadband decoupling Sequences. *J. Magn. Reson.*, **1982,** *49* (3), 517-521.
88. Shaka, A. J.; Keeler, J., Broadband spin decoupling in isotropic liquids. *Prog. Nucl. Magn. Reson. Spectrosc.*, **1987,** *19*, 47-129.
89. Fu, R.; Cross, T. A., SOLID-STATE NUCLEAR MAGNETIC RESONANCE INVESTIGATION OF PROTEIN AND POLYPEPTIDE STRUCTURE. *Annual Review Biophysics Biomolecular Structure* **1999,** *28*, 235-268.
90. Teng, Q.; Iqbal, M.; Cross, T. A., Determination of the 13C Chemical Shift and 14N Electric Field Gradient Tensor Orientations with Respect to the Molecular Frame in a Polypeptide. *J. Am. Chem. Soc.*, **1992,** *114*, 5312-5321.
91. Wei, Y.; Lee, D. K.; Ramamoorthy, A., Solid-State 13C NMR Chemical Shift Anisotropy Tensors of Polypeptides. *J. Am. Chem. Soc.*, **2001,** *123*, 6118-6126.
92. Hartzell, C. J.; Whitfield, M.; Oas, T. G.; Drobny, G. P., Determination of the 15N and 13C Chemical Shift Tensors of L-[13C]Alanyl-L-[15N]alanine from the Dipole-Coupled Powder Patterns. *J. Am. Chem. Soc.*, **1987,** *109*, 5966-5969.
93. Hong, M., Solid-State NMR Determination of 13CR Chemical Shift Anisotropies for the Identification of Protein Secondary Structure. *J. Am. Chem. Soc.*, **2000,** *122*, 3762-3770.
94. Brender, J. R.; Taylor, D. M.; Ramamoorthy, A., Orientation of Amide-Nitrogen-15 Chemical Shift Tensors in Peptides: A Quantum Chemical Study. *J. Am. Chem. Soc.*, **2001,** *123*, 914-922.
95. Oas, T. G.; Hartzell, C. J.; McMahon, T. J.; Drobny, G. P.; Dahlquist, F. W., The Carbonyl 13C Chemical Shift Tensors of Five Peptides Determined from 15N Dipole-Coupled Chemical Shift Powder Patterns. *J. Am. Chem. Soc.*, **1987,** *109*, 5956-5962.
96. Lee, D. K.; Santos, J. S.; Ramamoorthy, A., Application of One-Dimensional Dipolar Shift Solid-State NMR Spectroscopy To Study the Backbone Conformation of Membrane Associated Peptides in Phospholipid Bilayers. *J. Phys. Chem. B*, **1999,** *103*, 8383-8390.
97. Lee, D. K.; Wittebort, R. J.; Ramamoorthy, A., Characterization of 15N Chemical Shift and 1H-15N Dipolar Coupling Interactions in a Peptide Bond of Uniaxially Oriented and Polycrystalline Samples by One-Dimensional Dipolar Chemical Shift Solid-State NMR Spectroscopy. *J. Am. Chem. Soc.*, **1998,** *120*, 8868-8674.
98. Asakawa, N.; Kuroki, S.; Kurosu, H.; Ando, I.; Shoji, A.; Ozaki, T., Hydrogen-Bonding Effect on 13C NMR Chemical Shifts of L-Alanine Residue Carbonyl Carbons of Peptides in the Solid State. *J. Am. Chem. Soc.*, **1992,** *114*, 3261-3265.
99. Pake, G. E., Nuclear Resonance Absorption in Hydrated Crystals: Fine Structure of the Proton Line. *J. Chem. Phys.*, **1948,** *16* (4), 327-336.
100. Abragram, A., *Principles of Nuclear Magnetism*. 1982.
101. Andrew, E. R.; Bradbury, A.; Eades, R. G., Magnetic Resonance Spectra from a Crystal Rotated at High Speed. *Nature*, **1958,** *182*, 1.
102. Lowe, I. J., Free Induction Decays of Rotating Solids. *Phys. Rev. Lett.*, **1959,** *2* (7), 285-287.
103. Maricq, M. Matti; Waugh, J. S., NMR in rotating solids. *J. Chem. Phys.*, **1979,** *70* (7), 3300-3316.
104. Brunner, E.; Freude, D.; Gerstein, B.C.; Pfeifer, H., Residual Linewidth of NMR Spectra of Spin 1/2 Systems under Magic-Angle Spinning. *J. Magn. Reson.*, **1990,** *90*, 90-99.
105. Challoner, R.; McDowell, C.A., Three-Spin Systems in Rotating Solids and the X approximation. *J. Magn. Reson.*, **1992,** *98*, 123-133.
106. Levitt, M. H.; Raleigh, D. P.; Creuzet, F.; Griffin, R. G., Theory and simulations of homonuclear spin pair systems in rotating solids. *J. Chem. Phys.*, **1990,** *92* (11), 6347-6364.
107. Malar, A. A.; Smith-Penzel, S.; Camenisch, G. M.; Wiegand, T.; Samoson, A.; Bockmann, A.; Ernst, M.; Meier, B. H., Quantifying proton NMR coherent linewidth in proteins under fast MAS conditions: a second moment approach. *Phys. Chem. Chem. Phys.*, **2019,** *21* (35), 18850-18865.
108. Nakai, Toshihito; McDowell, Charles A., Application of Floquet theory to the nuclear magnetic resonance spectra of homonuclear two‐spin systems in rotating solids. *J. Chem. Phys.*, **1992,** *96* (5), 3452-3466.
109. Filip, C. ; Hafner, S.; Schnell, I. ; Demco, D. E.; Spiess, H. W., Solid-state nuclear magnetic resonance spectra of dipolar-coupled multi-spin systems under fast magic-angle spinning. *J. Chem. Phys.*, **1999,** *110*, 423-440.
110. Penzel, S.; Oss, A.; Org, M. L.; Samoson, A.; Bockmann, A.; Ernst, M.; Meier, B. H., Spinning faster: protein NMR at MAS frequencies up to 126 kHz. *J. Biomol. NMR.*, **2019,** *73* (1-2), 19-29.
111. Schnell, Ingo; Spiess, Hans Wolfgang, High-Resolution 1H NMR Spectroscopy in the Solid State: Very Fast Sample Rotation and Multiple-Quantum Coherences. *J. Magn. Reson.*, **2001,** *151* (2), 153-227.
112. Sternberg, U.; Witter, R.; Kuprov, I.; Lamley, J. M.; Oss, A.; Lewandowski, J. R.; Samoson, A., (1)H line width dependence on MAS speed in solid state NMR - Comparison of experiment and simulation. *J. Magn. Reson.*, **2018,** *291*, 32-39.

113. Zorin, V. E.; Brown, S. P.; Hodgkinson, P., Origins of linewidth in 1H magic-angle spinning NMR. *J Chem Phys*, **2006,** *125* (14), 144508.
114. Pines, A.; Gibby, M. G.; Waugh, J. S., Proton-enhanced NMR of dilute spins in solids. *J. Chem. Phys.*, **1973,** *59* (2), 569-590.
115. Wickramasinghe, A.; Wang, S.; Matsuda, I.; Nishiyama, Y.; Nemoto, T.; Endo, Y.; Ishii, Y., Evolution of CPMAS under fast magic-angle-spinning at 100 kHz and beyond. *Solid State Nucl. Magn. Reson.*, **2015,** *72*, 9-16.
116. Agarwal, V.; Penzel, S.; Szekely, K.; Cadalbert, R.; Testori, E.; Oss, A.; Past, J.; Samoson, A.; Ernst, M.; Bockmann, A.; Meier, B. H., De novo 3D structure determination from sub-milligram protein samples by solid-state 100 kHz MAS NMR spectroscopy. *Angew. Chem. Int. Ed. Engl.*, **2014,** *53* (45), 12253-6.
117. Kobayashi, T.; Mao, K.; Paluch, P.; Nowak-Krol, A.; Sniechowska, J.; Nishiyama, Y.; Gryko, D. T.; Potrzebowski, M. J.; Pruski, M., Study of intermolecular interactions in the corrole matrix by solid-state NMR under 100 kHz MAS and theoretical calculations. *Angew. Chem. Int. Ed. Engl.*, **2013,** *52* (52), 14108-11.
118. Lin, Y. L.; Cheng, Y. S.; Ho, C. I.; Guo, Z. H.; Huang, S. J.; Org, M. L.; Oss, A.; Samoson, A.; Chan, J. C. C., Preparation of fibril nuclei of beta-amyloid peptides in reverse micelles. *Chem. Commun. (Camb.)*, **2018,** *54* (74), 10459-10462.
119. Nishiyama, Y.; Malon, M.; Ishii, Y.; Ramamoorthy, A., 3D (1)(5)N/(1)(5)N/(1)H chemical shift correlation experiment utilizing an RFDR-based (1)H/(1)H mixing period at 100 kHz MAS. *J. Magn. Reson.*, **2014,** *244*, 1-5.
120. Hahn, Erwin L., Spin Echoes. *Phys Rev*, **1950,** (80), 580-590.
121. De Paepe, G.; Giraud, N.; Lesage, A.; Hodgkinson, P.; Böckmann, A.; Emsley, L., Transverse Dephasing Optimized Solid-State NMR Spectroscopy. *J. Am. Chem. Soc.*, **2003,** *125*, 13938-13939.
122. Hahn, E. L., Spin Echoes. *Phys. Rev.*, **1950,** *80* (4), 580-594.
123. Nishiyama, Y.; Hou, G.; Agarwal, V.; Su, Y.; Ramamoorthy, A., Ultrafast Magic Angle Spinning Solid-State NMR Spectroscopy: Advances in Methodology and Applications. *Chem. Rev.*, **2023,** *123* (3), 918-988.
124. Asami, S.; Szekely, K.; Schanda, P.; Meier, B. H.; Reif, B., Optimal degree of protonation for (1)H detection of aliphatic sites in randomly deuterated proteins as a function of the MAS frequency. *J. Biomol. NMR.*, **2012,** *54* (2), 155-68.
125. Agarwal, V.; Reif, B., Residual methyl protonation in perdeuterated proteins for multi-dimensional correlation experiments in MAS solid-state NMR spectroscopy. *J. Magn. Reson.*, **2008,** *194* (1), 16-24.
126. Reif, B., Ultra-high resolution in MAS solid-state NMR of perdeuterated proteins: implications for structure and dynamics. *J. Magn. Reson.*, **2012,** *216*, 1-12.
127. Reif, B.; van Rossum, B.; Castellani, F.; Rehbein, K.; Diehl, A.; Oschkinat, H., Characterization of 1H-1H Distances in a Uniformly 2H,15N-Labeled SH3 Domain by MAS Solid-State NMR Spectroscopy. *J. Am. Chem. Soc.*, **2003,** *125* (6), 1488-1489.
128. Chevelkov, V.; Zhuravleva, A. V.; Xue, Y.; Reif, B.; Skrynnikov, N. R., Combined Analysis of 15N Relaxation Data from Solid- and Solution-State NMR Spectroscopy. *J. Am. Chem. Soc.*, **2007,** *129*, 12594-12595.
129. Agarwal, V.; Xue, Y.; Reif, B.; Skrynnikov, N. R., Protein Side-Chain Dynamics As Observed by Solution- and Solid-State NMR Spectroscopy: A Similarity Revealed. *J. Am. Chem. Soc.*, **2008,** *130*, 16611-16621.
130. Barbet-Massin, E.; Pell, A. J.; Retel, J. S.; Andreas, L. B.; Jaudzems, K.; Franks, W. T.; Nieuwkoop, A. J.; Hiller, M.; Higman, V.; Guerry, P.; Bertarello, A.; Knight, M. J.; Felletti, M.; Le Marchand, T.; Kotelovica, S.; Akopjana, I.; Tars, K.; Stoppini, M.; Bellotti, V.; Bolognesi, M.; Ricagno, S.; Chou, J. J.; Griffin, R. G.; Oschkinat, H.; Lesage, A.; Emsley, L.; Herrmann, T.; Pintacuda, G., Rapid proton-detected NMR assignment for proteins with fast magic angle spinning. *J. Am. Chem. Soc.*, **2014,** *136* (35), 12489-97.
131. Gerstein, B. C.; Pembleton, R. G.; Wilson, R. C.; Ryan, L. M., High resolution NMR in randomly oriented solids with homonuclear dipolar broadening: Combined multiple pulse NMR and magic angle spinning. *J. Chem. Phys.*, **1977,** *66* (1), 361-362.
132. Leskes, Michal; Steuernagel, Stefan; Schneider, Denis; Madhu, P. K.; Vega, Shimon, Homonuclear dipolar decoupling at magic-angle spinning frequencies up to 65kHz in solid-state nuclear magnetic resonance. *Chem. Phys. Lett.*, **2008,** *466* (1-3), 95-99.
133. Salager, Elodie; Dumez, Jean-Nicolas; Stein, Robin S.; Steuernagel, Stefan; Lesage, Anne; Elena-Herrmann, Bénédicte; Emsley, Lyndon, Homonuclear dipolar decoupling with very large scaling factors for high-resolution ultrafast magic angle spinning 1H solid-state NMR spectroscopy. *Chem. Phys. Lett.*, **2010,** *498* (1-3), 214-220.
134. Gan, Zhehong; Madhu, P. K.; Amoureux, Jean-Paul; Trébosc, Julien; Lafon, Olivier, A tunable homonuclear dipolar decoupling scheme for high-resolution proton NMR of solids from slow to fast magic-angle spinning. *Chem. Phys. Lett.*, **2011,** *503* (1-3), 167-170.
135. Elena, Bénédicte; de Paëpe, Gaël; Emsley, Lyndon, Direct spectral optimisation of proton–proton homonuclear dipolar decoupling in solid-state NMR. *Chem. Phys. Lett.*, **2004,** *398* (4-6), 532-538.
136. Halse, M. E.; Emsley, L., Improved phase-modulated homonuclear dipolar decoupling for solid-state NMR spectroscopy from symmetry considerations. *J. Phys. Chem. A*, **2013,** *117* (25), 5280-90.
137. Samoson, A., H-Mas. *J. Magn. Reson.*, **2019,** *306*, 167-172.
138. Venkatesh, A.; Hung, I.; Boteju, K. C.; Sadow, A. D.; Gor'kov, P. L.; Gan, Z.; Rossini, A. J., Suppressing (1)H Spin Diffusion in Fast MAS Proton Detected Heteronuclear Correlation Solid-State NMR Experiments. *Solid State Nucl. Magn. Reson.*, **2020,** *105*, 101636.
139. Zhang, R.; Chen, Y.; Rodriguez-Hornedo, N.; Ramamoorthy, A., Enhancing NMR Sensitivity of Natural-Abundance Low-gamma Nuclei by Ultrafast Magic-Angle-Spinning Solid-State NMR Spectroscopy. *Chemphyschem*, **2016,** *17* (19), 2962-2966.

140. Althaus, S. M.; Mao, K.; Stringer, J. A.; Kobayashi, T.; Pruski, M., Indirectly detected heteronuclear correlation solid-state NMR spectroscopy of naturally abundant 15N nuclei. *Solid State Nucl. Magn. Reson.*, **2014,** *57-58*, 17-21.
141. Nehra, Ekta; Sehrawat, Neelam; Kobayashi, Takeshi; Nishiyama, Yusuke; Pandey, Manoj Kumar, Proton-detected 15N-1H dipolar coupling/1H chemical shift correlation experiment for the measurement of NH distances in biological solids under fast MAS solid-state NMR. *J. Magn. Reson. O.*, **2022,** *10-11*.
142. Zhang, R.; Nishiyama, Y.; Ramamoorthy, A., Exploiting heterogeneous time scale of dynamics to enhance 2D HETCOR solid-state NMR sensitivity. *J. Magn. Reson.*, **2019,** *309*, 106615.
143. Barbet-Massin, E.; Pell, A. J.; Jaudzems, K.; Franks, W. T.; Retel, J. S.; Kotelovica, S.; Akopjana, I.; Tars, K.; Emsley, L.; Oschkinat, H.; Lesage, A.; Pintacuda, G., Out-and-back 13C-13C scalar transfers in protein resonance assignment by proton-detected solid-state NMR under ultra-fast MAS. *J. Biomol. NMR.*, **2013,** *56* (4), 379-86.
144. Hou, G.; Byeon, I. J.; Ahn, J.; Gronenborn, A. M.; Polenova, T., 1H-13C/1H-15N heteronuclear dipolar recoupling by R-symmetry sequences under fast magic angle spinning for dynamics analysis of biological and organic solids. *J. Am. Chem. Soc.*, **2011,** *133* (46), 18646-55.
145. Liang, L.; Ji, Y.; Zhao, Z.; Quinn, C. M.; Han, X.; Bao, X.; Polenova, T.; Hou, G., Accurate heteronuclear distance measurements at all magic-angle spinning frequencies in solid-state NMR spectroscopy. *Chem. Sci.*, **2021,** *12* (34), 11554-11564.
146. Linser, R.; Dasari, M.; Hiller, M.; Higman, V.; Fink, U.; Lopez del Amo, J. M.; Markovic, S.; Handel, L.; Kessler, B.; Schmieder, P.; Oesterhelt, D.; Oschkinat, H.; Reif, B., Proton-detected solid-state NMR spectroscopy of fibrillar and membrane proteins. *Angew. Chem. Int. Ed. Engl.*, **2011,** *50* (19), 4508-12.
147. Linser, R.; Fink, U.; Reif, B., Narrow carbonyl resonances in proton-diluted proteins facilitate NMR assignments in the solid-state. *J. Biomol. NMR.*, **2010,** *47* (1), 1-6.
148. Marchetti, Alessandro; Jehle, Stefan; Felletti, Michele; Knight, Michael J.; Wang, Yao; Xu, Zhi-Qiang; Park, Ah Young; Otting, Gottfried; Lesage, Anne; Emsley, Lyndon; Dixon, Nicholas E.; Pintacuda, Guido, Backbone Assignment of Fully Protonated Solid Proteins by1H Detection and Ultrafast Magic-Angle-Spinning NMR Spectroscopy. *Angew. Chem.*, **2012,** *124* (43), 10914-10917.
149. Vasa, S. K.; Singh, H.; Rovo, P.; Linser, R., Dynamics and Interactions of a 29 kDa Human Enzyme Studied by Solid-State NMR. *J. Phys. Chem. Lett.*, **2018,** *9* (6), 1307-1311.
150. Zhang, R.; Ramamoorthy, A., Constant-time 2D and 3D through-bond correlation NMR spectroscopy of solids under 60 kHz MAS. *J. Chem. Phys.*, **2016,** *144* (3), 034202.
151. Zhou, D. H.; Shea, J. J.; Nieuwkoop, A. J.; Franks, W. T.; Wylie, B. J.; Mullen, C.; Sandoz, D.; Rienstra, C. M., Solid-state protein-structure determination with proton-detected triple-resonance 3D magic-angle-spinning NMR spectroscopy. *Angew. Chem. Int. Ed. Engl.*, **2007,** *46* (44), 8380-3.
152. Demers, J. P.; Chevelkov, V.; Lange, A., Progress in correlation spectroscopy at ultra-fast magic-angle spinning: basic building blocks and complex experiments for the study of protein structure and dynamics. *Solid State Nucl. Magn. Reson.*, **2011,** *40* (3), 101-13.
153. Franks, W. T.; Atreya, H. S.; Szyperski, T.; Rienstra, C. M., GFT projection NMR spectroscopy for proteins in the solid state. *J. Biomol. NMR.*, **2010,** *48* (4), 213-23.
154. Franks, W. T.; Kloepper, K. D.; Wylie, B. J.; Rienstra, C. M., Four-dimensional heteronuclear correlation experiments for chemical shift assignment of solid proteins. *J. Biomol. NMR.*, **2007,** *39* (2), 107-31.
155. Schuetz, A.; Wasmer, C.; Habenstein, B.; Verel, R.; Greenwald, J.; Riek, R.; Bockmann, A.; Meier, B. H., Protocols for the sequential solid-state NMR spectroscopic assignment of a uniformly labeled 25 kDa protein: HET-s(1-227). *Chembiochem*, **2010,** *11* (11), 1543-51.
156. Sperling, L. J.; Berthold, D. A.; Sasser, T. L.; Jeisy-Scott, V.; Rienstra, C. M., Assignment strategies for large proteins by magic-angle spinning NMR: the 21-kDa disulfide-bond-forming enzyme DsbA. *J. Mol. Biol.*, **2010,** *399* (2), 268-82.
157. Huber, M.; Hiller, S.; Schanda, P.; Ernst, M.; Bockmann, A.; Verel, R.; Meier, B. H., A proton-detected 4D solid-state NMR experiment for protein structure determination. *Chemphyschem*, **2011,** *12* (5), 915-8.
158. Xiang, S.; Chevelkov, V.; Becker, S.; Lange, A., Towards automatic protein backbone assignment using proton-detected 4D solid-state NMR data. *J. Biomol. NMR.*, **2014,** *60* (2-3), 85-90.
159. Xiang, S.; Biernat, J.; Mandelkow, E.; Becker, S.; Linser, R., Backbone assignment for minimal protein amounts of low structural homogeneity in the absence of deuteration. *Chem. Commun. (Camb.)*, **2016,** *52* (21), 4002-5.
160. Zinke, M.; Fricke, P.; Samson, C.; Hwang, S.; Wall, J. S.; Lange, S.; Zinn-Justin, S.; Lange, A., Bacteriophage Tail-Tube Assembly Studied by Proton-Detected 4D Solid-State NMR. *Angew. Chem. Int. Ed. Engl.*, **2017,** *56* (32), 9497-9501.
161. Fraga, H.; Arnaud, C. A.; Gauto, D. F.; Audin, M.; Kurauskas, V.; Macek, P.; Krichel, C.; Guan, J. Y.; Boisbouvier, J.; Sprangers, R.; Breyton, C.; Schanda, P., Solid-State NMR H-N-(C)-H and H-N-C-C 3D/4D Correlation Experiments for Resonance Assignment of Large Proteins. *Chemphyschem*, **2017,** *18* (19), 2697-2703.
162. Trease, Nicole M.; Clark, Ted M.; Grandinetti, Philip J.; Stebbins, Jonathan F.; Sen, Sabyasachi, Bond length-bond angle correlation in densified silica—Results from 17O NMR spectroscopy. *J. Chem. Phys.*, **2017,** *146* (18).
163. Hanrahan, M. P.; Chen, Y.; Blome-Fernandez, R.; Stein, J. L.; Pach, G. F.; Adamson, M. A. S.; Neale, N. R.; Cossairt, B. M.; Vela, J.; Rossini, A. J., Probing the Surface Structure of Semiconductor Nanoparticles by DNP SENS with Dielectric Support Materials. *J. Am. Chem. Soc.*, **2019,** *141* (39), 15532-15546.
164. Davies, E.; Muller, K. H.; Wong, W. C.; Pickard, C. J.; Reid, D. G.; Skepper, J. N.; Duer, M. J., Citrate bridges between mineral platelets in bone. *Proc. Natl. Acad. Sci. U S A*, **2014,** *111* (14), E1354-63.

165. Brus, J.; Kobera, L.; Schoefberger, W.; Urbanova, M.; Klein, P.; Sazama, P.; Tabor, E.; Sklenak, S.; Fishchuk, A. V.; Dedecek, J., Structure of framework aluminum Lewis sites and perturbed aluminum atoms in zeolites as determined by 27Al1H REDOR (3Q) MAS NMR spectroscopy and DFT/molecular mechanics. *Angew. Chem. Int. Ed. Engl.*, **2015,** *54* (2), 541-5.
166. Bonhomme, C.; Gervais, C.; Laurencin, D., Recent NMR developments applied to organic-inorganic materials. *Prog. Nucl. Magn. Reson. Spectrosc.*, **2014,** *77*, 1-48.
167. Alanazi, A. Q.; Kubicki, D. J.; Prochowicz, D.; Alharbi, E. A.; Bouduban, M. E. F.; Jahanbakhshi, F.; Mladenovic, M.; Milic, J. V.; Giordano, F.; Ren, D.; Alyamani, A. Y.; Albrithen, H.; Albadri, A.; Alotaibi, M. H.; Moser, J. E.; Zakeeruddin, S. M.; Rothlisberger, U.; Emsley, L.; Gratzel, M., Atomic-Level Microstructure of Efficient Formamidinium-Based Perovskite Solar Cells Stabilized by 5-Ammonium Valeric Acid Iodide Revealed by Multinuclear and Two-Dimensional Solid-State NMR. *J. Am. Chem. Soc.*, **2019,** *141* (44), 17659-17669.
168. Schmidt-Rohr, K.; ; Spiess, H. W., *Multidimensional Solid-State NMR and Polymers*. Academic PRess: London, 1996.
169. Ishii, Y.; Yesinowski, J. P.; Tycko, R., Sensitivity Enhancement in Solid-State 13C NMR of Synthetic Polymers and Biopolymers by 1H NMR Detection with High-Speed Magic Angle Spinning. *J. Am. Chem. Soc.*, **2001,** *123*, 2921-2922.
170. Takahashi, H.; Ayala, I.; Bardet, M.; De Paepe, G.; Simorre, J. P.; Hediger, S., Solid-state NMR on bacterial cells: selective cell wall signal enhancement and resolution improvement using dynamic nuclear polarization. *J. Am. Chem. Soc.*, **2013,** *135* (13), 5105-10.
171. Wang, T.; Phyo, P.; Hong, M., Multidimensional solid-state NMR spectroscopy of plant cell walls. *Solid State Nucl. Magn. Reson.*, **2016,** *78*, 56-63.
172. Duan, P.; Li, X.; Wang, T.; Chen, B.; Juhl, S. J.; Koeplinger, D.; Crespi, V. H.; Badding, J. V.; Schmidt-Rohr, K., The Chemical Structure of Carbon Nanothreads Analyzed by Advanced Solid-State NMR. *J. Am. Chem. Soc.*, **2018,** *140* (24), 7658-7666.
173. Nagarkar, S. S.; Kurasho, H.; Duong, N. T.; Nishiyama, Y.; Kitagawa, S.; Horike, S., Crystal melting and glass formation in copper thiocyanate based coordination polymers. *Chem. Commun. (Camb.)*, **2019,** *55* (38), 5455-5458.
174. Ishii, Y.; Tycko, R., Sensitivity Enhancement in Solid State 15N NMR by Indirect Detection with High-Speed Magic Angle Spinning. *J. Magn. Reson.*, **2000,** *142*, 199-204.
175. Andreas, L. B.; Jaudzems, K.; Stanek, J.; Lalli, D.; Bertarello, A.; Le Marchand, T.; Cala-De Paepe, D.; Kotelovica, S.; Akopjana, I.; Knott, B.; Wegner, S.; Engelke, F.; Lesage, A.; Emsley, L.; Tars, K.; Herrmann, T.; Pintacuda, G., Structure of fully protonated proteins by proton-detected magic-angle spinning NMR. *Proc. Natl. Acad. Sci. U S A*, **2016,** *113* (33), 9187-92.
176. Brown, Steven P., Probing proton–proton proximities in the solid state. *Prog. Nucl. Magn. Reson. Spectrosc.*, **2007,** *50* (4), 199-251.
177. Brown, S. P., Applications of high-resolution 1H solid-state NMR. *Solid State Nucl Magn Reson*, **2012,** *41*, 1-27.
178. Jain, M. G.; Lalli, D.; Stanek, J.; Gowda, C.; Prakash, S.; Schwarzer, T. S.; Schubeis, T.; Castiglione, K.; Andreas, L. B.; Madhu, P. K.; Pintacuda, G.; Agarwal, V., Selective (1)H-(1)H Distance Restraints in Fully Protonated Proteins by Very Fast Magic-Angle Spinning Solid-State NMR. *J Phys Chem Lett*, **2017,** *8* (11), 2399-2405.
179. Potnuru, L. R.; Duong, N. T.; Ahlawat, S.; Raran-Kurussi, S.; Ernst, M.; Nishiyama, Y.; Agarwal, V., Accuracy of (1)H-(1)H distances measured using frequency selective recoupling and fast magic-angle spinning. *J Chem Phys*, **2020,** *153* (8), 084202.
180. Schanda, P.; Ernst, M., Studying Dynamics by Magic-Angle Spinning Solid-State NMR Spectroscopy: Principles and Applications to Biomolecules. *Prog Nucl Magn Reson Spectrosc*, **2016,** *96*, 1-46.
181. Zhang, R.; Ramamoorthy, A., Selective excitation enables assignment of proton resonances and (1)H-(1)H distance measurement in ultrafast magic angle spinning solid state NMR spectroscopy. *J Chem Phys*, **2015,** *143* (3), 034201.
182. Zhang, R.; Ramamoorthy, A., Dynamics-based selective 2D (1)H/(1)H chemical shift correlation spectroscopy under ultrafast MAS conditions. *J Chem Phys*, **2015,** *142* (20), 204201.
183. Bennett, A. E.; Griffin, R. G.; Ok, J. H.; Vega, S., Chemical shift correlation spectroscopy in rotating solids: Radio frequency‐driven dipolar recoupling and longitudinal exchange. *J. Chem. Phys.*, **1992,** *96* (11), 8624-8627.
184. Ji, Y.; Liang, L.; Guo, C.; Bao, X.; Polenova, T.; Hou, G., Zero-Quantum Homonuclear Recoupling Symmetry Sequences in Solid-State Fast MAS NMR Spectroscopy. *Acta Phys. Chim. Sin.*, **2020,** *36* (4), 1905029_1905040.
185. Ishii, Yoshitaka, 13C-13C dipolar recoupling under very fast magic angle spinning in solid-state nuclear magnetic resonance: Applications to distance measurements, spectral assignments, and high-throughput secondary-structure determination. *J. Chem. Phys.*, **2001,** *114* (19), 8473-8483.
186. Ishii, Y.; Balbach, J. J.; Tycko, R., Measurement of dipole-coupled lineshapes in a many-spin system by constant-time two-dimensional solid state NMR with high-speed magic-angle spinning. *Chem. Phys.*, **2001,** *266*, 231-236.
187. Shen, M.; Hu, B.; Lafon, O.; Trebosc, J.; Chen, Q.; Amoureux, J. P., Broadband finite-pulse radio-frequency-driven recoupling (fp-RFDR) with (XY8)4(1) super-cycling for homo-nuclear correlations in very high magnetic fields at fast and ultra-fast MAS frequencies. *J. Magn. Reson.*, **2012,** *223*, 107-19.
188. Nishiyama, Y.; Zhang, R.; Ramamoorthy, A., Finite-pulse radio frequency driven recoupling with phase cycling for 2D (1)H/(1)H correlation at ultrafast MAS frequencies. *J. Magn. Reson.*, **2014,** *243*, 25-32.
189. Teymoori, G.; Pahari, B.; Eden, M., Low-power broadband homonuclear dipolar recoupling in MAS NMR by two-fold symmetry pulse schemes for magnetization transfers and double-quantum excitation. *J. Magn. Reson.*, **2015,** *261*, 205-20.
190. Zhang, R.; Nishiyama, Y.; Sun, P.; Ramamoorthy, A., Phase cycling schemes for finite-pulse-RFDR MAS solid state NMR experiments. *J. Magn. Reson.*, **2015,** *252*, 55-66.

191. Hellwagner, J.; Wili, N.; Ibanez, L. F.; Wittmann, J. J.; Meier, B. H.; Ernst, M., Transient effects in pi-pulse sequences in MAS solid-state NMR. *J. Magn. Reson.*, **2018,** *287*, 65-73.
192. Feike, M.; ; Demco, D. E.;; Graf, R.; ; Gottwald, J.; ; Hafner, S.; ; Spiess, H. W., Broadband Multiple-Quantum NMR Spectroscopy. *J. Magn. Reson. Series A*, **1996,** *122*, 214.
193. Lee, Y. K.; Kurur, N. D.; Helmle, M.; Johannessen, O. G.; Nielsen, N. C.; Levitt, M. H., Efficient dipolar recoupling in the NMR of rotating solids. A sevenfold symmetric radiofrequency pulse sequence. *Chem. Phys. Lett.*, **1995**, 304-309.
194. Carravetta, M.; Eden, M.; Johannessen, O. G.; Luthman, H.; Verdegem, P. J. E.; Lugtenburg, J.; Sebald, A.; Levitt, M. H., Estimation of Carbon-Carbon Bond Lengths and Medium-Range Internuclear Distances by Solid-State Nuclear Magnetic Resonance. *J. Am. Chem. Soc.*, **2001,** *123*, 10628-10638.
195. Nielsen, N. C.; Bildso/e, H.; Jakobsen, H. J.; Levitt, M. H., Double-quantum homonuclear rotary resonance: Efficient dipolar recovery in magic-angle spinning nuclear magnetic resonance. *J. Chem. Phys.*, **1994,** *101* (3), 1805-1812.
196. Hohwy, M.; Jakobsen, H. J.; Edén, M.; Levitt, M. H.; Nielsen, N. C., Broadband dipolar recoupling in the nuclear magnetic resonance of rotating solids: A compensated C7 pulse sequence. *J. Chem. Phys.*, **1998,** *108* (7), 2686-2694.
197. Brinkmann, Andreas; Edén, Mattias; Levitt, Malcolm H., Synchronous helical pulse sequences in magic-angle spinning nuclear magnetic resonance: Double quantum recoupling of multiple-spin systems. *J. Chem. Phys.*, **2000,** *112* (19), 8539-8554.
198. Hohwy, M.; Rienstra, C. M.; Griffin, R. G., Band-selective homonuclear dipolar recoupling in rotating solids. *J. Chem. Phys.*, **2002,** *117* (10), 4973-4987.
199. Kristiansen, P. E.; Mitchell, D. J.; Evans, J. N., Double-quantum dipolar recoupling at high magic-angle spinning rates. *J. Magn. Reson.*, **2002,** *157* (2), 253-66.
200. Wi, Sungsool; Hwang, Son-Jong, Multiple-quantum 13C solid-state NMR spectroscopy under moderate magic-angle spinning. *Chem. Phys. Lett.*, **2006,** *426* (1-3), 187-191.
201. Mafra, L.; Siegel, R.; Fernandez, C.; Schneider, D.; Aussenac, F.; Rocha, J., High-resolution 1H homonuclear dipolar recoupling NMR spectra of biological solids at MAS rates up to 67 kHz. *J. Magn. Reson.*, **2009,** *199* (1), 111-4.
202. Lafon, O.; Trebosc, J.; Hu, B.; De Paepe, G.; Amoureux, J. P., Observing 13C-13C connectivities at high magnetic fields and very high spinning frequencies. *Chem. Commun. (Camb.)*, **2011,** *47* (24), 6930-2.
203. Saalwachter, K.; Lange, F.; Matyjaszewski, K.; Huang, C. F.; Graf, R., BaBa-xy16: robust and broadband homonuclear DQ recoupling for applications in rigid and soft solids up to the highest MAS frequencies. *J Magn Reson*, **2011,** *212* (1), 204-15.
204. Ren, J.; Eckert, H., A homonuclear rotational echo double-resonance method for measuring site-resolved distance distributions in I=(1/2) spin pairs, clusters, and multispin systems. *Angew. Chem. Int. Ed. Engl.*, **2012,** *51* (51), 12888-91.
205. Ren, J.; Eckert, H., DQ-DRENAR: a new NMR technique to measure site-resolved magnetic dipole-dipole interactions in multispin-1⁄2 systems: theory and validation on crystalline phosphates. *J. Chem. Phys.*, **2013,** *138* (16), 164201.
206. Tan, K. O.; Nielsen, A. B.; Meier, B. H.; Ernst, M., Broad-Band DREAM Recoupling Sequence. *J. Phys. Chem. Lett.*, **2014,** *5* (19), 3366-72.
207. Ren, J.; Eckert, H., Measurement of homonuclear magnetic dipole-dipole interactions in multiple 1/2-spin systems using constant-time DQ-DRENAR NMR. *J. Magn. Reson.*, **2015,** *260*, 46-53.
208. Dekhil, M.; Mollica, G.; Bonniot, T. T.; Ziarelli, F.; Thureau, P.; Viel, S., Determining carbon-carbon connectivities in natural abundance organic powders using dipolar couplings. *Chem. Commun. (Camb.)*, **2016,** *52* (55), 8565-8.
209. Hellwagner, J.; Sharma, K.; Tan, K. O.; Wittmann, J. J.; Meier, B. H.; Madhu, P. K.; Ernst, M., Optimizing symmetry-based recoupling sequences in solid-state NMR by pulse-transient compensation and asynchronous implementation. *J. Chem. Phys.*, **2017,** *146* (24), 244202.
210. Marker, K.; Hediger, S.; De Paepe, G., Efficient 2D double-quantum solid-state NMR spectroscopy with large spectral widths. *Chem. Commun. (Camb.)*, **2017,** *53* (65), 9155-9158.
211. Kristiansen, Per Eugen; Carravetta, Marina; Lai, Wai Cheu; Levitt, Malcolm H., A robust pulse sequence for the determination of small homonuclear dipolar couplings in magic-angle spinning NMR. *Chem. Phys. Lett.*, **2004,** *390* (1-3), 1-7.
212. Nishiyama, Y.; Agarwal, V.; Zhang, R., Efficient symmetry-based gamma-encoded DQ recoupling sequences for suppression of t(1)-noise in solid-state NMR spectroscopy at fast MAS. *Solid State Nucl. Magn. Reson.*, **2021,** *114*, 101734.
213. Moutzouri, P.; Paruzzo, F. M.; Simoes de Almeida, B.; Stevanato, G.; Emsley, L., Homonuclear Decoupling in (1) H NMR of Solids by Remote Correlation. *Angew Chem Int Ed Engl*, **2020,** *59* (15), 6235-6238.
214. Moutzouri, P.; Simoes de Almeida, B.; Torodii, D.; Emsley, L., Pure Isotropic Proton Solid State NMR. *J Am Chem Soc*, **2021,** *143* (26), 9834-9841.
215. Cordova, M.; Moutzouri, P.; Simoes de Almeida, B.; Torodii, D.; Emsley, L., Pure Isotropic Proton NMR Spectra in Solids using Deep Learning. *Angew. Chem. Int. Ed. Engl.*, **2023,** *62* (8), e202216607.
216. Cordova, M.; Balodis, M.; Hofstetter, A.; Paruzzo, F.; Nilsson Lill, S. O.; Eriksson, E. S. E.; Berruyer, P.; Simoes de Almeida, B.; Quayle, M. J.; Norberg, S. T.; Svensk Ankarberg, A.; Schantz, S.; Emsley, L., Structure determination of an amorphous drug through large-scale NMR predictions. *Nat. Commun.*, **2021,** *12* (1), 2964.
217. Rehman, Z.; Franks, W. T.; Nguyen, B.; Schmidt, H. F.; Scrivens, G.; Brown, S. P., Discovering the Solid-State Secrets of Lorlatinib by NMR Crystallography: To Hydrogen Bond or not to Hydrogen Bond. *J. Pharm. Sci.*, **2023,** *112* (7), 1915-1928.
218. Reif, Bernd; Ashbrook, Sharon E.; Emsley, Lyndon; Hong, Mei, Solid-state NMR spectroscopy. *Nat. Rev. Methods Primers*, **2021,** *1* (1).
219. Ray, S.; Vinogradov, E.; Boender, G.; Vega, S., Proton MAS NMR Spectra at High Magnetic Fields and High Spinning Frequencies: Spectral Simulations Using Floquet Theory. *J. Magn. Reson.*, **1998,** *125*, 418-426.

220. Schledorn, M.; Malar, A. A.; Torosyan, A.; Penzel, S.; Klose, D.; Oss, A.; Org, M. L.; Wang, S.; Lecoq, L.; Cadalbert, R.; Samoson, A.; Bockmann, A.; Meier, B. H., Protein NMR Spectroscopy at 150 kHz Magic-Angle Spinning Continues To Improve Resolution and Mass Sensitivity. *Chembiochem*, **2020,** *21* (17), 2540-2548.
221. Hellwagner, Johannes; Grunwald, Liam; Ochsner, Manuel; Zindel, Daniel; Meier, Beat H.; Ernst, Matthias, Origin of the residual line width under frequency-switched Lee–Goldburg decoupling in MAS solid-state NMR. *Magn. Reson.*, **2020,** *1* (1), 13-25.
222. Suter, D.; Ernst, R. R., Spin diffusion in resolved solid-state NMR spectra. *Phys. Rev. B: Condens. Matter*, **1985,** *32* (9), 5608-5627.
223. Kubo, A.; McDowell, C.A., Spectral Spin Diffusion in Polycrystalline Solids under Magic-angle Spinning. *Journal of the Chemical Society, Faraday Transactions 1*, **1988,** *84* (11), 3713-3730.
224. Dumez, J. N.; Butler, M. C.; Salager, E.; Elena-Herrmann, B.; Emsley, L., Ab initio simulation of proton spin diffusion. *Phys. Chem. Chem. Phys.*, **2010,** *12* (32), 9172-5.
225. Veshtort, M.; Griffin, R. G., Proton-driven spin diffusion in rotating solids via reversible and irreversible quantum dynamics. *J. Chem. Phys.*, **2011,** *135* (13), 134509.
226. Grommek, Andreas; Meier, Beat H.; Ernst, Matthias, Distance information from proton-driven spin diffusion under MAS. *Chem. Phys. Lett.*, **2006,** *427* (4-6), 404-409.
227. Agarwal, V., The origin of negative cross-peaks in proton-spin diffusion spectrum of fully protonated solids at fast MAS: Coherent or incoherent effect? *J. Magn. Reson.*, **2020,** *311*, 106661.
228. Scholz, Ingo; Huber, Matthias; Manolikas, Theofanis; Meier, Beat H.; Ernst, Matthias, MIRROR recoupling and its application to spin diffusion under fast magic-angle spinning. *Chem. Phys. Lett.*, **2008,** *460* (1-3), 278-283.
229. Scholz, I.; van Beek, J. D.; Ernst, M., Operator-based Floquet theory in solid-state NMR. *Solid State Nucl. Magn. Reson.*, **2010,** *37* (3-4), 39-59.
230. Bengs, C.; Levitt, M. H., SpinDynamica: Symbolic and numerical magnetic resonance in a Mathematica environment. *Magn. Reson. Chem.*, **2018,** *56* (6), 374-414.
231. Hogben, H. J.; Krzystyniak, M.; Charnock, G. T.; Hore, P. J.; Kuprov, I., Spinach--a software library for simulation of spin dynamics in large spin systems. *J. Magn. Reson.*, **2011,** *208* (2), 179-94.
232. Mueller, Leonard J., Tensors and rotations in NMR. *Concepts Magn. Reson. Part A*, **2011,** *38A* (5), 221-235.
233. Haeberlen, U.; Waugh, J. S., Coherent Averaging Effects in Magnetic Resonance. *Phys. Rev.*, **1968,** *175* (2), 453-467.
234. Brinkmann, Andreas, Introduction to average Hamiltonian theory. I. Basics. *Concepts Magn. Reson. Part A*, **2016,** *45A* (6).
235. Bak, M.; Nielsen, N, REPULSION, a novel approach to efficient powder averaging in solid-state NMR. *J. Magn. Reson.*, **1997,** *125*, 132-139.
236. Moutzouri, P. ; Simões de Almeida, B.; Torodii, D. ; Emsley, L., Pure Isotropic Proton Solid State NMR. *J. Am. Chem. Soc.*, **2021,** *143* (26), 9834-9841.
237. Moutzouri, P.; Simoes de Almeida, B.; Emsley, L., Fast remote correlation experiments for (1)H homonuclear decoupling in solids. *J. Magn. Reson.*, **2020,** *321*, 106856.
238. Chávez, Matías; Wiegand, Thomas; Malär, Alexander A.; Meier, Beat H.; Ernst, Matthias, Residual dipolar line width in magic-angle spinning proton solid-state NMR. *Magn. Reson.*, **2021,** *2* (1), 499-509.
239. VanderHart, D.L.; Earl, William L.; Garroway, A.N., Resolution in 13C NMR of Organic Solids Using High Power Proton Decoupling and Magic-Angle Sample Spinning. *J. Magn. Reson.*, **1981,** *44*, 361-401.
240. Alla, M; Lippmaa, E., Resolution Limits In Magic-Angle Rotation NMR Spectra Of Polycrystalline Solids. *Chem. Phys. Lett.*, **1982,** *87* (1), 30-33.
241. Samoson, A., In *The 62nd Experimental NMR Conference*, 2021; p p. 26.
242. Paruzzo, F. M.; Emsley, L., High-resolution (1)H NMR of powdered solids by homonuclear dipolar decoupling. *J. Magn. Reson.*, **2019,** *309*, 106598.
243. Nishiyama, Y.; Lu, X.; Trebosc, J.; Lafon, O.; Gan, Z.; Madhu, P. K.; Amoureux, J. P., Practical choice of (1)H-(1)H decoupling schemes in through-bond (1)H-X HMQC experiments at ultra-fast MAS. *J. Magn. Reson.*, **2012,** *214* (1), 151-8.
244. Ding, S.; McDowell, C. A., High-Resolution Proton NMR Spectra in Solids by Single-Pulse Excitation. *J. Magn. Reson. Series A*, **1994,** *111*, 212-214.
245. Ding, S.; McDowell, C. A., High-Resolution NMR Spectra of Nuclear Spin Systems under Homogeneous Interactions in Solids Exhibiting Line Narrowing Induced by the Memory Effect. *J. Magn. Reson. Series A*, **1995,** *117*, 171-178.
246. Zorin, V. E.; Elena, B.; Lesage, A.; Emsley, L.; Hodgkinson, P., On the orientational dependence of resolution in 1H solid-state NMR, and its role in MAS, CRAMPS and delayed-acquisition experiments. *Magn. Reson. Chem.*, **2007,** *45 Suppl 1*, S93-100.
247. Oschkinat, H.; Pastore, A.; Pfändler, P.; Bodenhausen, G., Two-Dimensional Correlation of Directly and Remotely Connected Transitions by z-Filtered COSY. *J. Magn. Reson.*, **1986,** *69*, 559-566.
248. Pell, A. J.; Edden, R. A.; Keeler, J., Broadband proton-decoupled proton spectra. *Magn. Reson. Chem.*, **2007,** *45* (4), 296-316.
249. Simoes de Almeida, B.; Moutzouri, P.; Stevanato, G.; Emsley, L., Theory and simulations of homonuclear three-spin systems in rotating solids. *J Chem Phys*, **2021,** *155* (8), 084201.
250. Pell, A. J.; Keeler, J., Two-dimensional J-spectra with absorption-mode lineshapes. *J. Magn. Reson.*, **2007,** *189*, 293-299.
251. Bloembergen, N., On the Interaction Of Nuclear Spins in a Crystalline Lattice. *Phsysica*, **1949,** *15*, 386-425.

252. Caravatti, P.; Neuenschwander, P.; Ernst, R. R., Characterization of Heterogeneous Polymer Blends by Two-Dimensional Proton Spin Diffusion Spectroscopy. *Macromolecules*, **1985,** *18*, 119-122.
253. Halse, M. E.; Zagdoun, A.; Dumez, J. N.; Emsley, L., Macroscopic nuclear spin diffusion constants of rotating polycrystalline solids from first-principles simulation. *J. Magn. Reson.*, **2015,** *254*, 48-55.
254. Avalos, C. E.; Walder, B. J.; Viger-Gravel, J.; Magrez, A.; Emsley, L., Chemical exchange at the ferroelectric phase transition of lead germanate revealed by solid state (207)Pb nuclear magnetic resonance. *Phys. Chem. Chem. Phys.*, **2019,** *21* (3), 1100-1109.
255. Davis, M. C.; Shookman, K. M.; Sillaman, J. D.; Grandinetti, P. J., TOP-PASS: a processing algorithm to reduce 2D PASS acquisition time. *J. Magn. Reson.*, **2011,** *210* (1), 51-8.
256. Paruzzo, F. M.; Walder, B. J.; Emsley, L., Line narrowing in (1)H NMR of powdered organic solids with TOP-CT-MAS experiments at ultra-fast MAS. *J. Magn. Reson.*, **2019,** *305*, 131-137.
257. Walder, B. J.; Dey, K. K.; Kaseman, D. C.; Baltisberger, J. H.; Grandinetti, P. J., Sideband separation experiments in NMR with phase incremented echo train acquisition. *J. Chem. Phys.*, **2013,** *138* (17), 174203.
258. Brown, S. P.;; Wimperis, S., Two-Dimensional Multiple-Quantum MAS NMR of Quadrupolar Nuclei: A Comparison of Methods. *J. Magn. Reson.*, **1997,** *128*, 42-61.
259. Brown, S. P.; ; Wimperis, S., Two-Dimensional Multiple-Quantum MAS NMR of Quadrupolar Nuclei. Acquisition of the Whole Echo. *J. Magn. Reson.*, **1997,** *124*, 279-285.
260. Grandinetti, P. J.; Baltisberger, J.H; Llor, A.; Lee, Y.K.; Werner, U.; Eastman, M.A.; Pines, A., Pure-Absorption-Mode Lineshapes and Sensitivity in Two-Dimensional Dynamic-Angle Spinning NMR. *J. Magn. Reson. Series A*, **1992,** *103*, 72-81.
261. Massiot, D.; Touzo, B.; Trumeau, D.; Coutures, J.P.; Virlet, J.; Florian, P.; Grandinetti, P. J., Two-dimensional magic-angle spinning isotropic reconstruction sequences for quadrupolar nuclei. *Solid State Nucl. Magn. Reson.*, **1996,** *6*, 73-83.
262. Massiot, D.; Hiet, J.; Pellerin, N.; Fayon, F.; Deschamps, M.; Steuernagel, S.; Grandinetti, P. J., Two-dimensional one pulse MAS of half-integer quadrupolar nuclei. *J. Magn. Reson.*, **2006,** *181* (2), 310-5.
263. Castanar, L., Pure shift (1) H NMR: what is next? *Magn. Reson. Chem.*, **2017,** *55* (1), 47-53.
264. States, D.J.; Haberkorn, R.A.; Ruben, D.J., A Two-Dimensional Nuclear Overhauser Experiment with Pure Absorption Phase in Four Quadrants. *J. Magn. Reson.*, **1982,** *48*, 286-292.
265. Foroozandeh, M.; Adams, R. W.; Kiraly, P.; Nilsson, M.; Morris, G. A., Measuring couplings in crowded NMR spectra: pure shift NMR with multiplet analysis. *Chem. Commun. (Camb.)*, **2015,** *51* (84), 15410-3.
266. Frydman, Lucio; Peng, J., Non-Cartesian Sampling Schemes And The Acquisition Of 2D NMR Correlation Spectra From Single-Scan Experiments. *Chem. Phys. Lett.*, **1994,** *222* (4), 371-377.
267. Frydman, Lucio; Chingas, Gerard C.; Lee, Young K.; Grandinetti, Philip J.; Eastman, Margaret A.; Barrall, Geoffrey A.; Pines, Alexander, Variable‐angle correlation spectroscopy in solid‐state nuclear magnetic resonancea). *J. Chem. Phys.*, **1992,** *97* (7), 4800-4808.
268. Frydman, L.; Scherf, T.; Lupulescu, A., The acquisition of multidimensional NMR spectra within a single scan. *Proc. Natl. Acad. Sci. U S A*, **2002,** *99* (25), 15858-62.
269. Chen, J.; Mandelshtam, V. A.; Shaka, A. J., Regularization of the two-dimensional filter diagonalization method: FDM2K. *J. Magn. Reson.*, **2000,** *146* (2), 363-8.
270. Chen, J.; De Angelis, A. A.; Mandelshtam, V. A.; Shaka, A. J., Progress on the two-dimensional filter diagonalization method. An efficient doubling scheme for two-dimensional constant-time NMR. *J. Magn. Reson.*, **2003,** *162* (1), 74-89.
271. Rovnyak, D; Hoch, J. C.; Stern, A.S.; Wagner, G., Resolution and sensitivity of high field nuclear magnetic resonance spectroscopy. *J. Biomol. NMR.*, **2004,** *30*, 1-10.
272. Nagayama, K; Bachmann, P.; Wüthrich, K; Ernst, R. R., The Use of Cross-Sections and of Projeetiom in Two-d4meagioftal
NMR Spectroscopy. *J. Magn. Reson.*, **1978,** *31* (1), 133-148.
273. Kupce, E; Freeman, R., Projection-Reconstruction of Three-Dimensional NMR Spectra. *J. Am. Chem. Soc.*, **2003,** *27* (4), 383-387.
274. Dumez, J. N.; Butler, M. C.; Emsley, L., Numerical simulation of free evolution in solid-state nuclear magnetic resonance using low-order correlations in Liouville space. *J. Chem. Phys.*, **2010,** *133* (22), 224501.
275. Lesage, A.; Sakellariou, D.; Steuernagel, S.; Emsley, L, Carbon-Proton Chemical Shift Correlation in Solid-State NMR by
Through-Bond Multiple-Quantum Spectroscopy. *J. Am. Chem. Soc.*, **1998,** *120*, 13194-13201.
276. Bielytskyi, Pavlo; Gräsing, Daniel; Zahn, Stefan; Alia, A.; Matysik, Jörg, 15N–1H Transfer of Light-Induced Nuclear Hyperpolarization in Frozen Photosynthetic Reaction Centers. *Appl. Magn. Reson.*, **2019,** *50* (5), 695-708.
277. Pandey, M. K.; Zhang, R.; Hashi, K.; Ohki, S.; Nishijima, G.; Matsumoto, S.; Noguchi, T.; Deguchi, K.; Goto, A.; Shimizu, T.; Maeda, H.; Takahashi, M.; Yanagisawa, Y.; Yamazaki, T.; Iguchi, S.; Tanaka, R.; Nemoto, T.; Miyamoto, T.; Suematsu, H.; Saito, K.; Miki, T.; Ramamoorthy, A.; Nishiyama, Y., 1020MHz single-channel proton fast magic angle spinning solid-state NMR spectroscopy. *J. Magn. Reson.*, **2015,** *261*, 1-5.
278. Lu, H.; Liu, Y.; Ahlawat, P.; Mishra, A.; Tress, W. R.; Eickemeyer, F. T.; Yang, Y.; Fu, F.; Wang, Z.; Avalos, C. E.; Carlsen, B. I.; Agarwalla, A.; Zhang, X.; Li, X.; Zhan, Y.; Zakeeruddin, S. M.; Emsley, L.; Rothlisberger, U.; Zheng, L.; Hagfeldt, A.; Gratzel, M., Vapor-assisted deposition of highly efficient, stable black-phase FAPbI(3) perovskite solar cells. *Science*, **2020,** *370* (6512).
279. LeCun, Y.; Bengio, Y.; Hinton, G., Deep learning. *Nature*, **2015,** *521* (7553), 436-44.
280. Worswick, S.G.; Spencer, J.A.; Jeschke, G; Kuprov, I., Deep neural network processing of DEER data
. *Sci. Adv.*, **2018,** *4*, eaat5218.

281. Lecun, Y.; Bottou, L.; Bengio, Y; Haffner, P, Gradient-Based Learning Applied
to Document Recognition. *Proc. IEEE*, **1998,** *86*, 2278.
282. Krizhevsky, Alex; Sutskever, Ilya; Hinton, Geoffrey E., ImageNet classification with deep convolutional neural networks. *Commun. ACM*, **2017,** *60* (6), 84-90.
283. Liu, J.; Osadchy, M.; Ashton, L.; Foster, M.; Solomon, C. J.; Gibson, S. J., Deep convolutional neural networks for Raman spectrum recognition: a unified solution. *Anlst*, **2017,** *142* (21), 4067-4074.
284. Karunanithy, G.; Hansen, D. F., FID-Net: A versatile deep neural network architecture for NMR spectral reconstruction and virtual decoupling. *J. Biomol. NMR.*, **2021,** *75* (4-5), 179-191.
285. Chen, D.; Wang, Z.; Guo, D.; Orekhov, V.; Qu, X., Review and Prospect: Deep Learning in Nuclear Magnetic Resonance Spectroscopy. *Chem.*, **2020,** *26* (46), 10391-10401.
286. Qu, X.; Huang, Y.; Lu, H.; Qiu, T.; Guo, D.; Agback, T.; Orekhov, V.; Chen, Z., Accelerated Nuclear Magnetic Resonance Spectroscopy with Deep Learning. *Angew. Chem. Int. Ed. Engl.*, **2020,** *59* (26), 10297-10300.
287. Luo, J.; Zeng, Q.; Wu, K.; Lin, Y., Fast reconstruction of non-uniform sampling multidimensional NMR spectroscopy via a deep neural network. *J. Magn. Reson.*, **2020,** *317*, 106772.
288. Karunanithy, G.; Mackenzie, H. W.; Hansen, D. F., Virtual Homonuclear Decoupling in Direct Detection Nuclear Magnetic Resonance Experiments Using Deep Neural Networks. *J. Am. Chem. Soc.*, **2021,** *143* (41), 16935-16942.
289. Li, D. W.; Hansen, A. L.; Yuan, C.; Bruschweiler-Li, L.; Bruschweiler, R., DEEP picker is a deep neural network for accurate deconvolution of complex two-dimensional NMR spectra. *Nat. Commun.*, **2021,** *12* (1), 5229.
290. Hochreiter, S.; Schmidhuber, J.;, Long Short-Term Memory. *Neural Comput.*, **1997,** *9*, 1735.
291. Kong, Weicong; Dong, Zhao Yang; Jia, Youwei; Hill, David J.; Xu, Yan; Zhang, Yuan, Short-Term Residential Load Forecasting Based on LSTM Recurrent Neural Network. *IEEE Trans. Smart Grid*, **2019,** *10* (1), 841-851.
292. Graves, A.; Jaitly, N.; Mohamed, A.R., HYBRID SPEECH RECOGNITION WITH DEEP BIDIRECTIONAL LSTM. *Proc. IEEE Workshop Autom.*
Speech Recognit. Understand. (ASRU), **2013**, 273.
293. Sundermeyer, M.; Schluter, R.; Ney, H. , LSTM Neural Networks for Language Modeling. *Proc. Interspeech*, **2012,** (1-3), 194-197.
294. Hansen, D. F., Using Deep Neural Networks to Reconstruct Non-uniformly Sampled NMR Spectra. *J. Biomol. NMR.*, **2019,** *73* (10-11), 577-585.
295. Moutzouri, P. , Simões de Almeida, B., Torodii, D. , Emsley, L., submitted. **2021**.
296. Gu, Z.; Ridenour, C.F.; Bronnimann, C.E.; Iwashita, T.; McDermott, Ann, Hydrogen Bonding and Distance Studies of Amino Acids and Peptides Using Solid State 2D 1H-13C Heteronuclear Correlation Spectra. *J. Am. Chem. Soc.*, **1996,** *118*, 822-829.
297. Lesage, A.; Auger, C.; Caldarelli,, S.; Emsley, L., Determination of Through-Bond Carbon-Carbon Connectivities in Solid-State NMR Using the INADEQUATE Experiment. *J. Am. Chem. Soc.*, **1997,** *119*, 7867-7868.
298. Lesage, A.; Bardet, M.; Emsley, L., Through-Bond Carbon-Carbon Connectivities in Disordered Solids
by NMR. *J. Am. Chem. Soc.*, **1999,** *121*, 10987-10993.
299. Jain, Varun; Biesinger, Mark C.; Linford, Matthew R., The Gaussian-Lorentzian Sum, Product, and Convolution (Voigt) functions in the context of peak fitting X-ray photoelectron spectroscopy (XPS) narrow scans. *Appl. Surf. Sci.*, **2018,** *447*, 548-553.
300. Shi, X.J., Chen, Z.R.; Wang, H.; Yeung, D.Y.; Wong, W. K.; Woo, W. C.; , Convolutional LSTM Network: A Machine Learning Approach for Precipitation Nowcasting. *Adv Neur In*, **2015,** *1*, 802.
301. Lee, G. S. H.; Taylor, R.C.; Dawson, M.; Kamali Kannangara, G. S.; Wilson, M. A., High-resolution solid state 13C nuclear magnetic resonance spectra
of 3,4-methylenedioxyamphetamine hydrochloride and related
compounds and their mixtures with lactose. *Solid State Nucl. Magn. Reson.*, **2000,** *16*, 225-237.
302. Giannozzi, P.; Andreussi, O.; Brumme, T.; Bunau, O.; Buongiorno Nardelli, M.; Calandra, M.; Car, R.; Cavazzoni, C.; Ceresoli, D.; Cococcioni, M.; Colonna, N.; Carnimeo, I.; Dal Corso, A.; de Gironcoli, S.; Delugas, P.; DiStasio, R. A., Jr.; Ferretti, A.; Floris, A.; Fratesi, G.; Fugallo, G.; Gebauer, R.; Gerstmann, U.; Giustino, F.; Gorni, T.; Jia, J.; Kawamura, M.; Ko, H. Y.; Kokalj, A.; Kucukbenli, E.; Lazzeri, M.; Marsili, M.; Marzari, N.; Mauri, F.; Nguyen, N. L.; Nguyen, H. V.; Otero-de-la-Roza, A.; Paulatto, L.; Ponce, S.; Rocca, D.; Sabatini, R.; Santra, B.; Schlipf, M.; Seitsonen, A. P.; Smogunov, A.; Timrov, I.; Thonhauser, T.; Umari, P.; Vast, N.; Wu, X.; Baroni, S., Advanced capabilities for materials modelling with Quantum ESPRESSO. *Journal of Physics: Condensed Matter*, **2017,** *29* (46), 465901.
303. Giannozzi, P.; Baroni, S.; Bonini, N.; Calandra, M.; Car, R.; Cavazzoni, C.; Ceresoli, D.; Chiarotti, G. L.; Cococcioni, M.; Dabo, I.; Dal Corso, A.; de Gironcoli, S.; Fabris, S.; Fratesi, G.; Gebauer, R.; Gerstmann, U.; Gougoussis, C.; Kokalj, A.; Lazzeri, M.; Martin-Samos, L.; Marzari, N.; Mauri, F.; Mazzarello, R.; Paolini, S.; Pasquarello, A.; Paulatto, L.; Sbraccia, C.; Scandolo, S.; Sclauzero, G.; Seitsonen, A. P.; Smogunov, A.; Umari, P.; Wentzcovitch, R. M., QUANTUM ESPRESSO: a modular and open-source software project for quantum simulations of materials. *J. Condens. Matter Phys.*, **2009,** *21* (39), 395502.
304. Morimoto, B.H.; Lovell, S.; Kahr, B., Ecstasy: 3,4-methylenedioxymethamphetamine (MDMA). *Acta Crystallogr. C.*, **1998,** *54*, 229.
305. Perdew, J. P.; Burke, K.; Emzehof, M., Generalized Gradient Approximation Made Simple. *Phys. Rev. Lett.*, **1996,** *77*, 3865.
306. Grimme, S., Semiempirical GGA-type density functional constructed with a long-range dispersion correction. *Journal of Computational Chemistry*, **2006,** *27* (15), 1787-99.

307. Dal Corso, Andrea, Pseudopotentials periodic table: From H to Pu. *Computational Materials Science*, **2014,** *95*, 337-350.
308. Monkhorst, Hendrik J.; Pack, James D., Special points for Brillouin-zone integrations. *Phys. Rev. B*, **1976,** *13* (12), 5188-5192.
309. Pickard, Chris J.; Mauri, Francesco, All-electron magnetic response with pseudopotentials: NMR chemical shifts. *Phys. Rev. B*, **2001,** *63* (24).
310. Yates, Jonathan R.; Pickard, Chris J.; Mauri, Francesco, Calculation of NMR chemical shifts for extended systems using ultrasoft pseudopotentials. *Phys. Rev. B*, **2007,** *76* (2).
311. Jeener, J.; Meier, B. H.; Bachmann, P.; Ernst, R. R., Investigation of exchange processes by two ‐ dimensional NMR spectroscopy. *J. Chem. Phys.*, **1979,** *71* (11), 4546-4553.
312. Klukowski, P.; Augoff, M.; Zieba, M.; Drwal, M.; Gonczarek, A.; Walczak, M. J., NMRNet: a deep learning approach to automated peak picking of protein NMR spectra. *Bioinform.*, **2018,** *34* (15), 2590-2597.
313. Lee, H. H.; Kim, H., Intact metabolite spectrum mining by deep learning in proton magnetic resonance spectroscopy of the brain. *Magn. Reson. Med.*, **2019,** *82* (1), 33-48.
314. Schmid, N.; Bruderer, S.; Paruzzo, F.; Fischetti, G.; Toscano, G.; Graf, D.; Fey, M.; Henrici, A.; Ziebart, V.; Heitmann, B.; Grabner, H.; Wegner, J. D.; Sigel, R. K. O.; Wilhelm, D., Deconvolution of 1D NMR spectra: A deep learning-based approach. *J. Magn. Reson.*, **2023,** *347*, 107357.
315. Gerrard, W.; Bratholm, L. A.; Packer, M. J.; Mulholland, A. J.; Glowacki, D. R.; Butts, C. P., IMPRESSION - prediction of NMR parameters for 3-dimensional chemical structures using machine learning with near quantum chemical accuracy. *Chem. Sci.*, **2020,** *11* (2), 508-515.
316. Chaker, Z.; Salanne, M.; Delaye, J. M.; Charpentier, T., NMR shifts in aluminosilicate glasses via machine learning. *Phys. Chem. Chem. Phys.*, **2019,** *21* (39), 21709-21725.
317. Paruzzo, F. M.; Hofstetter, A.; Musil, F.; De, S.; Ceriotti, M.; Emsley, L., Chemical shifts in molecular solids by machine learning. *Nat. Commun.*, **2018,** *9* (1), 4501.
318. Cordova, M.; Engel, E. A.; Stefaniuk, A.; Paruzzo, F.; Hofstetter, A.; Ceriotti, M.; Emsley, L., A Machine Learning Model of Chemical Shifts for Chemically and Structurally Diverse Molecular Solids. *J. Phys. Chem. C Nanomaterials Interfaces*, **2022,** *126* (39), 16710-16720.
319. Han, B.; Liu, Y.; Ginzinger, S. W.; Wishart, D. S., SHIFTX2: significantly improved protein chemical shift prediction. *J. Biomol. NMR.*, **2011,** *50* (1), 43-57.
320. Shen, Y.; Bax, A., SPARTA+: a modest improvement in empirical NMR chemical shift prediction by means of an artificial neural network. *J. Biomol. NMR.*, **2010,** *48* (1), 13-22.
321. Liu, S.; Li, J.; Bennett, K. C.; Ganoe, B.; Stauch, T.; Head-Gordon, M.; Hexemer, A.; Ushizima, D.; Head-Gordon, T., Multiresolution 3D-DenseNet for Chemical Shift Prediction in NMR Crystallography. *J. Phys. Chem. Lett.*, **2019,** *10* (16), 4558-4565.
322. Li, D.; Bruschweiler, R., PPM_One: a static protein structure based chemical shift predictor. *J. Biomol. NMR.*, **2015,** *62* (3), 403-9.
323. Zambrello, M. A.; Craft, D. L.; Hoch, J. C.; Rovnyak, D.; Schuyler, A. D., The influence of the probability density function on spectral quality in nonuniformly sampled multidimensional NMR. *J. Magn. Reson.*, **2020,** *311*, 106671.
324. Cobas, C., NMR signal processing, prediction, and structure verification with machine learning techniques. *Magn. Reson. Chem.*, **2020,** *58* (6), 512-519.
325. Becker, M.; Lehmkuhl, S.; Kesselheim, S.; Korvink, J. G.; Jouda, M., Acquisitions with random shim values enhance AI-driven NMR shimming. *J. Magn. Reson.*, **2022,** *345*, 107323.
326. Ernst, R. R.; Bodenhausen, G.; Wokaun, A., *Principles of nuclear magnetic resonance in one and two dimensions*. 1987.
327. Cadars, S.; Lesage, A.; Emsley, L., Chemical Shift Correlations in Disordered Solids. *J Am Chem Soc*, **2005,** *127*, 4466-4476.
328. Sakellariou, D.; Brown, S. P.; Lesage, A.; Hediger, S.; Bardet, M.; Meriles, C. A.; Pines, A.; Emsley, L., High-Resolution NMR Correlation Spectra of Disordered Solids. *J Am Chem Soc*, **2003,** *125* (14), 4376-4380.
329. Fabbiani, Marco; Al-Nahari, Shadi; Piveteau, Laura; Dib, Eddy; Veremeienko, Vasyl; Gaje, Arnold; Dumitrescu, Dan G.; Gaveau, Philippe; Mineva, Tzonka; Massiot, Dominique; van der Lee, Arie; Haines, Julien; Alonso, Bruno, Host–Guest Silicalite-1 Zeolites: Correlated Disorder and Phase Transition Inhibition by a Small Guest Modification. *Chem. Mater.*, **2021,** *34* (1), 366-387.
330. Cadars, Sylvian; Layrac, Géraldine; Gérardin, Corine; Deschamps, Michaël; Yates, Jonathan R.; Tichit, Didier; Massiot, Dominique, Identification and Quantification of Defects in the Cation Ordering in Mg/Al Layered Double Hydroxides. *Chem. Mater.*, **2011,** *23* (11), 2821-2831.
331. Fayon, F.; Massiot, D.; Levitt, M. H.; Titman, J. J.; Gregory, D. H.; Duma, L.; Emsley, L.; Brown, S. P., Through-space contributions to two-dimensional double-quantum J correlation NMR spectra of magic-angle-spinning solids. *J Chem Phys*, **2005,** *122* (19), 194313.
332. Corlett, Emily K.; Blade, Helen; Hughes, Leslie P.; Sidebottom, Philip J.; Walker, David; Walton, Richard I.; Brown, Steven P., An XRD and NMR crystallographic investigation of the structure of 2,6-lutidinium hydrogen fumarate. *CrystEngComm*, **2019,** *21* (22), 3502-3516.

333. Wu, X.; Hong, Y. L.; Xu, B.; Nishiyama, Y.; Jiang, W.; Zhu, J.; Zhang, G.; Kitagawa, S.; Horike, S., Perfluoroalkyl-Functionalized Covalent Organic Frameworks with Superhydrophobicity for Anhydrous Proton Conduction. *J. Am. Chem. Soc.*, **2020,** *142* (33), 14357-14364.
334. Hanrahan, M. P.; Venkatesh, A.; Carnahan, S. L.; Calahan, J. L.; Lubach, J. W.; Munson, E. J.; Rossini, A. J., Enhancing the resolution of (1)H and (13)C solid-state NMR spectra by reduction of anisotropic bulk magnetic susceptibility broadening. *Phys. Chem. Chem. Phys.*, **2017,** *19* (41), 28153-28162.
335. Robbins, A. J.; Ng, W. T.; Jochym, D.; Keal, T. W.; Clark, S. J.; Tozer, D. J.; Hodgkinson, P., Combining insights from solid-state NMR and first principles calculation: applications to the 19F NMR of octafluoronaphthalene. *Phys. Chem. Chem. Phys.*, **2007,** *9* (19), 2389-96.
336. Deschamps, M.; Fayon, F.; Cadars, S.; Rollet, A. L.; Massiot, D., 1H and 19F ultra-fast MAS double-quantum single-quantum NMR correlation experiments using three-spin terms of the dipolar homonuclear Hamiltonian. *Phys. Chem. Chem. Phys.*, **2011,** *13* (17), 8024-30.
337. Schwerk, U.; Michel, D.; Pruski, M., Local Magnetic Field Distribution in a Polycrystalline Sample Exposed to a Strong Magnetic Field. *Journal of Magnetic Resonance, Series A*, **1995,** *119*, 157-164.
338. Cadars, S.; Lesage, A.; Pickard, C. J.; Sautet, P. and Emsley, L., Characterizing Slight Structural Disorder in Solids by Combined Solid-State NMR and First Principle Calculations. *J. Phys. Chem. A*, **2008,** *113* (5), 902-911.
339. Aue, W. P.; Karhan, J.; Ernst, R. R., Homonuclear broad band decoupling and two ‐ dimensional J ‐ resolved NMR spectroscopy. *J Chem Phys*, **1976,** *64* (10), 4226-4227.
340. Samoson, A.; Tuherm, T.; Gan, Z., High-field high-speed MAS resolution enhancement in 1H NMR spectroscopy of solids. *Solid State Nucl Magn Reson*, **2001,** *20* (3-4), 130-6.
341. Burum, D.P.; Rhim, W. K., Analysis of multiple pulse NMR in solids. III. *J Chem Phys*, **1979,** *71*, 944-956.
342. Stoll, M. E.; Majors, T.J., Reduction of Magnetic Susceptibility Broadening in NMR by Susceptibility Matching. *J Magn Reson*, **1982,** *46*, 283-288.
343. Grey, C. P.; Dobson, C. M.; Cheetham, A. K., Susceptibility Matching in MAS NMR. The Determination of Hyperfine Tensors from Paramagnetic Stannates. *J Magn Reson*, **1992,** *98*, 414-420.
344. Cadars, S., Lesage, A.; Pickard, C. J.; Sautet, P. and Emsley, L., Characterizing Slight Structural Disorder in Solids by Combined Solid-State NMR and First Principle Calculations. *J Phys Chem A*, **2008,** *113* (5), 902-911.
345. Cadars, S.; Mifsud, N.; Lesage, A.; Epping, J. D.; Hedin, N.; Chmelka, B. F.; Emsley, L., Dynamics and Disorder in Surfactant-Templated Silicate Layers Studied by Solid-State NMR Dephasing Times and Correlated Line Shapes. *J Phys Chem C*, **2008,** *112*, 9145-9154.
346. Heise, H.; Luca, S.; de Groot, B. L.; Grubmuller, H.; Baldus, M., Probing conformational disorder in neurotensin by two-dimensional solid-state NMR and comparison to molecular dynamics simulations. *Biophys J*, **2005,** *89* (3), 2113-20.
347. Ovidiu, C.; Andronesi, S. F., Seidel, K.; Heise, H.; Young, H. S.; Baldus, M., Determination of Membrane Protein Structure and Dynamics by Magic-Angle-Spinning Solid-State NMR Spectroscopy. *J Am Chem Soc*, **2005,** *127*, 12965-12974.
348. Lesage, A.; Auger, C.; Caldarelli, S.; Emsley, L., Determination of Through-Bond Carbon-Carbon Connectivities in Solid-State NMR Using the INADEQUATE Experiment. *J Am Chem Soc*, **1997,** *119*, 7867-7868.
349. Lesage, A.; Duma L.; Sakellariou, D.; Emsley, L., Improved Resolution in Proton NMR Spectroscopy of Powdered Solids. *J Am Chem Soc*, **2001,** *123*, 5747-5752.
350. Petrakis, L., Spectral line shapes: Gaussian and Lorentzian functions in magnetic resonance. *J Chem Educ*, **1967,** *44* (8), 432-436.
351. Wertheim, G. K.; Butler, M. A.; West, K. W.; Buchanan, D. N. E., Determination of the Gaussian and Lorentzian content of experimental line shapes. *Rev Sci Instrum*, **1974,** *45* (11), 1369-1371.
352. Bruce, S.; Higinbotham, J.; Marshall, I.; Beswick, P. H., An Analytical Derivation of a Popular Approximation of the Voigt Function for Quantification of NMR Spectra. *J Magn Reson*, **2000,** *142*, 57-63.
353. Marshall, I.; Higinbotham, J.; Bruce, S.; Freise, A., Use of Voigt lineshape for quantification of in vivo 1H spectra. *Magn Reson Med*, **1997,** *37* (5), 651-7.
354. Ahlner, A.; Carlsson, M.; Jonsson, B. H.; Lundstrom, P., PINT: a software for integration of peak volumes and extraction of relaxation rates. *J Biomol NMR*, **2013,** *56* (3), 191-202.
355. Niklasson, M.; Otten, R.; Ahlner, A.; Andresen, C.; Schlagnitweit, J.; Petzold, K.; Lundstrom, P., Comprehensive analysis of NMR data using advanced line shape fitting. *J Biomol NMR*, **2017,** *69* (2), 93-99.
356. Dudley, J. A.; Park, S.; MacDonald, M. E.; Fetene, E.; Smith, C. A., Resolving overlapped signals with automated FitNMR analytical peak modeling. *J Magn Reson*, **2020,** *318*, 106773.
357. Penzel, S.; Smith, A. A.; Ernst, M.; Meier, B. H., Setting the magic angle for fast magic-angle spinning probes. *J Magn Reson*, **2018,** *293*, 115-122.
358. Pigliapochi, R.; O'Brien, L.; Pell, A. J.; Gaultois, M. W.; Janssen, Y.; Khalifah, P. G.; Grey, C. P., When Do Anisotropic Magnetic Susceptibilities Lead to Large NMR Shifts? Exploring Particle Shape Effects in the Battery Electrode Material LiFePO(4). *J Am Chem Soc*, **2019,** *141* (33), 13089-13100.
359. Trease, Nicole M.; Zhou, Lina; Chang, Hee Jung; Zhu, Ben Yunxu; Grey, Clare P., In situ NMR of lithium ion batteries: Bulk susceptibility effects and practical considerations. *Solid State Nuclear Magnetic Resonance*, **2012,** *42*, 62-70.
360. Zhou, Lina; Leskes, Michal; Ilott, Andrew J.; Trease, Nicole M.; Grey, Clare P., Paramagnetic electrodes and bulk magnetic susceptibility effects in the in situ NMR studies of batteries: Application to Li1.08Mn1.92O4 spinels. *Journal of Magnetic Resonance*, **2013,** *234*, 44-57.

361. Kinnun, Jacob J.; Leftin, Avigdor; Brown, Michael F., Solid-State NMR Spectroscopy for the Physical Chemistry Laboratory. *Journal of Chemical Education*, **2013,** *90* (1), 123-128.
362. Kwon, H. T.; Jeong, H.; Lee, A. S.; He, S. A.; Lee, J. S., CCDC 1429243. *Exp. Cryst. Struc. Det.*, **2015**.
363. Perdew, J. P.; Burke, K.; Ernzerhof, M., Generalized Gradient Approximation Made Simple. *Phys Rev Lett*, **1996,** *77* (18), 3865-3868.
364. Hubig, S. M.; Lindeman, S. V.; Kochi, J. K., CCDC 138870. *Exp. Cryst. Struc. Det.*, **2001**.
365. Callear, S. K.; Hursthouse, M. B., CCDC 1010510. *Exp. Cryst. Struc. Det.*, **2008**.
366. Frey, Michel N.; Koetzle, Thomas F.; Lehmann, Mogens S.; Hamilton, Walter C., Precision neutron diffraction structure determination of protein and nucleic acid components. X. A comparison between the crystal and molecular structures of L‐tyrosine and L‐tyrosine hydrochloride. *J. Chem. Phys.*, **1973,** *58* (6), 2547-2556.

Curriculum Vitae

Bruno Simões de Almeida
Avenue de Saugiaz 15 (1020 Renens)
brunosalmeida94@gmail.com
bruno.simoesdealmeida@epfl.ch
+ 78 648 64 90

Physical Chemistry Researcher
Nuclear Magnetic Resonance Spectroscopist
Machine Learning Experience

Professional experience

2019- 2023

Doctoral Assistant, Laboratory of Magnetic Resonance
ECOLE POLYTECHNIQUE FEDERALE DE LAUSANNE (EPFL)

Method development for solid-state Nuclear Magnetic Resonance, with experimental and machine learning approaches on improving the ^{1}H spectral resolution. Involved in three different projects that obtained the best ^{1}H resolution to date

2019- 2023

Teaching Assistant, Laboratory of Magnetic Resonance
ECOLE POLYTECHNIQUE FEDERALE DE LAUSANNE (EPFL)

Design and supervision of a new experimental physical chemistry course taking place during a whole semester for a class of sixty students that was met with their positive feedback.
Supervision of two master students during one semester each.
Involved in the teaching of two different bachelor courses (>900 hours cumulated).

2019

Master Student Research Assistant, Chemoinformatics Lab
FACULDADE DE CIÊNCIAS E TECNOLOGIA NOVA (FCT-NOVA), LISBOA

Involved for a semester in a machine learning classification project of organic molecules according to their optical rotation

Education

2019- 2023

PhD in Chemistry
ECOLE POLYTECHNIQUE FEDERALE DE LAUSANNE (EPFL)

Title of the thesis: “Development of strategies to improve 1H resolution in NMR of solids at 100 kHz MAS”

2017- 2019

Master in Chemoinformatics
Université de Strasbourg

2015-2017

Bachelor in Chemistry
Université de Genève

Languages

Portuguese (Native) French (Fluent) English (Proficient) German (Elementary) Spanish (Elementary)

Awards

Shimon Vega Travel Award (2023)

Dean's Award for Excellence in Teaching (2021-2022, EPFL)

SCS Fall Meeting Best Oral Presentation Award (2022, Zurich)

Journal of Magnetic Resonance Young Scientist Award (2021, online)

List of Publications

1. Moutzouri, P.; Paruzzo, F. M.; Simões de Almeida, B.; Stevanato, G.; Emsley, L., Homonuclear Decoupling in ^{1}H NMR of Solids by Remote Correlation. *Angew Chem Int Ed Engl* **2020,** *59* (15), 6235-6238.
2. Moutzouri, P.; Simões de Almeida, B.; Emsley, L., Fast remote correlation experiments for ^{1}H homonuclear decoupling in solids. *J Magn Reson* **2020,** *321*, 106856.
3. Simões de Almeida, B.; Moutzouri, P.; Stevanato, G.; Emsley, L., Theory and simulations of homonuclear three-spin systems in rotating solids. *J Chem Phys* **2021,** *155* (8), 084201.
4. Moutzouri, P.; Simões de Almeida, B.; Torodii, D.; Emsley, L., Pure Isotropic Proton Solid State NMR. *J Am Chem Soc* **2021,** *143* (26), 9834-9841.
5. Cordova, M.; Moutzouri, P.; Simões de Almeida, B.; Torodii, D.; Emsley, L., Pure Isotropic Proton NMR Spectra in Solids using Deep Learning. *Angew Chem Int Ed Engl* **2023,** *62* (8), e202216607.
6. Moutzouri, P.; Cordova, M.; Simões de Almeida, B.; Torodii, D.; Emsley, L., Two-dimensional Pure Isotropic Proton Solid State NMR. *Angew Chem Int Ed Engl* **2023,** *62* (21), e202301963.
7. Simões de Almeida, B.; Torodii, D.; Moutzouri, P.; Emsley, L., Barriers to Resolution in ^{1}H NMR of Rotating Solids, *J Magn Reson*, **2023**, 233, 10755
8. Cordova, M.; Balodis, M.; Hofstetter, A.; Paruzzo, F.; Nilsson Lill, S. O.; Eriksson, E. S. E.; Berruyer, P.; Simoes de Almeida, B.; Quayle, M. J.; Norberg, S. T.; Svensk Ankarberg, A.; Schantz, S.; Emsley, L., Structure determination of an amorphous drug through large-scale NMR predictions. *Nat Commun*, **2021,** *12* (1), 2964.
9. Cordova, M. Balodis, M.; Simões de Almeida, B.; Ceriotti, M.; Emsley, L., Bayesian probabilistic assignment of chemical shifts in organic solids. *Science Advances*, **2021,** *7*, eabk2341.
10. Simões de Almeida, B.; Emsley, L., Improvements in Resolution of 1H NMR of solids. *Chimia*, **2023,** *77* (4).

Presentations

1. Simões de Almeida, B.; Moutzouri, P.; Emsley, L. Fast Remote Correlation Experiments for 1H Homonuclear Decoupling in Solids, *EUROMAR 2020, 7th-8th December 2020, online* (oral presentation)
2. Simões de Almeida, B.; Moutzouri, P.; Emsley, L. Fast Remote Correlation Experiments for 1H Homonuclear Decoupling in Solids at 1.2 GHz and 100 kHz MAS, *ENC 2021, 29th-31st March 2021, online* (poster presentation)
3. Simões de Almeida, B.; Moutzouri, P.; Stevanato, G.; Emsley, L. Resonances in ^{1}H MAS spectra are not centered at the isotropic chemical shift, *EUROMAR 2021, 5th-8th July 2021, online* (oral presentation)
4. Simões de Almeida, B.; Moutzouri, P.; Torodii, D.; Emsley, L. Pure Isotropic Proton Solid State NMR, *ENC 2022, 24th-29th April 2022, Orlando (USA),* (poster presentation)
5. Simões de Almeida, B.; Moutzouri, P.; Torodii, D.; Emsley, L. Pure Isotropic Proton Solid State NMR, *SCS Fall Meeting 2022, 8th September 2022, Zurich (Switzerland),* (oral presentation)
6. Simões de Almeida, B.; Torodii, D.; Moutzouri, P. ; Emsley, L. Barriers to Proton Resolution in Solids, *ISMAR 2023, 8th September 2022, Brisbane (Australia),* (oral presentation)